GEOCHEMICAL INVESTIGATION OF HYDROTHERMAL AND VOLCANIC SYSTEMS IN ICELAND, NEW MEXICO AND ANTARCTICA.

By

Lara Bevan Owens

DISSERTATION

Submitted in Partial Fulfillment
of the Requirements for

Doctorate of Philosophy in Earth & Environmental Science
(Geochemistry)

New Mexico Institute of Mining & Technology
Department of Earth & Environmental Science

Socorro, New Mexico
August, 2013

ABSTRACT

Four studies are presented using various petrologic, gaseous and aqueous geochemical methods to investigate volcanic and hydrothermal systems in different geologic settings. Each study contributes to aspects of geothermal exploration: from the theoretical in investigating the occurrence of water-rock interaction at Erebus volcano (Antarctica), to the practical in locating the depths of acidic feed zones in the Krafla (Iceland) production wells as well as testing new low-temperature geothermal exploration methods in Socorro, New Mexico..

The Socorro Geothermal Area in New Mexico represents a low-temperature, geothermal system demonstrated by several hot springs and an exploration slim hole drilled at the base of Socorro Peak. Low temperature reservoirs typically lack surface manifestations and equilibrated sample fluids necessary to assess the extent and economic potential of the resource. Extensive past work performed on Socorro Peak, including temperature gradient drilling and heat flow model (*Barroll and Reiter, 1991; Mailloux et al., 1999*), allows us to test alternative methods for exploring similar blind, low temperature resources. Two methods tested here included soil mapping by selective extraction and a multi-isotope fluid chemistry survey. Selective extraction soil mapping, a method common in mineral exploration, applies two distinct biosynthetic leaches, Enzyme leach and Terrasol leach, used to liberate volatilized compounds adhered to the soil's MnOx surface. Hydrothermal systems generate weak self-potential cells which produce anomalous concentrations of these compounds at the surface. Sampling transects deployed over mapped range front structures reveal strong anomalous concentrations of rare earth elements, high field strength elements, base metals and soil pH. Transects covering the rift basin exhibit remarkable anomalies trending parallel to the main range bounding structure, suggesting geothermal upflow along buried, synthetic faults. Geothermal indicator elements, such as As, Se, Zn and Ce which are found within local warm springs and temperature gradient wells, also correlate strongly with selective extraction soil profiles. This argues for hydrologic dispersion as

a potential source for certain soil anomalies rather than electrochemical cell formation alone. Selective extraction soil mapping is demonstrated as a potential reconnaissance level geothermal exploration tool, particularly for identifying up flow of geothermal waters or saturated bedrock below buried faults.

To address the lack of reliable geothermometry in a low temperature geothermal system like Socorro, we administer an alternative geochemical tool-set for characterizing the geothermal potential. This tool-set includes a suite of conservative and non-conservative chemical tracers such as Cl/Br ratios; Li,B, As concentrations and variation in the isotopes of $^{87}Sr/^{86}Sr$, $\delta^{11}B$, $\delta^{34}S$, $\delta^{13}C$, $\delta^{18}O$, $\delta^{2}H$, ^{14}C and ^{3}H. Exploration well NMTG2 drilled to a depth of 330 m at the base of Socorro Peak, provides the most primary end member fluid samples for the investigation of this system. Na-Cl NMTG2 fluids exhibited elevated $^{87}Sr/^{86}Sr$ concentrations (0.721904) supporting deep recharge through Precambrian basement granite or metasediments. $\delta^{18}O/\delta^{2}H$ elevation profiles and ^{14}C radiometric dating describe a 17.6ka flow path losing over 1000m of hydrologic head from the point of recharge in the Magdalena Mountains. Conversely, nearby Socorro springs indicate a much shorter and shallower pathway of 9.1ka penetrating through Cenozoic volcanics ($^{87}Sr/^{86}Sr = 0.712814$). Mixing models with high Cl thermal fluids along the Bosque del Apache support geothermal upwelling as a source of mobilizing saline sedimentary brines. A review of geothermal equilibria throughout the Socorro geothermal area demonstrates that mixing and conductive cooling play a significant role in invalidating the use of these tools. Geothermometer calculations and speciation models on partially equilibrated NMTG2 fluids predict 60-80°C at economic depths (1-2km), corresponding with hydrologic models. Where mixing is suspected within high-solute geothermal fluids, plots of Mg, SO_4 and Ca concentrations help delineate thermal from non-thermal brines, owing to retrograde solubility of Mg-clays and gypsum.

The 60MW Krafla geothermal field in NE Iceland produces highly acidic steam and non-condensable gas components from many production wells nearing 2000m depth. Well cuttings are examined by cold-crush fluid inclusion gas analyses to investigate the processes and depth intervals associated with these problematic feed zones, for possible mitigation while drilling in real time. Fissure eruptions of basaltic lava near the geothermal field from 1975-1984 affected the field. Good producing geothermal wells soon exhibited high CO_2 concentrations coupled with increased acidic character attributed to pervasive magmatic gases within the reservoir. Wells drilled following the eruptions produced much lower CO_2 concentrations, however, HCl-rich superheated steam was a continuous problem from otherwise prolific wells. Molten lava was encountered during drilling in at least three production wells . Two such wells completed in separate ends of the field; IDDP-1 in Lierbotnar and KJ-39 in Suðurhlíðar, exhibit the highest flow rates, enthalpies and most corrosive character in Krafla. Fluid inclusion gas signatures associated with direct input of magmatic gases is characterized as elevated CO_2, high total-gas content and presumable HCl. Magmatic gases in with the Leirbotnar field also exhibit SO_2 and He spikes, associated with the recent magma intrusions near these wells. H_2S and H_2 are absent from magmatic gas-flux profiles suggesting rapid modification by the reservoir following exsolution from the nearby magma. Superheated boiling is mapped 300m above molten magmatic intrusions, based on CO_2/N_2 vs total gas concentrations, coupled with excess CO_2 in gas-rich inclusions, and production of HCl vapor. Some wells without direct magmatic gas influx still exhibit acidic character if superheating conditions exist, owing to residual concentrated Cl brine from the basaltic intrusions.

Oxygen isotope analysis of minerals (olivine and anorthoclase) in alkalic lavas from Erebus volcano, Ross Island, Antarctica, illustrates an anomalous trend of depletion with fractionation of the lavas from basanite to phonolite. The frozen climate and lack of evidence for assimilation of crustal materials makes this a unique location to investigate factors contributing to

oxygen isotope depletion. Thirty lavas from Erebus volcano, ranging from parental basanite to anorthoclase phonolite, along with glass, feldspar, and olivine separates were analyzed using silicate fluorination and stable oxygen isotope determination by mass spectrometry. Forward models indicate an ideal enrichment of 0.8–2.0‰ in modern lavas due to Raleigh fractionation, but this is not observed in either glass or mineral separate analysis. Olivines exhibit a clear trend of isotopic depletion from a typical mantle value of $\delta^{18}O$ +5.0‰ in the parental source to 3.8‰ in recently erupted lava bombs, correlating strongly with the olivine Fo contents. Feldspar and glasses exhibit modern isotopic values well below predicted values, averaging 6.0‰ and 5.7‰, respectively, and are in fractionation disequilibrium with olivine compositions at measured magmatic temperatures of 1000°C within the persistently convecting lava lake. Isotopic depletion of the whole melt may be accounted for by incorporation of 7.7-11% hydrothermally altered volcanic edifice over time assuming water–rock interaction from strongly depleted Antarctic precipitation. Enhanced disequilibrium with olivine phenocrysts, particularly during the latest stages of Erebus construction, appears to be strongly associated with the occurrence of the modern lava lake configuration calling for differential fractionation of olivines and feldspars from their respective melts, and slow O-diffusion of olivines while in the shallow lava lake prior to eruption.

Keywords: geothermal, volcanology, Erebus, Socorro, Krafla, fluid inclusions

ACKNOWLEDGEMENTS

I would like to thank the many faculty, NMT departments, labs and funding agencies that made this work possible. Thanks to EMRTC for their support of our fieldwork and drilling near Socorro Peak. Thanks to the DOE-GREDIII program and NMT Physical Plant for funding the Socorro Geothermal Area exploration studies and drilling efforts. Special thanks to Andy Campbell, Bill Chavez, Bonnie Frey, Zach Sharp, Nelia Dunbar, Jungho Park, Joseph Moore, Greg Hill and Nigel Blamey whose laboratories and expertise provided for the various analytical works contained within. Thanks to Wilfred Elders, Omar Friðleifsson and Annette Mortenson for making me a part of the Iceland Deep Drilling Project team and the opportunity to work in Krafla. Very special thanks to Phil Kyle for bringing me to Socorro in the first place, and taking me in when tragedy struck. Thanks to Mark Person for bringing new life to the NMT geothermal project and giving me the opportunity to continue research in this field. Thanks to Jim Witcher for giving me my first lessons on a drill rig and teaching me everything I know about New Mexico geothermal. Last but not least, thanks to my late advisor, David Norman who will always have a special place in my heart.

TABLE OF CONTENTS

LIST OF TABLES

LIST OF FIGURES

INTRODUCTION

"Chemistry is king"

Recently, as a staff geologist, I was assigned to a geothermal prospect in Chile hosted near two active stratavolcanoes. Geothermal manifestations included low lying acid-sulfate hotsprings, distal mixed SO_4^{-2} – HCO_3^- springs and superheated fumaroles along the flanks of the volcano. The original developers performed a detailed magnetotelluric (MT) and transient electromagnetic (TEM) survey over the prospect with 3-D inversions, totaling over 60 stations. The results were a beautiful subsurface image illustrating a thin, low-resistivity clay cap forming within the volcanic ash-dominated units, overlaying a moderate resistivity "reservoir". Resistivity anomalies corresponding with possible hydrothermal upflow or magmatic intrusions were also evident near the volcanic base. A single shallow temperature gradient well had reached the smectite-illite boundary revealing high thermal gradients yet no permeability. Such conditions are not uncommon within the capping clay units of a well-developed geothermal system. Chemical gas analysis of the fumarolic discharge, however, painted a less optimistic story. The occurrence of HCl, SO_2 and H_2 within the steam suggested an abundance of primary magmatic gases and little or no interaction with a mature hydrothermal system at depth. In addition, the H_2 concentrations suggested an equilibrated steamphase or vapor cap which often prevails in immature volcanic systems with low permeability.

Due to the promising reservoir model inferred from the MT data and favorable temperatures encountered within the TG well, the prospect was reviewed by several additional geophysical experts in attempts to quantify the likelihood of a geothermal reservoir and thus the risk of additional exploration drilling at this prospect. Each reviewer had a positive interpretation of the resistivity survey, yet insisted on learning about the geochemistry. Bill Cummings, a well renowned expert in MT processing, summarized their concerns best, "when it

comes to geothermal exploration, chemistry is king." No other exploration method can form a unique solution to the dataset.

The prospect was ultimately passed on and new developers drilled several dry exploration wells, proving the immaturity and low permeability of the system. Had the geochemistry been trusted in the first place, the future developers would have saved themselves hundreds of thousands of dollars on geophysical investigations and subsequent millions on exploration slimholes.

For geothermal exploration, development and reservoir analysis, no other tool set is as widely applicable as the study of water-gas-rock interactions and mineral equilibria. The earliest studies of geothermal systems (Ellis and Mahon, 1964; Browne, 1978; Giggenbach, 1980; 1981) were so precise at characterizing the various processes (boiling, condensation, absorption of magmatic gases) and defining their relationships to pressure, temperature and permeability, that we still use these fundamental studies today. The continued exploitation of brine-dominated, deep circulation systems such as those in the Great Basin have resulted in an expansion of geochemical models to deal with lower temperature equilibrium relationships in non-volcanic host rocks lacking the important contribution of acidic volcanic gases.

Stable isotopes have long been used to identify the degree of water rock interaction and/or magmatic input using $\delta^{18}O$ and $\delta^{2}H$ ratios (Craig, 1963; Giggenbach, 1992). Less common stable isotopes such as B and Li are increasingly being investigated to fingerprint geothermal inputs (Millot et al., 2010; 2012). Radiogenic isotopes play a crucial role in dating geothermal waters using ^{3}H, ^{36}Cl and ^{14}C, and identifying magmatic input with $^{3}He/^{4}He$ ratios (Kennedy and van Soest, 2006). Shorter half-life radiogenic isotopes(^{131}I [$t½ = 8.0197\ days$], ^{3}H [$t½ = 12.32yrs$]) are commonly employed as reservoir tracers and to study the effects of phase

separation (McCabe et al., 1981). Fluid inclusion studies have long been used in quanitifying the potential and tracking the progression of a geothermal field (Moore et al., 2001; 2008).

The following chapters involve four studies in three unique geologic systems, both magmatic and non-magmatic, whose chemistries define a distinctive story of water-rock interaction and magmatic evolution.

The first study occurs within a low-temperature geothermal system along the Rio Grande Rift near Socorro, New Mexico. This system was originally recognized based on a handful of dilute warm springs issuing along the range front of Socorro Peak. Historic investigations of this system, including temperature gradient studies, gravity, aeromagnetics and hydrologic modeling, had led to a proposal for drilling an exploration well to locate a source of low-temperature thermal fluids for district heating of the New Mexico Tech campus. Predrilling exploration work included a detailed soil chemistry study to investigate potential upflow of geothermal fluids within the accessible range front structures or buried at depth within the Socorro Basin [*Chapter 1*]. Electrochemical cells form between a sequestered, reducing hydrothermal system and the oxidizing surface allowing for the redistribution of volatile and electrostatic complexes along lines of potential. At the evaporation front, chemical complexes adhere to the soil's Mg-oxide coating. Soil chemistry maps were created using weak digestions (Enzyme leach and Terrasol leach) and ICP-MS analysis revealing patterns aligned with the range front fault, namely in the vicinity of Woods Tunnel, as well as other buried piedmont faults suggesting upflow of a reducing geothermal fluid.

Two geothermal exploration wells drilled within the footwall of the Socorro Peak uplift, identified 42°C brackish fluid discharging along the Woods Tunnel Fault and sourcing from Precambrian crystalline basement. A suite of groundwater environmental tracers were employed

to characterize the flowpath of the geothermal waters and assess the potential for deeper, warmer fluids within the study area in lieu of reliable use of geothermometry in this low temperature system [*Chapter 2*]. Environmental tracers were subsequently used to investigate the extent of leakage of the geothermal waters in surrounding aquifers including the Rio Grande River. Cl/Br, Li, B, As $^{87}Sr/^{86}Sr$, $\delta^{11}B$, $\delta^{34}S$, $\delta^{13}C$, $\delta^{18}O$, $\delta^{2}H$, ^{14}C and ^{3}H ultimately revealed that geothermal exploration well fluids derive from a deep, ~20,000 yr flowpath within Precambrian metasediments and indicate a possible 60-65°C resource within exploitable depths using speciation and heat transport models (Mailloux et al., 1999). Nearby Socorro Spring fluids represent a unique pathway of slightly faster recharge through Oligocene volcanics associated with the Socorro Cauldron. Geothermal fluids along the Socorro reach of the Rio Grande do not contribute substantially to river salinity, however buoyant thermal waters likely play an important role in upwelling deep basinal brines.

The second case study includes a geothermal reservoir analysis of the 60MW Krafla field in northwest Iceland [*Chapter 3*]. The Krafla system is hosted within the magmatic rift and fed entirely by dilute meteoric fluids. Superheated wells discharging volatized HCl represent a major source of corrosion and operational and maintenance (O&M) costs for the powerplant. Acidic and non-condensable magmatic gases entrained within the reservoir fluids, sourcing from periodic eruptions of the Krafla volcano, provide additional difficulty for electrical production. Cuttings from multiple wells at Krafla associated with acidic fluids, elevated non condensable gases and even encounters with molten lava in the borehole, were analyzed using fluid inclusion gas analysis by cold-crush method on a quadrapole mass spectrometer. Gaseous profiles included H_2O, H_2, CO_2, H_2S, SO_2, CH_4, He, N_2 and Ar molar concentrations as a function of depth. Trapping of volcanic gases proximal to their exsolution from magmatic intrusions allowed us to identify a unique chemical signature associated with problematic feedzones, containing un-modified magmatic volatiles such as CO_2, SO_2 and He coupled with high total gas concentrations.

Occurrence of these signatures may be tied to an influx of volcanic HCl and superheated acidic steam. Zones of superheating or deep boiling were also identified, which may produce dry acidic steam with little excess chloride. Wells which encountered molten intrusions exhibit tell-tale magmatic gaseous signatures upwards of 300m above the actual intrusion. Applying fluid inclusion gas of cuttings analysis while drilling would allow for real-time decision making regarding casing off problematic feedzones or cessation of drilling before encountering superheated acidic steam or magma.

A final study takes place on Erebus volcano, in the Ross Sea area of Antarctica [*Chapter 4*]. Erebus is the site of a persistently convecting phonolitic lava lake and a unique suite of depleted oxygen isotope lavas derived from fractional crystallization of a basanite parental magma. Samples were compiled from the volcanic flanks, edifice and deep exploratory core representing a continuously evolved suite dating back to 1.3Ma. Olivine, feldspar and glass mineral separates revealed a trend of overall depletion since the evolution of the basanite resulting in modern glass values of $\delta^{18}O$ and olivines values as low as 6.02‰ in modern lava bombs. Cogenetic whole rock, feldspar and olivine pairs also exhibit poor isotopic agreement, particularly in late-stage phonolite melt. Entrainment of hydrothermally altered volcanic edifice into the intermediate depth magma chamber is proposed as a source for whole-system depletion over time. Hydrothermal water-rock interaction with isotopically light Antarctic meteoric fluids allows for the incorporation of only ~10% altered units overtime to create the degree of depletion observed in the Erebus Lineage Enhanced depletion in olivines is systemic throughout the EL lineage, particularly since the crystallization of anorthoclase phonolite melt, identified by Δ(olv-feld) and Δ(olv-melt) disequilibrium. Fluids at Erebus find repose in the shallow persistently convecting lava lake for approximately 300 years prior to eruption. Enhanced magnetite precipitation is forced within the lave lake due to continuous degassing and decreasing fO_2, thus causing the $\delta^{18}O$ of the melt to increase. The slower time scale for oxygen diffusion in olivines

would allow for these phenocrysts to retain their $\delta^{18}O$ signature on the order of 10^2yrs in a wholly enriched shallow melt.

REFERENCES

Browne, P.R.L., 1978. Hydrothermal alteration in active geothermal fields. Annual Review Earth and Planetary Sciences. 6, 229-250.

Craig, H., 1963. The isotopic geochemistry of water and carbon in geothermal areas: Nuclear Geology on Geothermal Areas, CNR, Pisa, p. 17–53.

Ellis, A.J. and Mahon, W.A.J., 1964. Natural hydrothermal systems and experimental hot-water/rock interactions. Geochim. Cosmochim. Acta, 28, 1323-1357.

Giggenbach, W.F., 1981. Geothermal mineral equilibria. Geochemica et Cosmochimica Acta 45, 393-410.

Giggenbach, W.F., 1980. Geothermal gas equilibria. Geochemica et Cosmochimica Acta 44, 2021-2032.

Giggenbach, W.F. 1992. Isotopic shifts in waters from geothermal and volcanic systems along convergent plate boundaries and their origin: Earth and Planetary Science Letters. 113, 495-510.

Kennedy, B.M., van Soest, M.C., 2006. A helium isotope perspective on the Dixie Valley, Nevada, hydrothermal system. Geothermics. 35, 26-43.

McCabe, W.J., Barry, B.J., Manning, M.R., 1983. Radioactive tracers in geothermal underground water flow studies. Geothermics. 12, 83-110.

Millot, R., Scaillet, B., Sanjaun, B., 2010. Lithium isotopes in island arc geothermal systems: Guadeloupe, Martinique (French West Indies) and experimental approach. Geochemica et Cosmochimica Acta. 74, 1852-1871.

Millot, R., Hegan, A., Negrel, P., 2012. Geothermal waters from the Taupo Volcanic Zone, New Zealand: Li, B and Sr isotopes characterization. Applied Geochemistry. 27, 677-688.

Moore, J.N., Norman, D.I., Kennedy, B.M. 2001. Fluid inclusion gas compositions from an active magmatic-hydrothermal system: a case study of The Geysers geothermal field, USA. Chemical Geology. 173, 3-30.

Moore, J.N., Allis, R.G., Necok, M., Powell., T.S., Bruton, C.J., Wannamaker, P.E., Raharjo, I.B., Norman, D.I., 2008. The evolution of volcano-hosted geothermal systems based on deep wells from Karaha-Telaga Bodas, Indonesia. American Journal of Science. 308, 1-48.

CHAPTER 1:

Exploration of a Blind Geothermal System using Geochemical Mapping by Selective Extraction: example from the Socorro Geothermal Area

ABSTRACT

Geochemical mapping using the selective extraction of soils is an approach utilized in the mineral and environmental industry for locating buried reducing bodies and is introduced in this study for the investigation of a blind geothermal resource. Selective extraction methods used here are two distinct biosynthetic leaches, Enzyme leach and Terrasol leach, to liberate weakly-bound volatilized compounds adhered to the soil's amorphous manganese-oxide coating, without dissolving the mineral substrate. ICP-MS analysis of the leachate reveals over 60 major and trace elements at the sub-ppm level. Soil-slurry pH analyses are also conducted to assess a low-cost, quickly-executed alternative to selective extraction methods. The low temperature geothermal system near Socorro, New Mexico, hosted along the Rio Grande Rift, was selected as a study area for this technique. Soil sampling transects reveal strong anomalous concentrations of rare earth elements (REE), high field strength elements (Zr, Hf, etc.) and soil pH overlapping the range-bounding fault, which is demonstrated to source geothermal upflow. Base metal elements indicate anomalous concentrations near mining adits, drowning out any signal from a weaker geothermal system. Normalizing base metals compositions to Mn concentrations reduces the effect of these artifacts and illuminates additional signatures within the study area correlating with rare earth element and high field strength element anomalies. Soil transects covering the rift basin exhibit remarkable anomalies trending parallel to the main range bounding structure, suggesting geothermal upflow along buried synthetic faults. Geothermal indicator elements, such as As, Se, Zn and Ce which are found within local warm springs and temperature gradient wells, correlate strongly with selective extraction soil profiles. This argues for hydrologic dispersion as

a potential source for certain soil anomalies rather than electrochemical cell formation alone. Stronger leaching agents, such as Terrasol leach, exhibit stronger anomalies, particularly over buried faults. Selective extraction surveys identified multiple basinward anomalies for testing of a blind, low-temperature geothermal resource.

INTRODUCTION

Development of geothermal energy has reached a new threshold by which many of the known systems in the US have actively been exploited, leaving a large reserve of hidden or "blind" geothermal systems yet to be discovered. Blind systems lack typical surface expressions such as fumaroles, mature hotsprings, argillic or propylitic alteration, or hydrothermal sinter and travertine deposits. The nature of high-temperature, high-pressure geothermal fluids, often with acidic gas-charged geochemistry, require depressurization of the system in the form of fumaroles or hotsprings as well as reaction of the thermal fluids with bedrock in the form of alteration or precipitation. Examples of low to moderate temperature geothermal systems (<165°C) in the Basin and Range and Imperial Valley has demonstrated that such blind reservoirs can exist (Matlick and Jayne, 2008; Kratt et al., 2009; Hinz et al., 2010; Faulds et al., 2011; Hinz et al., 2011), where the thickness of capping units or low-topography of the reservoir overrides the potential energy of the system.

Binary power generation and direct use makes exploitation of these lower temperatures economical (Bronicki, 2011; EERE-USDOE, 2012); however, the risk of uncovering such a resource often trumps the cost of more expensive and sophisticated exploration techniques. Exploration of a geothermal systems in the western US often begins with reconnaissance mapping of surface features, geochemical interpretation of springs, or establishment of elevated temperature gradients from historic drilling databases. Once the region of interest has been narrowed, electrical, potential field or seismic surveys are deployed to define the reservoir

geometry in the subsurface and site exploration drilling targets. In the case of a blind geothermal system without equilibrated hot springs or temperature gradient wells, the ability to narrow the scope of a geophysical survey is often curtailed. Over 60,000 MWt of direct use (<90°C) and 120,000 MWe of unidentified geothermal electrical potential (>150°C) is estimated for the southwest US largely involving adjective or conductive systems with little or no surface expression (Green and Nix, 2006). Advancement of a low-cost reconnaissance tool for detecting blind geothermal systems over a broad study area is necessary for the expansion and future application of this renewable resource.

Here we attempt a new approach to geothermal exploration using a traditional method of geochemical mapping used in environmental studies and greenfield mineral exploration. Geochemical soil mapping involves sampling and analysis of soil composition to discern anomalies found in the overburden or downstream of an ore deposit or contamination plume (De Vivo, et al., 1997; Marjoribanks, 2010). Traditional analytical methods, such as total digestion and Aqua Regia [nitro-hydrochloric acid], dissolve or partially dissolve soil regolith to expose trace element concentrations derived from ore deposits buried in the subsurface. Selective extraction is an expansion of this technique which attempts to extract only those trace elements weakly adhered to the soil's amorphous oxide coating without interfering with its indigenous composition. Selective extraction has had reported success in several case-studies, many involving young or weakly developed hydrothermal mineralization (Williams and Gunn, 2002; Noble and Stanley, 2009; Bajc, 1998).

Enzyme leach (EL) and Terrasol leach (TS), two proprietary selective leaches, and soil pH were used to map the surficial expression of a possible blind, low-temperature geothermal system in Socorro, NM. Rigorous statistical analysis of the geochemical data and correlations to the geologic model for the Socorro geothermal system are used to characterize the effectiveness of this method as a reconnaissance geothermal exploration tool. Geochemical maps reveal apical

anomalies forming over the Socorro Canyon range-front fault strongly correlating with a previously discovered heatflow anomaly. Similar N-S trending anomalies paralleling the strike of the range front fault form within the Socorro Basin, suggesting possible geothermal upflow along buried synthetic faults. We find that selective extraction may be utilized as a geothermal reconnaissance tool and should be further tested over a demonstrated resource.

THEORY OF SELECTIVE EXTRACTION IN GEOTHERMAL EXPLORATION

The application of selective extraction as an exploration tool invokes the theory that buried, reducing bodies (e.g. ore deposits, petroleum and geothermal reserves) will propel or redistribute inorganic compounds at the surface creating recognizable patterns of anomalous concentrations in the soil (Smee, 1999; Clark et al., 2003; Hamilton et al., 2004; Mann et al., 2005; Hill et al., 2006). The formation of these anomalies relies fundamentally on the principle that geothermal systems, like other economic deposits, have well-developed self-potential (SP) fields (Corwin & Hoover, 1979; Ross et al., 1995). Naturally occurring hydrothermally-induced self-potential differences may be caused by electrokinetic, thermoelectric and electrochemical processes in the subsurface. Electrokinetic sources are induced by flowing, charged fluids. In robust geothermal areas with active transport and high concentrations of total dissolved solids, electrokinetic processes are commonly thought to be the source of SP signatures (Anderson and Johnson, 1976). Thermoelectric processes are the result of thermal gradients which induce diffusion of electrolytic solutions, yet often produce SP anomalies several orders of magnitudes weaker than electrokinetic. Electrochemical responses originate from isothermal aqueous diffusion involving "geobatteries" or redox cells in the subsurface. Buried, low-temperature geothermal systems may act as a reducing source, driving an electrochemical potential between the system and the closest body of oxygen, the atmosphere.

The distribution of elements at the surface is believed to be affected by a self-potential variation, though the precise transport mechanisms are not well understood. Geothermal reservoirs confined within permeable strata may act as a reduction diode, producing a 'reducing chimney' between it and the oxidized vadose zone above (Sato and Mooney; 1960, Clark, 1993). The vertically positioned electrochemical cell aids in the transport of reduced species towards the water table which acts as a cathode (Fig 1). Positively charged ions, namely H^+, and oxidized volatiles migrate along electropotential lines towards the cathode while reduced anions migrate outwards forming anomalous concentrations in the soil along the evaporation horizon as dictated by the perimeters of the reducing chimney (Govett, 1984; Tompkins, 1990; Clark, 1993; Hamilton et al., 2004). Elements already residing at the surface may reposition along to the potential field forming similar surficial anomalies in the soil. In practice, this type of buried redox cell forms circular, or "halo-shaped" anomalies of anionic compounds, such as halides and oxyanions surrounding centralized zones of depletion (Clark, 1996; Hill and Clark, 2000; Hill et al., 2001). Likewise, oxidized metals, H^+ and cationic species tend to form anomalous highs above the center of the reducing body due to oxidation at the cathode (Smee, 1998; Hamilton et al., 2004).

The method of transportation of trace elements through unfractured substrata is a source of considerable controversy surrounding the application of selective extraction in exploration. Simple diffusion, particularly through thick vadose zones and clay units is too slow a process to be effective over the average lifetime of an epithermal system (10^4-10^6 yrs) (Smee, 1983; Cameron, 2004). Adherence of trace element compounds to volatiles may, however, aid in the transport through the vadose zone (Clark, 1996; Clark, 1997). Electrochemical redistribution of cations at the surface above a reduced column may be the most reasonable process in these geologic settings (Hamilton, 1998; Cameron et al., 2004).

Transportation of geothermal fluids along faults may also be identified. The formation of oxidized elements at the interface between the saturated, reduced footwall block and O_2-rich basin fill sediments produce apical anomalies ,or sharp concentration spikes, controlled by the angle and trace of the fault and depth to water table (Hamilton et al., 2004) as illustrated in Fig 2. Resulting geochemical signatures may be expected in Basin & Range-type, or fault-controlled, geothermal systems situated in arid environments with the greatest depth-to-watertable. Studies involving Enzyme leach in particular cite considerable anomaly formation over faults aligning over the subcrop of the structure (Clark, 1997; Bajc, 1998; Williams & Gunn, 2002; Cameron et al., 2004). Faults and fractures appear to facilitate transport of trace elements to the surface. Possible mechanisms involve some form of advection, including barometric pumping of gases (i.e. halogens) or volatile metal halides or simple hydrolithic transport. Structural anomalies may also be associated with seismic pumping of pore fluids during micro-seismic events forcing these fluids out of fractures and depositing at the surface (Cameron et al., 2002; Cameron et al., 2004).

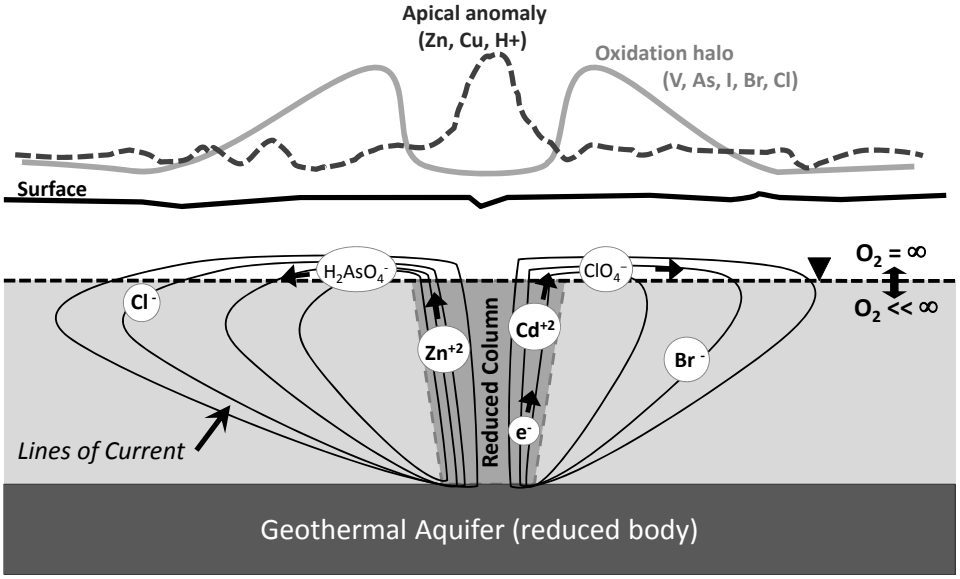

Fig. 1. Model of oxidation cell anomalies, illustrating the formation of a reduced column between the geothermal aquifer and the vadose zone above. Halo shaped anomalies featuring oxidation-suite elements form at the surface outlining the perimeter of reduced column; a central depletion of these elements are formed directly above the resource. Central apical anomalies are often observed featuring elements concentrated in the resource as well as mobile species forming immobile complexes by oxidation above the reduced column. Figure modified from Clark et al., 2003 and Hamilton et al., 2004.

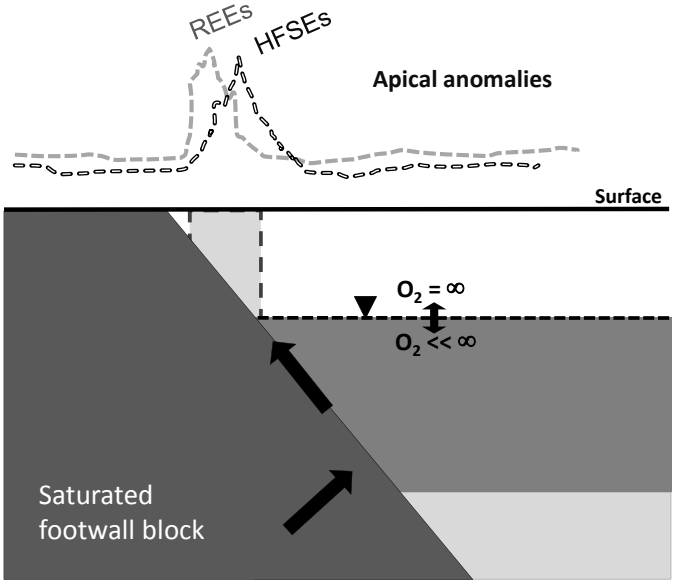

Fig. 2. Model of 1-D apical anomaly formation over faults. Cartoon illustrates formation of oxidized compounds, particularly featuring High Field Strength Elements (HFSEs) and Rare Earth Elements (REEs), at interface between saturated, reduced footwall block and O_2-rich basin fill sediments above the water table. Resulting geochemical anomalies are expected in Basin & Range-type geothermal systems where geothermal upflow is directed along range-front faults. Cartoon illustrates common spatial offset of apical anomalies at the surface for different suites of elements may be observed based on differences in molecular diffusivity. Figure modified from Clark et al., 2003.

GEOLOGIC BACKGROUND

Geologic Setting

The Socorro Geothermal Area (SGA), in central New Mexico, is located along the Rio Grande Rift, a continental rift system with elevated background heat flows upwards of 100mW/m^2 (Reiter et al., 1986; Reiter, 2009) and host to multiple low-temperature geothermal systems along its extent (Boyd et al., 2011). The rift supports a Basin-and-Range-type geothermal setting, serving as both a source of conductive heat input as well as a hydrologic sink bounded by extensional faulting aiding in deep circulation of meteoric waters and advective heat transport.

The SGA is hosted within an uplifted Precambrian basement fault block, bounded to the east by the Socorro Canyon fault (Fig. 3 and 4). Socorro Peak boasts a stratigraphic sequence of

alternating permeable and impermeable Proterozoic to mid-Tertiary units juxtaposed by domino-style fault-blocking (Chapin, 1979; Chamberlin, 1999). This assemblage is fundamental to models supporting deep fluid circulation and discharge through hydrologic windows (Witcher, 1988). Fractured Paleozoic limestones and indurated shales conformably overlie the Precambrian units, which may represent cooperative aquifer and aquitard units. Overlying Oligocene volcanics and volcaniclastics, which include brittle and well-jointed welded ash-flow tuffs and lava flows, exhibit good fracture permeability and are generally considered the main hydrologic unit in this system supplying the warm springs to the south (Chapin, 1979; Barroll and Reiter,1990; Mallouix 1999). Lastly, syn-rift forming fanglomerates and interfingering playa facies deposited during early Rio Grande Rifting are impermeable and possible insulating caps for hydrothermal fluids particularly in the La Jencia and Socorro Basins.

Local permeability for the SGA is likely hosted along the Socorro Canyon fault, a north-trending dip-slip normal fault. Upwelling along the range front expression of this fault or buried synthetic faults within Socorro Basin (Chamberlin, 1999) are the likely targets for this system. The northeastern rim of the Socorro Cauldron ring fracture, an Oligocene caldera-collapse feature, transects the Socorro Peak horst block providing possible structural permeability within the range front and basinward units (Fig. 3). In addition, the SGA occurs only a few km north of the Socorro Accommodation Zone (SAZ). Proximity to this major transverse shear zone may provide enhanced dilation along the SCF as well as aid in deep circulation of meteoric recharge from the west along structural conduits (Chapin, 1978).

Geothermal Model for Socorro Geothermal Area

Though lacking in surficial physical expression, past geologic and hydrologic studies of the SGA elude to a geothermal resource within the Socorro Peak horst block (Sanford,1977; Reiter and Smith, 1977; Chapin,1979; Gross and Wilcox, 1983; Barroll and Reiter,1990;

Mallouix 1999). Heatflow studies identify a strong north-south trending thermal anomaly along the range front, as defined by elevated temperature gradients within the uplifted horst block. A maximum heatflow value of 490 mW/m^2 was derived from a mine-shaft well located beneath Socorro Peak, drilled into thermally conductive Precambrian bedrock (Barroll, 1989). Depressed heatflow values in La Jencia basin support a forced convection model of deep recharge originating from the Magdalena Mountains to the west and upflowing beneath Socorro Peak (Barroll and Reiter, 1990; Maillox, 1999). Apart from the Socorro warm springs issuing along the range front (Fig. 3 and Fig. 5), there is no significant discharge near Socorro Peak of geothermal fluids associated with the apparent heatflow anomaly. Discharge across the range bounding fault into downfaulted syn-rift conglomerate units may represent a buried geothermal reservoir beneath the Socorro Basin (Fig. 4). Thick, insulating playa deposits overlie the permeable conglomerates and prevent the identification of such a reservoir through thermal gradient studies.

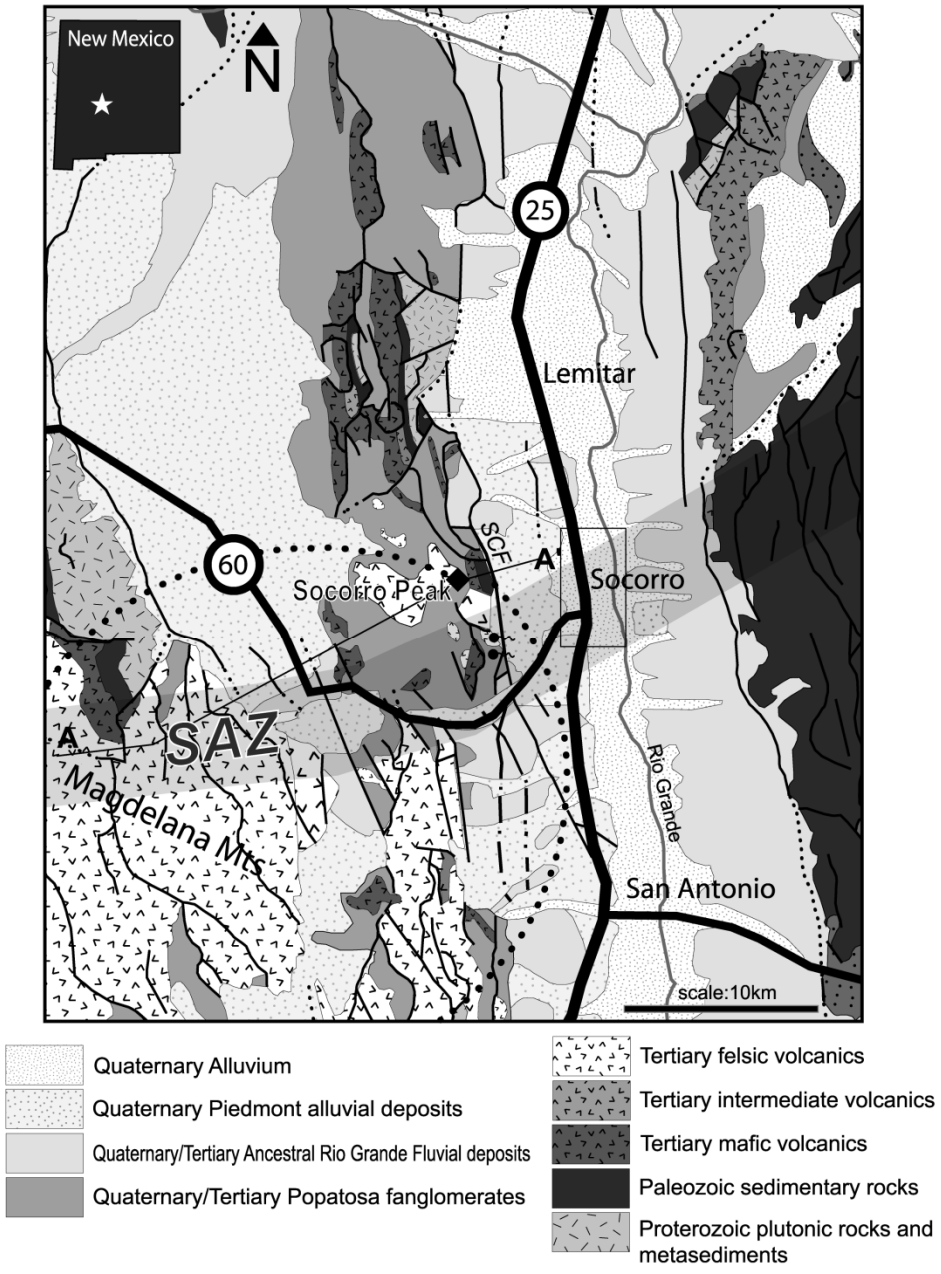

Fig. 3. Simplified geologic map of Socorro area along Rio Grande rift in central New Mexico. Transect (A-A') corresponds to trace of hydro-stratigraphic cross-section illustrated in Figure 4. Dashed circle indicates perimeter of Socorro Caldron ring fracture system. Socorro Accommodation Zone (SAZ), a transverse shear zone, bounds the Socorro Geothermal Area to the south. The range-bounding Socorro Canyon Fault (SCF) illustrated trending N-S to the east of Socorro Peak. Modified from Chapin, 1978 and Scholle, 2003.

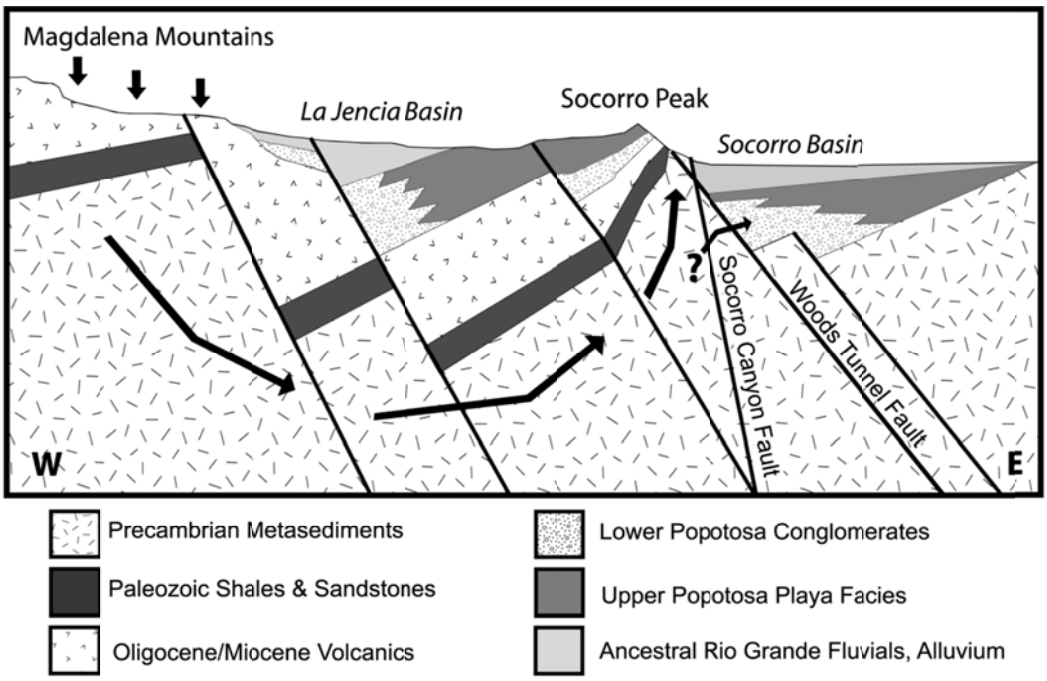

Fig. 4. Generalized hydrologic cross section of west (A) to east (A') through La Jencia Basin and Socorro Mountain Block illustrating fluids advecting to several km depth beneath playa deposits and upflow along permeable strata. Deeply buried hydrostratigraphic units with the Socorro Basin are a hypothesized reservoir for upwelling geothermal fluids.

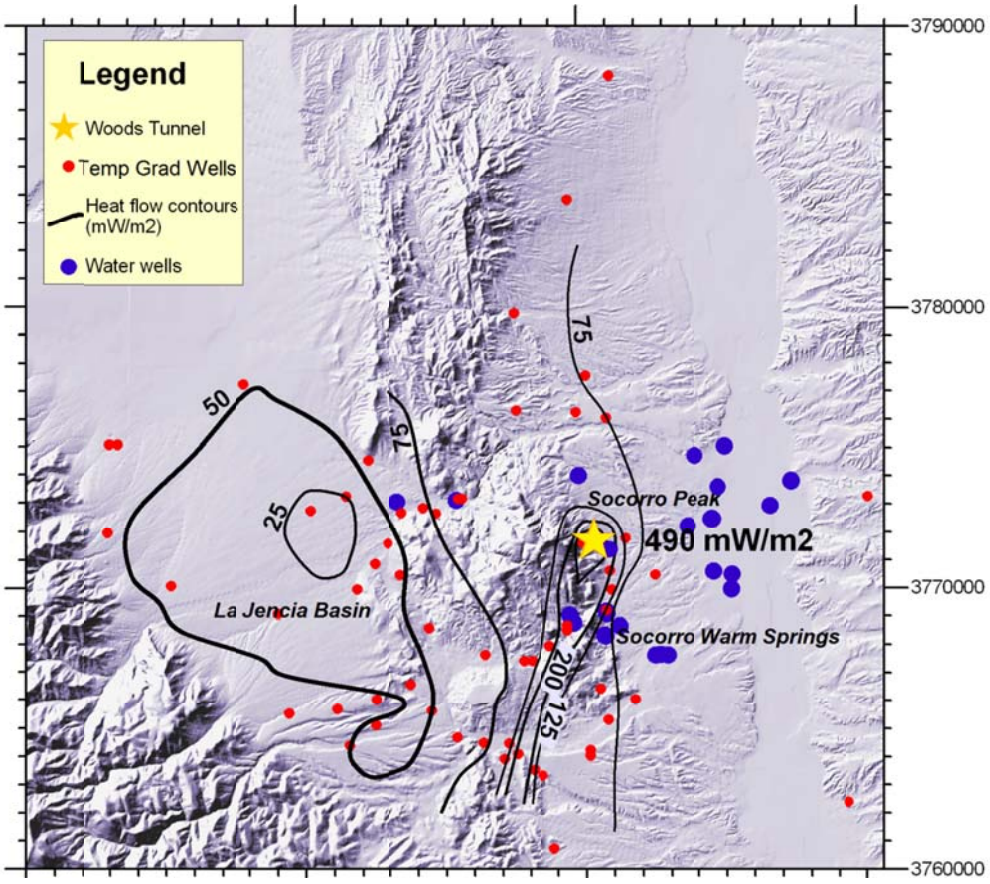

Fig 5. Map of heat flow and locations of wells in the Socorro Peak area. Heat flow is contoured in mW/m^2 (Barroll and Reiter, 1990). Heat flow measurements were calculated using least-mean-square temperature gradients and thermal conductivities measured from cuttings. In the case of heat flow perturbations due to fluid flow in the wells, heat flows were estimated using bottom-hole temperatures and surface temperatures. Uncertainty for heat flow measurements and heat flow contours range from 10% to 20%.

Mineral deposition near Socorro Peak

Care must be taken in the interpretation of this geochemical mapping technique to avoid confusing anomalies associated with that of ore-deposits or other reducing bodies. Primary hydrothermal mineralization in the SGA is limited to barite and fluorite; however, mineral deposits containing Pb, Au, Ag, W, V, As and Br occur along narrow veins in the Socorro Peak rhyolite and Popotosa Formation (North, 1983). The Torrence, Merrit and Woods Tunnel mine adits occur along the range front of Socorro Peak and may contribute trace amounts ore-rich tailings to the alluvial fan units (Ennis, 1996).

Warm spring chemistry

Thermal fluids in the Socorro KGRA have 2 distinct compositions. The Socorro, Sedillo, Cook, and Blue Canyon warm springs (29-32°C), located to the south of Socorro Peak (Fig. 5), discharge from a fractured volcanic unit uplifted along the range bounding fault. Springs are characterized by low Cl fluid with elevated concentrations of As and SiO_2 (Table 2). Warm fluids (42°C) are contained within a recently drilled, 330m deep geothermal exploration well near the Woods Tunnel mine adit sunk into Precambrian metasediments. The well waters exhibit elevated salinity and dissolved silica, yet appear geochemically isolated from the warm springs to the south despite being conflated within the same N-S trending heat flow anomaly. These fluids also contain high concentrations of geothermal indicator elements such as B and Li (Ellis and Mahon, 1964). The group of warm springs to the south and test well to the north are separated by the east-west trending Socorro Caldron boundary which transects through the center of the geothermal study area. Local meteoric waters exhibit low Cl and As concentrations and represent the source of shallow aquifer drinking waters in the Socorro Basin.

Table 1. Geochemical composition of warm wells and springs in the Socorro study area. All concentrations are in parts per millon (ppm). Temperatures are measured at time of sampling from screen depth. Compositions from studies by ‡Brandvolt (2001), * Summers et al. (1981), **City of Socorro (2003) and ‡this author (see Chapter 2).

	pH	Cl	Na	SiO_2	As	B	Li	Zn	Temp (°C)
THERMAL WATERS 1	7.7	17	65	23		0.11	0.040		
Cook Springs*	7.8	11	50	22	0.04	0.07	0.047	0.003	29
Sedillo Springs**	8.0	11	50	23	0.04	0.07	0.048	0.001	24
Socorro Springs**	7.8	19	57	26	0.03	0.10	0.050	0.160	29
Blue Canyon†	7.7	17	65	23		0.11	0.040		27
THERMAL WATERS 2									
Woods Tunnel test well‡	7.9	935	625	34	0.03	0.82	1.144	<0.005	42

METHODS AND MATERIALS

Selective Extraction

EL and TS used in this study are both proprietary extraction methods developed by ActLabs, Ontario and are discussed in further detail by Clark (1995). Geochemical mapping methods often involve varying degrees of dissolution of the soil's crystalline and amorphous oxide coating with different reactants, including ammonium acetate, hydroxylamine hydrochloride, acetic acid, and Mobile Metal Ion. Very weak reactants such as EL intend to dissolve only the amorphous oxyhydroxide soil coatings liberating the weakly-bound volatile compounds and trace elements, leaving the crystalline MnO_2 coating and indigenous soil material intact (Clark, 1995). By eliminating concentrations derived from the soil substrate, the elevated background signatures are removed, allowing for more sensitive detection of residual anomalies (Hill, 2006). This is particularly desirable for the study of a modern geothermal system such as the Socorro Geothermal Area where past occurrences of mineralization near the surface may be incorporated into the eroded surface strata and confuse the location of an active resource.

EL and TS both use the protein glucose oxidase to catalyze the oxidation of dextrose in a reaction forming gluconic acid and hydrogen peroxide (Reaction 1). The hydrogen peroxide produced reacts with amorphous MnO_2, releasing trapped trace elements into the resulting solution (Reaction 2).

$$C_6H_{12}O_6 + O_2 + H_2O \leftrightarrow \text{glucose oxidase} \leftrightarrow C_6H_{12}O_7 + H_2O_2 \qquad \text{Reaction 1}$$

$$MnO_{2(s)} + H_2O_2 + 2H^+ \rightarrow Mn^{2+}{}_{(aq)} + O_2 + 2H_2O \qquad \text{Reaction 2}$$

Amorphous MnO_2 coating is uniquely capable of trapping a wide variety of gases, compounds and ions because of a large surface area and multi-charged surface (Clark, 1995; Clark et al., 2003). Amorphous MnO_2 dissolves much faster than its crystalline counterpart, thus

cutting off the digestion before advancing into the indigenous soil (Hill, 2006). Once the amorphous MnO_2 is completely dissolved, Reaction 2 slows and the excess H_2O_2 builds causing the first reaction to slow as well. As a result, the mineral substrate containing crystalline MnO_2 form is minimized. TS is a stronger solution involving the addition of acetic acid and is designed to dissolve both amorphous MnO_2 and FeO_2 phases (Reaction 3).

$$MnO_{2(s)} + 2\ CH_3CO_2H \rightarrow 4\ CH_3CO_2^- + Mn^{2+}_{(aq)} + H_2O \qquad \text{Reaction 3}$$

Soil sampling for EL and TS

Soil samples for EL and TS analyses were collected at 50-100m intervals along E-W transects (Figure 6). Six lines were spaced across the study area, incorporating both the alluvial basin and foothill topography, intersecting major N-S trending range-bounding faults to investigate fracture permeabilty within this system. Sampling coverage within Socorro basin is designed to test for deeply buried geothermal fluids beneath the confining playa deposits. Twenty-five gram soil samples were collected from B horizon at ~5-10cm depth and sieved to collect a fraction <1mm.

Samples were analyzed by Activation Laboratories in Tucson, AZ. A 0.75g soil sample was reacted in the Enzyme leach or Terrasol leach solution at 30°C for 1 hour. The resulting solutions are analyzed on a Perkin Elmer ELAN 6000, 6100 or 9000 ICP-MS by EPA 200.8 standard methods and reported for numerous elements (Table 2).

Table 2. List of element groups designated for the interpretation of selective extraction anomalies and detection limits from ICP-MS analyses in parts per billion (ppb).

Oxidation Suite:		Base Metals:		Chalcophiles:		HFSEs:		REEs:		Lithophiles:	
Cl	2000	Co	1	Ga	1	Ti	100	La	0.1	Li	2
Br	5	Ni	3	Ge	0.5	Cr	20	Ce	0.1	Be	2
I	2	Cu	3	Ag	0.2	Y	0.5	Pr	0.1	Sc	100
V	1	Zn	10	Cd	0.2	Zr	1	Nd	0.1	Mn	1
As	1	Pb	1	In	0.1	Nb	1	Sm	0.1	Rb	1
Se	5			Sn	0.8	Hf	0.1	Eu	0.1	Sr	1
Mo	1			Tl	0.1	Ta	0.1	Gd	0.1	Cs	0.1
Sb	0.1			Bi	0.8			Tb	0.1	Ba	1
Te	1							Dy	0.1		
W	1							Ho	0.1		
Re	0.01							Er	0.1		
Au	0.05							Tm	0.1		
Hg	1							Yb	0.1		
Th	0.1							Lu	0.1		
U	0.1										

Element classifications

Analyses are reported according to their Goldschmidt classification (Table 2). Oxidation type anomalies forming over buried, reduced bodies appear to liberate volatile halogen complexes that form anomalies among the halogens and elements that form hydroxyanion compounds (Cl, Br, I, Mo, As, Sb, W, Re, V, Se, Te, U, and Th (Clark, 1997; Clark and Russ, 1991). Anomalies represented by high field strength elements (HFSE) sometimes occur within the central low and commonly at the interface between a central low and a halo (Hill and Clark, 2000). Base metal and commodity elements (those elements concentrated in the source) also occur as a central high above the source. Less mobile cations, including rare earth elements (REEs) and high field strength elements, tend to form anomalies over fractures (Clark, 1997).

Soil pH

The use of soil pH as an exploration method is applied alongside EL and TS in this study. Hydrogen ions form in anomalous concentrations along with other oxidized elements and are released by redox reactions across electrochemical cells (Govett, 1976; Hamilton, 2004). The analysis and mapping of soil pH has reported use in the oil, gas and mineral exploration fields

(Smee, 1983; Smee, 1999). The measurement and mapping of soil pH using deionized water is a simplified, real-time approach which may identify hydrothermal anomalies with comparable results. We applied the technique here to investigate its validity as a low-cost substitute for identifying buried structures and fluids within a geothermal system.

Sampling and analysis of soil pH

Soil samples for pH measurements were collected along 9 E-W trending transects spaced 400m apart, roughly overlapping the same target area as the EL and TS survey (Figure 6). Tight 30-50m sample spacing along each transect was utilized across the range front in order to better identify fluid movement directed by faulted permeability. Sample spacing was increased to 100m in the basin where the anomalies are thought to be more diffuse. Soil was sampled from upper 5-10cm depth in soil profile, with special attention to avoid vegetation, organic peat or caliche. If caliche was detected at >10cm depth, soil was collected in upper 5cm of profile and tested for excess acidity. Samples were seived to <1mm and all organic matter removed. Three milligrams soil was mixed with 50mL reverse osmosis water (pH buffered to 6.0). The pH of soil slurries were tested following 2 minutes of agitation and pH meter was calibrated every 2 hours. (Smee, 1999). Analyses were conducted in the lab < 2 hours after collection to minimize barometric influences. Results of these analyses are discussed here in both pH (standard units) as well as $[H^+]$ concentration (mol/kg) for better comparison with trace element concentrations.

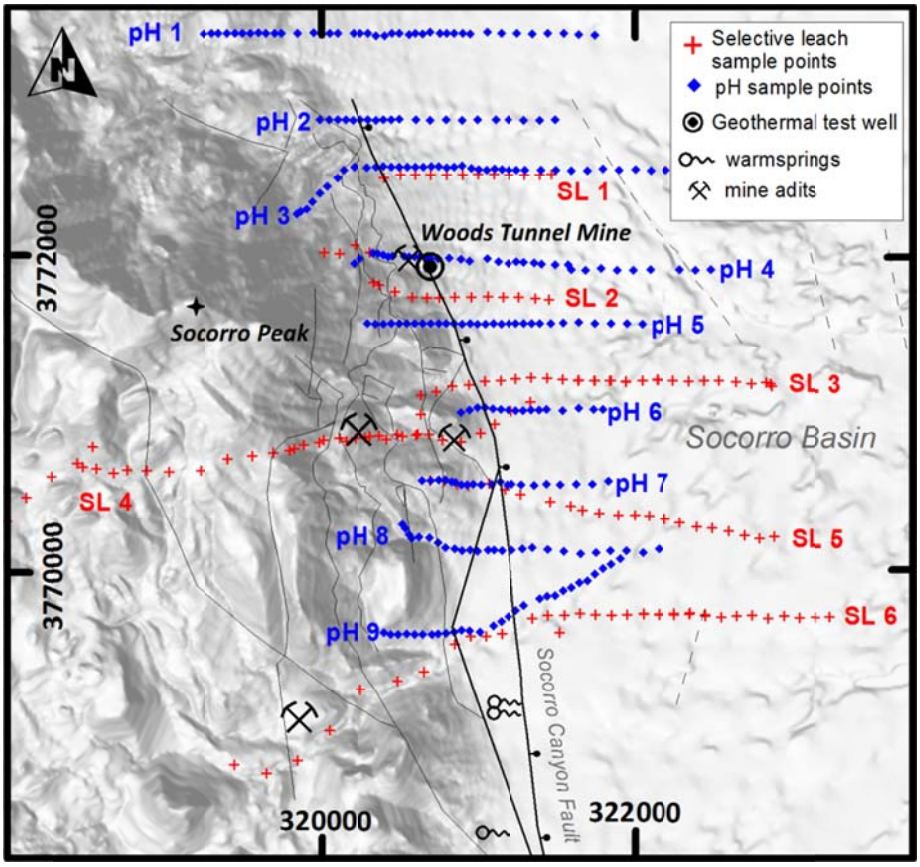

Fig. 6. Sample transects for EL and TS selective extraction (SL 1- 6) and soil pH analyses (pH 1- 9). Socorro Canyon range bounding fault borders Socorro Peak to the west and Socorro Basin to the west.

RESULTS AND INTERPRETATION

SL and pH results and statistics

Enzyme leach and Terrasol leach concentrations are reported for each suite of elements in Appendix 2 and 3. Results of the pH analysis are found in Appendix 4. Simple statistics for all data sets are found in Table 3 below. Lithophile elements exhibit the highest concentrations with median values of 20-2500ppb for EL and 5-100,000ppb for TS. Rare earth elements consistently report median values 2-orders-of-magnitude lower, between 0.5-3ppb for EL and 30-3000ppb for TS. High field strength elements exhibit the lowest concentrations with values below detection limits for multiple elements (<1-0.1ppb). Oxide suite elements, namely Cl, Br, Mo and U exhibit quite variable concentrations with the highest contrasting values ranging from below detection limits to over 2.0E5 ppb for both EL and TS. Mn concentrations are among the highest of all analytes with maximum values of 2.2 E4 ppb and 2.2 E6 ppb for EL and TS, respectively. Soil pH analyses ranged from median values of pH > 9.2 to a minimum of pH = 5.6.

Anomalous concentrations are distinguished from background populations using histogram analysis and cumulative probability plots (Appendix 5 and 6). No single data set exhibits a normal or random distribution, as exemplified by the non-linearity in the cumulative probability plots. Statistical contrast between background and minimal anomalous concentrations are reported in Table 3. Oxide suite and lithophile elements form the greatest contrasting anomalies at least 3-7 times that of background levels. REEs profiles exhibit the least contrast with anomalous concentrations averaging only 2-4 times that of background values.

Many elements exhibit maximum concentrations of 10's – 1000's times the detection limit, illustrating either the robustness of the anomaly or the possibility for contamination in the data set. Histograms are used to identify extreme outliers from elemental profiles with high contrast values and corrected where contamination is suspected.

Correlation Analysis

Elemental Suite Correlations

Correlation analyses (Pearson R values) of the reported elemental concentrations help distinguish between groups with strong geochemical associations related to the nature of the geothermal system and artifacts from the leaching and sampling process. Oxidation suite elements processed with EL indicate a fair correlation between the halogens, Br, I, Cl, and V, averaging R = 0.47 between each pair, and Mo, I, As, Ni, and U, averaging R = 0.59. Base metal and chalcophile elements exhibit good correlations within their groups, averaging R = 0.72. All rare earth elements exhibit excellent correlations, averaging 0.74 with some pairs as high as 1.00. TS analyses indicate very poor correlation between the oxide suite elements. Base metals Cu, Zn and Pb indicate very strong correlations (R_{ave} = 0.82), possibly corresponding to the enhanced dissolution of Fe compounds with TS dissolutions. REE's also exhibit excellent correlation (R_{ave} = 0.82) as a group, with increasing R values with increasing atomic number. High field strength elements Y, Zr, Hf, Ta, Nb also exhibit notable correlations averaging R = 0.64.

Correlations between Mn concentrations and the remaining suite of elements may provide evidence of excess soil substrate involved in the leaching reaction. EL values of Mn have good association with Co, Cd, Tl (R >0.5) and fair association (R >0.35) with base metals Ni, Cu, Zn, Pb. All other elements have an R<0.35 and indicate negligible dissolution of the crystalline MnO_2 substrate. TS analyses, however, indicate a significant correlation between Mn and Sb, W, Hg, Th, Co, Ti, Y, Zr, Hf, Be (R >0.5) and all REEs (R_{ave} = 0.64) possibly related to the increased strength of the leach.

Table 3. Simple statistics for EL, TS and pH datasets. Concentrations reported in ppb. Contrast values are reported for maximum/median and anomalous/background. Soil pH contrast values reported in [H+] molarity.

	Oxidation Suite Elements																			
	Cl		Br	I	V		As		Se		Mo		Sb		Te		W		Re	
	EL	TS	EL	EL	EL	TS	EL	TS	EL	TS	EL	TS	EL	TS	EL	TS	EL	TS	EL	TS
Min	1000	<2000	16	<2	39	63	9	69	<5	<5	2	<1	2	<0.1	<1	<1	3	<1	<0.01	<0.01
Max	199000	238000	2410	4480	848	1820	716	3900	43	234	2750	11000	75	153	2	-	416	1400	0.06	-
Mean	4544	1700	81	65	164	440	86	556	1	3	43	155	19	40	-	-	26	85	0.06	-
Stdev	16387	20115	195	358	136	362	86	526	4	28	220	945	13	29	-	-	39	183	0.06	-
Median	1000	<2000	51	19	123	311	62	416	<5	<5	11	17	15	33	<1	<1	16	<1	0.06	<0.01
Contrast (Max/Med)	199	119	47	242	7	6	12	9	9	47	244	643	5	5	2	-	26	1400	1	-
Background			46.4	17.3	113	356	73.4	368	<5		15.4	43.6	8.5	30.6	<1		9.93	<1	<0.01	
Anomalous			137	118	407	1088	330	2623	7.9		71	142	61.9	139	1		62.4	275	0.03	
Contrast (AN/BG)			3	7	4	3	4	7	-		5	3	7	5	-		6	-	-	

	Au		Hg		Th		U	
	EL	TS	EL	TS	EL	TS	EL	TS
Min	<0.05	<0.05	<1	<1	<0.1	57	<0.1	8
Max	0.29	25.10	-	179	1.94	1290	36.60	2110
Mean	0.29	0.89	-	22	0.46	426	0.42	73
Stdev	0.29	3.46	-	34	0.33	249	2.95	200
Median	0.29	<0.05	<1	11	0.37	361	<0.1	28
Contrast (Max/Med)	1	-	-	17	5	4	366	76
Background	<0.05	<0.05		12.2	0.27	365	0.21	35.8
Anomalous	0.1	7.54		57.7	1.57	982	0.54	118
Contrast (AN/BG)	-	-		5	6	3	3	3

	High-Field Strength Elements										Lithophile Elements									
	Ti		Cr		Y		Zr		Nb		Hf		Ta		Li		Be		Sc	
	EL	TS	EL	TS	EL	TS	EL	TS	EL	TS	EL	TS	EL	TS	EL	TS	EL	TS	EL	TS
Min	<100	<100	<20	<20	1	805	<1	164	<1	<1	<0.1	4.2	<0.1	<0.1	9	47.7	<2	<2	<100	<2
Max	146	5480	-	1040	17	11900	9	5670	19	165	-	134.0	0.7	2.9	189	881.0	4	686	-	578
Mean	-	1213	-	11	4	3663	1	1228	-	7	-	27.6	-	0.2	36	169.8	-	98	-	4
Stdev	26	1259	0	99	2	1996	2	1153	2	15	-	24.3	-	0.5	25	130.3	-	155	-	49
Median	<100	609	<20	<20	3	3040	1	704	<1	5	<0.1	17.1	<0.1	<0.1	30	132.0	<2	26	<100	<2
Contrast (Max/Med)	-	9	-	52	5	4	8	8	19	33	-	8	7	29	6	7	2	26	-	289
Background		747			3.27	2654	<1	623	<1	<1	0.15	15			25.4	117		52.6		
Anomalous		3113			16.2	6353	3.36	2917	2.65	8.3	0.24	79.9			107	395		341		
Contrast (AN/BG)		4			5	2	-	5	-	-	2	5			4	3		6		

	Lithophile Elements															
	Mn		Rb		Sr		Cs		Ba							
	EL	TS	EL	TS	EL	TS	EL	TS	EL	TS						
Min	147	8050	11	410	554	7800	<0.1	19	111	1990						
Max	22100	2200000	153	2430	36100	232000	19.7	766	9530	365000						
Mean	3493	207512	30	895	2876	33630	0.3	59	2831	117469						
Stdev	3944	350098	17	351	3455	24499	1.6	73	1583	67133						
Median	2215	74150	26	821	2270	28250	<0.1	45	2565	102500						
Contrast (Max/Med)	10	30	6	3	16	8	19.7	17	4	4						
Background	2143	200000	24.1	915	3785	26483	<0.1	45.3	1824	62492						
Anomalous	14117	1000000	114	2430	13480	100000	3.5	112	7818	300000						
Contrast (AN/BG)	7	5	5	3	4	4	-	2	4	5						

	Rare Earth Elements																			
	La		Ce		Pr		Nd		Sm		Eu		Gd		Tb		Dy		Ho	
	EL	TS	EL	TS	EL	TS	EL	TS	EL	TS	EL	TS	EL	TS	EL		EL	TS	EL	TS
Min	0.7	160.0	0.7	575.0	0.1	133.0	0.6	668.0	0.1	160.0	<0.1	55.5	0.1	143.0	<0.1		<0.1	142.0	<0.1	27.6
Max	8.8	3800.0	26.2	14000.0	2.8	1610.0	12.0	8420.0	2.8	2210.0	1.8	492.0	2.3	2150.0	0.4		1.8	2010.0	0.4	388.0
Mean	2.9	1526.5	6.0	3427.2	0.9	681.5	3.7	3302.0	0.8	823.3	0.5	189.3	0.7	747.1	0.1		0.6	685.4	0.1	127.8
Stdev	1.6	947.8	3.8	2548.5	0.5	327.1	2.3	1564.2	0.5	401.7	0.3	85.1	0.4	374.5	0.1		0.4	359.5	0.1	67.9
Median	2.4	1345.0	4.9	2420.0	0.7	621.5	3.1	3035.0	0.7	763.0	0.5	174.0	0.6	665.0	0.0		0.5	591.5	0.0	108.0
Contrast (Max/Med)	4	3	5	6	4	3	4	3	4	3	4	3	4	3	4		4	3	4	4
Background	2.16	1070	5.34	1694	0.61	502	2.65	2606	0.62	673	0.57	165	0.52	645	<0.1		0.43	609	<0.1	87.7
Anomalous	6.57	3193	26.2	6169	1.58	1364	9.92	6482	2.06	1527	1.41	274	1.73	1314	0.19		0.95	1232	0.14	208
Contrast (AN/BG)	3	3	5	4	3	3	4	2	3	2	2	2	3	2	-		2	2	-	2

	Rare Earth Elements									
	Er		Tm		Yb		Lu			
	EL	TS	EL	TS	EL	TS	EL	TS		
Min	<0.1	75.3	<0.1	9.9	0.0	66.9	<0.1	11.9		
Max	1.4	1080.0	0.2	142.0	1.4	900.0	0.2	134.0		
Mean	0.3	344.8	-	44.3	0.3	283.1	-	39.5		
Stdev	0.2	185.0	-	24.8	0.2	163.0	-	23.4		
Median	0.3	285.0	<0.1	35.6	0.2	223.0	<0.1	30.8		
Contrast (Max/Med)	5	4	2	4	6	4	2	4		
Background	1.1	578	0.12	76	0.96	622	73			
Anomalous	4	2	-	2	3	3	2			

	Chalcophile Elements																Base Metals										Soli pH
	Ga		Ge		Ag		Cd		Sn		Tl		Bi		In		Co		Ni		Cu		Zn		Pb		
	EL	TS	EL	TS	EL	TS	EL	TS	EL	TS	EL	TS	EL	TS	EL	TS	EL	TS	EL	TS	EL	TS	EL	TS	EL	TS	
Min	<1	8	<0.5	<0.5	<0.2	<0.2	<0.2	<0.2	<0.8	<0.8	<0.1	<0.1	<0.8	<0.8	<0.1	<0.1	2	194	<3	<3	<3	118	<10	<10	<1	<1	5.68
Max	2	125	4	24	-	898	62	5440	1	-	1	237.0	1	6.5	-	11.3	237	29100	174	11200	324	25500	1510	70500	812	142000	9.72
Mean	-	36	-	3	-	122	2	308	-	-	0.1	3.4	-	0.2	-	0.4	15	1670	11	345	27	1396	21	2368	30	3231	8.79
Stdev	-	22	-	6	-	239	5	541	-	-	0.2	21.8	0.1	1.1	-	1.7	25	3325	17	1104	33	2428	123	6368	77	12831	0.79
Median	<1	29	<0.5	<0.5	<0.2	<0.2	1	134	<0.8	<0.8	0.1	<0.1	<0.8	<0.8	<0.1	<0.1	8	615	7	<3	21	762	<10	781	13	112	9.04
Contrast (Max/Med)	2	4	8	49	-	4490	65	41	1	-	23	2370	1	8	-	113	28	47	25	3733	15	33	151	90	65	1274	0.21*
Background		27.2		<0.5		<0.2	0.79	449				<0.1					6.41	870	13.1	<3	26.7	2233	17.5	672	14.7	798	9.2
Anomalous		95		12.9		611	4.29	2264				0.24					30.7	3572	62	2725	146	4348	31.9	2630	81.4	6030	8.2
Contrast (AN/BG)		3		-		-	5	5				-					5	4	5	-	5	2	2	4	6	8	10*

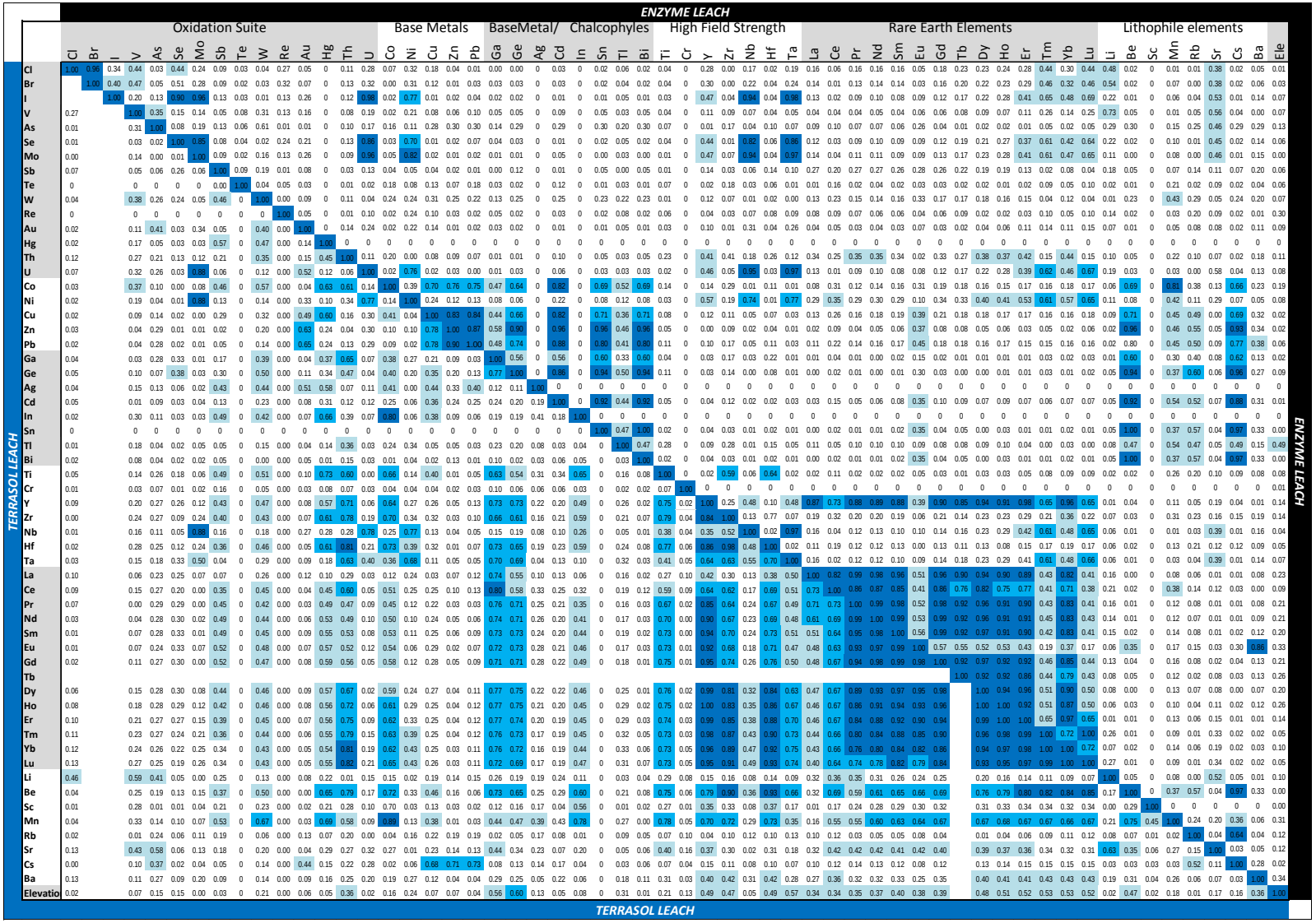

Fig 7. Correlation analysis chart between elemental suites. Pearson R values for EL are found in upper right; values for TS are found in lower left.

Correlation with Topography

Elevation is also investigated as a source of bias for anomaly formation due to the widely variable topography of the field area. EL analyses do not indicate any notable correlation with elevation. TS REEs and lithophiles, however, do correlate with sample elevation (R = 0.34 – 0.53), possibly related to the soil thickness above bedrock or volume of amorphous coating available for ionic adsorption. Correlation between $[H^+]$ concentration in the soil and elevation is also poor (R = 0.18).

Correlation between EL and TS

Enzyme leach and Terrasol leach both dissolve a nominal amount of oxyhydroxide soil coating to obtain a trace element signature. The difference in strength and precision of each leach may be examined by comparing the results from both methods. Terrasol leach reports concentrations 100-1000 times greater than corresponding values measured by Enzyme leach (Figure 7), however the relative magnitude of the anomalies in both data sets correlate well. Oxide suite elements Cl, V, As, Mo, W, U and Sb exhibited excellent agreement between the two leaches (R_{ave} = 0.85). Base metals Ni, Cu, Zn, Pb, Co and lithophile group elements Li, Ba, Sr, Mn, Cs and Rb also exhibited good correlations (R_{ave} = 0.78 and R_{ave} = 0.77, respectively.) Despite excellent correlation within their respective groups, REEs and HFSEs demonstrated very poor agreement between Terrasol and Enzyme leach values (R_{ave} <0.15). The Enzyme leach is a weaker dissolving agent, thus may detect only shallower (100-500m depth) resources resonating a stronger geochemical signal. Terrasol leach, which dissolves greater amounts of amorphous oxide soil coatings, may uniquely detect more deeply seated (>500m) resources that EL cannot (Hill et al., 2001). It appears HFSE and REE elements and the volatile compounds they adhere to are most susceptible to this factor.

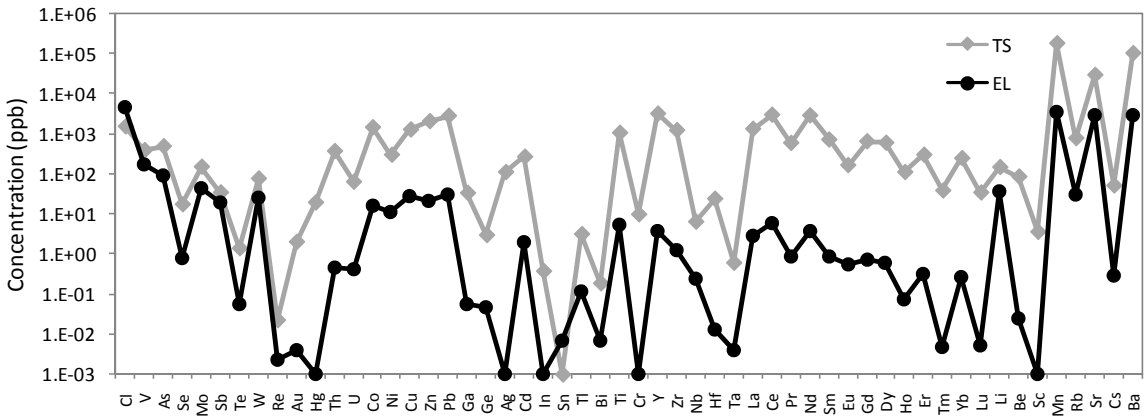

Fig 8. Comparison of average analytical concentrations for Enzyme leach and Terrasol leach. Concentrations are calculated as mean from all values analyzed and reported in parts per billion (ppb).

Transect Analysis

Elemental concentrations are plotted along their 1-D transects to observe correlations with known geologic features (Fig. 9). Apical anomalies observed within the range front indicate a strong response to mapped structures. Both EL and TS transects reveal apical anomalies over the Socorro Canyon range bounding fault and associated landslide scarps, as well as several implied blind faults transecting the Socorro Basin. There is no surface expression for other buried faults, however domino-style faulting associated with the Socorro peak uplift suggests that synthetic faults may propagate well into the basin below the valley fill (Chamberlin,1999). Enzyme leach REE profiles (La-Lu) and HFS elements (Zr, Nb, Hf, Ta) indicate at least several buried paralleling faults within the basin as well as significant responses along the Socorro Canyon Fault, particularly southward along the SL6 transect (Fig 9.a). Terrasol leach REEs, HFSEs and lithophiles (Ba, Eu, Sr, Tm, Yb, La) illustrate these basinward apical anomalies with remarkable repeatability (Fig. 9.b).

A plot of Enzyme leach intensity across the Socorro Canyon main boundary fault and Woods Tunnel fault confirm a strong correlation with structural conduits (Fig.10). The

distribution of these anomalies to the east of the main boundary fault also represents preferred migration through the low angle footwall block where volatiles are liberated at varying depths. These linear anomalies tend to retain the same geometry from element-suite to element-suite, though offset one another in an east-west sense. Figure 9 represents a repeating pattern of EL REE apical anomalies occurring approximately 150m to the west of lithophile and base metal anomalies over the Woods Tunnel fault. This rotated fault dips to the east at approximately 30° (Chamberlin, 1999), allowing REEs to liberate from the fault at shallower depths and lithophiles from a greater depth (Clark 1997) creating an exaggerate offset. This anomaly pattern confirms a shallow dip to the conduit structure as surmised by Hamilton (2004) in a model for Basin and Range-type block-faulted geothermal systems (Fig. 2).

Comparing EL and TS profiles, particularly the REE and HFSE groups, suggests the occurrence of volatile anomalies forming along faults. Figure 11 illustrates the location of anomalies for both EL and TS REE profiles, using the example of La values. TS profiles illustrate multiple apical anomalies aligned parallel to mapped and unmapped structures. EL profiles of the same elements reveal fewer anomalies clustering closer to the Socorro Canyon fault, yet occupy the same locations as those mapped by TS. TS is a stronger leach and expected to detect a greater number of anomalies from a deeper or less robust electrochemical source. Those anomalies detected by both EL and TS along Socorro Canyon fault may also represent more permeable and active conduits for trace element migration and geothermal fluids at depth, possibly indicating an upflow zone.

Apical anomalies corresponding with mapped structures may also be observed near the top of the mountain range. A single E-W trending sampling line (SL 4) traverses the Socorro Mountains just to the south of Socorro Peak. Paired or “rabbit ear” anomalies are observed mainly within oxide suite/commodity profiles (I, Br, V, As) and most lithophile suite profiles, particularly for Sr, Y, Li (Fig. 12). Multiple TS elemental profiles show very strong responses

within this part of the sampling area (La, Th, Sb, Yb, Tm, Be Zr, Hf) suggesting possible permeable structures west of the range front. The near vertical nature of mapped faults in this area results in strong overlap between anomalies of different element groups. Unfortunately, these anomalies are only represented by a single sampling transect, thus a 2-D surface geometry may not be deduced.

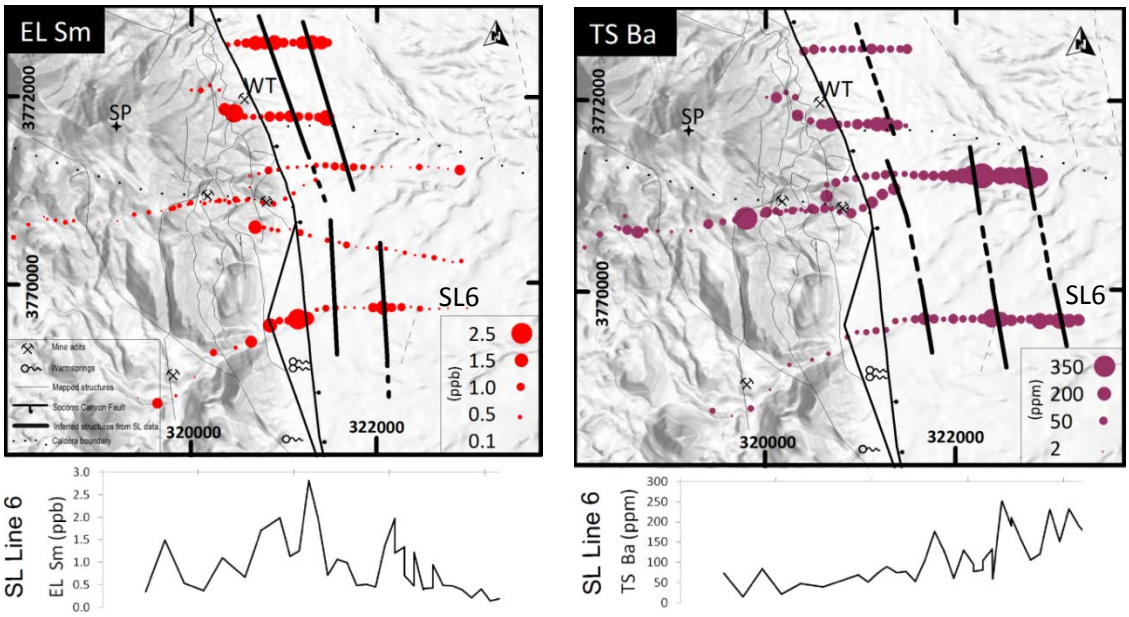

Fig 9. a) Relative concentrations of Sm as extracted by Enzyme leach. Size of filled circles illustrates relative intensity of anomalies. Concentrations are plotted linearly. Similar EL profiles are demonstrated for all REEs and HFSEs. Underlying graph represents concentrations plotted for SL6 (southern-most transect) illustrating apical peaks associated with mapped anomalies. b) Relative concentrations of Ba as extracted by Terrasol leach. Similar TS profiles are mapped for several REEs, HFSEs, and other lithophile elements. Legend found in Fig.9.a applies to all future maps. Mapped faults and trace of Socorro canyon fault are from Chamberlin, 1999. Socorro Peak (SP), Woodstunnel mine (WT), Merrit mine (MM) and Dewey-lode mine (DL), and Socorro Canyon Fault (SCF) are illustrated in future maps.

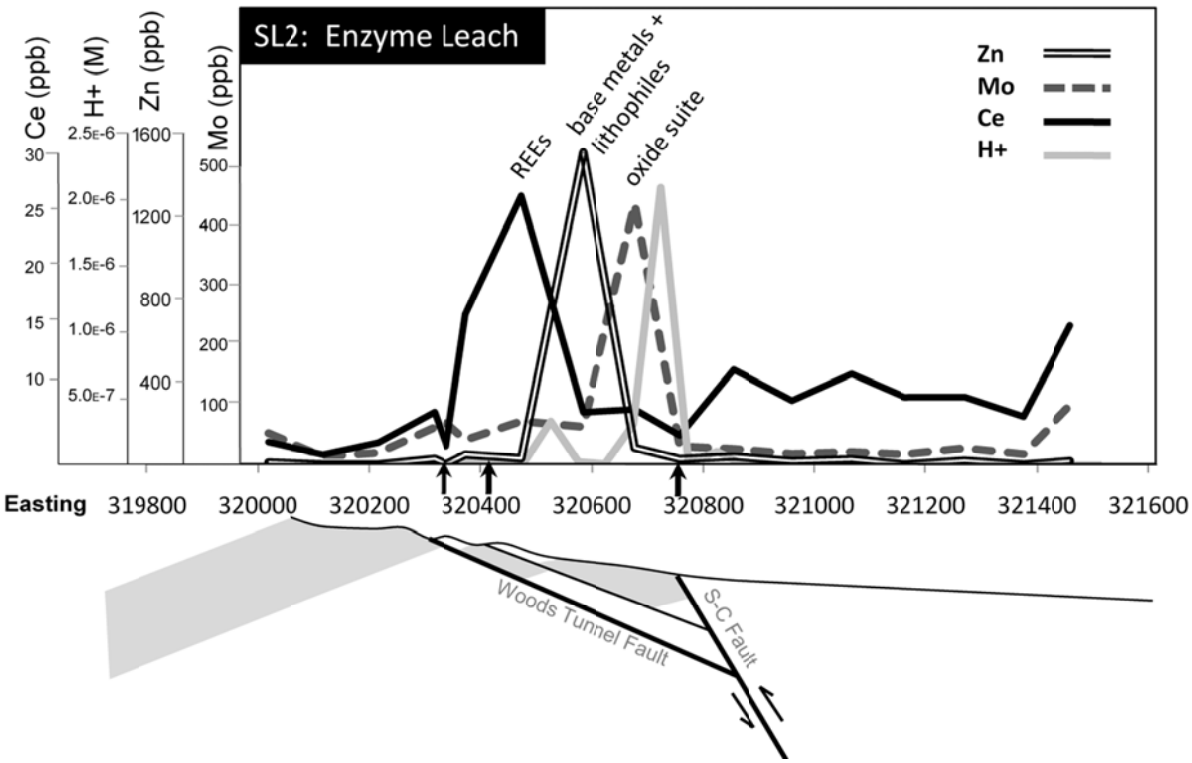

Fig 10. Apical peaks of common element groups mapped across the Woods Tunnel fault and cross-cutting Socorro Canyon fault illustrated in cross-section below. Peaks are offset eastward from the Woods tunnel fault moving down-dip within the footwall. Black arrows indicate location of fault traces mapped at surface.

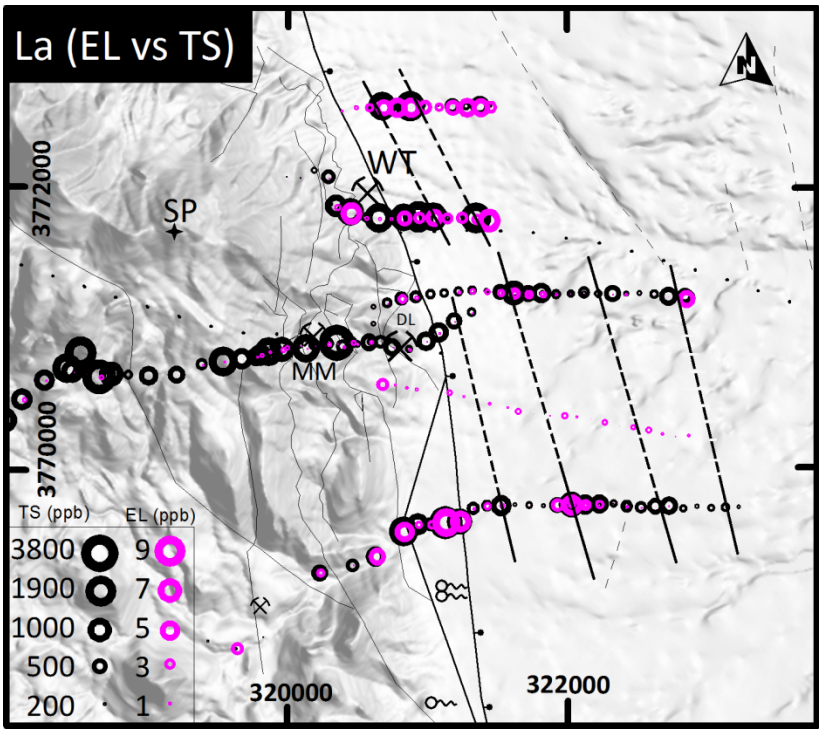

Fig 11. Comparison of anomalies formed by EL and TS REE profiles. Black symbols represent TS La values; pink symbols represent EL La values. Dashed lines represent interpreted structures from apical anomalies. Similar profiles are indicated for all HFSE and REE elements.

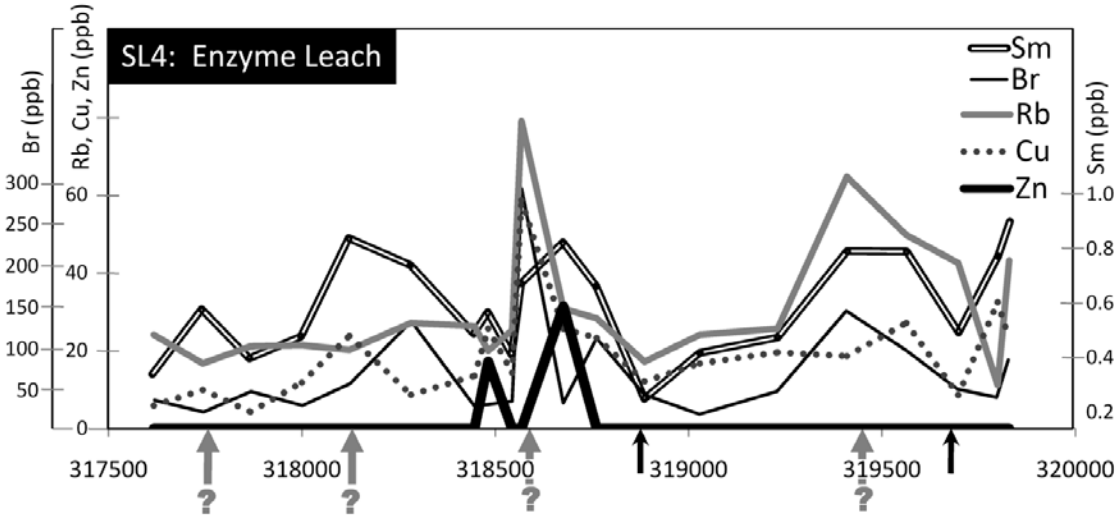

Fig 12. Apical anomalies forming along SL4 transect crossing the ridge of Socorro Hill. Anomalies for various element groups analyzed by Enzyme leach overlap without offset correlating well with high angle structures. Black arrows illustrate location of mapped faults. Gray arrows illustrate locations off possible unmapped structures corresponding with apical anomalies.

Base Metals

Certain base metal (Co, Cu, Zn, Pb) and chalcophile (Cd, Bi, Sn) profiles for both EL and TS illustrate strong apical peaks along the range front focused near Woods Tunnel and the western edge of transect SL5 (Fig. 13.a). Though no significant base metal or chalcophile responses were measured directly over the Merrit mine or Dewey lode mine adits or their tailings piles, the focus of anomalies in the vicinity of these mineralized fracture zones is conspicuous. This group of elements forms cations which are strongly adsorbed by negatively charged Mn- and Fe-oxyhydroxides in the soil. Over time, these metals become incorporated into the crystalline soil coatings and soil regolith forming a more robust geochemical anomaly detectable by stronger leaches. Base metal concentrations are normalized to Mn values to test the hypothesis that observed base metal anomalies are caused by enhanced dissolution of Mn oxide coatings related to a past mineral deposit rather than a modern, ephemeral geothermal anomaly (Fig. 13.b). Normalization to Mn reduces the overall concentrations near mines and tailings piles; however these regions still exhibit strong anomalies, focusing the response along range-front faults. Apical anomalies within Socorro basin may also be resolved from the Mn-normalized profiles. These basinward anomalies correspond with some REE –interpreted structures (Fig. 9).

Soil pH

Soil pH transects illustrate an overall trend of anomalously high H^+ concentrations (pH ~ 6.5) along the range front fault, decreasing to background values within the alluvial basin (>9.2) (Fig. 14). These profiles also reveal significant responses along mapped structures particularly those paralleling the Socorro Canyon fault to the west within the foothills. The trace of the soil pH anomalies, however, is offset slightly from REE and HFSE anomalies in a general east-west sense (Fig 10). Soil pH anomalies do not correlate well to inferred lineaments within Socorro Basin as illustrated by selective extraction profiles.

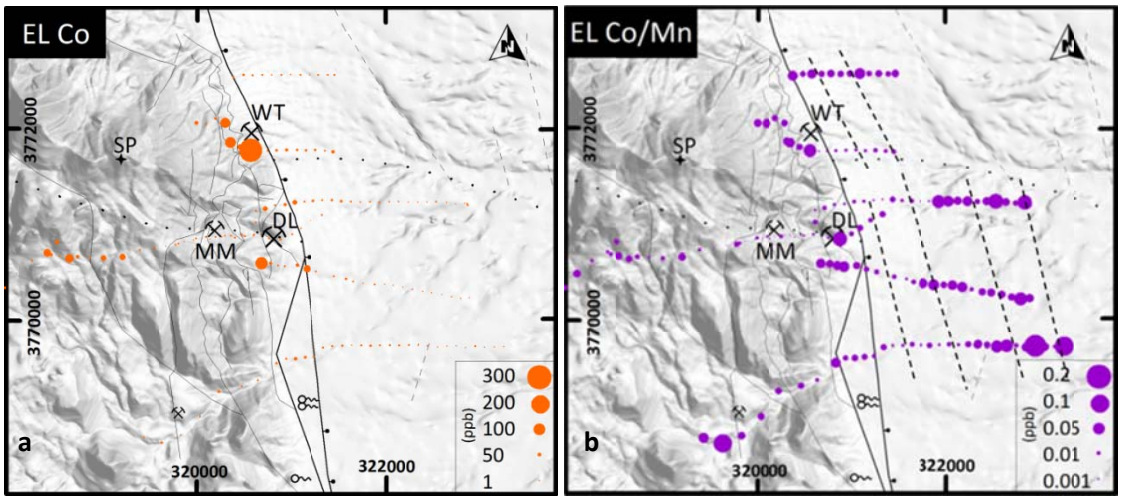

Fig. 13. a) Map of cobalt concentrations (ppb) prepared with Enzyme leach. Apical anomalies form near Woods Tunnel mine entrance (WT) and south of Merrit Mine (MM) and Dewey Lode Mines (DL). b) EL cobalt concentrations (ppb) divided by EL manganese concentrations (ppb). Residual values illustrate similar anomaly locations in Socorro basin corresponding with inferred structures from REEs profiles in Fig. 11 (dashed lines).

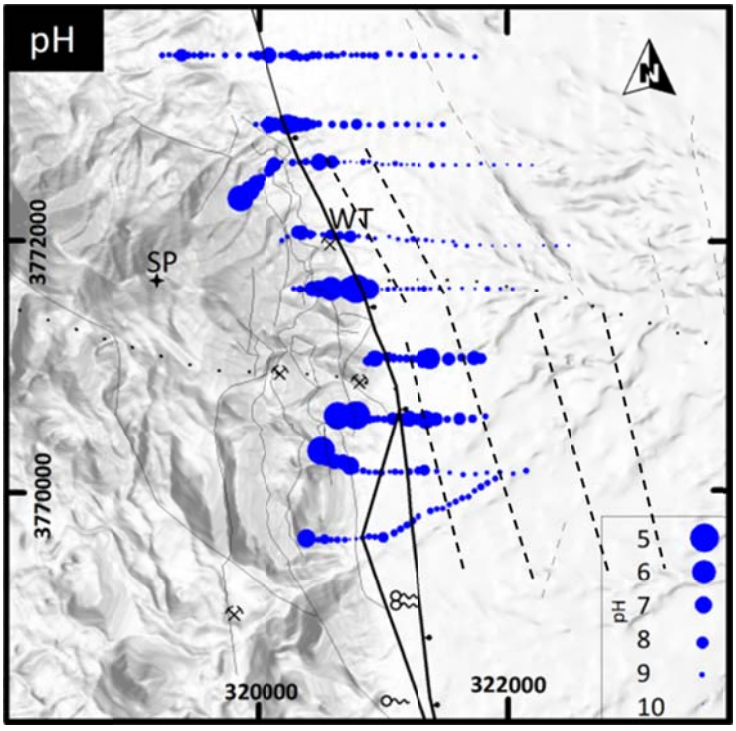

Fig. 14. Relative soil pH concentrations plotted along sample transects. Size of filled circle correlates with relative acidity or inverse of pH. Inferred structures from REE profiles (Fig. 11) are shown as dashed lines.

Gridded analysis

Oxidation type anomalies typically form above a reduced body buried beneath thick clays or alluvium (Clark, 1996). These anomalies typically take the shape of circular highs or "halos" circumscribing the outer boundaries of the buried body with a central low or "depletion" anomaly marking the scavenging of mobile ions to the outer edges of the geobattery formed near the surface. To investigate the occurrence of deeply buried geothermal fluids within the Socorro Basin, we plot 2-dimensional profiles of EL and TS concentrations and the formation of oxidation-type anomalies. Linear transects are declustered into a more equally spaced grid patterns to aid in krigging of the concentration data. Sets of data points are averaged every 500m, incorporating between 3-5 sample values, depending on transect spacing.

Contoured profiles of halogens (Cl, I, Br) and certain oxide suite elements (As, Mo, W, V, Ni, Se) illustrate major depletions occurring in Socorro Basin and may indicate tentative oxidation-type anomalies (Fig. 15). The center of these depletions occur over N3770000,E322000 within the basin, repeating over multiple elements. Terrasol leach W and Se profiles illustrate a central high at N3769721,E321779 within these larger depletions adding credence to a possible oxidation cell formed above a buried geothermal reservoir within the basin. A corresponding halo anomaly surrounding the central low, however, is not well defined within the limited extent of the survey.

Correlations with Groundwater

Geothermal fluids in this region are characterized by two geochemical endmembers, including the Woods Tunnel Test well, a moderate As, high Zn, high Na-Cl water; and the Socorro Springs cluster, a low Cl, low Zn, high As, Na-HCO_3-type water. The character and locality of these waters is likely governed by the type of a hydrologic unit from which these fluids are derived. The low Cl, high As warm springs appear to discharge locally from a fractured

Oligocene volcanic unit, while the high Cl geothermal fluids produce from a Proterozoic crystalline metasediment. For the most part, M-Mountain acts as a local catchment for meteoric waters, which make up the majority of shallow groundwater within Socorro Basin. These groundwaters are low in dissolved constituents, including Cl and As, and do not exhibit measurable mixing with the upwelling geothermal fluids within the basin.

Selective extraction 2-D profiles indicate a strong depletion in soluble oxide suite elements, particularly oxyanions Cl, As, Br, I, V, W, along the heavily fractured, E-W trending Socorro Caldron ring fracture zone with an apparent outflow plume within the basin (Fig.16.a). Selective extraction anomalies are often ephemeral and those compounds most soluble in water are likely to be influenced or eliminated by flooding events and surface water. Certain non-halogenated semi-volatiles, however, such as As and Se do exhibit a spatial correlation between groundwater concentrations and soil anomalies (Fig.16.b). Elevated concentration of these groundwater constituents may have a larger influence on anomalous soil concentrations than electrochemical cell formation.

EL and TS base metal anomalies appear to be heavily influenced by zones of mineralization as well as groundwater sources. Most metal concentrations in the warm springs and non-thermal groundwaters are very low, often below detection limits. Zn is, however, concentrated near the Woods Tunnel test well fluids and in selective extraction profiles (Fig.17.a and b). Zinc dissolves as a cation and is not very soluble in water, thus less likely to be carried far from its source or be disrupted by superficial flooding events. The source of the base metal soil anomalies near zones of mineralization is likely influenced by redistribution of mine regolith aided by upwelling geothermal fluids along the range front.

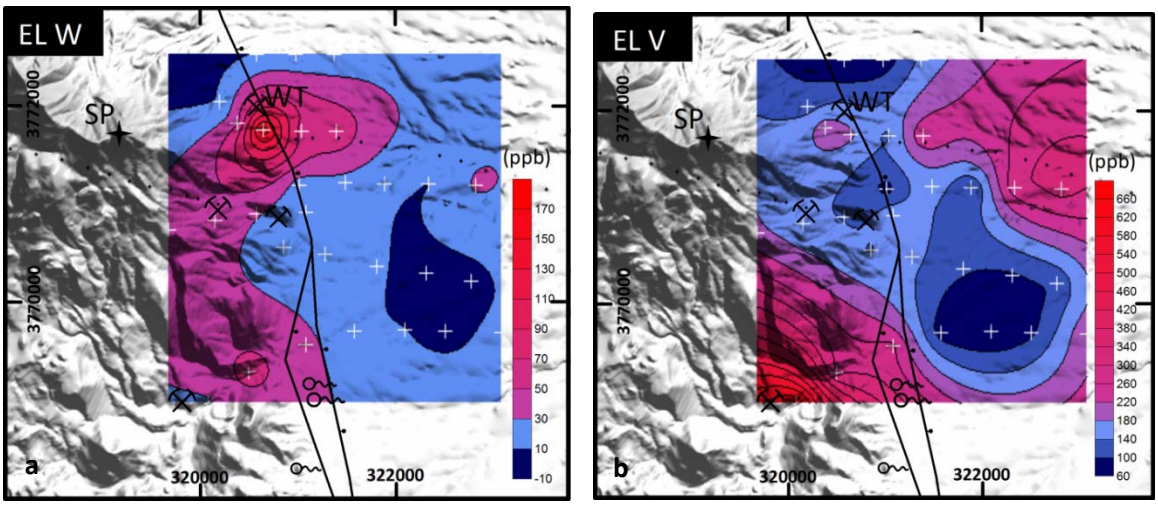

Fig. 15. Contoured concentrations of W and V prepared with Enzyme leach illustrating a large depletion occurring within Socorro Basin reporting at or below detection limits for both elements. White crosses mark locations for declustered data grid.

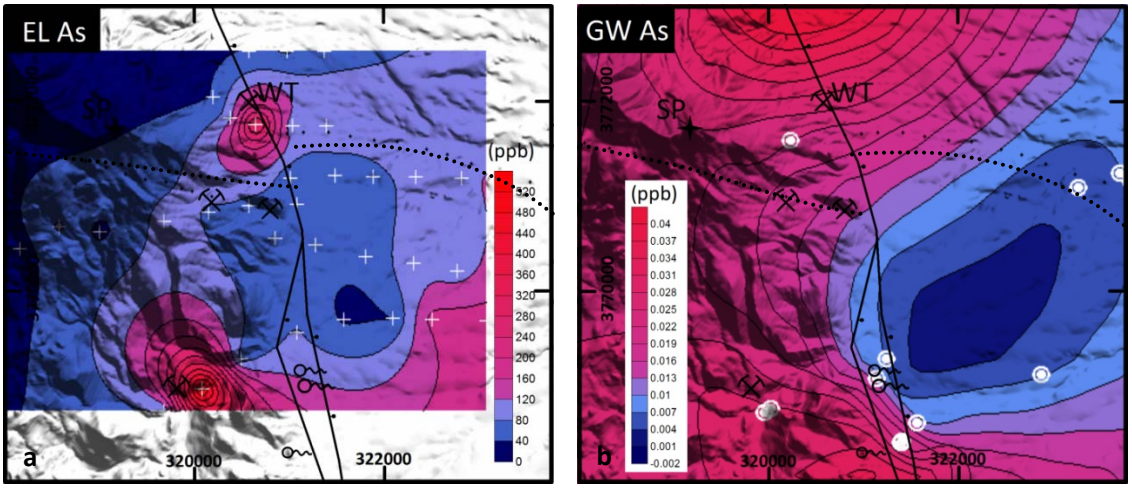

Fig. 16. (a) Contoured concentrations of arsenic prepared by Enzyme leach (ppb levels). White crosses indicate declustered data point locations. b) Contoured concentrations of arsenic in groundwater (measured in ppm). White circles indicate locations of sampled wells and spring galleries used for contour profile (all well locations shown in Fig.5). Black dotted line outlines trace of Socorro Cauldron.

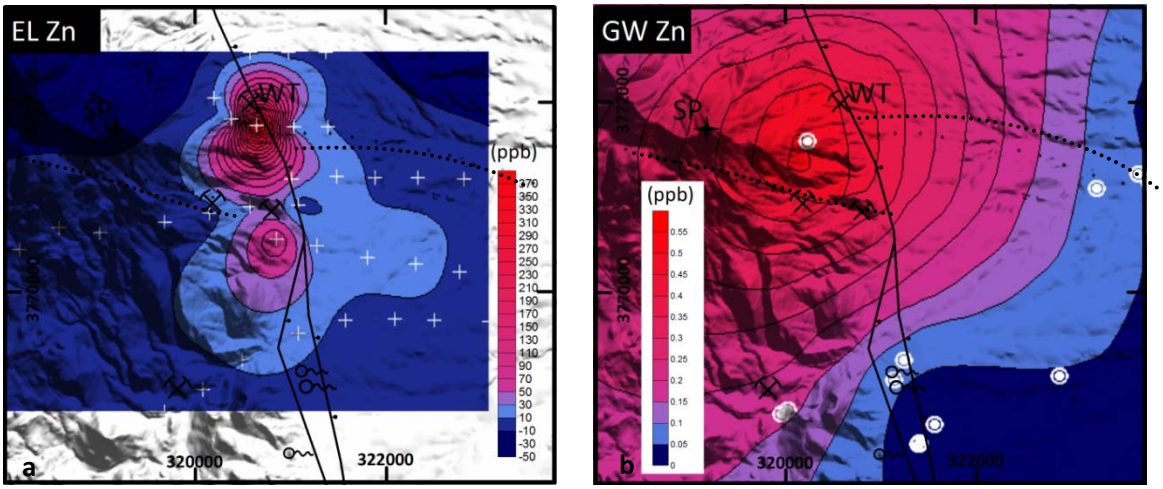

Fig. 17. (a) Contoured concentrations of zinc prepared by Enzyme leach (ppb levels). b) Contoured concentrations of zinc in groundwater (measured in ppm). Same symbols as represented in Fig. 16.

DISCUSSION

Influence of Structures on 1-D profiles

Locating zones of high structural permeability is important in geothermal exploration as it is often the target of test and production wells. Selective extraction profiles for both Enzyme leach and Terrasol leach methods illustrate resounding apical anomalies corresponding with mapped structural traces and implied buried faults paralleling the range bounding fault extending both east with the basin and west through Socorro Hills uplift. Strong responses occurring over the Socorro Canyon fault for EL, TS and pH profiles indicate that this structure may act as a primary conduit for geothermal fluid upflow or at least represent the boundary between saturated footwall strata and oxygenated basin fill at reservoir depths. Additional apical anomalies within the foothills indicate the importance of fracture permeability in focusing geothermal fluids within the uplifted horst block which has resulted in the north-south trending heat flow anomaly. High

fracture permeability, however, may not always produce elevated heatflow near the surface, particularly when insulated by thick overburden. This reality underlines the value of innovative exploration techniques, such as geochemical mapping by selective extraction, particularly in the case of a blind resource. South of Socorro Peak, hydrologic windows created within permeable volcanics express as thermal springs and high thermal gradients. The heat flow anomaly terminates north of Socorro Peak, however apical anomalies mapped by EL, TS and soil pH indicating high fracture permeability are still strong. Hydrologic units are likely faulted against impermeable units and buried deeply beneath alluvial fill. Similarly, several apical anomalies forming N-S trending structures may be illuminated within the Socorro Basin. These anomalies suggest the presence of buried permeable faults capped and thermally insulated by thick overburden and a shallow alluvial aquifer. Apical responses over the Socorro Caldron ring fracture zone along transects SL3 and SL4 are surprisingly poor, resulting in an apparent depletion for most element profiles west of the range bounding fault. Conversely, apical anomalies along the westward extent of SL4 suggest a great deal of fracture permeability within the uplifted mountain block. Anecdotal reports of warm springs and snow-melt observed within the westward slope at higher elevations of Socorro Peak supports the possible occurrence of permeable faults accessing geothermal fluids at depth.

The influence on permeable structures in the formation of apical anomalies appears to be significant in this case-study. Strong apical responses over Socorro Canyon fault, particularly to the south of the study area near Socorro Springs and other historic warm springs, verify the geologic mechanisms described for selective leach by Hamilton et al. (2004) and others. Using apical anomalies to target hidden structures at depth may prove to be the most powerful application of this tool.

Investigation of a Basinward Geothermal Aquifer

Hydrologic models predict the possible occurrence of deeply buried geothermal fluids within the Socorro Basin beneath thick clay-rich playa deposits. Proximity to New Mexico Tech campus and other sites for direct use make exploration in the basin desirable. The eastward extent of the selective leach transects were designed to occupy as much of the Socorro basin as possible and 2-D profiles were constructed to investigate the appearance of halo-shaped oxidation anomalies related to geothermal fluids at depth. Large depletions with values below detection limits for most oxidation-suite profiles(Cl, I, Br, Mo, W, V, Ni, Se) were mapped within the basin, centering in the middle of the study spanning nearly 2000 meters in diameter. Two TS profiles (W and Se) indicate tentative oxidation-type anomalies with the detection of focal highs at the center of the larger depletions, yet no definitive halo shapes forming along the perimeter of the depletions may be identified. It should be noted that likely extent of a stratified geothermal resource would eclipse the limited size of the study area and thus the observation of an outward halo anomaly. An alternative explanation for the occurrence of the basinward depletions may involve shallow groundwater effects. Meteoric runoff and occasional flash flooding from the Socorro Mountains feeds shallow water wells hosted within the Sierra Ladrones alluvial aquifer perched above the underlying playa deposits at >400m depth within the basin. These shallow waters are fresh and contain low dissolved solids, such as As, Cl, Br, Mo and Se. Weak, ephemeral anomalies formed at evaporation fronts in the soil may be subject to frequent removal by shallow groundwaters in this catchment setting.

Strong apical anomalies mapped within the basin strongly suggest domino-style faulting of basement strata at depth. These N-S trending faults are observed as far eastward as the boundary of the study area (~E323000) corresponding with several distal Quaternary faults mapped within the alluvium. Deeply buried geothermal fluids beneath impermeable strata may

still be signaled to the surface along open and active faults despite a lack of halo anomaly formation and elevated heat flow. The electrochemical response from low-temperature geothermal fluids may simply not be strong enough to form robust oxidation-type anomalies such as those found over more reducing ore bodies. In addition, the Socorro basin is also uniquely beset with several obstacles to volatile transmission including a thick playa clay zone, a perched shallow aquifer and a deep vadose zone isolating the buried target from the surface. Open and recently-active faults may penetrate these capping layers, however, allowing for greater transmission of trace elements to the soil evaporation front.

Agreement with other Geothermal Indicators

Heat flow studies are typically one of the most important tools in geothermal exploration yet may be hindered in certain blind systems. The local heat flow anomaly trends roughly N-S focused along the range front, incorporating the Woods Tunnel test well and Socorro warm springs. A similar trend is defined by apical anomalies, namely the clustering of certain Enzyme leach REE and LILE profiles along this Socorro Canyon fault. In addition, we see the continuation of high fracture permeability in the ridge top along SL4 where the heat flow contours extend eastward. A lack of thermal gradient wells at more rugged elevations, however, results in poor constraint of the heat flow anomaly in this area.

Microseepage of geothermal fluids along permeable faults appears to have a direct effect on the formation of soil anomalies at the surface. High apical anomalies for nearly all suites of elements show up near Blue Canyon thermal well and the Woods Tunnel geothermal test well, emphasizing mobile geothermal constituents, such as As and Cl. Woods Tunnel test well fluids represent the highest salinity and predicted temperature in the geothermal study area and likely resemble the composition of isolated geothermal fluids beneath Socorro Basin if such a reservoir

exists. The elevated salinity and thermal character of fluids from the Woods Tunnel well appear to correlate with the intensity of the apical and contoured anomalies in the area. This would argue that geothermal anomalies in this case study are largely derived from a hydrologic process involving advection or dispersion of dissolved constituents to the surface rather than unique dependence on electrochemical cell formation.

Base metal and chalcophile concentrations are largely below detection limits in the hydrothermal fluids within the study area, which is reflected in the lack of EL or TS anomalies for base metals near any of these hydrothermal targets. Base metals, however are concentrated in certain areas along the range front corresponding with possible mine-adits and mine tailings. Suspicion of extraneous base metal concentrations in the leachate derived from soil regolith rather than those weakly adsorbed on the surface is confirmed. Due to evolving tectonic and hydrologic regimes, many geothermal systems in the Basin and Range province overprint older epithermal systems laced with various amounts of ore deposition and hydrothermal alteration. Delineating responses from reducing ore bodies and modern geothermal fluids proves difficult. Normalizing base metal and other regolith-forming elements by leached Mn or Fe values removes superfluous concentrations related to ore formation and reveals only weak anomalies associated with active, ephemeral electrochemical phenomenon. This method of correction, however, may work with only small or uneconomic-grade ore deposits as is the case of Socorro Peak. A larger deposit would likely form electrochemical responses overpowering the geothermal fluids thus restricting the use of selective extraction for hydrothermal exploration.

Assessment of Soil pH Method

The soil pH profile overlaps a large portion of the selective extraction sampling area yet does not occupy the same sampling locations allowing for only indirect comparisons between the

two methods. The formation of volatilized hydrogen ions in the soil atmosphere is similar to that of other compounds tested for with weak leaching methods thus we would expect near identical profiles. Though we observe good agreement along the range front, these correlations disappear within Socorro Basin. Halo shaped anomalies within Socorro Basin are not detected here by soil pH methods. Differences between the soil pH profiles and selective extraction may be related to (1) the rate or mode of volatilization and transport mechanism of H^+ in the subsurface, (2) the simple washing method from which H^+ is removed or "extracted" from soil coatings in this study, (3) differences in soil retention of H^+ volatiles on soil coatings and its susceptibility to changes in the soil atmosphere (e.g. barometric pressure, evaporation), (4) inherent differences in soil pH as a result of organics, carbonates, Al^{+3} concentrations, or buffering by other non-detected factors. Each of these factors warrants further investigation for ideal application of the technique.

Application of soil surveys to geothermal exploration

The sensitivity and accuracy of geochemical mapping by selective extraction and soil pH in identifying a low temperature geothermal reservoir can only be quantified by comparison to geothermal wells which demonstrate the temperature and extent of the resource. A shallow test well near Woods Tunnel identified a feed zone sourcing from Woods Tunnel fault producing 42°C fluids with geothermometers estimating 60-65°C (Chapter 2). Resounding soil anomalies across the surface trace of the Woods Tunnel fault (Fig.10) are presumably derived from this shallow upflow zone. Testing of basinward anomalies cannot be fully realized without a deep exploration well penetrating the alluvium and capping Upper Popatosa playa units. In the meantime, we may still draw some conclusions about this method's universal application based on this case study.

These methods are proven here to be extremely capable at identifying microseepage along open faults and fractures. The large occurrence of H^+, LREE and LILE anomalies along mapped fault traces attests to the usefulness of the technique to resolve geothermal upwelling as these elements are likely to be the most mobile of all those analyzed. In the case of low angled faults, the distribution of element-groups may allow for the rough calculation of fault dip or depth to resource. Application of soil surveys to other geothermal systems, particularly those associated with Rio Grande rifting, is specifically recommended for locating zones of high fracture permeability. Resources such as Dixie Valley, NV and Lightning Dock, NM, boasting a basal reservoir fed from fault-driven advection of deep geothermal fluids may also benefit from this form of surficial exploration. Deeper, confined geothermal aquifers without pervasive faulting may not generate sufficient electrochemical responses to be identified with this method. The occurrence of high salinity and high concentrations of dissolved geothermal indicator species in the prospect waters may enhance the results of this technique as it appears that dispersion may play an important role in the formation of soil anomalies.

There are many significant drawbacks and uncertainties associated with this method which may limit its application for both low and high temperature geothermal. (1) Geochemical mapping utilizing the selective extraction of trace elements requires the compilation of multiple profiles, each agreeing and contradicting each other to some degree, in order to develop a coherent model. As a result, certain factors are harder to distinguish, such as depth to resource. (2) The genesis of electrochemical signals, particularly those resolved by migration of volatilized trace elements, is not well understood. As a result, complications due to stratigraphic heterogeneity, variable barometric pressure and interference from other electrokinetic potentials may not be quantitatively accounted for. Knowledge of these factors may be applied in a multivarient treatment of the soil concentration data to best identify true geothermal signatures. (3) Areas where mine tailings and mine deposits at depth are known should be avoided.

Geothermal systems in the Basin and Range benefit from multiple generations of active extension and volcanism, and are likely to encounter overprinting from a paleohydrothermal system and associated mineralization. Future research in identifying anomalies featuring volatile and oxyanion-forming elements that are uniquely responsive to geothermal systems would help eliminate false positives above complicated hydrothermal provinces.

Calibration of this technique using known systems of well characterized temperature, stratigraphy and reservoir parameters is also suggested. Furthermore, the application of self-potential surveys over a known hydrothermal system would best delineate induced potential strengths and illuminate the degrees to which geothermal reserves induce electrochemical cells.

CONCLUSIONS

The investigation of selective extraction mapping over a low-temperature geothermal system has afforded insight on both the extent of the geothermal resource as well as the mechanisms involved in the formation of geochemical anomalies in such a setting. Apical anomalies forming over mapped faults imply a genetic relationship between structural conduits for geothermal fluids and the accumulation of anomalous trace element concentrations at the surface. Such anomalies commonly involve REEs, HFSE and geothermal indicator elements like As. Additional apical anomalies are formed basinward aligning parallel to the mapped range-bounding fault, suggesting possible upflow along buried faults beneath capping units within Socorro Basin. Oxidation-type halo anomalies were not convincingly observed in this case study, likely due to the weakness of the electrochemical cells produced. Anomalously high concentrations of elements, including As, Ba, Se, W, V, Zn and Ce, however, correlated with the

location of springs and wells in the study area exhibiting similar geochemistry. Terrasol leach profiles (a stronger leach) result in more intense anomalies populating more locations than Enzyme leach profiles, possibly due to a greater incorporation of trace elements into the soil regolith over time. Selective extraction methods are recommended for reconnaissance exploration of a blind geothermal resource and appear to identify hydrologic upflow of even low temperature geothermal fluids within a faulted basin.

REFERENCES

Anderson, L. and Johnson G., 1976, Application of self-potential method to geothermal exploration in Long Valley, California: Journal Geophysical Research 81, 1527-1532.

Bajc, A.F., 1998. A comparative analysis of enzyme leach and mobile metal ion selective extractions; case studies from glaciated terrain, northern Ontario: Journal of Geochemical Exploration 61, 113–148.

Barroll, M.W., 1989, Analysis of the Socorro hydro-geothermal system, central New Mexico [PhD Dissertation]: New Mexico Institute of Mining and Technology, 239 p.

Barroll, M.W. and Reiter, M. 1990, Analysis of the Socorro Hydrogeothermal system: Central New Mexico: J. Geophys. Res. 95, 21,949-21,963.

Boyd, T., Hall, J., Boyle, R., Cole, S., McBride, K., Hass, C., Anderson, A., Miranda, J., Benedict, M., Maddi, P., Evans, J., Coulson, C., 2011. The Feasibility of Geothermal Potential in the Rio Grande Rift Area of New Mexico and Texas. GRC Transactions. 35, 1551-1556.

Brandvolt, L., 2001. Arsenic in ground water in the Socorro Basin, New Mexico. New Mexico Geology 23, 2-8.

Bronicki, L.Y. "Geothermal Power Stations." Ormat. 2011. Web. http://www.ormat.com/research/papers/geothermal

Cameron, E.M., Hamilton, S.M., Leybourne, M.I., Hall, G.E.M., McClenaghan, M.B., 2004. Finding deeply buried deposits using geochemistry. Geochemistry: Exploration, Environment, Analysis 4, 7-32.

Cameron E.M., Leybourne, M.I. and Kelley, D.I., 2002. Exploring for deeply-covered mineral deposits: formation of geochemical anomalies in northern Chile by earthquake-induced surface flooding of mineralized groundwaters. Geology. 30, 1007-1010.

Chamberlin, R.M.,1999, Preliminary geologic map of the Socorro quadrangle, Socorro County, New Mexico: New Mexico Bureau of Geology and Mineral Resources: Open-file Digital Map Series OF-DM-34, 46 p. (scale 1:24,000).

Chapin, C.E., and Cather, S.M., 1994, Tectonic setting of the axial basins of the northern and central Rio Grande rift, *in* Keller, G.R., and Cather, S.M., eds., ***Basins of the Rio Grande rift: Structure, stratigraphy, and tectonic setting:*** Geological Society of America Special Paper 291, 5-25.

Chapin, C.E., A.R. Sanford, D.W. White, R.M. Chamberlin, G.R. Osburn, 1979. Geologic Investigation of the Socorro Geothermal Area (N.M. Bur. Mines and Min. Res. Rpt. NMERDI 2-65-2301), 70 p.

Chapin, C. E., R. M. Chamberlin, G. R. Osburn, D. W. White, and A. R. Sanford, 1978. Exploration framework of the Socorro Geothermal Area, New Mexico, in Field Guide to Selected Cauldrons and Mining Districts of the Datil-Mogollon Volcanic Field, Spec. Publ. N. M. Geol. Soc. 7, 114-129.

Clark, J.R. and Russ, G.P., 1991, A New Enzyme Partial leach enhances anomalies in pediment soils near buried gold deposits (abs.): Assoc. Explor. Geochem. Symp., Reno, NV, USA.

Clark, J.R., 1993, Enzyme-induced leaching of B-horizon soils for mineral exploration in areas of glacial overburden: Trans. Instn. Min. Metall., (Sect. B: Appl. Earth Sci.)102, B19-B29.

Clark, J.R., 1995, Method of geochemical prospecting, United States Patent 5,385,827, 20 p.

Clark, J.R., 1996. Unique significant Enzyme leach anomaly patterns in areas of tropical/subtropical weathering. Queen's University Conference Proceedings, Kingston, ON, 241–256.

Clark, J.R., Yeager, J.R., Rogers, P. and Hoffman, E.L., 1997, Innovative Enzyme Leach Provide Cost-Effective Overburden/Bedrock Penetration: Proceedings of Exploration 97, 371-374.

Clark, J.R., Hill, G.T., and Tompkins, R., 2003, Mapping of Reservoirs and Subsurface Structures Using Selective Analysis of the Surface Chemistry of Soil Particles: Trans. AAPG Annual Convention.

Corwin, R. and Hoover, D.,1979, The self-potential method in geothermal exploration: Geophysics 44, 226-245.

De Vivo, B., Belkin, H.E., Lima, A. 1997. Environmental Geochemistry: Site Characterization, Data Analysis and Case Histories. Elsevier.

EERE. "Direct Use of Geothermal Energy". DOE. 2012. Web. http://www1.eere.energy.gov/geothermal/directuse.html

Eggleston, T.L., Norman, D.I., Chapin, C.E., Savin, S., 1983., Geology, alteration, and genesis of the Luis Lopez manganese district, New Mexico. New Mexico Geological Society Guidebook 34, 241–246.

Ellis, A.J. and Mahon, W.A.J., 1964. Natural hydrothermal systems and experimental hot-water/rock interactions. Geochim. Cosmochim. Acta, 28, 1323-1357.

Ennis, D.J., 1996, The effects of K-metasomatism on the mineralogy and geochemistry of silicic ignimbrites near Socorro, New Mexico [*Masters Thesis*]: New Mexico Institute of Mining and Technology, 160 p.

Faulds, J., Drakos, P., Vice, G., Mayhew, B., Noel, D., 2011. The Pyramid Lake Paiute Reservation, Western Nevada (USA): Exploration for Blind Geothermal Systems in a Transtensional Displacement Transfer Zone. Proceedings of the New Zealand Geothermal Workshop. 33, 5p.

Fritz, D.E., Farmer, G.L., Verplanck, E.P, 2006. Application of Sr isotopes in secondary silicate minerals to paleogroundwater hydrology: An example from K-metasomatized rocks in the western U.S. Chemical Geology 235, 276-285.

Govett, G.J.S., 1976. Detection of deeply buried and blind sulphide deposits by measurement of Hq and conductivity of closely spaced surface soil samples. J. Geochem. Explor. 6, 359–382.

Govett, G.J.S., Dunlop, A.C. and Atherden, P.R. 1984. Electrogeochemical techniques in deeply weathered terrain in Australia. Journal of Geochemical Exploration, 21, 311–331.

Green, B.D. and Nix, R.G.,2006, Geothermal—The Energy Under Our Feet Geothermal Resource Estimates for the United States, National Renewable Energy Laboratory Technical Report: NREL/TP-840-40665, 21 p.

Gross, G.W. and Wilcox R., 1983, Groundwater Circulation in the Socorro Geothermal Area: NMGS Guidebook, 34th Field Conference, pp. 311-318.

Hamilton, S.M., 1998. Electrochemical mass-transport in overburden: a new model to account for the formation of selective leach geochemical anomalies in glacial terrain. Journal of Geochemical Exploration 63, 155–172.

Hamilton, S.M., Cameron, E.M., McClenaghan, M.B., and Hall, G.E.M., 2004, Redox, pH and SP variation over mineralization in thick glacial overburden. Part I: methodologies and field investigation at the Marsh Zone gold property: Geochem.: Explor., Environ., Anal. 4, 33-44.

Hill, G.T. and Clark, J.R., 2000, Enzyme leach signatures of the Marigold Eight North and Clay Pit gold deposits, Humboldt County, Nevada: Geol. Soc. Nevada, Symp. 2000 Proceedings, p. 903-918.

Hill, G.T., Clark, J.R., and Lovstrom, K.A., 2001, Complementary selective extraction and biogeochemical patterns at the I-10 and Dragoon skarn/porphyry deposits, Cochise County, Arizona, Abs.: 20th IGES Abstract Volume, p. 79-81.

Hill, G., Norman, D.I., L. Owens, L.B., 2006, Surface Geochemistry in Exploration for a Buried Geothermal System, Socorro, New Mexico: Proceedings 31st Workshop on Geothermal Reservoir Engineering, Standford University.

Hinz, N., Faulds, J.E., Moeck, I., Bell, J.W., Oldow, J.S. 2010. Structural Controls of Three Blind Geothermal Resources at the Hawthorne Ammunition Depot, West-Central Nevada. GRC Transactions. 34, 785-790.

Hinz, N.H., Faulds, J. E., Stroup, C. 2011. Stratigraphic and Structural Framework of the Reese River Geothermal Area, Lander County, Nevada: A New Conceptual Structural Model. GRC Transactions. 35, 827-832.

Kratt, C., Coolbaugh, M., Peppin, B., Sladek, C., 2009. Identification of a New Blind Geothermal System with Hyperspectral Remote Sensing and Shallow Temperature Measurements at Columbus Salt Marsh, Esmeralda County, Nevada. GRC Transactions. 33, 481-486.

Matlick, S., Jayne, T., 2008. Brawley--Resurrection of a Previously Developed Geothermal Field. GRC Transactions. 32, 159-162.

Mailloux, B. et al, 1999, Tectonic controls on the hydrogeology of the Rio Grande Rift, NM: Wat. Res. Resear. 35, 2641-2659.

Mann, A.W. , Birrell, R.D., Fedikow, M.A.F., de Souza, H.A.F., 2005, Vertical ion migration: mechanisms, soil anomalies, and sampling depth for mineral exploration: Geochemistry: Exploration, Environment, Analysis 5, 201-210.

Marjoribanks, R., 2010. Geological Methods in Mineral Exploration and Mining, 2nd ed. Chapman & Hall, London.

Newton, B.T., 2005, Geologic Controls on Shallow Groundwater Quality in the Socorro Basin, New Mexico. [Masters Thesis]: New Mexico Institute of Mining and Technology, 174 p.

Noble, R.R.P. and Stanley, C.R. 2009. Traditional and novel geochemical extractions applied to a Cu-Zn soil anomaly: a quantitative comparison of exploration accuracy and precision. Geochemistry-Exploration Environment Analysis 9, 159-172.

Norman, D.I., Bazrafshan, K., Eggleston, T.L., 1983, Mineralization of the Luis Lopez epithermal manganese deposits in light of fluid inclusion and geologic studies. New Mexico Geological Society Guidebook 34, 247–251.

North, R.M. 1983. History and Geology of the precious metal occurrences in Socorro County, NM. New Mexico Geological Society Guidebook 34, 261-268.

Reiter, M. and Smith, R., 1977, Subsurface Temperature Data in the Socorro Peak KGRA, New Mexico: Geothermal Energy Magazine 5, 37-42.

Reiter, M., Eggleston, R.E., Broadwell, B.R., and Minier, J.,1986, Estimates of terrestrial heat flow from deep petroleum tests along the Rio Grande rift in central and southern New Mexico: Journal of Geophysical Research, v. 91, p. 6225–6245.

Reiter, M. 2009. Heat-flow anomalies crossing New Mexico along La Ristra seismic profile. Lithosphere. 1, 88-94.

Ross, H., Blackett, R., Witcher, J., 1995, The Self-potential method: Cost-effective exploration for moderate-temperature geothermal resources. Proceedings: World Geothermal Congress.

Sanford, A.R., 1977, Temperature gradient and heat-flow measurements in the Socorro, New Mexico area, 1965-1968: New Mexico Institute of Mining and Technology, Geoscience Dept. Open-File Rep. 15, 19 p.

Sato, M., Mooney, H.M., 1960. The electrochemical mechanism of sulphide self-potentials. Geophysics 25, 226–249.

Scholle P.A. 2003. Geologic Map of New Mexico, New Mexico Bureau of Geology and Mineral Resources, Scale 1:500,000.

Smee, B.W., 1983. Laboratory and field evidence in support of the electrochemically enhanced migration of ions through glaciolacustrine sediment. Journal of Geochemical Exploration 19, 277-304.

Smee, B.W., 1998. A new theory to explain the formation of soil geochemical responses over deeply covered gold mineralization in arid environment. Journal of Geochemical Exploration 61, 149–172.

Smee, B.W., 1999, The effect of soil composition on weak leach solution pH: a potential exploration tool in arid environments: Explore 102, 4-7.

Summers, W.K., 1976. Catalog of Thermal Waters in New Mexico: New Mexico Bureau of Mines and Mineral Resources Hydrologic Report 4, 44-51.

Summers, W.K., Colpitts R.M.J., and Schwab, G.E., 1981. Hydrogeologic Evaluation of the Industrial Park Area, Socorro NM. Summers & Associates: Report to the City of Socorro Utilities Department. 105p.

Tompkins, R., 1990, Direct location technologies: a unified theory. Oil and Gas Journal, 126-134.

Witcher, J.C., 1988, Geothermal resources of southwestern New Mexico and southeastern Arizona: Field Conference Guidebook N.M. 39, 191-197.

Williams, T.M. and Gunn, A.G., 2002. Application of enzyme leach soil analysis for epithermal gold exploration in the Andes of Ecuador: Applied Geochemistry 17, 367–385.

CHAPTER 2:

Geochemical exploration of a low temperature geothermal system near Socorro peak, New Mexico using a multi-environmental-tracer approach

ABSTRACT

Geochemical exploration in low temperature geothermal settings is problematic, particularly owing to the lack of mineral-solute equilibria from extensive conductive cooling, mixing or dilution with groundwaters. We investigate an alternative geochemical tool-set for characterizing the geothermal potential of a well-studied low-temperature system near Socorro, New Mexico, including a suite of conservative and non-conservative chemical tracers such as Cl/Br, Li, B, As, $^{87}Sr/^{86}Sr$, $\delta^{11}B$, $\delta^{34}S$, $\delta^{13}C$, $\delta^{18}O$, $\delta^{2}H$, ^{14}C and ^{3}H. Exploration well NMTG2 drilled near Socorro Peak, provided the most primary endmember fluid samples for the investigation of this system. Na-Cl NMTG2 fluids exhibited elevated $^{87}Sr/^{86}Sr$ concentrations (0.721904) supporting deep recharge through Precambrian basement granite or metasediments. $\delta^{18}O/\delta^{2}H$ elevation profiles and C-14 radiometric dating describe a 17.6ka flow path losing over 1000m of hydrologic head from the point of recharge in the Magdalena mountains. Conversely, nearby Socorro springs indicate a much shorter and shallower pathway of 9.1ka penetrating through Cenozoic volcanics ($^{87}Sr/^{86}Sr = 0.712814$). Mixing of NMTG2 geothermal fluids is identified southward along the Socorro Canyon range front fault, yet not laterally within the Socorro Basin wells. Mixing models of high Cl thermal fluids within the Bosque del apache support geothermal upwelling as a source of mobilizing saline sedimentary brines. Review of geothermal equilibria relationships and the application of geothermometer calculations in the Socorro geothermal area demonstrates that mixing and conductive cooling play a significant role in invalidating the use of these tools. Near steady-state prograde and retrograde reactions with chalcedony and Mg-chlorite supports the tentative application of fast reacting silica and K/Mg geothermometers for high flow rate, unmixed fluids such as NMTG2. Geothermometer

calculations and speciation models predict 60-80°C at economic depths, corresponding with hydrologic models (Mailloux et al., 1999). Where mixing is suspected within high-solute geothermal fluids, plots of Mg, SO_4 and Ca concentrations help delineate thermal from non-thermal brines, owing to retrograde solubility of Mg-clays and gypsum.

INTRODUCTION

The State of New Mexico in particular is endowed with relatively high background heat flow (Reiter, 2009) and permeable, fractured bedrock (Mailloux et al. 1999). This combination has given rise to numerous low-temperature (< 80°C) geothermal systems throughout the southwest (Summers, 1976; Witcher,2002; 2005). Many of these unconventional geothermal resources have been utilized for aquaculture and greenhouse industries. Witcher (2002) reports that a total of 52 acres of greenhouses are being heated by geothermal energy generating annual gross receipts of 12 million dollars. Geothermal heat is also used in Tilapia farming in southwestern New Mexico. The USGS (Williams et al. 2008) and our own temperature estimates indicate that the known geothermal potential in New Mexico is between 163-170 MW of energy. These low enthalpy geothermal systems are also becoming of increasing importance in the field of energy development and direct use as enhanced technologies make more efficient use out of lower and lower temperatures. Electrical production is possible with fluids as low as 130°C with efficient cooling (Bronicki, 2011) and direct use applications have been applied with temperatures near 20°C (EERE-USDOE, 2012).

Traditional geochemical exploration techniques for geothermal systems rely on identifying modified groundwater compositions resulting from elevated temperatures, often greater than 200°C, including the use of geothermometery, stable isotopes and tracking thermally mobile constituents to name a few (Giggenbach, 1981, 1988; Craig, 1961; Ellis & Mahon, 1977). The

application of geothermometer calculations in lower temperature systems, is particularly flawed, as these suffer from re-equilibration of fluids at shallow temperatures, as well as mixing and contamination with sedimentary evaporite basins which can denigrate or mask any geothermal signature. The goal of this study is to assess the applicability of alternative geochemical indicators and non-thermal groundwater tracers to a low temperature system. Our study is focused on the Socorro Geothermal Resource Area because the plumbing and depth of circulation of this geothermal system is reasonably well known from prior studies (Barroll and Reiter,1990; Mailloux et al. 1999) and can be used to test our assumptions based on the multi-tracer approach.

The Socorro Geothermal Area is a classic example of a forced convection-type geothermal system (Smith and Chapman 1983; Forster and Smith, 1991). Two geothermal slim holes that were drilled to assess the viability of installing a district heating system on the campus of New Mexico Tech also provide new constrains on this geothermal system. This paper discusses the geochemistry of the thermal fluids (temperatures > 28°C) in the Socorro area, including the newly developed NMTG2 slimhole fluids, and attempts to characterize the hydrologic sources and pathways of the geothermal waters using a multi-isotope-tracer approach. A suite of conservative and non-conservative chemical tracers including [Cl]/[Br], [Li],[B], [As], $^{87}Sr/^{86}Sr$, $\delta^{11}B$, $\delta^{34}S$, $\delta^{13}C$, $\delta^{18}O$, $\delta^{2}H$, ^{14}C and ^{3}H, as well as several thermally-controlled mineral equilibrium relationships, are employed to (1) characterize and fingerprint the various fluids defining the resource, (2) delineate the source and main hydrostratigraphic units or structures controlling the transport of the geothermal fluids, (3) identify mixing or compartmentalization of geothermal fluids with adjacent aquifers, namely the contribution of high saline fluids to the Rio Grande, (4) evaluate and recommend a geochemical toolkit for the exploration of similar low temperature systems, including the tempered use of problematic geothermometer calculations.

GEOLOGIC BACKGROUND

The Socorro Peak area has long been recognized as a geothermal resource due to the expression of the thermal Socorro Springs, and has since been the subject of multiple geology and hydrology characterization studies (Anderholm, 1987; Barroll and Reiter, 1990; Chapin et al, 1978; Reiter and Smith, 1977; Sanford, 1968; Mailloux et al, 1999; Ennis et al, 2000). Extensive thermal gradient studies of the resource define a N-S-trending heatflow anomaly along the uplifted range front of the Socorro Mountains paralleling the Rio Grande Rift (Fig. 1). A significant heatflow depression in La Jencia Basin to the west of the mountains was also identified supporting the hydrologic model of deep fluid circulation and adjective transport of heat from depth (Fig. 2). Recharge from the topographically higher Magdalena Mountains is driven deep along steeply dipping stratigraphic conduits and recharged along the Socorro peak range front attributing to the observed heatflow profile. Warm springs occurring along the southern extent of the heatflow anomaly discharge across the range-bounding Socorro Canyon fault through hydrologic windows. Until recently, these springs were the only thermal waters observed and studied within the Socorro Peak Geothermal Area. They are characterized as dilute, arsenic-enriched 32°C fluids, yet have limited potential for geothermal use. Notably, the potable quality of the springs has made them one of the largest municipal water sources for the town of Socorro. The apex of heatflow calculated at 490mW/m^2 is measured inside Woods Tunnel, an abandoned silver adit below Socorro Peak, hosted within the crystalline Precambrian basement of the uplifted Socorro Peak horstblock (Fig. 2). This feature represents the site of the exploration slim hole NMTG2 which was drilled to 1100' in January 2010 accessing a new brackish geothermal endmember. In light of these new fluids, we attempt to investigate the hydrologic dynamics of the using geochemical fingerprinting.

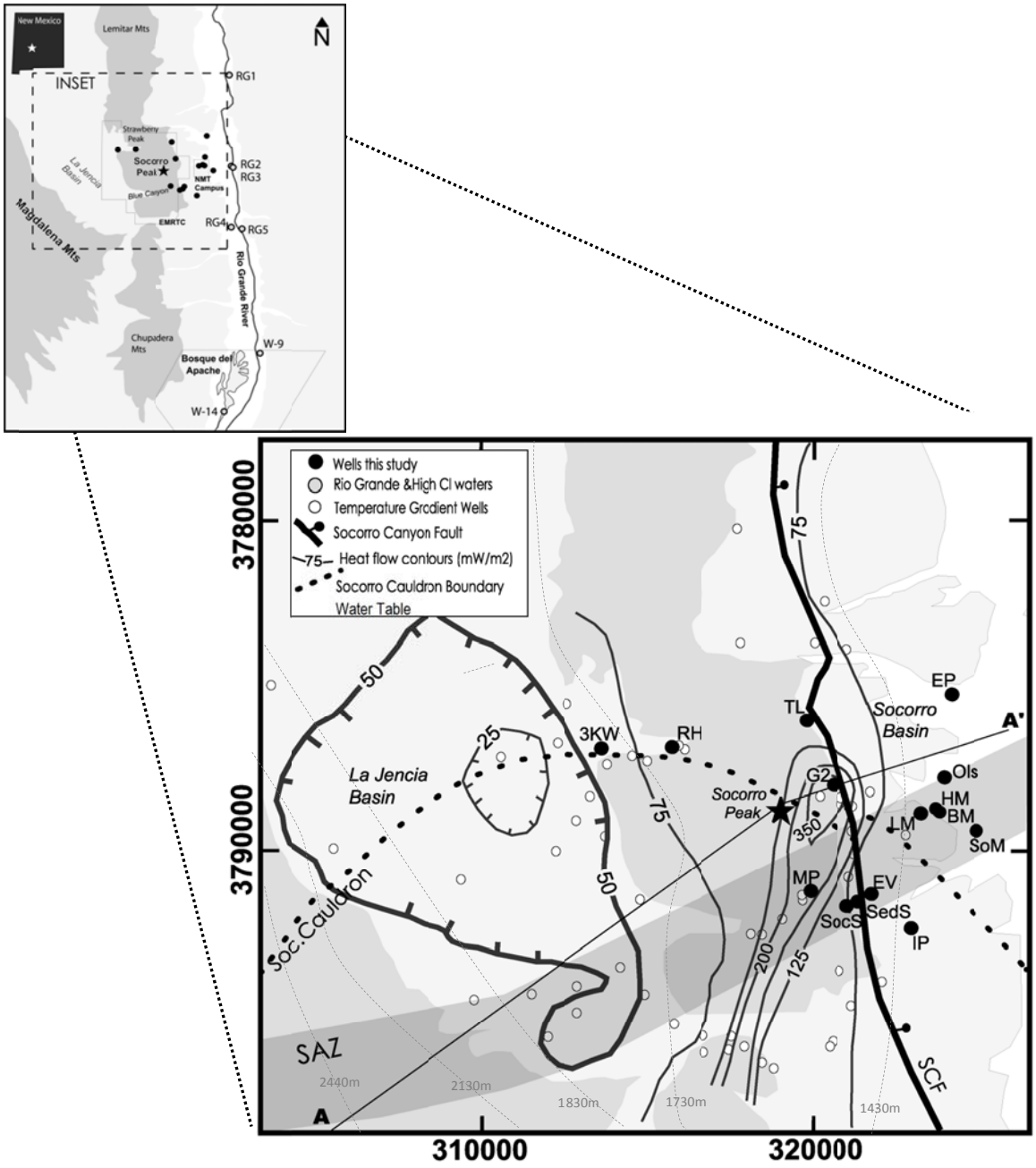

Fig. 1. Location of the Socorro Peak Geothermal anomaly, modified from Barroll and Reiter (1990). Figure on left hand side illustrates location of New Mexico Tech's property boundary, campus, Rio Grande Rift and Bosque del Apache, as well as several representative fluids from the Rio Grande watershed (RG1, RG2, RG3, RG4, RG5) and high Cl endmember fluids south of Socorro Peak near the Bosque del Apache (W-9 ,W-14). Inset figure on the right illustrates location of Socorro Peak, Socorro Canyon Range-Bounding Fault (SCF), Socorro Accommodation Zone (SAZ), the approximate boundary of the Socorro Cauldron, and multiple temperature gradient wells compiled by Barroll and Reiter (1990). Locations of fluids sampled for this study include: 3-K West (3KW), Rockhouse Lab (RH), Torres Lab (TL), Main Pad (MP), Eagle Pitcher (EP), Olsen (Ols), School of Mines (SoM), Evergreen (EV), Industrial Park (IP), Holmes (HM), Bushman (BM), Lattman(LM), Socorro Springs (SocS), Sedillo Springs (SedS), NMT Geothermal Test Well (G2).

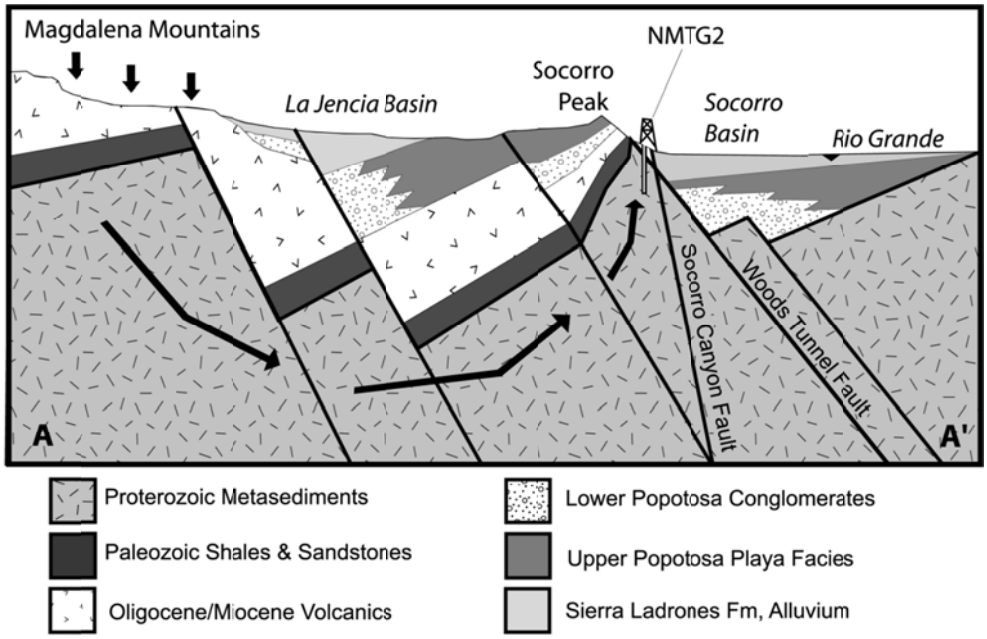

Fig. 2. Simplified stratigraphic cross section of the study area, representing A-A' transect in Fig. 1. Cartoon (*not to scale*) illustrates recharge in the Magdalena Mountains and observed upflow beneath Socorro Peak near NMTG2 exploration well.

Structural & stratigraphic controls

The Socorro Peak geothermal system is located in central New Mexico at the intersection of the Rio Grande Rift, Socorro Accommodation Zone (SAZ) and Socorro Caldron (Fig. 1), each with significant contribution to the structural complexity. Fault block rotation breaches a regional confining unit creating a hydrologic window and appears to be the locus of groundwater discharge at the base of Lemitar Mountains. Extentional block-faulting mechanism, which juxtaposes permeable units against one another at an angle, allows meteoric recharge to circulate much deeper in the earth's crust, whereby heating it to economic temperatures (Fig. 2). Various hydrologic studies (Barroll & Reiter, 1990; Mailloux et al., 1999) support this model near Socorro, invoking (a) recharge in the Magdelena Mountains to the west, (b) deep circulation

through fractured crystalline bedrock (Fritz et al. 2006) beneath the La Jencia Basin within downfaulted permeable strata, (c) advective upflow beneath at the base of Socorro Peak where water table elevations are thousands of feet lower, (d) demonstrating elevated heat flow values within the mountain block. Transport of heated fluids within the Socorro Peak horst block is likely aided by fracture permeability resulting from Socorro Cauldron ring-fracturing. The boundaries of this structural feature transect the Socorro Canyon fault near the center of the heatflow anomaly as measured by Reiter and Smith (1977). The N-S trending, range-bounding Socorro Canyon fault dividing the uplifted horst block and the Socorro Basin is likely a major component of vertical and horizontal flow in this hydrologic model. Lateral permeability across this fault feeding a deeper aquifer buried below Socorro Basin is also a central question addressed in this study.

Permeable crystalline and Paleoozic sedimentary rocks as well as a lateral stratigraphic sequence of alluvial fan and playa units block-faulted by Rio Grande rifting is fundamental to our conceptual model of deep fluid circulation and discharge through hydrologic windows (Witcher, 1988, Mallioux et al., 1999; Chapin et al., 1979). Socorro Peak is an uplifted fault block composed of Precambrian argillite overlain by alternating sequences of fractured Paleozoic limestones and less permeable Sandia shales. Volcanoclastics of the Spears formation would provide an overlying impermeable cap (Chapin et al., 1979). Oligocene welded tuffs are generally well-jointed, brittle and exhibit high K_2O overprinting associated with a paleogeothermal system alluding to their potential as modern reservoirs (Chapin et al., 1979; Fritz et al, 2006). Many current hydrologic models invoke these volcanic units as the main hydrologic conduit transporting recharge in the Magdalena Mountains to the Socorro warm springs (Maillox et al., 1999; Gross and Wilcox, 1983). Overlying landslide deposits associated with the collapse of the Socorro Caldera, also exhibit significant fracture permeability and may act locally as a hydrologic window for the Socorro hot springs (Chapin et al., 1979; Anderholm, 1987). Popatosa

Formation rift-fill units vary regionally in composition, thickness and hydrologic properties. Locally, the upper Popatosa represents a thick, impermeable, clay-rich playa facies, while the lower Popatosa contains more permeable quartzite and volcanic fanglomerates. In the Socorro and La Jencia basins, the upper and lower Popatosa units may act as an aquifer and capping aquitard capable of hosting a deep seated geothermal fluid.

Hydrologic setting and sampling locations

The structure of the Socorro Peak geothermal area is investigated by studying thermal and nonthermal fluids in the vicinity of the heatflow anomaly. Watertable elevation varies from about 2400 to 1700m above sea-level within the La Jencia Basin and drops down to 1400m in the Socorro Basin. This strong west-east hydrologic gradient drives interbasin transfers of fluids and is an important factor in explaining the position of springs at the base of Socorro peak. Water wells located within the perimeter of elevated heatflow near Socorro Peak are not common. This is largely due to the mountain topography and limited development on the hillslopes, as well as restricted public access to M-mountain within the confines of the New Mexico Tech Energetic Materials Research and Testing Center (EMRTC) security zone which utilizes the area for explosives testing and Homeland Security training. Thermal fluids include several high flow rate warm springs (~29°-33°C) near Blue Canyon, including Socorro Springs, Sedillo Springs and EMRTC Main Pad well, which have since been dug into galleries and are pumped for industrial or municipal water use. These waters issue from well jointed Oligocene volcanics faulted against lower Popatosa playa deposits, forcing the fluids to the surface. They are good quality waters with moderate As and SiO_2 concentrations, yet past tritium analyses indicate substantial dilution by surface waters (Gross & Wilcox, 1983). Cooler groundwater wells located proximal to Socorro Peak thermal fluids include Torres Lab well, 3K West well and the Rockhouse well, each sourcing from quaternary gravels, Popatosa conglomerates and playa units. Multiple wells situated downdip of Socorro Peak within Socorro Basin draw from the shallow aquifer of the

Sierra Ladrones formation of the Ancestral Rio Grande floodplain facies, including Evergreen, Industrial Park, Bushman, Lattman, Holmes, Olsen, Eagle Pitcher and School of Mines wells.

Additional endmember waters are included here as potential mixing components with the geothermal fluids investigated in this study. Surface and groundwaters along the Socorro reach of the Rio Grande may be characterized as dilute Na-Ca-HCO_3 fluids (Newton, 2004). Thermal and non-thermal high-chloride fluids are observed along the San Antonio-Bosque del Apache reach of the Rio Grande and have been thought to contribute to the step-wise increase in salinity of the river in this area (Mills, 2003; Hogan et al., 2007). Two unique waters are highlighted here. The Bosque del Apache W-14 is a moderately warm (29-32°C) brackish well water with approximately 1000ppm Cl (Brandvolt, 2001). Bosque del Apache well W-9 is a cooler (16-21°C) fluid yet brackish water with near 4000ppm Cl (Newton, 2004). Studies investigating the causes of Rio Grande salinization attribute the chloride in these wells to seepage of sedimentary brines (Newton, 2004; Phillips et al., 2003; Mills, 2003). Mapped and projected structures crossing the Rio Grande make it plausible that deep basinal brines are mobilized by thermal fluids transported from large distances away.

Fluid temperature profiles (Fig. 3), hydraulic head gradients, and fluid chemistry were collected from the recently drilled near Woods Tunnel below Socorro Peak to test the thermal potential of the study area. Well NMT4-67T is a corehole with total depth of 100m with static water encountered at 66m. NMTG2 is slimhole later deepened to 335m which penetrated several faulted units composed of Pennsylvanian aged sandstones and shales before crossing the low angle Woods Tunnel fault at 137m and entering the Precambrian metasediment bedrock. The static water table rose to 45m after well completion indicating a point of upflow. This yields a vertical hydraulic a gradient of about 0.1. Flow rates measured during drilling with air were consistently around 60L/s. Both of these observations suggest that the shallow bedrock and hydrothermally altered sedimentary units are highly fractured and permeable. Bottomhole

temperatures only rose to 42°C exhibiting an isothermal temperature profile associated with the Woods Tunnel fault zone. The near isothermal temperature profile near the bottom of the well suggests strong upward advection of heat up to the water table. We estimate a vertical thermal Peclet number as high as 10 using the well data. Advection of heat to the water table produced very high conductive thermal gradients within the unsaturated zone helping to explain the high heat flow measurements from shallow gradient holes. However, there are temperature overturns at a depth of 110 m suggesting transient, lateral fluids flow (Ziagos & Blackwell, 1986). An alteration assemblage of pyrite-galena-sphalerite-barite-quartz was encountered in veins throughout the mineralized core and cuttings derived from NMT4-67T and NMTG2, namely the within the Woods Tunnel fault. Calcite was prevalent in fractures and found superimposed on other mineralized zones. Stable isotopes of $\delta^{13}C$, $\delta^{34}S$ and $\delta^{18}O$ were analyzed for these secondary minerals to characterize their relationship to the historic and present-day thermal fluids.

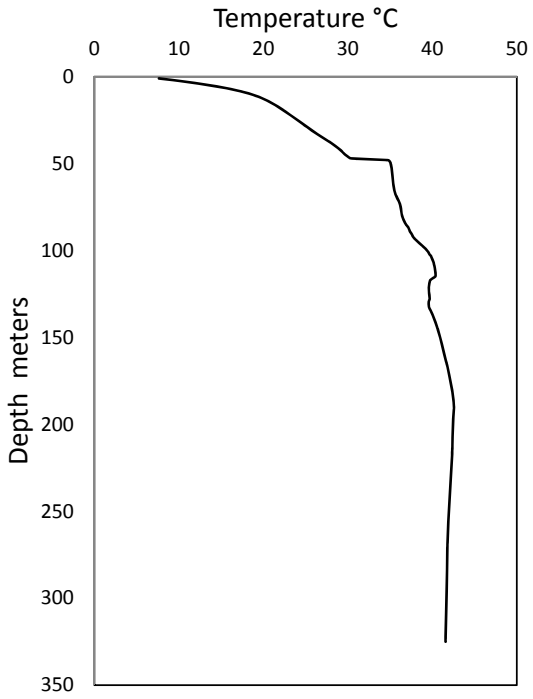

Fig. 3. Temperature with depth profile for NMTG2 slimhole. Data collected by Marshal Reiter, January 2010, 1 month following completion.

METHODS

Sixteen groundwater wells and springs within the study area were collected over multiple synoptic sampling events from 2005 to 2010. Well waters were sampled following the purging of at least 3 well volumes by pump, each well demonstrated high flow rates and permeability thus little contamination from storage. Fluids from NMT4-67T were bailed using a Teflon bailer with the water table at 65m. Several baleful were collected; both first and last samples were analyzed yet indicated no measurable change in chemistry. Specimens collected for major and trace element chemistry and ^{11}B isotope analyses were filtered to 0.45μm. Dissolved metal samples were preserved with ultrapure nitric acid to pH <2.0. Samples collected for sulfur and carbon isotopes were filtered to 1 μm.

Major chemistry was performed at the Bureau of Geology and Mineral Resources. Inorganic anions were determined by ion chromatography using a Dionex DX 600 ion chromatograph with an AS 50 auto sampler (EPA 300.0). Metals were determined using an Agilent 7500 ICP-MS (EPA 200.8). Alkalinity was determined by the titrimetric method (EPA 310.1) and reported as bicarbonate units. High chloride samples required dilutions up to 100x thus limiting reporting accuracy in some cases.

Oxygen, hydrogen, sulfur and carbon stable isotopes of waters and mineral separates from the NMT4-67 core and NMTG2 cuttings were prepared and analyzed at the New Mexico Tech Stable Isotope Lab. Aqueous SO_4^{-2} was prepared by precipitating as barium sulfate, dried and powdered. Barite, sphalerite, pyrite and galena mineral separates were collected from core samples. All samples were packed in tin cups and combusted at 1020°C in EA. SO_2 gas was run in continuous flow mode with Conflow II and Delta XP Mass Spectrometer. Mineral standards (AJC barite, NBS123 sphalerite and NZ2 Ag_2S) were used for the correction of the data and reporting with respect to VCDT (‰$\delta^{34}S$).

Carbon and oxygen isotopes were measured from aqueous DIC and calcite minerals. Barium carbonate precipitate was prepared from sample fluids. Carbonate powders were transferred to glass vials, flushed with helium gas, and treated with phosphoric acid. CO_2 gas was analyzed with Delta XP Mass Spectrometer in conjunction with a PAL autosampler and Gas Bench II continuous flow gas delivery system. Mineral standards (NBS-18, Solenhofen Limestone, and IAEA CO-9) within the run allowed for correction of the data and reporting with respect to PDB (‰$\delta^{13}C$) and VSMOW (‰$\delta^{18}O$).

All fluid samples were analyzed for oxygen and hydrogen isotopes. The oxygen composition was measured on 1mL samples of water using the CO_2 / H_2O equilibration method using a Thermo Finnigan Gasbench operated in continuous flow mode. The hydrogen gas was generated by metal reduction with powdered chromium at 850°C in an H-Device and analyzed in dual inlet mode. Both CO_2 and H_2 were analyzed on a Delta XP Mass Spec. All stable isotope results are reported as ‰$\delta^{18}O$ and ‰$\delta^{2}H$ with respect to VSMOW.

Oxygen isotopes of quartz and opaline mineralization were analyzed on a traditional silicate fluorination line. Silica separates were powered and placed in nickel reaction vessels. Contents of evacuated vessels were exposed to 500bar ClF_3 at 500°C for eight hours to liberate O_2 from silicates. Free oxygen was converted to CO_2 by heated carbon rods and collected in liquid nitrogen traps. The liberated CO_2 gas was analyzed with a Delta XP Mass Spec. Analyses were calibrated to oxygen isotope standards NBS-28 quartz and reported with respect to VSMOW (‰$\delta^{18}O$).

Strontium isotopes are measured at the University of Texas in Austin Clean facility using a Finnigan-MAT 261 thermal ionization mass spectrometer using NIST SRM 987 standards with a mean value of 87Sr/86Sr = 0.71024. Boron stable isotopes are measured at the Geochemical Technologies Co. Laboratory in Waco, Texas using a VG 336 thermal ionization mass

spectrometer using the extraction technique of Bassett et al. (1995) and standard NBS-951 with an accepted $^{11}B/^{10}B$ ratio of 4.04362. Carbon-14 isotopes were analyzed at Beta Analytic by accelerated mass spectrometry (AMS). Reported (raw) Apparent Radiocarbon Ages were reported in RCYBP (radiocarbon years before present; present = 1950), using the modern reference standard of 95% the 14-C activity of the NIST Oxalic Acid SRM 4990C, calculated using the Libby 14-C half-lift of 5568yrs. Conventional radiocarbon ages reported were corrected for isotopic fractionation using the carbon isotope $\delta^{13}C$ composition (Aggarwal et al., 2005). Tritium (H-3) values were determined at the University of Utah Dissolved and Noble Gas Laboratory by the method of helium ingrowth (Schlosser et al., 1988; 1989) following 8 weeks He-3 buildup from the decay of H-3 and analysis by a Mass Analyzers Products 215-50 Magnetic Sector Mass Spectrometer.

Table 1. Major Chemistry of spring and well fluids. All concentration values are in mg/L.
* Newton (2004)
†City of Socorro (2003)
‡City of Socorro (2000)

	Abr.	Easting	Northing	Elev (m)	Date	Temp (°C)	pH	Cond. (µS/cm)	TDS (mg/L)	CaCO3 (mg eq/L)	HCO3-	Br-	Cl-	F-	NO3-	PO4-3	SO4-2	Na	K	Mg	Ca	Cl/Br
EMRTC wells																						
3K West Site	**3KW**	313611	3773061	1739	3/13/09	7.3	8.6	285	147	31	115	<0.1	5	0.62	3.3	<0.5	13	44	1.7	3	7	….
3K West Site	**3KW**	313611	3773061	1739	11/11/08	7.3	8.5	275	145	37	125	<0.1	5.2	0.59	3.3	<0.5	13	46	1.8	3.6	8.7	….
3K West Site	**3KW**	313611	3773061	1739	2/18/10	7.3	….	….	….	….	….	0.067	4.9	….	….	….	….	….	….	….	….	74
RockHouse	**RH**	315717	3773115	1697	3/13/09	9.9	8.1	953	553	125	225	<0.5	63	0.55	3.0	<2.5	160	145	2.2	9	35	….
RockHouse	**RH**	315717	3773115	1697	11/11/08	9.9	8	940	544	136	245	0.30	62	0.47	3.1	<0.5	155	150	2.4	9.5	39	207
RockHouse	**RH**	315717	3773115	1697	3/13/05	9.9	8.2	840	546	109	240	<0.5	54	0.53	3.2	<2.5	140	135	2.5	6.8	33	….
RockHouse	**RH**	315717	3773115	1697	2/18/10	9.9	….	….	….	….	….	0.28	61	….	….	….	….	….	….	….	….	218
Torres Lab	**TL**	320084	3774004	1540	3/13/09	12	7.9	2113	1388	388	105	<1.0	57	1.79	6.9	<5.0	820	300	7.8	37	94	….
Torres Lab	**TL**	320084	3774004	1540	11/11/08	12	8.1	2130	1447	438	120	0.76	60	1.70	6.8	<2.5	845	315	8.9	41	108	79
Torres Lab	**TL**	320084	3774004	1540	2/18/10	12	….	….	….	….	….	0.67	57	….	….	….	….	….	….	….	….	84
Socorro Basin alluvial wells (NMT Campus Irrigation wells & City of Socorro Municipal wells)																						
Bushman	**BM**	323793	3771184	1413	3/10/09	21	7.7	1045	642	287	255	0.21	48	<0.5	2.1	<2.5	230	100	2.6	13	94	224
Eagle Pitcher	**EP**	324199	3774727	1430	3/6/09	19.1	8.1	389	226	131	135	0.06	14	0.42	0.71	<0.5	53	29	1.7	8.6	38	250
Eagle Pitcher	**EP**	324199	3774727	1430	5/17/05	19.1	8.1	385	234	122	150	<0.1	13	0.41	0.41	<0.5	51	28	1.8	7.1	38	
Evergreen	**EV**	321544	3768646	1487	3/10/09	18.6	8.1	738	428	117	175	0.09	68	0.91	<0.5	<2.5	110	100	3.2	9.3	32	725
Holmes	**HM**	323685	3771269	1419	3/19/09	20	7.8	514	301	161	155	0.11	22	0.40	1.50	<0.5	83	39	1.7	6.5	54	200
Olsen	**Ols**	323957	3772203	1430	5/16/05	20	7.9	475	293	139	170	<0.1	19	0.40	0.3	<0.5	68	40	2.1	6.4	46	….
Olsen†	**Ols†**	323957	3772203	1430	3/5/03	20	7.4	428	320	158	185	<0.1	21	0.46	0.57	<0.5	75	45	1.3	6.8	52	….
School of Mines	**SoM**	324916	3770597	1418	5/18/05	20	8	1090	674	291	255	<0.5	84	<0.5	<0.5	<2.5	210	102	5	11	100	….
School of Mines†	**SoM†**	324916	3770597	1418	3/5/03	20	7.5	850	640	290	249	0.21	82	0.36	0.24	<0.5	200	96	3.7	11	98	390
Industrial Park†	**IP†**	322985	3767640	1496	3/5/03	21.7	7.5	990	690	198	245	0.35	190	0.99	1.7	<0.5	86	150	9.3	11	61	543
Industrial Park‡	**IP‡**	322985	3767640	1496	9/6/00	21.7	7.7	1132	….	….	240	1.94	140	0.90	1.17	….	79.6	134	11.1	9.9	92	72
Lattman‡	**Latt‡**	323246	3771126	1433	2/11/00	20.9	7.8	669	….	….	176	0.35	33.9	0.43	3.43	….	156	55	2.22	8.1	84	98
Warm springs/wells																						
MainPad/ Blue Canyon	**MP**	319932	3768760	1591	3/13/09	33.3	8.4	424	233	68	145	0.50	17	0.64	2.3	<0.5	43	57	2.8	5	19	33
Sedillo Springs	**SedS**	321378	3768435	1504	5/14/05	33.1	8.3	330	211	61	155	0.12	12	0.56	1.9	<0.5	29	50	2.9	4.2	18	100
Sedillo Springs†	**SedS†**	321378	3768435	1504	3/5/03	33	7.8	289	220	58	156	<0.1	11	0.64	1.9	<0.5	28	50	2.5	3.8	17	
Socorro Springs	**SocS**	321064	3768297	1508	3/6/09	32.5	8.3	347	205	62	145	0.10	12	0.61	2.0	<0.5	29	50	2.6	4.8	17	123
Socorro Springs	**SocS**	321064	3768297	1508	5/15/05	32.5	8.2	330	237	59	155	0.08	12	0.59	1.9	<0.5	29	49	2.9	4.1	17	150
Socorro Springs†	**SocS†**	321064	3768297	1508	3/5/03	30.4	8	293	220	59	155	<0.1	11	0.63	1.9	<0.5	28	50	2.4	4	17	
NMT geothermal exploration well																						

NMT4-67T	**G**	320524	3771972	1564	1/8/07	34	11	2140	400	75	….	….	….	….	….	….	….	356	13	< 1.0	31	….
NMT4-67T	**G**	320524	3771972	1564	6/26/07	34	9.7	2708	….	….	….	….	….	….	….	….	….	495	21	….	56	….
NMT4-67T	**G**	320524	3771972	1564	4/12/08	34	8.2	3530	1868	209	150	1.2	865	1.20	<0.5	<2.5	220	570	24	9.1	70	721
NMT4-67T	**G**	320524	3771972	1564	3/4/09	34	7.3	3671	1970	361	300	1.4	880	1.40	<1.0	<5.0 (0.5)	190	560	25	20	110	638
NMT4-67T	**G**	320524	3771972	1564	11/11/08	34	8.7	3440	1802	224	99	1.2	850	1.40	<1.0	<5.0	210	580	25	7.8	77	708
NMTG2-450'	**G2**	320524	3771972	1564	11/17/09	42	8	3510	1961	330.8	290	<1.0	865	1.38	<1.0	<5.0	185	580	25	20	100	….
NMTG2-633'	**G2**	320524	3771972	1564	1/11/10	42	8	3860	2142	370	325	1.3	935	1.23	<0.5	<2.5	185	650	27	17	120	713
NMTG2-977'	**G2**	320524	3771972	1564	1/11/10	42	8	3780	2119	341	315	1.3	945	1.24	<0.5	<2.5	185	635	27	16	110	713
NMTG2-1085'	**G2**	320524	3771972	1564	1/11/10	42	8	3740	2092	328	305	1.3	935	1.24	<0.5	<2.5	190	625	26	16	105	696
Bosque del Apache High-Cl waters																						
W-14(warm well)	**W-14**	326200	3742344	1378	….	32.7	7.3	4528	3110	450	357	1.0	973	0.65	3.6	….	541	831	33	39	124	953
W-9(highCl)	**W83**	330343	3749068	1384	….	19	7.0	….	13890	2730	1065	3.7	3950	0.3	1.07	0.33	4500	3815	153	293	610	1068
Rio Grande Waters Socorro Reach*																						
W-Thomas1	**RG1**	326784	3781822	1405	ave 02-03	14	7.2	….	707	417.00	266	0.16	71	0.23	….	….	250	74	5.17	20	133	435
W-99.59	**RG2**	327085	3771091	1402	ave 02-03	14	7.6	….	403	217	223	0.15	37	0.43	….	….	99	57	4.43	11	69	239
R-99.59	**RG3**	327247	3771052	….	ave 02-03	14	7.9	….	424	212	209	0.17	42	0.50	1.95	0.56	113	62	5.16	11	67	251
BRN-E01	**RG4**	326998	3763940	….	ave 02-03	14	7.5	….	453	231	237	0.24	41	0.40	0.11	….	118	61	4.80	12	73	173
BRN-E06A	**RG5**	328299	3763779	….	ave 02-03	14	7.0	….	730	394	288	0.17	81	0.40	0.13	<0.5	240	87	7.8	23	120	476

Table 2. Trace Chemistry of springs and well fluids. All concentration values are in mg/L.

	Al	As	Ba	B	Cr	Cu	Pb	Li	Mn	Mo	SiO_2	Sr	U	V	Zn	Fe
EMRTC Wells																
3K West Site	0.001	0.037	0.012	0.09	0.010	0.001	<0.001	0.021	<0.001	0.001	22.7	0.08	0.00	0.070	0.014	<0.05
Rockhouse	<0.001	0.010	0.022	0.28	0.002	0.009	<0.001	0.194	<0.001	0.008	59.8	0.74	0.01	0.019	0.022	0.18
Torres Lab	<0.005	0.068	0.012	1.26	<0.005	0.009	<0.005	0.281	<0.005	0.066	55.1	2.89	<0.005	0.026	0.010	<0.25
Socorro Basin alluvial wells (NMT Campus Irrigation wells & City of Socorro Municipal wells)																
Bushman	<0.005	0.010	0.058	0.24	<0.005	<0.005	<0.005	0.059	0.024	0.005	29.7	0.56	0.11	<0.005	<0.005	<0.25
Eagle Pitcher	0.001	0.008	0.099	0.076	0.001	0.001	<0.001	0.068	<0.001	0.004	26.4	0.25	0.024	0.007	0.002	<0.05
Evergreen	0.001	0.010	0.045	0.17	0.002	0.003	<0.001	0.062	<0.005	0.013	41.0	0.71	0.007	0.017	0.002	<0.25
Holmes	<0.001	0.011	0.073	0.094	0.001	0.001	<0.001	0.041	0.029	0.004	27.9	0.32	0.051	0.004	0.002	<.05
Olsen†	0.007	0.009	0.044	0.15	<0.001	0.007	0.002	0.038	0.001	0.003	25.0	0.288	0.034	0.004	0.004	0.075
School of Mines†	<0.001	0.027	0.13	0.3	<0.001	0.001	0.002	0.046	0.76	0.005	26.0	0.73	0.007	0.001	0.002	0.14
Industrial Park†	0.002	0.024	0.078	0.16	0.003	0.003	0.003	0.2	<0.001	0.005	52.0	1.5	0.005	0.011	0.005	0.064
Warm springs/wells																
Main Pad/Blue Canyon	0.002	0.031	0.097	0.10	0.002	0.003	<0.001	0.057	0.008	0.003	21.4	0.40	0.00	0.012	0.029	<0.05
Sedillo Springs†	0.001	0.04	0.12	0.065	0.005	0.001	0.002	0.047	<0.001	0.002	22.0	0.31	0.002	0.011	0.003	0.002
Socorro Springs	0.001	0.045	0.14	0.080	0.006	0.002	<0.001	0.064	0.001	0.002	25.3	0.34	0.002	0.012	0.002	0.024
NMT geothermal exploration well																
NMT4-67T	<0.02	0.03	0.18	0.64	<0.02	0.05	<0.02	0.93	0.82	0.06	27.9	2.3	<0.02	<0.02	<0.02	0.053
NMT4-67T	<0.005	0.021	0.057	0.81	<0.005	0.014	<0.005	1.1	0.033	0.005	30.5	3.9	0.007	<0.005	0.57	<0.5
NMTG2-450	<0.02	0.029	<0.1	0.74	<0.02	0.034	<0.02	1.0	0.17	0.023	32.0	3.7	0.14	<0.02	<0.02	<1.0
NMTG2-450dup	<0.02	0.029	<0.1	0.76	<0.02	0.033	<0.02	1.1	0.17	0.027	32.1	3.7	0.14	<0.02	<0.02	<1.0
NMTG2-633	0.029	0.037	0.071	0.85	<0.005	0.006	0.007	1.2	0.26	<0.005	36.6	4.1	0.021	0.008	0.006	0.25
NMTG2-977	0.008	0.034	0.066	0.84	<0.005	<0.005	<0.005	1.1	0.24	0.005	34.4	4.1	0.024	<0.005	<0.005	<0.05
NMTG2-1085	<0.005	0.033	0.065	0.82	<0.005	<0.005	<0.005	1.1	0.20	<0.005	33.5	4.0	0.030	<0.005	<0.005	<0.05
Bosque del Apache High-Cl waters																
W-14 (warm well)	0.006	0.039	….	0.885	<0.001	0.015	<0.005	0.93	0.22	….	27.0	5.7	….	….	<0.03	1.25
W-9 (highCl)	<0.001	0.017	….	0.76	….	….	….	4.0	….	….	54	15.7	….	….	….	….
Rio Grande Waters Socorro Reach*																
W-Thomas1	….	….	….	0.09	….	….	….	….	….	….	….	1.10	….	….	….	….
W-99.59	….	….	….	0.13	….	….	….	….	….	….	….	0.85	….	….	….	….
R-99.59	….	….	….	0.13	….	….	….	….	….	….	….	0.73	….	….	….	….
BRN-E01	….	….	….	0.11	….	….	….	….	….	….	….	0.74	….	….	….	….
BRN-E06A	….	….	….	0.09	….	….	….	….	….	….	….	0.99	….	….	….	….

RESULTS

Major & trace geochemistry

Major and trace chemical values for the waters in the study area are presented in Tables 1 and 2. Piper diagrams of major geochemistry of the fluids in the study area (Fig. 4) reveal a strong correlation between composition and location, but with notable exceptions. Socorro Basin fluids, hosted within the Popatosa playa units and Sierra Ladrones aquifer may generally be characterized as a Ca-Na-HCO_3 fluids with strong overlap with Rio Grande waters along the Socorro Reach. Socorro Warm Springs are of a Na-HCO_3 type, while NMT geothermal fluids are a high TDS, Na-Cl type setting them apart from both thermal and non-thermal waters in the Socorro area. NMT geothermal fluids do exhibit a striking similarity to the Bosque high Cl and warm well fluids (W-14 and W-9) located 20 km south of the Socorro study area.

Plots of common geothermal indicators, namely Li and B, exhibit a strong correlation with TDS and Cl concentrations among thermal and non-thermal fluids (Fig. 5a & 5b). An even stronger correlation between Na:Cl (R = 0.97) and Sr:Cl (R=0.92) (Fig. 5c & 5e) is observed. Outliers include Torres Lab containing elevated B and Li concentrations and Bosque well W-9 containing far less boron than expected for its high Cl-composition. Arsenic concentrations are extremely scattered for this study area and are most elevated in the Socorro Warm Springs as well as Torres Lab well (Fig. 5d). We also observe a poor correlation between sampling temperature and chloride composition (Fig. 5f), underlining the unique difficulty in applying traditional chemical fingerprints in low temperature geothermal systems. Bosque warm well fluids (W-14) overlap with NMT geothermal fluids for all plotted constituents (Fig. 5a-5f).

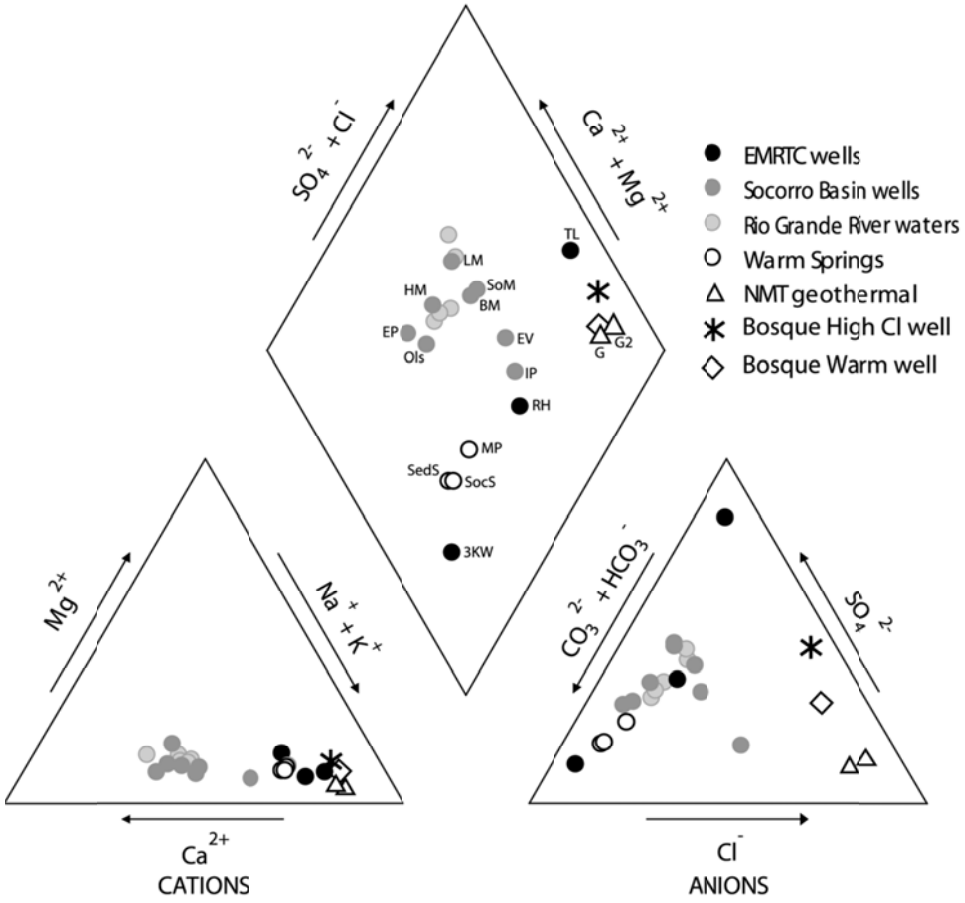

Fig. 4. Piper diagram illustrating mean chemical compositions for all fluids in study area corresponding to values in Table 1.

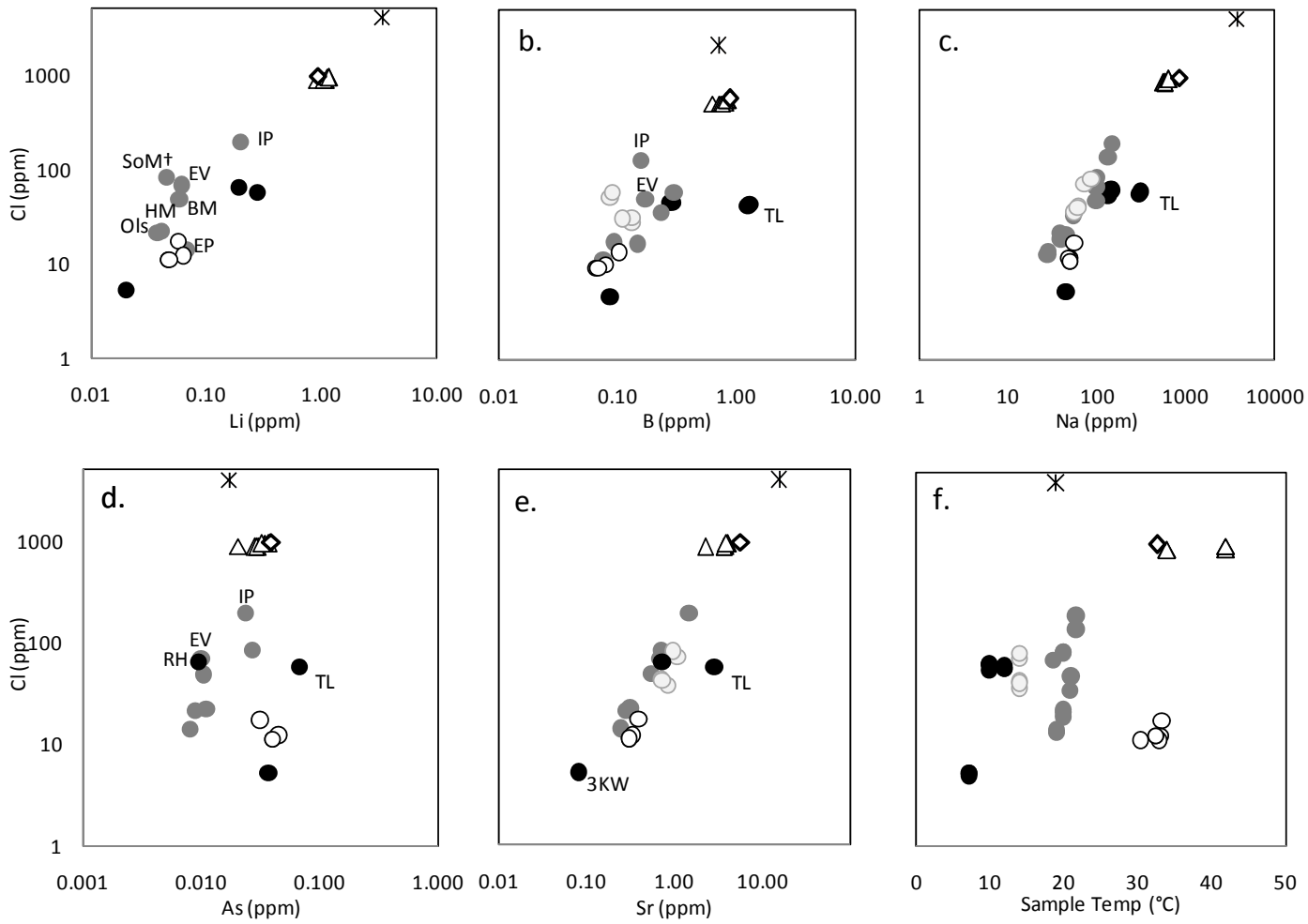

Fig. 5. (a-e) Plots of chloride concentrations versus common geothermal dissolved constituents. (f) Plot of chloride versus temperature of fluids at the time of sampling. Symbols found in Fig. 3.

Table 3. Stable isotope and radiogenic isotope values for selected sample locations.

	Date Sampled	$^{87}Sr/^{86}Sr$	$\delta^{34}S$-SO4 (‰)	$\delta^{18}O$-SO4 (‰)	$\delta^{13}C$-HCO3 (‰)	$\delta^{11}B$ (‰)	$\delta^{18}O$ (‰)	$\delta^{2}H$ (‰)	^{3}H (TU)	^{14}C (fraction mod C)	corrected ^{14}C age (yr)
EMRTC wells											
3K West Site	3/13/09	0.712394				3.7	-9.5	-63.2			
3K West Site	2/18/10				-14.5		-9.4	-63.6			
RockHouse	12/1/05						-9.4	-67.4			
RockHouse	3/13/09	0.711487				18.2	-9.5	-65.8			
RockHouse	2/17/10		5.4	6.9	-10.7		-9.5	-65.9			
Torres Lab	12/1/05	0.711873				19.0	-11.8	-86.3			
Torres Lab	3/13/09						-11.7	-85.9			
Torres Lab	2/17/10		6.1	7.0	-15.7		-11.8	-86.9			
Socorro basin alluvial wells (NMT Campus Irrigation wells & City of Socorro Municipal wells)											
Bushman	3/10/09	0.710103					-12.2	-90.6			
Bushman	2/17/10		0.9		-10.4		-12.2	-91.5			
Eagle Pitcher	12/1/05						-12.7	-93.7			
Eagle Pitcher	3/6/09	0.710138				4.2					
Eagle Pitcher	2/17/10		2.3	7.3	-10.6		-12.9	-95.4			
Evergreen	3/10/09	0.710262				10.3	-12.4	-90.7			
Evergreen	2/17/10		5.5	6.4	-9.6		-12.3	-91.0			
Holmes	3/19/09						-12.5	-92.7			
Holmes	2/18/10		1.1	4.1	-10.3		-12.8	-94.8			
Olsen	12/1/05						-12.7	-89.5			
School of Mines	12/1/05						-12.3	-90.1			
Industrial Park	2/17/10		5.9	6.5	-10.3		-9.8	-68.7			
Lattman	2/17/10		3.0		-11.8		-12.3	-92.4			
Warm springs/wells											
MainPad	12/1/05						-10.2	-70.9			
MainPad	3/13/09	0.712725				19.1					
MainPad	2/18/10		5.8	6.2	-13.3		-10.0	-69.4			
Sedillo Springs	5/14/05						-9.9	-66.5			
Sedillo Springs	7/15/10		6.1		-10.0						
Socorro Springs	12/1/05						-10.0	-65.2			
Socorro Springs	3/6/09	0.712814				7.7			0.15 ±0.10	0.2628	9,120
Socorro Springs	2/18/10		6.2	3.8	-10.0		-10.0	-69.2			
NMT geothermal exploration well											
NMT4-67T	3/4/09	0.721904	7.4	6.8	-6.2	14.7	-10.7	-74.5	0.39 ±0.19	0.0756	17,630
NMTG2-633'	1/11/10				-7.1		-10.6	-73.9			
NMTG2-977'	1/11/10		7.8	4.8	-6.9		-10.7	-75.2			
NMTG2-1085'	1/11/10						-10.6	-75.2			
Bosque del Apache High-Cl waters											
W-14 (warm well)	7/15/10		10.2		-9.5		-11.3	-86.7			
W-9 (highCl)	7/15/10		9.2		-14.7		-11.5	-89.6			

Table 4. Stable Isotope values for secondary mineralization obtained from NMTG2 drill cuttings and NMT4-67T core. Equilibrium temperature calculations for $\Delta^{18}O$ (calcite-H2O) from Friedman and O-Neil (1977); Temperature for $\Delta^{18}O$(quartz-H2O) calculated from Sharp & Kirschner(1994); Temperatures for $\Delta^{34}S$(sphalerite-galena) calculated from Li &Liu (2006) and Kiyosu (1973). Oxygen isotope geothermometers calculated from NMTG2 fluids (-10.7‰).

Depth (meters)		Isotopic Value (‰)		Equilibrium Temperature (°C)
Calcite	**δ13C**	**δ18O**	**δ34S**	**Δ 18O (calcite-H2O)**
66	-3.34	17.42		25
149	-5.03	6.09		94
198	-5.15	4.00		110
201	-6.47	3.73		113
250	-3.52	10.26		65
268	-4.85	11.95		55
287	-4.80	4.43		107
326	-6.63	4.35		108
Quartz				**Δ 18O (quartz-H2O)**
116		3.83		161
121		4.16		158
134		6.09		137
131		4.17		157
201		5.53		143
268		4.17		157
287		6.32		136
Sulfides/Sulfates				**Δ 34S (sphal-gal)**
98	*Sphal*		-6.26	
116	*Gal*		-8.12	243
	Bar		9.87	
	Sphal		-5.23	
125	*Py*		-3.69	
137	*Gal*		-10.42	287
	Sphal		-8.20	
	Bar		9.33	
201	*Gal*		-8.73	389
	Sphal		-7.46	
	Bar		9.76	
250	*Sphal*		-8.12	
265	*Py*		-6.62	
280	*Sphal*		-6.62	

Isotopic tracers

Oxygen-18 and Deuterium

Stable and radiogenic isotope values for selected fluid samples are located in Table 3. Oxygen and deuterium stable isotope concentrations for the study area, including the NMT Geothermal fluids, fall largely on the meteoric water line (Fig. 6), exhibiting no measurable amount of oxygen enrichment due to crustal exchange at high temperatures (Craig, 1961; 1963). Socorro warm springs appear slightly enriched compared to the NMT geothermal fluids underlining the apparent uniqueness between these two thermal waters. Most Socorro Basin wells overlap with Rio Grande surface and groundwater values yet cluster near the intersection of the meteoric water line and the evaporation-derived (RGWL) Rio Grande Water Line (Mills, 2003). Bosque warm and high-Cl fluids fall considerably off of the MWL and overlap with river waters and the RGWL. Because the Bosque del Apache is a surface water feature fed by the Rio Grande, the shared stable isotope compositions of these saline groundwaters with river waters may be merely coincidental. These saline fluids may alternatively plot as an extension of a formation water line representing deep paleofluids (Hoefs, 2004; Taylor, 1974) or exchange with a hydrologically isolated sedimentary basin.

Elevation Models

The conservative nature of oxygen and deuterium stable isotopes may aid in determining the elevation and provenance of geothermal fluids near Socorro Peak. Snow pack recharge studies by Earman et al.(2006) observed an isotopic depletion relative to altitude effects for the 3,300m high Magdalena Mountain range to the west of Socorro Peak, a likely source of recharge for Socorro's geothermal fluids. A tentative altitude depletion line is derived locally for the Magdalena Mountains based on composite recharge compositions from snowpack and summer precipitation values (Fig.7a). To make a reasonable fit, this line excludes data from the highest

elevations (3243m) which may be skewed during sampling due to exposure and frequent storm conditions (Earman et al., 2006). The resulting slopes of Δ^2H/Δelevation (-1.34‰/100m) and $\Delta^{18}O/\Delta$elevation (-0.22‰/100m) are similar to other studies in New Mexico (Vuataz & Goff, 1986). The $\Delta^{18}O/\Delta$elevation trends are applied to determine the possible recharge elevations for the various waters near Socorro Peak (Fig.7b). Similar results are produced using Δ^2H/Δelevation trends. The lightest waters in this suite belong to the Socorro Basin alluvial wells which likely derive their isotopic composition from the depleted Rio Grande which sources from the higher altitudes of the Colorado Rockies. The next lightest fluids are the NMT Geothermal fluids which may correspond to recharge in the Magdalena Mountains as predicted by multiple hydrologic models discussed above. These results discount significant recharge within La Jencia basin which would likely produce much heavier isotopic waters. Slightly enriched Socorro warm springs correlate with either lower-elevation recharge in the Magdalena mountains or mixing between local (Socorro Peak catchment) and distal (Magdalena catchment) fluids. The dilute nature of these warm springs makes the latter scenario more probable. Rockhouse and 3K West wells are among the most dilute and isotopically heaviest waters in the area. Their location on the foothills of Socorro Peak and Strawberry Peak make these likely recharge catchments for the EMRTC fluids rather than upwelling from a deeper fluid source.

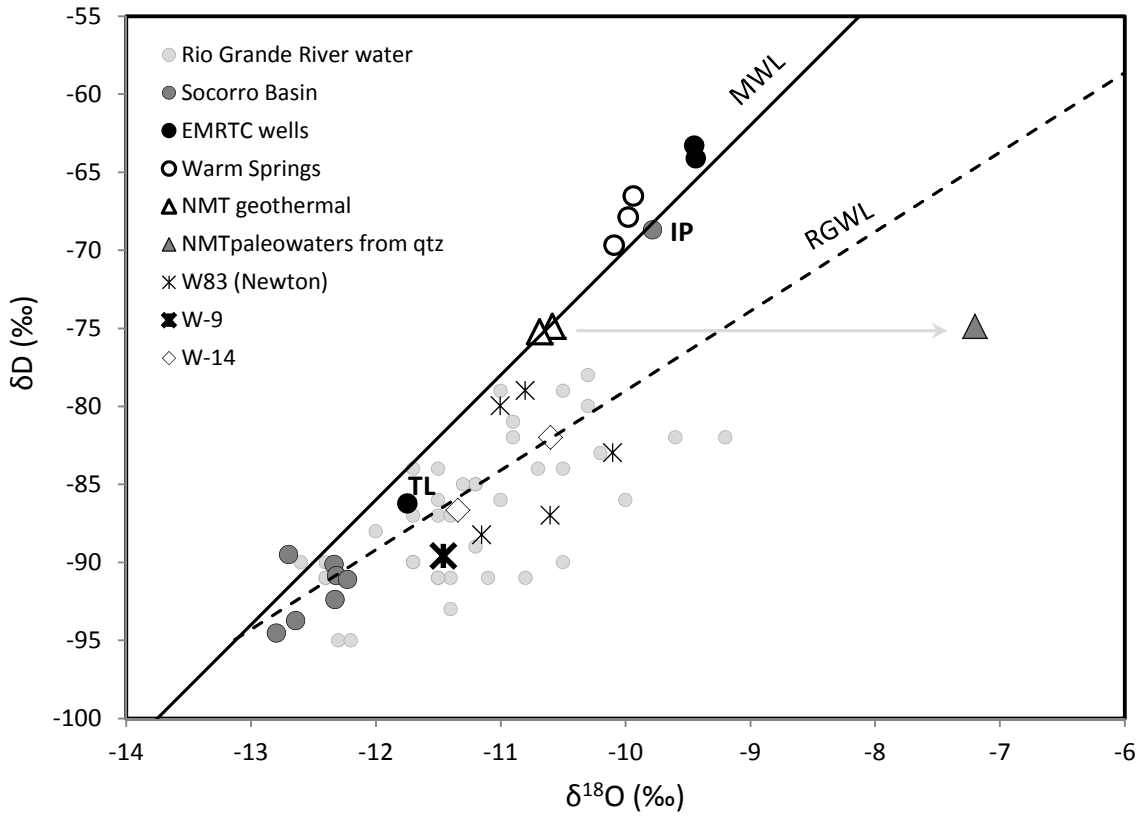

Fig. 6. Stable oxygen and dueterium isotope compositions of regional waters. Global meteoric Water Line (MWL) from Craig (1961). Rio Grande Water Line from Mills (2003).

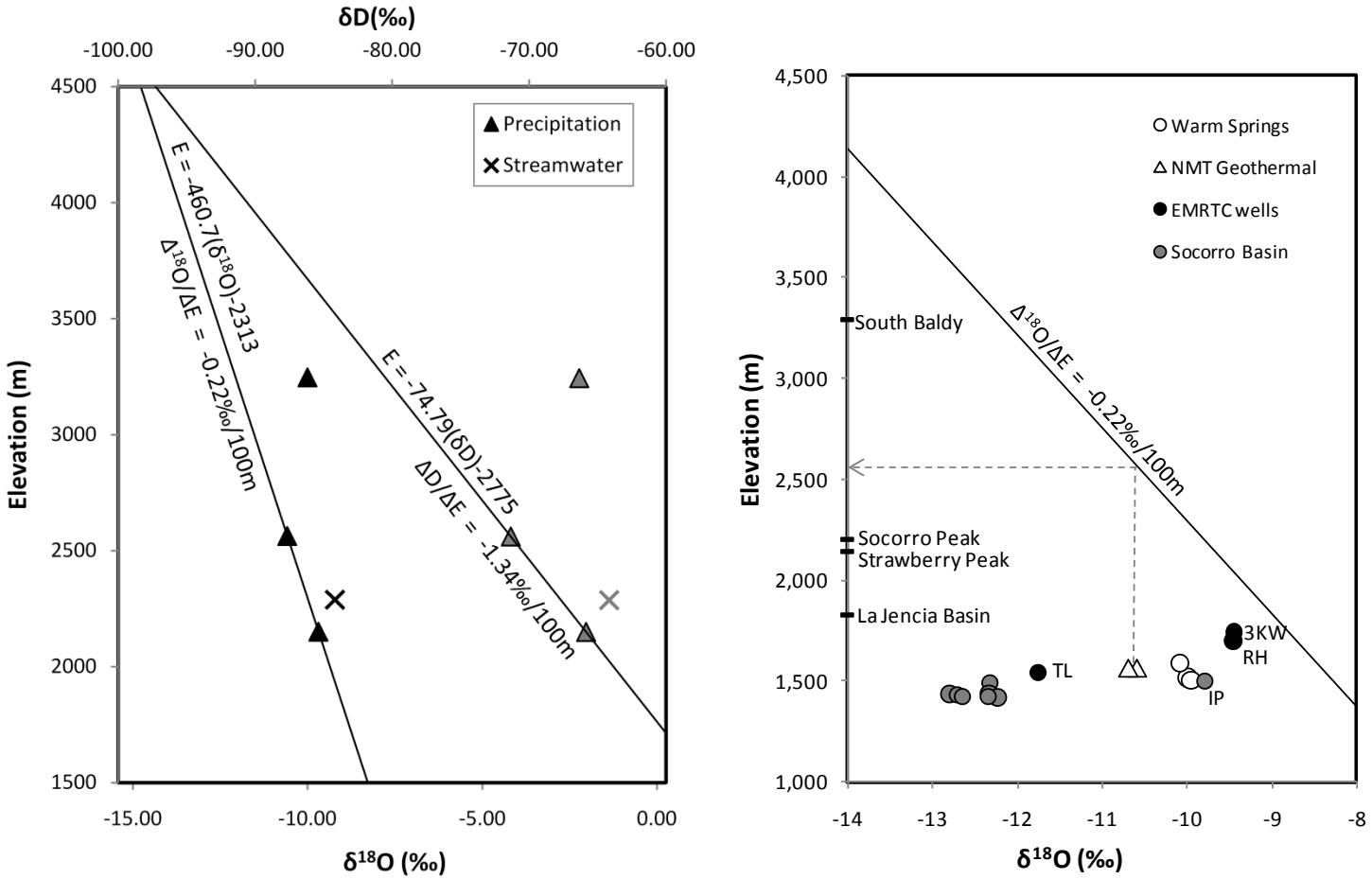

Fig. 7. (a) Plot of $\delta^{18}O$ (black symbols) and δD (grey symbols) as a function sample elevation. Snowpack and rain precipitation values from Earman et al. (2006); steamwater collected on Langmuir road following rain event in March 2010. Trends of $\Delta^{2}H/\Delta$elevation and $\Delta^{18}O/\Delta$elevation used for estimating source-water elevations are shown. (b) Plot of $\delta^{18}O$ compositions of sample waters as a function of actual sample elevations and possible recharge elevations in correlation with regional $\Delta^{18}O/\Delta$elevation trend. Elevations of local topographic features are shown.

Carbon-13, Sulfur-34, Boron-11 and Strontium-87/86

Waters in the study area exhibit $\delta^{13}C$ values ranging from -6 to -16‰ (Fig. 8). Our geothermal samples occupy a range of values near atmospheric CO_2 and overlap with secondary calcite values sampled from the NMTG slimhole. NMTG2 $\delta^{13}C$ values are consistent with mantle CO_2 values, however such a correlation is hardly conclusive. $^3He/^4He$ isotopic analysis of thermal fluids is recommended to investigate contributions from a magmatic source along this stretch of the Rio Grande Rift. Socorro Basin fluids as well as Socorro warm springs range from -9.6 to -11.8‰ nearing $\delta^{13}C$ values observed within the Rio Grande as well as CO_2 soil gas values.

Sulfur istopes ($\delta^{34}S$) values for Socorro area fluids range from 7.8 to 0.9‰ (Fig. 9). Most fluids overlap Rio Grande waters, namely Socorro Basin waters which are typically lower due to sulfate loading of $\delta^{34}S$ fertilizers (Szynkiewicz et al., 2010). Socorro Warm springs, Eagle Pitcher, Industral Park wells and EMRTC wells strongly associate with observed sulfate values from Paleozoic sedimentry units. NMT Geothermal fluids are the heaviest of those located in Socorro intermediate between precipitation values and NMTG2 barite, yet may derive from dissolution of Precambrian bedrock hosting enriched sulfate evaporites. NMTG2 $\delta^{34}S$ values are not consistent with having a large magmatic component, as observed in geothermal systems such as the Salton Sea or Steamboat (Field and Fifarek, 1985). Bosque wells W-9 and W-14 are much heavier than Socorro area fluids approaching values of evaporites found ubiquitously throughout New Mexico playa units and Permian sediments (Szynkiewicz et al., 2011).

Stable boron isotopes $\delta^{11}B$ were investigated for a subset of samples for the study area. All analyzed samples fell between 4 and 20‰ (Fig. 10). NMT geothermal fluids were measured at 14.7 ‰. All samples fell along a trend of increasing $\delta^{11}B$ with increased total boron

concentration (ppm) indicating possible fractionation within the solute source or mixing between a dilute/depleted reserve and a concentrated/enriched reserve.

$^{87}Sr/^{86}Sr$ isotopes were analyzed for select fluids within the study area (Fig. 11). Shallow Socorro Basins waters range from 0.7010-0.7026 nearing Rio Grande values along the Socorro reach. Warm spring fluids and EMRTC well waters range from 0.7114-0.7128 overlapping the values of local Oligocene and Miocene volcanic units as well as atmospheric precipitation values. NMT geothermal fluids are the most radiogenic strontium (0.721904) in the study with values greater than most known reservoirs in the region with the exception of the Precambrian units from the Magdalena Mountains. Elevated $^{87}Sr/^{86}Sr$ values observed within K-metasomatized Upper Lemitar tuffs in Socorro dated at ~7-8 My, also support a hydrologic path sourcing from the highly radiogenic Precambrian units (Fritz et al., 2006). Ratios of calcium and strontium concentrations in the waters plot along two separate trend lines illustrating two possible sources of strontium in the study area (Fig. 12). Socorro Basin waters plot alongside Rio Grande river values with a [Ca]/[Sr]ratio of approximately 108. NMTG, warm springs and deeper Socorro Basin wells (Evergreen and Industrial Park) form a shallower trend line with a [Ca]/[Sr]ratio of approximately 25, possibly related to enhanced Sr contributions from weathering of volcanic clinopyroxenes or Ca-bearing mineralization where Sr strongly substitutes.

Groundwater dating methods

Tritium and radiogenic Carbon-14 values for NMT Geothermal fluids and Socorro Springs are located in Table 3**.** Tritium is valuable for analyzing mixing from young waters, due to the short half-life of 12.4yrs. Tritium values for these waters range from 0.15 to 0.39 tritium units (TU) falling in the range of sub-modern waters recharged prior to the 1950's bomb peak, which may be estimated at <0.8 TU. Though modern meteoric recharge is a possible component of these thermal fluids, it is not volumetrically significant. Because the very low values of these

tritium measurements are on the same order as the detection limits, apparent ages derived from these two sites are indistinguishable. Carbon -14 values aid in assessing recharge on a much greater timescale owing to the longer half-life of C-14 of 5568yrs. C-14 values for NMT geothermal fluids reveal a corrected groundwater age of 17.6ky. Socorro Springs C-14 values, however, correspond to a groundwater age of 9.1ky. These ages may be considered comparable in geologic time yet suggest a slightly deeper/longer or slower pathway for the NMT geothermal fluids.

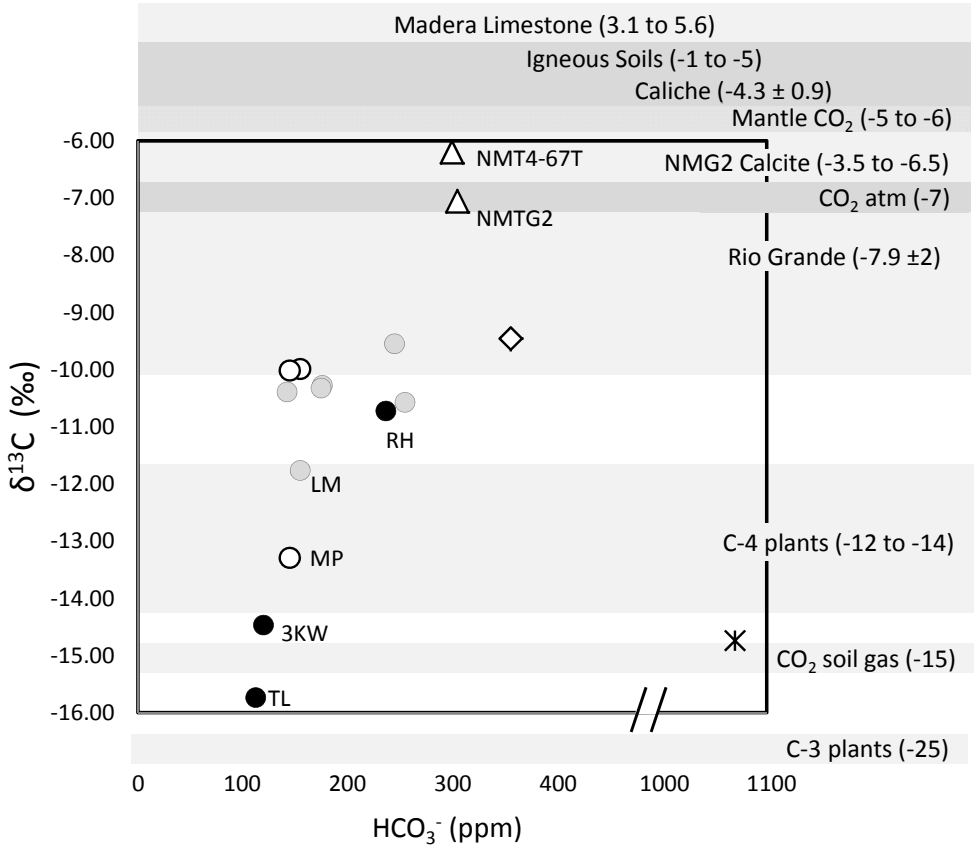

Fig. 8. Plot of stable carbon isotope composition vs DIC (reported as ppm HCO3-). Ranges of regional carbon reservoirs shown: Madera Limestone from Chamberlin (1999); Rio Grande fluids from Hogan (2007); other values from Sharp (2006) and Plumber et al. (2004).

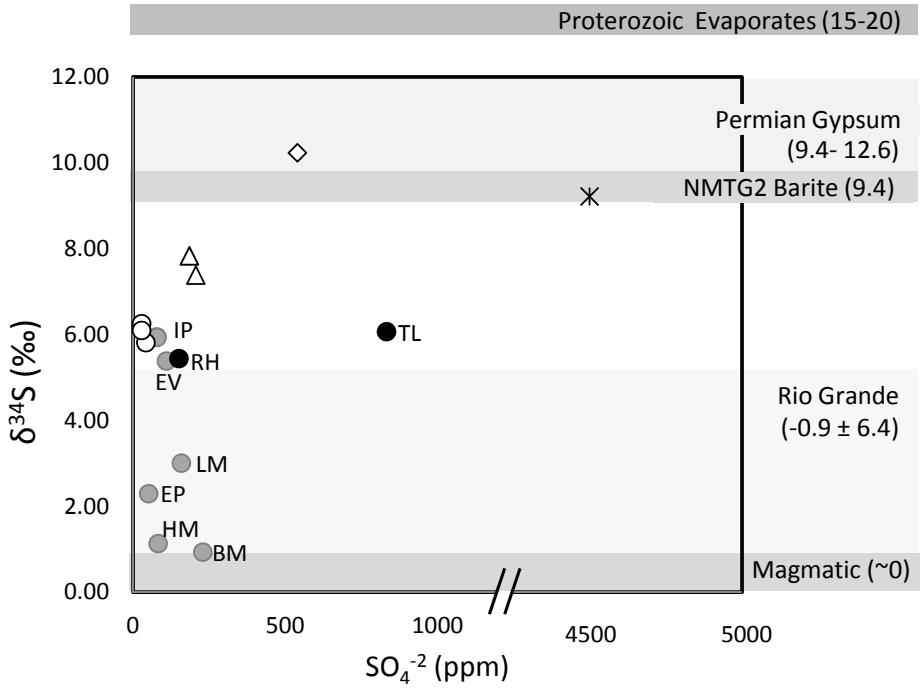

Fig. 9. Plot of stable sulfur isotope composition as a function of total sulfate. Local sulfate reservoirs are shown: Rio Grande and Permian gypsum from Szynkiewicz et al. (2011); Proterozoic evaporates from Sharp (2006); magmatic sulfur from Field and Fifarek (1985).

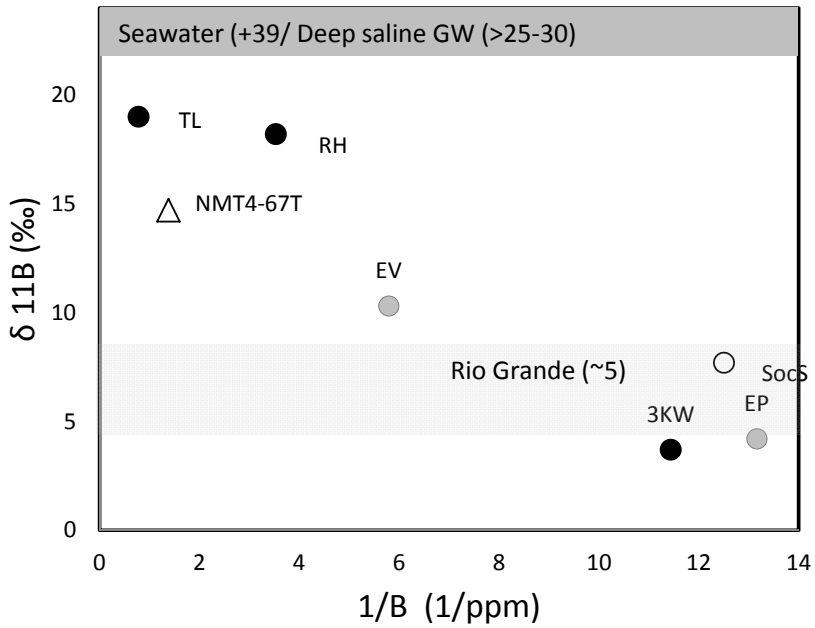

Fig. 10. Plot of stable boron isotope compositions versus the inverse of total boron (ppm). Rio Grande reservoir values from Moore et al. (2008); seawater and deep saline groundwaters from Vengosh et al. (1994); Vengosh et al. (1992).

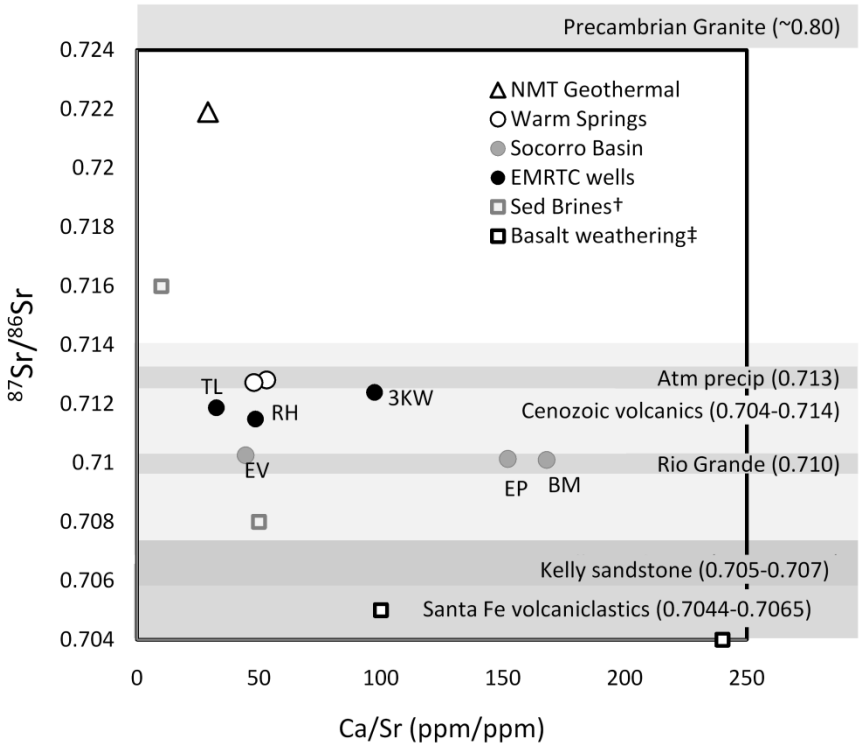

Fig. 11. Plot of radiogenic strontium concentrations ($^{87}Sr/^{86}Sr$) versus ratios of dissolved calcium to strontium (wt/wt). Radiogenic strontium values of local reservoirs are shown: local rock formations from Chapin (1979) and Witcher (pers. Comm. 2008); Rio Grande from Hogen et al. (2007); Precambrian Granite from Condie (1987) and White (1978); Atmospheric precipiation form Graustein and Armstrong (1983); Basalt weathering from Dugan et al (1986); Rio Grande waters from Hogan et al.(2007) and Plummer (2004).

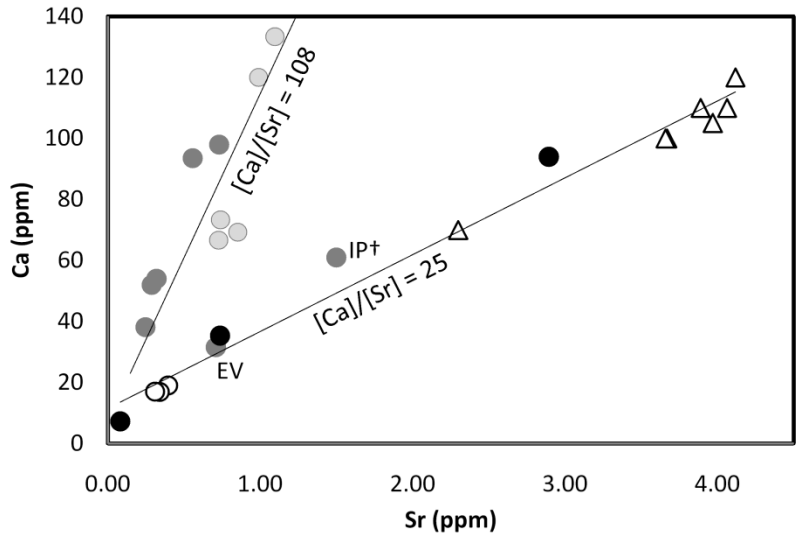

Fig. 12. Plot of calcium versus strontium for Socorro region waters illustrating 2 apparent (wt/wt) trend lines.

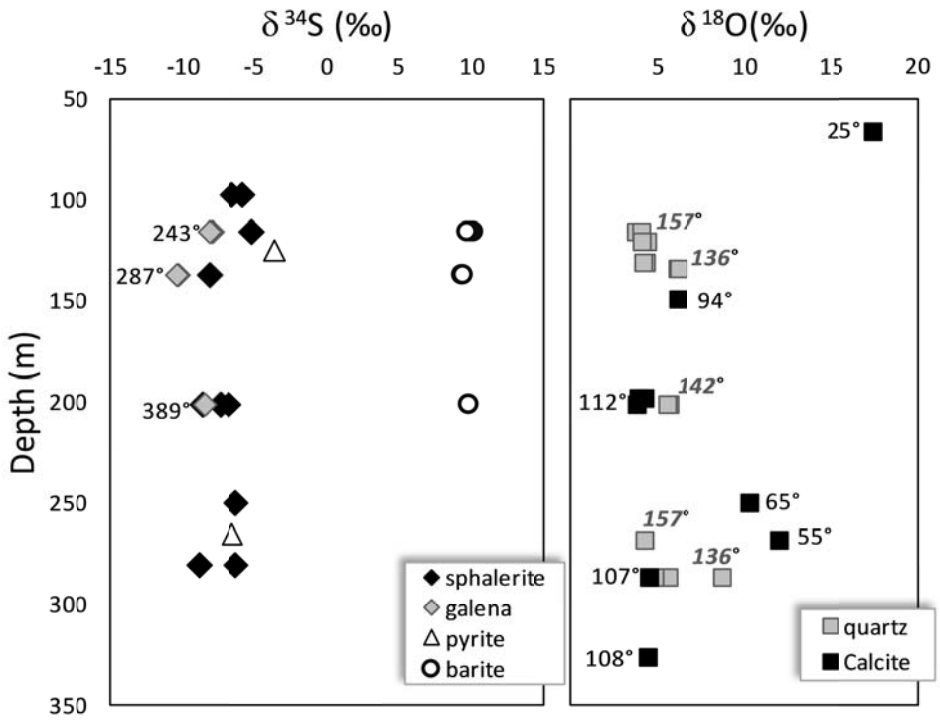

Fig. 13. Stable oxygen and sulfur compositions of secondary minerals from NMT4-67T core and NMTG2 cuttings. Geothermometers calculated from mineral pairs are shown where available.

Alteration Mineralization Isotopic Composition

Minerals collected from the NMTG2 & NMT4-67T core and cuttings were analyzed for stable isotopes (Table 4). Sulfide minerals galena, sphalerite and pyrite are common with the highly fractured argillite and appear to grow cogenically, overprinted with barite. $\delta^{34}S$ compositions do not change substantially with depth (Fig. 13). Equilibrium geothermometers for sulfide pairs $\Delta^{34}S$(sphal-gal) are calculated indicating possible emplacement temperatures of 243 to 389°C. These values correlate well with fluid inclusion evidence from nearby Mn-mineral districts supporting the existence of a paleo-geothermal system of at least 3-6 Ma (Chamberlin, 1980; Lueth et al., 2004) with temperatures between 150 to 375°C°C (Norman et al. 1983; Eggleston et al., 1983). Secondary quartz mineralization averages $\delta^{18}O$ values of 4.0 ± 0.17‰ with the exception of fractures near the Woods Tunnel fault which exhibit slightly heavier values.

Oxygen isotope geothermometers $\Delta^{18}O(qtz\text{-}H_2O)$ are applied using the estimated geothermal H_2O composition of modern NMTG2 fluids (-10.7‰). Estimated precipitation temperatures range from 136-161°C, markedly cooler than sulfide pairs. Alternatively, we may calculate the $\delta^{18}O$ isotope composition of paleofluids assuming emplacement temperatures similar to sulfide mineralization. At 243°C, silica quartz would fractionate from enriched waters with values of -7.2‰ requiring either substantial water-rock interaction (Fig. 6). Near surface boiling of geothermal brine may contribute to the enrichment of the isotopic composition, yet only by a few per mil. Calcite mineralization is found commonly in both cuttings and core, especially as large bladed crystals forming within alluvial fill. Calcite mineralization exhibits quite varied $\delta^{18}O$ compositions of 3.7 to 17.4‰. Geothermometers for $\Delta^{18}O(calcite\text{-}H_2O)$ using modern NMTG2 fluid compositions indicate temperatures of 25 to 113°C, with lowest temperature fluids correlating with major fracture-dominated loss zones encountered during drilling, namely calcite at 66m found near the depth to water table.

DISCUSSION

Tracing sources of thermal waters in the Socorro geothermal area

NMT geothermal fluids are a high conductivity, Na-Cl type water exhibiting elevated concentrations of certain geothermal indicators such as SiO_2, Li, and B. Radiogenic strontium for this water (0.7219) plots above groundwaters all known hydrostratigraphic units in the region, namely the Cenozoic volcanics and Paleozoic sediments, with the exception of Precambrian granitic units outcropping in the Magdalena mountains and regional plutons exhibiting $^{87}Sr/^{86}Sr$ values of 0.8 to 1.1 (White, 1978, Condie, 1987). The $^{87}Sr/^{86}Sr$ isotopic isotopic data is consistent with the hypothesis of fluid circulation and water rock exchange of groundwaters with the Precambrina bedrock. This supports the hydrothermal modeling results from Mailloux et al. (1999) for the study area. These authors found that in order to match heat flow anomalies (Fig.1),

fluid circulation had to extend to depths of at least 2 km into the Precambrian bedrock below the Paleozoic sedimentary units within the La Jencia Basin reaching temperatures of about 130 ^{o}C (Fig.14). Highly fractured Precambrian-aged metasediments penetrated by the NMTG2 exploration well are a likely hydrologic conduit for geothermal fluids at depth. Through model calibration to observed heat flow data (Fig.1), Mailloux et al. (1999) found that the permeability of the Precambrian basement to be about 10^{-14} m^2 (100 mD). In addition, δ^{13}C values and low DIC concentrations indicate minimal exchange with other carbonaceous units observed in the NMTG2 well including the Paleozoic shales and limestones. δ^{34}S values (7.6 ±0.2) coincide with dissolution of evaporate-rich metisedimentary bedrock. Not enough data exists to identify contributions from a magmatic source. Meteoric δ^{18}O and δ^{2}H values and atmospheric δ^{13}C values for these geothermal fluids also suggest fast infiltration of precipitation at the point of recharge, meaning negligible exchange with soil gas CO_2 or other units. For the temperatures predicted by Mailloux et al. (1999) one would expect minimal fluid-rock δ^{18}O isotopic exchange. Stable isotope altitude models correlate with recharge elevations between La Jencia Basin and South Baldy peak indicating probable deposition at intermediate elevations within the Magdalena mountains. This scenario is supported by C-14 groundwater ages which estimate a reasonable groundwater flow-rate of >1.4 m/yr along a theoretical horizontal path, assuming meteoric recharge of the NMT geothermal fluids from a somewhat distant source (~25km),.

Deep recharge to several kilometers depth beneath La Jencia basin and 25km of lateral flow would allow for enough heat to be mined supporting the heat flow anomaly near Socorro Peak (Forster and Smith, 1989) , yet requires intense fracture permeability within deep seated Precambrian units. Close proximity to the Socorro Accommodation Zone may provide such tensile fracturing and permeability at these depths. Maps of seismic epicenters within the Rio Grande Rift system (Fig.15) illustrates a cluster of >3 magnitude earthquakes within La Jencia Basin transecting between Magdelena Peak and Socorro Peak, outlining the most direct pathway

of deep hydrologic transmission of geothermal fluids. Geothermometers from alteration mineralogy paint a story of a waning hydrothermal system focused near Socorro which may have reached temperatures as high as 280°C as evidenced by isotopic sulfide pairs, overprinted with modern calcite representing the current low temperature upwelling fluids (<65°C).

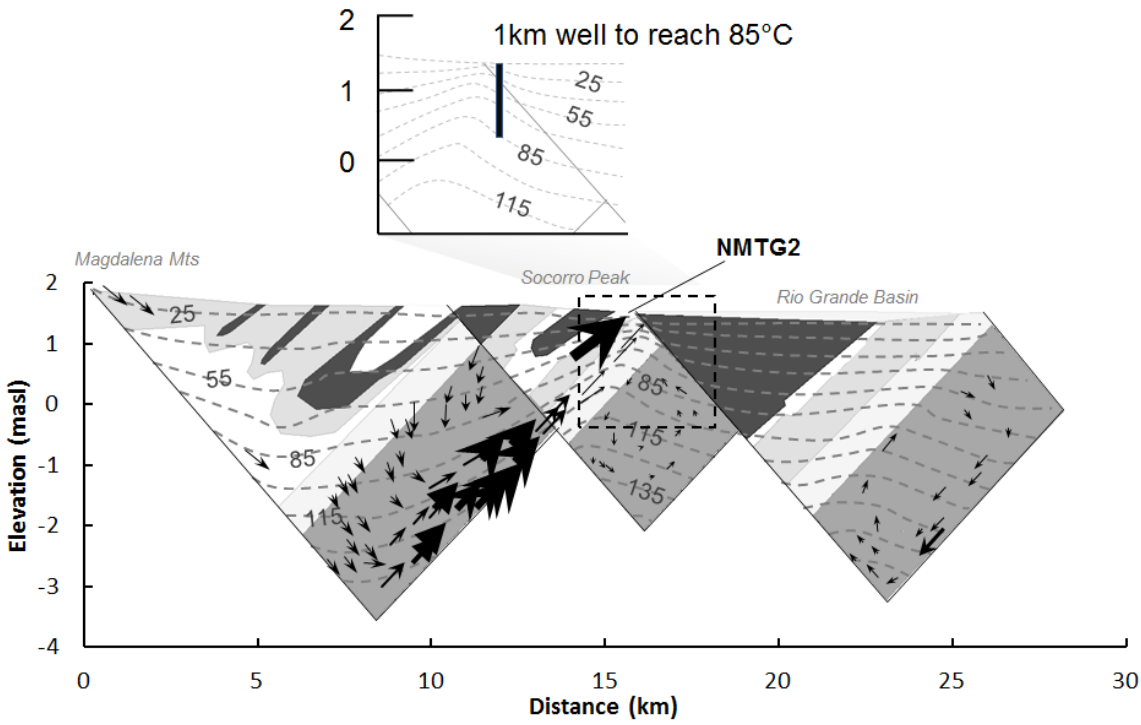

Fig. 14. Computed present-day groundwater flow directions (vectors), velocities (vector sizes) and temperatures (in degrees C) along an east west cross section of the Rio Grande Rift near Woods Tunnel, from Mailloux et al., (1999). Location of NMTG2 335m well would penetrate 45°C contours according to model. Theoretical 1km deep well (INSET) drilled from Socorro Basin, east of Socorro Peak and range bounding fault, would tap 85°C. Hydrostratigraphic units are according to Mailloux, et al. (1999): include prerift deposits (solid grey) overlain by Oligocene volcanics (pale grey), overlain by synrift deposits that are gradationally deposited with coarse-grained deposits (light) adjacent to the Magdalena Mountains and fine-grained playa deposits (dark grey) in the eastern central portions of the rift.

Socorro Warm springs appear to have a different source-path and point of recharge than the NMT geothermal fluids, despite their close proximity and common occurrence along the range bounding fault and N-S trending heatflow anomaly. These thermal springs are each very dilute Na-HCO_3 type waters with elevated SiO_2 and As indicating dissolution of volcanic rhyolitic glass at elevated temperatures (Ellis and Mahon, 1977). Socorro springs, Sedillo springs and Main Pad well each issue from fractured volcanics which likely represent a hydrologic significant unit for these fluids. This is supported by 0.7127-0.7128 $^{87}Sr/^{86}Sr$ values which indicate exchange with the more felsic tuffs and flows in the study area (Chapin et al, 1979). Cenozoic volcanic units penetrate deep near the site of the warm springs, as thick infill within the collapsed Socorro Caldera (Chamberlin, 1999), however the dilute nature of the fluids, lower temperatures and younger groundwater ages indicated a shallower and more fracture-driven flow path than for the NMTG geothermal fluids (Gross & Wilcox, 1983).

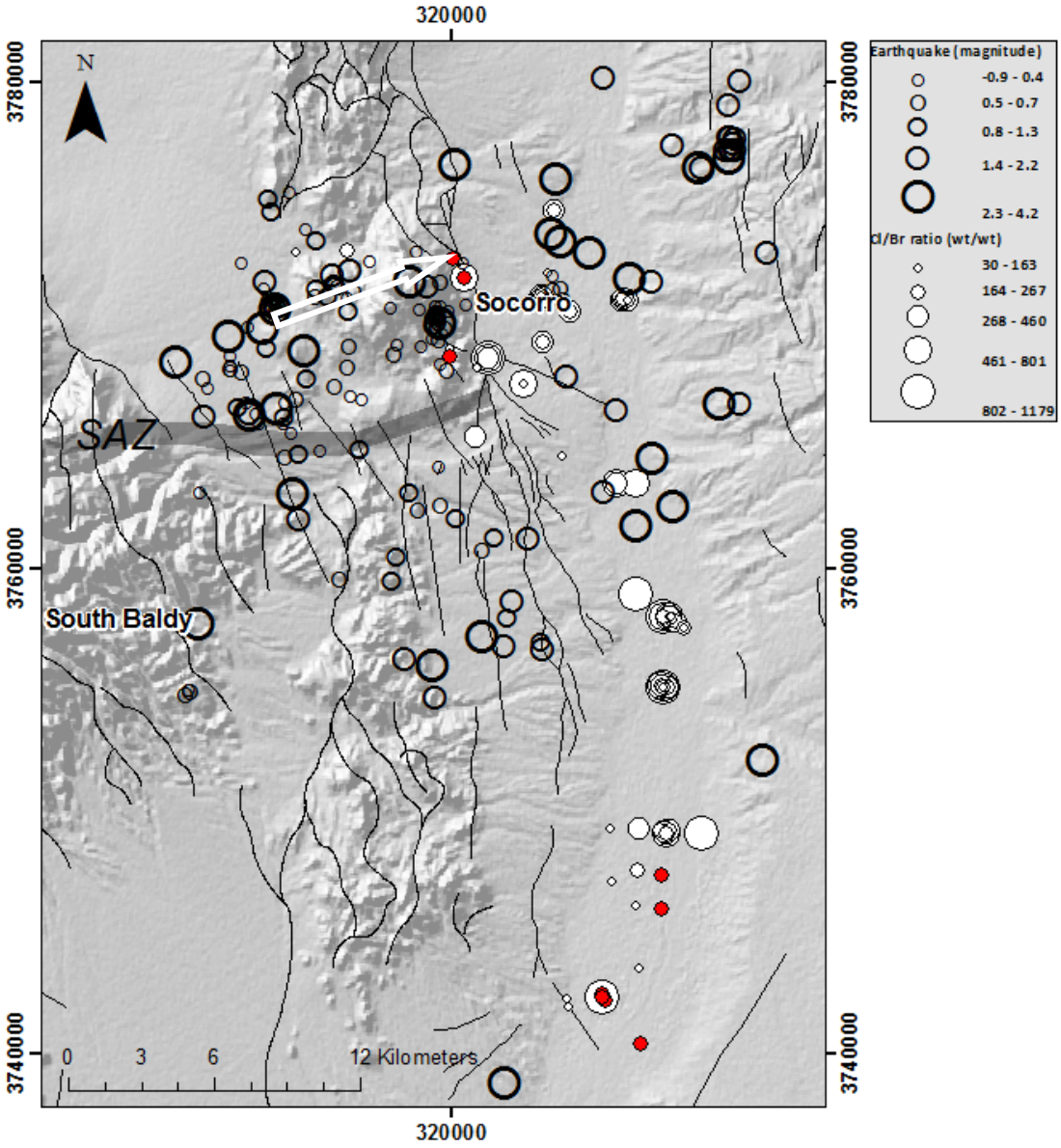

Fig. 15. Map of earthquake epicenter within Rio Grande Rift near Socorro. Arrow designates presumed deep circulation flow path from Magdalena Mountains to Socorro aided by tectonic activity. Earthquake magnitudes from Stankova-Pursley, New Mexico Tech Seismic center, personal communication (Appendix 9). Cl/Br ratios and notable locations of thermal waters (T>29°C highlighted as red point) from Summers (1976); WATSTORE (1993); Newton (2004); Anderholm (1987); Brandvolt (2001), and this study (Appendix 10).

Mixing of geothermal fluids in Socorro Basin and Rio Grande watershed

Contributions to Rio Grande Salinity

Geothermal fluids represent a possible source of salinity for the Rio Grande, as is observed in more southern watersheds such as Mesilla Basin (Witcher, et al 2004). Both thermal and nonthermal high-Cl groundwaters have been identified along the Rio Grande, including the non-thermal W-9 Bosque well with Cl values of >4000ppm and thermal W-14 Bosque well with Cl values of >1000ppm. Each has largely been attributed to leakage of sedimentary brines with possible transport aided by buoyant geothermal fluids. Piper diagrams demonstrate a shared chemical profile between Bosque del Apache thermal waters W-14 and non-thermal W-9 with NMT geothermal fluids (Fig.4). To investigate possible relationships between Socorro geothermal fluids and Cl contributions to the Rio Grande, we compare the chemical signatures of these thermal and nonthermal Cl waters using both whole chemistry and Cl/Br mixing models.

Modeling high Cl W-9 fluids with NMT geothermal fluids reveals an optimized mixture which closely matches the chemical composition of Bosque warm well W-14 (Table 5). A mixture of 6 to 8% W-9 brine with 94-92% NMT geothermal fluids matches within a few percent for most constituents, including geothermal indicators Li and B. A more accurate mixing model involves a contribution from NMT geothermal fluids (30%), Rio Grande waters (53%) and W-9 brines (17%), which sees better matching among conservative halogens Cl, F, Br. Mixtures with other possible endmembers exhibiting poor agreement with W-14 are shown here for comparison.

Table 5. Major chemistry mixing models between Bosque W-9 high chloride fluids and other ground waters in the Socorro region. Composition of target geothermal fluid (W-14) issuing along Rio Grande shown here for comparison.

	Brine	*Host fluids mixed with Brine*							Target
	W-9	**3KW**	**SocS**	**RG2**	**RG5**	**NMTG2-977'**	**NMTG2-977'**	**NMTG2 + RG5**	**W-14**
% Brine in Mix	*100%*	*80%*	*84%*	*80%*	*82%*	*92%*	*94%*	*30%+53%*	
TDS	13930	2904		3125	3106	3064	2857	3220	3110
Na	3817	799	653	813	758	890	834	868	831
K	153	32	27	35	34	37	35	36	33
Ca	583	122	108	170	203	148	140	174	124
Mg	285	59	49	66	70	38	33	61	39
HCO3	1070	306	415	381	429	375	362	398	356
SO4	4547	920	883	988	1015	534	458	885	541
Li	3.4	0.7	---	---	---	1.3	1.2	---	0.9
As	0.02	0.04	---	---	---	0.03	0.03	---	0.04
Sr	15.7	3.2	2.8	3.7	3.6	5	4.8	4.3	5.7
B	0.72	0.22	0.75	0.25	0.2	0.83	0.83	0.43	0.89
SiO2	54	29.2	29.64	---	---	35.6	35.25	---	26.95
F	0.34	0.56	0.56	0.47	0.39	1.13	1.15	0.64	0.65
Br	3.9	0.84	1.63	0.92	0.84	1.51	1.46	1.15	1.02
Cl	3967	797	645	827	780	1187	1134	974	972
Cl/Br	1017	954	395	903	928	787	775	850	953

Chloride/bromide (Cl/Br) ratios, however, can often be a more powerful tracer for identifying fluid sources. The conservative nature of chloride and bromide in solution allows for mixing relationships to be preserved over large temperature ranges and between stratigraphically diverse aquifers. Elevated Cl/Br fluids are identified along the Rio Grande, seeping particularly near thermal springs and saline wells, as illustrated in Fig.16. NMT geothermal fluids have an average Cl/Br ratio of 700 which has been observed among many geothermal systems (Ellis & Mahon, 1977), yet is much higher than fluids typically derived from granitic or metamorphic host rocks (e.g. 200-300; Davis et al, 1998) from which these waters are extracted. Precambrian metasediments may have formerly contained low-Br evaporites sediments effecting this composition. Bosque high Cl waters exhibit slightly higher Cl/Br ratios of ~1000, which is often attributed to dissolution of halite (Davis et al, 1998). Three mixing models are built between

dilute groundwaters and high Cl fluids to explore the possible contribution of these endmembers to intermediate well waters in the study area (Fig.16). Mixing Line 1 involves the incremental addition of a W-9 type brine (Cl: 4000ppm, Cl/Br:1000) to a dilute precipitation-derived fluid (Cl: 10ppm, Cl/Br:200); Mixing Line 2 involves the addition of an NMTG2 type fluid (Cl:880ppm, Cl/Br:700) with a dilute fluid (Cl:10ppm, Cl/Br:100); Mixing Line 3 investigates the direct mixing of NMG2 with a concentrated basinal brine represented by W-9 fluids. W-14 warm waters falls along the first mixing trend with an approximate 20% contribution from the W-9 endmember and 80% contribution from a low Cl source such as river water, however Cl/Br mixing models cannot account for the disagreement in SO_4 concentrations (Table 5).

While it is inconclusive that W-14 brines may be product of NMTG2-type geothermal fluids, it is quite likely that high Cl fluids along the Rio Grande rift are mobilized by buoyant geothermal fluids. Warm fluids near the Bosque del Apache appear to occur along NNE synrift structures near the intersection of NNW cross structures forming a right step in the range front. Differences in chemical profiles between the NMTG2 thermal waters, W-14 thermal waters and W-8 brines are likely associated with differences in bedrock types. NMTG2 solutes are likely derived from metasediment evaporite salts while southern Bosque fluids have encountered variable degrees of Permian sulfate evaporites as evidence from sulfur isotope profiles. Thermal waters are expected to have undergone additional alteration with regards to higher temperature fluid-mineral reactions, thus differentiating them from non-thermal brines. Expansion of this study using $^{87}Sr/^{86}Sr$ isotopes and C-14 isotopes of thermal fluids along the Rio Grande could investigate the depth of recharge and a shared geothermal host rock as NMTG2.

Geothermal in Socorro Basin

Transfer of NMTG2-type fluids, and thus permeability, across the range bounding Socorro Canyon fault is necessary to the formation of a geothermal resource within Socorro

Basin. Corresponding studies have attempted to find evidence of a blind system located within the basin using magnetotellurics and geochemical soil mapping (Baars et al., 2006), which support possible saline fluid beneath the capping Popotosa playa units and geothermal upflow along peidmont faults. Mixing models may be applied to investigate NMTG2 contributions to adjacent wells and springs.

Socorro Basin and its shallow alluvial aquifer are situated along a losing stretch of the Rio Grande, causing strong overlap of major chemistry and Cl/Br values with river waters, yet no indication of mixing with NMTG2 fluids (Fig. 4 and 16). Industrial Park, drilled 300ft within alluvial gravels and the Sierra Ladrones, exhibits elevated Cl, Na, Li, Sr, As above the other basin fluids and have $\delta^{18}O$, $\delta^{2}H$, $\delta^{34}S$ and $\delta^{13}C$ values plotting intermediate between local recharge and NMT geothermal fluids indicating possible leaking of geothermal fluids southwards along the range bounding fault. Cl/Br mixing models of the Industrial Park well exhibits a good fit incorporating Socorro Warm Springs and NMTG2 waters and may be a combination of these endmembers. Evergreen well falls along mixing line 1 involving a 0.1% and 1.4% contribution of a sedimentary brine endmember. Evergreen well is screened approximately 30m above the stratigraphic contact with the upper Popatosa playa facies which may contribute to the more evaporite-derived Cl/Br values. EMRTC wells dug west of the Socorro Canyon fault are also absent contributions from NMTG2 fluids. Torres Lab well located along this structure, and north of the temperature gradient anomaly, lacks apparent northward transport of the fluids along this fault. 3KWest and Rockhouse wells are dilute, locally derived meteoric fluids lacking contribution from an NMTG2 or Socorro Spring type thermal fluid indicating little upflow within the Socorro Peak fault block or along fracturing of the Socorro Cauldron ring structure.

The occurrence of possible mixing of NMTG fluids in the fault-adjacent Industrial Park well suggests possible transport of thermal waters southward along the Socorro Canyon fault with lateral transmission along hydrologic windows, or within shallow alluvial units. A lack of

NMTG signature further east within the Socorro Basin shallow may speak to localized compartmentalization along the range front near NMTG2, however lateral permeability across the Socorro Canyon fault may still occur at depth if transmission is permitted across juxtaposing permeable units.

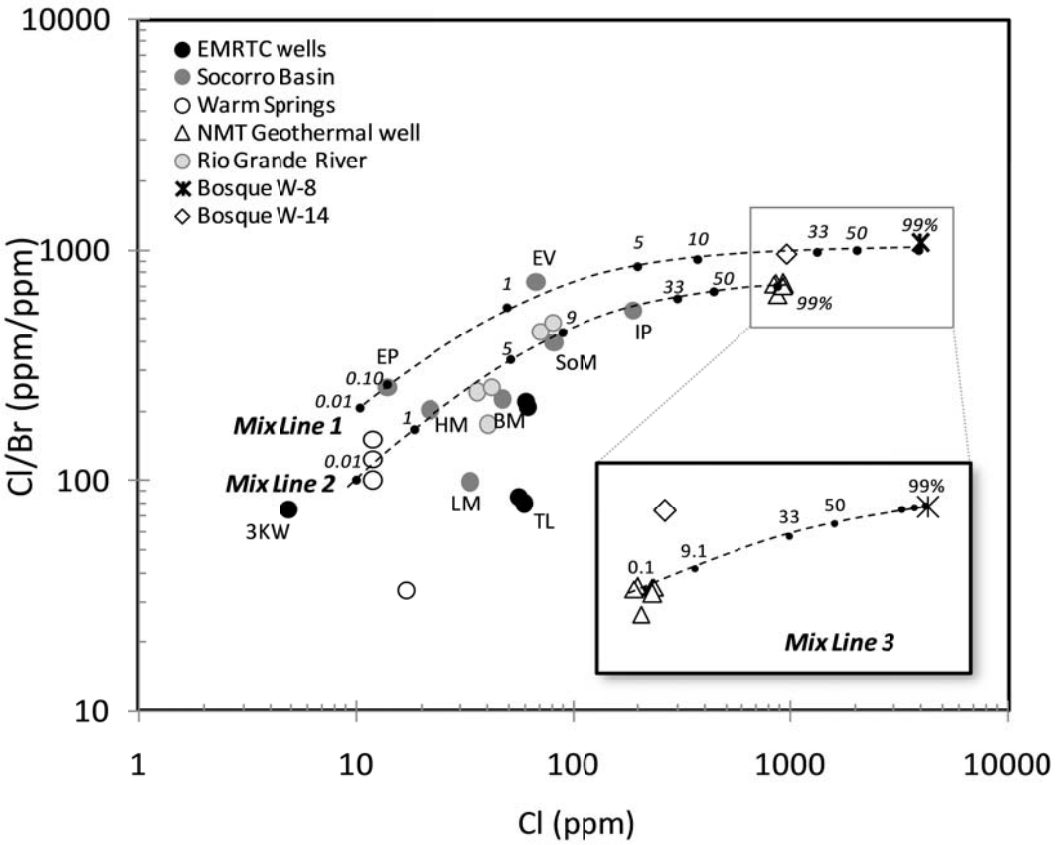

Fig. 16. Cl/Br ratios vs Cl concentrations illustrating 2 mixing lines attributing to the formation of Bosque waters W-9 and W-14.

Estimated temperatures of Socorro warm fluids

Geothermometers

Geothermometery is a commonly used tool in the investigation of geothermal systems allowing for the estimation of deep reservoir temperatures from much-cooled springs and shallow wells; however, their application is often precarious in low-temperature systems. Aqueous

geothermometers are based on slow-reacting, temperature-dependent mineral-solute equilibria relationships. Assumptions for the application of geothermometers include (1) that specific mineral equilibrium is achieved, (2) fluids neither mix nor re-equilibrate with shallow circulating fluids during ascent to the surface, and (3) that conductive heat loss is minimal. Slow or limited flows to surface following discharge through a tight fracture system or shallow alluvial unit can allow for precipitation of minerals, altering the silica and alkali metal concentrations (Fournier, 1985; Giggenbach, 1988). Mixing with shallow groundwater can also dilute or alter the ratios of dissolve solutes. As exhibited above, formations with high levels of evaporites can have overwhelming effects on the dissolved solids, much to the impedance of geothermal equilibrium reactions. Studies focused on Basin-and-Range type geothermal systems with increasing limitations towards lower temperature resources are actively addressing this issue (Spycher et al, 2011; Shevenell and Coolbaugh, 2011). We evaluate here the applicability of common geothermometer calculations as well as other geothermal indicator elements to exploration in low temperature systems. Geothermometer calculations for thermal fluids in this study area are found in Table 6.

A-priori knowledge about the geologic and hydrologic system is necessary for the proper application of geothermometer calculations. For example, chalcedony is the preferred silica-phase geothermometer for systems below 150°C (Fournier, 1985). Socorro warm springs, however, may exhibit enhanced SiO_2 dissolution from amorphous silica in volcanic tuffs which can overestimate resource temperatures. Both area warm springs and NMTG2 fluids are hosted within feldspar-bearing igneous or metamorphic bedrock making alkali geothermometers applicable. Slow reaction Na-K geothermometers derived from ion exchange between Na- and K- feldspars may predict the highest temperatures achieved by this system (Fournier & Truesdell, 1973), however are not valid below 200°C. Considerably faster equilibrium reactions represented by the K-Mg geothermometer (Giggenbach et al, 1983; Henley et al, 1984) predict

much lower temperatures and likely represent conditions closest to the surface in an advective system. Mg-corrected Na-K-Ca thermometers appear to predict the most plausible temperature estimates for thermal fluids by incorporating both fast and slow mineral equilibria (Fournier, 1981; Giggenbach, 1988), however the depths at which these temperatures exist may be much greater than economically feasible for a low temperature resource area. Sulfate oxygen isotope geothermometers for NMTG2 fluids provide temperature estimates with reasonable agreement with other fast-equilibrating methods (Mizutani and Rafter, 1969).

Geothermometer calculations for NMTG2 fluids range from 55°C to 100°C (**Table 6**), while values for Socorro Springs and similar wells (Sedillo Springs and Main Pad well) average 48°C. Bosque warm well W-14 geothermometers predict reservoir temperatures between 43 and 80°C. High Cl W-9 fluids, also predict elevated temperatures with some equilibrium calculations, however Mg-corrected Na-Ca-K geothermometer (Fournier, 1981) accurately conforms to the low sampling temperature of the fluids.

Speciation models

Estimation of reservoir temperatures associated with the Socorro system was also investigated with mineral speciation models (Fig.17.a and b.). Models are created in Geochemist Workbench with thermodynamic constants from the Lawrence Livermore National Lab (LLNL) database. Bicarbonate and pH values are reconstructed for NMTG-2 in equilibrium with calcite to account for lost CO_2 gas. Aluminum values are reconstructed using methods of Reed and Spycher (1998). We discover from plotting mineral saturation indices as a function of varying temperature that our fluids are not in full equilibrium with mineral phases known to be present. This is often the case in geothermal systems and instead our fluids achieve a complex steady-state representing the combined effects of mineral dissolution at high temperatures and retrograde mineral precipitation at decreasing temperatures (Giggenbach, 1981), with possible dilution and

mixing. Mineral equilibrium is never achieved, limited by differing kinetics of mineral buffers, however plots may still illuminate the various processes underway. A lower-temperature steady state is depicted averaging approximately 60°C for NMTG2 fluids associated with the dissolution of chalcedonic SiO_2 and precipitation of K, Mg- bearing clays. Initially calcite was supersaturated with respect to this fluid at equilibrium temperatures, possibly due to a loss of CO_2 and corresponding increase in pH at time of sampling. Albite dissolution does not appear to be controlling the Na- composition of the fluids, suggesting possible contamination from a sedimentary Na-source. Similarly, speciation models of W-14 Bosque warm wells identify a partial-equilibrium composition between 50-60°C despite the apparent influence of evaporite-dominated brines.

Speciation models are recommended here for best assessment of resource temperatures, particularly to assess the degree of equilibrium achieved; however, a combination of chalcedony and K-Mg geothermometer calculations produce the most accurate predictions for the Socorro low temperature springs and wells. Study-wide, silica geothermometers are most unambiguously tied to temperature due to its single-variable equilibrium relationship. Care, however, must be taken to apply the proper silica solubility phase and make corrections for boiling, mixing or excess dissolution from CO_2-rich fluids if indicated (Fournier, 1985; Fournier, 1979; Witcher and Stone, 2005).

Predicted NMTG2 reservoir temperatures

Modeled temperature profiles estimated by Mailloux et al. (1999) predict both the shallow sampled temperatures (42°C) from the 335m NMTG2 well, as well as reservoir temperatures at exploitable depths (56-83°C), as determined from SiO_2 and K-Mg geothermometers (Fig.14). The kinetics of silica precipitation due to conductive cooling are on the order of days thus limiting, the resource depth to a mere 10's of meters assuming flow rates of

1.4m/yr. Conductive cooling is proportional to the distance traveled, and inversely proportional to flowrate. Truesdell et al. (1977) calculated for a vertical pipe flow, that temperatures are reduced by half for waters flowing at 0.4 L/s from a 1km deep reservoir. NMTG2 produced over 60L/s while drilling thus limiting the effect of conduction within the highly fractured shallow units, yet may play a more important role at greater depth as overburden restricts permeability along the upflow path. Alkali geothermometer kinetics are relevant over the course of weeks to months, thus are expected to preserve higher, yet deeper reservoir temperatures. 100-117°C as predicted by Na-K-Ca, Mg-Na-K-Ca, Na/Li and $\delta^{18}O$ may represent fluids at 1.7km depth as predicted by thermal models.

Fig. 17. Mineral equilibria models for select thermal fluids within the study area.

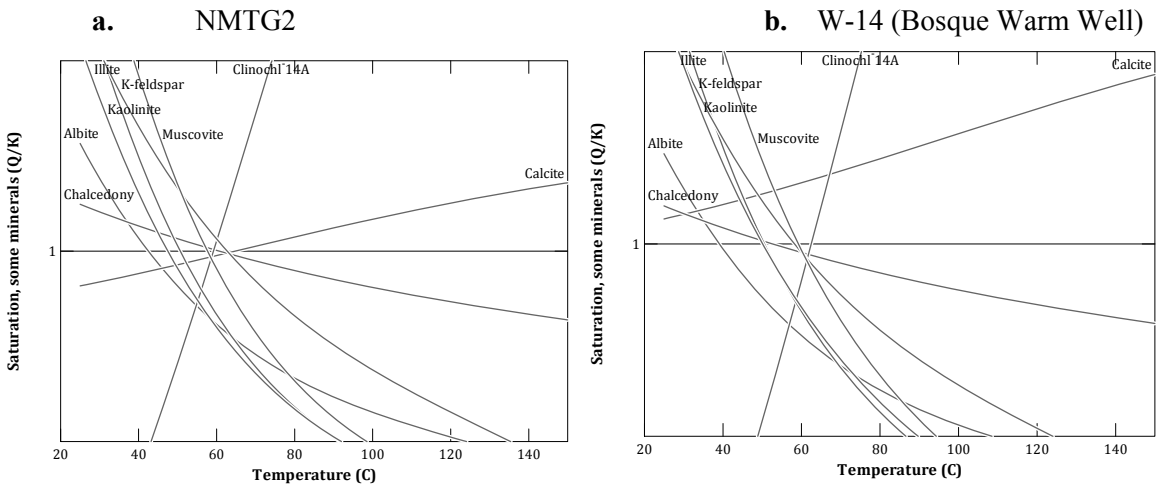

Table 6. Geothermometer temperature calculations for warm fluids (and high-Cl W-9 well).

	Sample Temp (°C)	Cl(ppm)	Geothermometer Calculated Temp (°C)							
			Qtz.	Chalc.	Na/K	Na-K-Ca	Mg-corr.	Na/Li	K-Mg	$\delta^{18}O$ (H_2O-SO_4)
Main Pad	33	17	66	34	163	54	54	78	48	
Sedillo Springs	33	12	60	28	169	53	53	74	49	
Socorro Springs	32	12	79	47	168	53	53	84	48	127
NMT4-67T	34	865	87	56	152	120	101	108	83	91
NMTG2	42	909	84	53	153	117	100	112	83	110
Bosque W-14	33	973	75	43	149	127	67	83	80	
Bosque W-9	19	3950	106	76	149	158	20	79	93	

Geothermal indicator elements

Other geothermal indicators may assist in reconnaissance of low temperature systems. Elevated concentrations of Cl, Li, B, As are common conservative elements in geothermal fluids as they readily dissolve from interstitial spaces rather than requiring complete dissolution of the silicate structure and do not participate in temperature dependent precipitation or ion-exchange reaction (Ellis & Mahon, 1977; Nicholson, 1993). However, plots of Li and B for both thermal and non-thermal waters catalogued along the Rio Grande (Appendix 11) reveal a strong correlation with Cl (Fig. 5) indicating either a mixing relationship between geothermal and non-geothermal endmembers or a common factor influencing the solubility and mobilization of Cl and trace elements in the waters, such as temperature (Fig. 17). An even stronger correlation between Na:Cl (R=0.97) and Sr:Cl (R=0.92) suggests that the degree of water-rock interaction, and not just temperature, may play an important role in effecting the concentrations of these dissolved constituents. Non-thermal fluids or those with a significant source of dissolved species from sedimentary brines can, however, give false indication of thermal character. These brines also contain elevated Cl, Li and B as well as Cl/Br ratios within the range of geothermal fluids (7000-1000). This highlights the unique difficulty of applying tradition geochemical exploration methods to deep circulating geothermal systems, along such rift basins as the Rio Grande hosting multiple lithologies and solute sources.

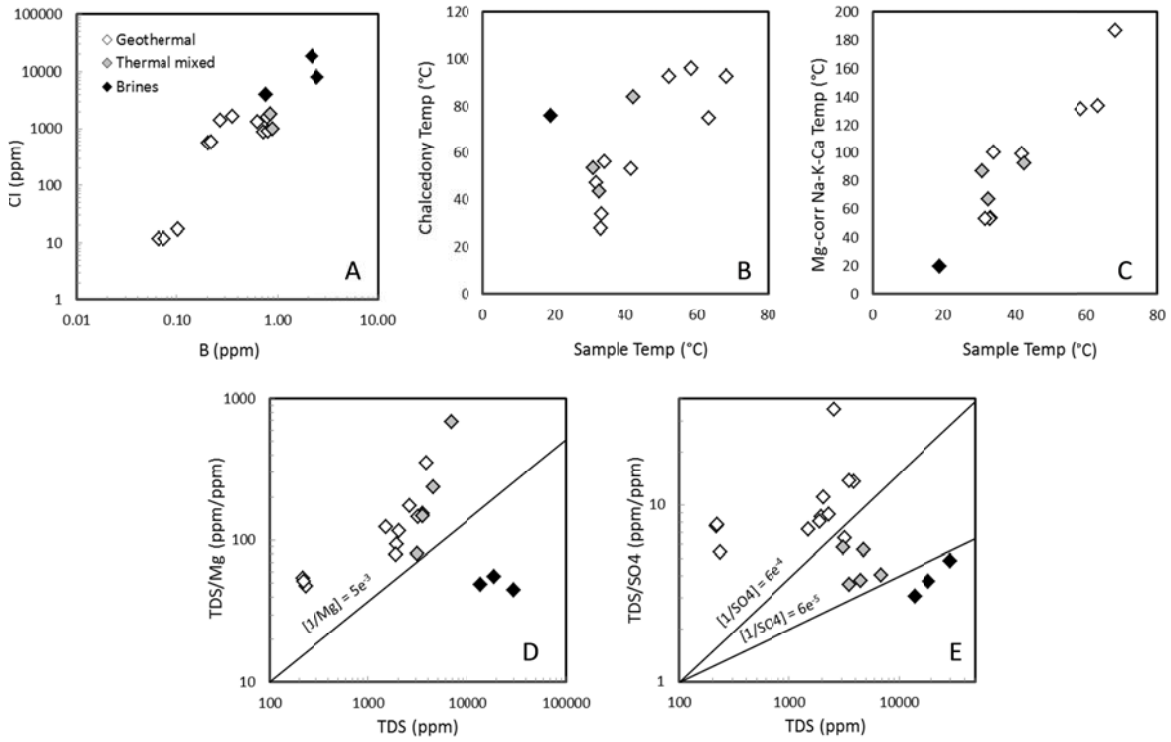

Fig. 18. Chemical comparisons of thermal and non-thermal brines in Socorro study area.

Concentrations of certain solutes such as SO_4, Ca and Mg, however are distinctly depleted in thermal waters within this system and may be used to eliminate high Cl brines with a non-thermal or sediment-derived source. Figs.17.d and 17.e illustrate thermal and mixed fluids thermal fluids (T>30°C) exhibit 1/Mg ratios of $>5e^{-3}$ and $1/SO4 > 6e^{-4}$. The inverse solubility of calcite and gypsum or anhydrite may be responsible for this particular trend. Selection of springs suitable for geothermometer calculations may be performed by identifying those whose geothermal indicator elements such as SiO_2, Li, As, B or Cl plot inversely with Mg, SO_4 and Ca.

SUMMARY & CONCLUSIONS

1. A hydrologic pathway for the Socorro geothermal system is evaluated using a number of environmental tracers. Fluids sampled from the NMTG2 exploration well represent the most primary geothermal endmember of all the thermal waters identified in the Socorro area. A combination of radiogenic Sr, C-14 and stable $\delta^{18}O$ values indicate recharge at higher elevations within the Magdelana mountains, deep circulation in Precambrian granitic or metasediment bedrock along a 17,630yr pathway. Socorro Springs fluids indicate a comparatively shorter path with lower elevation recharge, shallower circulation through Cenozoic volcanics in a matter of 9,120yrs. The higher temperatures predicted for NMTG2 must be attributed to the deeper recharge pathway, aided by greater hydrologic potential and enhanced fracture permeability within the crystalline basement, supported by earthquake epicenter maps. Speciation models predict our targeted resource temperatures of >60°C at economic depths, corresponding with hydrologic models (Mailloux et al., 1999). Flowing temperatures of 42°C were produced from NMTG2 with TD of 335m corresponding to an isothermal profile within the wellbore. Higher resource temperatures are hypothesized from deeper, less permeable units or at greater depth along the fault. Shallow leakage of thermal NMTG fluids is not evident in the Socorro Basin wells drawing from the Sierra Ladrones formation. Southward transport along the range front is suggested by mixing in the Industrial Park well.
2. Rio Grande salinity does not appear to be uniquely sourced from geothermal fluids within the Socorro Basin based on major chemistry and Cl/Br mixing models and Permian evaporite-derived sulfur isotope signatures of Bosque del apache high Cl waters. Geothermal waters do, however, appear to play a role in mobilizing sedimentary brines to the surface along intersecting structures within the Rio Grande rift.

3. The application of geothermometry in a low temperature setting is believed to be inherently flawed and often misapplied to predict resource temperatures in the presence of mixing and substantial conductive cooling. Large spreads in geothermometer calculations for most of the warm fluids in the study verify a lack of chemical equilibrium, likely due to mixing with meteoric or riverwaters or contamination with deep sedimentary brines as established with Cl/Br mixing models. High volume flow rates from NMTG2 and lack of mixing, however, support minimal conductive cooling near the surface and possible application of fast-reacting chalcedony and K/Mg geothermometer calculations. Speciation models exhibit disequilibrium for NMTG2 fluids, however a steady-state system is approached buffered by chalcedonic silica and Mg-chlorite clays between 60-80°C, supporting the tentative application of these geothermometers where guiding assumptions are met and temperatures agree, even in low enthalpy environments.
4. In lieu of reliable geothermometry, analyses of several groundwater tracers and geothermal indicator elements were reviewed for the evaluation of low temperature fluids in a Basin & Range type geothermal system.

a. Traditionally high dissolved solids with elevated concentrations of Cl, B, SiO_2, and an elevated Na/K ratio are associated with mature geothermal fluids in most hostrocks. In the Socorro geothermal study area, these indicator elements correlate linearly with Sr, As, Na and Li concentrations as often observed in fault-dominated geothermal systems, however non-thermal sedimentary derived brines also exhibit such correlations and, in the case of Bosque del Apache chloride wells, erroneously imply the presence of a geothermal source as well produce the highest silica and alkali geothermometers.
b. A further evaluation of the relative Mg, SO_4 and Ca concentrations may be used to accurately delineate non-thermal brines from thermal waters by identifying those with depleted concentrations of these elements. Reduced Mg concentrations are often associated with Mg-clay formation in maturing geothermal regimes. Reduced Ca and SO_4

concentrations may be linked with the inverse solubility of calcite and gypsum, particularly powerful in evaporite-rich sedimentary or meta-sedimentary host rocks.

c. Enriched radiogenic Sr, depleted $\delta^{18}O/\delta^{2}H$ values and millennial groundwater ages support high elevation precipitation and deeper recharge in older, basement units.

d. Non-unique sources for $\delta^{13}C$, $\delta^{34}S$ and $\delta^{11}B$ stable isotopes made application of these tracers for identifiying flowpaths in the Socorro area difficult, however mixing relationships were strongly implied.

e. Cl/Br mixing models evaluated the chemical relationship between different geothermal fluids, finding that mixing played as strong role in distributing parental NMTG2 fluids and delineating different geothermal endmembers, such as the Bosque del Apache warm springs which fall along a unique mixing trend.

REFERENCES

Aggarwal, P.K., Gat, J.R., Froehlich, K.F.O. (eds), 2005. Isotopes in the Water Cycle: Present and Future of a Developing Science. IEA. 221-241.

Anderholm, S.K., 1987. Hydrogeology of the Socorro and La Jencia basins, Socorro County, New Mexico: U.S.G.S. Water Resource Investigations Report. 84-4342.

Baars, R.M., Owens, L.O., Tobin, H., Norman, D., Cummings, W., Hill, G., 2006. Exploration and Targeting of the Socorro, New Mexico direct use geothermal exploration well, a GRED III project. Proceedings, Thirty-First Workshop on Geothermal Reservoir Engineering Stanford University. 8p.

Barroll, M.W. and Reiter, M., 1990. Analysis of the Socorro hydrogeothermal system: Central New Mexico. J. Geophys. Res. 95, 21,949-21,963.

Bassett, R.L., Buszka, G.R., Davidson, G.R., Chong-Diaz, D., 1995. Identification of groundwater solute sources using boron isotope composition. Environmental Science and Technology. 29, 2915-2922.

Bothern, L.R., 2003. Geothermal salt intrusion into Mesilla Basin aquifers and the Rio Grande, Dona Ana County, NM. [Masters Thesis]: New Mexico State University, 126 p.

Brandvolt, L., 2001. Arsenic in ground water in the Socorro Basin, New Mexico. New Mexico Geology. 23, 2-8.

Bronicki, L.Y. "Geothermal Power Stations." Ormat. 2011. Web. http://www.ormat.com/research/papers/geothermal

City of Socorro, 2003. Water quality reports [Data file].

City of Socorro, 2000. Water quality reports [Data file].

Chamberlin, R. M., 1980. Cenozoic stratigraphy and structure of the Socorro Peak volcanic center, central New Mexico [Ph.D. thesis]: Golden, Colorado School of Mines, 495 p.

Chamberlin, R.M., 1999. Preliminary geologic map of the Socorro quadrangle, Socorro County, New Mexico: New Mexico Bureau of Geology and Mineral Resources. Open-file Digital Map Series OF-DM-34, p. 46 (scale 1:24,000).

Chapin, C.E., Sanford, A.R., White, D.W., Chamberlin, R.M., Osburn, G.R., 1979. Geologic Investigation of the Socorro Geothermal Area. NMERDI 2-65-2301, 70p.

Chapin, C.E., Chamberlin, R.M., Osburn, G.R., White, D.W., Sanford, A.R., 1978. Exploration framework of the Socorro Geothermal Area, New Mexico: Field Guide to Selected

Cauldrons and Mining Districts of the Datil-Mogollon Volcanic Field. Spec. Publi. N.M. Geol. Soc. 7, 114-129.

Condie, K.C., 1978. Geochemistry of Precambrian granitic plutons from New Mexico, U.S.A. Chemical Geology. 21, 131-149.

Craig, H., 1961. Isotopic variations in meteoric waters. Science. 133, 1702-1703.

Craig, H., 1963. The isotopic geochemistry of water and carbon in geothermal areas: Nuclear Geology on Geothermal Areas, CNR, Pisa, p. 17–53.

Davis, S., Whittemore, D.O., Fabryka-Martin, J., 1998. Uses of Chloride/Bromide Ratios in Studies of Potable Water. Groundwater. 36, 338-350.

Dungan, M.A., Lindstrom, M.M., McMillan, N.J., Moorbath, S., Hoefs, J., Haskin, L.A., 1986. Open system magmatic evolution of the Taos Plateau volcanic field northern New Mexico. Journal of Geophysical Research. 91, 5999-6028.

Earman, S.A., Campbell, A.R., Phillips, F.M., Newman, B.D. , 2006. Isotopic exchange between snow and atmospheric water vapor: Estimation of the snowmelt component of groundwater recharge in the southwestern United States. Journal of Geophysical Research. 111, D09302.

EERE. "Direct Use of Geothermal Energy". DOE. 2012. Web. http://www1.eere.energy.gov/geothermal/directuse.html

Eggleston, T.L., Norman, D.I., Chapin, C.E., Savin, S., 1983. Geology, alteration, and genesis of the Luis Lopez manganese district, New Mexico. New Mexico Geological Society Guidebook. 34, 241–246.

Ennis, D.J., Dunbar, N.W., Campbell, A.R., Chapin, C.E., 2000. The effects of K-metasomatism on the mineralogy and geochemistry of silicic ignimbrites near Socorro, New Mexico. Chemical Geology. 167, 285-312.

Ellis, A.J. and Mahon, W.A.J., 1977. Chemistry and Geothermal Systems. Academic Press.

Field, C.W., and Fifarek, R.H., 1985. Light Stable Isotope Systematics in the Epithermal Environment, in Berger, B.R. and Bethke, P.M.,eds., Geology and Geochemistry of Epithermal Systems; Reviews in Economic Geology, Vol. 2, Society of Economic Geologists, Univ. Texas, El Paso, TX.

Forster, C., Smith, L. 1989. The influence of groundwater flow on thermal regimes in mountainous terrain: A model study. Journal of Geophysical Research. 94, 9439-9451.

Fournier R.O., 1979. Geochemical and hydrological considerations and the use of enthalpy-chloride diagrams in the prediction of underground conditions in hot-spring systems. Journal Volcanology Geothermal Research. 5, 1-16.

Fournier, R.O., 1981. Application of water geochemistry to geothermal exploration and reservoir engineering; Chapt. 4 in Geothermal Systems: Principles and Case Histories, L. Ryback and L.J.P. Muffler eds., Wiley New York, 109-143.

Fournier, R.O, and Truesdell, A.H., 1973. An empirical Na-K-Ca geothermometer for natural waters. Geochemica et Cosmochimica Acta. 37, 1255-1275.

Fournier, R.O., 1985. The behavior of silica in hydrothermal solutions. In Berger, B.R. and Bethke, P.M. (eds.), Geology and Geochemistry of Epithermal Systems, Society of Economic Geologists, 45-61.

Fritz, D.E., Farmer, G.L. and Verplanck, E.P., 2006. Application of Sr isotopes in secondary silicate minerals to paleogroundwater hydrology: An example from K-metasomatized rocks in the western U.S. Chemical Geology. 235, 276–285.

Friedman, I. and O'Neil, J.R., 1977. Compilation of stable isotope fractionation factors of geochemical interest. USGS 440-KK, 11p.

Giggenbach, W.F., 1988. Geothermal solute equilibria-Derivation of Na-K-Mg-Ca geoindicators. Geochemica et Cosmochimica Acta. 52, 2749-2765.

Giggenbach, W.F., Gonfiantini, R., Jangi, B.L., Truesdell, A.H., 1983. Isotopic and chemical composition of Parbati Valley geothermal discharges, NW Himalaya, India. Geothermics. 12, 199-222.

Giggenbach, W.F., 1981. Geothermal mineral equilibria. Geochimica et Cosmochimica Acta. 45, 393-410.

Glorieta Geosciences, 2004. Geologic and Geochemical evaluation of the Evergreen Drive Municipal Well: Internal report to the City of Socorro.

Graustein, W.C., and Armstrong, R.L., 1983. The use of strontium-87/strontium-86 ratios to measure atmospheric transport into forested watersheds. Science. 219, 289-292.

Gross, G.W. and Wilcox R., 1983. Groundwater circulation in the Socorro Geothermal Area. New Mexico Geol. Soc. Guidebook, 39th Field Conf., 311-318.

Henley, R.W., Truesdell, A.H., Barton, P.B., 1984. Fluid-Mineral Equilibria in Hydrothermal Systems; Reviews in Economic Geology, Vol. 1, Society of Economic Geologists, Univ. Texas, El Paso, TX.

Hoefs, J., 2004. Stable Isotope Geochemistry. Spring-Verlag Berlin. 285p.

Hogan, J.F., Phillips, F.M., Mills, S.K., Hendrickx, J.M.H., Ruix, J., Chesley, J.T., Asmerom, Y., 2007. Geologic origins of salinization in a semiarid river: The role of sedimentary basin brines. Geology. 35, 1063-1066.

Kiyosu, Y., 1973. Sulfur isotope fractionation among sphalerite, galena and sulfide ions. Geochemical Journal. 7, 191-199.

Li, Y.B., Liu J.M., 2006. Calculation of sulfur isotope fractionation in sulfides. Geochimica et Cosmochimica Acta. 70, 1789-1795.

Lueth, V.W., Chamberlin, R.M., Peters, L., 2004. Age of mineralization in the Luis Lopez manganese district, Socorro county, New Mexico, as determined by 40Ar/39Ar dating of

cryptomelane. New Mexico Bureau of Geology and Mineral Resources Bulletin. 160, 239–249.

Mailloux, B., Person, M., Kelly, S., Dunbar, N., Cather, S., Strayer, L., Hudleston, P., 1999. Tectonic controls on the hydrogeology of the Rio Grande Rift, NM. Water Resources Research. 35, 2641-2659.

McNutt, R.H., 2000. Strontium Isotopes, *in* Cook, P., and Herczeg, A.L., eds., Environmental Tracers in Subsurface Hydrology, Kulwer Academic Publishers, p. 233-260.

Mills, S.K. 2003. Quantifying Salinization of the Rio Grande Using Environmental Tracers. [Masters Thesis]: New Mexico Institute of Mining and Technology, 448 p.

Mizutani, Y. and Rafter, T.A. 1969. Oxygen isotopic composition of sulphates, 3. Oxygen isotopic fractionation in the bisulfate ion-water system. N.Z. Journal of Science., 12, 54-59.

Moore, S.J., Bassett, R.L., Liu, B., Wolf, S.P., Doremus, D., 2008. Geochemical tracers to evaluate hydrogeologic controls on river salinization. Groundwater. 46, 489–50.

Newton, B.T., 2004. Geologic controls on shallow groundwater quality in the Socorro Basin, New Mexico. [Masters Thesis]: New Mexico Institute of Mining and Technology, 174 p.

Nicholson, K., 1993. Geothermal Fluids: Chemistry and Exploration Techniques. Springer-Verlag. 263p.

Norman, D.I., Bazrafshan, K., Eggleston, T.L., 1983. Mineralization of the Luis Lopez epithermal manganese deposits in light of fluid inclusion and geologic studies. New Mexico Geol. Soc. Guidebook, 34th Field Conf., 247–251.

Phillips, F.M., Hogan, J.F., Mills, S.K., Hendrickx, J.M.H., 2003. Environmental tracers applied to quantifying causes of salinity in arid region rivers: Preliminary results from the Rio Grande, Southwestern USA, in Water Resources, Perspectives: Evaluation, Management and Policy. Elsevier, 327-334.

Plummer, L.N., Bexfield, L.M., Anderholm, S.K., Sanford, W.E., Busenberg, E., 2004. Geochemical characterization of ground-water flow in the Santa Fe Group aquifer system, Middle Rio Grande Basin, New Mexico. USGS WRIR 03-4131, 395p.

Reed M. H. and Spycher N. F., 1998. User's guide for CHILLER: a program for computing water–rock reactions, boiling, mixing and other reaction processes in aqueous–mineral-gas systems and minplot guide (Department of Geological Sciences, University of Oregon, Corvallis, Oregon), 3rd edn.

Reiter, M. and Smith, R., 1977. Subsurface temperature data in the Socorro Peak KGRA, New Mexico. Geothermal Energy Magazine. 5, 37-42.

Sanford, A.R., 1968. Gravity survey in Central Socorro County, New Mexico. SBMMR Circlular, 91.

Schlosser P., Stute, M., Dorr, H., Sonntag, C., and Munnich, K.O., 1988. Tritium/3He dating of shallow groundwater. Earth and Planetary Science Letters. 89, 353-362.

Schlosser P., Stute, M., Sonntag, C., Munnich, K.O., 1989. Tritiogenic ^{3}He in shallow groundwater. Earth and Planetary Science Letters. 94, 245-256.

Shevenell, L. and Coolbaugh, M., 2011. A New Method of Evaluation of Chemical Geothermometers for Calculating Reservoir Temperatures from Thermal Springs in Nevada. GRC Transactions. 35, 657-661.

Sharp, Z. D., and Kirschner, D. L., 1994. Quartz-calcite oxygen isotope themometry:a calibration based on natural isotopic variations. Geochimica et Cosmochimica Acta. 58, 4491-4501.

Sharp, Z., 2006. Principles of Stable Isotope Geochemistry. Prentice Hall, 360p.

Spycher, N., Sonnenthal, E., Kennedy, B.M., 2011. Integrating Multicomponent Chemical Geothermometry with Parameter Estimation Computations for Geothermal Exploration. GRC Transactions. 35, 663-666.

Summers, W.K., 1976. Catalog of thermal waters in New Mexico: New Mexico Bureau of Mines and Mineral Resources Hydrologic Report. 4, 44-51.

Summers, W.K., Colpitts R.M.J., and Schwab, G.E., 1981. Hydrogeologic Evaluation of the Industrial Park Area, Socorro NM. Summers & Associates: Report to the City of Socorro Utilities Department. 105p.

Szynkiewicz A., Witcher J., Modelska M., Borrok D.B., Pratt L.M., 2011. Anthropogenic sulfate loads in the Rio Grande, New Mexico. Chemical Geology. 283, 194-209.

Szynkiewicz A., Moore C.H., Glamoclija M., Bustos D., Pratt L.M., 2010. The origin of coarsely crystalline gypsum domes in a saline playa environment at the White Sands National Monument, New Mexico. Journal of Geophysical Research. 115, F02021.

Stankova-Pursley, J., 2008. Earthquake epicenter database for Rio Grande Rift near Socorro, NM. New Mexico Tech Seismic Center. Personal communication.

Taylor, H.P., 1974. The application of oxygen and hydrogen isotope studies to problems of hydrothermal alterations and ore deposition. Economic Geology. 69, 843-883.

Truesdell, A.H., Nathenson, M., Rye, R.O., 1977. The effects of subsurface boiling and dilution on the isotopic compositions of Yellowstone thermal waters. Journal of Geophysical Research. 8, 3694–704.

Vuataz, F.D. and Goff, F., 1986. Isotope Geochemistry of Thermal and Nonthermal Waters in the Valles Caldera, Jemez Mountains, Northern New Mexico. Journal of Geophysical Research. 91, 1835-1853.

White, D.L., 1978. Rb–Sr isochron ages of some Precambrian plutons in South-central New Mexico. Isochron-West. 21, 8-13.

Witcher, J.C., 1988. Geothermal resources of southwestern New Mexico and southeastern Arizona. New Mexico Geological Society Guidebook, 39th Field Conf., 191-197.

Witcher, J., 2002. Geothermal Energy in New Mexico. Oregon Institute of Technology-Geo Heat Center Bulletin. 23, 2-6.

Witcher, J.C., King, P.J, Hawley, J.W., Kennedy, J.F., Williams, J., Cleary, M., Bothern, L.R., 2004. Sources of salinity in the Rio Grande and Mesilla Basin groundwater. WRRI Technical Completion Report No. 330, 184p.

Witcher, J.C., Stone, C. 2005. A CO2 silica geothermometer for low temperature geothermal resource assessment with application to resources in the Safford Basin, Arizona. Arizona Geologic Survey, CR-05-B. 160p.

Witcher, J.C., 2005. Geothermal Resource Data Base New Mexico 2005. Southwest Technology Development Institute New Mexico State University. Las Cruces, NM.

Witcher, J.C., 2008. Unpublished $^{87}Sr/^{86}Sr$ values from New Mexico Volcanic Units. Personal communication.

Vengosh, A., Starinsky, A., Kolodny, Y., Chivas, A.R., Raab, M., 1992. Boron isotope variations during fractional evaporation of sea water: New constraints on the marine vs. non-marine debate. Geology. 20,799- 802.

Vengosh, A., Heumann, K. G., Juraske, S. Kasher, R., 1994. Boron isotope application for tracing sources of contamination in groundwater. Environmental Science & Technology. 28, 1968-1974.

WATSTORE, 1997. USGS, Water Storage and Retrieval System.

Williams, C.F., Reed, M.J., and Mariner, R.H., 2008. A review of methods applied by the U.S. Geological Survey in the assessment of identified geothermal resources: U.S. Geological Survey Open-File Report 2008-1296.

Ziagos, J.P., Blackwell, D.D., 1986. A model for the transient temperature effects of horizontal fluid flow in geothermal systems. Journal of Volcanology and Geothermal Research. 27, 371-397.

CHAPTER 3:

Identification of problematic feedzones using fluid inclusion gas analysis: A study of acidic production fluids at Krafla, NE Iceland

ABSTRACT

Krafla well cuttings are examined by cold-crush fluid inclusion gas analyses to investigate the processes and depth intervals associated with problematic feedzones, for possible mitigation in real time. Krafla produces highly acidic steam and non-condensible gases (NCGs) from many production wells nearing 2000m depth. During the Krafla fires from 1975-1984, good producers soon exhibited high CO_2 concentrations coupled with increased acidic character attributed to pervasive magmatic gases within the reservoir. Wells drilled following this event saw CO_2 concentrations return to near-background levels, however HCl-rich superheated steam is a continuous problem from otherwise prolific wells. Molten lava has been encountered in at least three production wells while drilling. Two such wells completed in separate ends of the field; IDDP-1 in Lierbotnar and KJ-39 in Suðurhlíðar, exhibit the highest flow rates, enthalpies and most corrosive character in Krafla. Fluid inclusion gas signatures associated with direct input of magmatic gases may be characterized as having elevated CO_2, high total-gas wt percent and presumable HCl. Magmatic gases in with the Leirbotnar field also exhibit SO_2 and He spikes, associated with the recent intrusions of the Krafla fires near these wells. H_2S and H_2 are absent from magmatic gas-flux profiles suggesting rapid modification by the reservoir following exsolution from the nearby magma. Superheated boiling is mapped upwards of 300m above molten intrusions, mapped from CO_2/N_2 vs total gas concentrations, coupled with excess CO_2 in gas-rich inclusions, highlighting feedzones capable of producing vaporized HCl. Wells without direct magmatic gas influx may still exhibit acidic character if superheating conditions exist, owing to residual concentrated Cl brine from the Krafla fires.

INTRODUCTION

The Krafla geothermal field in northeast Iceland is home to some of the hottest and most productive wells in the world. Since the completion of 60MW powerplant in 1977, the drilling and reservoir engineers have struggled to generate enough steam to meet capacity due to a myriad of problems, including pervasive magmatic gases and NCGs, corrosion and scaling from acidic steam, and molten intrusions encountered within the wellfield. A large volcanic swarm in Krafla during the 1975-1984 Krafla fires resulted in spikes of CO_2 and low pH of production fluids throughout the field. Though the CO_2 concentrations have returned to normal levels, highly acidic fluids occur pervasively at depth related to shallow emplacement of these volcanic gases and magmatic dikes and affect nearly a third of the wells drilled at Krafla (Gudmundsson, 2001). Magmatic intrusions have also been encountered in three production wells while drilling, manifesting as quenched volcanic glass in cuttings and the cause of near blowouts. One such well was the Iceland Deep Drilling Project-1 (IDDP-1) drilled with a target depth of 4.5km, in search of supercritical phase water, yet was terminated prematurely with the intersection of a felsic dike at 2047m. Aside from obvious drilling difficulties, wells encountering molten lava exhibit strongly corrosive production fluids and have yet to be made fully productive.

Mitigation of such problematic production zones might involve blocking off specific depth intervals with cemented casing or blank production liner. A preferred method would involve the cessation of drilling before such intervals or magma bodies were fully penetrated. Determining a production fluids' chemical and physical character cannot be achieved until after liner has been installed and a flow test is performed. During a flow test, fluids from individual feed zones mix and the source of problematic zones are difficult to identify. Intersection of both felsic and basaltic magmatic intrusions has resulted in months of drilling delays and millions of

dollars due to lost circulation and stuck drill pipe. Identification of problematic feedzones after well completion is extremely difficult and often too late for mitigating efforts. Insitu characterization of the reservoir conditions while drilling would allow for timely changes to the drill program and casing design.

We attempt the use of fluid inclusion gas analysis to characterize downhole conditions and identify unique signatures associated with problematic production zones, such as the addition of magmatic gases and superheated phase separation. Reservoir-wide fluid-inclusion stratigraphy models may also be implemented to map specific regions of the field which may host problematic fluids. Commercial fluid inclusion gas analyses are common-place in oil and gas drilling, providing rapid analysis to inform on payzone locations. Similar real-time data collection may be applied one day to the geothermal drilling industry to modify reservoir targets and well completions to prevent the production of problematic acidic fluids.

BACKGROUND

Geologic setting at Krafla

The Krafla geothermal field is a high temperature system located within the Krafla caldera in northeast Iceland and currently produces 60MW from over 25 active wells (Gudmundsson, 2001; Landsvirkjun, 2013). The field is situated within a structurally complex volcanic depression along the NNE trending fissure swarm. The central Krafla volcano sits above a magma chamber seismically imaged at 3-8km depth (Einarsson, 1978). Volcanic activity is episodic, occurring at 250-1000yr intervals. The most recent event was the "Krafla Fires" which lasted from 1975 to 1984 and introduced significant magmatic gases into the wellfield (Ármannsson et al., 1989). At least three producing sub-fields, Leirbotnar, Suðurhlíðar and Hvíthólar have been identified based on surface activity and the properties of well fluids (Fig. 1). Leirbotnar wells generally exhibit a high permeability, low enthalpy upper-zone (down to 1100m)

and a two-phase deeper zone with temperatures reaching 350°C to at least 2200m (Fig. 2). The Suðurhlíðar reservoir is two-phase from surface down to total depth. The Hvíthólar field exhibits shallow boiling conditions down to 600m, but suffers from a cool, temperature reversal below this (Ármannsson et al., 1987).

The major lithologic units within the Krafla caldera are a thick hyaloclastite package prevalent down to 1000m, underlain by basaltic lava and hyaloclastite interbeds down to 1400m. Basaltic and doleritic dikes and sills are common within the lava bed succession. Thin, sheeted intrusive units dominate below 1400 which grade into larger intrusive bodies of gabbro and occasional felsite, or 'granophyre' as it is referred to in Iceland, below 1800m. The highly permeable, fractured granophyre units make up the targeted reservoir rock (Ármannsson et al., 1987; Friðleifsson et al., 2006). Bimodal compositions are not uncommon among the Krafla rock suite, as minor volumes of subglacial rhyolitic ridges are found outside the margins of the caldera. Felsic units in Krafla, as much of Iceland, likely form from near-solidus differentiation of partially melted basaltic crust and are emplaced mainly as veins and dikes by deformation-induced melt segregation (Jónasson, 1994; Jónasson, 2007).

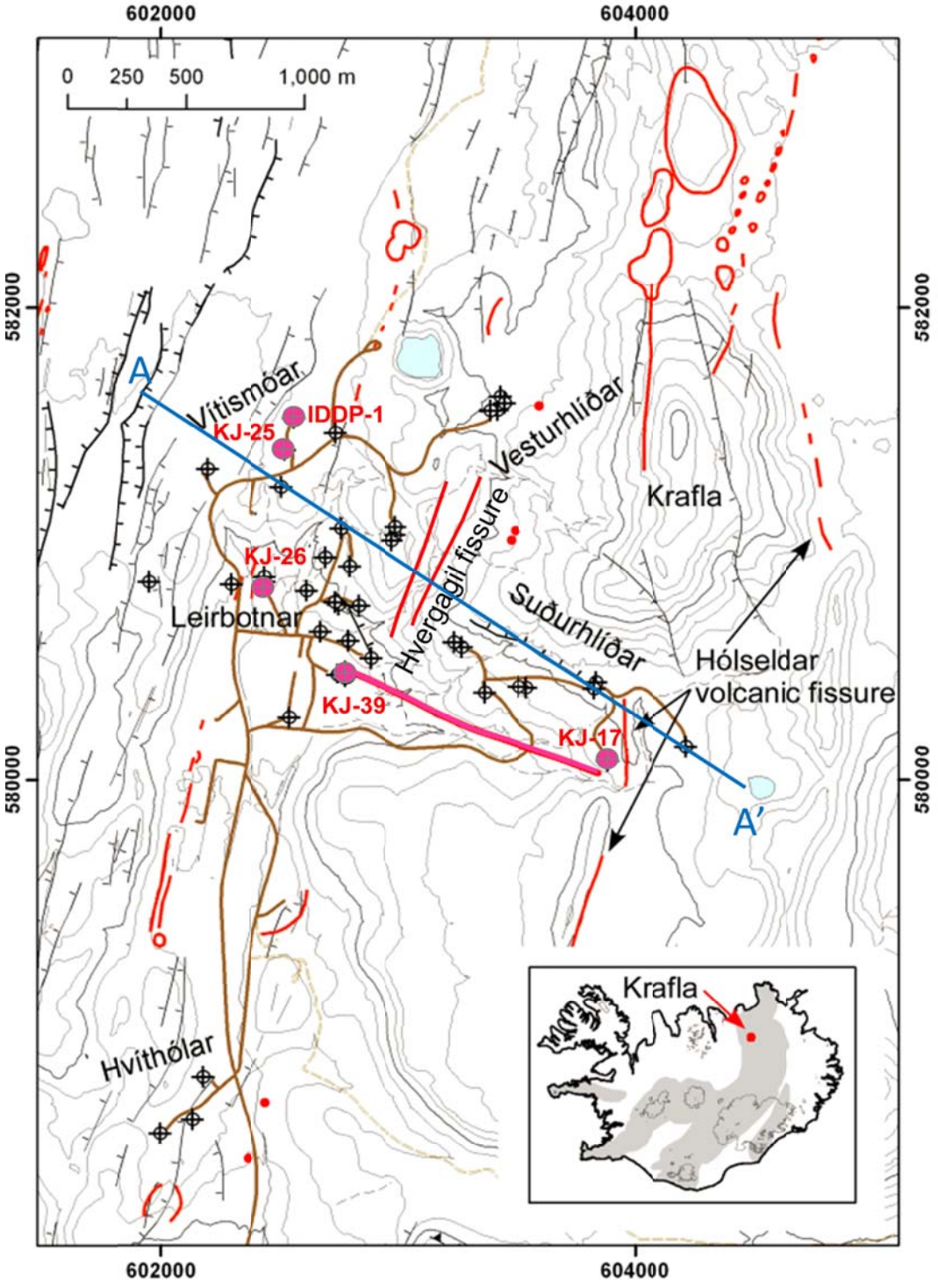

Fig. 1. Wellfield map of Krafla. Wells included in this study and directional well paths highlighted in pink. Location of magmatic fissures and fumaroles illustrated in red. Modified from Mortenson et al. (2010).

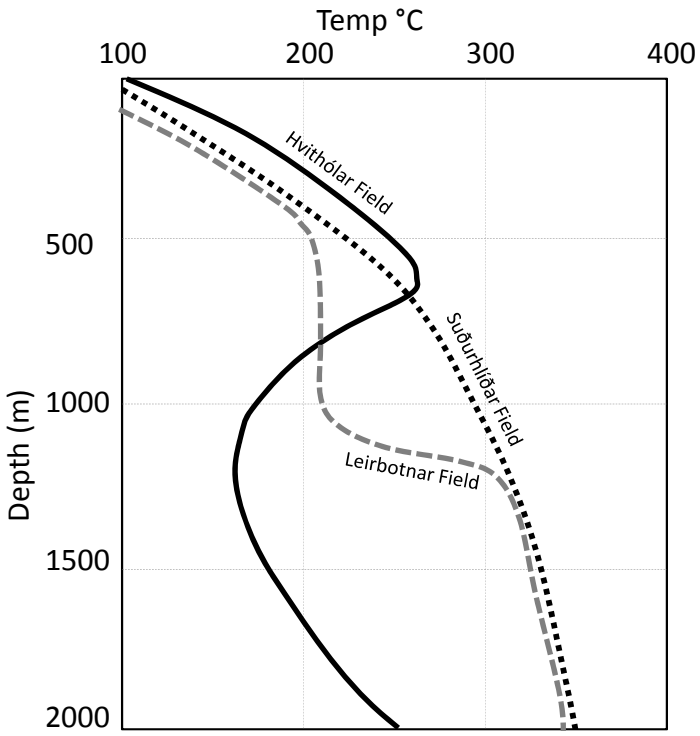

Fig. 2. Idealized formation temperature profiles for the three producing wellfields at Krafla. From Ármannsson et al. (1987).

History of development

Surface exploration of Krafla began in 1970 with the first full-sized production wells drilled in 1974. By 1975, construction of a dual turbine 60MW powerplant was underway. The volcanic events of the Krafla Fires coincided with an invasion of magmatic gases throughout the planned production field. NCG concentrations in the geothermal fluid increased and pH declined dramatically. Due to the large invested cost in the project, drilling continued in search of unaffected parts of the field (Gudmundsson, 2001). Drilling moved from the highly ranked Leirbotnar field to Suðurhlíðar, and later to Hvitholar, as no signs of magmatic gases were found in fumarole fluids from these two subfields (Ármannson et al., 1982). The flux of magmatic gas reached their highest levels from 1976-1980, as indicated by CO_2 concentrations reaching over

60,000ppm in monitored production wells (Gudmundsson, 2001). CO_2 concentrations began to decrease in 1981 as the eruption activity started to wane, yet average values still remain higher than before the Krafla fires. Wells drilled after the eruption subsided in 1984, targeted similar granophyric feedzones near 2000m depth in the Lierbotnar field with hopes of finding uncontaminated reservoir fluids similar to pre-1975 conditions. In many cases, initial flow tests revealed high productivity and low gas, yet the wells quickly dropped pressure and began producing black, low pH liquid full of corroded steel casing and sulfide scale debris. Continued drilling until the year 2000 focused on the productive Hveragil fracture in the Leirbotnar valley allowing for the plant to meet its full 60MW capacity. The most productive wells also yielded elevated NCGs and slight acidity, yet have been dealt with at great operational cost. Currently, additional wells in Krafla are drilled as needed to replace damaged wells and maintain plant capacity; however plans for expansion are stunted until risk of drilling more acidic steam can be mitigated.

Acidic wells

Over 15 wells produce acidic fluid throughout the Krafla field. Superheated wells may produce acidic steam when HCl is volatilized into the vapor phase, which in turn creates super-concentrated HCl liquid upon condensation. HCl in dry steam is nonreactive and may be utilized without corrosion if the steam remains superheated upon delivery to the plant, such is the case of the Geysers (Truesdell, 1991). This is rarely possible at Krafla where sub-boiling feedzones within the borehole induce condensation or mixing with the superheated steam before production at the wellhead where it may be chemically treated. Corrosion and iron sulfide scaling are commonly identified downhole near lower-temperature feedzones (Einarsson et al., 2010). Krafla typically produces neutral, low Cl fluids (<30ppm) owing to equilibrated meteoric recharge in a basaltic volcanic setting (Gudmundsson and Arnorsson, 2005), thus excess chloride is necessary

to create HCl in the vapor phase with superheated conditions (Truesdell, 1991; Truesdell et al., 1989). Excess chloride has been deemed the culprit for acidic production in saturated-steam wells throughout Krafla, particularly in association with fluxing magmatic CO_2 during the Krafla fires (Armannson et al., 1982; Gudmundsson, 2001). We define excess chloride here as chloride equivalent concentrations significantly greater than the sum of equivalent concentrations of cations other than H^+ such as HCl gas from a magmatic steam. Though we cannot measure chloride concentrations by means of fluid inclusion gas analysis in this study, determination of related magmatic gas concentrations and superheated conditions can be used as a tool for identifying the likelihood of finding acidic fluids.

Five production wells with acidic character or proximity to magmatic gases have been selected to investigate the reservoir conditions responsible for problematic production. Production wells KJ-25 and KJ-26 were drilled in 1990-1991 following the Krafla fires to test the quality of fluid in the Leirbotnar field. KJ-25 was completed near Viti crater (Fig. 1) to a depth of 2104m in a granophyre-hosted feedzone. This well initially exhibited high productivity, 50% steamfraction and <1% wt/wt NCG concentration which was a positive sign for improvement of the field. After ten weeks of production, however, the pH of the fluid fell below 2.0 and the liner of the well was destroyed (Helgadottir, 2008). Well KJ-26 was later drilled to a final depth of 2127m to the south of KJ-25 (Friðleifsson et al., 2006). During the first flow test, the well initially produced high enthalpy steam, yet experienced rapid pressure drawdown and began producing black brine enriched in iron, sulfur and silica indicative of scaling and corrosion. The well quickly lost permeability and was eventually converted to an injection well. Fluid chemistry from this well indicated very different compositions from the upper and lower parts of the well, possibly responsible for the quick formation of scale upon mixing in the borehole. Discharge fluids revealed that CO_2 concentrations in KJ-26 had returned to pre-eruptive conditions in this

portion of the Krafla field despite the high Cl concentration of the fluids (608ppm) and mild acidity (4.1 pH).

Production well KJ-39 was directionally drilled in 2008 within the Suðurhlíðar field to a depth of 2865m, targeting the Hólseldar fissure-forming fracture. After reaching TD (total depth) the drill string became stuck and had to be backed off with the aid of explosives. The deepest recovered drill pipe contained cuttings of fresh holocrystalline basalt and quenched silicic glass suggesting magma had flowed into the borehole below 2800m (Mortensen et al., 2010). Petrologic analysis of the silica glass indicates a strongly subalkaline, peraluminous composition (hornfels facies) resulting from the anatexis of hydrated basalts associated with the intruding basaltic dike. Maximum temperatures of 386°C were measured with a Kuster tool at 2822m within the stuck drill string, however, corresponding reservoir pressures could not be carried out to quantify supercritical conditions within the reservoir. The well was ultimately plugged back with cement to 2620m depth as high temperatures and vicinity to magma raised the concern that fluid from bottomhole would be acidic and cause damage to the well and render it unsuitable for steam generation. Despite this modification, superheated steam still produces from the lowermost feedzones, at approximately 2400m, resulting in volatilized HCl and severe corrosion to the liner upon mixing with saturated feedzones in the shallow well.

IDDP-1, located in the northern Leirbotnar field near KJ-25, was drilled in 2008-2009 in attempts of finding 450°C fluids at 3.5-4.0km depth, near the brittle/ductile boundary above the Krafla magma chamber to produce supercritical phase fluids (Friðleifsson and Elders, 2005; Friðleifsson et al., 2010). The well encountered magma at 2100m following weeks of problems with lost circulation and stuck drillpipe. Drill cuttings revealed the lowest 20m of the well was plugged by quenched obsidian. Petrologic studies indicated the rhyolite formed from a mantle-derived magma assimilating partially melted hydrothermally altered basalt at near 900°C (Elders

et al., 2011). The well was flow tested in 2010 and determined to still be a highly productive well (25MW) capable of producing 380°C superheated steam at over 100bar wellhead pressure. The steam contains a high Cl concentration, yet low CO_2/H_2S ratio compared to other superheated wells (Ármannsson, 2010). The casing is being redesigned to handle more corrosive fluids.

Well KJ-17, drilled in 1983 in the Suðurhlíðar field near the bottomhole target of KJ-39 (Fig. 1), also encountered fresh silicic glass in cuttings from 2156m composed of hornfels-facies rhyolite (Óskarsson and Grönvold, 2009). Despite its proximity to a molten intrusion and ongoing volcanic activity, this well did not produce acidic fluids, making it an important control to further examine the relationship between production character and geologic setting.

Hydrothermal gases at Krafla

Hydrothermal gas compositions at Krafla derive from equilibrium reactions with volcanic gases in meteoric water and basaltic rock. Icelandic volcanism produces olivine-tholeiitic mid-ocean ridge basalts (MORB). Gas inputs in mid-ocean ridge and hot-spot volcanoes descend directly from the mantle thus have moderate contributions of C and S and are relative depleted in H_2O (Symonds et al., 1994; Giggenbach, 1997). CO_2 and SO_2 make up the majority of a typical volcanic dry gas suite; HCl makes up between 0.5 and 1mol% dry gas(Table 1). H_2 and H_2S still represent a significant portion of fresh volcanic gas. Icelandic systems also exhibit substantial molar concentrations of He, namely mantle-derived ^3He with $^3He/^4He$ values ranging from 11 to 26 times the atmospheric ratio (R/R_a). Conservative species such as He, N_2 and Ar plot near the He apex of the magmatic-source-ternary developed by Giggenbach (1995, 1997). N_2/Ar ratios should reflect air-saturated meteoric water as there is no source of subducted marine sediments to contribute excess N_2 in Iceland MORBs. Ar values can only be attributed to a meteoric source, thus we may ratio other gas components against Ar as a means of comparing volatile inputs.

Reactive gas species in the Krafla reservoir are efficiently buffered by the quartz + calcite + epidote + prehnite + pyrrhotite + pyrite mineral assemblage. Arnorsson and Gunnlaugsson (1985) calibrated the thermodynamic relationships of CO_2, H_2S, H_2 using real data from Icelandic systems to create gas geothermometers which are still part of the standard methodoloy today (Arnorsson et al., 1990; Gudmundsson and Arnórsson, 2002; Gudmundsson and Arnórsson, 2005). Above 230°C, CO_2 is buffered by epidote + prehnite + calcite + quartz by the temperature relationship:

$$t_{CO2} = -44.1 + 269.25Q - 76.88Q^2 + 9.52Q^3 \quad \text{(eq 1)}$$

For reservoir fluids above 300°C, H_2S and H_2 are buffered by pyrite + epidote + prehnite + chlorite by the relationships:

$$t_{H2S\text{-}high} = +246.7 + 44.81Q \quad \text{(eq 2)}$$

$$t_{H2\text{-}high} = +277.2 + 20.99Q, \quad \text{(eq 3)}$$

where temperature is in °C and gas concentrations, Q, are in mmoles per kg steam.

For lower temperature reservoir fluids between 200-300°C, H_2S and H_2 are buffered by pyrite + pyrrhotite + epidote + prehnite by the relationships:

$$t_{H2S\text{-}low} = +173.2 + 65.04Q \quad \text{(eq 4)}$$

$$t_{H2\text{-}low} = +212.2 + 38.59Q, \quad \text{(eq 5)}$$

Gas-gas equilibrium between CO_2, CH_4 and H_2 is closely approached in geothermal systems (Giggenbach, 1980), however this is not to be the case in Krafla demonstrated by a poor fit between aquifer temperatures and those thermodynamically predicted by Fisher Tropsch reactions. The limited availability of methane and the reduction reaction of CO_2 is too slow to compete with other mineral buffers (Arnórsson and Gunnlaugsson, 1985; Stefánsson and Arnórsson, 2002).

Gas concentrations from fluid inclusion gas analysis may be applied to calculate theoretical formation temperatures and comparison to measured static temperatures. Poor agreement between the actual and theoretical formation temperatures may be used to identify a disruption in the equilibrium relationships described above, such as a flux of excess magmatic gas into the reservoir. During the eruption of the Krafla fires, excess gases identified in production fluids had a unique signature of CO_2/H_2S >30 (Gudmundsson, 2001) as CO_2 appeared to be contributed in greater amounts than H_2S. A comparison of fumarole compositions before and during the eruptions saw similar trends with an average excess gas component made up of CO_2 = 98.8%, H_2S = 1.2%,H_2 = 0% (Armannson et al., 1982). If gases emanating from a magmatic source are at all similar to the volcanic assemblage discussed above, the fluids must have modified considerably before production. SO_2, in particular, is extremely soluble and forms a strong acid upon dissolution in water, which may then disproportionate into H_2S and SO_4^{-2} (eq 6 and 7). These products will react with divalent iron, which is abundant in reactive forms such as in basaltic glass, magnetite and pyroxene in Krafla rocks, and forms pyrite and pyrrhotite (eq 8 and 9). The dramatic decrease in $\Sigma S/\Sigma C$ from volcanic gases to the hydrothermal system is likely related to iron sulfide deposition which is observed in abundance in Krafla wells.

$$SO_2 + H_2O \leftrightarrow SO_3^{-2} + 2H^+ \leftrightarrow H_2SO_3 \qquad \text{(eq 6)}$$

$$4H_2SO_3 \leftrightarrow 6H^+ + 4SO_4^{-2} + H_2S \quad \text{(eq 7)}$$

$$4Fe^{+2} + 7H_2S + SO_4^{-2} \leftrightarrow 4FeS_2 + 4H_2O + 6H^+ \quad \text{(eq 8)}$$

$$Fe^{+2} + H_2S \leftrightarrow FeS + 2H^+ \quad \text{(eq 9)}$$

Reservoir conditions such as boiling and condensation may also affect the mineral equilibrium relationships. Superheated boiling, in particular, will form vapor-rich fluids inclusion with elevated gas concentrations, driving geothermometer values above expected formation temperature. Such conditions may be identified with the use of fluid inclusion gas analysis by observing bimodal inclusions exhibiting variable amounts of gas/liquid components (Norman et al., 1996). Boiling within the reservoir will also preferentially partition less soluble gases such as N_2 and H_2 into the vapor phase over more soluble gases such as CO_2 and H_2S. Condensation of magmatic gases or gas-rich steam within the reservoir will exhibit an opposite effect of increasing soluble gases with increasing total gas content. Plots of CO_2/N_2 vs total molar gas % provide for easy identification of these processes (Norman et al., 2002).

Superheated conditions should be manifested as boiling or vapor-dominated fluids within the reservoir as a result of temperatures exceeding that expected for saturated steam at a given formation pressure (i.e. plotting above the boiling point curve).

Sample	Sample Temp °C	Sample Pressure Bar-g	Enthalpy kJ/kg	Mol gas /kg H_2O	*mol% dry gas*												
					H_2	He	N_2	O_2	CH_4	Ar	CO_2	H_2S	SO_2	CO	S_2	HCl	HF
Surtsey basalt ¥	1125	atm		12.35	15.52						51.50	4.93	22.84	3.82	1.39	0.5-1	nd
Iceland**	300					0.003	0.25			0.004	85.00					2	
K-30*	290	28.5	2508	0.47	2.33		0.66	0.008	0.004	0.010	87.58	9.40					
K-20	280	9.8	2306	0.73	2.58		0.29	0.005	0.033	0.005	92.80	4.28					
K-20	280	12.8	2370	0.74	3.60		0.21	0.000	0.047	0.004	91.97	4.17					
K-12	275	13.3	1831	0.18	3.70		0.36	0.009	0.098	0.009	87.74	8.08					
K-17	275	21.7	1881	0.13	12.03		0.87	0.000	0.324	0.020	74.94	11.82					
K-15	265	11.7	1790	0.16	6.75		0.60	0.011	0.014	0.011	79.91	12.71					
K-27	250	10.5	1716	0.09	12.54		1.62	0.033	0.141	0.033	74.23	11.40					
K-14	245	8.5	2267	0.29	8.11		0.47	0.010	0.046	0.010	82.90	8.45					

Table 1. Compilation of volcanic and hydrothermal gases from Iceland and Krafla fields.

¥ Symonds et al., 1994

**Giggenbach, 1997

* Gudmundsson and Arnórsson, 2002 (*all Krafla wells*)

METHODS

Fluid inclusion gas analysis

Fluid inclusion gas analysis by rapid crush methods provides quantitative gas concentrations which could not otherwise by obtained by thermometric methods or Raman spectroscopy, and offers improved gas extraction to thermal decrepitation methods which may alter the chemical suite at elevated temperatures (Norman et al., 1996). Typical analyses are performed on larger secondary mineralization suites handpicked from core samples. Drill cuttings from large diameter geothermal wells rarely provide adequate sized samples for discrete analysis of a single vein or paragenesis suite, however, strain rates allow continuous trapping of gases in secondary mineralization and micro-veining. Cold crush bulk analysis of whole cuttings involves extracting trapped fluids from such micro-veins, resulting in a statistical representation of the reservoir composition. Previous studies (McLin et al., 2006; Dilley et al., 2006) demonstrate that active geothermal reservoirs constantly reprint geothermal signatures within fluid inclusions in response to evolving fracture permeability, temperature and chemical equilibrium, which inherently force changes on the secondary minerals and their inclusions.

Analytical procedure

Six wells in the Krafla fields were selected for assessing processes associated with magmatic gas influx, corrosive fluid production or supercritical conditions. Well cuttings were collected at 50-100m intervals, or as often as available, for crush-fast-scan fluid inclusion gas analyses as described in Norman et al. (1996). Cuttings with secondary vein material were prioritized for crushing, however, pure secondary mineral separates were extremely rare. Secondary mineral samples were set aside for comparative analyses of CO_2, H_2S, H_2 and Cl concentrations by Laser Ablation-ICP-MS in an associated study, however no inclusions were identified large enough (>40um) for such analysis below ~1000m depth (Mortenson, 2010

personal communication). 100g samples were cleaned with NaOH and distilled water and allowed to dry under low heat <40°C for two days. Cuttings were placed in crushers and evacuated while heating to 60°C overnight until a pressure $<10^{-7}$ Torr was attained. The analysis is performed by means of two Pfeiffer Vacuum Prisma mass spectrometers operating in a fast-scan, peak-hopping mode. The cold crush method involves opening inclusions by a swift crush in the vacuum chamber housing the mass spectrometers and released volatiles are quickly removed by the vacuum pumping system. Between two and five crushes were obtained from the same sample depending on the number and volume of fluid inclusions. Opening a 10-20 μm inclusion or equivalent volume of smaller inclusions provides the ideal amount of volatiles for analysis. This pulse is recorded by operating the quadrupoles in a fast scan mode with measurements every 200 to 250 millisecond. The mass peak areas are used to determine the relative concentration of each species. Predetermined sensitivity factors, peakstripping algorithms and matrix-inversion programs were designed in-house to refine the concentration outputs. Species routinely recorded are H_2, He, CH_4, H_2O, N_2, O_2, H_2S, Ar, CO_2 and SO_2. The mass spectrometer is calibrated with commercial gas mixtures, artificial inclusions filled with gas mixtures, and an in-house fluid inclusion standard. The gas/water ratio of the standard inclusions (Hansonburg Fluorite-1) is known to ~ 0.1% by Penfield-tube analysis, thus allowing water calibration with an error less than 0.2%.Measurement precision is <5% for major gaseous species and ~10% for less representative species.

RESULTS

Well KJ-39

Fluid inclusion gas analysis profiles plotted as a function of depth for well KJ-39 are illustrated in Fig. 3. Gas geothermometers are plotted against static temperature profiles and boiling point curves for this well. H_2S and CO_2 geothemometers appear to match measured

temperature profiles between 950 and 2500m depth, with over and under predictions >30°C, slightly greater than the expected error estimated by Arnorsson and Gunnlaugsson (1985). t_{H2} geothermometers exhibit the best correlation with the boiling point curve in this formation. Geothermometer temperatures strongly diverge below 2550m resulting from a rapid increase in CO_2 concentration and gas fractions. A pronounced spike in CO_2 (mol%), total gas concentrations, N_2/Ar ratios, and CO_2/N_2 ratios may also be observed at 2800 total depth, corresponding with a molten felsic glass and a basaltic intrusion. A primary geothermal feedzone is identified immediately above this at 2735m as determined from waterloss test temperature logs. A temperature reversal observed within the static logs for KJ-39 at 2500m, immediately below a superheated zone, is matched by H_2S and H_2 geothermometer profiles which illustrate a similar trend.

A plot of CO_2/N_2 ratios vs. total gas concentrations (Fig. 8-a) illustrate a possible input of CO_2 (as well as N_2) at 2800m, followed by boiling within the formation up towards 1750m indicated by decreasing CO_2/N_2 values with increasing total gas. Phase separation forming coeval gas-rich and gas-poor fluid inclusions is apparent in Figs. 3 and 8-a. Subsequent condensation of the partitioned geothermal gases is the dominate process between 450 and 1550m depth.

Relative N_2, Ar and He contributions are illustrated on a ternary diagram (Fig. 9-a) showing N_2/Ar values between air and air-saturated water for most samples. N_2 enriched samples at 2800m anomalously plot within the arc-volcanic zone as defined by Giggenbach (1997), which is unexpected for Icelandic MORBs. Other slighty N_2 enriched samples occur at 2650-2550m directly above the magmatic intrusion, and at 2150-2050m. Excessive N_2 may be the product of partitioning of this insoluble gas during phase separation which can create vapor-phase fluid inclusions with N_2/Ar upwards of 110 from a meteoric water due to differing liquid/vapor dissociation constants between the two gases (Moore et al., 2001); however KJ-39 exhibits N_2/Ar

ratios upwards of 210. Excess N_2 could also suggest contamination, such as a quenching of drilling fluids in molten glass, however, the occurrence of elevated N_2/Ar in the 400 meters of cuttings collected above the intrusion rule out this potential source. Enriched He molar concentrations are indicated for most samples plotting off the N_2/Ar axis, with elevated values in samples from 2400-2650m, 1950m and 1150-1200m depth. These plot towards the mantle-apex, illustrating that geothermal fluids in KJ-39 are strongly influenced by mantle-derived magmatic gases.

Well IDDP-1

Fluid inclusion gas profiles are plotted for well IDDP-1 in Fig. 4. H_2 geothermometers correlate quite closely with reservoir temperatures; however, H_2S geothermometers diverge strongly upwards of 100°C from measured temperatures even when incorporating contributions from SO2 (Fig.4). CO_2 geothermometers illustrate a 30-60°C underestimate from the formation temperature above 1700m depth, with better convergence at greater depth (1900-2000m). A strong spike in CO_2 concentrations and t_{CO2}correlates with a spike in total gas concentration between 2000-2072m depth. An additional spike in He/Ar ratios, He mol%, SO_2, and N_2/Ar ratios are most pronounced at 2032-2046m, located 12 meters above the felsic intrusion, supporting an influx of magmatic CO_2, SO_2, He and N_2 gas.

CO_2/N_2 ratios are relatively constant (1.5-4.0) with depth, yet do slightly increase near bottomhole. Plots of CO_2/N_2 vs. total gas (Fig. 8-b) illustrate complicated boiling and condensation dynamics within the reservoir. A zone of magmatic gas influx from 2046m is characterized by a CO_2/N_2 ratio of 5.0-6.0 with near 33-55% total gas concentrations. This gas-charged fluid is subsequently boiled into liquid and steam phases above the superheated rock-formation from 2041 and 2000m depth. The low CO_2/N_2 condensate product of this boiling

forms a second superheated gas-charged steam reservoir between 1900-2000m depth. Condensation of these partitioned gases is indicated above 1850m in a non-flashing reservoir.

He-Ar-N_2 ternary diagram (Fig. 9-b) illustrates an interesting mix of magmatic volatiles occurring below 1250m depth. The N_2/Ar ratio from 1250-1600m is consistent with air or air-saturated waters with increasing concentrations of magmatic He. The anomalous He concentrations may be a contribution from partitioned gases in the boiling reservoir below, or a localized flux of magmatic gas. Fluids trapped below 1700m exhibit elevated N_2/Ar ratios >200 as observed in well KJ-39 at 2800m. Unlike KJ-39, sample points scatter throughout the ternary diagram and do not follow normalized trends associated with distinct magmatic inputs as defined by Giggenbach (1997). The scatter between points from the same depth argues for phase separation or boiling occurring in the reservoir which is partitioning gases of different solubilities. Fluids with the highest N_2 concentration appear to be sourcing from 2046m depth immediately above the molten glass.

Well KJ-25

Geothermometer values, as well as other gas profiles for well KJ-15, are found in Fig. 5. CO_2 geothermometers correlate well with static temperature profiles, particularly within the sub-boiling zone above 1150m characteristic of the Leirbotnar field wells. t_{H2S} profiles follow the formation temperature within the shallow steam zone, yet strongly diverge at greater depths. SO_2 dominates over H_2S near bottom hole, which is used to project total-S corrected $t_{H2S+SO2}$ profiles. t_{H2} profiles more closely match the proposed boiling point curve. All geothermometer profiles increase in concert below 1200m suggesting mineral equilibrium conditions dictate the chemical composition of the fluid inclusion gases and not localized phase separation or gas-input. This is supported by CO_2/N_2 and total gas plots (Fig. 5 and 8-c) which illustrate few coexisting vapor and liquid-rich inclusions, as well as a lack of boiling or condensation trends. A steam-phase is

strongly evident from 350-1050m based on the isothermal static temperature profiles. Magmatic gas input is evident at 2104m corresponding with CO_2/N_2 values of 2-3 and 11 mol% total gas. Minor phase separation is apparent between 2002 and 2104m possibly associated with magmatic steam and localized superheating near bottomhole.

He-Ar-N_2 ternary diagram indicates mainly air-saturated N_2/Ar waters with minimal contribution from a He-enriched magmatic gas in KJ-25 (Fig. 9-c). Samples plotting off the N_2/Ar axis largely correspond with the temperature inflection and reservoir boundary postulated between 1250-1450m, possibly related to a gas cap trapping insoluble gases such as He.

Well KJ-26

Well KJ-26 (Fig. 6) exhibits similar geothermometer profiles as KJ-25. CO_2 and H_2S geothermometers strongly correlate with formation temperatures between 694-959m within the capping low-enthalpy reservoir. t_{H2} values largely follow the presumed boiling point curve. All geothermometers between 1250-1750m largely change in parallel indicating partial chemical equilibrium within these depths. Boiling is evident between 1800-2100m based on dual-phase fluid inclusions based on CO_2/N_2 vs total gas plots (Fig. 6 and 8-d) resulting in vapor-filled inclusions exhibiting elevated t_{CO2} He, CO_2 and SO_2 concentrations. Phase separation is observed where where static temperature profiles approach the boiling point curve, thus superheating would not have been detected from downhole logs alone in this case. The He-Ar-N_2 ternary diagram indicates mainly air-saturated N_2/Ar waters with limited magmatic He (Fig. 9-d).

Well KJ-17

Well KJ-17 geothermometers strongly diverge from measured or predicted formation temperatures at all depths, which largely follows the boiling point curve within the Suðurhlíðar reservoir (Fig. 7). H_2 geothermometers overpredict the formation temperatures by ≤60°C. H_2S and CO_2 geothermometers generally share similar values below 900m depth, yet under-predict

formation temperatures by an average of 45°C. KJ-17 exhibits low total gas concentrations (<2 mol%) and near constant CO_2/H_2S ratios with depth. Elevated N_2/Ar ratios are identified at 2100-2150m, directly above the melted felsic glass encountered at 2156m, corresponding with minor spikes in t_{CO2} and He concentrations. He-Ar-N_2 ternary plots (Fig. 9-e) confirm this occurrence with scattered values plotting above air and air-saturated water concentrations trending towards arc-type magmatic values.

Limited phase separation or gas-input may be observed within this borehole based on CO_2/N_2 vs total gas plots (Fig. 7 and 8-e). A minor boiling trend is observed between 1150-1950m, while a possible condensation trend is observed between 300-1050m. Very minor total gas increases may be observed near the felsic glass at 2150m.

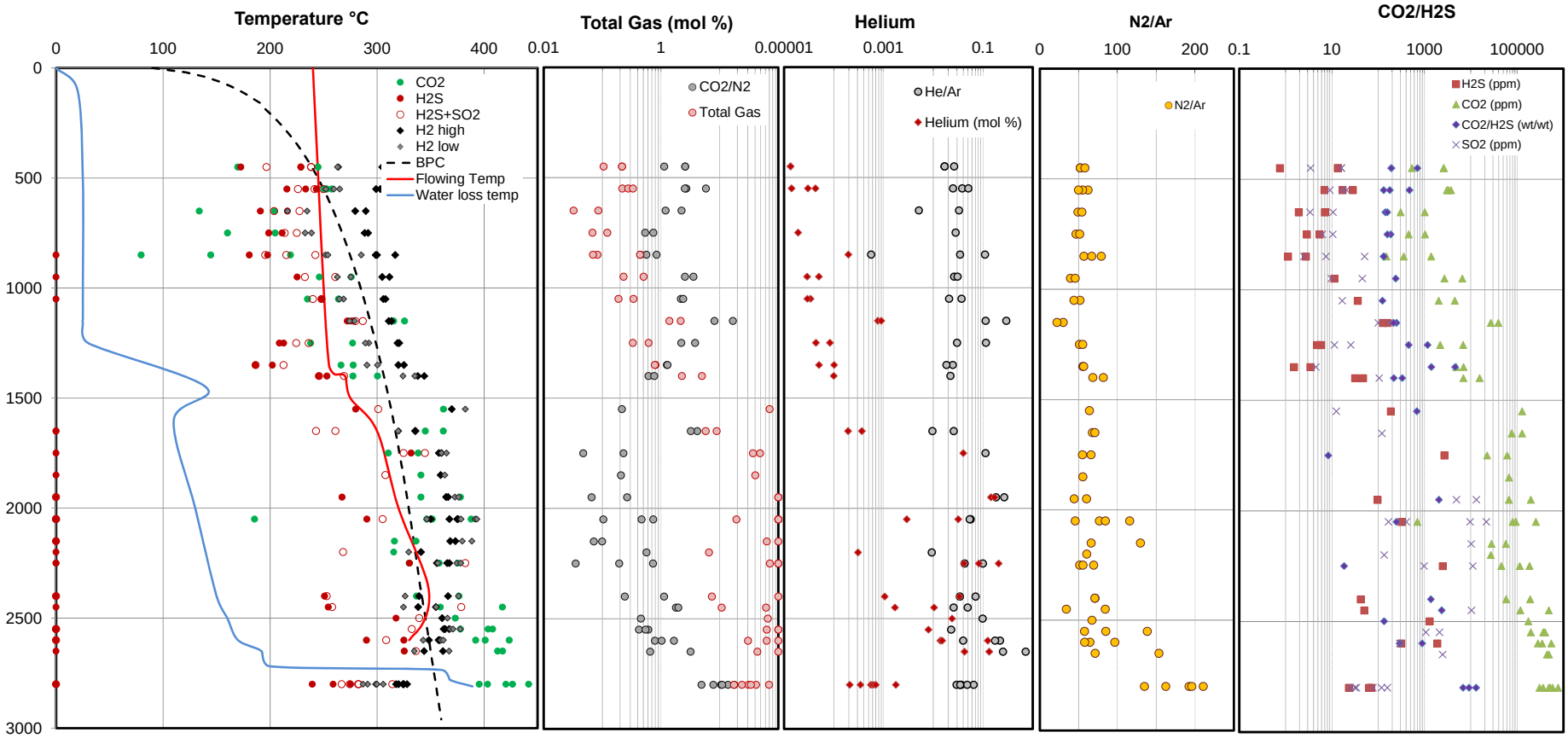

Fig. 3. Well KJ-39 fluid inclusion profile. CO_2, H_2S, H_2-high, H_2-low temperatures based on equations in Section 2.4. H_2S+SO_2 temperatures are calculated from the H_2S-high geothermometer equation using ΣSO_2+H_2S (molar concentration). Boiling point curves calculated based on depth of watertable and fluid density; flowing temperatures derived from downhole logs during flow test; measured temperatures derived from static logs where available; water loss test temperatures derived from logs during steady injection into the borehole illustrating feedzone locations. Total gas, CO_2/N_2, He/Ar, He, N_2/Ar values represent molar concentrations. H_2S, CO_2, CO_2/H_2S and SO_2 represent ppm-wt concentration.

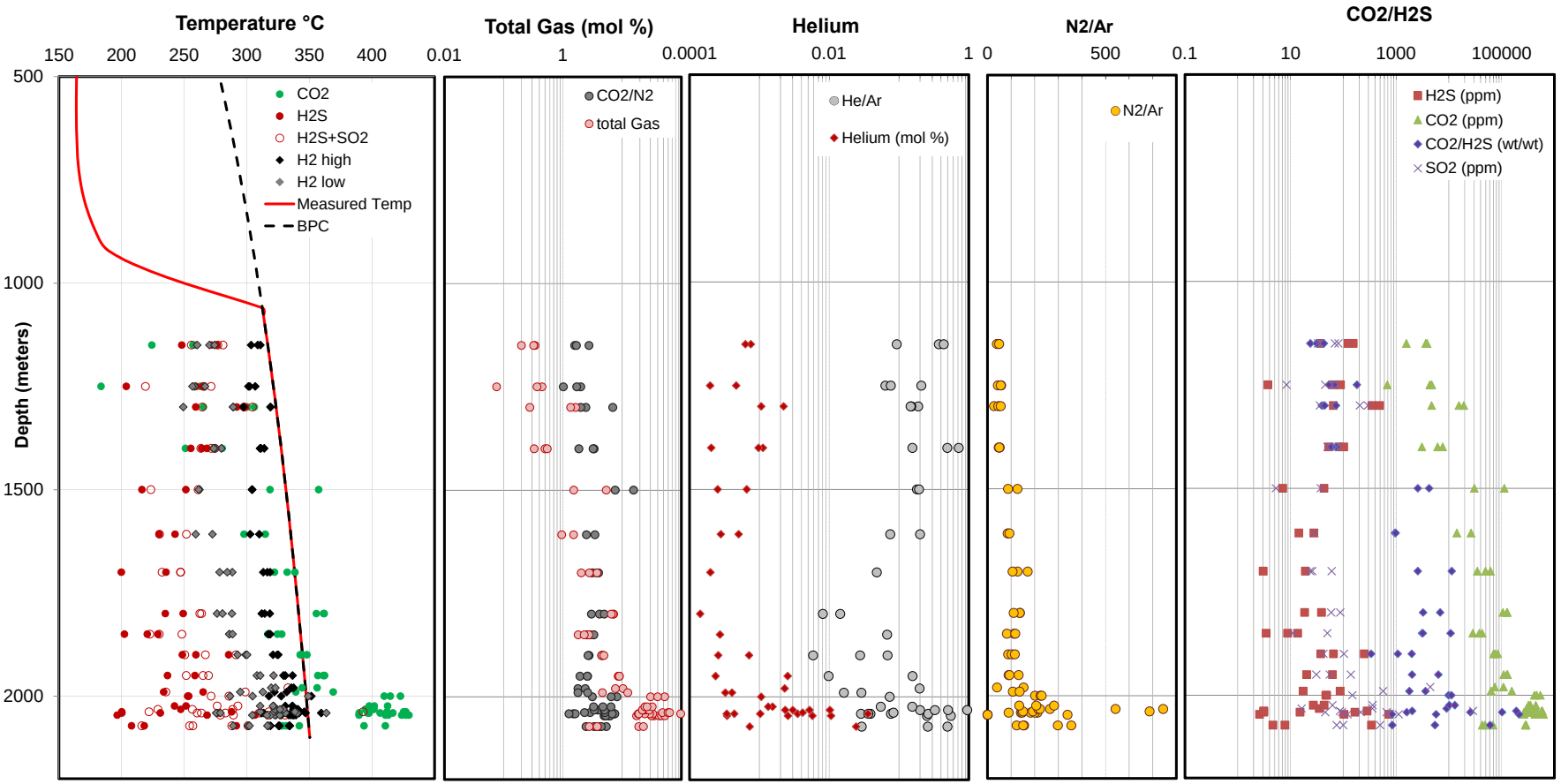

Fig. 4. Well IDDP-1 fluid inclusion profiles. See Fig.3 caption for explanation.

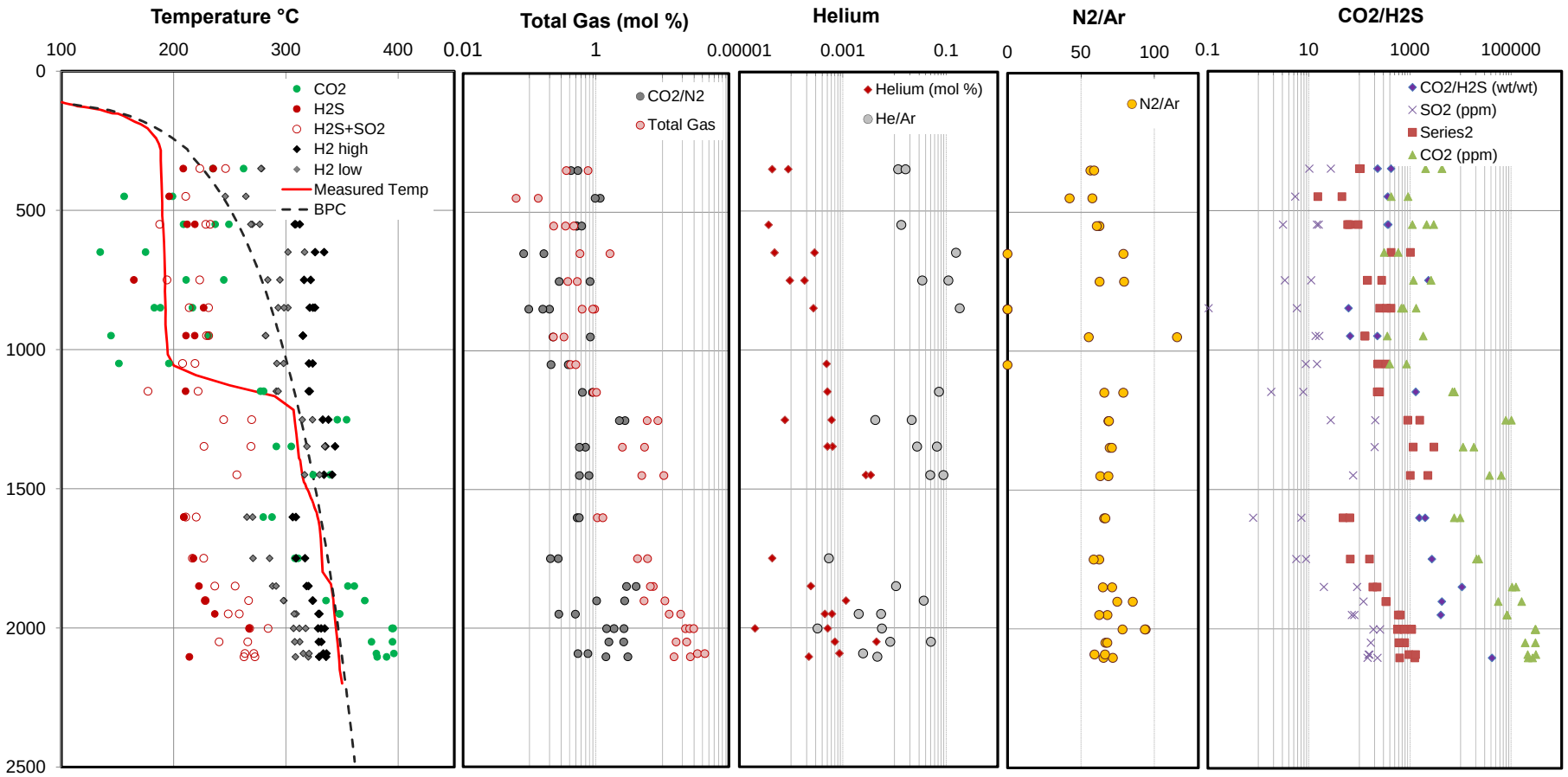

Fig. 5. Well KJ-25 fluid inclusion profiles. See Fig.3 caption for explanation.

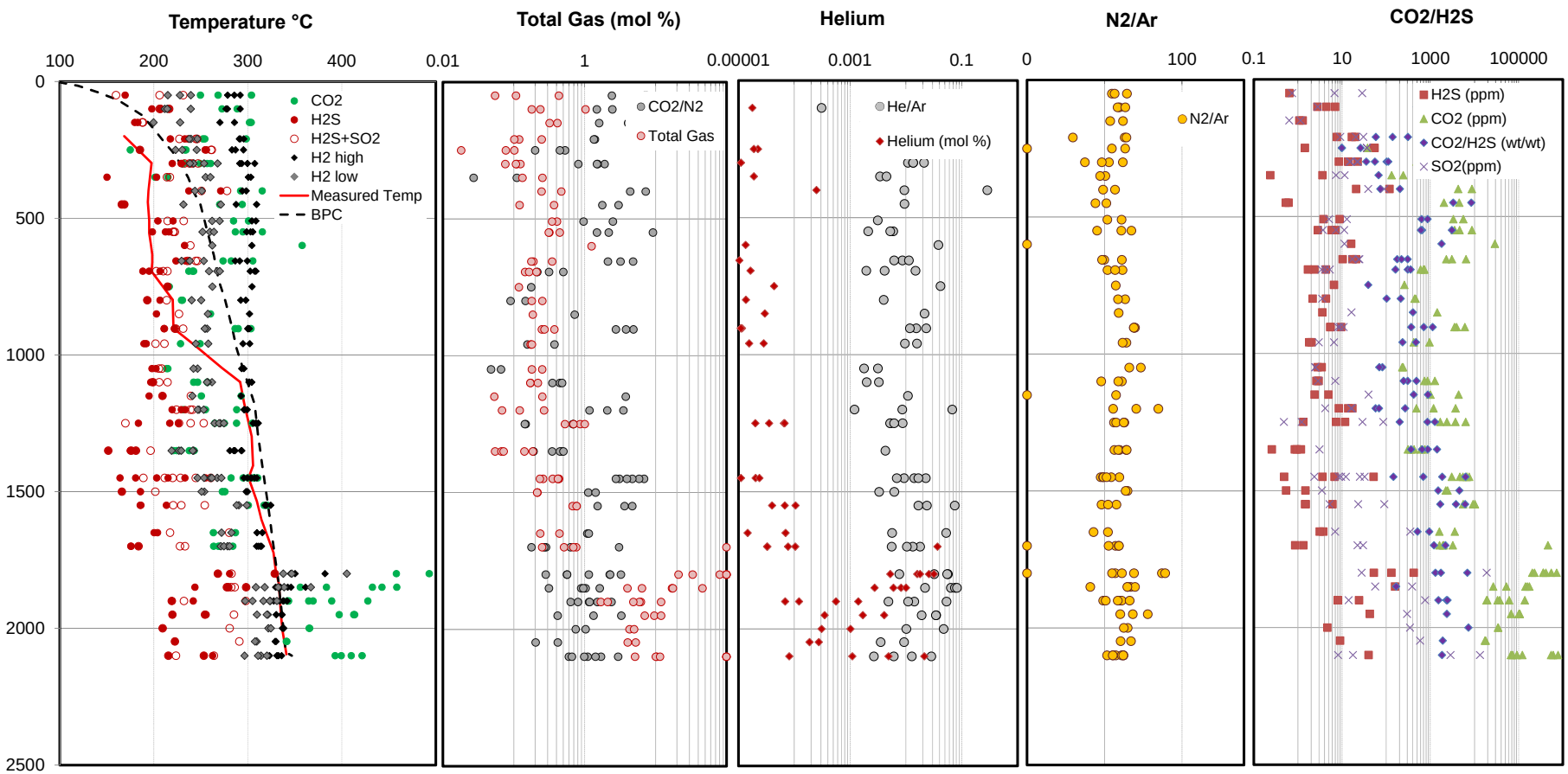

Fig. 6. Well KJ-26 fluid inclusion profiles. See Fig.3 caption for explanation.

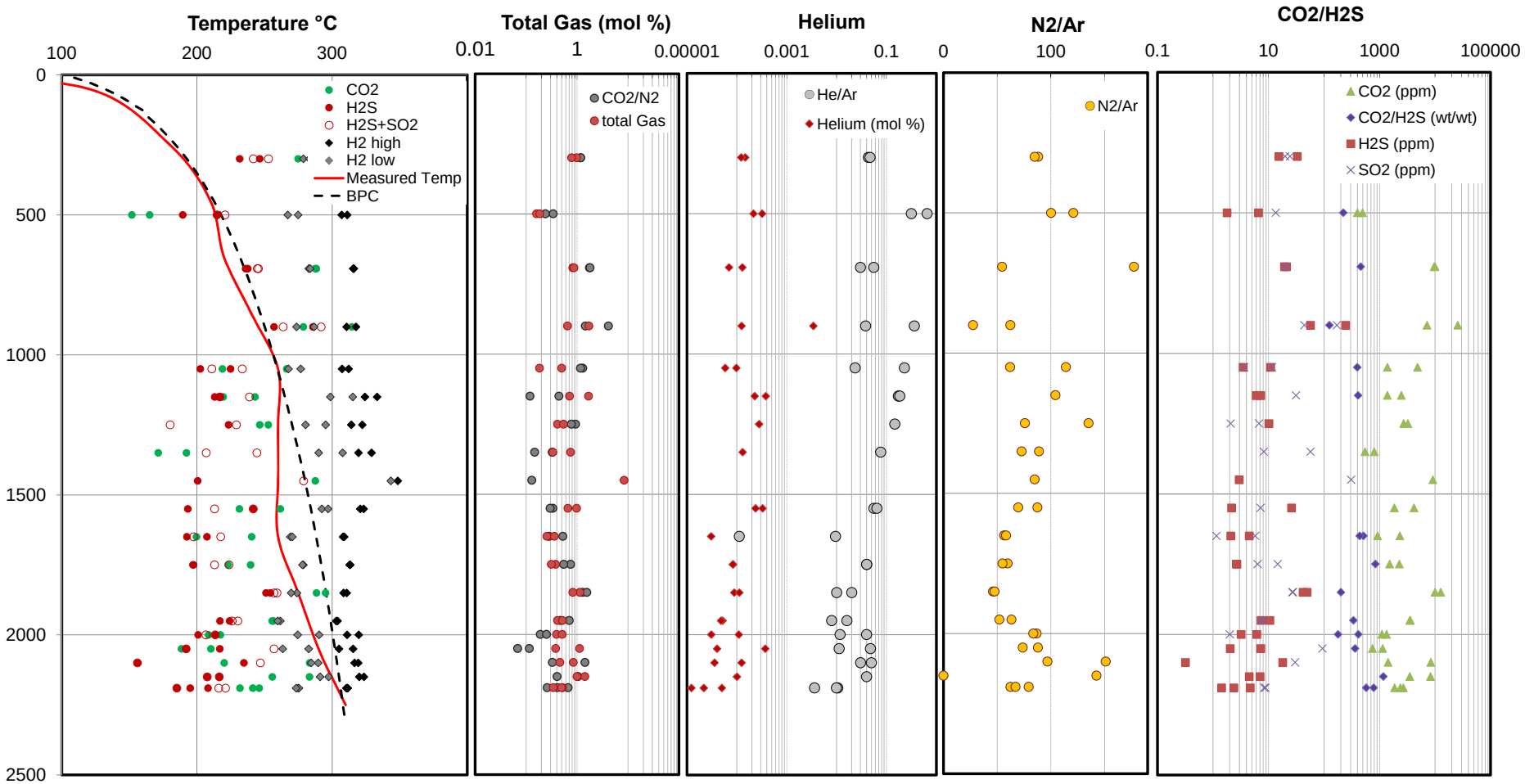

Fig. 7. Well KJ-17 fluid inclusion profiles. See Fig.3 caption for explanation.

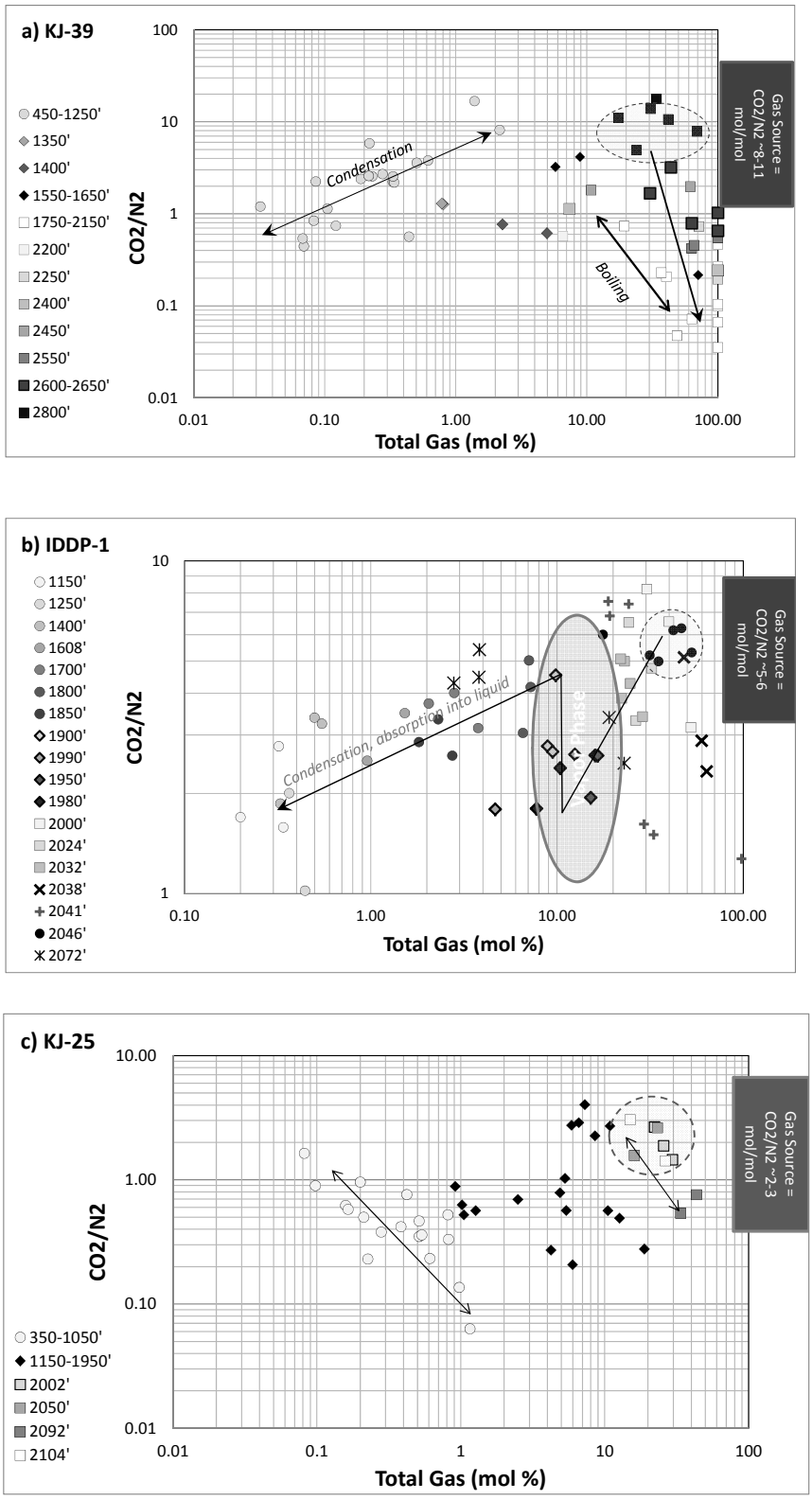

Fig. 8. CO_2/N_2 vs total gas plots illustrating magmatic gas input, condensation and boiling conditions.

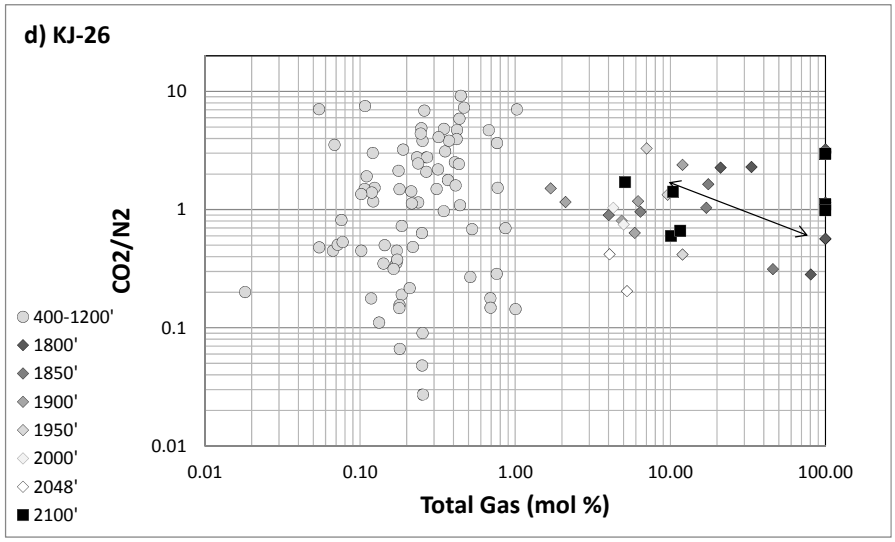

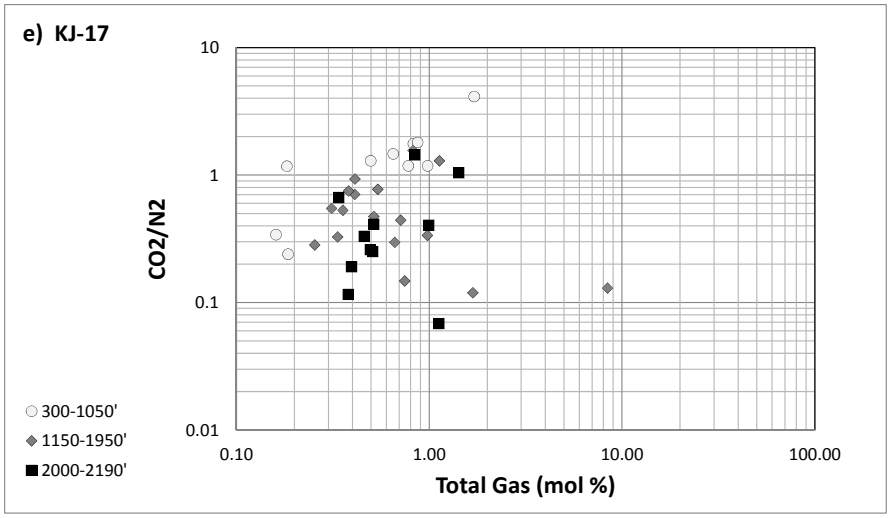

Fig. 8 *cont*. CO_2/N_2 vs total gas plots illustrating magmatic gas input, condensation and boiling conditions.

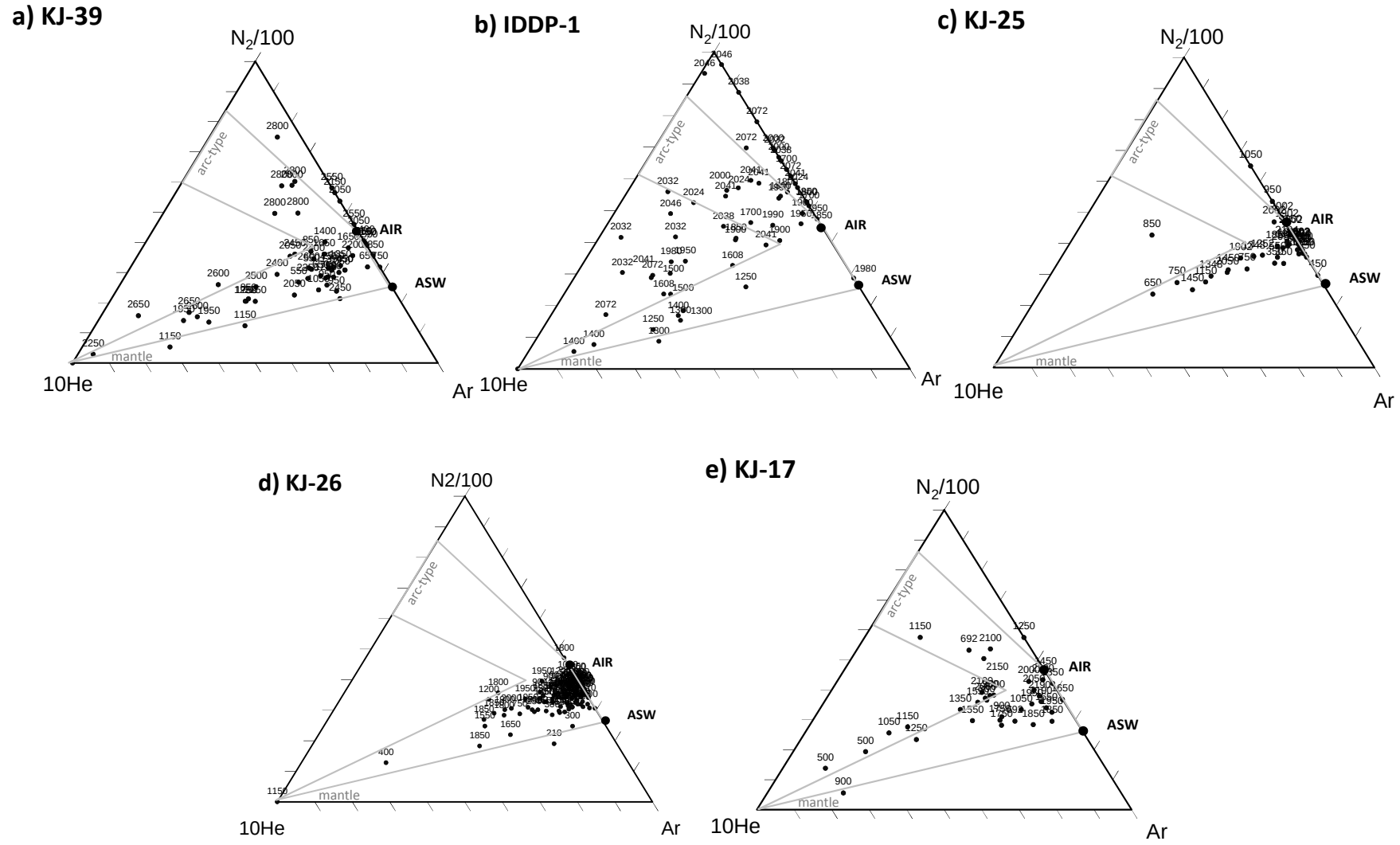

Fig. 9. N_2-Ar-He ternary diagrams, format from Giggenbach (1997).

DISCUSSION

Geothermometers

Gas geothermometers agree best with formation temperatures for equilibrated wells and those sections unaffected by magmatic gas input. Wells KJ-26, KJ-25 and KJ-17 exhibit good agreement with t_{CO2} and t_{H2} values, particularly below 1000m depth. $t_{H2\text{-}high}$ exhibits good agreement for static temperatures above 300°C; $t_{H2\text{-}low}$ exhibits improved agreement below 300°C as defined by the empirical calibration (Arnórsson and Gunnlaugsson,1985). t_{CO2} agrees most closely with all wells above 1000m and below 300°C, demonstrating more rapid equilibrium with single phase or sub-boiling reservoirs. $t_{H2S\text{-}high}$ consistently underpredicts formation temperatures, particularly for depths >250°C, suggesting poor equilibrium with buffer minerals. The rapid removal of sulfur from fresh magmatic gas in both surface fumaroles as well as fluid inclusion profiles, suggests efficient scrubbing by precipitating iron sulfides as observed in many of the geothermal well cuttings. Such precipitation reactions are enhanced by flashing, which locally increases the pH and is expected near the exsolution of magmatic steam in an aqueous environment.

SO_2 is rarely detected among geothermal fluids or hydrous fumarole discharges due to the rapid dissociation in water. H_2S geothermometers are recalculated for ΣS assuming all SO_2 is available for conversion to H_2S by the reaction in equation 6 and 7. Predicted temperatures are only a few degrees (~20°C) higher than calculated for H_2S alone despite the near doubling of molar ΣS for most depths.

CO_2 geothermometers clearly exhibit signs of disequilibrium associated with superheated or acidic wells. KJ-39, KJ-25, KJ-26 and IDDP-1 each exhibit t_{CO2} spikes >50°C above the boiling point curve near bottomhole associated with an influx of magmatic gas. This disequilibrium subsides at shallower depths as the CO_2 is diluted or buffered out of the system.

t_{CO2} values also best correlate with temperature fluctuations below the boiling point curve in the Leirbotnar field wells reinforcing the decoupled mineral buffers and efficient solubility reactions associated with CO_2(g) concentrations.

H_2 gas was not identified amongst the magmatic gas flux measured in fumaroles during the Krafla fires, and thus it was suggested by some authors (Ármannsson et al, 1982; Gudmundsson and Arnórsson, 2002) that the H_2 geothermometer may provide an ideal method for monitoring reservoir temperature as it is not effected by magmatic gas contamination. The knowledge that H_2 is a significant component of fresh basaltic volcanic gas provides an opportunity to examine the kinetics at which H_2 concentrations are modified within the system. Elevated CO_2 geothermometers accurately pinpoint depths at which an influx of magmatic gas permeates the borehole, however such spikes are not coupled with similar unequilibrated t_{H2} (or t_{H2S}) values. This indicates that either (1) reactions with fresh H_2 gas is efficient, taking place between the borehole and the point of exsolution from the magma; (2) that insoluble H_2 gas is rapidly removed from the system when magmatic steam mix with geothermal fluids; or (3) that the buffering of fresh CO_2 gas is markedly slower, indicating that the source is some great distance from the borehole and not proximal to the intersected magma. The identification of soluble SO_2 in IDDP-1 suggests that, at least in this case, that the magmatic gas was emplaced very near to the borehole. A strong correlation between H_2 and He molar concentrations suggests that insolubility plays an important role in efficiently removing these species from the system.

Composition of magmatic gas input

Analysis of fluid inclusions near a magmatic intrusion in a geothermal system allows for the direct "sampling" and characterization of the Krafla magmatic-steam compositions and the subsequent modification into a magmatic-hydrothermal phase. Wells IDDP-1, KJ-39 and KJ-25 each exhibit spikes in CO_2 concentrations, CO_2/H_2S ratios and consequently t_{CO2} values elevated

above formation temperatures. Coupled with sharp increases in total gas concentrations, we may attribute a flux of fresh CO_2 in each of these wells at their respective depths. Spikes in SO_2 and He are also observed in IDDP-1 and KJ-25, correlating with the addition of CO_2, favoring the presence of fresh magmatic condensate as described by volcanic gas profiles from other Icelandic volcanoes (Table 1). Conversely, KJ-39 exhibited a decrease in SO_2 and steady He/Ar values with depth. Elevated N_2/Ar values >110m were observed in IDDP-1, KJ-39 and KJ-17. Such values are typically associated with magmatic gases in andesitic arc-type volcanoes, and not MORBs, however Arnórsson (1986) identified multiple occurrences of elevated N_2/Ar in geothermal wells and fumaroles, particularly at Krafla. Strong acidic character of IDDP-1, KJ-39 and KJ-25 supports a coupling of concentrated HCl with elevated CO_2 concentrations.

Leirbotnar vs Suðurhlíðar magmatic gases

The unique character of magmatic gas in different parts of the Krafla field is evident. A cartoon illustrating the reservoir conditions and magmatic compositions for both Leirbotnar and Suðurhlíðar fields, as related to the analyzed wells, is found in Fig. 10. Proximity of KJ-25 to well IDDP-1 in Leirbotnar, though drilled 18 years prior during the subsidence of the Krafla fires, explains the similarity between the two well's fluid inclusion profiles, including the unique trend of CO_2, SO_2 and He gaseous input as well as production of acidic steam. Well IDDP-1 targeted a zone above the Krafla magma chamber estimated at >3.5km depth, yet evidently encountered magma at 2204m likely associated with the Vitismóar fissure, a possible conduit for the recent Krafla eruption. The molten rhyolite glass has been attributed to partial melting of a hydrothermally altered basalt combined with an anhydrous basaltic melt, based on δ^2H and $\delta^{18}O$ studies (Elders et al, 2011; Pope, 2010). Elders et al. (2011) estimated that the felsic intrusion must have been at least 50m thick to remain molten at the time of drilling, assuming it was emplaced during the 1975-1984 Krafla fires. Localized emplacement of sizable magmatic dikes

may be responsible for a flux of magmatic gases containing CO_2, SO_2, He, N_2, and HCl in both IDDP-1 and KJ-25.

Well KJ-39 bottomhole was also drilled near KJ-17, but 30 years later and 322m vertically deeper at bottomhole within the Suðurhlíðar field (Fig. 1). Both wells encountered similar felsic glasses from anetexis melt, yet the magma from KJ-39 also contained a corresponding holocrystalline basaltic intrusion predicted to be a dolerite dike from a partially molten crystal mush (Óskarsson and Grönvold, 2009). The fluid inclusion and production chemistry of the two wells is still very different. The strong flux of CO_2 and HCl from KJ-39 may be the product of a younger doleritic intrusion associated with the Hóldelsar volcanic fissure not emplaced at the time of drilling KJ-17; or simply was not 'sampled' by the shallower KJ-17 borehole. The partially-melted hydrothermally-altered basalts forming the anetexis felsic glass are likely to be degassed of magmatic volatiles and not a strong contributor for CO_2, HCl, SO_2 or He. Likewise, the molten doleritic dike in KJ-39 may have been a largely degassed, solidifying crystal mush, as suggested by a lack of SO_2 and He in the KJ-39 gas-rich fluid inclusions. Intrusions in Suðurhlíðar may be decoupled from the recent Krafla eruption which derived directly from the Krafla magma chamber to the west bringing a fresh batch of magmatic gas, suggesting that the Hólseldar intrusives source from a more degassed intermediate chamber, or are formed in-situ by the partial melting of hydrated basalt. The occurrence of elevated N_2/Ar in both KH-17 and KJ-39, however, could be a unique signature of the anatexis melt, assuming the altered basalts derived from once shallower depths where they may have interacted with seawater or N_2-fixing processes.

Superheating conditions

Superheated steam is necessary to vaporize HCl and produce acidic conditions in the borehole. Wells KJ-39, IDDP-1, KJ-25 and KJ-26 each exhibited some degree of superheated

boiling near bottom-hole as demonstrated by high total gas concentrations, dual phase fluid inclusions and t_{CO2} values above the boiling point curve. Excess HCl from magmatic steam is postulated in wells KJ-29, IDDP-1 and KJ-25 by the presence of other magmatic gas indicators, however KJ-26 exhibited acidic production fluids without such evident magmatic gas flux or a molten intrusion. KJ-26, did however, exhibit a substantial boiling trend near bottom hole from 1800-2100m. Reservoir boiling and dry steam production is often the result of depressurization near the wellbore due to continuous production with inadequate recharge or reinejection; such is the case at the Geysers and Cierra Prieto (Truesdell, 1991). Excess enthalpy will be evident at the wellhead over time as pressure may continue to drop despite the increased steam fraction. A deep-seated equilibrium steam phase in an un-stressed field such as Krafla, however, can only be the result of additional heat provided to the reservoir and usually associated with localized zones of low permeability. The addition of heat in Iceland most likely results from intrusive dikes, or proximity to the shallow emplacement of the Krafla magma chamber. In the case of IDDP-1 and KJ-39, a strong influx of supercritical magmatic gas (exsolving at magmatic tempertures) provides enough heat to support superheated phase separation. Well KJ-26 experiences superheating below 2000m as seen by other Leirbotnar wells with high enthalpies and acidic nature (Einarsson et al., 2010).

The formation of acidic production steam still requires a Cl component for vaporization. Distribution coefficients (B_{HCL}) for the vaporization of HCl allows us to estimate the concentration available in the formation necessary to produce the flashed HCl identified in the superheated steam at the wellhead (Truesdell et al, 1989). Following a long term flow test where the fluids became increasingly acidic, well KJ-26 produced dry steam with a maximum 600ppm Cl and estimated pH of 4.1, prior to shutting in due to intense erosion of the casing (Friðleifsson et al, 2006). Shallower feedzones in KJ-26 produced neutral, equilibrated fluids with 22ppm Cl and pH of 7.1. Assuming mixing with the shallower feedzone forcing condensation of the

superheated Cl, Friðleifsson et al. (2006) estimated a primary composition of the of the deep acidic steam to have approximately 610ppm Cl and pH 3.6 using a mass balance of the combined enthalpies. Assuming a 350°C reservoir temperature, a brine of ~4000ppm Cl is necessary to create acidic superheated steam with the conditions observed in KJ-26 (Fig. 11). KJ-25 exhibited slightly lower Cl in the production fluids; however, this well was shut in prematurely during the flow test prior to stabilization, thus had not yet revealed the maximum enthalpy and acidity related to the reservoir conditions. A minimum reservoir brine of 1000ppm Cl is necessary to produce 68ppm Cl identified in the KJ-25 production fluids.

The thermodynamics of HCl vaporization require that a concentrated, yet localized, Cl-brine must be available in the Krafla reservoir to produce acidic steam. Superheating of the dilute, low chloride reservoir fluids alone is insufficient to create the corrosive conditions observed in the many acidic wells. Despite the lack of trapped primary magmatic steam in the KJ-26 cuttings, this well must still have been exposed to magmatic gas-entrained fluids in the reservoir as evidenced by the increasing CO_2/H_2S concentrations in the produced fluids correlating with increasing enthalpy and Cl during the flow test. Good transmissivity within the productive units would allow for rapid distribution of magmatic gases to wells such as KJ-26 upon drawdown, increasing the risk of finding acidic steam anywhere below ~2000m in the Leirbotnar field. CO_2/H_2S ratios have dropped dramatically in the wellfield as well as the Vítismóar and Hveragil fumaroles since the subsidence of the Krafla eruptions in 1984, however, these reactive gases may be buffered by mineral equilibria reactions within the reservoir. The conservative nature of Cl ions, even following neutralization of HCl fluids, would require physical dispersion of the concentrated brine to decrease the Cl concentration in the deep Leirbotnar reservoir – a process likely to be much slower than the chemical buffering of CO_2 gas. As a result, wells with indications of superheated conditions from fluid inclusions may still be regarded as potential acidic wells.

Analysis while drilling

Detection of problematic feedzones while drilling or before running casing is possible by rapid analysis of fluids inclusion gases. Zones associated with acidic steam production are demonstrated by the following characteristics:

- Elevated CO_2-geothermometers above the boiling point curve, illustrating signs of disequilibrium and an influx of magmatic gas
- Elevated SO_2, He and N_2/Ar concentrations, suggesting an influx of magmatic gas
- Dual phase fluids inclusions or boiling below 2000m, particularly in association with the above signatures

Fluid inclusion analysis for the entire well may be completed in real time, using an onsight lab, or with expedited turn-around by a commercial lab. Several days are required to cool the well following drilling and before running liner, during which FI-logs could be produced and problematic zones could be sealed off with cement or blank casing. KJ-25 represents a good example of a well which may have benefited from a modified completion. Magmatic gas indicators become evident below 2002m. The well could have been plugged back below this depth and rig-tested to determine if adequate permeability exists without the problematic feedzone, before completing with liner.

Fluid inclusions associated with molten intrusions exhibited the following signatures, upwards of 400m above the intrusion itself:

- Magmatic gas infux including elevated CO_2-geothermometers above the boiling point curve, SO_2, He, N_2/Ar
- Superheating (gas-dominated dual-phase fluid inclusions) occurring in conjunction with geothermometer temperatures at or above the boiling point curve.

Each well that encountered molten lava while drilling also experienced dramatic drilling issues including stuck drill pipe, severe lost circulation or superheated steam (>100°C at atm) in the mud-returns. These drilling indicators in conjunction with fluid inclusion data should provide adequate warning to cease drilling 50-100m above an intrusion. KJ-39 and IDDP-1 are excellent examples of wells that could have greated benefited from this technique as multiple drilling delays due to lost circulation and stuck pipe would have allowed time for diagnostic fluid inclusion analysis.

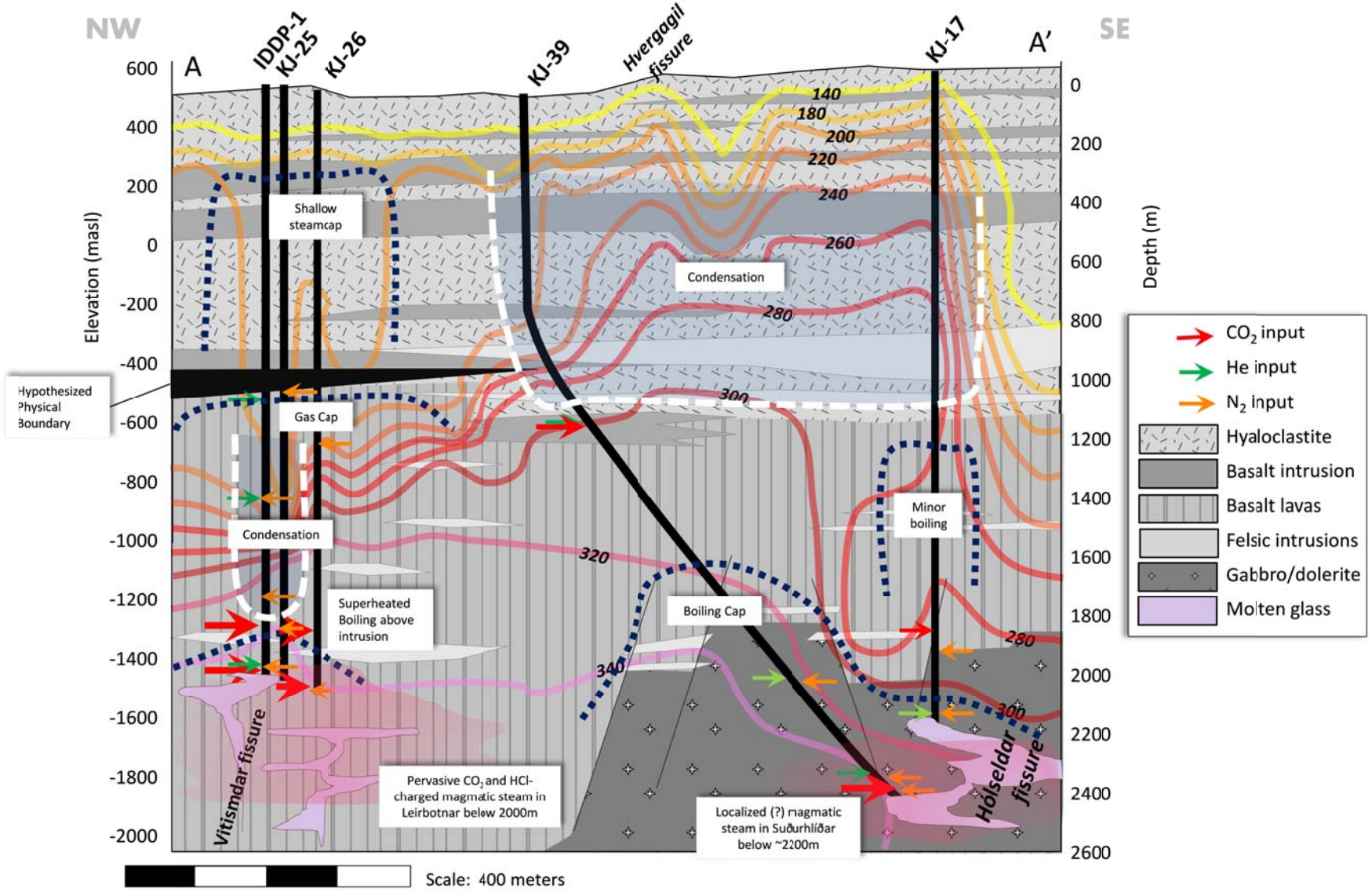
NW
A
IDDP-1
KJ-25
KJ-26
KJ-39
Hvergagil fissure
KJ-17
A'
SE
Elevation (masl)
Depth (m)
600
400
200
0
-200
-400
-600
-800
-1000
-1200
-1400
-1600
-1800
-2000
0
200
400
600
800
1000
1200
1400
1600
1800
2000
2200
2400
2600
140
180
200
220
240
260
280
300
320
340
Shallow steamcap
Condensation
Hypothesized Physical Boundary
Gas Cap
Condensation
Superheated Boiling above intrusion
Minor boiling
Boiling Cap
Vitismar fissure
Pervasive CO_2 and HCl-charged magmatic steam in Leirbotnar below 2000m
Localized (?) magmatic steam in Suðurhlíðar below ~2200m
Hólseldar fissure
Scale: 400 meters
CO_2 input
He input
N_2 input
Hyaloclastite
Basalt intrusion
Basalt lavas
Felsic intrusions
Gabbro/dolerite
Molten glass

Fig. 10. (*previous page*) Cartoon illustrating reservoir conditions in the Krafla field surrounding wells IDDP-1,KJ-25, KJ-26, KJ-39 and KJ-17. Cross-section refers to A-A' transect from Figure 1. Field-wide temperature contours from Gundmundsson (1991); lithologies from Ármannsson et al. (1987). Magmatic gas is pervasive through the Leirbotnar field influencing the 3 wells sunk below 2000m associated with multiple acidic intrusions from the Krafla fires. A superheated boiling cap exists below 1800m. Condensation of magmatic steam is apparent in IDDP-1 and KJ-25 upwards of 1100m depth where a gas cap forms beneath a proposed physical barrier, such as a clay cap or impermeable lavaflow. A shallow steamcap is evident in the shallow Leirbotnar wells above 1000m depth. Magmatic gas is also apparent, though localized to KJ-39 below 2200m vertical depth, in the Suðurhlíðar field most likely associated with the Hólseldar volcanic fissure. A superheated boiling cap is evident near the upper boundary of the dolerite intrusive complex characteristic of the Suðurhlíðar wells below 2000m, possibly associated with decreased permeability within these units. A zone of condensation is observed above 1100m east of Hvergagil, likely derived from steady state degassing of the deeper intrusive units.

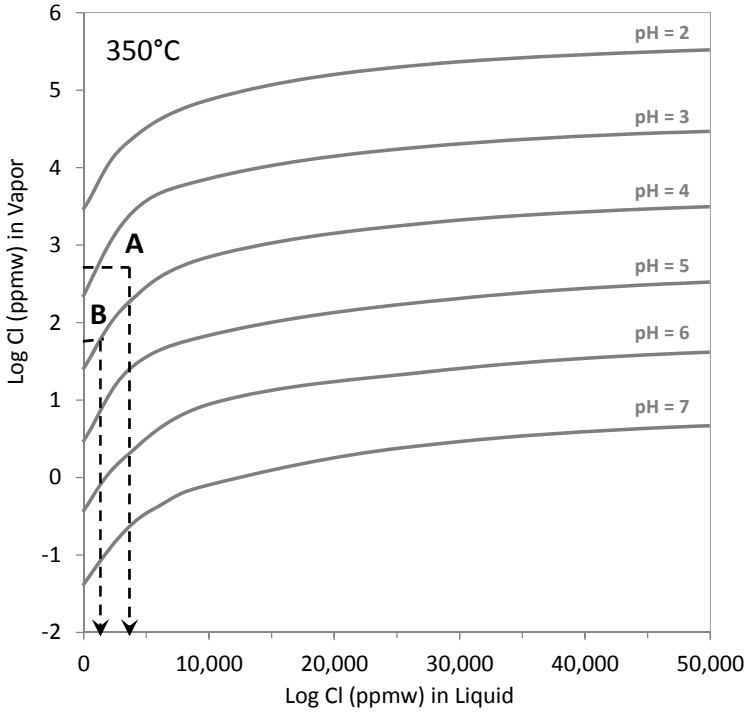

Fig. 11. CI in reservoir liquid versus Cl in reservoir vapor, in ppmw at 350°C and various pH values (modified from Truesdell et al, 1989). Conditions from production test in KJ-26 represented by path A; conditions from KJ-25 represented by path B.

CONCLUSIONS

Magmatic gas in Krafla is ubiquitously rich in CO_2 and generally H_2S and H_2 poor, corresponding to the elevated CO_2/H_2S ratios identified in the contaminated wells and fumaroles during the Krafla Fires. Leirbotnar wells exhibit elevated SO_2, He and N_2/Ar >110 in correlation with elevated CO_2 input. Identification of primary magmatic components such as SO_2 and He, though extremely rare in hydrothermal environments, supports a nearby source of degassing magmatic steam such as a molten intrusion derived from the Krafla magma chamber. Suðurhlíðar wells merely exhibit elevated CO_2 and some enriched N_2/Ar, arguing for a unique magmatic source.

Wells with magmatic gas signatures also exhibit acidic character, supporting the hypothesis that HCl is a major component of the pervasive magmatic gas within the wellfield. This correlation bolsters the method of identifying feedzones within the well that may source excess HCl, by looking for other magmatic gas signatures.

Superheated phase conditions or boiling, in addition to excess HCl, is necessary to produce superheated steam and volatilize HCl. The general boundary for encountering both these conditions is below 2000m in the Lieirbotnar field and below 2200m in the Suðurhlíðar field. HCl-concentrated magmatic gases must result in at least 1000ppm Cl to support acidic steam conditions, as was demonstrated in KJ-25. Much higher Cl concentrations are expected for highly corrosive wells such as KJ-39 and IDDP-1.

Magmatic intrusions, which are inherently problematic while drilling and potential catastrophic precursors to a blow-out, are strongly correlated with magmatic gas signatures in the borehole, at least was the case for IDDP-1 and KJ-39. High fluxes of excess CO_2 and superheated conditions were detectable in fluid inclusions for 100s of meters above the intrusion. KJ-17, however, exhibited no signs of significant magmatic gases with the exception of elevated

N_2/Ar, which were also characteristic of the gases associated with IDDP-1 and KJ-39 melts. Additional petrographic work is needed to address the source of elevated N_2/Ar (200-1000 mol/mol) associated with these melts and whether or not this signature may represent a legitimate precursor to identifying a molten lava along the wellpath.

The unique chemical profile of each borehole, particularly those located very near to each other yet drilled over a decade apart, supports the hypothesis that fluid inclusion signatures rapidly change in response to changing reservoir conditions and may be used 'sample' and characterize insitu or 'downhole' conditions. Such assumptions are necessary to identify ever-changing conditions such as boiling and condensation in response to wellfield stresses, magmatic gas input or a recently emplaced intrusion. The latter effects have been demonstrated to modify reservoir conditions within a few years, marking the minimal time needed to reprint a fluid inclusion profile in a dynamic geothermal system such as Krafla.

REFERENCES

Ármannsson, H. 2010. The Chemistry of the Krafla Geothermal System in Relation to the IDDP Well. Proceedings World Geothermal Congress 2010, Indonesia. 5p.

Ármannsson, H., Benjaminsson, J., Jeffrey, W.A., 1989. Gas changes in the Krafla geothermal system, Iceland. Chemical geology. 76, 175-196.

Ármannsson, H., Gudmundsson, A., Steingrimsson, B.S., 1987. Exploration and development of the Krafla geothermal area. Jokull. 37, 13-30.

Ármannsson, H., Gíslason, G., Hauksson, T., 1982. Magmatic gases aid the mapping of the flow pattern in a geothermal system. Geochimica et Cosmochimica Acta. 46, 167-177.

Arnórsson, S.,Gunnlaugsson, E. 1985. New gas geothermometers for geothermal exploration-Calibration and application. Geochemica et Cosmochimica Acta. 49, 1307-1325.

Arnórsson, S. 1986. Chemistry of gases associated with geothermal activity and volcanism in Iceland: a review. Journal of Geophysical Research. 91, 12261-12268.

Arnórsson, S., Björnsson, S., Muna, Z.W., Bwire-Ojiambo, S.B., 1990. The use of gas chemistry to evaluate boiling processes and initial steam fractions in geothermal reservoirs with an example from the Olkaria Field, Kenya. Geothermics. 19, 497-514.

Dilley, L.M., Norman, D.I., Moore, J., McCulloch, J. 2006. Fluid stratigraphy of the Coso geothermal reservoir. Proceedings, 31st Workshop on geothermal reservoir engineering. Stanford University, California. 6p.

Elders, W.A., Friðleifsson, G.O., Zierenberg, R.A., Pope, E.C., Mortensen, A.K., Gudmundsson, A., Lowenstern, J.B., Marks, N.E., Owens, L., Bird, D.K., Reed, M., Olsen, N.J., Schiffman, P., 2011. Geology. Origin of a rhyolite that intruded a geothermal well while drilling at the Krafla volcano, Iceland. 39, 231-234.

Einarsson, K., Pálsson, Gudmundsson, Á., Hólmgeirsson, S., Ingason, K., Matthíasson, J., Hauksson, T., Ármannsson, H., 2010. Acid Wells in the Krafla Geothermal Field. Proceedings World Geothermal Congress 2010, Indonesia. 6p.

Einarsson P., 1978. S-wave shadows in the Krafla caldera in NE-Iceland, evidence for a magma chamber in the crust, Bulletin of Volcanology. 41, 1-9.

Friðleifsson, G.O., Ármannsson, H., Mortensen, A.K., 2006. Geothermal conditions in the Krafla caldera with focus on well KG-26: A review in relation to the Iceland Deep Drilling Project. ISOR internal report. 38p.

Friðleifsson, G.O., Elders, W.A., 2005. The Iceland Deep Drilling Project: a search for deep unconventional geothermal resources. Geothermics. 34, 269-285.

Friðleifsson, G.O., Pálsson, B., Stefánsson, B., Albertsson, A., Gunnlaugsson, E., Ketilsson, J., Lamarche, R., Andersen, P.E., 2010. Iceland Deep Drilling Project. The first IDDP Drill Hole

Drilled and Completed in 2009. Proceedings World Geothermal Congress 2010, Indonesia. 4p.

Giggenbach, W.F., 1980. Geothermal gas equilibria. Geochemica et Cosmochimica Acta. 44, 2021-2032.

Giggenbach, W. F., 1997. The origin and evolution of fluids in magmatic-hydrothermal systems. In Barnes, H. L., editors, Geochemistry of hydrothermal ore deposits. Wiley and Sons, 737-796.

Giggenbach, W.F., 1995. Composition of magmatic components in hydrothermal fluid, in, Thompson, J.F.H.,editors, Magmas, fluids, and ore deposits. Mineralogical Association of Canada Short Course. 23, 247-261.

Gudmundsson, B.T. and Arnórsson, S., 2002. Geochemical monitoring of the Krafla and Námafjall geothermal areas, N-Iceland. Geothermics. 31, 195-243.

Gudmundsson, B.T. and Arnórsson, S., 2005. Secondary mineral-fluid equilibria in the Krafla and Námafjall geothermal systems, Iceland. Applied Geochemistry. 20, 1607-1625.

Gundmundsson, A., 2001. An expansion of the Krafla power plant from 30 to 60 MWe – Geothermal consideration. GRC Transactions. 25, 741-746.

Helgadóttir, H.M. 2008. Krafla- Well KG-15 Drilling, geology and geochemistry. ISOR internal report. 34p.

Jónasson, K., 1994. Rhyolite volcanism in the Krafla central volcano, north-east Iceland. Bulletin of Volcanology. 56, 516-528.

Jónasson, K., 2007. Silicic volcanism in Iceland: Composition and distribution within the active volcanic zones. Journal of Geodynamics. 43, 101-117.

Landis, G.P., Rye, R.O., 2005. Characterization of gas chemistry and noble-gas isotope ratios of inclusion fluids in magmatic-hydrothermal and magmatic-steam alunite. Chemical Geology. 215, 155-184.

Landsvirkin “Kröflustod Power Station" 2013. Web. http://www.landsvirkjun.com/Company/PowerStations/KraflaPowerStation/

McLin, K.S., Moore, J.N., Hulen, J., Bowman, J.R., Berard, B. 2006. Mineral characterization of scale deposits in injection wells: Coso and the Salton Sea Geothermal fields, CA. Proceedings, 31st Workshop on geothermal reservoir engineering. Stanford University, California. 8p.

Moore, J.N., Norman, D.I., Kennedy, B.M., 2001. Fluid inclusion gas compositions from an active magmatic-hydrothermal system: a case study of The Geysers geothermal field, USA. Chemical Geology. 173, 3-30.

Mortensen, A.K., Grönvold, K., Gudmundsson, A., Steingrimsson, B., Egilson, P., 2010. Quenched silicic glass from Well KJ-29 in Krafla, Northeast Iceland. Proceedings World Geothermal Congress 2010, Indonesia. 6p.

Norman, D.I., Blamey, N., Moore, J.N., 2002. Interpreting geothermal processes and fluid sources from fluid inclusion organic compounds and CO2/N2 ratios. Proceedings 27th Workshop on geothermal reservoir engineering. Stanford University, California. 9p.

Norman, D.I., Moore, J.N., Yonaka, B., Musgrave, J., 1996. Gaseous species in fluid inclusions: A tracer of fluids and an indicator of fluid processes. Proceedings 21st Workshop on geothermal reservoir engineering. Stanford University, California. 233-240.

Óskarsson, N., Grönvold, K., 2009. Fresh plutonic minerals and sililic glass from geothermal wells in Krafla: evidence for anatexis in hornels facies. ISOR internal report. 7p.

Pope, E.C., Bird, D.K., Arnorsson, S., Fridriksson, T., Elders, W.A., Fridleifsson, G.O., 2010. Iceland Deep Drilling Project (IDDP): Stable isotope evidence of fluid evolution in Icelandic geothermal systems. Proceedings World Geothermal Congress 2010. 7p.

Stefánsson, A., Arnórsson., S. 2002. Gas pressures and redox reactions in geothermal fluids in Iceland. Chemical Geology. 190, 251-271.

Symonds, R.B., Rose, W.I., Bluth, G.J.S., Gerlach, T.M., 1994. Volcanic-gas studies: Methods, results, and applications. In Carroll, M.R., and Holloway, J.R., editors, Volatiles in magmas: Mineralogical Society of America, Reviews in Mineralogy. 30, 1-66.

Truesdell, A.H. 1991. Origins of acid fluids in geothermal reservoirs. GRC Transactions. 15, 289-296.

Truesdell, A.H., Haizlip, J.R., Armannsson, H., D'Amore, F., 1989. Origin and transport of chloride in superheated geothermal steam. Geothermics. 18, 295-304.

CHAPTER 4:

Oxygen Isotope Fractionation of Alkalic lavas from Erebus volcano, Antarctica

ABSTRACT

Oxygen isotope analysis of minerals in alkalic lavas from Erebus volcano, Ross Island, Antarctica, indicates an anomalous trend of depletion with fractionation from basanite to phonolite. The frozen climate and lack of evidence for assimilation of crustal materials makes this a unique location to investigate factors contributing to oxygen isotope depletion. Thirty lavas from Erebus volcano, ranging from parental basanite to anorthoclase phonolite, along with glass, feldspar, and olivine separates were analyzed using silicate fluorination and stable oxygen isotope determination by mass spectrometry. Forward models indicate an ideal enrichment of 0.8–2.0‰ in modern lavas due to Raleigh fractionation, but this is not observed in either glass or mineral separate analysis. Olivines exhibit a clear trend of isotopic depletion from a typical mantle value of $\delta^{18}O$ +5.0‰ in the parental source to 3.8‰ in recently erupted phonolite lava bombs, correlating strongly with Fo content in olivines. Feldspar and glasses exhibit modern isotopic values well below predicted values, averaging 6.0‰ and 5.7‰, respectively, and are in fractionation disequilibrium with olivine compositions at measured magmatic temperatures of 1000°C within the persistently convecting lava lake. Isotopic depletion of the whole melt may be accounted for by incorporation of 7.7-11% hydrothermally altered volcanic edifice over time assuming water–rock interaction from strongly depleted Antarctic precipitation. Enhanced disequilibrium with olivine phenocrysts, particularly during the latest stages of Erebus construction, appears to be strongly associated with the occurrence of the modern lava lake configuration calling for differential fractionation of olivines and feldspars from their respective melts, and slow O-diffusion of olivines while in the shallow lava lake prior to eruption.

INTRODUCTION

Volcanic systems exhibiting depleted $\delta^{18}O$ have been noted in Yellowstone, Iceland, Hawaii, Greenland, and the Marianas (Harmon and Gerbe, 1992; Eiler et al., 1996; Bindeman and Valley, 2001; Bindeman and Valley, 2000; Bindeman and Valley, 2001; Gurenko and Chaussidon, 2002; Wang et al., 2003; Marks et al., 2004; Wade et al., 2005; Bindeman et al., 2006; Thirlwall et al., 2006; Wang and Eiler, 2008). The cause for such occurrences is often attributed to assimilation of meteoric water or hydrothermally altered strata, while depletions in other systems are not as easily explained. Erebus volcano, located on Ross Island, Antarctica, is an active, silica-undersaturated alkaline stratovolcano hosting one of the world's few visibly and persistently convecting lava lakes. This study reveals depleted oxygen isotope values for modern lavas well below parental HIMU and DMM mantle values (Eiler, 2001). Erebus lavas derive almost linearly from a basanite parent magma via fractional crystallization with no perceivable evidence for crustal assimilation (Kyle et al., 1992; Kelly et al., 2008; Sims et al., 2008); thus, they provide a unique opportunity to investigate alternative mechanisms for the formation of isotopically depleted magmas.

Complete geochemical studies of the modern and historic lavas of Erebus and surrounding volcanic centers have provided a well-established evolutionary history for the regional magmatic system (Kyle, 1981; Moore & Kyle, 1987; Kyle et al., 1992; Kelly et al., 2008; Sims et al., 2008). Samples collected from outcropping lava flows record a progressive suite of strongly silica-undersaturated magmas, ranging from basanite through anorthoclase phonolite. This suite, termed the Erebus lineage (EL) will be the main focus of this study. A contemporaneous yet volumetrically minor suite of iron-rich trachyte and trachyandesite flows on Erebus volcano, referred to as the enriched-Fe suite (EFS), is believed to have evolved from a unique parental source with incorporation of assimilated crustal components. This suite is

included here to compare mechanisms driving the formation of low-$\delta^{18}O$ lavas. The Dry Valley Drilling Project (DVDP) core taken from nearby Hut Point Peninsula (Kyle, 1981) also represents a complete evolutionary suite of silica-undersaturated magmas and may be used for context. Although the DVDP lineage evidently followed a slightly different evolutionary path, it is believed to share a common basanite parent with the EL; thus, it provides a valuable end member in the characterization of oxygen fractionation trends for Erebus lavas.

In this study we analyzed whole rock and feldspar–olivine mineral pairs from the Erebus lineage to characterize temporal variations in oxygen isotope compositions and discern the events and mechanisms responsible for the anomalous isotopic depletions. Mineral pairs uniquely allow for temperature-dependent isotopic fractionation calculations for each stage of magmatic differentiation and qualification of crystal–melt equilibrium conditions. Whole-rock oxygen isotopic data also provide comparison of overall fractionation trends between the EL, DVDP, and EFS magmatic suites.

EREBUS VOLCANO

Volcanic setting

Erebus is an alkaline stratovolcano located on Ross Island and surrounded by several smaller volcanic centers, each derived from the same Cenozoic interplate rifting and are part of the more extensive McMurdo Volcanic Group which occurs in the western Ross Sea area (Kyle, 1990). Volcanoes from this group likely developed from a common mantle source with possible mixing of HIMU and DMM end members (Sims et al., 2008); however, the occurrence of a mantle plume beneath Erebus is still subject to speculation (e.g. Storey et al., 1999; Panter et al., 2000; Gupta et al., 2009). Each volcanic center in the McMurdo Volcanic Group records a

slightly different evolutionary path, with the central Erebus volcanic lineage exhibiting the hottest, deepest magmatic plumbing system (Kyle et al., 1992).

Petrology of Erebus suites and mantle source

The Erebus lineage consists of parental basanites, phonotephrite, tephriphonolite and anorthoclase-bearing phonolites (Kyle et al., 1992). Mg-rich olivines, high-Al and -Ti clinopyroxenes, titanomagnetites, and feldspars represent the main mineral phases in the fractional crystallization history of the melt, with trace amounts of nepheline, pyrrhotite, and apatite occurring throughout. Olivines range from Fo_{89} in basanites to Fo_{47} in anorthoclase phonolites, while feldspars range from $An_{50}Ab_{46}Or_4$ in less evolved samples to $An_{16}Ab_{66}Or_{18}$ in the phonolites. Major element and trace element compositions for EL lavas exhibit smooth fractionation trends on geochemical variation diagrams, supporting the fractional crystallization of the mineral phases mentioned above. This scenario is supported by least-squares mass balance models developed by Kyle et al. (1992) for each stage of fractionation and by the uniform ratios between incompatible and compatible elements observed throughout the EL suite.

The EFS lineage lavas are rare on Erebus volcano and consist of more silica-saturated trachyandesites, trachytes and phonolites with microphenocrysts of olivine, clinopyroxene, opaque oxides, kaersutite, and alkali to plagioclase feldspars. The groundmass and olivines are more iron-rich than their silica-undersaturated counterparts. Plots of incompatible elements are distinct from those of EL, indicating a unique fractionation history. Low Sr, Ba, and K/Rb values, large Eu anomalies, and elevated Pb and Sr isotopic ratios in EFS trachytes suggest derivation from an extremely fractionated residual fluid and/or evolution by assimilation fractional crystallization (Kyle et al., 1992).

The DVDP core samples exhibit similar mineral compositions to the EL, with the addition of kaersutite occurring as a major fractionating phase in these lavas (Kyle, 1981; Kyle et al., 1992). Major and trace elements plot linearly and similarly to EL lavas, with the exception of kaersutite fractionation as evidenced by decreased TiO_2, FeO, and Y values and enrichment in K and Rb in more evolved DVDP lavas. Greater P_2O_5 is also observed in more primitive samples due to early apatite fractionation in the DVDP system, which may represent a distinct departure from a common parental lineage with EL lavas, as apatite solubility is strongly controlled by decreasing temperatures in the magma chamber (Watson, 1979; Kyle et al., 1992). This point of evidence combined with the lack of kaersutite suggests that EL lavas were formed in a deeper, hotter, less hydrous magma chamber than DVDP lavas throughout most of their evolution. The DVDP lineage likely derives from fractional crystallization of olivine, clinopyroxene, magnetite, feldspar, and kaersutite, agreeing well with the least-squares fit models of Kyle (1981).

Radiogenic isotopes have been used to identify the mantle source and paths of differentiation for the Erebus lavas. Near constant $^{87}Sr/^{86}Sr$ values, below 0.7030 throughout the Erebus lineage and DVDP lavas, argue against crustal contamination (Kyle et al., 1992; Sims et al., 2008). EFS trachytes from Aurora Cliff exhibit elevated $^{87}Sr/^{86}Sr$ ratios (0.70425) and crustal xenoliths suggesting a definite crustal contribution to the melt. Hf, Nd, and Pb isotopic analyses, demonstrate a slightly greater degree of isotopic variation in the earliest stages of differentiation among EL and DVDP basanites and phonotephrites, attributed to a heterogeneous mantle source (Sims et al., 2008). EL samples plot between HIMU and DMM mantle end members, and may be associated with an upwelling mantle plume. Other authors, however, attribute this source signature to lithospheric mantle impregnated with amphibole and phlogopite (Finn et al., 2005; Panter, 2006). Younger phonolitic lavas (<17 ka) exhibit no variation in Sr, Hf, Nd, or Pb isotopes, indicating a stable steady-state system, an isotopically homogenous source, or very efficient magma mixing with injected basanite (Kelly et al., 2008; Sims et al., 2008).

Eruptive history

$^{40}Ar/^{39}Ar$ dating and U-series isotopes have placed time constraints on the eruptive histories of Erebus and on residence times for their eruptive products (Reagan et al., 1992; Harpel et al., 2004; Esser et al., 2004; Kelly et al.2008b). Esser et al. (2004) indicated 1.3 Myr of subaerial eruptive activity at Erebus. Lavas collected from Fang Ridge spanning 1.07 Ma to 0.72 Ma outcrop unconformably over a mere 200m, indicating a possible period of repose associated with differentiation from basanite to phonotephrite/tephriphonolite lavas. Formation of the modern volcano began 250 ka, when anorthoclase-bearing phonolitic lava started erupting. $^{40}Ar/^{39}Ar$ studies also point to a significant injection of basanite into the Erebus magma chamber around 500 ka (Esser et al., 2004). The U-series data of Reagan et al. (1999) estimated the residence time of phonolite magmas in the shallow magma chamber system to be about 3 ka with final anorthoclase crystal growth occurring after injection into the shallow lava lake less than decades before eruption. Recent U-series work by Sims et al. (2013) supports a magma residence time of 100-10,000yrs.

Volcanic degassing

One of the most unique features of Erebus volcano is its persistently convecting lava lake with continuous degassing of CO_2 and SO_2 (Oppenheimer and Kyle, 2008; Oppenheimer et al., 2009; 2011). Measurements of the gaseous plume using LICOR flyovers and COSPEC/DOAS flux measurements estimated CO_2 emission rates averaging 1330–1930 Mt per day (Wardell et al., 2004; Oppenheimer and Kyle, 2008; Sweeney et al., 2008). Melt inclusions from eruptive products throughout the Erebus lineage indicate CO_2 partial pressures in equilibrium with both an intermediate magma chamber at 3–4 kbar and the shallow lava lake (Echenbacher, 1998;

Oppenheimer et al., 2011). The observed CO_2 flux, however, cannot be reconciled from these limited magma reservoirs alone and must be continuously streaming from a deeper (>8 kbar) CO_2-rich basanite reservoir (Wardell et al., 2004; Oppenheimer et al., 2011).

SAMPLE SELECTION AND METHODS

Thirty-one samples from the EL, EFS, and DVDP suites, each located on or near the Erebus edifice, were selected for oxygen isotope analyses (Fig. 1). Samples selected for this study were derived mainly from those used in the previous studies discussed above; thus allowed for direct comparison with corresponding geochemical data and interpretations based on other methods. Primitive basanite sample DVDP 2-105.53 was recognized by previous studies as a possible parental end member for the Erebus lineage and represents the parental magma composition for subsequent fractionation products (Kyle et al., 1992). Modern bombs representing the current condition of the convecting phonolite lava lake were collected during the 1982, 1997, and 2006 Austral field seasons.

Feldspar and olivine mineral separate pairs were collected from each sample. Field samples were crushed and sieved to 30 mesh and cleaned in an ultrasonic bath to remove matrix from phenocrysts. Mineral separates were handpicked under a binocular microscope to select pristine olivine and feldspar specimens with minimal inclusions. Whole-rock powders were also prepared for isotopic analysis by crushing to 60 mesh and pulverizing with a WC swing mill. Wherever possible, glasses were selected from modern phonolite bomb samples to allow mineral-groundmass comparisons. Microprobe analyses were performed on all mineral and glass separates to provide geochemical compositions and identify zoning and alteration for each sample; this also provided quality control of the separation and preparation processes.

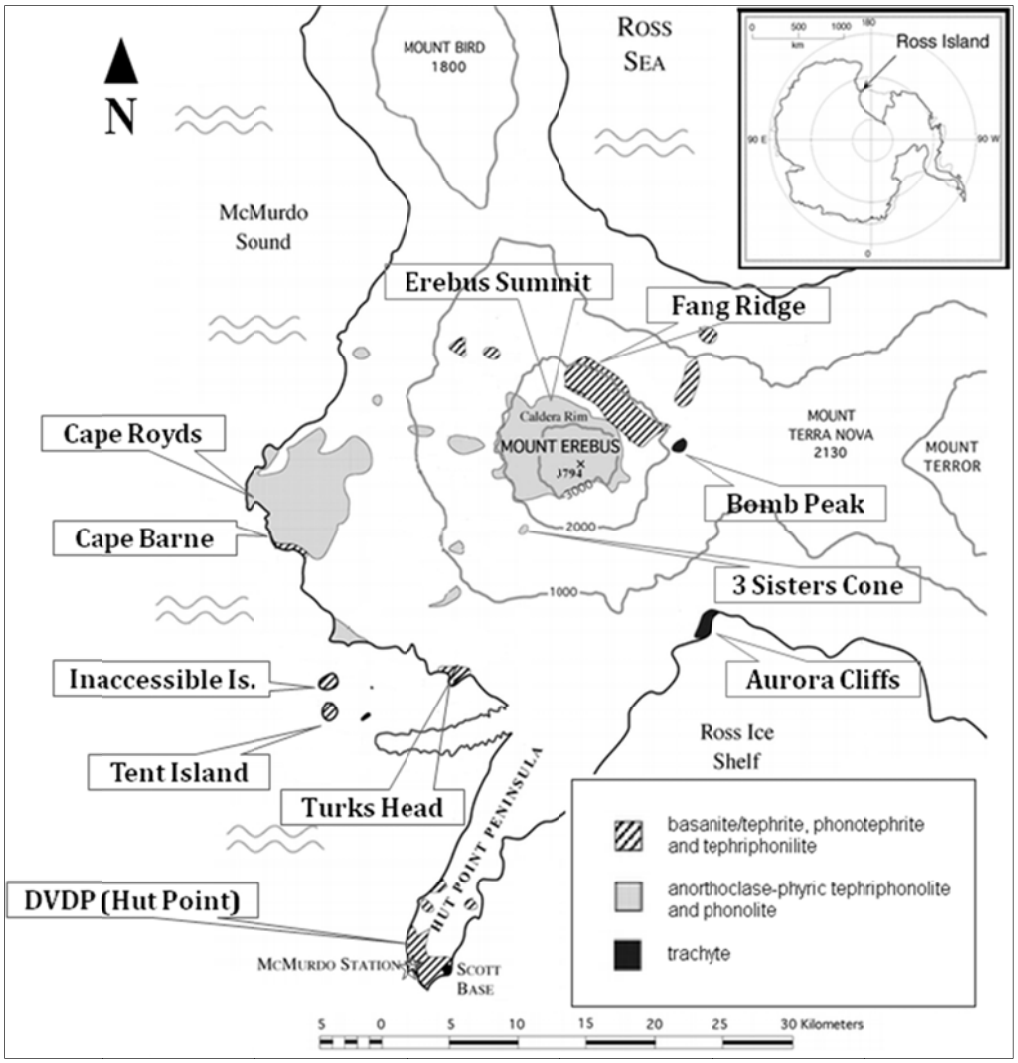

Fig 1. Sample locations for EL and EFS samples on Mt. Erebus, Ross Island, including location of DVDP core samples at Hut Point. Modified from Esser et al., 2004.

Geochemical compositions of whole-rock powders were previously analyzed by Kyle et al. (1992) (see Appendix 17). Whole rock and feldspar separates were analyzed for oxygen isotopes in New Mexico Tech's Stable Isotope Lab on a traditional silicate fluorination line (Ertchi and Silverman, 1951). Whole rock and feldspars were powdered and placed in nickel reaction vessels. Contents of evacuated vessels were exposed to 500 bar ClF_3 at 500°C for eight hours to liberate O_2 from silicates. Free oxygen was converted to CO_2 by activated carbon rods

and collected in liquid nitrogen traps. Lastly, CO_2 gas was analyzed with a Finnigan Delta Plus XP mass spectrometer. Analyses were calibrated to oxygen isotope standards NBS-28 quartz ($\delta^{18}O = 9.64‰$).

Analyses of refractory olivine separates were performed by laser fluorination (Sharp, 1990) at the Stable Isotope Laboratory at the University of New Mexico. Feldspar and glass duplicates were also analyzed by laser fluorination to assess reproducibility and standard error for the two methods. Mineral separates were placed in an evacuated laser extraction line and heated with a 25-W Merchantek CO_2 laser in BrF_5 gas. Liberated O_2 was collected in a zeolite cold finger and introduced into a Finnigan MAT Delta XL mass spectrometer. Olivine separates were calibrated with garnet standard UWG-2 ($\delta^{18}O = +5.8$); glasses and feldspars were calibrated to NBS-28 quartz. All data are reported in the standard notation relative to SMOW.

RESULTS

Major oxide geochemistry

Representative electron microprobe analysis of mineral separates are given in Table 1. (A complete listing of all analyses is given in Appendix 18-20). Feldspars for the EL suite range in composition from $An_{50}Ab_{46}$ Or_4 in less evolved phonotephrite to $An_{16}Ab_{66}Or_{18}$ in recently erupted anorthoclase megacrysts in phonolite bombs (Kyle et al.,1992; Kelly et al., 2008). Feldspars for the EFS suite are more albite-rich with values ranging from $An_2Ab_{81}Or_{17}$ to $An_4Ab_{60}Or_{36}$. EL olivines range from Fo_{89} to Fo_{47}. EFS olivines are also more iron-rich, with values as high as Fo_{06} in the more evolved samples. Little to no variation (within statistical error) was observed between mineral grains, implying a homogenous chemical composition in each stage of the melt. No xenocrystic compositions were identified. Olivines rims and cores were probed separately to identify evidence of resorption or regrowth; however, no apparent chemical zoning was observed.

Oxygen isotopes

Oxygen isotope analyses of feldspar and olivine mineral separates as well as whole-rock and glass analyses from the Erebus lineage are detailed in Table 2. Feldspars fell within a relatively narrow range from 6.5‰ to 5.3‰ following an overall trend of decreasing $\delta^{18}O$ values with increased fractionation and decreasing whole-rock MgO. Isotopic values of olivines displayed more pronounced depletion with increased fractionation, ranging from 5.3‰ for olivine from more primitive melts to 3.8‰ for more fayalitic olivine in modern Erebus ejecta. Olivines and whole-rock samples from parental basanite DVDP 2-105.53 exhibited values of 6.05‰ and 5.26‰, respectively, falling within the range of values predicted for HIMU mantle (Eiler, 2001). Modern Erebus phonolite glasses displayed slightly depleted (compared to their parental basanites) values of 5.7 ‰. Analysis of whole-rock powders by traditional fluorination produced scattered results for samples with MgO >3.0 wt%. Incomplete fluorination of refractory minerals such as clinopyroxene and olivine may be more pronounced in mafic samples, resulting in less reliable values (Sharp, 1990). Whole-rock data for more evolved samples with MgO <0.26 wt% indicate better reproducibility and representation of the host melt. Results of laser fluorination analysis of glass samples from modern anorthoclase phonolite bombs collected on Erebus Summit (EB-06-02, 97018) correlate well with those from traditional fluorination of whole rock powered from other modern samples; this increases confidence in the data for these more evolved samples. Phonolite xenolith sample 82431 indicates excessively depleted $\delta^{18}O$ values for all olivine, feldspar, and whole-rock separates, with values ranging from 0.17 to -2.10‰.

Whole-rock powders from four DVDP-2 core samples (from depths of 45.83, 61.23, 76.38 and 105.53 m) were analyzed (Table 2). Oxygen isotope values reported for these samples were 5.48, 5.49, 5.65 and 6.02 ‰, respectively. The primitive basanite 105.53, has the highest $\delta^{18}O$ which decreases with increased fractionation.

Isotopic values for the enriched-Fe series (EFS) are reported in Table 3. Trachyandesites and phonolite whole-rock samples produced values ranging between 5.92 and 4.82‰. Olivines range from 5.13 to 4.13‰ and all exhibited decreasing isotopic composition with increasing differentiation. Feldspars from Fe-enriched, alkali-poor phonolites and trachyandesites displayed averaged values between 5.92 and 5.88‰, correlating well with intermediate EL feldspar samples. Bomb Peak tephriphonolite (82405) exhibited the most enriched feldspar in either series.

Table 1. Average major oxide contents of representative phenocrysts in samples from the Erebus suites.

	EL and DVDP Series																				*EFS Series*				
Sample	**DVDP 105.53**	**83435**	**DVDP* 295.43**	**AW 82044**	**83409**	**AW 82038**	**7713***	**83415**	**DVDP 45.83**	**83417**	**83410**	**AW 82015**	**83452**	**83446**	**83448**	**80020**	**83400**	**97018**	**EB-06-03**	**82431**	**AW 82023**	**83407**	**82405**	**82403**	**AW* 82033**
Sample Location	DVDP parent basan.	Cape Barne	Hut Point	Turks Head	Inaccessible Island	Turks Head	Turks Head	Tent Island	DVDP	Tent Island	Inaccessible Island	Turks Head	Bomb Peak	Cape Royds	Cape Royds	3 Sisters Cone	Mt Erebus	Mt Erebus Summit	Fresh Bomb	Bomb Peak Xenolith	Lewis Bay	Inacc. Island	Bomb Peak	Summit Mt Erebus	Turks Head
Rock Type	Basan.	Basan.	Basan.	Basan.	Phono-tephrite	Phono-tephrite	Phono-tephrite	Phono-tephrite	Phono-tephrite	Phono-tephrite	Tephri-phon.	Tephri-phon.	Tephri-phon.	Tephri-phon.	Tephri-phon.	Anorth. Phon.	Anorth. Phon.	Anorth. Phon.	Anorth. Phon.	Anorth. Phon.	Trachy-andesite	Phonolite	Tephri-phon.	Cum. xenolith	Basaltic Trachy-andesite
Olivines																									
SiO2	40.67	39.09	39.00	39.65	39.00	37.16	35.00	37.82	39.10	36.55	35.85	35.22	33.53	35.57	35.61	34.84	34.60	34.88	35.41		33.90	31.31	29.85	31.12	39.00
FeO	10.41	18.92	14.00	15.52	17.95	27.61	31.00	24.52	17.20	30.79	33.79	36.95	41.39	35.73	35.55	38.73	40.16	39.26	39.79		43.47	55.92	63.21	57.69	21.00
MnO	0.11	0.29	0.20	0.18	0.21	0.58	0.70	0.55	0.24	0.99	1.01	1.56	2.54	1.79	1.80	2.36	2.32	2.38	2.48		1.72	2.89	2.99	2.65	0.30
MgO	48.27	41.91	45.00	44.04	42.45	34.12	32.00	36.87	42.80	31.58	29.06	25.84	21.06	26.72	26.84	23.65	22.67	23.48	24.00		20.52	8.96	2.56	7.61	40.00
CaO	0.12	0.33	0.32	0.36	0.29	0.40	0.44	0.35	0.30	0.37	0.41	0.42	0.49	0.41	0.43	0.49	0.51	0.47	0.48		0.38	0.58	0.72	0.47	0.30
Fa	**10.8**	**20.2**	**14.9**	**16.5**	**19.3**	**31.2**	**35.2**	**27.2**	**18.4**	**35.4**	**39.5**	**44.5**	**52.4**	**42.9**	**42.6**	**47.9**	**49.8**	**48.4**	**48.2**		**55.3**	**78.7**	**93.5**	**81.7**	**22.9**
Fo	**89.2**	**79.8**	**85.1**	**83.5**	**80.7**	**68.8**	**64.8**	**72.8**	**81.6**	**64.6**	**60.5**	**55.5**	**47.6**	**57.1**	**57.4**	**52.1**	**50.2**	**51.6**	**51.8**		**44.7**	**21.3**	**6.5**	**18.3**	**77.1**
Feldspar																									
SiO2				54.61	54.82	53.44		55.51		56.65	56.85	59.41	64.05	62.32	61.82	63.07	62.71	62.93	62.33	58.44	58.03	64.36	65.57	62.74	
Al2O3				28.25	27.51	28.99		27.63		26.06	26.69	24.24	21.22	22.09	22.64	21.80	21.99	22.69	23.06	25.33	23.30	20.38	19.35	22.29	
FeO				0.29	0.33	0.31		0.26		0.25	0.26	0.25	0.21	0.21	0.22	0.21	0.20	0.20	0.21	0.34	1.15	0.15	0.19	0.14	
CaO				9.81	9.62	10.64		9.07		7.97	7.95	5.75	2.32	3.40	3.98	3.01	3.22	3.07	3.41	7.00	0.42	1.56	0.61	3.33	
Na2O				5.12	5.39	4.70		5.57		6.11	6.14	6.96	7.63	7.36	7.38	7.56	7.55	7.60	7.53	7.58	13.16	7.32	6.88	8.13	
K2O				0.73	0.69	0.58		0.87		1.04	0.99	1.59	3.97	3.15	2.70	3.37	3.18	3.32	3.01	1.05	4.25	4.99	6.42	2.12	
SrO				0.35	0.39	0.38		0.38		0.40	0.37	0.38	0.16	0.27	0.27	0.23	0.23	0.30	0.31	0.29	0.04	0.05	0.01	0.31	
BaO				0.08	0.10	0.07		0.10		0.12	0.06	0.21	0.25	0.29	0.21	0.25	0.27	0.29	0.26	0.14	0.00	0.38	0.23	0.24	
An				**49.2**	**47.6**	**34.9**		**44.9**		**39.3**	**39.3**	**28.4**	**11.1**	**16.6**	**19.4**	**14.5**	**15.6**	**14.8**	**16.5**	**31.9**	**1.4**	**7.5**	**3.0**	**16.2**	
Ab				**46.4**	**48.3**	**62.9**		**50.0**		**54.6**	**54.9**	**62.2**	**66.2**	**65.1**	**65.0**	**66.1**	**66.1**	**66.2**	**66.1**	**62.4**	**81.3**	**63.9**	**60.1**	**71.5**	
Or				**4.4**	**4.0**	**2.3**		**5.1**		**6.1**	**5.8**	**9.4**	**22.7**	**18.3**	**15.6**	**19.4**	**18.3**	**19.0**	**17.4**	**5.7**	**17.3**	**28.6**	**36.9**	**12.3**	

* values from Eschenbacher, 1998

Table 2. Oxygen isotope analysis of olivine, feldspar, and whole-rock powders and glasses for DVDP basanite and Erebus lineage rocks.

Sample	**DVDP 105.53**	**83435**	**DVDP 295.43**	**83437**	**AW 82044**	**79300**	**83432**	**DVDP2-76.38**	**83409**	**AW 82038**	**7713**	**83415**	**DVDP2-45.83**	**83417**	**83410**	**DVDP2-61.23**	**AW 82015**	**83452**	**83446**	**83448**	**80020**	**83400**	**97018**	**EB-06-03**	**82431**
Rock Type	Basan.	Basan.	Basan.	Basan.	Basan.	Basan.	Basan.	Phono-tephrite	Phono-tephrite	Phono-tephrite	Phono-tephrite	Phono-tephrite	Phono-tephrite	Phono-tephrite	Tephri-phon.	Tephri-phon.	Tephri-phon.	Tephri-phon.	Anorth. Phon.	Anorth. Phon.	Anorth. Phon.	Anorth. Phon.	Anorth. Phon.	Anorth. Phon.	Anorth. Phon. Xeno
MgO (wt%)	12.13	6.77	5.65	4.92	4.74	4.69	4.21	3.72	3.47	3.13	3.10	3.00	2.67	2.51	2.20	2.07	1.81	1.64	1.30	1.23	0.99	0.95	0.85	0.83	1.14
δ18O(‰)																									
Whole Rock/	*n=3*						*n=2*			*n=2*			*n=2*			*n=2*		*n=2*		*n=2*		*n=2*		*n=2*	
glass	6.02	5.34		6.35	4.62	5.28	4.41	5.66	6.10	5.05			5.48	5.61	4.55	5.49		5.86	5.55	5.61		6.26	5.68	5.74	0.17
2-sigma	*0.18*						*0.14*			*0.13*			*0.28*			*0.17*		*0.09*		*0.08*		*0.25*		*0.01*	
Feldspar					*n=2*				*n=2*	*n=3*		*n=2*		*n=3*	*n=2*		*n=3*	*n=4*	*n=3*	*n=5*	*n=2*	*n=3*	*n=3*	*n=4*	*n=3*
					5.59				6.50	6.00	6.18	5.98		5.96	5.31		5.95	5.99	5.63	5.89	6.02	5.81	6.03	5.99	-0.20
2-sigma									*0.28*	*0.30*		*0.36*		*0.27*						*0.13*		*0.41*	*0.30*	*0.39*	*1.22*
Olvines	*n=4*	*n=2*	*n=3*		*n=2*				*n=3*		*n=2*						*n=2*			*n=2*		*n=4*	*n=2*		
	5.26	5.41	5.61		5.42				5.91	5.10	5.39	5.26		5.00			4.50		4.63	5.03		3.83	3.99	4.27	-2.1
2-sigma	*0.12*	*0.19*	*0.32*		*0.22*				*0.02*		*0.15*						*0.22*			*0.30*		*0.16*	*0.30*		
$\Delta^{18}O$(a-b)																									
(Olv-Feld)					**0.17**				**0.59**	**0.90**	**0.79**	**0.72**		**0.96**			**1.46**		**1.00**	**0.86**		**1.98**	**2.05**	**1.72**	**1.91**
(Feld- WR)					**0.97**				**0.40**	**0.95**				**0.35**	**0.76**			**0.13**	**0.07**	**0.28**		**-0.04**	**0.35**	**0.24**	**-0.37**
(Olv - WR)	**-0.76**	**0.07**			**0.80**				**-0.19**	**0.04**				**-0.61**					**-0.92**	**-0.88**		**-2.43**	**-1.40**	**-1.48**	**-2.27**

Table 3. Oxygen isotope analysis of olivine, feldspar, and whole-rock powder for enriched-Fe series (EFS).

Sample	**83412**	**AW82023**	**83407**	**82405**	**82403**	**AW82033**
Location	Inacc. Island	Lewis Bay	Inacc. Island	Bomb Peak	Summit Mt Erebus	Turks Head
Rock Type	Trachy-andesite	Trachy-andesite	Phono lite	Tephri-phonolite	Cumulate xenolith	Basaltic Trachy-andesite
MgO (wt%)	**1.57**	**1.35**	**0.37**	**0.14**	**2.5**	**1.39**
δ18O‰		*n=2*	*n=2*			
Whole Rock	**4.82**	**5.92**	**5.71**			
2-sigma		*0.25*	*0.39*			
				n=3		*n=2*
Feldspars			**5.88**	**6.88**	**5.25**	**5.92**
2-sigma				*0.31*		*0.15*
Olivines		**4.43**	**4.13**			**5.13**

DISCUSSION

Predicted fractionation trends

The Erebus lineage exhibits a notable pattern of decreasing oxygen isotope values with increasing petrologic fractionation (Fig. 2). Modern anorthoclase phonolites represent a 0.23 wt fraction of parental basanite melts with a HIMU–peridotite mantle source (Kyle et al., 1992). Here, an isotopic fractionation model was developed using Rayleigh distillation of crystallization products, as described by Kyle et al. (1992) for each stage of fractionation from a basanite to a modern anorthoclase phonolite and plotted against MgO whole-rock composition (Fig. 2). Initial (F = 0) $\delta^{18}O$ compositions were determined from olivine and melt (e.g., whole-rock) measurements from DVDP parental basanite and correlate well with published HIMU oxygen isotope values (Eiler, 2001) and values for other primitive olivines in similar alkalic lavas from Marie Byrd Land, West Antarctica (Perinelli et al., 2006; Nardini et al., 2009). Forecasted $\delta^{18}O$ values for this model were calculated based on $1000ln\alpha$(min–melt) by Clayton et al. (1989), Chiba et al. (1989), Eiler (2001), and Zhoa and Zhang (2003) and can be found in Appendix 21. The fractionation model predicts a slight increase in $\delta^{18}O$ for melt, feldspar, and olivine values from the parental basanite stage through the phonolite stage due to the strong crystallization and settling of depleted $\delta^{18}O$ minerals such as olivine, Fe–Ti–Cr oxides, and clinopyroxene. In this model, an additional stage of crystallization from F = 0.23 to F = 0.21 was imposed to observe the effects of the persistently convecting phonolitic lava lake and equilibrium crystallization of anorthoclase megacrysts as well as degassing of CO_2. Crystallization of isotopically enriched anorthoclase feldspar (An_{22}) crystals in this final stage resulted in a slight depletion of whole-rock $\delta^{18}O$; an additional one-time total degassing of 0.5 wt% CO_2 resulted in a combined 0.11‰ decrease in the final modeled melt.

Measured melt and phenocryst isotopic compositions are strongly depleted compared to the modeled fractionation trends for the entire Erebus lineage, diverging as early as the basanite melt stage. Modern anorthoclase feldspar compositions are 1.0‰ or more lighter, olivine compositions 1.8‰ lighter, and whole-rock compositions nearly 0.8‰ lighter than predicted values. Measured feldspar and olivine $\delta^{18}O$ values form a smooth depletion trend with increased fractionation, which argues for a systematic change affecting the entire melt from the basanite stage onward.

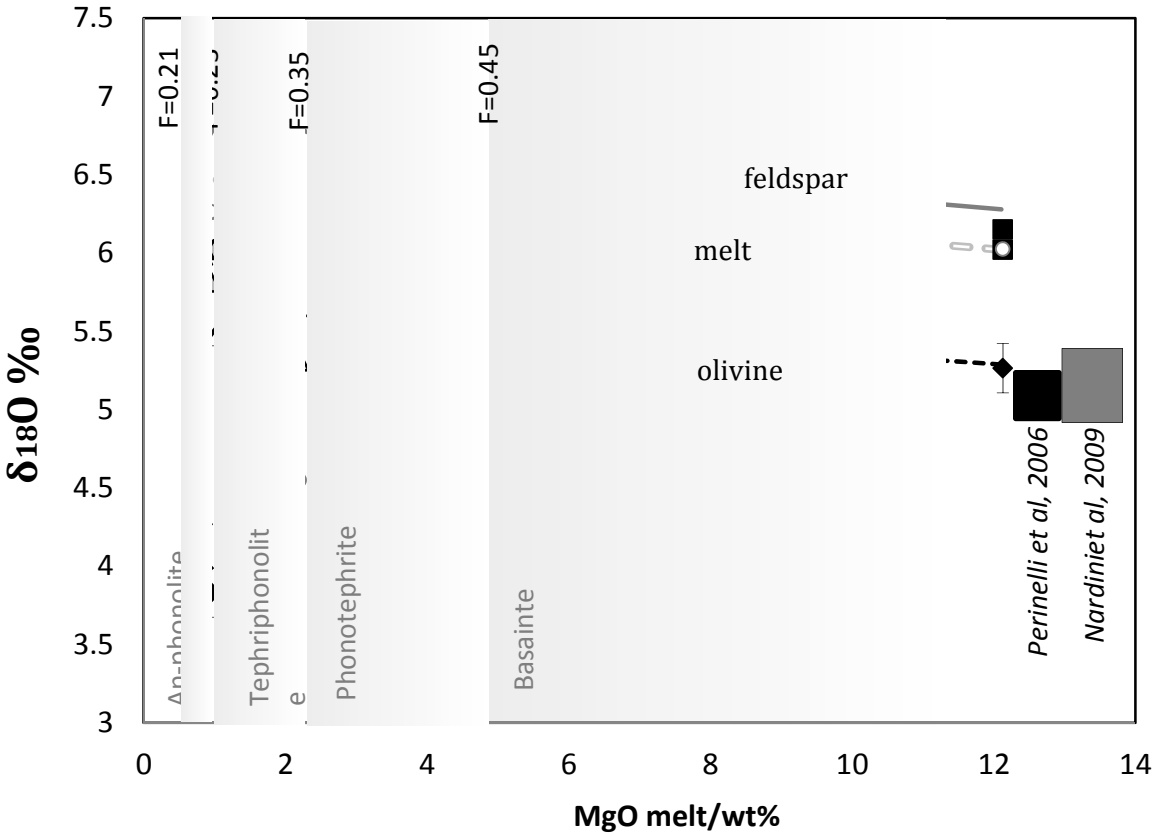

Fig. 2. Modeled $\delta^{18}O$ fractionation trend for Erebus lineage melt originating from DVDP parental basanite. Corresponding trends for feldspar and olivine crystallization products calculated and averaged from various authors (Chiba et al., 1989; Chacko et al., 2001; Eiler, 2001; Zhao and Zheng, 2003) at progressively lower fractionation temperatures. Values and calculations for model can be found in Appendix 21. Measured $\delta^{18}O$ values for EL and DVDP olivines (black diamonds), feldspars (grey triangles), and melt (open circle) compositions also shown. Error bars represent 1-standard deviation. Values of primitive olivines from alkali basalts of northern Victoria Land (Perinelli et al., 2006; Nardini et al., 2009).

To investigate these depletions, we compared $\Delta^{18}O$ of mineral–mineral and mineral–melt pairs to determine the apparent disequilibrium for each stage of fractionation. Fractionation factors $\Delta^{18}O(a–b)$ were modeled at estimated temperatures for each stage and compared to actual $\Delta^{18}O$ of mineral–melt pairs from the Erebus lineage (Fig. 3). Comparison to models indicated a strong disequilibrium between (feld–olv) and (melt–olv) in the Erebus lineage for most intermediate stages from basanite through tephriphonolite (MgO = 7.0 thru 1.8 wt%). Predicted values of $\Delta^{18}O$ (feld–melt) were small to negligible for magmatic temperatures of 1000–1200°C; these values overlap with those measured in modern anorthoclase phonolites to phonotephrite, indicating equilibrium between the feldspar and the host melt during these later stages. Such equilibrium in modern bomb samples agrees with the long residence time of anorthoclase phenocrysts in the currently openly convecting lava lake and the compositional invariance of the modern lava lake in historic times (Reagan et al., 1998; Kelly et al., 2008; Sims et al., 2008). Fractionation between olivine and other phases, however, exhibited much stronger disequilibrium during intermediate petrologic stages. Actual values of $\Delta^{18}O(olv–melt)$ only converged toward predicted values in the initial differentiation stages of the phonolite melts. In summary, it appears that olivines maintained strong disequilibrium with the melt following fractionation with the parental basanite, resulting in strongly depleted $\delta^{18}O$ olivine values superimposed on a systematic depletion influencing the entire system.

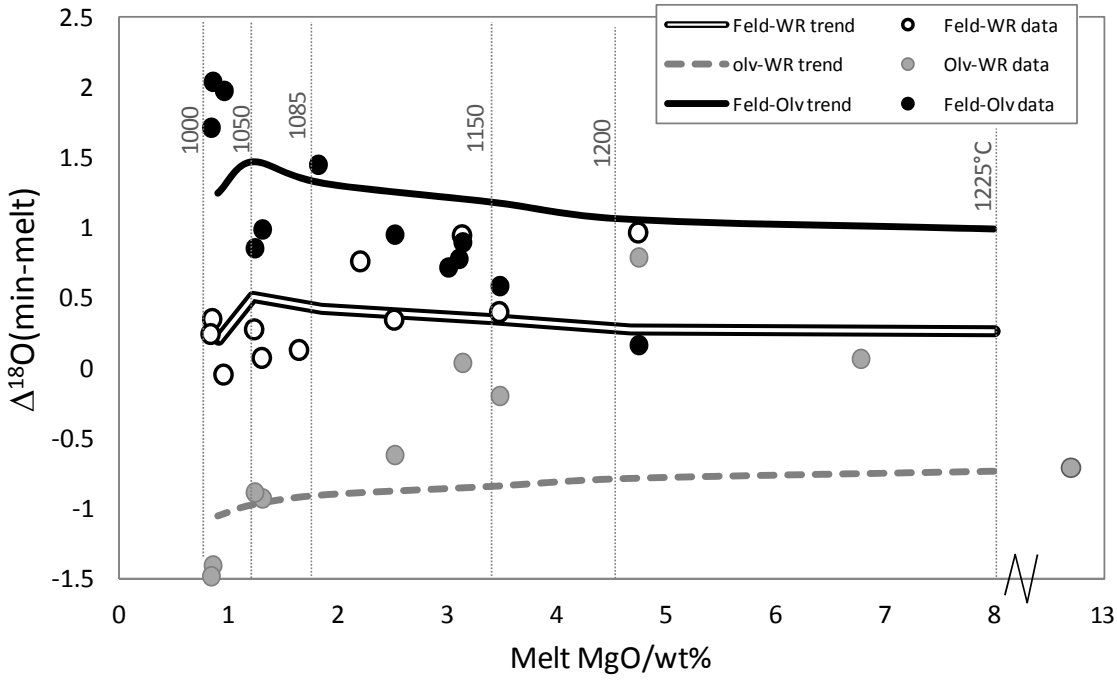

Fig. 3. Modeled temperature-dependent fractionation factors between mineral and melt pairs with actual fractionation factors for Erebus lineage. Temperatures (°C) used to calculate modeled $\Delta^{18}O$(min–melt) for each stage of fractionation are shown.

Geothermometry

Geothermometers calculated from $\Delta^{18}O$(min–melt) and $\Delta^{18}O$(min–min) were recorded for each fractionation stage of the Erebus lineage (Table 4) based on models by Chiba et al. (1989) and Zhao & Zhang (2003) and data compiled by Eiler (2001). Equilibrium temperatures for modern melts averaged 1000°C, which corresponds with values measured by Fourier transform infrared spectroscopy (FTIR) of the convecting lava lake (Calkins et al., 2008) and Fe–Ti geothermometry (Kelly et al., 2008). Temperatures ranged from 467 to 1416°C for intermediate values, indicating prominent disequilibrium at certain sample locales including Turks Head and Inaccessible Island. Temperatures calculated for DVDP2-105.53 were 1232°C, which falls within the expected range for partial melt basanites at >8 kbar depth (Oppenheimer et al., 2011). Fe–Ti oxide equilibrium geothermometers previously predicted 1081°C for phonotephrite assuming

equilibrium conditions (Kyle et al., 1992); however, sensible isotopic temperatures could not be resolved for these samples.

Anorthoclase phonolite samples from Cape Royds, 83446 and 83448, both indicated higher equilibrium temperatures than would be expected for this degree of fractionation in the Erebus lineage. It is possible that this sample underwent separate, accelerated fractionation, apart from the main magma chamber and at higher temperatures.

Table 4. Geothermometer values (°C) for fractionation pairs in Erebus lineage. Unrealistic values omitted.

Sample	**105.53** DVDP parental basanite	**AW82044** Turks Head	**83409** Inaccessible Island	**AW82038** Turks Head	**83417** Tent Island	**83410** Inaccessible Island	**AW82015** Turks Head	**83446** Cape Royds	**83448** Cape Royds	**83400** Mt Erebus Summit	**97018** Mt Erebus Summit	**EB-06-03** Fresh Bomb
MgO (wt%)	**12.13**	**4.74**	**3.47**	**3.13**	**2.51**	**2.20**	**1.81**	**1.30**	**1.23**	**0.95**	**0.85**	**0.83**
T(Olv-Feld)		-	1651	1252	1260		1000	1307	1416	850	829	923
T(Feld-WR)		467	877	475	965	525			1109	1000	956	1000
T(Olv-WR)	1232	-	-	-	1396			1086	1116	563	828	800

Trends in isotopic depletion

Olivine compositions for the Erebus lineage formed an overall trend of decreasing $\delta^{18}O$ with increasing fractionation, as discussed above. A strong correlation was observed between olivine Fo values and olivine $\delta^{18}O$ (R = 0.7)for Erebus lineage samples and for olivines from less differentiated Cenozoic basalts in Northern Victoria Land (Fig. 4), as described by Nardini et al. (2009). This correlation suggests that nonlinear factors other than simple fractionation of the melt affected both olivine MgO:FeO ratios and isotopic content.

Other significant observations include the isotopic depletions observed in the DVDP and EFS samples. These lineages are known to have evolved under unique physical parameters including temperature, depth, and rate of differentiation (Kyle et al., 1992; Kyle et al., 1981).

Like the EL samples, DVDP and EFS samples also exhibited apparent isotopic depletions in their evolutionary paths. EFS olivines displayed steady isotopic depletion with decreasing Fo content (Fig. 4, inset), supporting a common mechanism that affected all regional samples similarly, although possibly not to the same extent.

Departures of certain samples of the Erebus lineage from the overall trends (Fig. 2) may help elucidate the unique factors responsible for this overall depletion. Samples from Inaccessible Island (83410 and 83409), part of the Delbridge Islands, exhibited systematically higher $\delta^{18}O$ for both olivines and feldspars, while those from Turks Head (AW82044 and 7713) exhibited smaller enriched $\delta^{18}O$ values but strong disequilibrium between melt phases. Esser et al. (2004) identified a non-linear Mg# vs. $^{40}Ar/^{39}Ar$ dating trend among the Delbridge Islands succession, including Inaccessible Island, Turks Head, and Trygger Point, indicating that these lavas evolved in a magma chamber separate to that of Erebus. These eruptive centers may have been active for as little as 150 kyr (Esser et al., 2004); thus, they would have evolved at an accelerated pace (Moore and Kyle, 1987) under unique pressure and temperature conditions, isolating them from the specific factors that depleted the main Erebus lineage.

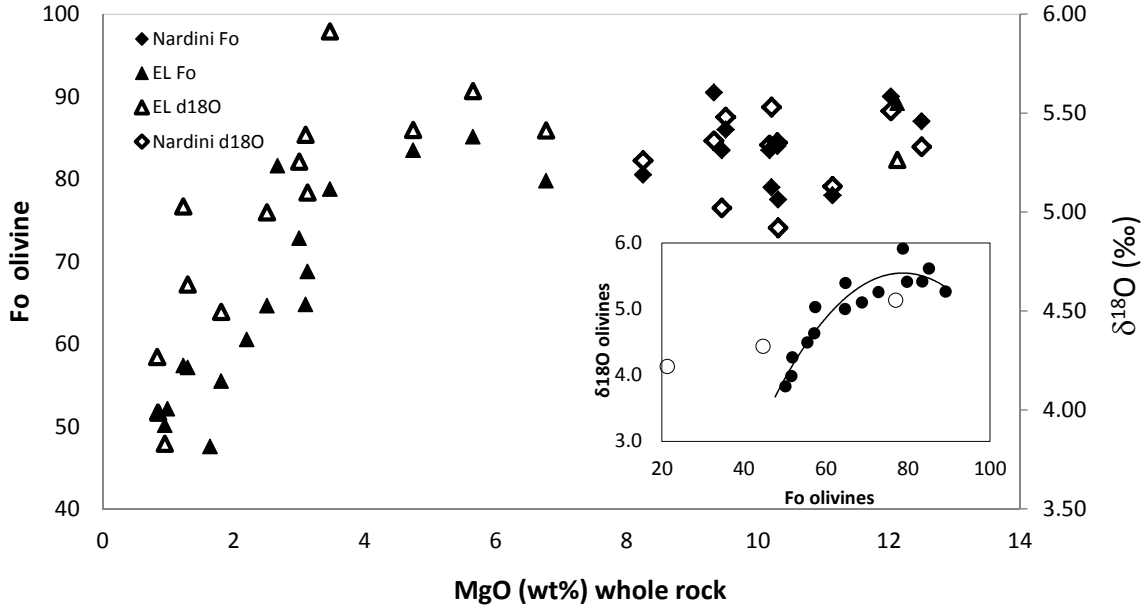

Fig. 4. Comparison of molar forsterite content (*left y-axis*) and oxygen isotope composition (*right y-axis*). Values are plotted as a function of MgO wt% of whole rock. Triangles represent olivines from the Erebus lineage. Diamonds represent less evolved olivines from Northern Victoria Land basalts (Nardini et al., 2009), illustrating similar correlation between $\delta^{18}O$ and forsterite content. Inset: plot of $\delta^{18}O$ of olivines from Erebus lineage (black circles) vs. forsterite content; good correlation between these two factors is indicated by the polynomial relationship $y = -0.0019x^2 + 0.3036x - 6.4063$; $R = 0.89$. EFS olivines (open circles) diverge from this trend but still represent a decrease in $\delta^{18}O$ with decreasing Fo content.

Effects of a heterogeneous mantle

Much speculation surrounds the presence or absence of a mantle plume to explain the volcanism at Erebus volcano and rift activity in the western Ross Sea. Heterogeneous mantle sources are often suggested to explain variations in isotopic or chemical compositions of volcanic products. A mantle plume could easily provide a unique source of depleted $\delta^{18}O$ magma amidst a reservoir of HIMU mantle; however, a depleted mantle source could not explain the systematic depletion of the differentiated melt with time. Isotopic compositions of mantle xenoliths located in southern Ross Sea indicate similar compositions to HIMU mantle. DVDP 2-105.53 isotopic analyses fell within this range, verifying the DVDP basanite as a likely parental representation of

the Erebus lineage; however, this does not need to be the case. A more isotopically depleted magma could represent the parental end-member, or our limited sampling of the DVDP basanite could be an erroneous representation of the isotopic composition of this melt. In any case, a wholly lowered starting point for this system could not explain the trend of temporal depletion encountered.

Degassing of CO_2

Fractionation factors for magmatic degassing Δ(melt–gas) are quite large, upward of several tenths of a permil at magmatic temperatures (Eiler, 2001), implying a possible important source for isotope depletion. This process, however, requires near-complete degassing of melt's CO_2 and H_2O to achieve as much as 0.5‰ $\delta^{18}O$ whole-rock depletion. Mt. Erebus' persistent convecting lava lake has exhibited steady-state CO_2 degassing of >1300 Mg/day (Wardell, et al. 2004), far outweighing the potential dissolved CO_2 in an initial volume of melt estimated at 4080 km^3 (Kyle et al., 1992). This phenomenon has led authors to propose a more deep-seated magmatic source providing a constant stream of CO_2 to both the intermediate magma chamber and the convecting lava lake (Oppenheimer et al., 2008, 2011). We present two models for open-system and closed-system degassing of CO_2 from a theoretical basanite melt at 4 kbar, representing conditions of a reposed magma chamber beneath the Erebus summit. The models were designed based on the CO_2 flux rates (calculated from correlatable SO_2 flux rates) of Sweeney et al. (2008) and the dissolved CO_2 contents in basanite melt inclusions of Oppenheimer et al. (2011), assuming unlimited replenishment of CO_2 from a mantle source. Complete closed-system degassing of 4080 km^3 of basanite melt with 0.06 wt% CO_2 predicted a maximum depletion of 0.02‰ of the original melt, insufficient to cause the observed depletions (Fig. 5). Open-system degassing assuming complete replenishment of CO_2 from a deeper source with values of 6.02‰ and continuous degassing at current rates for 1300ka since the initial stages of

construction of Mt. Erebus would achieve upwards of 0.20‰ depletion of the primary melt. This process of long-term CO_2 degassing could be a major contributor to the current depletion of modern Erebus glasses with $\delta^{18}O$ values of 5.7± 0.15‰. Fractionation of CO_2 from the melt at lower temperatures (<1050°C) and doubling the flux of CO_2 could increase this depletion to near the observed values.

Several caveats, however, are inherent to this model. The calculations do not take into account isotopic enrichment due to Rayleigh distillation of crystallization products over time, predicting a 0.4‰ increase in $\delta^{18}O$ values over the primary melt and effectively cancelling out any depletion due to continuous degassing. The calculations also assume a constant source of CO_2 with a $\delta^{18}O$ signature of 6.02‰, representing an infinite reservoir of CO_2-saturated HIMU partial melt. Even at mantle temperatures near the melting point of peridotite, fractionated CO_2 from a basanite melt is likely to have much higher isotopic values near 8.5‰, ultimately increasing the isotopic composition of the replenished shallow melt (Eiler, 2001). In addition, the assumption that continuous degassing at present rates for the duration of Erebus' construction is largely untested and generally considered a unique manifestation of the current open-system lava lake. Similarly, observed isotopic depletions in EFS and DVDP lavas would require the same mechanism of open-system fluxing of CO_2 over time to replicate this effect. Measurements of continuously decreasing $\delta^{18}O$ of CO_2 in melt inclusions for the Erebus lineage and similarly depleted $\delta^{18}O$ of presently degassing CO_2 from the summit crater could verify this particular model.

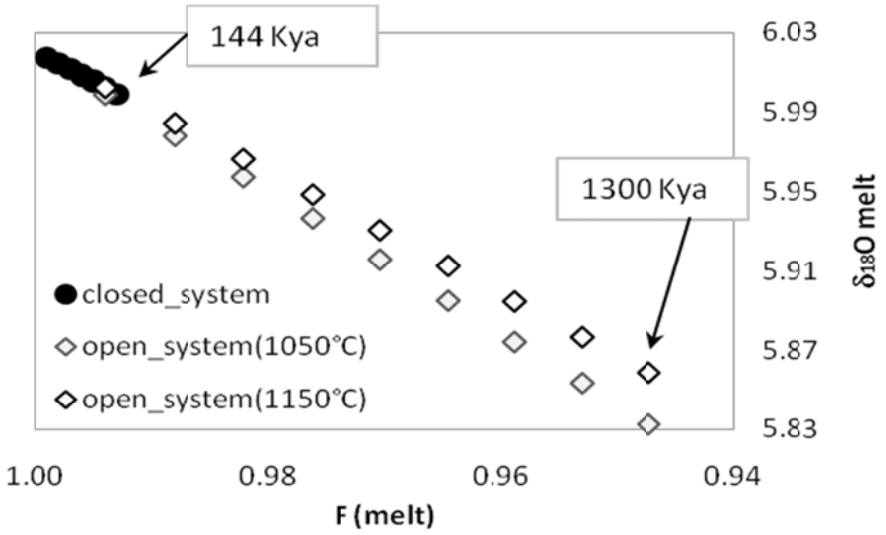

Fig. 5. Isotopic depletion of melt assuming open- and closed-system degassing of CO_2 from an intermediate depth magma chamber. Closed-system degassing is estimated at progressively decreasing fractionation temperatures from 1250 to 1000°C. Complete degassing of the original volume of basanite melt required for the formation of Erebus magmas would conclude in 144 kyr. Open-system degassing at current flux rates assuming completely replenishable concentrations of CO_2 dissolved in an intermediate magma chamber were modeled at temperatures of 1050°C and 1150°C. Optimistic calculations at 1050°C predicted a final melt composition of 5.83‰ following 1.3 Ma of continuous degassing.

Assimilation of cumulates or hydrothermally altered edifices

Subsurface scavenging of cumulate olivines has been invoked to explain small depletions for low $\delta^{18}O$ systems such as Laki (Bindeman et al., 2006) and Galunggung volcanoes (Harmon, 1992). Such models involve sidewall melting and scouring of the crystalline roof into the shallow magma chamber. Significant remelting of high-Fo cumulates could cause depletion of the melt; however, this process would be limited by the isotopic composition of the incorporated material. Olivine cumulates have been identified on Mt. Erebus (Kyle et al., 1992), but their compositions are likely to resemble parental basanites or HIMU averaging 5.0‰, thus limiting any depletions below this value.

Assimilated material with even greater depletions, however, could be derived from hydrothermally altered volcanic edifices, such has been proposed for Hawaii (Wang et al., 2003;

Wang and Eiler, 2008) and Yellowstone (Bindeman and Valley, 2000; 2001). All volcanoes are host to some form of hydrothermal system, even immature ones characterized as exhibiting a low water:rock ratio (Hedenquist, 1986). The occurrence of multiple ice caves forming near the modern volcanic edifice, largely associated with ring fracturing (Giggenbach, 1976), supports structural pathways for the formation of hydrothermal cells at greater depth. Significant crustal contamination in the main Erebus lineage is not discernible from radiogenic isotopes or trace elements. Yet, hydrothermal alteration by meteoric water can change the isotopic composition of rock without altering its bulk chemical composition, including trace elements and radiogenic $^{87}Sr/^{86}Sr$ signatures (Taylor, 1979; Wade and Eiler, 2008; Bindeman, 2008). Incorporation of altered volcanic units in shallow crustal environments is aided by continual caldera collapses and buildup of the volcanic edifice, which brings the altered units deeper towards the melting zone (Fig. 6). Hydrothermal alteration also aids with volatile flux to support re-melting and mechanical incorporation of the glassy, porous units (Bindeman, 2008). The extremely depleted nature of the Ross Ice Shelf and Antarctic meteoric precipitation (Dansgaard et al., 1977; Grootes & Suiver, 1986) would result in significant isotopic depletion of the altered units with much smaller water–rock ratios.

Anorthoclase phonolite xenoliths (82431)located on Bomb Peak exhibit extremely depleted $\delta^{18}O$ whole-rock values of 0.17‰, illustrating a possible altered endmember for incorporation into the melt. Plots of whole-rock K_2O vs. Rb concentrations align with other Erebus lineage samples, indicating little change to trace or major element compositions outside the evolutionary path that signifies crustal assimilation. Prolific geothermal systems exhibits a $\delta^{18}O$ enrichment of approximately 5‰ in thermal fluids (Craig, 1963; Taylor, 1979); much higher enrichments are expected for systems with low water:rock ratios. The formation of a 0.17‰ altered unit from a 5.68‰ phonolite by the +10‰ enrichment of a -35‰ Antarctic water may be achieved with a minimum 1 to 3.5 water:rock ratio using a closed-system box model (Appendix

22). Two fractionation models are presented that involve the increasing incorporation of such a depleted edifice into the fractionating melt (Fig. 7). A total 11.0% contribution of altered material over time is needed to produce the modern olivine compositions; a 7.7% contribution is needed to produce the modern anorthoclase phonolite melt (calculations in Appendix 23).

Phase 1 – Early basanite evolution during proto-Erebus shield building phase. During initial subaerial phase, hydrothermal alteration with meteoric water is minimal , however has large impact on d18O of EL series

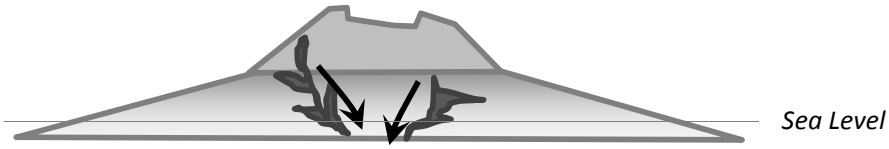

Phase 2 – Phototephrite evolution, form steeper cone on slopes of proto-Erebus volcano, followed by caldera forming event which destroys summit.
Larger degrees of crustal contamination with hydrothermally altered units are incorporated following major collapses.
Equilibration of melt in intermediate magma chamber, olivines are slow to equilibrate due to slower diffusion

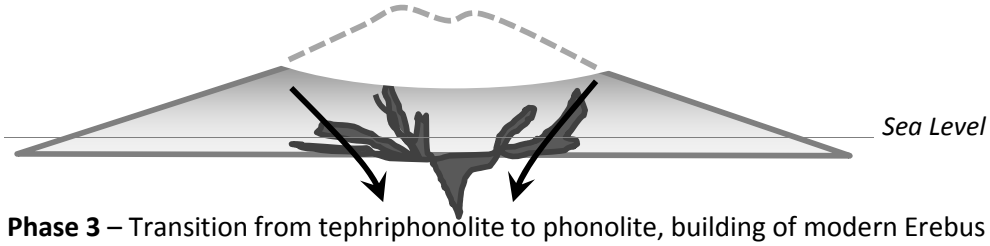

Phase 3 – Transition from tephriphonolite to phonolite, building of modern Erebus cone
Hydrothermal system is more mature, additional collapse events of modern Erebus caldera means greater crustal contamination with hydrothermally altered units
Equilibration of melt in intermediate magma chamber; Olivines reach equilibrium with melt

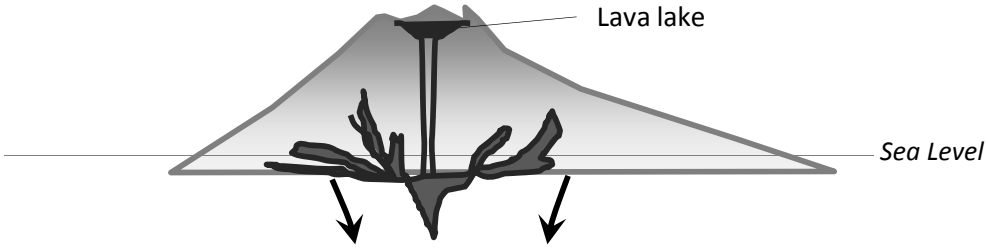

Phase 4 – Modern Erebus anorthoclase phonolite lavalake. Late stage incorporation of altered material is negligible, yet would have migrated deep below the surface. Melt reaches lava lake for period of repose, fractionation of anortthoclase megacrysts and magnetite increases the melt $\delta^{18}O$. Olivines are slow to equilibrate with new melt $\delta^{18}O$ due to diffusion.

Fig. 6. Cartoon illustrating incorporation of hydrothermally altered volcanic edifice through the various Erebus building phases.

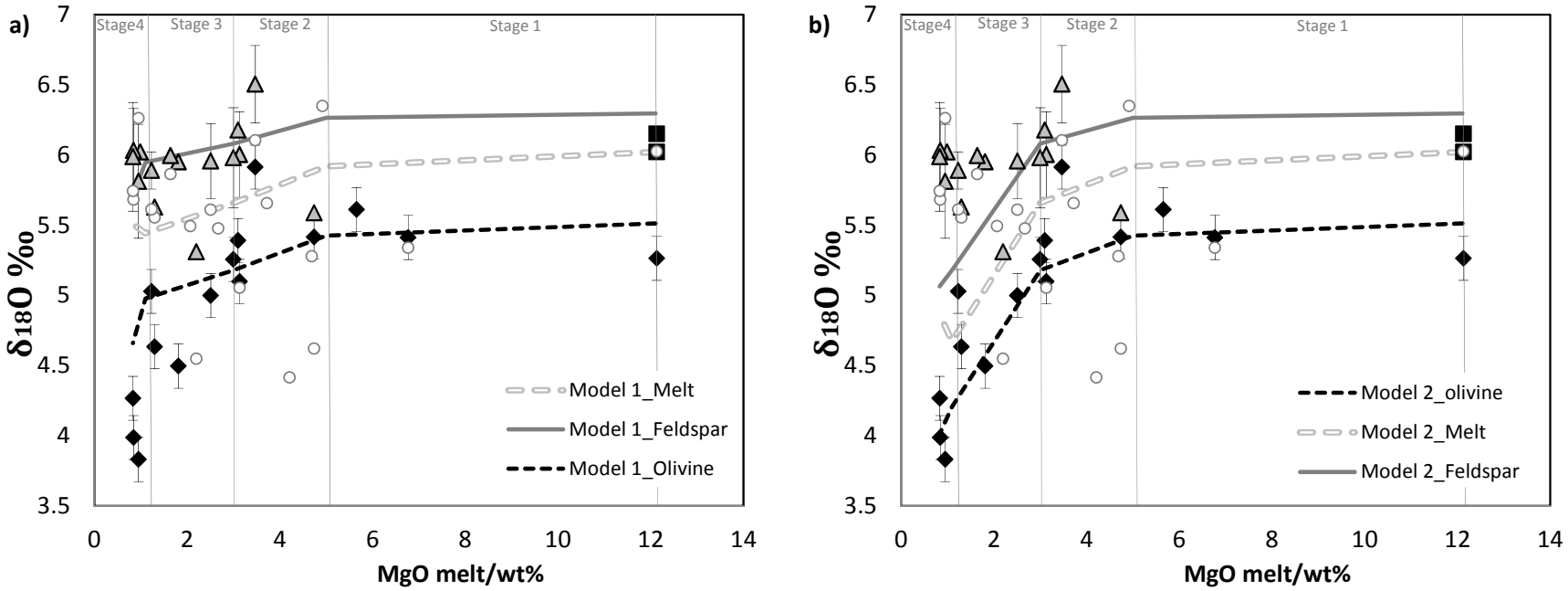

Fig. 7. a) Fractionation model involving the incorporation of 7.7% altered volcanic edifice over time. Resulting values agree with observed melt, olivine and feldspar pairs through Stage 4: the formation of modern anorthoclase phonolite melt, however diverge strongly for olivine phases in modern samples.
b) Fractionation model involving 11.0% altered edifice over time, with greatest contribution during Stage 3: the evolution from tephriphonolite to phonolite melt associated with large caldera collapse of modern Erebus caldera. Isotopic values of feldspar and melt strongly diverge in An-phonolite samples < MgO ≈ 3.

Excess isotopic depletion in olivines

Many studies rely on olivines as sole proxies for monitoring isotopic trends in the melt, due to their refractory nature which limits oxygen diffusion and simple Fe–Mg solid solution that results in negligible fractionation (Eiler, 2001; Bindeman, 2008). This study observed a disequilibrium of the olivines with the melt and feldspar suites at most stages of fractional crystallization and, most notably, in the modern anorthoclase phonolites (Fig. 7). The systematic depletion of the melt or whole-rock compositions observed here may be rectified by various geologic factors described above; however, these alone cannot explain the uniquely enhanced depletion witnessed amongst the olivines.

We propose a model whereby two stages of equilibration take place, first within an intermediate-depth magma chamber where incorporation of altered units forms a depleted melt with equally depleted olivine phases; followed by temporary repose in the shallow lava lake where anorthoclase megacrysts are formed over the course of $10^{1\text{-}2}$ yrs prior to eruption. Olivine phenocrysts may not have enough time to re-equilibrate their O-isotopic values via diffusion and thus record a lower $\delta^{18}O$ phase within shallow melt. The coincidence of strong olivine $\Delta^{18}O$ disequilibrium with the formation of the modern anorthoclase-rich phonolite melt and shallow lava lake, argues for differential fractionation with the other analyzed phases. The variability between modern olivine values amongst different samples, where MgOwt% < 2, also supports a heterogeneous or sporadic process for which depleted olivines are incorporated into the modern assemblage, such as eruptive periodicity.

Olivines are rare in modern bombs and occur as smaller, subhedral phenocrysts compared to their more mafic counterparts. Microprobe analyses, however, have not identified apparent zoning or unique rim compositions that would indicate partial re-equilibration of relic olivines with a shallow magma chamber. Diffusion of oxygen in olivines is a slow process and estimated

to take ~126ka for a 2mm long olivine to re-equilibrate with its host melt's $\delta^{18}O$ composition (Bindeman, 2008; Ryerson et al., 1989). In addition, chemical variation has not been identified in olivines undergoing oxygen diffusion (Bindeman, 2008) unless undersaturation calls for resorption, thus leaving little chemical indication for such a process without single crystal isotopic transects. As discussed above, the isotopic compositions of the olivines appear to be strongly coupled with their FeO content, specifically with Fo composition. Oppenheimer et al. (2011) observed a marked decrease in the fO_2 composition of the shallow lava lake in comparison to melt inclusions from the repose chamber at intermediate depths. This phenomenon was attributed to buffering by FeO and increased magnetite precipitation in the shallow chamber. It is possible that olivine isotopic compositions are strongly affected by decreasing oxygen fugacity in either the intermediate depth magma chamber or shallower melt. These arguments may be addressed by olivine crystallization studies in the presence of changing volatile compositions.

CONCLUSIONS

Isotopically depleted lavas and mineral separates were identified at Erebus volcano, exhibiting a trend of increasingly depleted $\delta^{18}O$ values with increased fractional crystallization of the melt. A primitive DVDP basanite lava, representing a parental end member for the Erebus lineage, exhibited whole-rock and olivine isotopic values of 6.02‰ and 5.26‰, respectively, which is consistent with a HIMU mantle source. Modern anorthoclase phonolites exhibited depleted feldspar, melt, and olivine isotopic compositions of 6.0‰, 5.7‰, and 3.8‰, respectively. Contemporaneously emplaced lavas of the enriched-Fe series (EFS) also exhibited a trend of decreasing isotopic values with increased differentiation.

Forward models were constructed by calculating the equilibrium fractionation factors ($\Delta^{18}O$) between melt–mineral and mineral–mineral pairs at slowly evolving magmatic

temperatures. Feldspar phenocrysts appeared to be in near-isotopic equilibrium with the melt throughout the intermediate to late stage melts within the Erebus lineage. Olivine phenocrysts, however, remained in stark disequilibrium with the melt and feldspars throughout.

Scavenging and incorporation of altered and isotopically depleted volcanic edifice through the intermediate magma chamber is proposed as a possible cause for the observed isotopic trends. Extremely light Antarctica snow and ice from the Ross Ice Sheet would impose strong depletions on shallowly intruded basalts with little contribution from mass. A water-to-rock mass ratio of approximately 1:4 would be required to alter the volcanic edifice at geothermal temperatures (300°C) to form the isotopic composition of the light phonolite xenoliths observed on Mt. Erebus. Incorporation of 7.7-11% altered material over time would be required to produce the modern depleted melts. This model has the advantage of explaining the similar isotopic depletions observed in the EFS lavas emplaced in close proximity to the Erebus lineage lavas. Strong $\Delta^{18}O$ disequilibrium between olivines and feldspar/melt pairs correlates strongly with the formation of the modern Erebus configuration and convecting lava lake. Olivine isotopic compositions correlated strongly with their forsterite contents, more so than SiO_2 or MgO in the melt, indicating additional unique factors influencing the olivines alone. Differential precipitation of olivines in the intermediate magma chamber and feldspars in the shallow lava lake may result in depleted olivines in the modern mineral assemblage if olivines are slow to equilibrate their isotopic composition via diffusion. Additional factors, such as variable fO_2 should be investigated to examine the cause of olivine disequlibrium.

Continuous degassing of CO_2 from a primitive mantle source was also investigated. Models assuming complete "resetting" of the dissolved CO_2 in our melt with mantle values of 6.02‰, followed by open-system degassing for 1.3 Ma, achieved a final melt composition of 5.82‰; this was still slightly higher than the observed composition of the anorthoclase phonolite glasses. This model, however, did not account for additional enrichment of the melt prescribed by

fractional crystallization or for changes in rates of degassing over time. To further investigate this later mechanism, we propose the measurement of CO_2 in the Erebus plume, to be compared with $\delta^{18}O$ of CO_2 in temporally staggered melt inclusions of the Erebus lineage to investigate possible changes in CO_2 composition of the melt.

The abundance of depleted oxygen-isotopic systems may be drastically overlooked in the tertiary volcanic record (Bindeman, 2008), thus calling for a largely universal method for such depletions which may affect volcanic systems in various geologic and climatic settings. The Erebus lineage lavas offer a unique opportunity to study these mechanisms due to the lack of meteoric precipitation and apparent crustal assimilation. The incorporation of hydrothermally altered volcanic edifice may represent a more common process than previously thought, largely due to the lack of chemical fingerprints related to meteoric-alteration of similar volcanic lithologies to the melt. Very little water:rock interaction is required to produce altered units and frequent dome or caldera collapses aid in introducing edifice material into the melt.

REFERENCES

Bindeman, I.N. 2008. Oxygen isotopes in mantle and crustal magmas as revealed by single crystal analysis. Reviews in Mineralogy and Geochemistry. 69, 445-478.

Bindeman, I.N., Sigmarsson, O., Eiler, J., 2006. Time constraints on the origin of large volume basalts derived from O-isotope and trace element mineral zoning and U-series disequilibria in the Laki and Grímsvötn volcanic system. Earth and Planetary Science Letters. 245, 245–259.

Bindeman, I.N., and Valley, J.W., 2001. Low $\delta^{18}O$ rhyolites from Yellowstone: magmatic evolution based on analyses of zircons and individual phenocrysts. Journal of Petrology. 42, 1491-1517.

Bindeman, I.N., and Valley, J.W., 2000. Formation of low $\delta^{18}O$ rhyolites after caldera collapse at Yellowstone, Wyoming. Geology. 28, 719-722.

Calkins, J., Oppenheimer, C., Kyle, P.R., 2008. Ground-based thermal imaging of the lava lakes at Erebus volcano, Antarctica. Journal of Volcanology and Geothermal Research. 177, 695-704.

Criss, R.E., Taylor,H.P., 1986. Meteoric hydrothermal systems. In: Stable Isotopes in High Temperature Geological Processes. Valley, J.W., Taylor,H.P., O'Neil, J.R. (eds), Reviews in Mineralogy. 16, 373-422.

Craig, H., 1963. The isotopic geochemistry of water and carbon in geothermal areas: Nuclear Geology on Geothermal Areas, CNR, Pisa, p. 17–53.

Chiba H., Chacko T., Clayton R.N., Goldsmith J.R., 1989. Oxygen isotope fractionations involving diopside, forsterite, magnetite, and calcite: Applications to geothermometry. Geochimica et Cosmochimica Acta. 53, 2985-2995.

Dansgaard, W., Johnsen, S.J., Clausen, H.B., Hammer, C.U., Langway, C.C., 1977. Stable isotope profile through the Ross Ice Shelf at Little America V, Antarctica. In: Isotopes and impurities in snow and ice (Proc. Grenoble Symp., August-September1975), pp. 322-325. IAHS Publ. no. 118.

Eiler, J.M., 2001. Oxygen isotope variations of basaltic lavas and upper mantle rocks. In: Valley, J.W., Cole, D.R. (eds), Stable Isotope Geochemistry, Reviews in mineralogy.43, 319-364.

Eiler, J.M., Valley, J.W., Stolper, E.M., 1996. Oxygen isotope ratios in olivine from the Hawaii Scientific Drilling Project. Journal of Geophysical Research. 101, 11807-11813.

Eschenbacher, A., 1998. Open-system degassing of a fractionating, alkaline magma, Mount Erebus, Ross Island, Antarctica. Masters Thesis, New Mexico Institute of Mining and Technology.

Esser R.P., Kyle P.R., McIntosh W.C., 2004. 40Ar/39Ar dating of the eruptive history of Mount Erebus, Antarctica: Volcano evolution. Bull. Volcanol. 66, 671-686.

Ertchi P. and Silverman S.R. 1951. The determination of the relative abundance of the oxygen isotopes in silicate rocks. Geochim. et Cosmochim. Acta 1, 317-328.

Finn, C.A., Muller, R.D., Panter, K.S. 2005. A Cenozoic diffuse alkaline magmatic province (DAMP) in the southwest Pacific without rift or plume origin. Geochemistry geophysics geosystems. 6, 1-26.

Giggenbach, W.F. 1976. Geothermal ice caves on Mt Erebus, Ross Island, Antarctica. New Zealand Journal of Geology and Geophysics. 19, 365-372.

Grootes, P.M., Stuiver, M., 1986. Ross Ice Shelf oxygen isotopes and West Antarctic climatehistory. Quaternary Research. 26, 49-67.

Gupta, S., Zhao, D.P., Rai, S.S., 2009. Seismic imaging of the upper mantle under the Erebus hotspot in Antarctica. Gondwana Research. 16, 109-118.

Gurenko, A.A., Chaussidon, M., 2002. Oxygen isotope variations in primitive tholeiites of Iceland: evidence from a SIMS study of glass inclusions, olivine phenocrysts and pillow rim glasses. Earth and Planetary Science Letters. 205, 63-79.

Harmon, R.S., Gerbe, M., 1992. The 1982–83 Eruption at Galunggung Volcano, Java (Indonesia): Oxygen Isotope Geochemistry of a Chemically Zoned Magma Chamber. Journal of Petrology. 33, 585-609.

Harpel, C.J., Kyle, P.R., Esser, R.P., McIntosh, W.C., Caldwell, D.A., 2004. 40Ar/39Ar dating of the eruptive history of Mount Erebus, Antarctica: summit flows, tephra, and caldera collapse. Bull Bull Volcanol. 66, 687–702.

Harris, A.J.L., Flynn, L.P., Rothery, D.A., Oppenheimer, C., Sherman, S.B., 1999. Mass flux measurements at active lava lakes: Implications for magma recycling. J. Geophys. Res. 104, 7117-7136.

Hedenquist J.W., 1986. Geothermal systems in the Taupo volcanic zone; their characteristics and relation to volcanism and mineralisation. In: Late Cenozoic volcanism in New Zealand (I.E.M. Smith, Ed.) Bulletin – Royal Society of New Zealand. 23, 134-168.

Kelly, P.K., 2006. Geochemistry and mineralogy of the phonolite lava lake, Mount Erebus volcano, Antarctica: 1972-2004 and comparison with older lavas. Masters Thesis, New Mexico Institute of Mining and Technology.

Kelly, P.J., Kyle, P.R., Dunbar, N.W., Sims, K.W.W., 2008. Geochemistry and mineralogy of the phonolite lava lake, Mount Erebus volcano, Antarctica: 1972–2004 and comparison with older lavas. Journal of Volcan. Geothermal Res. 177, 589-605.

Kyle, P.R., 1981. Mineralogy and geochemistry of a basanite to phonolite sequence at Hut Point Peninsula, Antarctica, based on core from Dry Valley Drilling Project drillholes 1, 2, and 3. J. Petrology. 22, 451-500.Kyle, P.R., 1990. McMurdo Volcanic Group Western Ross Embayment: Introduction In:"Volcanism of the Antarctic Plate and Southern Oceans" (Ed. W. LeMasurier, J. Thompson). Antarctic Research Series, Vol. 48, American Geophysical Union, 18-25.

Kyle, P.R., Moore, J.A., Thirlwall, M.F., 1992. Petrologic evolution of anorthoclase phonolite lavas at Mt Erebus, Ross Island, Antarctica. J. Petrol. 33, 849-875.

Marks, M., Vennemann, T., Wolfgang, S., Markl, G., 2004. Nd-, O-, and H-isotopic evidence for complex, closed-system fluid evolution of the peralkaline Ilı´maussaq intrusion, South Greenland. Geochimica et Cosmochimica Acta. 68, 3379–3395.

Moore, J.A. and Kyle, P.R., 1987. Volcanic Geology of Mount Erebus, Ross Island, Antarctica. Proc. NIPR Symp. Antarct. Geosci. 1, 48-65.

Nardini, I., Armienti, P., Rocchi, S., Dallai, L., Harrison, D., 2009. Sr-Nd-Pb-He-O Isotope and Geochemical Constraints on the Genesis of Cenozoic Magmas from theWest Antarctic Rift. Journal of Petrology 50, 1359-1375.

Oppenheimer, C., Kyle, P.R., 2008. Probing the magma plumbing of Erebus volcano, Antarctica, by open-path FTIR spectroscopy of gas emissions. J. Volcanol. Geotherm. Res. 177, 743-754.

Oppenheimer, C., Lomakina, A.S., Kyle, P.R., Kingsbury, N., Boichu, M., 2009. Pulsatory magma supply to a phonolite lava lake. Earth Planetary Science Letters 284, 392-398.

Oppenheimer, C., Moretti, R., Kyle, P.R., Eschenbacher, A., Lowenstern, J.B. Hervig, R.L., Dunbar, N.W., 2011, Mantle to surface degassing of alkalic magmas at Erebus volcano, Antarctica. Earth and Planetary Science Letters. 306, 261–271.

Perinelli, C., Armienti, P., Dallai, L. 2006., Geochemical and O-isotope constraints on the evolution of lithospheric mantle in the Ross Sea rift area (Antarctica). Contrib. Mineral. Petrol. 151, 245–266.

Panter, K. S., Hart, S. R., Kyle, P., 2000. Evidence for a Cretaceous Antarctic plume (‘Erebus Plume’) in New Zealand. EOS Transactions, AGU. 81, F1357.

Panter, K.S., Blusztajn, J., Hart, S.R., Kyle, P.R., Esser, R., McIntosh, W.C., 2006. The Origin of HIMU in the SW Pacific: Evidence from Interplate Volcanism in Southern New Zealand and Subantarctic Islands. Journal of Petrology. 47, 1673-1704.

Reagan, M.K., Volpe, A.M., Cashman, K.V., 1992. U-238 Series Chronology of Phonolite Fractionation at Mount Erebus, Antarctica. Geochimica et Cosmochimica Acta. 56, 1401-1407.

Ryerson F.J., Durham, W.D., Cherniak, D.J. 1989. Oxygen diffusion in olivine- effect of oxygen fugacity and implications for creep. Journal of Geophysical Research. 94, 4105-4118.

Sharp, Z.D., 1990. A laser-based microanalytical method for the in-situ determination of oxygen isotope ratios of silicates and oxides. Geochim. Cosmochim. Acta. 54, 1353-1357.

Sims, K.W.W., Blichert-Toft, J., Kyle, P.R., Pichat, S., Bluzstajn, J., Kelly, P.J., Ball, L.A., Layne, G. D., 2008. A Sr, Nd, Hf, and Pb isotope perspective on the genesis and long-term evolution of alkaline magmas from Erebus volcano, Antarctica. Journal of Volcanology and Geothermal Research. 177, 606-618.

Storey, B. C., Leat, P. T., Weaver, S. D., Pankhurst, R. J., Bradshaw, J. D., Kelly, S., 1999. Mantle plumes and Antarctica–New Zealand rifting: evidence from mid-Cretaceous mafic dykes. Journal of the Geological Society, London. 156, 659–671.

Sweeney, D., Kyle, P.K., Oppenheimer, C., 2008. Sulfur dioxide emissions and degassing behavior of Erebus volcano, Antarctica. J. Volcanol. Geotherm. Res. 177, 725-733.

Taylor, H.P., Jr., 1979. Oxygen and hydrogen isotope relationships in hydrothermal mineral deposits. In Geochemistry of Hydrothermal Ore Deposits (ed. H.L. Barnes), pp. 236-277. New York: J.Wiley and Sons.

Thirlwall, M.F., Gee, M.A.M., Lowry, D., Mattey, D.P., Murton, B.J., Taylor, R.N., 2006. Low d18O in the Icelandic mantle and its origins: Evidence from Reykjanes Ridge and Icelandic lavas. Geochimica et Cosmochimica Acta. 70, 993–1019.

Wade, J.A., Planka, T., Stern, R.J., Tollstrup, D.L., Gill, J.B., O'Leary, J.C., Eiler, J.M, Moore, R.B., Woodhead, J.D., Trusdell, F., Fischer, T.P., Hilton, D.R., 2005. The May 2003 eruption of Anatahan volcano, Mariana Islands: Geochemical evolution of a silicic island-arc volcano. Journal of Volcanology and Geothermal Research. 146, 139– 170.

Wang, Z., Kitchen, N.E., Eiler, J.M., 2003. Oxygen isotope geochemistry of the second HSDP core. Geochemistry, Geophysics, Geosystems. 4, 1-29.

Wang, Z., Eiler, J.M., 2008. Insights into the origin of the low-$\delta^{18}O$ basaltic magmas in Hawaii revealed from in situ measurements of oxygen isotope compositions of olivines. Earth and Planetary Science Letters. 269, 377-387.

Wardell, L.J, Kyle, P.R., Chaffin, C., 2004. Carbon dioxide and carbon monoxide emission rates from an alkaline intra-plate volcano: Mt. Erebus, Antarctica. J. Volcanol. Geotherm. Res. 131, 109-121.

Watson, 1979. Apatite saturation in basic and intermediate magmas. Geophys. Res. Lett. 6, 937-40.

Zhao, Z. F., Zheng, Y. F., 2003. Calculation of oxygen isotope fractionation in magmatic rocks. Chemical Geology. 193, 59-80.

Appendix 1. Locations for Enzyme Leach and Terrasol Leach soil samples

Sample Number	Easting (UTM)	Northing (UTM)	Elevation (meters)
SL Line 1			
1	320404	3772530	1546
2	320509	3772551	1536
3	320603	3772550	1528
4	320703	3772551	1518
5	320803	3772553	1507
6	320903	3772552	1502
7	321001	3772555	1497
8	321104	3772554	1489
9	321203	3772553	1483
10	321303	3772553	1482
11	321403	3772552	1478
12	321475	3772554	1475
SL Line 2			
13	320373	3771848	1614
14	320473	3771805	1599
15	320584	3771768	1564
16	320678	3771764	1542
17	321270	3771771	1476
18	321375	3771763	1469
19	321460	3771754	1467
20	321163	3771769	1481
21	321067	3771773	1487
22	320960	3771771	1499
23	320854	3771768	1512
24	320758	3771765	1525
25	320018	3772053	1670
26	320117	3772047	1667
27	320216	3772100	1634
28	320316	3772053	1608
29	320338	3771862	1632
SL Line 3			
30	321547	3771241	1470
31	321645	3771235	1466
32	321747	3771232	1463
33	321842	3771235	1455
34	321946	3771226	1452
35	322052	3771233	1459
36	322146	3771240	1457
37	322251	3771233	1454
38	322351	3771230	1451
39	322448	3771232	1447
40	322544	3771235	1446
41	322651	3771227	1446
42	322751	3771213	1440
43	322844	3771221	1436
44	322871	3771215	1434
45	322880	3771200	1433
46	320012	3770853	1765
47	320115	3770867	1746
48	320216	3770868	1714
49	320315	3770879	1672
50	320421	3770860	1623
51	320520	3770877	1604
52	320619	3770892	1578
53	320639	3771020	1615
54	320638	3771140	1572
55	320737	3771164	1544
56	320839	3771198	1523
57	320943	3771206	1512
58	321046	3771229	1496
59	321147	3771234	1489
60	321248	3771245	1483
61	321345	3771253	1478
62	321448	3771251	1474
63	321547	3771241	1470
64	321648	3771237	1466
65	321749	3771232	1462
66	321850	3771232	1454
67	321946	3771229	1452
68	322050	3771235	1459
69	322149	3771236	1457
SL Line 4			
70	319889	3770823	1806
71	319985	3770839	1770
72	320157	3770845	1737
73	320282	3770869	1688
74	320375	3770882	1642
75	320488	3770890	1612
76	320609	3770886	1579
77	320691	3770890	1563
78	320774	3770853	1548
79	320895	3770841	1538
80	321018	3770896	1513
81	321108	3770956	1499
82	321217	3771038	1491
83	321343	3771098	1481
84	317617	3769980	1939
85	317744	3770099	1935
86	317867	3770189	1911
87	318000	3770338	1913
88	318123	3770486	1922
89	318282	3770621	1955
90	318446	3770704	1960
91	318544	3770813	2004
92	318482	3770682	1952
93	318568	3770669	1943
94	318676	3770644	1925
95	318762	3770664	1924
96	318886	3770658	1915
97	319029	3770650	1899
98	319230	3770660	1903
99	319409	3770732	1901
100	319563	3770753	1894
101	319697	3770771	1879
102	319799	3770787	1848
103	319829	3770799	1836
SL Line 5			
104	320698	3770595	1597
105	320789	3770593	1585
106	320871	3770572	1546
107	320941	3770562	1523
108	321073	3770575	1502
109	321176	3770536	1496
110	321280	3770508	1493
111	321466	3770458	1482
112	321595	3770434	1474
113	321671	3770405	1470
114	321777	3770387	1471
115	321898	3770374	1470
116	322004	3770375	1467
117	322093	3770368	1466
118	322195	3770349	1463
119	322292	3770326	1457
120	322401	3770300	1458
121	322498	3770291	1459
122	322606	3770272	1459
123	322708	3770246	1457
124	322801	3770226	1457
125	322896	3770236	1451
SL Line 6			
126	322057	3769746	1470
127	322156	3769743	1469
128	322258	3769747	1467
129	322359	3769753	1464
130	322455	3769732	1464
131	322557	3769725	1463
132	322658	3769732	1461
133	322754	3769736	1459
134	322857	3769717	1458
135	322957	3769733	1456
136	323056	3769722	1454
137	323159	3769724	1453
138	323256	3769730	1452
139	319452	3768784	1634
140	319654	3768728	1610
141	319851	3768808	1587
142	320053	3769002	1570
143	320253	3769263	1550
144	320489	3769316	1529
145	320657	3769378	1512
146	320855	3769554	1507
147	320957	3769604	1501
148	321053	3769604	1497
149	321154	3769618	1495
150	321255	3769625	1490
151	321354	3769717	1488
152	321451	3769735	1481
153	321556	3769738	1482
154	321654	3769746	1478
155	321755	3769741	1478
156	321855	3769738	1475
157	321954	3769742	1475
158	322057	3769743	1470
159	322154	3769741	1469
160	322256	3769742	1467
161	322354	3769743	1464
162	322455	3769742	1464

Appendix 2.1 Results of Enzyme Leach Analysis for Oxidation Suite, Base metals and Chalcophile elements.

	Oxidation Suite Elements												Base Metals						Chalcophile Elements								
Sample Number	Cl	Br	I	V	As	Se	Mo	Sb	Te	W	Re	Au	Hg	Th	U	Co	Ni	Cu	Zn	Pb	Ga	Ge	Ag	Cd	In	Sn	Tl	Bi
SL Line 1																												
1	2470	57	<2	81	56	<5	9	12	<1	10	<0.01	<0.05	<1	0.50	<0.1	13.4	6.9	12.8	<10	2	<1	<0.5	<0.2	0.4	<0.1	<0.8	<0.1	<0.8
2	11300	47	<2	81	48	<5	9	18	<1	15	<0.01	<0.05	<1	0.24	<0.1	14.9	18.5	27.8	11	11	<1	<0.5	<0.2	0.7	<0.1	<0.8	<0.1	<0.8
3	4680	57	<2	39	35	<5	9	19	<1	9	<0.01	<0.05	<1	0.64	<0.1	11.0	7.3	16.8	12	<1	<1	<0.5	<0.2	0.4	<0.1	<0.8	<0.1	<0.8
4	2080	63	<2	65	38	<5	6	18	<1	11	<0.01	<0.05	<1	0.53	<0.1	11.4	7.6	21.7	<10	20	<1	<0.5	<0.2	0.8	<0.1	<0.8	<0.1	<0.8
5	<2000	30	<2	56	30	<5	3	17	<1	6	<0.01	<0.05	<1	0.45	<0.1	6.0	4.3	13.1	<10	3	<1	<0.5	<0.2	<0.2	<0.1	<0.8	<0.1	<0.8
6	<2000	32	<2	80	37	<5	4	20	<1	14	<0.01	<0.05	<1	0.33	<0.1	8.9	5.2	12.5	<10	9	<1	<0.5	<0.2	0.5	<0.1	<0.8	<0.1	<0.8
7	<2000	29	<2	55	22	<5	2	7	<1	6	<0.01	<0.05	<1	0.63	<0.1	6.0	4.6	12.9	<10	10	<1	<0.5	<0.2	0.5	<0.1	<0.8	<0.1	<0.8
8	<2000	46	<2	103	49	<5	4	19	<1	11	<0.01	<0.05	<1	0.49	<0.1	6.4	4.9	9.3	<10	<1	<1	<0.5	<0.2	<0.2	<0.1	<0.8	<0.1	<0.8
9	<2000	36	<2	67	43	<5	2	11	<1	6	<0.01	<0.05	<1	0.74	<0.1	4.8	4.0	7.5	<10	3	<1	<0.5	<0.2	0.4	<0.1	<0.8	<0.1	<0.8
10	<2000	56	<2	95	64	<5	4	14	<1	10	<0.01	<0.05	<1	0.73	<0.1	9.2	6.3	10.9	<10	5	<1	<0.5	<0.2	0.3	<0.1	<0.8	<0.1	<0.8
11	<2000	35	<2	125	59	<5	4	27	<1	10	<0.01	<0.05	<1	0.52	<0.1	8.2	6.1	15.8	<10	7	<1	<0.5	<0.2	<0.2	<0.1	<0.8	<0.1	<0.8
12	<2000	57	44	307	89	<5	12	28	<1	27	<0.01	<0.05	<1	0.30	0.3	12.3	12.2	17.4	<10	<1	<1	<0.5	<0.2	<0.2	<0.1	<0.8	<0.1	<0.8
SL Line 2																												
13	3930	64	13	154	66	<5	33	17	<1	60	<0.01	<0.05	<1	0.25	0.3	105.0	48.9	31.0	48	136	<1	<0.5	<0.2	14.9	<0.1	<0.8	<0.1	<0.8
14	4140	102	11	311	136	<5	66	33	<1	76	<0.01	<0.05	<1	0.47	<0.1	48.7	49.9	61.0	30	118	<1	<0.5	<0.2	6.1	<0.1	<0.8	0.1	<0.8
15	8230	31	<2	72	413	<5	56	28	<1	136	<0.01	<0.05	<1	0.24	1.7	237.0	27.6	324.0	1510	812	2	4.2	<0.2	61.6	<0.1	1.1	1.2	1.1
16	5390	90	26	282	716	<5	437	19	<1	416	<0.01	<0.05	<1	0.19	0.5	28.3	31.5	60.7	81	74	<1	<0.5	<0.2	4.4	<0.1	<0.8	0.3	<0.8
17	5400	44	3	174	93	<5	19	30	<1	72	<0.01	<0.05	<1	0.38	<0.1	14.2	22.3	21.3	19	33	<1	<0.5	<0.2	1.0	<0.1	<0.8	<0.1	<0.8
18	7500	72	<2	150	97	<5	9	41	<1	43	<0.01	<0.05	<1	0.23	<0.1	10.3	11.9	20.4	<10	25	<1	<0.5	<0.2	0.7	<0.1	<0.8	<0.1	<0.8
19	7360	169	76	437	157	<5	93	56	<1	88	<0.01	<0.05	<1	0.67	0.2	28.6	45.5	69.2	17	36	<1	<0.5	<0.2	1.8	<0.1	<0.8	0.2	<0.8
20	2760	58	<2	194	111	<5	9	38	<1	73	<0.01	<0.05	<1	0.21	<0.1	14.7	19.1	22.7	<10	45	<1	<0.5	<0.2	0.6	<0.1	<0.8	<0.1	<0.8
21	7550	32	<2	115	70	<5	13	28	<1	50	<0.01	<0.05	<1	0.25	<0.1	16.9	17.5	34.1	25	80	<1	<0.5	<0.2	2.5	<0.1	<0.8	<0.1	<0.8
22	<2000	18	<2	137	94	<5	9	42	<1	63	<0.01	<0.05	<1	0.20	<0.1	23.7	20.0	39.9	16	45	<1	<0.5	<0.2	3.7	<0.1	<0.8	<0.1	<0.8
23	<2000	40	<2	97	85	<5	18	23	<1	57	<0.01	<0.05	<1	0.32	<0.1	18.8	14.6	40.9	38	102	<1	<0.5	<0.2	4.0	<0.1	<0.8	<0.1	<0.8
24	2950	59	<2	81	92	<5	22	22	<1	29	<0.01	<0.05	<1	0.28	<0.1	10.8	7.4	20.1	27	50	<1	<0.5	<0.2	2.3	<0.1	<0.8	<0.1	<0.8
25	14700	135	26	72	40	7	45	30	<1	11	0.06	<0.05	<1	0.65	0.2	31.2	47.8	32.1	10	<1	<1	<0.5	<0.2	1.4	<0.1	<0.8	0.1	<0.8
26	10500	84	21	69	30	5	5	8	<1	5	<0.01	<0.05	<1	1.02	<0.1	8.4	6.6	28.2	<10	<1	<1	<0.5	<0.2	0.7	<0.1	<0.8	<0.1	<0.8
27	8430	46	13	100	33	<5	11	11	<1	5	<0.01	<0.05	<1	0.42	<0.1	17.8	10.4	21.3	<10	2	<1	<0.5	<0.2	0.8	<0.1	<0.8	<0.1	<0.8
28	18100	56	31	242	65	<5	55	10	<1	25	<0.01	<0.05	<1	<0.1	<0.1	98.4	46.2	34.4	27	14	<1	<0.5	<0.2	3.9	<0.1	<0.8	<0.1	<0.8
29	20500	109	65	250	142	<5	63	15	<1	29	<0.01	<0.05	<1	0.30	0.5	33.0	23.9	50.2	<10	37	<1	<0.5	<0.2	3.7	<0.1	<0.8	<0.1	<0.8
SL Line 3																												
30	<2000	39	12	107	60	<5	18	15	<1	20	<0.01	<0.05	<1	0.73	0.1	18.9	11.9	37.9	44	50	<1	<0.5	<0.2	4.1	<0.1	<0.8	0.1	<0.8
31	<2000	60	11	91	43	<5	11	13	<1	13	<0.01	<0.05	<1	0.91	<0.1	6.2	6.3	15.5	<10	15	<1	<0.5	<0.2	1.8	<0.1	<0.8	<0.1	<0.8
32	<2000	37	4	64	71	<5	11	13	<1	18	<0.01	<0.05	<1	0.25	<0.1	3.3	4.8	17.1	<10	19	<1	<0.5	<0.2	1.7	<0.1	<0.8	<0.1	<0.8
33	<2000	31	<2	46	30	<5	6	10	<1	12	<0.01	<0.05	<1	1.16	<0.1	4.2	9.6	26.5	24	35	<1	<0.5	<0.2	1.8	<0.1	<0.8	0.2	<0.8
34	<2000	54	19	86	35	<5	4	5	<1	5	<0.01	<0.05	<1	0.44	<0.1	3.3	<3	17.7	<10	16	<1	<0.5	<0.2	1.0	<0.1	<0.8	<0.1	<0.8
35	<2000	45	14	92	67	<5	4	6	<1	5	<0.01	<0.05	<1	0.22	<0.1	5.2	3.5	30.1	<10	3	<1	<0.5	<0.2	1.1	<0.1	<0.8	<0.1	<0.8
36	<2000	28	12	64	47	<5	3	20	<1	5	<0.01	<0.05	<1	0.25	<0.1	3.4	<3	<3	<10	<1	<1	<0.5	<0.2	0.9	<0.1	<0.8	<0.1	<0.8
37	<2000	39	32	361	133	<5	7	13	<1	10	<0.01	<0.05	<1	<0.1	0.2	2.3	<3	<3	<10	<1	<1	<0.5	<0.2	0.4	<0.1	<0.8	<0.1	<0.8
38	<2000	35	52	715	92	<5	17	14	<1	20	<0.01	<0.05	<1	0.54	0.4	4.1	<3	<3	<10	4	<1	<0.5	<0.2	1.0	<0.1	<0.8	<0.1	<0.8
39	<2000	84	38	131	130	<5	5	23	<1	6	<0.01	<0.05	<1	1.77	0.2	4.1	<3	<3	<10	<1	<1	<0.5	<0.2	0.7	<0.1	<0.8	<0.1	<0.8
40	<2000	150	122	405	78	<5	10	7	<1	13	<0.01	<0.05	<1	0.16	0.2	7.8	7.6	16.9	<10	<1	<1	<0.5	<0.2	0.5	<0.1	<0.8	<0.1	<0.8
41	<2000	60	38	307	85	<5	5	11	<1	34	<0.01	<0.05	<1	0.14	0.5	4.7	3.2	9.3	<10	1	<1	<0.5	<0.2	0.6	<0.1	<0.8	<0.1	<0.8
42	<2000	32	18	127	44	<5	3	10	<1	18	<0.01	<0.05	<1	0.48	0.1	2.6	<3	8.9	<10	6	<1	<0.5	<0.2	0.8	<0.1	<0.8	<0.1	<0.8
43	<2000	42	42	220	175	<5	6	14	<1	20	<0.01	<0.05	<1	<0.1	0.3	3.3	<3	<3	<10	<1	<1	<0.5	<0.2	0.3	<0.1	<0.8	<0.1	<0.8
44	<2000	34	104	667	124	<5	18	4	<1	64	<0.01	<0.05	<1	0.30	4.2	6.1	5.8	4.5	<10	<1	<1	<0.5	<0.2	0.5	<0.1	<0.8	<0.1	<0.8
45	43100	666	4480	253	157	43	2750	2	<1	27	0.01	0.10	<1	0.98	36.6	13.3	174.0	15.8	<10	<1	<1	<0.5	<0.2	4.0	<0.1	<0.8	<0.1	<0.8
46	8660	128	63	230	115	6	24	43	<1	38	<0.01	<0.05	<1	0.49	0.1	6.9	7.6	22.3	<10	<1	<1	<0.5	<0.2	0.4	<0.1	<0.8	0.2	<0.8
47	2580	46	15	69	49	<5	7	53	<1	20	<0.01	<0.05	<1	0.34	<0.1	7.4	4.3	9.1	<10	<1	<1	<0.5	<0.2	0.2	<0.1	<0.8	<0.1	<0.8
48	6420	35	13	130	64	<5	18	42	<1	34	<0.01	<0.05	<1	0.42	<0.1	7.4	5.3	14.7	<10	<1	<1	<0.5	<0.2	0.5	<0.1	<0.8	0.1	<0.8
49	3630	46	7	108	46	<5	42	29	<1	36	<0.01	<0.05	<1	0.51	<0.1	5.9	4.5	13.0	<10	<1	1	<0.5	<0.2	0.4	<0.1	<0.8	0.1	<0.8
50	2470	53	11	147	61	<5	29	23	<1	50	<0.01	<0.05	<1	0.43	<0.1	10.8	10.7	20.5	<10	2	<1	<0.5	<0.2	1.1	<0.1	<0.8	0.1	<0.8
51	2460	62	33	162	147	<5	12	47	<1	36	<0.01	<0.05	<1	0.21	<0.1	9.4	8.9	21.0	<10	<1	<1	<0.5	<0.2	0.4	<0.1	<0.8	<0.1	<0.8
52	2180	62	11	121	62	<5	15	26	<1	39	<0.01	<0.05	<1	0.54	<0.1	8.2	8.0	23.9	<10	6	<1	<0.5	<0.2	0.8	<0.1	<0.8	<0.1	<0.8
53	<2000	51	34	124	56	<5	8	44	<1	18	<0.01	<0.05	<1	0.26	<0.1	7.9	6.7	20.3	<10	3	<1	<0.5	<0.2	0.5	<0.1	<0.8	<0.1	<0.8
54	13600	56	58	146	53	<5	99	6	<1	29	<0.01	<0.05	<1	0.33	0.6	8.7	15.0	137.0	239	37	<1	<0.5	<0.2	12.9	<0.1	<0.8	<0.1	<0.8
55	22000	61	9	148	40	<5	43	14	2	33	<0.01	<0.05	<1	0.23	<0.1	42.2	24.4	26.3	50	24	<1	<0.5	<0.2	5.8	<0.1	<0.8	0.1	<0.8

Appendix 2.1 cont. Results of Enzyme Leach Analysis for Oxidation Suite, Base metals and Chalcophile elements.

	Oxidation Suite Elements												Base Metals							Chalcophile Elements							
Sample Number	Cl	Br	I	V	As	Se	Mo	Sb	Te	W	Re	Au	Hg	Th	U	Co	Ni	Cu	Zn	Pb	Ga	Ge	Ag	Cd	In	Sn	Tl	Bi
SL Line 3 cont.																												
56	5670	114	13	89	67	5	24	22	<1	24	<0.01	<0.05	<1	0.44	<0.1	10.8	17.0	56.0	21	25	<1	<0.5	<0.2	2.9	<0.1	<0.8	0.1	<0.8
57	4790	40	6	91	49	<5	28	13	1	19	<0.01	<0.05	<1	0.17	<0.1	23.4	17.3	34.7	90	40	<1	<0.5	<0.2	5.2	<0.1	<0.8	<0.1	<0.8
58	2020	35	8	101	43	<5	22	8	1	15	<0.01	<0.05	<1	0.14	<0.1	43.2	24.0	35.6	49	22	<1	<0.5	<0.2	6.6	<0.1	<0.8	<0.1	<0.8
59	12400	35	14	60	19	<5	5	13	<1	13	<0.01	<0.05	<1	0.26	<0.1	10.5	4.7	50.6	43	26	<1	<0.5	<0.2	1.8	<0.1	<0.8	<0.1	<0.8
60	<2000	23	<2	96	52	<5	17	28	<1	23	<0.01	<0.05	<1	0.11	<0.1	19.8	7.7	19.0	38	41	<1	<0.5	<0.2	3.2	<0.1	<0.8	<0.1	<0.8
61	2230	20	<2	73	26	<5	6	15	<1	15	<0.01	<0.05	<1	0.41	<0.1	9.2	4.3	28.1	34	34	<1	<0.5	<0.2	3.2	<0.1	<0.8	<0.1	<0.8
62	22700	138	80	459	92	<5	28	6	<1	42	<0.01	<0.05	<1	0.58	0.4	14.1	21.4	42.4	20	10	<1	<0.5	<0.2	1.4	<0.1	<0.8	<0.1	<0.8
63	5030	33	13	147	63	<5	14	27	<1	32	<0.01	<0.05	<1	0.27	<0.1	14.8	12.2	24.2	26	31	<1	<0.5	<0.2	2.4	<0.1	<0.8	<0.1	<0.8
64	<2000	39	17	107	64	<5	7	21	<1	18	<0.01	<0.05	<1	0.36	<0.1	7.0	4.5	19.3	<10	27	<1	<0.5	<0.2	1.4	<0.1	<0.8	<0.1	<0.8
65	2060	47	10	73	110	<5	13	33	<1	23	<0.01	<0.05	<1	0.32	<0.1	6.1	11.0	22.2	12	26	<1	<0.5	<0.2	2.1	<0.1	<0.8	<0.1	<0.8
66	<2000	28	4	62	49	<5	5	14	<1	18	<0.01	<0.05	<1	0.23	<0.1	5.5	11.0	18.9	15	33	<1	<0.5	<0.2	1.4	<0.1	<0.8	<0.1	<0.8
67	3700	82	40	175	76	<5	3	24	<1	13	<0.01	<0.05	<1	0.36	<0.1	8.7	6.8	34.3	<10	13	<1	<0.5	<0.2	0.7	<0.1	<0.8	<0.1	<0.8
68	<2000	50	19	175	175	<5	10	23	<1	14	<0.01	<0.05	<1	0.17	0.1	6.1	5.7	27.1	<10	<1	<1	<0.5	<0.2	<0.2	<0.1	<0.8	<0.1	<0.8
69	<2000	27	4	57	39	<5	2	11	<1	4	<0.01	<0.05	<1	0.12	<0.1	5.5	<3	18.1	<10	18	<1	<0.5	<0.2	0.4	<0.1	<0.8	<0.1	<0.8
SL Line 4																												
70	<2000	58	14	193	132	<5	27	19	<1	84	<0.01	<0.05	<1	0.58	<0.1	4.1	5.2	17.4	<10	<1	<1	0.6	<0.2	0.6	<0.1	<0.8	0.4	<0.8
71	<2000	43	8	159	68	<5	11	32	<1	47	<0.01	<0.05	<1	0.95	<0.1	4.4	4.5	16.7	<10	<1	<1	0.8	<0.2	0.4	<0.1	<0.8	0.3	<0.8
72	3470	84	15	116	42	<5	22	22	<1	17	<0.01	<0.05	<1	0.37	<0.1	4.8	5.0	16.0	<10	<1	<1	<0.5	<0.2	0.6	<0.1	<0.8	0.2	<0.8
73	<2000	87	45	172	93	6	19	41	<1	62	0.01	<0.05	<1	0.22	<0.1	4.9	6.8	9.5	<10	<1	<1	<0.5	<0.2	0.5	<0.1	<0.8	0.3	<0.8
74	<2000	69	7	159	45	<5	32	19	<1	61	<0.01	<0.05	<1	0.59	<0.1	7.6	6.9	19.8	<10	<1	<1	<0.5	<0.2	0.7	<0.1	<0.8	0.4	<0.8
75	<2000	42	42	185	104	<5	8	48	<1	32	<0.01	<0.05	<1	1.50	0.2	12.2	7.3	<3	<10	2	<1	0.6	<0.2	2.0	<0.1	<0.8	0.2	<0.8
76	<2000	25	9	105	36	<5	37	7	<1	16	<0.01	<0.05	<1	0.79	<0.1	6.3	3.1	17.2	<10	12	<1	<0.5	<0.2	1.1	<0.1	<0.8	<0.1	<0.8
77	<2000	35	24	100	51	<5	41	3	<1	8	<0.01	<0.05	<1	0.19	0.2	4.1	<3	3.3	<10	<1	<1	<0.5	<0.2	0.9	<0.1	<0.8	<0.1	<0.8
78	3740	131	37	124	81	<5	111	13	<1	25	<0.01	<0.05	<1	0.25	0.2	11.8	22.9	37.2	<10	9	<1	<0.5	<0.2	1.5	<0.1	<0.8	0.1	<0.8
79	<2000	161	37	124	93	5	15	23	<1	15	0.02	<0.05	<1	0.47	<0.1	13.2	11.7	33.2	<10	2	<1	<0.5	<0.2	0.8	<0.1	<0.8	0.1	<0.8
80	<2000	59	25	183	62	<5	9	20	<1	16	<0.01	<0.05	<1	0.73	<0.1	8.2	8.6	11.4	<10	<1	2	<0.5	<0.2	0.5	<0.1	<0.8	0.1	<0.8
81	<2000	42	18	173	70	<5	4	15	<1	12	<0.01	<0.05	<1	0.71	<0.1	6.3	11.1	19.4	<10	2	<1	<0.5	<0.2	0.4	<0.1	<0.8	<0.1	<0.8
82	<2000	37	9	94	20	<5	3	10	<1	7	<0.01	<0.05	<1	0.79	<0.1	4.9	3.8	7.7	<10	<1	<1	<0.5	<0.2	0.5	<0.1	<0.8	<0.1	<0.8
83	<2000	56	45	336	119	<5	5	22	<1	21	<0.01	<0.05	<1	0.29	<0.1	6.8	6.4	7.1	<10	<1	<1	<0.5	<0.2	0.7	<0.1	<0.8	<0.1	<0.8
84	<2000	41	<2	106	19	<5	32	3	<1	9	0.02	<0.05	<1	0.17	<0.1	27.1	7.5	5.9	<10	<1	<1	<0.5	<0.2	1.5	<0.1	<0.8	0.1	<0.8
85	<2000	30	13	129	9	<5	13	5	<1	8	<0.01	<0.05	<1	0.84	<0.1	7.4	3.1	9.9	<10	<1	<1	<0.5	<0.2	0.7	<0.1	<0.8	<0.1	<0.8
86	<2000	49	18	47	17	<5	7	8	<1	8	<0.01	<0.05	<1	0.58	<0.1	2.8	<3	4.3	<10	<1	<1	<0.5	<0.2	0.7	<0.1	<0.8	0.2	<0.8
87	<2000	36	6	80	10	<5	28	4	<1	8	<0.01	<0.05	<1	0.32	<0.1	17.8	7.0	11.8	<10	5	<1	<0.5	<0.2	1.4	<0.1	<0.8	0.1	<0.8
88	<2000	56	17	69	15	<5	4	2	<1	4	<0.01	<0.05	<1	0.57	<0.1	2.7	5.4	23.8	<10	<1	<1	0.6	<0.2	0.7	<0.1	<0.8	0.1	<0.8
89	<2000	116	161	288	39	<5	7	6	<1	16	<0.01	<0.05	<1	0.25	0.3	7.7	7.4	8.7	<10	<1	<1	<0.5	<0.2	0.3	<0.1	<0.8	0.5	<0.8
90	<2000	35	4	234	42	<5	152	7	<1	22	<0.01	<0.05	<1	0.36	<0.1	70.1	33.6	13.5	<10	<1	<1	<0.5	<0.2	1.9	<0.1	<0.8	1.1	<0.8
91	<2000	40	6	184	128	<5	28	6	<1	11	<0.01	<0.05	<1	<0.1	<0.1	33.5	13.5	14.3	<10	5	<1	<0.5	<0.2	1.2	<0.1	<0.8	0.6	<0.8
92	<2000	37	5	121	37	<5	34	8	<1	9	<0.01	<0.05	<1	0.14	<0.1	25.6	26.2	25.7	17	24	<1	<0.5	<0.2	1.4	<0.1	<0.8	0.3	<0.8
93	2480	243	104	575	189	<5	23	14	<1	91	0.03	<0.05	<1	0.28	0.3	8.6	13.2	58.6	<10	3	<1	<0.5	<0.2	0.8	<0.1	<0.8	0.1	<0.8
94	<2000	38	20	167	36	<5	27	4	<1	4	<0.01	<0.05	<1	<0.1	<0.1	81.1	32.2	25.6	31	12	<1	<0.5	<0.2	3.7	<0.1	<0.8	0.2	<0.8
95	<2000	100	17	191	43	<5	61	12	<1	19	0.01	<0.05	<1	0.27	<0.1	27.8	19.6	23.3	<10	5	<1	<0.5	<0.2	1.2	<0.1	<0.8	0.8	<0.8
96	<2000	46	17	83	24	<5	40	29	<1	26	<0.01	<0.05	<1	0.35	<0.1	12.3	5.4	12.1	<10	<1	<1	<0.5	<0.2	0.7	<0.1	<0.8	0.6	<0.8
97	<2000	27	<2	140	34	<5	96	7	<1	22	<0.01	<0.05	<1	0.20	<0.1	48.2	21.9	16.7	<10	3	<1	<0.5	<0.2	1.5	<0.1	<0.8	0.5	<0.8
98	<2000	49	<2	148	19	<5	234	4	<1	10	0.03	<0.05	<1	0.14	<0.1	55.0	16.9	19.6	<10	3	<1	<0.5	<0.2	2.4	<0.1	<0.8	0.3	<0.8
99	5740	126	47	194	87	<5	19	19	<1	21	0.04	<0.05	<1	0.37	<0.1	6.4	7.1	18.6	<10	186	<1	<0.5	<0.2	0.5	<0.1	<0.8	0.2	<0.8
100	2480	89	23	257	169	<5	269	70	<1	96	0.01	<0.05	<1	0.36	<0.1	12.4	15.4	27.1	<10	6	<1	0.6	<0.2	1.0	<0.1	<0.8	0.4	<0.8
101	<2000	51	19	161	70	<5	6	22	<1	27	<0.01	<0.05	<1	0.46	<0.1	3.3	5.1	8.6	<10	<1	<1	<0.5	<0.2	0.6	<0.1	<0.8	0.2	<0.8
102	<2000	44	44	220	69	<5	5	17	<1	25	<0.01	0.29	<1	1.09	<0.1	6.9	4.8	32.5	<10	31	<1	<0.5	<0.2	0.9	<0.1	<0.8	<0.1	<0.8
103	<2000	79	18	119	77	<5	19	8	<1	17	0.03	<0.05	<1	0.56	<0.1	7.5	11.3	23.0	<10	<1	<1	<0.5	<0.2	0.9	<0.1	<0.8	0.2	<0.8
SL Line 5																												
104	6320	128	59	154	53	<5	13	6	1	10	<0.01	<0.05	<1	0.35	0.4	122.0	28.6	186.0	302	437	<1	<0.5	<0.2	11.0	<0.1	<0.8	0.3	<0.8
105	3690	92	45	102	37	<5	20	17	<1	13	<0.01	<0.05	<1	0.28	<0.1	23.0	9.7	51.4	18	82	<1	<0.5	<0.2	5.1	<0.1	<0.8	0.1	<0.8
106	7340	187	55	176	73	<5	5	11	<1	13	0.02	0.10	<1	0.42	<0.1	8.3	6.9	102.0	54	117	<1	<0.5	<0.2	2.8	<0.1	<0.8	0.1	<0.8
107	5910	145	40	118	56	<5	5	23	<1	6	0.04	<0.05	<1	0.34	<0.1	9.4	28.4	65.4	<10	32	<1	<0.5	<0.2	1.1	<0.1	<0.8	<0.1	<0.8
108	2080	48	20	185	48	<5	11	14	<1	19	<0.01	<0.05	<1	0.17	<0.1	27.4	13.5	12.9	<10	9	<1	<0.5	<0.2	0.8	<0.1	<0.8	0.1	<0.8
109	6100	64	55	173	72	<5	28	7	<1	17	<0.01	<0.05	<1	0.28	0.3	66.5	34.3	49.8	64	50	2	<0.5	<0.2	5.4	<0.1	<0.8	0.2	<0.8
110	2050	41	57	148	80	<5	5	18	<1	20	<0.01	<0.05	<1	0.53	0.2	8.1	7.0	20.9	<10	16	<1	<0.5	<0.2	0.4	<0.1	<0.8	<0.1	<0.8

Appendix 2.1 cont. Results of Enzyme Leach Analysis for Oxidation Suite, Base metals and Chalcophile elements.

	Oxidation Suite Elements												Base Metals							Chalcophile Elements							
Sample Number	Cl	Br	I	V	As	Se	Mo	Sb	Te	W	Re	Au	Hg	Th	U	Co	Ni	Cu	Zn	Pb	Ga	Ge	Ag	Cd	In	Sn	Tl	Bi
SL Line 5 cont.																												
111	2430	37	28	105	41	<5	3	9	<1	26	<0.01	<0.05	<1	0.79	0.1	8.7	9.3	34.5	10	34	2	<0.5	<0.2	1.4	<0.1	<0.8	0.1	<0.8
112	3350	24	20	94	32	<5	6	14	<1	12	<0.01	<0.05	<1	0.58	<0.1	16.9	7.1	20.3	24	32	<1	<0.5	<0.2	3.5	<0.1	<0.8	0.2	<0.8
113	3890	53	34	98	48	<5	6	22	<1	16	<0.01	<0.05	<1	0.41	0.2	10.2	9.2	35.6	18	33	<1	<0.5	<0.2	1.6	<0.1	<0.8	<0.1	<0.8
114	<2000	40	37	73	50	5	3	22	<1	7	<0.01	<0.05	<1	0.15	0.2	4.6	<3	19.4	<10	5	<1	<0.5	<0.2	0.6	<0.1	<0.8	<0.1	<0.8
115	2470	69	104	162	76	<5	4	17	<1	13	<0.01	<0.05	<1	0.39	0.2	6.5	<3	25.0	31	13	<1	<0.5	<0.2	0.9	<0.1	<0.8	0.1	<0.8
116	4440	65	43	104	43	<5	4	9	<1	10	<0.01	<0.05	<1	0.85	<0.1	4.9	3.5	25.7	<10	17	<1	<0.5	<0.2	1.2	<0.1	<0.8	<0.1	<0.8
117	3260	76	91	110	109	6	6	23	<1	10	<0.01	<0.05	<1	0.34	0.3	5.2	4.1	30.0	<10	14	<1	<0.5	<0.2	1.1	<0.1	<0.8	0.1	<0.8
118	3850	65	44	60	155	5	5	27	<1	5	<0.01	<0.05	<1	0.26	0.1	4.1	<3	23.6	153	22	<1	<0.5	<0.2	1.1	<0.1	<0.8	<0.1	<0.8
119	4590	54	24	60	35	<5	4	21	<1	7	<0.01	<0.05	<1	1.39	<0.1	5.5	4.6	28.2	<10	26	<1	<0.5	<0.2	1.4	<0.1	<0.8	0.2	<0.8
120	3770	50	37	54	55	<5	4	6	<1	5	<0.01	<0.05	<1	0.47	0.2	4.4	<3	29.3	<10	27	<1	<0.5	<0.2	1.2	<0.1	<0.8	0.2	<0.8
121	<2000	48	46	199	215	<5	6	35	<1	10	<0.01	<0.05	<1	0.55	0.2	3.5	<3	20.7	<10	6	<1	<0.5	<0.2	0.2	<0.1	<0.8	0.2	<0.8
122	4990	56	38	80	49	<5	3	9	<1	5	<0.01	<0.05	<1	0.78	0.1	5.0	<3	31.4	<10	63	<1	<0.5	<0.2	1.4	<0.1	<0.8	0.1	<0.8
123	3050	54	46	86	43	<5	3	6	<1	6	<0.01	<0.05	<1	0.60	0.1	5.4	<3	25.3	<10	15	<1	<0.5	<0.2	0.7	<0.1	<0.8	0.2	<0.8
124	4210	54	79	189	234	<5	6	15	<1	6	<0.01	<0.05	<1	0.21	0.3	3.9	<3	34.5	<10	18	<1	<0.5	<0.2	0.9	<0.1	<0.8	0.1	<0.8
125	<2000	37	41	73	72	<5	3	8	<1	4	<0.01	<0.05	<1	0.27	0.2	4.0	<3	30.3	<10	53	<1	<0.5	<0.2	2.2	<0.1	<0.8	0.1	<0.8
SL Line 6																												
126	<2000	67	11	63	34	<5	19	21	<1	9	<0.01	<0.05	<1	0.82	<0.1	10.2	4.3	21.2	<10	29	<1	<0.5	<0.2	1.5	<0.1	<0.8	0.3	<0.8
127	<2000	31	5	72	27	<5	7	7	<1	9	<0.01	<0.05	<1	1.07	<0.1	7.1	<3	13.8	<10	12	<1	<0.5	<0.2	1.2	<0.1	<0.8	0.2	<0.8
128	<2000	62	12	82	116	<5	20	14	2	10	<0.01	<0.05	<1	1.25	<0.1	9.4	10.5	28.9	<10	115	<1	<0.5	<0.2	3.1	<0.1	<0.8	0.2	<0.8
129	<2000	51	40	124	143	<5	4	22	<1	17	<0.01	<0.05	<1	0.39	0.1	3.8	<3	6.1	<10	18	<1	<0.5	<0.2	0.7	<0.1	<0.8	<0.1	<0.8
130	<2000	69	47	87	278	<5	7	28	<1	4	<0.01	<0.05	<1	1.94	0.3	1.9	<3	<3	<10	18	<1	<0.5	<0.2	2.2	<0.1	<0.8	<0.1	<0.8
131	<2000	69	39	114	272	<5	13	20	<1	5	<0.01	<0.05	<1	0.20	0.1	3.4	<3	34.9	<10	116	<1	<0.5	<0.2	3.9	<0.1	<0.8	0.1	<0.8
132	<2000	73	32	75	220	<5	12	13	<1	4	0.01	<0.05	<1	0.30	0.1	1.6	<3	43.8	<10	148	<1	<0.5	<0.2	4.3	<0.1	<0.8	0.2	<0.8
133	<2000	38	21	81	81	<5	5	7	<1	4	<0.01	<0.05	<1	0.58	<0.1	1.7	<3	24.9	<10	108	<1	<0.5	<0.2	3.2	<0.1	<0.8	0.1	<0.8
134	<2000	60	82	163	170	<5	5	15	<1	8	<0.01	<0.05	<1	0.17	0.2	4.0	<3	11.6	<10	22	<1	<0.5	<0.2	1.3	<0.1	<0.8	0.1	<0.8
135	<2000	309	318	399	182	7	35	11	<1	24	<0.01	<0.05	<1	0.16	0.3	10.5	9.8	23.1	<10	7	<1	<0.5	<0.2	0.7	<0.1	<0.8	0.2	<0.8
136	<2000	68	74	142	231	<5	12	15	<1	8	<0.01	<0.05	<1	0.12	0.2	1.8	<3	6.1	<10	9	<1	<0.5	<0.2	0.9	<0.1	<0.8	0.1	<0.8
137	<2000	43	57	167	46	<5	3	6	<1	16	<0.01	<0.05	<1	0.30	0.2	3.4	13.3	6.8	<10	12	<1	<0.5	<0.2	0.9	<0.1	<0.8	0.2	<0.8
138	<2000	71	116	202	264	8	17	21	<1	13	<0.01	<0.05	<1	<0.1	0.3	4.6	<3	<3	<10	<1	<1	<0.5	<0.2	0.6	<0.1	<0.8	0.1	<0.8
139	2680	80	154	500	90	<5	21	22	<1	34	<0.01	<0.05	<1	0.23	0.8	6.3	4.1	13.2	<10	<1	<1	<0.5	<0.2	<0.2	<0.1	<0.8	<0.1	<0.8
140	199000	2410	777	848	75	15	154	4	<1	18	0.03	<0.05	<1	0.90	3.7	16.3	30.9	63.8	16	<1	<1	<0.5	<0.2	<0.2	<0.1	<0.8	<0.1	<0.8
141	7770	135	134	256	76	<5	12	4	<1	99	<0.01	<0.05	<1	0.28	1.3	5.6	5.2	18.0	<10	<1	<1	<0.5	<0.2	<0.2	<0.1	<0.8	<0.1	<0.8
142	12500	65	481	662	536	<5	265	8	<1	28	<0.01	<0.05	<1	0.38	7.0	8.3	12.0	32.8	<10	5	<1	<0.5	<0.2	0.5	<0.1	<0.8	0.3	<0.8
143	11700	102	95	627	105	<5	109	7	<1	129	<0.01	0.16	<1	0.31	0.2	21.6	32.3	109.0	11	41	<1	<0.5	<0.2	0.7	<0.1	<0.8	0.1	<0.8
144	6800	44	40	160	60	<5	13	4	<1	17	<0.01	<0.05	<1	0.60	0.1	10.0	11.1	58.6	19	17	<1	<0.5	<0.2	0.3	<0.1	<0.8	<0.1	<0.8
145	5010	41	8	103	26	5	16	5	<1	25	<0.01	<0.05	<1	1.16	<0.1	9.0	7.2	19.9	11	7	<1	<0.5	<0.2	0.2	<0.1	<0.8	0.3	<0.8
146	10100	182	28	374	154	<5	19	14	<1	41	<0.01	<0.05	<1	0.97	<0.1	14.1	13.8	42.8	16	30	<1	<0.5	<0.2	1.3	<0.1	<0.8	0.1	<0.8
147	22100	169	10	159	53	<5	19	21	<1	38	0.01	<0.05	<1	0.53	0.1	13.1	19.0	58.4	59	61	<1	<0.5	<0.2	3.4	<0.1	<0.8	0.2	<0.8
148	2310	28	<2	144	34	<5	12	20	<1	20	<0.01	<0.05	<1	0.25	<0.1	26.1	12.7	8.8	14	37	<1	<0.5	<0.2	1.4	<0.1	<0.8	0.1	<0.8
149	14500	80	12	392	113	<5	7	36	<1	41	<0.01	<0.05	<1	0.55	<0.1	21.4	15.6	13.3	<10	13	<1	<0.5	<0.2	<0.2	<0.1	<0.8	0.2	<0.8
150	6130	63	6	269	64	<5	9	32	<1	42	<0.01	<0.05	<1	0.97	<0.1	12.2	9.2	23.5	<10	16	<1	<0.5	<0.2	<0.2	<0.1	<0.8	0.1	<0.8
151	3680	34	<2	100	41	<5	11	23	<1	20	<0.01	<0.05	<1	0.53	<0.1	12.5	9.9	11.3	<10	4	<1	<0.5	<0.2	0.2	<0.1	<0.8	0.2	<0.8
152	<2000	16	<2	70	23	<5	7	9	<1	11	<0.01	<0.05	<1	0.76	<0.1	10.5	13.2	24.8	<10	20	<1	<0.5	<0.2	0.6	<0.1	<0.8	0.1	<0.8
153	11000	105	<2	134	57	<5	16	75	<1	24	<0.01	<0.05	<1	0.41	<0.1	13.7	8.4	12.2	<10	25	<1	<0.5	<0.2	<0.2	<0.1	<0.8	0.2	<0.8
154	2420	39	19	48	38	<5	3	32	<1	3	<0.01	<0.05	<1	0.22	<0.1	3.6	<3	7.7	<10	<1	<1	<0.5	<0.2	<0.2	<0.1	<0.8	<0.1	<0.8
155	<2000	19	4	49	19	<5	7	16	<1	5	<0.01	<0.05	<1	0.28	<0.1	10.5	3.6	12.9	26	17	<1	<0.5	<0.2	0.7	<0.1	<0.8	<0.1	<0.8
156	<2000	38	3	61	37	<5	16	16	2	8	<0.01	<0.05	<1	0.27	<0.1	16.7	7.7	16.5	<10	17	<1	<0.5	<0.2	2.2	<0.1	<0.8	0.1	<0.8
157	<2000	22	19	79	40	<5	6	59	<1	13	<0.01	<0.05	<1	0.53	<0.1	9.5	3.3	17.1	<10	34	<1	<0.5	<0.2	1.5	<0.1	<0.8	<0.1	<0.8
158	<2000	37	8	84	53	<5	15	55	<1	17	<0.01	<0.05	<1	0.89	<0.1	9.1	4.6	27.7	<10	26	<1	<0.5	<0.2	1.3	<0.1	<0.8	0.1	<0.8
159	4780	45	12	88	39	<5	11	11	<1	11	<0.01	<0.05	<1	1.10	<0.1	12.1	7.2	25.3	<10	18	<1	<0.5	<0.2	1.4	<0.1	<0.8	0.1	<0.8
160	2290	29	21	49	49	<5	6	6	<1	4	<0.01	<0.05	<1	0.45	<0.1	5.6	<3	28.4	<10	69	<1	<0.5	<0.2	3.1	<0.1	<0.8	<0.1	<0.8
161	<2000	41	35	103	146	<5	3	31	<1	7	<0.01	<0.05	<1	0.19	0.2	5.0	<3	25.1	<10	31	<1	<0.5	<0.2	1.4	<0.1	<0.8	<0.1	<0.8
162	<2000	25	20	64	131	<5	3	13	<1	3	<0.01	<0.05	<1	0.24	0.1	3.0	<3	28.9	<10	94	<1	<0.5	<0.2	3.4	<0.1	<0.8	<0.1	<0.8

Appendix 2.2 Results of Enzyme Leach Analysis for HFSE, REE and LILEs.

	High-Field Strength Elements							Rare Earth Elements														Lithophile Elements							
Sample Number	Ti	Cr	Y	Zr	Nb	Hf	Ta	La	Ce	Pr	Nd	Sm	Eu	Gd	Tb	Dy	Ho	Er	Tm	Yb	Lu	Li	Be	Sc	Mn	Rb	Sr	Cs	Ba
SL Line 1																													
1	<100	<20	3.2	<1	<1	<0.1	<0.1	2.4	4.7	0.7	3.6	0.9	0.7	0.6	0.1	0.6	0.1	0.3	<0.1	0.2	<0.1	15.5	<2	<100	1580	19	1720	<0.1	3760
2	<100	<20	3.8	<1	<1	<0.1	<0.1	2.9	4.9	0.9	4.0	1.1	1.0	0.9	0.1	0.7	0.1	0.3	<0.1	0.2	<0.1	18.3	<2	<100	2820	20	1750	0.1	4560
3	<100	<20	5.7	<1	<1	<0.1	<0.1	4.0	5.9	1.4	5.9	1.4	0.7	1.2	0.2	1.1	0.2	0.4	<0.1	0.3	<0.1	14.4	<2	<100	1390	17	2050	0.1	2700
4	<100	<20	7.4	<1	<1	<0.1	<0.1	5.9	8.8	1.9	8.7	2.0	0.8	1.7	0.3	1.2	0.2	0.6	<0.1	0.4	<0.1	11.5	<2	<100	2070	26	1860	0.1	2790
5	<100	<20	6.7	<1	<1	<0.1	<0.1	6.7	9.6	2.1	9.0	1.9	0.7	1.6	0.3	1.2	0.2	0.6	<0.1	0.5	<0.1	9.0	<2	<100	897	17	1660	<0.1	2290
6	<100	<20	6.9	<1	<1	<0.1	<0.1	6.7	10.1	2.2	9.5	2.1	0.7	1.6	0.3	1.3	0.3	0.6	<0.1	0.5	<0.1	11.5	<2	<100	1580	21	1210	<0.1	2430
7	<100	<20	5.4	1	<1	<0.1	<0.1	5.3	8.9	1.6	6.6	1.4	0.6	1.2	0.2	0.9	0.2	0.5	<0.1	0.4	<0.1	9.1	<2	<100	1020	20	1450	<0.1	2390
8	<100	<20	4.4	1	<1	<0.1	<0.1	4.0	7.1	1.2	5.3	1.2	0.9	1.1	0.2	0.8	0.2	0.4	<0.1	0.3	<0.1	14.9	<2	<100	685	16	2130	<0.1	4460
9	<100	<20	7.5	<1	<1	<0.1	<0.1	5.7	8.7	1.7	7.5	1.9	0.8	1.6	0.3	1.3	0.2	0.7	<0.1	0.5	<0.1	11.7	<2	<100	925	20	2140	0.1	3690
10	<100	<20	8.7	<1	<1	<0.1	<0.1	6.6	11.2	2.1	9.1	2.1	1.0	1.9	0.3	1.3	0.3	0.7	<0.1	0.5	<0.1	16.7	<2	<100	1510	24	2430	0.2	3640
11	<100	<20	7.2	1	<1	<0.1	<0.1	6.4	9.4	1.8	7.9	1.9	0.8	1.5	0.2	1.2	0.3	0.6	<0.1	0.5	<0.1	21.5	<2	<100	1670	17	3030	<0.1	3330
12	<100	<20	5.2	<1	<1	<0.1	<0.1	4.9	7.0	1.4	6.0	1.2	1.1	1.1	0.2	0.9	0.2	0.5	<0.1	0.4	<0.1	49.8	<2	<100	1900	17	4090	<0.1	5070
SL Line 2																													
13	<100	<20	7.5	3	<1	<0.1	<0.1	3.5	15.6	1.5	6.9	1.8	0.7	1.5	0.2	1.3	0.3	0.7	<0.1	0.7	<0.1	44.2	<2	<100	12800	23	810	<0.1	2380
14	<100	<20	9.5	1	<1	<0.1	<0.1	7.2	26.2	2.6	11.8	2.5	1.4	2.3	0.3	1.6	0.3	1.0	0.1	0.8	0.1	20.2	<2	<100	8670	37	2260	0.1	5010
15	<100	<20	2.7	2	<1	<0.1	<0.1	3.0	6.9	0.9	4.0	1.0	1.8	0.9	0.1	0.6	0.1	0.3	<0.1	0.2	<0.1	19.3	4	<100	22100	153	1100	19.7	9530
16	<100	<20	4.3	<1	<1	<0.1	<0.1	2.7	7.2	0.9	3.5	0.9	1.1	0.8	0.1	0.8	0.2	0.4	<0.1	0.3	<0.1	39.9	<2	<100	17200	26	2690	0.1	5690
17	<100	<20	5.1	1	<1	<0.1	<0.1	4.7	8.3	1.4	5.2	1.3	1.4	1.2	0.2	0.9	0.2	0.4	<0.1	0.4	<0.1	17.4	<2	<100	3390	34	2820	<0.1	7110
18	<100	<20	4.7	1	<1	<0.1	<0.1	4.5	6.5	1.4	5.7	1.3	1.0	1.1	0.2	0.8	0.2	0.4	<0.1	0.4	<0.1	32.3	<2	<100	2940	64	2460	<0.1	4510
19	<100	<20	8.2	1	<1	<0.1	<0.1	7.5	14.6	2.3	9.2	2.2	0.8	1.8	0.3	1.4	0.3	0.7	<0.1	0.5	<0.1	33.7	<2	<100	6440	58	4270	0.1	2240
20	<100	<20	5.1	<1	<1	<0.1	<0.1	4.7	8.2	1.4	5.8	1.3	1.4	1.1	0.2	0.8	0.2	0.5	<0.1	0.4	<0.1	23.1	<2	<100	5020	42	2660	<0.1	7270
21	<100	<20	6.9	1	<1	<0.1	<0.1	6.2	10.3	1.9	7.5	1.7	1.1	1.5	0.2	1.1	0.2	0.6	<0.1	0.5	<0.1	13.1	<2	<100	5570	40	2320	<0.1	5040
22	<100	<20	5.5	<1	<1	<0.1	<0.1	4.8	7.9	1.4	5.9	1.4	1.1	1.3	0.2	0.9	0.2	0.5	<0.1	0.4	<0.1	12.9	<2	<100	8110	20	2090	<0.1	5400
23	<100	<20	6.0	<1	<1	<0.1	<0.1	5.6	10.7	1.6	7.0	1.5	0.8	1.3	0.2	1.1	0.2	0.5	<0.1	0.4	<0.1	11.4	<2	<100	6610	23	2290	<0.1	2980
24	<100	<20	3.5	<1	<1	<0.1	<0.1	2.7	4.8	0.8	3.6	0.9	0.8	0.7	0.1	0.6	0.1	0.3	<0.1	0.2	<0.1	11.2	<2	<100	5060	18	2390	<0.1	3790
25	<100	<20	3.2	<1	<1	<0.1	<0.1	1.7	4.3	0.6	2.6	0.6	0.2	0.5	<0.1	0.4	<0.1	0.2	<0.1	0.2	<0.1	12.3	<2	<100	4600	47	2790	0.1	854
26	<100	<20	3.2	<1	<1	<0.1	<0.1	1.6	3.1	0.6	3.2	0.9	0.6	0.7	0.1	0.5	<0.1	0.2	<0.1	0.1	<0.1	21.7	<2	<100	1060	20	2480	<0.1	3750
27	<100	<20	3.3	<1	<1	<0.1	<0.1	1.7	4.2	0.6	2.4	0.7	0.3	0.6	<0.1	0.4	<0.1	0.2	<0.1	0.2	<0.1	20.9	<2	<100	3320	27	1900	<0.1	1310
28	<100	<20	3.2	2	<1	<0.1	<0.1	2.0	6.9	0.5	2.3	0.6	0.4	0.6	<0.1	0.4	<0.1	0.2	<0.1	0.2	<0.1	35.1	<2	<100	16200	27	1260	<0.1	2720
29	<100	<20	3.3	<1	<1	<0.1	<0.1	1.3	3.9	0.5	2.3	0.6	0.6	0.5	<0.1	0.4	<0.1	0.2	<0.1	0.2	<0.1	32.0	<2	<100	5120	31	3310	<0.1	4360
SL Line 3																													
30	145	<20	3.7	4	<1	0.1	<0.1	3.3	11.0	1.1	4.4	1.2	0.5	0.9	0.2	0.8	0.1	0.4	<0.1	0.3	<0.1	18.0	<2	<100	6740	40	724	0.6	1580
31	<100	<20	3.8	3	<1	<0.1	<0.1	3.6	7.5	1.0	4.1	0.9	0.4	0.7	<0.1	0.6	0.1	0.3	<0.1	0.3	<0.1	20.7	<2	<100	1910	34	1420	0.6	1800
32	<100	<20	2.9	<1	<1	<0.1	<0.1	2.5	4.8	0.7	2.7	0.7	0.5	0.5	<0.1	0.4	<0.1	0.2	<0.1	0.2	<0.1	27.2	<2	<100	1910	54	2660	0.1	2460
33	111	<20	3.5	7	1	0.2	<0.1	3.1	6.9	0.8	3.4	0.7	0.3	0.6	<0.1	0.5	0.1	0.3	<0.1	0.3	<0.1	41.2	<2	<100	2650	107	1560	1.2	1560
34	<100	<20	2.0	<1	<1	<0.1	<0.1	1.7	3.1	0.5	2.1	0.5	0.4	0.3	<0.1	0.3	<0.1	0.1	<0.1	0.2	<0.1	28.8	<2	<100	606	35	2360	<0.1	2450
35	<100	<20	2.0	<1	<1	<0.1	<0.1	1.6	2.7	0.4	1.8	0.3	0.5	0.3	<0.1	0.3	<0.1	0.1	<0.1	0.1	<0.1	26.1	<2	<100	664	31	2490	<0.1	3740
36	<100	<20	1.4	<1	<1	<0.1	<0.1	1.5	2.3	0.3	1.4	0.2	0.5	0.3	<0.1	0.2	<0.1	0.1	<0.1	<0.1	<0.1	19.6	<2	<100	522	19	2000	<0.1	4060
37	<100	<20	1.0	<1	<1	<0.1	<0.1	1.1	1.4	0.3	1.0	0.2	0.6	0.2	<0.1	<0.1	<0.1	<0.1	<0.1	<0.1	<0.1	110.0	<2	<100	271	15	3220	<0.1	4430
38	<100	<20	2.7	<1	<1	<0.1	<0.1	2.0	2.9	0.5	2.0	0.4	0.4	0.4	<0.1	0.3	<0.1	0.2	<0.1	0.2	<0.1	103.0	<2	<100	875	18	7130	<0.1	3010
39	<100	<20	5.3	4	<1	<0.1	<0.1	2.6	3.5	0.9	3.8	1.0	0.8	0.9	0.1	0.8	0.2	0.5	<0.1	0.5	<0.1	32.7	<2	<100	557	29	3280	0.3	4750
40	<100	<20	2.7	<1	<1	<0.1	<0.1	1.6	2.2	0.4	1.8	0.4	0.6	0.4	<0.1	0.4	<0.1	0.2	<0.1	0.2	<0.1	73.6	<2	<100	629	23	3380	<0.1	4020
41	<100	<20	2.3	<1	<1	<0.1	<0.1	1.4	1.9	0.4	1.5	0.4	0.5	0.3	<0.1	0.3	<0.1	0.2	<0.1	0.2	<0.1	53.2	<2	<100	694	25	3080	<0.1	3340
42	<100	<20	1.8	<1	<1	<0.1	<0.1	1.6	2.1	0.4	1.9	0.4	0.5	0.4	<0.1	0.3	<0.1	0.2	<0.1	0.2	<0.1	33.1	<2	<100	538	23	2160	<0.1	3460
43	<100	<20	0.8	<1	<1	<0.1	<0.1	0.7	0.7	0.1	0.6	0.1	0.7	0.1	<0.1	<0.1	<0.1	<0.1	<0.1	<0.1	<0.1	33.3	<2	<100	273	12	4480	<0.1	5570
44	<100	<20	2.0	<1	2	<0.1	<0.1	1.3	1.5	0.3	1.5	0.3	0.4	0.3	<0.1	0.2	<0.1	0.1	<0.1	0.1	<0.1	77.3	<2	<100	1340	18	11100	<0.1	2380
45	<100	<20	16.7	3	19	<0.1	0.7	6.1	7.1	1.6	7.3	1.5	0.2	1.5	0.3	1.6	0.4	1.4	0.2	1.4	0.2	54.4	<2	<100	2040	23	19900	0.2	111
46	<100	<20	3.8	1	<1	<0.1	<0.1	3.0	5.3	0.9	4.4	0.9	0.6	0.8	0.1	0.5	0.1	0.3	<0.1	0.2	<0.1	63.2	<2	<100	2170	42	5260	0.2	3580
47	<100	<20	2.3	<1	<1	<0.1	<0.1	2.1	3.5	0.6	2.3	0.5	0.3	0.4	<0.1	0.3	<0.1	0.1	<0.1	0.2	<0.1	16.7	<2	<100	2770	14	1510	<0.1	2050
48	<100	<20	2.2	<1	1	<0.1	<0.1	2.0	4.9	0.6	2.3	0.5	0.2	0.5	<0.1	0.4	<0.1	0.2	<0.1	0.2	<0.1	19.9	<2	<100	5190	21	1210	<0.1	1090
49	<100	<20	3.2	<1	<1	<0.1	<0.1	3.0	6.8	0.9	3.6	0.8	0.3	0.6	<0.1	0.4	0.1	0.3	<0.1	0.2	<0.1	15.1	<2	<100	3790	39	1580	0.2	1080
50	<100	<20	3.1	<1	1	<0.1	<0.1	2.6	9.2	0.8	3.6	0.8	0.3	0.6	<0.1	0.5	<0.1	0.3	<0.1	0.2	<0.1	22.2	<2	<100	6670	21	1120	0.1	970
51	<100	<20	2.8	<1	<1	<0.1	<0.1	2.3	3.7	0.6	2.7	0.6	0.4	0.6	<0.1	0.4	<0.1	0.2	<0.1	0.2	<0.1	32.1	<2	<100	4310	20	2660	<0.1	2280
52	<100	<20	3.2	<1	<1	<0.1	<0.1	2.8	6.4	0.8	3.6	0.8	0.4	0.6	<0.1	0.5	<0.1	0.3	<0.1	0.2	<0.1	25.2	<2	<100	2930	27	1680	<0.1	2680
53	<100	<20	1.7	<1	<1	<0.1	<0.1	1.6	3.4	0.5	2.2	0.4	0.4	0.4	<0.1	0.2	<0.1	<0.1	<0.1	<0.1	<0.1	60.3	<2	<100	1760	19	2030	<0.1	3470
54	<100	<20	2.5	<1	<1	<0.1	<0.1	1.8	4.8	0.6	2.6	0.6	0.3	0.5	<0.1	0.5	<0.1	0.2	<0.1	0.1	<0.1	26.7	<2	<100	4140	35	7410	0.3	1830
55	<100	<20	2.6	2	<1	<0.1	<0.1	2.0	8.2	0.6	2.6	0.6	0.5	0.5	<0.1	0.3	<0.1	0.2	<0.1	0.1	<0.1	32.2	<2	<100	10500	28	1020	<0.1	3170

Appendix 2.2 cont. Results of Enzyme Leach Analysis for HFSE, REE and LILEs.

	High-Field Strength Elements							Rare Earth Elements													Lithophile Elements								
Sample Number	Ti	Cr	Y	Zr	Nb	Hf	Ta	La	Ce	Pr	Nd	Sm	Eu	Gd	Tb	Dy	Ho	Er	Tm	Yb	Lu	Li	Be	Sc	Mn	Rb	Sr	Cs	Ba
SL Line 3 cont.																													
56	<100	<20	4.5	2	<1	<0.1	<0.1	4.2	9.1	1.3	5.3	1.2	0.5	0.9	0.1	0.7	0.1	0.3	<0.1	0.3	<0.1	20.1	<2	<100	3610	34	1540	<0.1	2020
57	<100	<20	2.7	2	<1	<0.1	<0.1	2.9	10.2	0.8	3.5	0.7	0.5	0.7	<0.1	0.4	<0.1	0.2	<0.1	0.2	<0.1	12.7	<2	<100	9190	20	795	0.1	2750
58	<100	<20	2.0	2	<1	<0.1	<0.1	1.8	6.9	0.5	2.6	0.6	0.4	0.5	<0.1	0.3	<0.1	0.1	<0.1	0.1	<0.1	31.8	<2	<100	12500	20	867	<0.1	2870
59	<100	<20	2.4	<1	<1	<0.1	<0.1	1.9	5.8	0.6	2.3	0.6	0.4	0.5	<0.1	0.4	<0.1	0.2	<0.1	0.1	<0.1	12.6	<2	<100	3470	22	1010	0.1	2620
60	<100	<20	2.5	1	<1	<0.1	<0.1	2.7	7.6	0.7	2.8	0.6	0.5	0.5	<0.1	0.4	<0.1	0.2	<0.1	0.1	<0.1	18.2	<2	<100	9360	18	853	0.2	3200
61	<100	<20	3.3	2	<1	<0.1	<0.1	3.3	8.7	1.0	4.0	0.9	0.4	0.7	<0.1	0.6	0.1	0.2	<0.1	0.2	<0.1	13.5	<2	<100	5070	23	784	0.4	1940
62	<100	<20	4.2	2	<1	<0.1	<0.1	3.4	7.7	1.1	4.4	1.0	0.4	0.9	0.1	0.7	0.1	0.4	<0.1	0.3	<0.1	91.5	<2	<100	2670	37	4880	<0.1	2100
63	<100	<20	4.0	2	<1	<0.1	<0.1	3.8	9.0	1.1	4.8	1.0	0.5	0.9	0.1	0.6	0.1	0.3	<0.1	0.2	<0.1	23.9	<2	<100	4790	28	889	0.4	2300
64	<100	<20	5.2	1	<1	<0.1	<0.1	4.7	7.9	1.4	6.3	1.4	0.6	1.1	0.2	0.8	0.1	0.4	<0.1	0.3	<0.1	19.7	<2	<100	1740	26	1810	<0.1	2930
65	<100	<20	3.9	1	<1	<0.1	<0.1	4.0	8.0	1.2	4.9	1.2	0.6	0.9	0.1	0.7	0.1	0.3	<0.1	0.3	<0.1	23.4	<2	<100	3040	34	2330	<0.1	3070
66	<100	<20	3.1	1	<1	<0.1	<0.1	3.6	7.0	0.9	4.0	0.9	0.5	0.7	<0.1	0.5	0.1	0.3	<0.1	0.2	<0.1	38.0	<2	<100	2840	52	2100	<0.1	3170
67	<100	<20	2.6	1	<1	<0.1	<0.1	2.5	4.4	0.7	3.1	0.6	0.6	0.6	<0.1	0.4	<0.1	0.2	<0.1	0.2	<0.1	30.8	<2	<100	811	27	2400	<0.1	4050
68	<100	<20	2.1	1	<1	<0.1	<0.1	1.9	3.5	0.5	2.2	0.4	0.4	0.4	<0.1	0.3	<0.1	0.2	<0.1	0.1	<0.1	36.3	<2	<100	678	23	2710	<0.1	3100
69	<100	<20	1.7	<1	<1	<0.1	<0.1	1.7	3.0	0.4	1.8	0.4	0.5	0.4	<0.1	0.2	<0.1	0.1	<0.1	<0.1	<0.1	16.7	<2	<100	790	15	1730	<0.1	4120
SL Line 4																													
70	<100	<20	3.3	<1	<1	<0.1	<0.1	2.6	6.3	0.8	3.2	0.8	0.3	0.7	<0.1	0.5	<0.1	0.3	<0.1	0.2	<0.1	21.8	<2	<100	3880	75	1610	0.4	1170
71	146	<20	3.2	9	<1	0.2	<0.1	3.2	6.1	0.8	2.9	0.6	0.3	0.6	<0.1	0.4	<0.1	0.3	<0.1	0.2	<0.1	29.9	<2	<100	2890	63	783	3.5	1270
72	<100	<20	3.0	1	<1	<0.1	<0.1	2.2	4.5	0.6	3.0	0.7	0.3	0.5	<0.1	0.4	<0.1	0.2	<0.1	0.2	<0.1	32.5	<2	<100	2280	42	1750	0.2	1050
73	<100	<20	2.4	<1	<1	<0.1	<0.1	1.8	4.2	0.6	2.6	0.6	0.4	0.6	<0.1	0.4	<0.1	0.2	<0.1	0.2	<0.1	35.8	<2	<100	1420	71	3040	0.4	1900
74	<100	<20	3.3	1	1	<0.1	<0.1	2.0	6.7	0.6	2.6	0.6	0.3	0.5	<0.1	0.4	<0.1	0.3	<0.1	0.2	<0.1	22.7	<2	<100	5020	58	1820	0.2	938
75	125	<20	4.1	7	1	0.2	<0.1	3.2	6.3	1.1	4.6	1.0	0.7	1.0	<0.1	0.6	0.1	0.4	<0.1	0.4	<0.1	33.5	<2	<100	5860	23	2730	0.3	3380
76	<100	<20	3.3	2	<1	<0.1	<0.1	2.3	5.9	0.6	2.6	0.8	0.4	0.6	<0.1	0.5	<0.1	0.3	<0.1	0.3	<0.1	14.4	<2	<100	4010	31	1920	0.3	1610
77	<100	<20	2.7	<1	<1	<0.1	<0.1	1.6	3.6	0.4	1.7	0.4	0.3	0.4	<0.1	0.3	<0.1	0.2	<0.1	0.2	<0.1	12.9	<2	<100	3180	33	4290	0.3	1500
78	<100	<20	4.0	<1	<1	<0.1	<0.1	2.2	5.0	0.7	3.1	0.7	0.3	0.6	<0.1	0.5	<0.1	0.3	<0.1	0.3	<0.1	36.2	<2	<100	4570	42	3760	0.1	1430
79	<100	<20	5.0	2	<1	<0.1	<0.1	2.5	4.5	0.9	3.8	0.9	0.5	0.8	0.1	0.6	0.1	0.4	<0.1	0.3	<0.1	47.0	<2	<100	1100	57	2300	<0.1	2130
80	<100	<20	3.5	4	<1	0.1	<0.1	2.2	3.9	0.7	2.9	0.8	0.3	0.7	<0.1	0.5	<0.1	0.3	<0.1	0.2	<0.1	57.2	<2	<100	1810	53	2080	1.3	1510
81	<100	<20	3.1	3	<1	<0.1	<0.1	2.4	4.3	0.7	3.2	0.7	0.4	0.6	<0.1	0.5	0.1	0.3	<0.1	0.2	<0.1	46.0	<2	<100	1140	32	1760	0.4	1850
82	<100	<20	2.5	3	<1	<0.1	<0.1	2.2	3.9	0.5	2.3	0.5	0.3	0.4	<0.1	0.3	<0.1	0.2	<0.1	0.2	<0.1	23.0	<2	<100	1110	28	1320	0.6	2230
83	<100	<20	3.0	<1	<1	<0.1	<0.1	2.2	3.9	0.7	3.1	0.7	0.5	0.6	<0.1	0.4	<0.1	0.2	<0.1	0.2	<0.1	52.1	<2	<100	1250	29	2310	<0.1	2890
84	<100	<20	1.9	3	<1	<0.1	<0.1	1.6	2.8	0.3	1.3	0.2	0.1	0.2	<0.1	0.2	<0.1	0.1	<0.1	0.2	<0.1	41.4	<2	<100	4680	24	836	<0.1	484
85	<100	<20	3.2	2	<1	<0.1	<0.1	2.4	4.2	0.6	2.5	0.5	0.2	0.4	<0.1	0.4	<0.1	0.3	<0.1	0.3	<0.1	27.9	<2	<100	1340	17	1090	<0.1	530
86	<100	<20	2.0	<1	<1	<0.1	<0.1	1.3	2.6	0.3	1.5	0.3	0.2	0.2	<0.1	0.2	<0.1	0.1	<0.1	0.2	<0.1	32.3	<2	<100	1250	21	1850	<0.1	1160
87	<100	<20	3.0	3	<1	<0.1	<0.1	1.8	4.0	0.5	1.8	0.4	0.2	0.3	<0.1	0.3	<0.1	0.2	<0.1	0.2	<0.1	40.1	<2	<100	3790	21	554	<0.1	495
88	<100	<20	4.8	4	2	<0.1	<0.1	3.0	4.2	0.9	3.6	0.8	0.2	0.7	<0.1	0.6	0.1	0.4	<0.1	0.4	<0.1	48.6	<2	<100	405	20	1070	0.2	520
89	<100	<20	3.4	1	<1	<0.1	<0.1	2.2	2.4	0.6	2.7	0.7	0.4	0.6	<0.1	0.5	<0.1	0.3	<0.1	0.3	<0.1	114.0	<2	<100	2460	27	4910	0.4	1920
90	115	<20	2.7	3	1	<0.1	<0.1	1.8	5.6	0.5	1.8	0.4	0.2	0.4	<0.1	0.3	<0.1	0.2	<0.1	0.2	<0.1	32.6	<2	<100	21400	26	1440	<0.1	957
91	<100	<20	2.2	2	<1	<0.1	<0.1	1.7	4.2	0.4	1.9	0.3	0.2	0.4	<0.1	0.3	<0.1	0.2	<0.1	0.2	<0.1	48.7	<2	<100	7020	25	984	<0.1	681
92	<100	<20	2.5	2	<1	<0.1	<0.1	1.9	5.2	0.5	2.4	0.5	0.2	0.4	<0.1	0.3	<0.1	0.2	<0.1	0.2	<0.1	43.3	<2	<100	7030	20	978	<0.1	1040
93	<100	<20	3.5	<1	<1	<0.1	<0.1	1.6	3.7	0.6	2.6	0.6	0.4	0.6	<0.1	0.5	<0.1	0.2	<0.1	0.2	<0.1	35.5	<2	<100	1370	79	4510	0.7	2610
94	<100	<20	4.0	3	<1	<0.1	<0.1	3.1	7.3	0.8	3.3	0.8	1.0	0.7	<0.1	0.6	<0.1	0.3	<0.1	0.3	<0.1	56.1	<2	<100	13700	31	1190	<0.1	5900
95	<100	<20	2.7	3	<1	<0.1	<0.1	1.9	6.2	0.5	2.5	0.6	0.2	0.5	<0.1	0.4	<0.1	0.3	<0.1	0.2	<0.1	39.9	<2	<100	6270	28	999	<0.1	1090
96	<100	<20	1.1	1	<1	<0.1	<0.1	0.7	2.7	0.2	0.7	0.1	<0.1	0.1	<0.1	<0.1	<0.1	0.1	<0.1	<0.1	<0.1	18.5	<2	<100	5270	17	1180	<0.1	599
97	<100	<20	1.8	3	<1	<0.1	<0.1	1.4	3.7	0.3	1.4	0.3	0.2	0.3	<0.1	0.2	<0.1	0.1	<0.1	0.1	<0.1	20.0	<2	<100	12900	24	1370	<0.1	824
98	<100	<20	2.0	3	<1	<0.1	<0.1	1.3	3.8	0.4	1.4	0.4	0.1	0.3	<0.1	0.2	<0.1	0.1	<0.1	0.1	<0.1	36.6	<2	<100	8320	26	759	0.1	693
99	<100	<20	3.0	1	<1	<0.1	<0.1	2.3	4.1	0.7	3.1	0.8	0.7	0.6	<0.1	0.5	<0.1	0.3	<0.1	0.3	<0.1	60.7	<2	<100	2060	65	4040	0.3	3680
100	<100	<20	3.7	1	<1	<0.1	<0.1	2.4	7.3	0.8	3.3	0.8	0.5	0.7	<0.1	0.5	<0.1	0.3	<0.1	0.2	<0.1	43.2	<2	<100	10800	50	1800	0.3	2180
101	<100	<20	2.3	<1	<1	<0.1	<0.1	1.8	3.3	0.5	1.8	0.4	0.3	0.3	<0.1	0.3	<0.1	0.2	<0.1	0.1	<0.1	35.8	<2	<100	2370	43	1490	0.3	1670
102	<100	<20	3.2	1	2	<0.1	<0.1	2.5	4.7	0.7	3.1	0.7	0.7	0.6	<0.1	0.4	<0.1	0.3	<0.1	0.2	<0.1	45.8	<2	<100	1420	11	1920	<0.1	5310
103	<100	<20	4.9	<1	<1	<0.1	<0.1	3.0	7.1	0.9	3.7	0.9	0.3	0.7	<0.1	0.6	0.1	0.4	<0.1	0.3	<0.1	27.3	<2	<100	2620	43	1760	0.2	1400
SL Line 5																													
104	103	<20	8.9	8	<1	0.2	<0.1	5.0	15.8	1.8	8.5	1.9	1.0	1.7	0.3	1.4	0.3	0.8	0.1	0.9	0.1	114.0	<2	<100	15000	37	858	<0.1	4300
105	<100	<20	3.5	3	<1	<0.1	<0.1	2.4	7.1	0.7	3.2	0.8	0.3	0.7	<0.1	0.5	0.1	0.3	<0.1	0.3	<0.1	44.6	<2	<100	3460	22	683	<0.1	1490
106	<100	<20	3.0	1	<1	<0.1	<0.1	2.6	5.4	0.7	3.1	0.7	1.2	0.7	<0.1	0.5	0.1	0.3	<0.1	0.2	<0.1	53.2	<2	<100	1090	25	2170	<0.1	7610
107	<100	<20	3.5	1	<1	<0.1	<0.1	2.7	5.4	0.8	3.8	0.7	1.2	0.7	<0.1	0.5	0.1	0.3	<0.1	0.3	<0.1	44.3	<2	<100	1050	24	2310	<0.1	8880
108	<100	<20	2.3	2	<1	<0.1	<0.1	1.8	4.2	0.5	2.1	0.4	0.5	0.4	<0.1	0.3	<0.1	0.2	<0.1	0.1	<0.1	47.1	<2	<100	4340	21	874	0.1	3380
109	<100	<20	4.8	4	<1	0.1	<0.1	3.3	10.3	1.1	4.7	1.1	0.5	0.9	0.2	0.8	0.1	0.4	<0.1	0.4	<0.1	59.5	<2	<100	13800	29	919	<0.1	2210
110	<100	<20	2.5	<1	<1	<0.1	<0.1	2.4	4.1	0.6	2.8	0.7	0.7	0.5	<0.1	0.4	<0.1	0.2	<0.1	0.2	<0.1	38.6	<2	<100	1770	21	2450	<0.1	4730

Appendix 2.2 cont. Results of Enzyme Leach Analysis for HFSE, REE and LILEs.

	High-Field Strength Elements							Rare Earth Elements														Lithophile Elements							
Sample Number	Ti	Cr	Y	Zr	Nb	Hf	Ta	La	Ce	Pr	Nd	Sm	Eu	Gd	Tb	Dy	Ho	Er	Tm	Yb	Lu	Li	Be	Sc	Mn	Rb	Sr	Cs	Ba
SL Line 5 cont.																													
111	<100	<20	2.6	4	<1	0.1	<0.1	2.6	6.0	0.8	3.2	0.8	0.5	0.6	<0.1	0.5	<0.1	0.3	<0.1	0.2	<0.1	35.4	<2	<100	2040	28	1050	0.7	2520
112	127	<20	2.4	3	1	0.1	<0.1	2.3	4.9	0.6	2.6	0.6	0.4	0.5	<0.1	0.4	<0.1	0.3	<0.1	0.2	<0.1	17.8	<2	<100	6110	30	689	0.6	3010
113	<100	<20	4.0	1	<1	<0.1	<0.1	3.5	5.8	1.1	4.8	1.1	0.7	1.0	0.2	0.8	0.1	0.4	<0.1	0.3	<0.1	23.0	<2	<100	2260	25	1930	<0.1	4280
114	<100	<20	1.4	<1	<1	<0.1	<0.1	1.2	1.9	0.3	1.2	0.4	0.7	0.3	<0.1	0.2	<0.1	<0.1	<0.1	<0.1	<0.1	24.5	<2	<100	531	20	2360	<0.1	5210
115	<100	<20	2.7	<1	<1	<0.1	<0.1	2.1	2.8	0.6	1.9	0.5	0.5	0.5	<0.1	0.4	<0.1	0.3	<0.1	0.2	<0.1	46.5	<2	<100	688	27	2600	<0.1	2990
116	<100	<20	3.5	<1	<1	<0.1	<0.1	3.5	4.9	1.0	3.7	0.9	0.4	0.7	0.1	0.6	0.1	0.3	<0.1	0.3	<0.1	29.9	<2	<100	824	26	1800	<0.1	2360
117	<100	<20	2.5	<1	<1	<0.1	<0.1	2.4	3.5	0.7	2.9	0.7	0.4	0.6	<0.1	0.5	<0.1	0.2	<0.1	0.2	<0.1	40.8	<2	<100	630	23	2770	<0.1	2750
118	<100	<20	1.7	<1	<1	<0.1	<0.1	1.6	2.1	0.4	1.7	0.4	0.3	0.3	<0.1	0.3	<0.1	0.2	<0.1	<0.1	<0.1	25.3	<2	<100	474	22	2170	<0.1	2440
119	<100	<20	3.5	3	<1	0.1	<0.1	3.3	6.2	1.0	3.9	0.7	0.4	0.7	0.1	0.6	<0.1	0.3	<0.1	0.3	<0.1	25.0	<2	<100	1390	31	1740	0.4	1590
120	<100	<20	2.2	<1	<1	<0.1	<0.1	1.8	3.1	0.5	2.2	0.4	0.5	0.5	<0.1	0.4	<0.1	0.2	<0.1	0.2	<0.1	20.5	<2	<100	691	30	2170	<0.1	3020
121	<100	<20	3.8	1	<1	<0.1	<0.1	3.2	3.7	0.9	4.2	0.7	0.5	0.8	0.1	0.6	0.1	0.4	<0.1	0.3	<0.1	81.2	<2	<100	506	26	3560	<0.1	2470
122	<100	<20	3.9	1	<1	<0.1	<0.1	3.4	4.7	0.9	3.9	0.9	0.4	0.7	0.1	0.6	0.1	0.3	<0.1	0.2	<0.1	32.1	<2	<100	743	23	2280	<0.1	2130
123	<100	<20	2.9	<1	<1	<0.1	<0.1	2.5	3.5	0.7	2.8	0.6	0.3	0.5	<0.1	0.4	<0.1	0.2	<0.1	0.2	<0.1	33.0	<2	<100	858	29	2270	<0.1	2270
124	<100	<20	2.4	<1	<1	<0.1	<0.1	1.9	2.6	0.5	2.1	0.5	0.4	0.4	<0.1	0.3	<0.1	0.2	<0.1	0.2	<0.1	61.8	<2	<100	357	26	3400	<0.1	2280
125	<100	<20	2.5	<1	<1	<0.1	<0.1	2.6	3.8	0.7	2.7	0.8	0.5	0.6	<0.1	0.4	<0.1	0.2	<0.1	0.2	<0.1	31.8	<2	<100	555	21	2480	<0.1	3250
SL Line 6																													
126	<100	<20	5.7	3	1	<0.1	<0.1	3.7	8.9	1.3	5.3	1.2	0.4	1.1	0.2	0.8	0.2	0.5	<0.1	0.5	<0.1	22.0	<2	<100	2380	50	2610	0.2	1420
127	<100	<20	3.9	3	<1	<0.1	<0.1	2.9	7.2	0.8	3.3	0.7	0.4	0.6	<0.1	0.5	0.1	0.3	<0.1	0.3	<0.1	16.2	<2	<100	2350	35	1980	0.3	1980
128	<100	<20	5.5	3	<1	<0.1	<0.1	4.0	11.1	1.4	6.3	1.2	0.4	1.0	0.2	0.9	0.2	0.5	<0.1	0.4	<0.1	22.3	<2	<100	1720	40	2260	0.2	1210
129	<100	<20	2.1	<1	<1	<0.1	<0.1	1.9	3.2	0.5	2.0	0.4	0.7	0.3	<0.1	0.3	<0.1	0.2	<0.1	0.1	<0.1	27.7	<2	<100	521	22	6150	<0.1	4800
130	<100	<20	5.8	3	<1	<0.1	<0.1	2.5	3.4	0.8	3.7	0.9	0.6	0.8	<0.1	0.7	0.1	0.5	<0.1	0.5	<0.1	39.8	<2	<100	387	26	4500	0.3	3940
131	<100	<20	2.6	<1	<1	<0.1	<0.1	2.2	2.7	0.5	2.1	0.5	0.4	0.4	<0.1	0.3	<0.1	0.2	<0.1	0.1	<0.1	42.3	<2	<100	329	25	3060	<0.1	2770
132	<100	<20	3.0	<1	<1	<0.1	<0.1	1.8	2.3	0.5	1.9	0.5	0.3	0.4	<0.1	0.4	<0.1	0.2	<0.1	0.2	<0.1	34.8	<2	<100	147	34	3540	<0.1	1790
133	<100	<20	2.5	<1	<1	<0.1	<0.1	2.0	2.3	0.5	1.9	0.4	0.4	0.4	<0.1	0.2	<0.1	0.2	<0.1	0.2	<0.1	31.5	<2	<100	394	25	2690	<0.1	2230
134	<100	<20	1.5	<1	<1	<0.1	<0.1	0.9	0.9	0.2	0.8	0.2	0.7	0.2	<0.1	0.1	<0.1	0.1	<0.1	0.1	<0.1	51.5	<2	<100	537	27	4380	<0.1	4600
135	<100	<20	2.4	<1	<1	<0.1	<0.1	1.5	2.1	0.4	1.7	0.4	0.5	0.3	<0.1	0.3	<0.1	0.2	<0.1	0.2	<0.1	99.9	<2	<100	580	26	5280	<0.1	3290
136	<100	<20	1.2	<1	<1	<0.1	<0.1	0.7	0.8	0.2	0.7	0.1	0.5	0.1	<0.1	<0.1	<0.1	<0.1	<0.1	<0.1	<0.1	53.9	<2	<100	259	23	3480	<0.1	3900
137	<100	<20	1.3	<1	<1	<0.1	<0.1	0.9	1.1	0.2	0.6	0.2	0.6	0.2	<0.1	0.1	<0.1	<0.1	<0.1	0.1	<0.1	34.2	<2	<100	873	28	4050	<0.1	4070
138	<100	<20	1.2	<1	<1	<0.1	<0.1	0.8	1.2	0.2	0.9	0.2	0.5	0.1	<0.1	0.1	<0.1	<0.1	<0.1	<0.1	<0.1	61.5	<2	<100	291	26	6050	<0.1	3460
139	<100	<20	2.3	<1	<1	<0.1	<0.1	1.9	2.2	0.5	2.1	0.4	0.4	0.4	<0.1	0.3	<0.1	0.2	<0.1	0.2	<0.1	100.0	<2	<100	717	21	4140	0.2	2090
140	<100	<20	8.1	1	<1	<0.1	<0.1	5.0	5.2	1.5	6.4	1.5	0.6	1.3	0.3	1.2	0.3	0.7	0.1	0.7	0.1	189.0	<2	<100	1070	20	14800	0.2	1920
141	<100	<20	2.6	<1	<1	<0.1	<0.1	1.9	3.4	0.6	2.3	0.5	0.6	0.5	<0.1	0.4	<0.1	0.2	<0.1	0.2	<0.1	41.6	<2	<100	837	28	6910	0.4	3120
142	<100	<20	1.9	<1	<1	<0.1	<0.1	1.1	2.2	0.3	1.9	0.4	0.3	0.4	<0.1	0.3	<0.1	0.1	<0.1	0.1	<0.1	129.0	<2	<100	1400	52	36100	0.7	1300
143	<100	<20	3.5	<1	<1	<0.1	<0.1	4.0	13.5	1.2	5.4	1.1	0.5	1.0	0.1	0.7	0.1	0.3	<0.1	0.2	<0.1	46.7	<2	<100	3600	33	2510	0.2	1760
144	<100	<20	2.5	<1	<1	<0.1	<0.1	2.1	6.5	0.7	3.1	0.7	0.4	0.6	<0.1	0.4	<0.1	0.2	<0.1	0.2	<0.1	24.2	<2	<100	1810	24	3050	0.2	1360
145	<100	<20	7.6	1	<1	<0.1	<0.1	6.1	17.1	1.9	8.0	1.7	0.6	1.6	0.3	1.4	0.2	0.7	<0.1	0.5	<0.1	26.1	<2	<100	2600	38	5360	0.2	1520
146	<100	<20	8.1	2	<1	<0.1	<0.1	6.7	14.6	2.0	8.8	2.0	0.7	1.6	0.3	1.5	0.3	0.7	<0.1	0.6	<0.1	45.6	<2	<100	1650	27	3350	0.1	1860
147	<100	<20	4.4	1	<1	<0.1	<0.1	3.7	8.6	1.2	5.0	1.1	0.5	0.9	0.2	0.9	0.2	0.4	<0.1	0.4	<0.1	24.7	<2	<100	2710	38	3580	0.2	1400
148	<100	<20	5.3	4	<1	0.1	<0.1	4.0	8.4	1.3	5.0	1.3	0.5	1.0	0.2	0.9	0.2	0.5	<0.1	0.4	<0.1	26.9	<2	<100	4490	21	1150	0.2	1770
149	<100	<20	10.2	3	<1	0.1	<0.1	8.8	19.5	2.8	12.0	2.8	1.0	2.3	0.4	1.8	0.3	1.0	0.1	0.9	0.1	36.9	<2	<100	4030	32	3770	0.1	3420
150	<100	<20	7.9	1	1	<0.1	<0.1	7.1	14.7	2.1	9.1	1.9	0.9	1.6	0.3	1.4	0.3	0.8	0.1	0.7	0.1	27.4	<2	<100	3050	29	4650	0.1	3150
151	<100	<20	2.9	6	<1	0.2	<0.1	2.6	6.2	0.8	3.2	0.7	0.4	0.7	0.1	0.5	<0.1	0.3	<0.1	0.3	<0.1	27.3	<2	<100	2300	30	972	1.2	1690
152	<100	<20	4.2	3	<1	<0.1	<0.1	3.8	11.0	1.3	5.6	1.1	0.5	1.0	0.2	0.8	0.2	0.4	<0.1	0.4	<0.1	11.3	<2	<100	3820	23	3430	1.0	1790
153	<100	<20	3.7	3	1	0.1	<0.1	3.1	8.2	1.0	4.4	1.0	0.7	1.0	0.1	0.7	0.1	0.4	<0.1	0.3	<0.1	25.8	<2	<100	4580	38	2270	0.9	2970
154	<100	<20	1.8	<1	<1	<0.1	<0.1	1.6	2.8	0.4	2.1	0.5	0.5	0.4	<0.1	0.3	<0.1	0.1	<0.1	0.1	<0.1	15.3	<2	<100	801	14	2430	<0.1	3510
155	<100	<20	2.2	<1	<1	<0.1	<0.1	1.8	4.0	0.5	2.2	0.5	0.3	0.5	<0.1	0.4	<0.1	0.2	<0.1	0.2	<0.1	18.3	<2	<100	2970	16	1540	<0.1	2310
156	<100	<20	2.0	1	<1	<0.1	<0.1	1.2	3.0	0.4	1.7	0.5	0.2	0.4	<0.1	0.3	<0.1	0.1	<0.1	0.2	<0.1	28.0	<2	<100	3220	20	1270	0.1	1340
157	<100	<20	5.4	1	<1	<0.1	<0.1	5.1	7.1	1.4	6.1	1.4	0.6	1.1	0.2	0.8	0.2	0.4	<0.1	0.4	<0.1	19.6	<2	<100	3570	19	2890	<0.1	3070
158	<100	<20	8.2	2	1	<0.1	<0.1	7.0	12.0	2.1	9.3	2.0	0.7	1.7	0.3	1.2	0.2	0.7	<0.1	0.6	<0.1	16.6	<2	<100	3980	27	4150	<0.1	2880
159	<100	<20	5.0	1	<1	<0.1	<0.1	4.6	10.9	1.4	6.3	1.3	0.5	1.2	0.2	0.9	0.2	0.5	<0.1	0.4	<0.1	15.9	<2	<100	4770	22	2520	<0.1	2330
160	<100	<20	2.2	<1	<1	<0.1	<0.1	1.8	3.3	0.5	1.9	0.5	0.4	0.4	<0.1	0.3	<0.1	0.2	<0.1	0.1	<0.1	15.5	<2	<100	1460	16	2480	<0.1	3190
161	<100	<20	1.9	<1	<1	<0.1	<0.1	1.4	2.2	0.4	1.5	0.4	0.6	0.4	<0.1	0.3	<0.1	0.1	<0.1	0.1	<0.1	27.4	<2	<100	699	16	3510	<0.1	5490
162	<100	<20	1.9	<1	<1	<0.1	<0.1	1.7	2.4	0.4	1.7	0.4	0.5	0.4	<0.1	0.2	<0.1	0.2	<0.1	0.1	<0.1	23.7	<2	<100	547	15	2850	<0.1	3890

Appendix 3.1 Results of Terrasol Leach Analysis for Oxidation Suite, Chalcophile elements and HFSEs.

Sample Number	Oxidation Suite Elements											Chalcophile Elements									High-Field Strength Elements								
	Cl	V	As	Se	Mo	Sb	Te	W	Re	Au	Hg	Th	U	Ga	Ge	Ag	Cd	In	Sn	Tl	Bi	Ti	Cr	Y	Zr	Nb	Hf	Ta
SL Line 1																												
1	<2000	257	552	<5	18	27.7	<1	<1	<0.01	<0.05	12	361.0	45.6	16	<0.5	<0.2	61.5	<0.1	<0.8	<0.1	<0.8	423	<20	2980	411	<1	11	<0.1
2	<2000	263	359	<5	13	41.6	<1	<1	<0.01	<0.05	17	310.0	44.3	14	<0.5	<0.2	81.1	<0.1	<0.8	<0.1	<0.8	379	<20	2740	347	<1	12	<0.1
3	<2000	148	326	<5	11	37.4	<1	<1	<0.01	<0.05	12	277.0	61.3	11	<0.5	<0.2	58.5	<0.1	<0.8	<0.1	<0.8	286	<20	3200	236	<1	9	<0.1
4	<2000	153	209	<5	<1	38.7	<1	<1	<0.01	<0.05	9	278.0	18.6	32	<0.5	<0.2	122.0	<0.1	<0.8	<0.1	<0.8	419	<20	3200	493	<1	13	<0.1
5	<2000	159	261	<5	<1	32.0	<1	<1	<0.01	<0.05	15	417.0	17.9	29	<0.5	<0.2	46.3	<0.1	<0.8	<0.1	<0.8	561	<20	2990	674	<1	17	<0.1
6	<2000	202	235	<5	<1	49.3	<1	<1	<0.01	<0.05	11	346.0	13.7	39	<0.5	<0.2	83.0	<0.1	<0.8	<0.1	<0.8	579	<20	3020	694	<1	19	<0.1
7	<2000	161	203	<5	<1	14.3	<1	<1	<0.01	<0.05	8	407.0	22.0	23	<0.5	<0.2	60.5	<0.1	<0.8	<0.1	<0.8	526	<20	2460	602	4	15	<0.1
8	<2000	263	510	<5	<1	17.8	<1	<1	<0.01	<0.05	15	560.0	38.4	18	<0.5	<0.2	33.3	<0.1	<0.8	<0.1	<0.8	446	<20	3130	413	<1	12	<0.1
9	<2000	177	280	<5	<1	20.9	<1	<1	<0.01	<0.05	9	302.0	18.6	22	<0.5	<0.2	62.5	<0.1	<0.8	<0.1	<0.8	395	<20	2320	335	<1	11	<0.1
10	<2000	210	361	<5	<1	23.1	<1	<1	<0.01	<0.05	11	308.0	25.1	19	<0.5	<0.2	59.0	<0.1	<0.8	<0.1	<0.8	367	<20	2270	304	<1	10	<0.1
11	<2000	239	383	<5	<1	35.2	<1	<1	<0.01	<0.05	12	381.0	18.9	26	<0.5	<0.2	51.7	<0.1	<0.8	<0.1	<0.8	475	<20	2650	513	<1	16	<0.1
12	<2000	512	652	<5	<1	19.9	<1	<1	<0.01	<0.05	11	570.0	51.2	18	<0.5	<0.2	29.4	<0.1	<0.8	<0.1	<0.8	371	<20	3700	447	<1	14	<0.1
SL Line 2																												
13	<2000	437	252	<5	95	27.5	<1	<1	<0.01	<0.05	18	366.0	88.7	40	<0.5	800.0	401.0	<0.1	<0.8	<0.1	<0.8	653	<20	3490	779	<1	29	<0.1
14	<2000	733	563	<5	78	72.8	<1	241	<0.01	6.9	27	361.0	34.8	53	10.1	677.0	499.0	<0.1	<0.8	<0.1	<0.8	631	<20	4020	965	<1	26	<0.1
15	<2000	247	2330	<5	146	50.1	<1	249	<0.01	25.1	114	56.5	852.0	23	13.7	898.0	1490.0	<0.1	<0.8	<0.1	<0.8	325	<20	1080	201	<1	9	<0.1
16	<2000	776	3430	<5	405	49.0	<1	###	<0.01	20.6	45	205.0	209.0	43	11.0	701.0	332.0	<0.1	<0.8	<0.1	<0.8	1070	<20	3730	631	8	19	<0.1
17	<2000	347	644	<5	14	42.9	<1	121	<0.01	7.7	22	482.0	35.0	23	<0.5	832.0	90.1	<0.1	<0.8	<0.1	<0.8	580	<20	3360	582	<1	14	<0.1
18	<2000	284	503	<5	<1	66.5	<1	<1	<0.01	5.3	18	287.0	13.5	37	<0.5	535.0	105.0	<0.1	<0.8	<0.1	<0.8	528	<20	3280	678	<1	16	<0.1
19	<2000	614	701	<5	74	61.7	<1	119	<0.01	<0.05	16	368.0	81.0	15	<0.5	576.0	127.0	<0.1	<0.8	<0.1	<0.8	489	<20	3020	366	<1	10	<0.1
20	<2000	338	610	<5	<1	56.6	<1	128	<0.01	6.7	23	372.0	18.3	30	<0.5	769.0	91.0	<0.1	<0.8	<0.1	<0.8	667	<20	3340	658	5	16	<0.1
21	<2000	316	408	<5	16	68.0	<1	155	<0.01	5.0	18	294.0	19.9	42	<0.5	565.0	247.0	<0.1	<0.8	<0.1	<0.8	862	<20	3050	714	6	18	<0.1
22	<2000	310	460	<5	11	92.8	<1	167	<0.01	5.0	19	316.0	19.5	42	<0.5	488.0	272.0	<0.1	<0.8	<0.1	<0.8	831	<20	3370	713	6	19	<0.1
23	<2000	257	402	<5	25	58.0	<1	153	<0.01	<0.05	29	334.0	22.2	39	<0.5	567.0	335.0	<0.1	<0.8	<0.1	<0.8	956	<20	2890	708	7	16	<0.1
24	<2000	184	532	<5	21	44.9	<1	<1	<0.01	6.9	27	382.0	39.6	24	<0.5	686.0	214.0	<0.1	<0.8	<0.1	<0.8	701	<20	4260	652	5	15	<0.1
25	<2000	228	245	<5	95	48.4	<1	<1	<0.01	<0.05	<1	91.2	47.3	8	<0.5	<0.2	29.4	<0.1	<0.8	<0.1	<0.8	284	<20	1880	271	<1	5	<0.1
26	<2000	326	249	<5	<1	25.8	<1	<1	<0.01	<0.05	<1	179.0	27.9	12	<0.5	<0.2	31.1	<0.1	<0.8	<0.1	<0.8	360	<20	2170	503	<1	12	<0.1
27	<2000	215	231	<5	24	32.7	<1	<1	<0.01	<0.05	5	159.0	28.1	26	<0.5	<0.2	181.0	<0.1	<0.8	<0.1	<0.8	912	<20	5630	1090	5	24	<0.1
28	<2000	1630	499	<5	561	110.0	<1	572	<0.01	<0.05	108	1240.0	306.0	67	14.7	608.0	594.0	11.3	<0.8	<0.1	<0.8	5170	<20	11900	5670	22	134	1
29	<2000	597	910	<5	110	34.8	<1	<1	<0.01	<0.05	22	106.0	232.0	16	<0.5	554.0	276.0	<0.1	<0.8	<0.1	<0.8	561	<20	4520	813	<1	18	<0.1
SL Line 3																												
30	<2000	401	288	<5	89	39.9	<1	261	<0.01	<0.05	58	532.0	21.5	64	<0.5	370.0	1460.0	<0.1	<0.8	<0.1	6.5	4210	<20	3540	1430	11	30	<0.1
31	<2000	245	226	<5	31	17.1	<1	<1	<0.01	<0.05	22	301.0	12.9	49	10.6	<0.2	948.0	<0.1	<0.8	<0.1	<0.8	1570	<20	3620	922	5	23	<0.1
32	<2000	84	344	<5	13	13.8	<1	<1	<0.01	<0.05	13	264.0	8.8	39	<0.5	<0.2	498.0	<0.1	<0.8	<0.1	<0.8	1290	<20	2610	528	<1	13	<0.1
33	<2000	180	201	<5	17	14.9	<1	<1	<0.01	<0.05	24	425.0	8.2	54	<0.5	<0.2	1240.0	<0.1	<0.8	<0.1	<0.8	2920	<20	2940	926	8	23	<0.1
34	<2000	214	192	<5	14	<0.1	<1	<1	<0.01	<0.05	<1	336.0	13.1	38	<0.5	<0.2	233.0	<0.1	<0.8	<0.1	<0.8	458	<20	1760	703	<1	13	<0.1
35	<2000	181	357	<5	<1	13.4	<1	<1	<0.01	<0.05	<1	526.0	13.8	28	<0.5	<0.2	44.8	<0.1	<0.8	<0.1	<0.8	371	<20	1860	538	<1	11	<0.1
36	<2000	246	435	<5	<1	14.2	<1	<1	<0.01	<0.05	<1	352.0	15.1	31	<0.5	<0.2	66.5	<0.1	<0.8	<0.1	<0.8	612	<20	1680	325	<1	8	<0.1
37	<2000	803	872	<5	<1	11.8	<1	<1	<0.01	<0.05	<1	309.0	24.5	26	<0.5	<0.2	14.2	<0.1	<0.8	<0.1	<0.8	488	<20	1490	164	<1	6	<0.1
38	<2000	1660	617	<5	30	13.9	<1	<1	<0.01	<0.05	<1	580.0	40.1	28	<0.5	<0.2	63.5	<0.1	<0.8	<0.1	<0.8	222	<20	2250	479	<1	12	<0.1
39	<2000	369	829	<5	<1	26.1	<1	<1	<0.01	<0.05	<1	387.0	16.6	19	<0.5	<0.2	10.2	<0.1	<0.8	<0.1	<0.8	459	<20	1920	365	<1	9	<0.1
40	<2000	999	456	<5	<1	16.6	<1	<1	<0.01	<0.05	<1	221.0	46.2	16	<0.5	<0.2	20.8	<0.1	<0.8	<0.1	<0.8	319	<20	1510	423	<1	9	<0.1
41	<2000	769	578	<5	<1	16.6	<1	<1	<0.01	<0.05	8	330.0	55.8	23	<0.5	<0.2	25.7	<0.1	<0.8	<0.1	<0.8	439	<20	1830	285	<1	8	<0.1
42	<2000	267	461	<5	<1	17.0	<1	<1	<0.01	<0.05	7	384.0	20.8	36	<0.5	<0.2	59.6	<0.1	<0.8	<0.1	<0.8	844	<20	2250	298	<1	9	<0.1
43	<2000	567	1110	<5	<1	16.0	<1	<1	<0.01	<0.05	<1	223.0	33.3	11	<0.5	<0.2	<0.2	<0.1	<0.8	<0.1	<0.8	230	<20	805	204	<1	4	<0.1
44	<2000	1620	757	<5	31	<0.1	<1	131	<0.01	<0.05	<1	231.0	339.0	18	<0.5	<0.2	19.2	<0.1	<0.8	<0.1	<0.8	<100	<20	2190	364	10	12	<0.1
45	<2000	808	565	<5	11000	10.5	<1	<1	<0.01	14.5	8	499.0	2110.0	18	<0.5	<0.2	234.0	<0.1	<0.8	<0.1	<0.8	867	<20	4330	3120	165	68	3
46	<2000	427	1100	<5	20	97.7	<1	<1	<0.01	<0.05	<1	285.0	22.8	17	<0.5	<0.2	24.8	<0.1	<0.8	<0.1	<0.8	474	1040	2970	742	<1	15	<0.1
47	<2000	148	380	<5	<1	42.8	<1	<1	<0.01	<0.05	<1	252.0	17.1	18	<0.5	<0.2	19.1	<0.1	<0.8	<0.1	<0.8	290	539	4070	930	7	16	<0.1
48	<2000	310	535	<5	29	70.2	<1	111	<0.01	<0.05	28	350.0	30.2	31	11.3	<0.2	132.0	<0.1	<0.8	<0.1	<0.8	1960	<20	6200	2760	20	43	<0.1
49	<2000	125	445	<5	50	56.6	<1	<1	<0.01	<0.05	17	316.0	21.5	29	10.9	<0.2	91.5	<0.1	<0.8	<0.1	<0.8	1430	<20	5600	1740	13	32	<0.1
50	<2000	597	411	<5	73	84.1	<1	292	<0.01	<0.05	31	511.0	36.9	43	12.6	<0.2	227.0	<0.1	<0.8	<0.1	<0.8	3500	<20	7460	2810	27	48	<0.1
51	<2000	341	1080	<5	11	48.0	<1	<1	<0.01	<0.05	7	235.0	23.1	21	<0.5	<0.2	28.5	<0.1	<0.8	<0.1	<0.8	278	<20	4010	809	<1	16	<0.1
52	<2000	216	590	<5	22	51.2	<1	109	<0.01	<0.05	10	303.0	28.5	25	<0.5	<0.2	178.0	<0.1	<0.8	<0.1	<0.8	1610	<20	4880	1470	8	25	<0.1
53	<2000	313	406	<5	<1	40.8	<1	<1	<0.01	<0.05	4	235.0	24.2	21	<0.5	<0.2	52.6	<0.1	<0.8	<0.1	<0.8	249	<20	3170	860	<1	13	<0.1
54	<2000	606	349	<5	323	34.7	<1	163	<0.01	<0.05	5	143.0	225.0	15	<0.5	<0.2	5440.0	<0.1	<0.8	<0.1	<0.8	<100	<20	2300	299	<1	10	<0.1
55	<2000	964	267	<5	387	130.0	<1	804	<0.01	<0.05	110	1060.0	120.0	49	12.5	625.0	1070.0	6.8	<0.8	<0.1	<0.8	5040	<20	8410	4790	32	101	1

Appendix 3.1 cont. Results of Terrasol Leach Analysis for Oxidation Suite, Chalcophile elements and HFSEs.

Sample Number	Oxidation Suite Elements											Chalcophile Elements								High-Field Strength Elements							
	Cl	V	As	Se	Mo	Sb	Te	W	Re	Au	Hg	Th	U	Ga	Ge	Ag	Cd	In	Sn	Tl	Bi	Ti	Cr	Y	Zr	Nb	Hf	Ta
SL Line 3 cont.																												
56	<2000	273	451	<5	49	63.1	<1	101	<0.01	<0.05	27	243.0	31.6	40	11.6	<0.2	483.0	<0.1	<0.8	<0.1	<0.8	2980	<20	6750	1780	13	36	<0.1
57	<2000	738	358	<5	210	99.2	<1	412	<0.01	<0.05	148	719.0	141.0	53	10.4	698.0	944.0	5.6	<0.8	<0.1	<0.8	4970	<20	7560	3610	25	77	<0.1
58	<2000	697	279	<5	280	60.9	<1	401	<0.01	<0.05	121	716.0	134.0	49	<0.5	520.0	637.0	8.9	<0.8	<0.1	<0.8	4170	<20	6390	3260	20	74	<0.1
59	<2000	380	228	<5	16	34.0	<1	<1	<0.01	<0.05	44	276.0	37.5	28	<0.5	<0.2	595.0	3.2	<0.8	<0.1	<0.8	2010	<20	4440	1710	11	37	<0.1
60	<2000	735	424	<5	129	145.0	<1	431	<0.01	<0.05	176	603.0	49.7	49	11.5	696.0	668.0	5.8	<0.8	<0.1	<0.8	5290	<20	6170	2850	25	56	<0.1
61	<2000	557	249	<5	32	68.5	<1	161	<0.01	<0.05	53	550.0	27.8	44	<0.5	436.0	951.0	3.5	<0.8	<0.1	<0.8	5480	<20	4650	1870	21	39	<0.1
62	<2000	1370	591	<5	16	23.8	<1	<1	<0.01	<0.05	7	352.0	69.1	18	<0.5	<0.2	48.3	<0.1	<0.8	<0.1	5.8	377	<20	3460	616	5	14	<0.1
63	<2000	894	482	<5	47	80.8	<1	287	<0.01	<0.05	73	452.0	32.4	46	12.1	472.0	548.0	4.1	<0.8	<0.1	<0.8	3260	<20	7000	2370	15	52	<0.1
64	<2000	232	495	<5	11	32.6	<1	<1	<0.01	<0.05	45	362.0	21.0	27	<0.5	320.0	293.0	<0.1	<0.8	<0.1	<0.8	1170	<20	4040	1070	7	24	<0.1
65	<2000	133	812	<5	13	37.6	<1	<1	<0.01	<0.05	34	162.0	10.3	21	<0.5	281.0	128.0	<0.1	<0.8	<0.1	<0.8	797	<20	2990	584	4	12	<0.1
66	<2000	142	480	<5	<1	40.5	<1	<1	<0.01	<0.05	38	406.0	16.7	26	<0.5	445.0	251.0	<0.1	<0.8	<0.1	<0.8	1990	<20	2620	860	9	17	<0.1
67	<2000	540	564	<5	<1	42.4	<1	<1	<0.01	<0.05	<1	382.0	20.5	19	<0.5	<0.2	41.9	<0.1	<0.8	<0.1	<0.8	394	<20	2020	704	<1	12	<0.1
68	<2000	485	1220	<5	18	37.9	<1	<1	<0.01	<0.05	3	563.0	22.0	19	<0.5	<0.2	26.4	<0.1	<0.8	<0.1	5.7	612	<20	2560	413	<1	8	<0.1
69	<2000	247	377	<5	<1	23.8	<1	<1	<0.01	<0.05	<1	405.0	18.2	19	<0.5	<0.2	42.0	<0.1	<0.8	<0.1	<0.8	412	<20	2080	519	<1	10	<0.1
SL Line 4																												
70	<2000	340	707	<5	47	56.9	<1	368	<0.01	<0.05	<1	360.0	16.2	74	17.7	<0.2	368.0	<0.1	<0.8	<0.1	<0.8	2250	<20	4830	1220	7	34	1
71	<2000	337	331	<5	23	56.1	<1	210	<0.01	<0.05	19	513.0	16.3	91	19.6	<0.2	423.0	<0.1	<0.8	<0.1	<0.8	3030	<20	5420	2530	7	62	1
72	<2000	133	301	<5	41	28.5	<1	<1	<0.01	<0.05	5	205.0	15.2	60	15.3	<0.2	332.0	<0.1	<0.8	<0.1	<0.8	1240	<20	5560	1540	8	32	1
73	<2000	265	766	<5	16	38.7	<1	<1	<0.01	<0.05	4	196.0	17.0	20	<0.5	<0.2	7.2	<0.1	<0.8	<0.1	<0.8	398	<20	1540	360	<1	8	<0.1
74	<2000	299	246	234	71	49.6	<1	338	<0.01	<0.05	14	950.0	17.2	103	19.9	<0.2	577.0	<0.1	<0.8	<0.1	<0.8	3920	<20	7990	2420	18	56	2
75	<2000	200	659	<5	<1	27.3	<1	<1	<0.01	<0.05	<1	401.0	19.8	33	<0.5	<0.2	30.9	<0.1	<0.8	<0.1	<0.8	439	<20	2310	425	<1	13	<0.1
76	<2000	288	253	<5	88	16.8	<1	<1	<0.01	<0.05	<1	225.0	30.7	33	<0.5	<0.2	555.0	<0.1	<0.8	<0.1	<0.8	1450	<20	2940	678	5	17	<0.1
77	<2000	299	283	<5	122	<0.1	<1	<1	<0.01	<0.05	<1	157.0	62.4	26	<0.5	<0.2	352.0	<0.1	<0.8	<0.1	<0.8	431	<20	2030	319	<1	10	<0.1
78	<2000	295	389	<5	293	30.9	<1	133	<0.01	<0.05	<1	167.0	60.7	37	<0.5	<0.2	497.0	<0.1	<0.8	<0.1	<0.8	557	<20	3200	634	<1	19	<0.1
79	<2000	219	418	<5	<1	24.2	<1	<1	<0.01	<0.05	<1	336.0	12.9	24	<0.5	<0.2	27.2	<0.1	<0.8	<0.1	<0.8	290	<20	2260	576	<1	12	<0.1
80	<2000	166	263	<5	15	15.8	<1	<1	<0.01	<0.05	9	283.0	19.2	51	<0.5	<0.2	197.0	<0.1	<0.8	<0.1	<0.8	799	<20	3720	701	<1	21	<0.1
81	<2000	177	379	<5	<1	21.5	<1	<1	<0.01	<0.05	<1	325.0	12.8	50	<0.5	<0.2	87.4	<0.1	<0.8	<0.1	<0.8	565	<20	3900	634	<1	20	<0.1
82	<2000	151	128	<5	12	<0.1	<1	<1	<0.01	<0.05	<1	312.0	12.1	46	<0.5	<0.2	136.0	<0.1	<0.8	<0.1	<0.8	309	<20	2790	672	<1	17	<0.1
83	<2000	401	593	<5	<1	15.6	<1	<1	<0.01	<0.05	<1	309.0	13.3	28	<0.5	<0.2	<0.2	<0.1	<0.8	<0.1	<0.8	205	<20	2680	358	<1	11	<0.1
84	<2000	579	120	<5	242	18.1	<1	189	<0.01	<0.05	28	1260.0	94.0	84	13.4	<0.2	499.0	<0.1	<0.8	<0.1	<0.8	2270	<20	7180	3950	13	92	1
85	<2000	337	92	<5	25	11.9	<1	<1	<0.01	<0.05	9	603.0	32.9	62	12.9	<0.2	490.0	<0.1	<0.8	<0.1	<0.8	1790	<20	7080	2130	8	48	1
86	<2000	102	169	<5	<1	10.0	<1	<1	<0.01	<0.05	<1	276.0	14.0	22	<0.5	<0.2	46.8	<0.1	<0.8	<0.1	<0.8	755	<20	1630	846	12	15	<0.1
87	<2000	375	69	<5	131	19.9	<1	133	<0.01	<0.05	17	1290.0	74.5	94	12.3	<0.2	617.0	<0.1	<0.8	<0.1	6.5	2520	<20	7380	4200	16	97	1
88	<2000	212	95	<5	11	10.9	<1	<1	<0.01	<0.05	<1	417.0	38.5	53	15.2	<0.2	421.0	<0.1	<0.8	<0.1	<0.8	1300	<20	5120	3000	33	57	1
89	<2000	495	185	<5	16	13.6	<1	<1	<0.01	<0.05	4	324.0	43.5	37	<0.5	<0.2	69.4	<0.1	<0.8	15.1	<0.8	462	<20	3770	1740	8	31	<0.1
90	<2000	823	182	<5	661	24.6	<1	311	<0.01	<0.05	69	1200.0	127.0	76	14.4	<0.2	499.0	<0.1	<0.8	237.0	<0.8	3250	<20	8670	2710	15	68	2
91	<2000	821	598	<5	135	36.7	<1	215	<0.01	<0.05	39	1190.0	98.0	106	15.3	<0.2	511.0	<0.1	<0.8	25.4	<0.8	2280	<20	7820	4300	9	95	2
92	<2000	438	215	<5	168	36.6	<1	195	<0.01	<0.05	43	944.0	89.4	87	14.6	<0.2	495.0	<0.1	<0.8	<0.1	<0.8	2150	<20	6350	3750	10	76	1
93	<2000	1440	1470	<5	42	51.2	<1	391	<0.01	<0.05	16	237.0	96.6	23	<0.5	<0.2	34.6	<0.1	<0.8	<0.1	<0.8	637	<20	2250	383	<1	13	<0.1
94	<2000	655	198	<5	270	20.0	<1	<1	<0.01	<0.05	100	826.0	77.8	125	14.7	573.0	569.0	2.0	<0.8	<0.1	<0.8	2920	<20	8750	2810	7	86	2
95	<2000	706	254	<5	235	53.7	<1	313	<0.01	<0.05	55	1190.0	116.0	86	14.0	<0.2	494.0	<0.1	<0.8	58.0	<0.8	2210	<20	7560	3990	13	82	2
96	<2000	164	197	<5	54	27.0	<1	<1	<0.01	<0.05	48	419.0	27.1	47	<0.5	<0.2	340.0	<0.1	<0.8	17.9	<0.8	2410	<20	2780	2160	10	36	<0.1
97	<2000	584	170	<5	630	28.3	<1	415	<0.01	<0.05	53	1060.0	133.0	62	10.6	<0.2	494.0	<0.1	<0.8	57.0	<0.8	2740	<20	6740	3070	12	67	1
98	<2000	655	111	<5	1990	22.5	<1	199	<0.01	<0.05	41	907.0	94.2	62	10.4	<0.2	495.0	<0.1	<0.8	<0.1	<0.8	2800	<20	5890	3730	12	79	1
99	<2000	212	476	<5	16	23.3	<1	<1	<0.01	<0.05	<1	257.0	14.0	27	<0.5	<0.2	24.5	<0.1	<0.8	<0.1	<0.8	432	<20	2550	792	<1	18	<0.1
100	<2000	406	703	234	405	153.0	<1	573	<0.01	<0.05	46	441.0	28.2	86	24.4	<0.2	299.0	<0.1	<0.8	<0.1	<0.8	2360	<20	7840	1670	9	47	2
101	<2000	180	320	<5	<1	27.4	<1	<1	<0.01	<0.05	<1	248.0	10.7	54	13.5	<0.2	172.0	<0.1	<0.8	<0.1	<0.8	528	<20	4120	1440	<1	37	<0.1
102	<2000	285	576	<5	<1	22.0	<1	<1	<0.01	7.8	9	282.0	30.5	39	11.9	313.0	206.0	<0.1	<0.8	<0.1	<0.8	609	<20	3870	1040	15	26	1
103	<2000	305	432	<5	38	21.5	<1	<1	<0.01	<0.05	3	240.0	25.9	45	11.6	<0.2	360.0	<0.1	<0.8	<0.1	<0.8	1390	<20	4150	1580	6	32	<0.1

Appendix 3.1cont. Results of Terrasol Leach Analysis for Oxidation Suite, Chalcophile elements and HFSEs.

Sample Number	Oxidation Suite Elements											Chalcophile Elements									High-Field Strength Elements							
	Cl	V	As	Se	Mo	Sb	Te	W	Re	Au	Hg	Th	U	Ga	Ge	Ag	Cd	In	Sn	Tl	Bi	Ti	Cr	Y	Zr	Nb	Hf	Ta
SL Line 5																												
126	<2000	173	220	<5	39	39.1	<1	<1	<0.01	<0.05	26	493.0	12.7	63	11.2	<0.2	969.0	<0.1	<0.8	<0.1	<0.8	2780	<20	4470	1650	12	36	1
127	<2000	196	162	<5	22	12.2	<1	<1	<0.01	<0.05	24	389.0	13.9	52	<0.5	<0.2	590.0	<0.1	<0.8	<0.1	<0.8	2320	<20	3210	1490	9	33	<0.1
128	<2000	209	634	<5	61	46.6	<1	<1	<0.01	<0.05	83	438.0	14.9	49	<0.5	300.0	1830.0	<0.1	<0.8	<0.1	<0.8	2770	<20	3420	1320	10	27	<0.1
129	<2000	244	980	<5	<1	31.0	<1	<1	<0.01	<0.05	<1	268.0	21.3	23	<0.5	<0.2	28.1	<0.1	<0.8	<0.1	<0.8	225	<20	1560	371	<1	8	<0.1
130	<2000	190	1700	<5	<1	42.0	<1	<1	<0.01	<0.05	<1	530.0	16.4	26	<0.5	<0.2	131.0	<0.1	<0.8	<0.1	<0.8	292	<20	2050	315	<1	10	<0.1
131	<2000	205	1580	<5	<1	39.8	<1	<1	<0.01	<0.05	<1	412.0	17.1	26	<0.5	<0.2	246.0	<0.1	<0.8	<0.1	<0.8	<100	<20	2100	344	<1	10	<0.1
132	<2000	145	1200	<5	<1	40.4	<1	<1	<0.01	<0.05	<1	638.0	16.7	32	<0.5	<0.2	464.0	<0.1	<0.8	<0.1	<0.8	<100	<20	2490	397	<1	13	<0.1
133	<2000	133	522	<5	14	21.9	<1	<1	<0.01	<0.05	<1	437.0	10.9	33	<0.5	<0.2	269.0	<0.1	<0.8	<0.1	<0.8	<100	<20	2610	426	<1	12	<0.1
134	<2000	355	887	<5	<1	26.5	<1	<1	<0.01	<0.05	<1	376.0	24.5	21	<0.5	<0.2	70.5	<0.1	<0.8	<0.1	<0.8	269	<20	1760	438	<1	9	<0.1
135	<2000	975	858	<5	47	23.4	<1	<1	<0.01	<0.05	<1	178.0	55.3	15	<0.5	<0.2	24.2	<0.1	<0.8	<0.1	<0.8	326	<20	1320	427	<1	7	<0.1
136	<2000	337	1450	<5	16	25.2	<1	<1	<0.01	<0.05	<1	413.0	33.3	17	<0.5	<0.2	33.2	<0.1	<0.8	<0.1	<0.8	529	<20	1530	273	<1	9	<0.1
137	<2000	383	290	<5	<1	13.1	<1	<1	<0.01	<0.05	<1	408.0	32.1	22	<0.5	<0.2	50.0	<0.1	<0.8	<0.1	<0.8	316	<20	1720	552	4	12	<0.1
138	<2000	413	1400	<5	13	24.1	<1	<1	<0.01	<0.05	6	306.0	39.7	12	<0.5	<0.2	25.6	<0.1	<0.8	<0.1	<0.8	413	<20	1210	268	<1	6	<0.1
139	<2000	1070	982	<5	15	19.3	<1	<1	<0.01	<0.05	14	560.0	178.0	14	<0.5	<0.2	34.1	<0.1	<0.8	<0.1	<0.8	403	<20	4040	691	5	18	<0.1
140	238000	1590	504	<5	131	15.4	<1	<1	<0.01	<0.05	16	783.0	228.0	24	<0.5	<0.2	10.7	<0.1	<0.8	<0.1	<0.8	526	<20	5730	1160	5	35	<0.1
141	<2000	746	1070	<5	16	12.4	<1	242	<0.01	<0.05	5	313.0	168.0	10	<0.5	<0.2	28.3	<0.1	<0.8	<0.1	<0.8	333	<20	1780	700	8	20	<0.1
142	<2000	1820	3900	<5	255	30.3	<1	<1	<0.01	<0.05	12	304.0	593.0	17	<0.5	<0.2	28.5	<0.1	<0.8	59.4	<0.8	424	<20	1890	1330	7	34	<0.1
143	<2000	1690	606	<5	128	24.8	<1	457	<0.01	13.2	15	299.0	77.9	36	<0.5	360.0	101.0	<0.1	<0.8	<0.1	<0.8	816	<20	1870	905	8	27	<0.1
144	<2000	511	472	<5	22	12.7	<1	<1	<0.01	<0.05	4	237.0	94.0	19	<0.5	<0.2	77.7	<0.1	<0.8	<0.1	<0.8	349	<20	1450	483	5	12	<0.1
145	<2000	211	309	<5	20	11.4	<1	<1	<0.01	<0.05	5	400.0	54.1	26	<0.5	<0.2	84.3	<0.1	<0.8	<0.1	<0.8	618	<20	2230	557	6	13	<0.1
146	<2000	651	670	<5	21	33.2	<1	<1	<0.01	<0.05	8	410.0	38.7	31	<0.5	287.0	158.0	<0.1	<0.8	<0.1	<0.8	631	<20	3030	664	5	15	<0.1
147	<2000	403	312	<5	26	35.9	<1	113	<0.01	<0.05	7	277.0	60.1	26	<0.5	308.0	327.0	<0.1	<0.8	<0.1	<0.8	546	<20	2090	530	6	13	<0.1
148	<2000	355	141	<5	20	40.0	<1	<1	<0.01	<0.05	11	327.0	30.2	32	<0.5	<0.2	105.0	<0.1	<0.8	<0.1	5.7	644	<20	2120	1140	5	34	<0.1
149	<2000	519	391	<5	<1	61.3	<1	<1	<0.01	<0.05	4	355.0	14.0	38	10.2	<0.2	41.6	<0.1	<0.8	<0.1	<0.8	453	<20	3830	887	6	23	<0.1
150	<2000	322	324	<5	<1	42.5	<1	<1	<0.01	<0.05	5	431.0	21.1	27	<0.5	<0.2	43.4	<0.1	<0.8	<0.1	<0.8	542	<20	2670	618	8	14	<0.1
151	<2000	263	171	<5	20	57.2	<1	<1	<0.01	<0.05	15	351.0	26.8	27	<0.5	<0.2	54.9	<0.1	<0.8	<0.1	<0.8	515	<20	1890	1290	5	34	<0.1
152	<2000	151	130	<5	11	15.0	<1	<1	<0.01	<0.05	3	152.0	19.4	16	<0.5	<0.2	46.8	<0.1	<0.8	<0.1	<0.8	318	<20	1280	410	5	13	<0.1
153	<2000	258	214	<5	22	124.0	<1	<1	<0.01	<0.05	8	367.0	18.6	34	<0.5	<0.2	56.1	<0.1	<0.8	<0.1	<0.8	609	<20	2860	948	8	25	<0.1
154	<2000	159	414	<5	13	31.8	<1	<1	<0.01	<0.05	11	345.0	14.6	19	<0.5	<0.2	35.7	<0.1	<0.8	<0.1	<0.8	783	<20	2290	749	6	12	<0.1
155	<2000	379	178	<5	47	68.8	<1	<1	<0.01	<0.05	68	679.0	38.4	36	<0.5	<0.2	393.0	5.8	<0.8	<0.1	<0.8	2990	<20	4760	4050	24	74	<0.1
156	<2000	539	280	<5	173	127.0	<1	195	<0.01	<0.05	106	853.0	122.0	30	<0.5	422.0	469.0	3.6	<0.8	<0.1	<0.8	3410	<20	4690	4690	31	79	<0.1
157	<2000	112	413	<5	14	85.6	<1	<1	<0.01	<0.05	179	535.0	14.1	36	<0.5	353.0	336.0	<0.1	<0.8	<0.1	<0.8	1730	<20	5730	1970	15	41	<0.1
158	<2000	63	483	<5	23	66.6	<1	<1	<0.01	<0.05	61	532.0	19.0	35	<0.5	<0.2	261.0	<0.1	<0.8	<0.1	<0.8	2030	<20	5870	1720	17	35	<0.1
159	<2000	292	281	<5	31	44.5	<1	<1	<0.01	<0.05	14	428.0	24.2	28	<0.5	<0.2	258.0	<0.1	<0.8	<0.1	<0.8	2850	<20	3670	1960	22	38	<0.1
160	<2000	213	513	<5	17	40.0	<1	<1	<0.01	<0.05	4	323.0	24.7	16	<0.5	<0.2	281.0	<0.1	<0.8	<0.1	<0.8	399	<20	1850	631	6	12	<0.1
161	<2000	312	1460	<5	<1	84.9	<1	<1	<0.01	<0.05	13	371.0	30.8	16	<0.5	<0.2	102.0	<0.1	<0.8	<0.1	<0.8	626	<20	2230	555	4	10	<0.1
162	<2000	233	1250	<5	12	84.8	<1	<1	<0.01	<0.05	<1	534.0	22.4	21	<0.5	<0.2	437.0	<0.1	<0.8	<0.1	<0.8	500	<20	2820	649	6	14	<0.1

Appendix 3.2. Results of Terrasol Leach Analysis for REEs, LILEs and Base metals.

	Rare Earth Elements													Lithophile Elements					Base Metals						
	La	Ce	Pr	Nd	Sm	Eu	Gd	Dy	Ho	Er	Tm	Yb	Lu	Lii	Be	Sc	Mn	Rb	Sr	Cs	Ba	Co	Ni	Cu	Zn	Pb
SL Line 1																										
1	273	873	285	1760	565	145	534	524	99	266	33	204	27	173	22	<2	43200	687	20800	53	124000	547	467	735	2660	50
2	211	839	254	1570	502	132	478	480	92	241	30	191	26	124	28	<2	78100	670	21400	51	133000	914	504	1180	4680	87
3	184	642	254	1640	556	135	537	554	105	277	36	220	29	93	21	<2	45300	595	26200	54	75600	510	350	436	2610	<1
4	3010	4810	892	3980	888	189	781	607	109	282	34	207	27	50	20	<2	62400	571	23500	37	83800	654	<3	483	1500	2980
5	385	1160	437	2500	679	156	593	560	107	286	36	228	31	88	25	<2	29800	698	20900	35	103000	438	156	602	922	<1
6	3190	5750	961	4210	885	189	782	617	112	291	35	218	30	61	24	<2	56800	725	15000	32	92200	864	<3	573	998	2890
7	465	1400	394	2090	534	125	481	459	87	239	31	196	27	106	25	<2	27500	640	21700	34	92900	376	<3	809	1360	<1
8	342	968	312	1910	586	150	546	569	111	302	39	246	34	223	16	<2	15500	597	26000	35	149000	226	352	527	949	<1
9	1720	2700	587	2700	620	143	560	461	83	216	26	162	22	77	23	<2	32100	536	27300	42	106000	317	<3	440	805	875
10	935	2070	463	2280	568	132	513	442	82	216	26	163	22	95	22	<2	37500	547	27500	43	93400	397	<3	362	670	212
11	2150	3110	725	3250	699	156	627	529	98	259	32	198	27	126	17	<2	39200	496	31800	28	99900	529	<3	502	430	727
12	456	928	388	2300	686	174	645	672	131	357	47	295	39	351	19	<2	26100	492	31500	35	134000	339	280	540	631	<1
SL Line 2																										
13	2430	8770	826	3820	862	189	858	687	128	335	40	242	34	94	39	<2	198000	598	8010	27	49200	3210	671	859	2130	26000
14	2910	10300	1030	4680	1050	234	982	783	144	382	47	298	42	95	41	<2	309000	780	21900	30	96200	3840	1100	883	4930	20400
15	1110	2430	340	1580	365	130	338	258	44	114	14	95	14	49	266	<2	112000	1960	13700	766	149000	5240	306	25500	70500	142000
16	3120	5460	929	4180	911	228	832	682	124	325	38	239	33	164	49	<2	495000	627	29400	31	197000	2000	954	1170	12600	12000
17	373	972	390	2270	659	175	605	617	118	320	41	264	36	161	16	<2	60600	1370	31500	37	218000	595	330	724	2070	118
18	3260	4200	975	4190	896	206	800	648	117	306	37	228	31	152	18	<2	72600	1880	25100	41	140000	741	<3	514	1070	4100
19	397	1220	405	2290	640	154	583	563	106	279	36	225	30	211	16	<2	73600	812	38600	30	56500	620	453	909	3860	77
20	1040	2070	631	3150	787	194	700	633	117	314	39	246	33	137	15	<2	84000	1480	29700	42	202000	753	<3	535	1800	253
21	3050	5550	879	3790	796	182	722	592	108	284	34	214	29	66	22	<2	124000	952	21600	26	136000	1090	216	898	4370	10300
22	3290	6320	978	4240	906	202	811	658	118	312	38	234	31	54	24	<2	137000	579	18700	21	141000	1320	326	835	2950	13100
23	2910	6060	828	3590	762	165	694	569	104	275	34	212	29	52	21	<2	133000	624	22800	26	88800	1120	142	1050	4980	18900
24	529	1490	531	2990	832	197	771	741	140	367	46	288	38	66	25	<2	110000	734	24900	31	114000	782	156	583	6420	147
25	204	768	196	1140	296	60	281	277	58	164	21	125	18	72	13	<2	105000	1240	35600	78	27400	893	<3	482	<10	52
26	247	914	266	1660	594	139	570	431	76	182	22	127	17	130	16	<2	19000	708	37100	34	152000	564	<3	379	4190	<1
27	796	2220	777	4400	1310	271	1170	1010	178	443	51	303	42	139	39	<2	178000	947	26500	47	69100	1150	<3	987	<10	<1
28	1620	8610	1610	8420	2210	492	2150	2010	388	1080	142	900	134	175	625	##	2040000	873	15200	36	84700	29100	<3	5190	<10	<1
29	473	1390	474	2700	780	190	802	704	136	358	42	244	36	191	18	<2	134000	953	43100	44	160000	865	<3	907	<10	<1
SL Line 3																										
30	1680	5360	675	3170	798	184	722	689	126	337	44	293	37	57	149	<2	458000	813	7800	53	65300	3280	1050	2830	18300	10800
31	2650	3260	884	3970	949	207	803	732	128	339	41	261	32	71	50	<2	109000	717	16800	30	101000	786	319	1580	3600	3760
32	1860	2370	683	3070	747	169	616	538	95	252	31	198	25	112	16	<2	44300	1370	27500	51	126000	284	<3	808	2040	947
33	2170	3310	728	3290	792	174	666	607	105	275	35	221	29	157	46	<2	129000	2100	17700	48	94100	625	618	1880	8360	5160
34	1140	1860	421	1920	455	112	375	350	64	170	21	142	18	125	14	<2	23800	838	27800	34	141000	319	<3	523	<10	365
35	925	1870	377	1810	438	114	373	356	67	185	24	154	20	119	9	<2	30000	919	28500	36	215000	445	<3	118	<10	<1
36	1320	2110	496	2340	520	137	428	321	59	160	20	130	18	151	9	<2	16800	838	30800	45	277000	387	375	319	<10	435
37	975	954	363	1760	403	127	329	271	52	143	19	126	18	639	<2	<2	11600	756	49800	42	365000	332	<3	292	<10	382
38	1860	1830	566	2500	554	130	461	419	80	216	29	186	25	411	23	<2	22000	557	79000	30	169000	266	<3	305	<10	189
39	712	1130	326	1620	429	118	359	359	69	188	25	163	23	177	10	<2	10900	911	32900	44	255000	287	<3	147	<10	<1
40	663	1130	277	1370	340	100	292	272	52	144	19	120	17	368	18	<2	27100	725	40400	35	232000	430	<3	162	<10	<1
41	1070	1590	374	1860	434	123	378	311	61	166	21	137	18	327	6	<2	25300	918	43700	48	254000	408	256	348	<10	<1
42	2040	2310	631	2840	635	167	533	415	76	214	24	157	20	245	15	<2	28300	1140	42000	61	333000	494	<3	200	<10	<1
43	343	639	133	668	160	68	143	142	28	75	10	67	12	166	8	<2	8450	410	47200	26	262000	284	<3	142	<10	<1
44	1730	1420	489	2210	489	103	446	390	75	206	27	169	24	295	27	<2	36200	508	104000	38	100000	335	<3	121	<10	<1
45	1920	1310	464	1900	461	56	455	670	150	475	78	577	85	192	189	<2	59700	480	78200	20	1990	668	11200	394	1160	885
46	637	1590	559	3000	749	179	664	540	100	264	32	181	24	341	17	<2	54900	1500	88200	119	151000	462	<3	571	2910	<1
47	824	1120	763	4000	965	197	855	748	140	375	48	284	39	101	33	<2	38000	617	26600	25	97900	436	<3	437	4190	<1
48	1260	2520	1100	5480	1400	276	1240	1140	207	558	72	452	65	109	94	<2	271000	912	22700	48	53200	848	<3	1640	<10	<1
49	1360	2790	1160	5840	1440	308	1290	1090	193	499	62	367	51	90	61	<2	172000	1420	28000	99	53300	457	<3	757	<10	<1
50	1510	5490	1310	6540	1670	359	1590	1400	256	671	87	543	78	121	164	<2	723000	1220	21700	80	55300	2210	<3	1980	<10	<1
51	858	1080	787	4040	1010	231	903	753	137	360	44	261	35	181	57	<2	63600	833	42600	35	108000	393	<3	527	3290	<1
52	893	2520	792	4060	1050	255	988	893	167	451	56	351	50	129	50	<2	120000	982	29400	38	118000	543	<3	916	<10	<1
53	649	1150	616	3200	833	194	734	602	110	288	36	211	29	318	27	<2	36500	943	35800	48	174000	452	<3	527	3570	<1
54	641	2270	450	2080	550	132	539	470	80	202	25	153	21	105	69	<2	907000	1020	87000	104	61600	1430	<3	2200	<10	<1
55	1190	7900	1110	5840	1550	355	1560	1410	273	733	96	607	88	119	629	<2	2200000	990	15000	43	116000	18600	<3	3490	<10	<1

Appendix 3.2. cont. Results of Terrasol Leach Analysis for REEs, LILEs and Base metals.

	Rare Earth Elements													Lithophile Elements								Base Metals					
	La	Ce	Pr	Nd	Sm	Eu	Gd	Dy	Ho	Er	Tm	Yb	Lu	Lii	Be	Sc	Mn	Rb	Sr	Cs	Ba	Co	Ni	Cu	Zn	Pb
SL Line 3 cont.																											
56	1540	3550	1320	6540	1650	362	1490	1230	219	562	70	422	58	106	107	<2	306000	1160	22600	55	74400	1190	<3	3180	<10	<1
57	1420	6960	1250	6340	1620	375	1530	1330	246	663	88	569	84	60	444	<2	1470000	863	10400	55	98000	8200	<3	5830	<10	<1
58	1160	6240	999	5120	1290	286	1260	1090	201	545	70	445	66	134	491	<2	1260000	863	10800	51	94400	9260	<3	5290	<10	<1
59	1050	3010	845	4090	1040	241	973	851	152	394	49	305	43	63	142	<2	357000	785	17000	57	114000	1770	<3	4030	<10	<1
60	1130	5930	998	5100	1320	314	1260	1120	205	548	72	473	68	90	325	<2	1210000	896	12500	59	120000	6830	<3	5580	<10	<1
61	1070	4830	932	4540	1150	275	1070	941	165	433	55	350	50	65	234	<2	669000	816	11800	60	79700	3150	<3	5590	<10	<1
62	661	2480	584	3070	783	173	744	628	119	325	41	252	37	484	27	<2	105000	947	65700	27	72900	578	<3	773	3540	<1
63	1540	5510	1320	6520	1720	384	1620	1370	238	618	76	488	69	133	287	<2	594000	973	16600	46	112000	4210	<3	6340	<10	<1
64	1150	2410	908	4300	1030	236	934	796	139	362	45	273	38	110	38	<2	89500	913	26700	38	137000	612	<3	1630	<10	<1
65	736	1580	643	3310	800	187	719	591	105	274	34	206	28	152	15	<2	75300	1440	37600	48	131000	410	<3	933	<10	<1
66	808	2320	623	2940	709	151	648	547	97	245	31	192	26	229	34	<2	128000	2420	34600	47	138000	598	<3	1410	<10	<1
67	436	1630	391	2000	503	129	451	392	73	197	24	162	23	179	10	<2	32300	883	38600	32	190000	529	<3	718	3860	<1
68	452	1720	419	2210	559	136	515	463	90	246	32	207	30	224	12	<2	29900	908	39100	29	156000	568	<3	1010	4350	<1
69	572	2020	458	2210	521	130	471	400	74	203	26	160	23	130	14	<2	29300	713	27100	34	203000	494	<3	458	3780	<1
SL Line 4																											
70	3030	5060	1150	5550	1370	331	1180	1030	185	481	59	352	46	75	167	<2	317000	1430	20900	120	62200	712	228	1030	2610	827
71	2700	4560	1080	5090	1320	318	1120	1100	197	530	68	425	56	104	287	<2	218000	1380	13800	129	103000	830	161	2070	1880	1580
72	3010	3350	1100	5260	1270	271	1090	1010	186	505	63	387	52	139	95	<2	133000	1220	29300	84	76400	718	<3	757	440	679
73	610	1110	267	1440	361	98	320	282	53	147	19	121	17	154	25	<2	36400	1680	41900	177	103000	272	<3	347	<10	<1
74	3800	9510	1540	7440	1910	404	1700	1650	303	807	103	624	84	81	206	<2	449000	1070	21700	62	50100	1700	515	1930	3230	2000
75	1150	1390	480	2370	586	138	485	452	84	234	31	191	30	140	30	<2	36600	789	30800	42	134000	292	<3	415	<10	97
76	1910	3340	616	2770	669	160	627	581	100	267	33	204	27	57	67	<2	320000	792	21200	68	76100	964	146	799	5830	3120
77	1500	2690	429	1870	463	118	446	434	73	181	23	146	19	48	20	<2	380000	712	36000	107	62400	764	130	355	2370	1490
78	1940	3140	657	3110	804	184	698	615	108	274	33	215	28	116	44	<2	347000	942	35700	63	72300	1290	333	858	2300	1640
79	908	1770	404	2120	548	135	453	443	85	230	28	190	25	208	9	<2	26900	1240	27100	28	138000	420	<3	329	<10	<1
80	2120	2280	790	3830	1010	230	868	766	134	334	41	248	33	219	23	<2	56200	926	25600	46	102000	406	<3	671	487	622
81	2200	2390	885	4290	1110	256	928	791	136	362	43	263	34	246	43	<2	50200	1040	31000	49	168000	444	<3	394	<10	52
82	1810	2360	652	3080	775	179	663	590	104	279	35	216	28	107	25	<2	34100	769	17700	43	153000	330	<3	517	<10	85
83	1080	1800	505	2580	673	163	560	498	97	263	34	214	29	236	<2	<2	25100	1140	32500	34	173000	319	<3	313	<10	<1
84	2760	7620	1000	4670	1170	249	1100	1210	238	676	93	649	93	150	513	<2	344000	659	10700	22	30100	4380	1540	1510	4110	808
85	3730	4950	1230	5700	1400	284	1260	1260	243	671	90	590	83	117	142	<2	71600	507	19700	19	47300	893	553	1560	1430	963
86	815	1550	315	1510	361	80	304	297	58	171	24	157	24	153	31	<2	23800	527	30000	44	71800	302	<3	306	<10	<1
87	2650	9100	969	4610	1180	255	1140	1270	254	725	102	709	102	156	553	<2	325000	626	8460	22	40400	2970	1190	2150	4690	1570
88	2320	2330	801	3640	919	184	808	877	176	493	71	484	72	210	206	<2	35300	584	20600	59	50400	467	<3	1010	279	1420
89	2280	2250	750	3510	859	183	731	708	134	358	45	281	39	390	36	<2	56400	573	58400	128	82600	388	182	379	<10	<1
90	3130	7750	1290	6350	1660	352	1470	1580	315	858	117	770	103	104	328	<2	1190000	536	10500	27	34100	9740	3840	1740	4850	693
91	3440	11000	1250	5810	1460	324	1380	1480	283	784	105	711	99	194	686	<2	520000	617	14700	29	46700	4780	2020	3020	4610	2100
92	2460	8080	893	4210	1100	260	1040	1120	221	619	86	578	82	169	584	<2	450000	609	16000	27	58700	3030	1320	1520	8830	6320
93	842	1670	385	2070	569	133	494	453	82	209	23	134	18	191	8	<2	50800	2430	56400	421	131000	533	287	612	<10	208
94	3670	14000	1460	7020	1760	394	1660	1680	318	879	110	689	95	158	586	<2	384000	925	9540	51	169000	3500	3110	2840	6290	2360
95	2650	9670	1020	4960	1360	307	1280	1390	273	746	102	676	95	144	437	<2	567000	635	17000	27	67000	4370	1980	4600	3520	2510
96	1090	2980	468	2250	602	131	521	562	108	292	40	270	41	84	133	<2	128000	535	17600	31	40900	722	259	3240	1560	636
97	2110	5340	882	4430	1150	254	1040	1150	229	641	89	598	84	73	341	<2	866000	665	13000	36	34800	8300	3100	2390	6620	1010
98	1920	5800	751	3680	948	201	903	986	203	571	80	528	72	108	301	<2	440000	672	8280	46	31500	5680	1870	1830	5280	1030
99	1340	1760	543	2640	649	157	539	477	90	238	30	186	25	205	16	<2	43700	1310	42300	108	136000	305	<3	230	<10	<1
100	3140	5660	1380	6820	1930	438	1640	1520	275	699	85	532	68	142	326	<2	528000	1060	19700	78	87500	1710	440	1850	2290	1050
101	2290	2090	936	4420	1070	257	911	829	149	399	50	305	38	119	83	<2	61500	1160	17700	99	93500	269	<3	760	567	105
102	2070	2000	830	3990	985	241	809	752	138	375	49	292	39	228	34	<2	25600	541	31700	22	332000	411	<3	1070	430	1570
103	2320	3350	855	4010	968	219	861	782	145	396	49	309	44	115	78	<2	150000	949	24100	72	91000	723	808	1130	3600	1240

Appendix 3.2. cont. Results of Terrasol Leach Analysis for REEs, LILEs and Base metals.

	Rare Earth Elements													Lithophile Elements						Base Metals						
	La	Ce	Pr	Nd	Sm	Eu	Gd	Dy	Ho	Er	Tm	Yb	Lu	Lii	Be	Sc	Mn	Rb	Sr	Cs	Ba	Co	Ni	Cu	Zn	Pb
SL Line 5																										
126	2720	5280	969	4460	1110	239	958	893	160	422	53	347	47	77	95	<2	186000	827	28000	48	78000	1160	251	1570	2470	8660
127	2130	3890	733	3310	810	181	700	648	115	310	40	260	35	65	67	<2	122000	724	22800	44	104000	831	145	1300	2390	3640
128	2070	4920	746	3480	858	184	752	687	128	341	44	277	38	71	82	<2	167000	783	27100	41	59900	1230	142	1150	3820	31500
129	969	1690	341	1600	366	107	321	287	55	153	20	135	19	131	8	<2	16700	794	77300	50	251000	276	<3	287	<10	980
130	1400	2020	475	2210	504	125	438	368	71	196	26	167	25	199	14	<2	8050	876	44500	54	210000	262	<3	326	<10	2190
131	1350	2000	484	2140	503	121	443	394	77	210	28	173	26	183	8	<2	11300	808	35200	50	155000	276	<3	341	<10	5840
132	1790	2490	577	2610	599	135	511	475	87	243	31	206	26	177	20	<2	12000	825	38100	44	106000	311	<3	358	<10	8770
133	1980	2490	620	2760	626	138	537	484	91	253	32	201	30	130	21	<2	16400	685	28900	38	121000	292	<3	294	<10	12400
134	918	1530	338	1620	389	107	336	319	60	172	22	146	22	247	14	<2	16600	839	47400	46	231000	308	<3	233	<10	638
135	623	1050	238	1180	290	77	243	223	45	120	16	104	13	458	<2	<2	24700	812	59800	49	152000	456	<3	327	<10	<1
136	885	1520	324	1560	375	101	309	276	53	147	19	128	19	313	13	<2	13100	843	41800	52	232000	301	<3	247	<10	60
137	1070	1960	365	1710	400	103	351	323	62	174	23	152	22	165	<2	<2	21400	750	42700	50	190000	277	<3	151	<10	219
138	511	957	203	970	244	67	212	206	42	118	16	105	13	313	<2	<2	9710	703	61000	41	164000	272	<3	233	<10	<1
139	359	758	336	2010	603	146	585	667	139	402	56	378	56	627	24	<2	17200	823	42900	103	73300	194	324	426	469	<1
140	407	777	430	2720	858	201	842	948	191	557	76	504	74	881	24	<2	27800	982	72200	60	15800	364	148	779	451	<1
141	190	624	173	1010	296	76	284	317	64	185	25	169	25	486	25	<2	28300	974	70300	178	85000	243	418	754	1210	<1
142	160	575	155	967	293	72	286	342	70	204	29	196	29	732	34	<2	84300	1550	232000	146	22400	406	618	879	1910	<1
143	1830	6640	532	2350	523	121	508	407	75	203	25	167	23	188	51	<2	141000	894	25000	91	47300	2620	997	2690	1880	21300
144	1470	3050	403	1740	364	79	333	277	52	141	17	114	16	157	19	<2	48600	699	40500	66	39600	572	<3	1690	4700	6510
145	2140	5580	595	2570	565	127	530	446	83	226	29	191	27	148	13	<2	99200	1200	75600	62	52800	726	<3	489	2350	1960
146	3140	5990	862	3650	766	172	711	587	108	291	37	232	32	203	20	<2	74700	670	42900	42	68800	781	<3	594	2970	5750
147	2350	4590	620	2610	553	137	500	421	78	213	27	172	24	122	21	<2	83800	790	39800	66	51300	668	<3	885	6860	9020
148	1550	6000	477	2160	493	113	479	416	80	215	28	183	27	69	32	<2	107000	704	14700	43	73700	1640	345	993	1420	5400
149	3460	7960	1000	4420	971	215	916	749	137	362	45	277	38	104	19	<2	123000	706	33100	34	89700	1680	<3	357	401	1660
150	2750	5110	738	3170	677	147	618	524	97	266	34	220	31	119	15	<2	58400	766	48200	42	74900	618	<3	420	553	1910
151	1440	4750	438	1990	441	101	420	366	70	192	25	167	24	73	37	<2	80200	710	13600	41	77300	1200	266	631	608	3300
152	1280	2780	348	1500	323	77	298	256	47	128	16	105	15	50	16	<2	50000	535	31700	52	52900	397	<3	520	757	1750
153	2260	7430	723	3270	764	174	717	583	106	280	36	226	32	71	28	<2	149000	925	25700	51	107000	1560	<3	334	804	2950
154	522	1680	461	2320	573	138	514	433	80	225	29	178	25	106	23	<2	24400	738	37100	40	177000	530	<3	611	4210	<1
155	865	4630	742	3730	1000	237	965	915	165	447	59	394	59	95	371	<2	393000	884	25500	54	126000	3500	<3	4700	<10	<1
156	602	3840	556	2920	810	183	822	829	162	465	64	434	68	125	428	<2	662000	862	20000	48	61100	8060	<3	3300	<10	<1
157	1730	3010	1280	6130	1450	316	1320	1140	204	535	66	405	56	117	83	<2	150000	859	41900	47	131000	1200	<3	2000	<10	<1
158	1560	3890	1230	6080	1480	326	1350	1170	210	546	67	425	59	96	81	<2	154000	973	50500	47	95100	819	<3	1520	<10	<1
159	1030	3760	783	3790	920	200	839	727	130	347	44	272	39	87	84	<2	239000	804	32200	46	82200	1380	<3	1710	<10	<1
160	567	2200	416	2020	464	111	426	365	68	187	23	149	21	122	17	<2	39600	729	34900	43	133000	548	<3	524	2610	<1
161	407	1360	340	1800	453	121	430	388	77	215	29	190	29	198	9	<2	21000	836	50500	45	247000	530	<3	763	4540	<1
162	740	2260	560	2690	642	153	582	495	94	259	33	217	32	170	19	<2	21000	818	42000	46	190000	516	<3	894	3010	<1

Appendix 4. Soil Slurry pH raw data

Sample Number	Easting (UTM)	Northing (UTM)	Elevation (meters)	pH
		pH Line 1		
1	319251	3773448	1672	***9.03***
2	319305	3773452	1670	***9.16***
3	319351	3773451	1665	***9.25***
4	319404	3773449	1665	***8.12***
5	319453	3773451	1660	***8.88***
6	319501	3773449	1650	***9.04***
7	319554	3773451	1634	***8.83***
8	319602	3773454	1625	***9.25***
9	319650	3773450	1617	***9.30***
10	319747	3773451	1594	***9.11***
11	319851	3773450	1582	***9.03***
12	319950	3773454	1569	***9.03***
13	320000	3773451	1564	***9.10***
14	320001	3773447	1564	***8.51***
15	320054	3773450	1559	***8.50***
16	320104	3773450	1554	***7.60***
17	320206	3773450	1542	***9.00***
18	320254	3773450	1536	***9.00***
19	320302	3773449	1532	***8.36***
20	320354	3773435	1529	***8.81***
21	320408	3773433	1526	***8.78***
22	320456	3773450	1521	***8.79***
23	320502	3773449	1518	***8.83***
24	320565	3773444	1512	***9.10***
25	320604	3773449	1510	***8.85***
26	320604	3773449	1510	***8.97***
27	320650	3773445	1507	***9.15***
28	320698	3773460	1505	***9.03***
29	320760	3773451	1501	***9.25***
30	320804	3773452	1499	***9.23***
31	320852	3773450	1497	***9.01***
32	320906	3773450	1494	***9.09***
33	320952	3773447	1492	***8.91***
34	321060	3773460	1488	***9.01***
35	321151	3773452	1485	***9.19***
36	321255	3773449	1482	***8.91***
37	321354	3773446	1478	***9.16***
38	321452	3773449	1476	***9.17***
39	321552	3773450	1471	***9.25***
40	321649	3773441	1469	***9.25***
41	321751	3773439	1465	***9.27***
		pH Line 2		
42	319990	3772904	1589	***9.18***
43	320050	3772904	1570	***8.97***
44	320102	3772902	1560	***7.50***
45	320152	3772902	1555	***7.91***
46	320200	3772901	1551	***9.10***
47	320252	3772902	1545	***7.04***
48	320301	3772902	1539	***7.49***
49	320352	3772900	1535	***7.95***
50	320399	3772903	1530	***7.98***
51	320451	3772903	1525	***8.61***
52	320503	3772907	1525	***8.98***
53	320608	3772904	1518	***8.88***
54	320700	3772900	1511	***8.72***
55	320801	3772902	1505	***8.37***
56	320902	3772901	1499	***9.25***
57	321000	3772901	1495	***8.86***
58	321116	3772903	1490	***9.14***
59	321200	3772903	1487	***9.03***
60	321299	3772900	1486	***9.14***
61	321401	3772901	1482	***9.20***
62	321499	3772903	1479	***9.22***
		pH Line 3		
63	319845	3772302	1684	***7.50***
64	319868	3772318	1675	***6.15***
65	319910	3772332	1665	***7.50***
66	319943	3772378	1649	***7.08***
67	319992	3772433	1631	***7.50***
68	320036	3772475	1622	***8.63***
69	320103	3772531	1605	***8.16***
70	320144	3772582	1596	***7.84***
71	320209	3772602	1585	***9.41***
72	320295	3772599	1563	***9.60***
73	320295	3772599	1563	***8.90***
74	320353	3772600	1551	***9.10***
75	320400	3772606	1545	***8.90***
76	320452	3772600	1537	***9.20***
77	320504	3772601	1530	***7.50***
78	320555	3772601	1529	***9.17***
79	320605	3772602	1525	***8.06***
80	320654	3772600	1521	***9.35***
81	320706	3772604	1517	***9.50***
82	320753	3772606	1513	***9.70***
83	320802	3772599	1508	***9.72***
84	320852	3772602	1505	***9.08***
85	320902	3772608	1501	***9.42***
86	320959	3772596	1498	***9.45***
87	321005	3772585	1495	***9.49***
88	321056	3772584	1492	***9.60***
89	321107	3772589	1488	***9.21***
90	321154	3772585	1487	***9.43***
91	321203	3772582	1486	***9.70***
92	321254	3772584	1484	***9.50***
93	321306	3772581	1482	***9.50***
94	321411	3772581	1478	***9.12***
95	321503	3772581	1475	***9.42***
96	321602	3772579	1471	***9.50***
97	321702	3772579	1469	***9.50***
98	321800	3772589	1463	***9.50***
99	321902	3772581	1463	***9.46***
100	322008	3772585	1466	***9.70***
101	322105	3772579	1463	***9.50***
102	322203	3772581	1457	***9.60***
		pH Line 4		
103	320209	3771984	1654	***9.26***
104	320250	3772015	1629	***9.30***
105	320333	3772050	1607	***8.09***
106	320366	3772047	1601	***7.82***
107	320400	3772039	1594	***8.71***
108	320433	3772029	1588	***8.67***
109	320460	3772033	1579	***9.12***
110	320533	3772031	1561	***9.26***
111	320566	3772028	1555	***9.06***
112	320600	3772029	1548	***8.42***
113	320633	3772026	1544	***9.37***
114	320671	3772021	1537	***8.71***
115	320700	3772015	1533	***9.21***
116	320750	3772015	1524	***8.18***
117	320818	3772018	1512	***9.34***
118	320893	3772011	1505	***9.25***
119	320947	3772000	1500	***9.39***
120	321060	3772014	1489	***9.47***
121	321132	3771997	1487	***9.40***
122	321200	3771983	1482	***9.42***
123	321254	3771995	1480	***9.12***
124	321300	3771993	1476	***9.32***
125	321366	3771987	1473	***9.35***
126	321415	3771979	1469	***9.52***
127	321580	3771978	1463	***9.50***
128	321501	3771978	1467	***9.44***
129	321600	3771945	1461	***9.41***
130	321690	3771943	1457	***9.41***
131	321790	3771951	1453	***9.53***
132	321890	3771940	1451	***9.64***
133	321990	3771941	1453	***9.68***
134	322100	3771947	1452	***9.57***
135	322293	3771945	1441	***9.60***
136	322393	3771942	1451	***9.54***
137	322493	3771945	1447	***9.69***
138	320300	3771600	1687	***9.26***
139	320351	3771599	1669	***8.87***
140	320399	3771599	1647	***9.20***
141	320450	3771600	1625	***7.69***
142	320501	3771600	1607	***7.45***
143	320550	3771600	1588	***8.14***
144	320600	3771601	1587	***6.48***
145	320650	3771600	1579	***7.61***
146	320700	3771600	1556	***8.06***
147	320751	3771600	1536	***6.51***
148	320800	3771602	1517	***5.68***
149	320850	3771600	1505	***7.73***
150	320901	3771599	1497	***6.99***
151	320950	3771600	1492	***9.15***
152	321000	3771596	1487	***9.58***
153	321050	3771599	1485	***9.27***
154	321100	3771600	1483	***9.35***
155	321150	3771599	1481	***9.49***
156	321201	3771600	1478	***9.35***
157	321250	3771601	1475	***9.32***
158	321301	3771600	1473	***9.25***
159	321350	3771600	1470	***9.12***
160	321400	3771600	1469	***9.50***
161	321470	3771600	1466	***9.57***
162	321550	3771604	1463	***9.55***
163	321649	3771607	1457	***9.48***
164	321751	3771602	1455	***9.58***
165	321850	3771600	1451	***9.20***
166	321951	3771600	1451	***9.44***
167	322050	3771599	1445	***9.49***
		pH Line 6		
168	320894	3771031	1551	***8.50***
169	320949	3771047	1524	***7.56***
170	320997	3771062	1512	***8.83***
171	321047	3771060	1502	***8.46***
172	321097	3771053	1495	***8.68***
173	321146	3771049	1492	***8.84***
174	321198	3771047	1491	***8.81***
175	321247	3771043	1489	***8.77***
176	321296	3771044	1488	***8.71***
177	321346	3771046	1485	***7.35***
178	321397	3771048	1483	***6.89***
179	321446	3771048	1480	***8.92***
180	321546	3771044	1473	***8.07***
181	321647	3771056	1470	***8.71***
182	321743	3771052	1465	***7.87***
183	321799	3771048	1465	***8.36***
		pH Line 7		
184	320648	3770598	1604	***5.96***
185	320703	3770597	1597	***6.77***
186	320751	3770602	1592	***6.90***
187	320797	3770599	1584	***5.84***
188	320834	3770588	1566	***8.77***
189	320859	3770584	1555	***8.80***
190	320899	3770570	1535	***8.66***
191	320934	3770570	1526	***8.96***
192	320970	3770573	1515	***8.97***
193	321022	3770570	1507	***8.87***
194	321089	3770574	1500	***8.13***
195	321145	3770588	1498	***8.95***
196	321189	3770568	1497	***7.96***
197	321221	3770573	1496	***7.63***
198	321286	3770569	1494	***8.16***
199	321365	3770566	1490	***7.26***
200	321445	3770571	1485	***7.96***
201	321532	3770570	1480	***8.88***
202	321632	3770574	1474	***8.14***
203	321734	3770574	1470	***8.72***
204	321836	3770592	1463	***9.08***
205	320521	3770316	1612	***5.85***
206	320541	3770287	1597	***7.46***
207	320564	3770249	1575	***8.07***
208	320579	3770223	1559	***9.26***
209	320626	3770233	1552	***7.76***
210	320694	3770227	1544	***7.79***
211	320750	3770198	1536	***7.36***
212	320796	3770168	1531	***8.93***
213	320853	3770160	1525	***9.00***
214	320901	3770147	1520	***9.18***
215	320953	3770149	1513	***9.15***
216	320999	3770145	1508	***8.95***
217	321064	3770152	1503	***9.40***
218	321106	3770150	1500	***9.02***
219	321155	3770148	1498	***9.20***
220	321222	3770151	1495	***8.97***
221	321293	3770158	1492	***8.65***
222	321354	3770165	1487	***8.32***
223	321453	3770156	1482	***9.19***
224	321555	3770144	1482	***9.33***
225	321659	3770128	1479	***9.23***
226	321756	3770134	1476	***9.31***
227	321848	3770145	1476	***9.31***
228	321948	3770146	1472	***9.27***
229	322054	3770137	1463	***9.29***
230	322154	3770158	1464	***9.11***
		pH Line 8		
231	320403	3769625	1584	***7.32***
232	320449	3769615	1574	***8.85***
233	320496	3769616	1563	***9.13***
234	320550	3769617	1555	***8.57***
235	320601	3769616	1544	***9.11***
236	320650	3769616	1534	***9.00***
237	320709	3769616	1522	***9.10***
238	320748	3769620	1516	***9.62***
239	320800	3769623	1509	***9.47***
240	320851	3769630	1505	***9.10***
241	320899	3769641	1503	***9.02***
242	320946	3769638	1501	***9.07***
243	321015	3769632	1500	***8.44***
244	321099	3769670	1496	***8.92***
245	321150	3769698	1494	***8.95***
246	321200	3769729	1493	***8.96***
247	321250	3769766	1492	***8.93***
248	321300	3769798	1491	***8.99***
249	321401	3769842	1487	***9.00***
250	321450	3769856	1486	***9.16***
251	321500	3769863	1484	***9.20***
252	321550	3769891	1483	***9.19***
253	321600	3769914	1482	***9.06***
254	321651	3769944	1481	***9.05***
255	321702	3769956	1478	***9.09***
256	321750	3769999	1477	***9.18***
257	321800	3770033	1476	***8.94***
258	321851	3770062	1475	***9.06***
259	321911	3770097	1473	***9.08***

Appendix 5.1 Histograms and cumulative probability plots for EL Oxide Suite Elements. Elements with extreme outliers were re-plotted without outlying points to better visualize distribution of data.

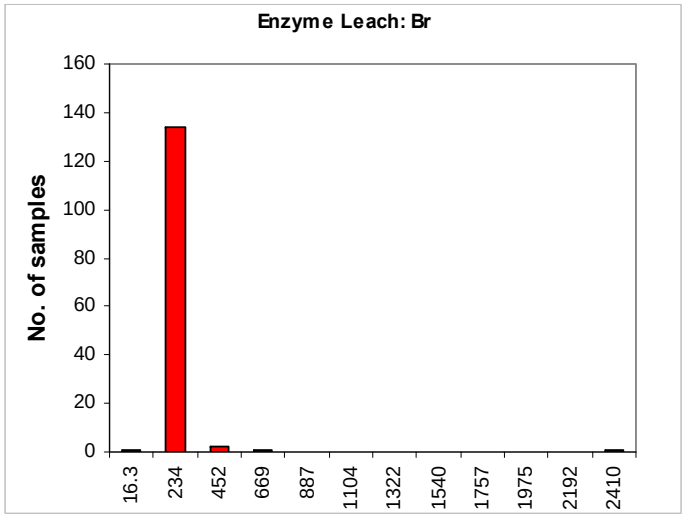

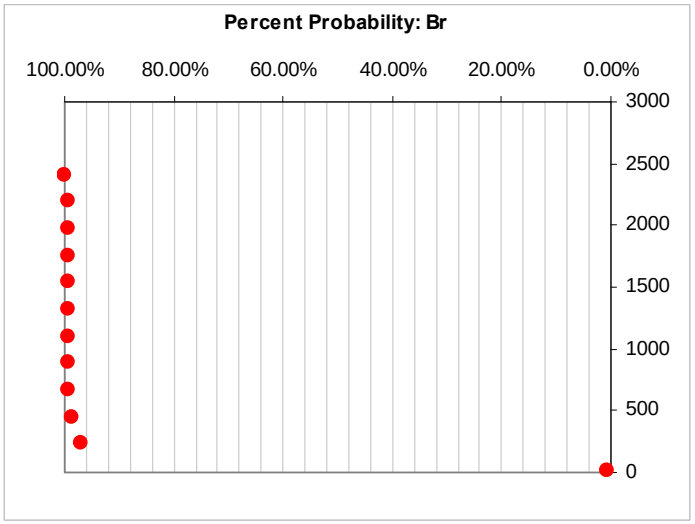

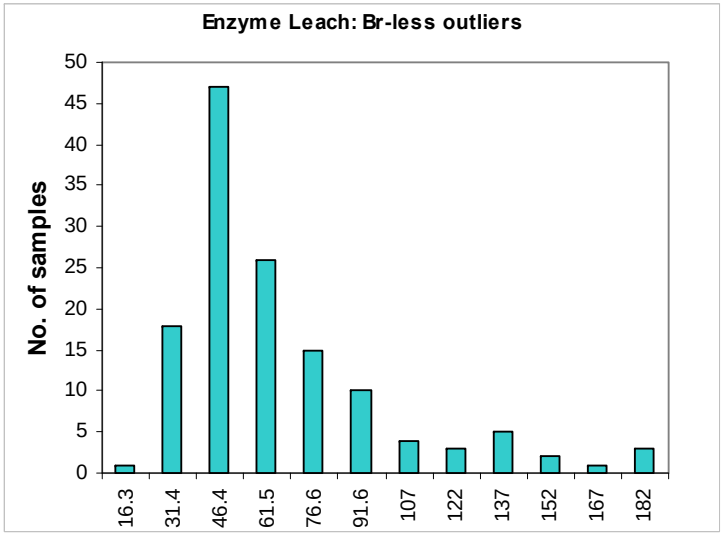

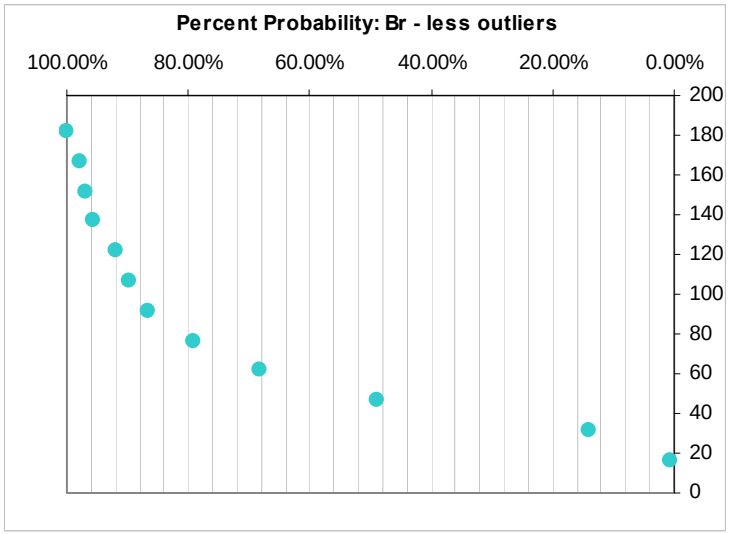

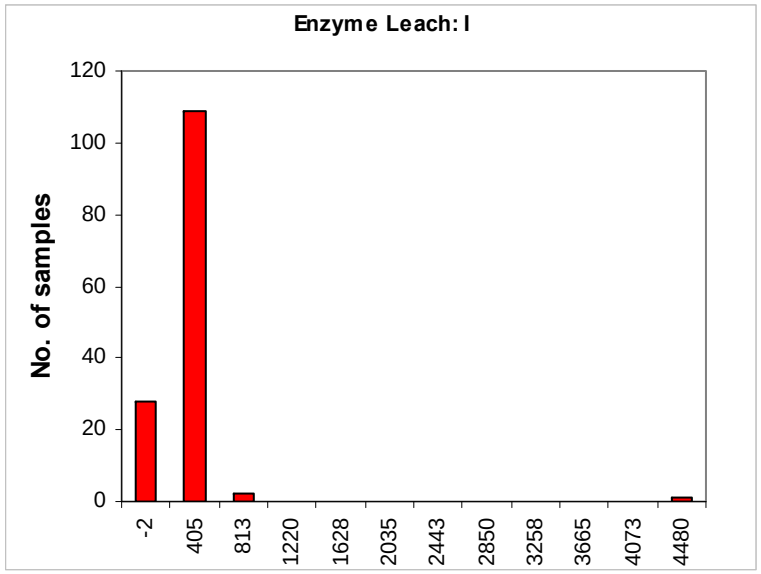
Enzyme Leach: I
No. of samples
120
100
80
60
40
20
0
-2
405
813
1220
1628
2035
2443
2850
3258
3665
4073
4480

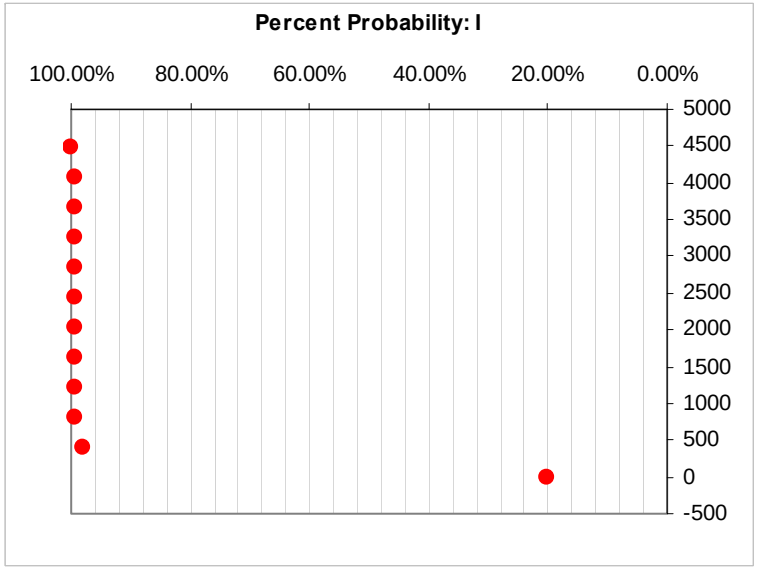
Percent Probability: I
100.00%
80.00%
60.00%
40.00%
20.00%
0.00%
5000
4500
4000
3500
3000
2500
2000
1500
1000
500
0
-500

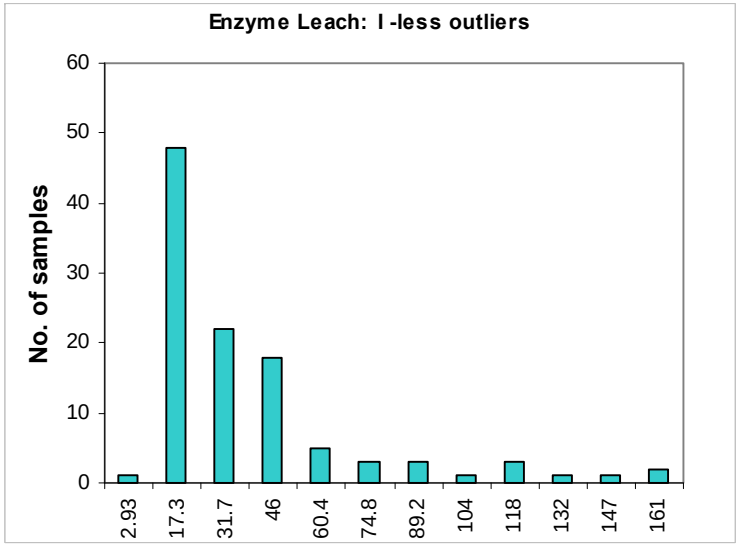
Enzyme Leach: I -less outliers
No. of samples
60
50
40
30
20
10
0
2.93
17.3
31.7
46
60.4
74.8
89.2
104
118
132
147
161

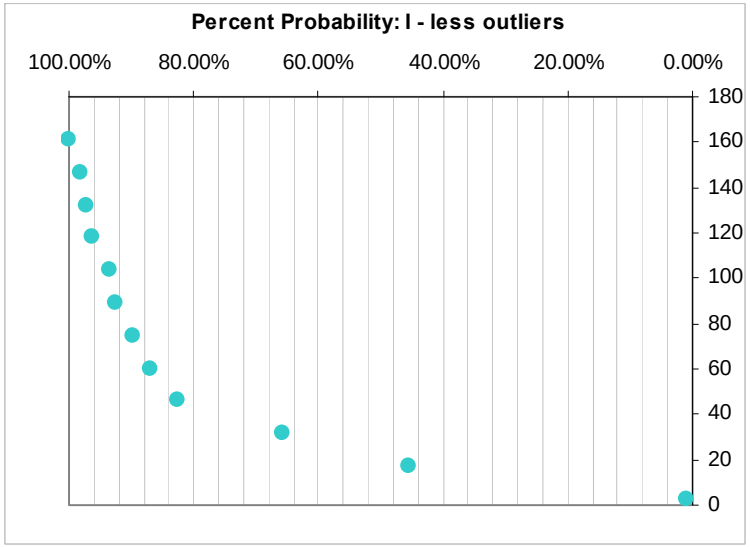
Percent Probability: I - less outliers
100.00%
80.00%
60.00%
40.00%
20.00%
0.00%
180
160
140
120
100
80
60
40
20
0

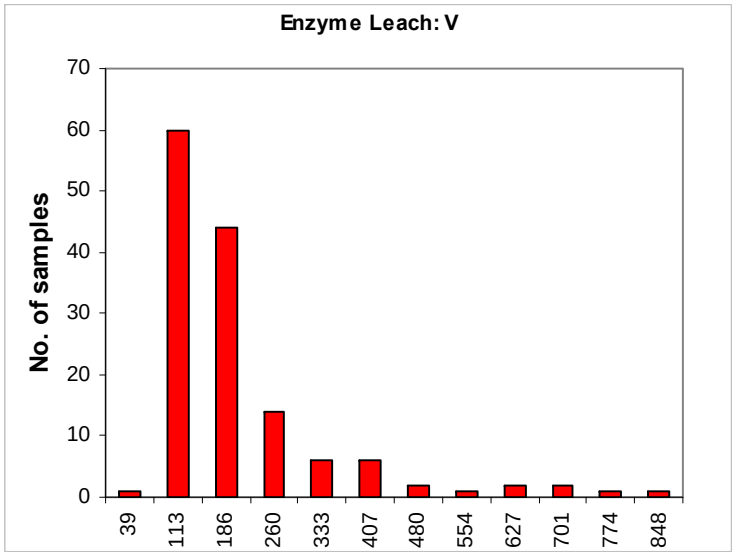
Enzyme Leach: V
No. of samples
70
60
50
40
30
20
10
0
39
113
186
260
333
407
480
554
627
701
774
848

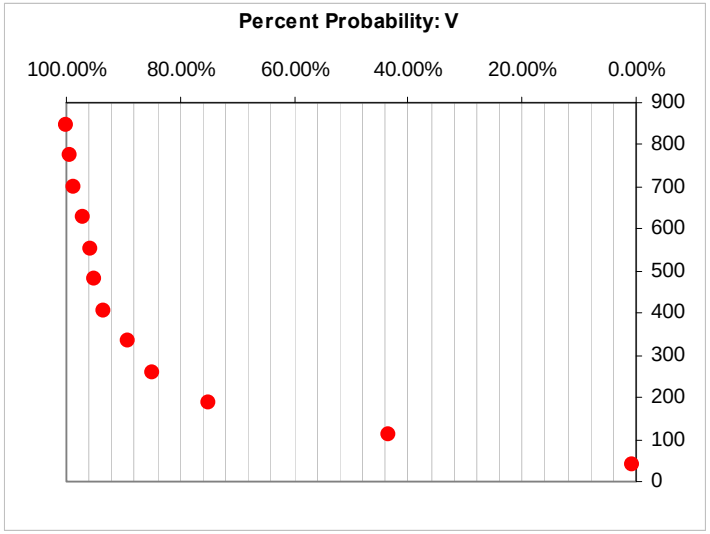
Percent Probability: V
100.00%
80.00%
60.00%
40.00%
20.00%
0.00%
900
800
700
600
500
400
300
200
100
0

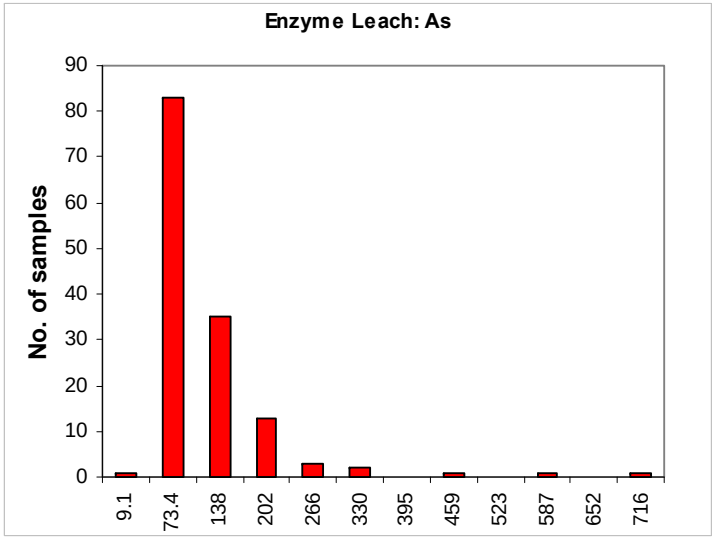
Enzyme Leach: As
No. of samples
90
80
70
60
50
40
30
20
10
0
9.1
73.4
138
202
266
330
395
459
523
587
652
716

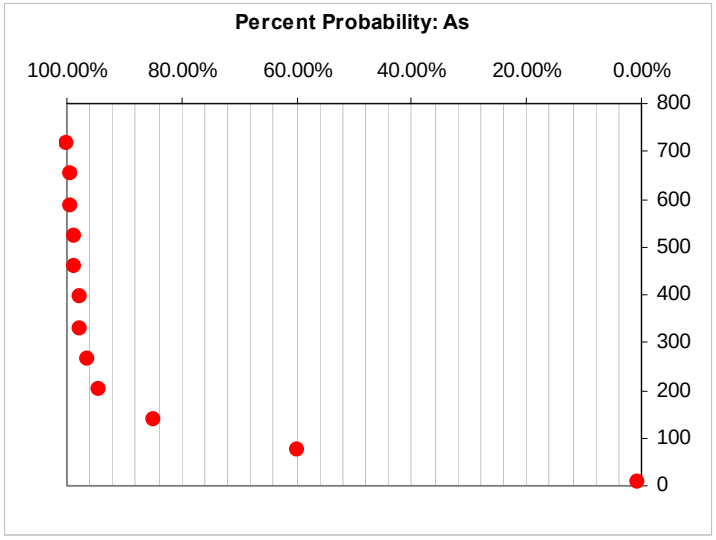
Percent Probability: As
100.00%
80.00%
60.00%
40.00%
20.00%
0.00%
800
700
600
500
400
300
200
100
0

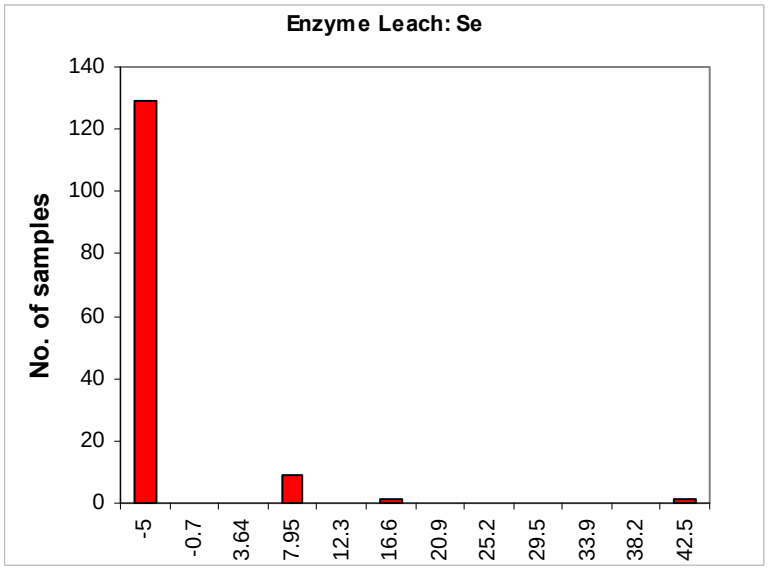
Enzyme Leach: Se
No. of samples
140
120
100
80
60
40
20
0
-5
-0.7
3.64
7.95
12.3
16.6
20.9
25.2
29.5
33.9
38.2
42.5

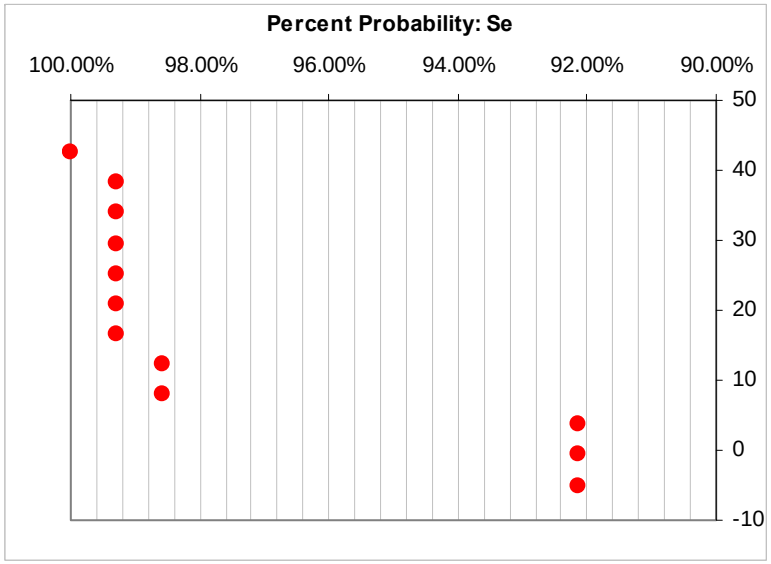
Percent Probability: Se
100.00%
98.00%
96.00%
94.00%
92.00%
90.00%
50
40
30
20
10
0
-10

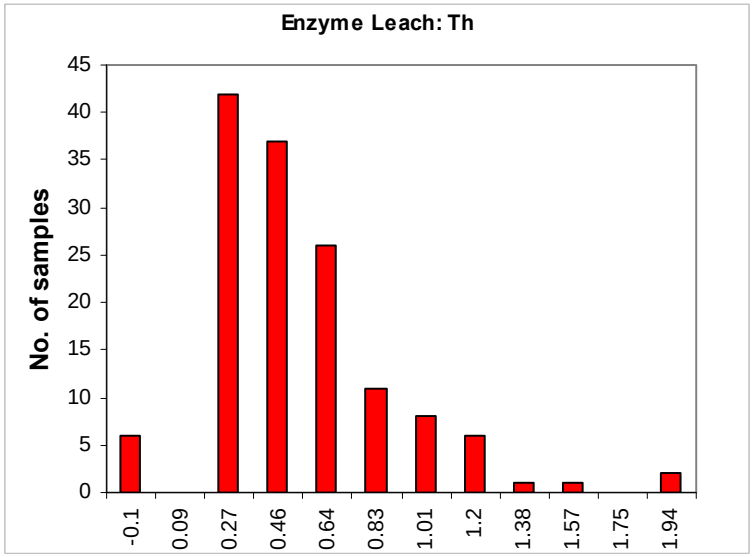
Enzyme Leach: Th
No. of samples
45
40
35
30
25
20
15
10
5
0
-0.1
0.09
0.27
0.46
0.64
0.83
1.01
1.2
1.38
1.57
1.75
1.94

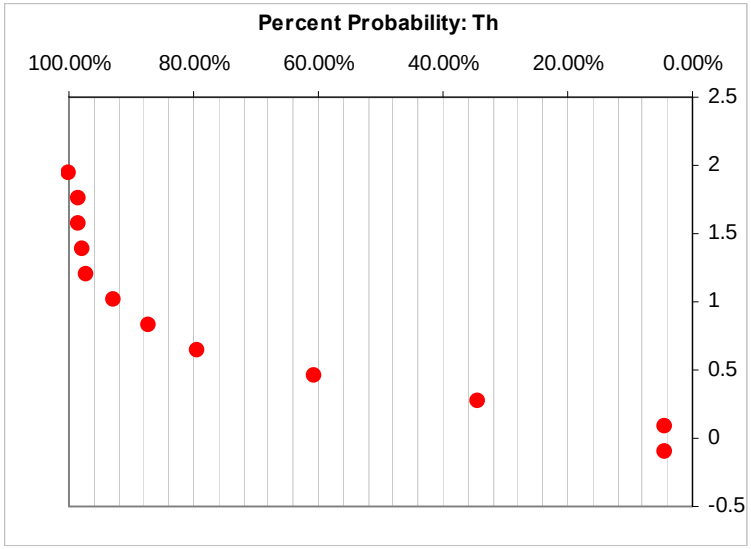
Percent Probability: Th
100.00%
80.00%
60.00%
40.00%
20.00%
0.00%
2.5
2
1.5
1
0.5
0
-0.5

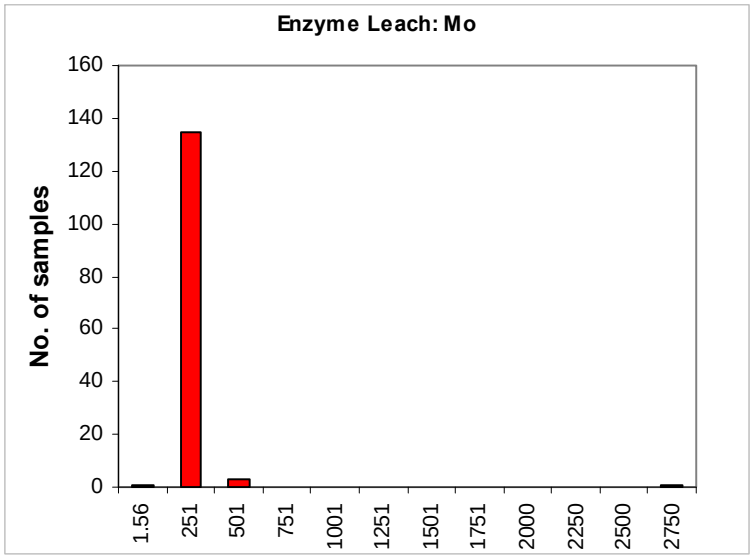
Enzyme Leach: Mo
No. of samples
160
140
120
100
80
60
40
20
0
1.56
251
501
751
1001
1251
1501
1751
2000
2250
2500
2750

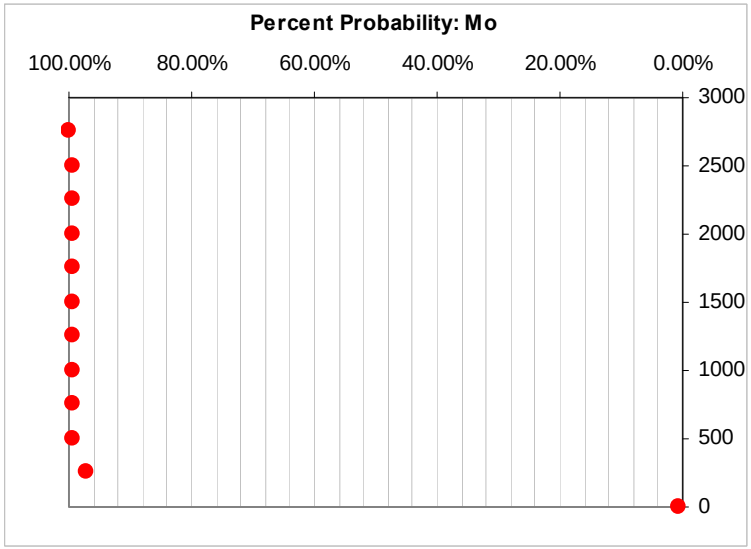
Percent Probability: Mo
100.00%
80.00%
60.00%
40.00%
20.00%
0.00%
3000
2500
2000
1500
1000
500
0

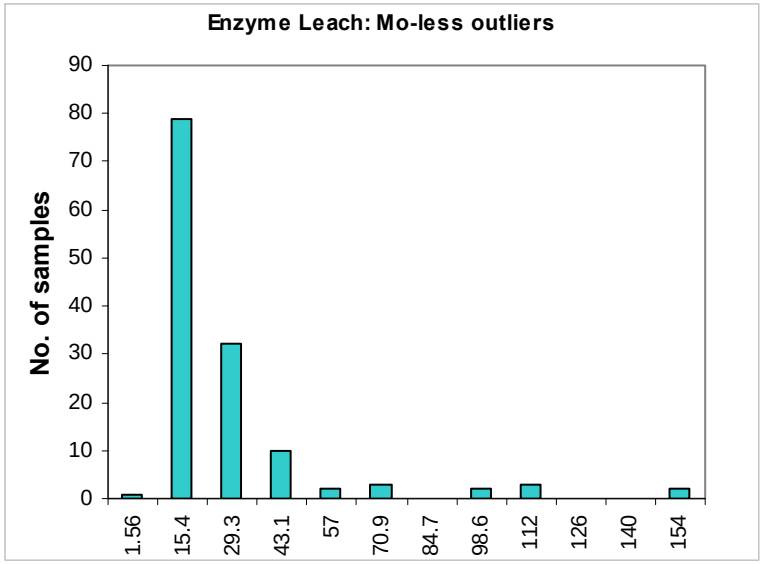
Enzyme Leach: Mo-less outliers
No. of samples
90
80
70
60
50
40
30
20
10
0
1.56
15.4
29.3
43.1
57
70.9
84.7
98.6
112
126
140
154

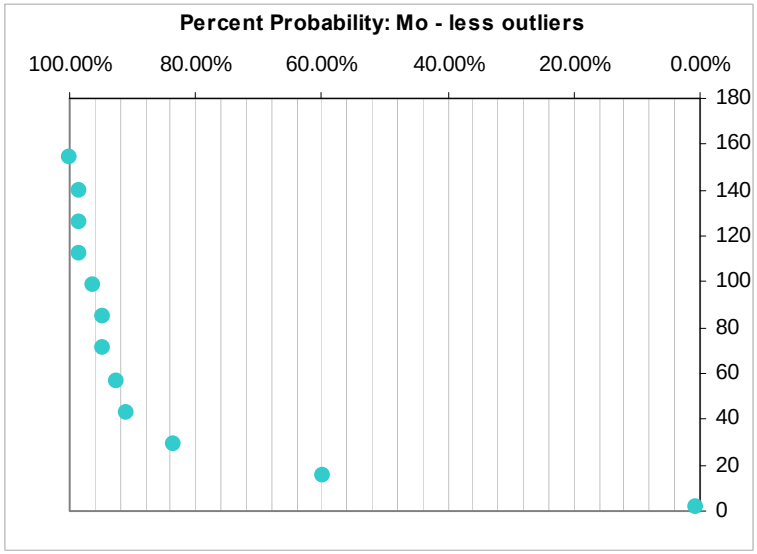
Percent Probability: Mo - less outliers
100.00%
80.00%
60.00%
40.00%
20.00%
0.00%
180
160
140
120
100
80
60
40
20
0

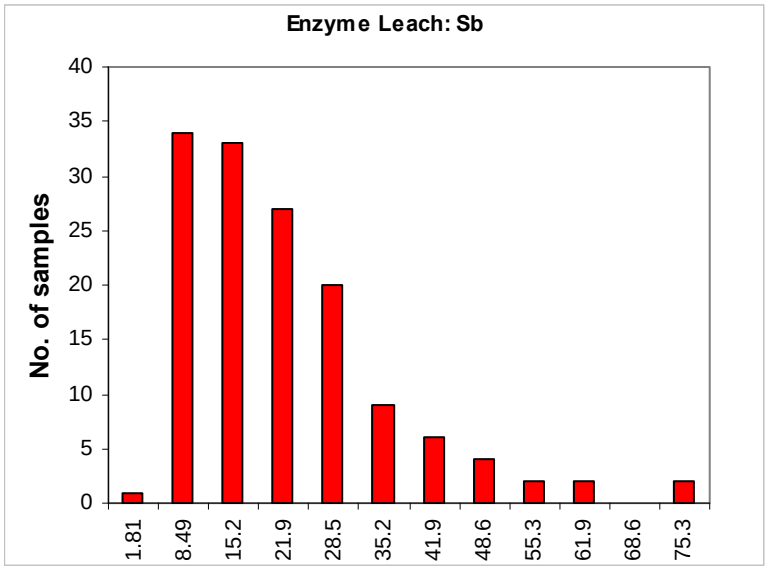
Enzyme Leach: Sb
No. of samples
40
35
30
25
20
15
10
5
0
1.81
8.49
15.2
21.9
28.5
35.2
41.9
48.6
55.3
61.9
68.6
75.3

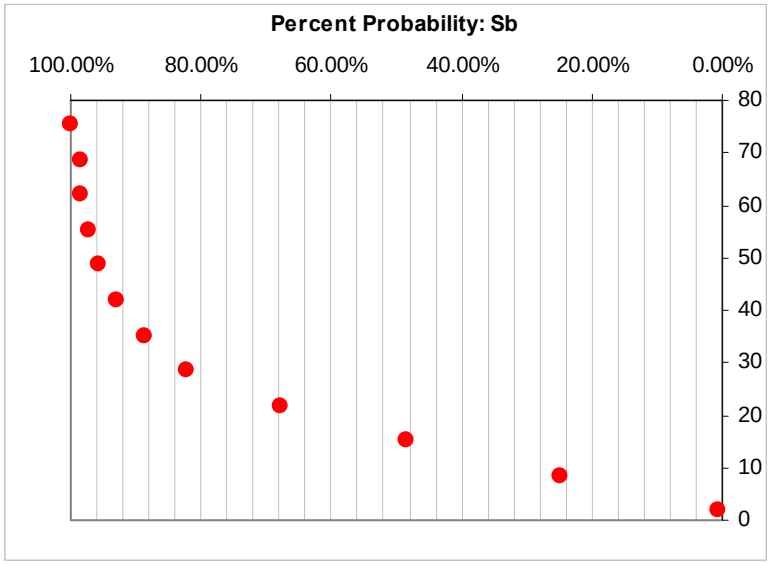
Percent Probability: Sb
100.00%
80.00%
60.00%
40.00%
20.00%
0.00%
80
70
60
50
40
30
20
10
0

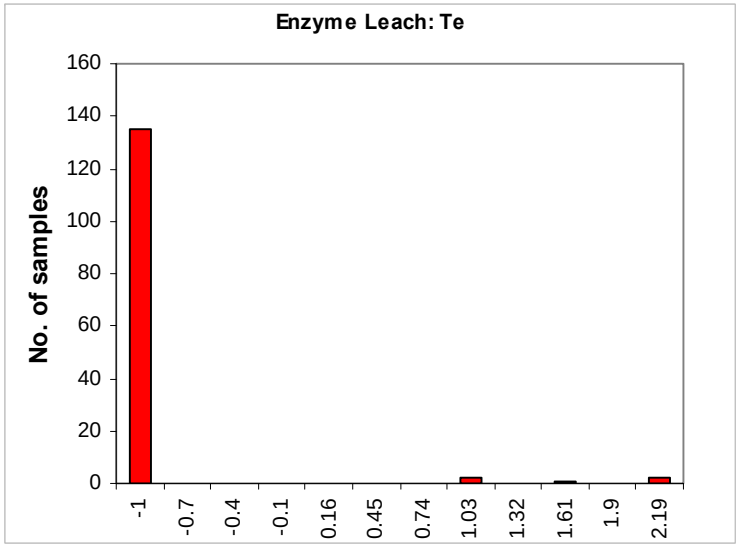
Enzyme Leach: Te
No. of samples
160
140
120
100
80
60
40
20
0
-1
-0.7
-0.4
-0.1
0.16
0.45
0.74
1.03
1.32
1.61
1.9
2.19

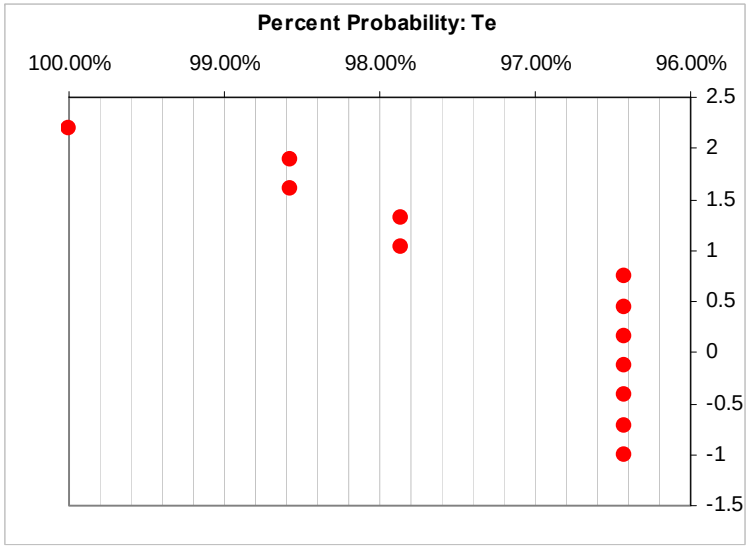
Percent Probability: Te
100.00%
99.00%
98.00%
97.00%
96.00%
2.5
2
1.5
1
0.5
0
-0.5
-1
-1.5

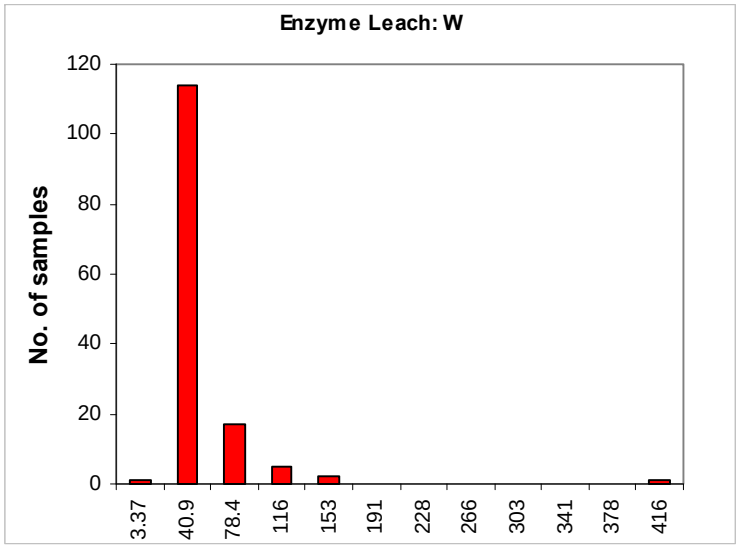
Enzyme Leach: W
No. of samples
120
100
80
60
40
20
0
3.37
40.9
78.4
116
153
191
228
266
303
341
378
416

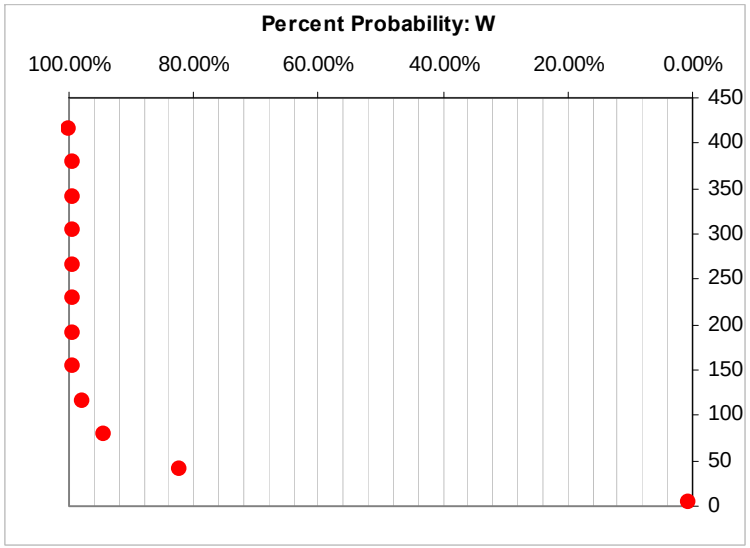
Percent Probability: W
100.00%
80.00%
60.00%
40.00%
20.00%
0.00%
450
400
350
300
250
200
150
100
50
0

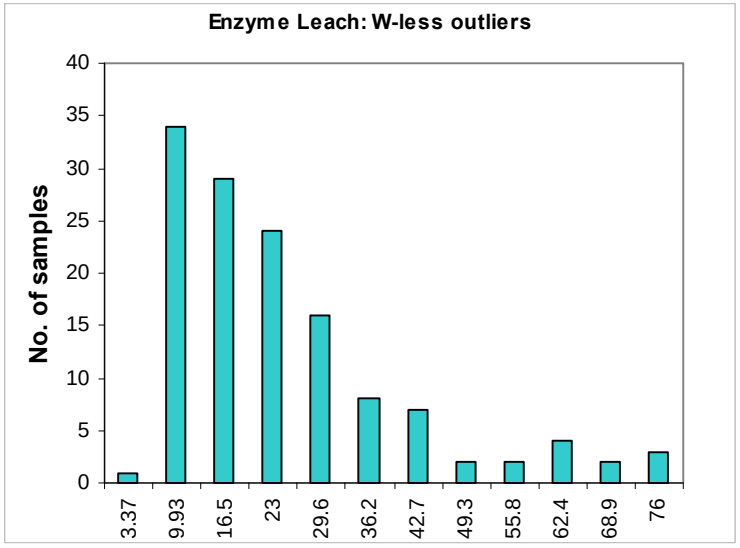
Enzyme Leach: W-less outliers
No. of samples
40
35
30
25
20
15
10
5
0
3.37
9.93
16.5
23
29.6
36.2
42.7
49.3
55.8
62.4
68.9
76

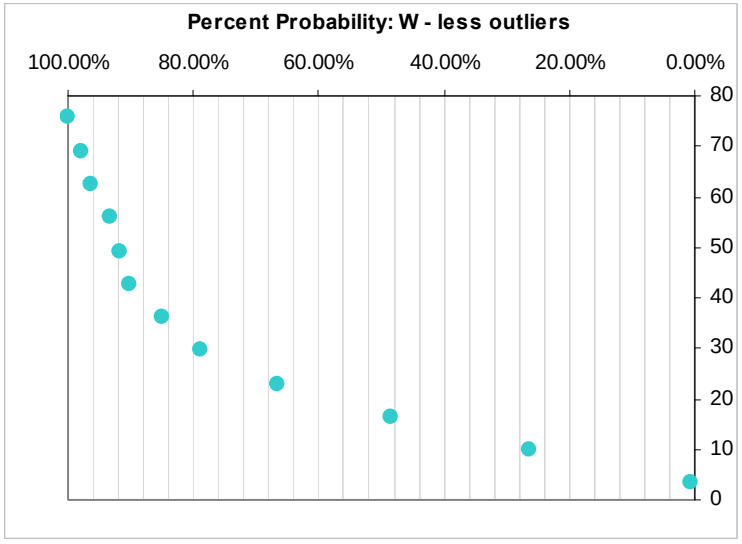
Percent Probability: W - less outliers
100.00%
80.00%
60.00%
40.00%
20.00%
0.00%
80
70
60
50
40
30
20
10
0

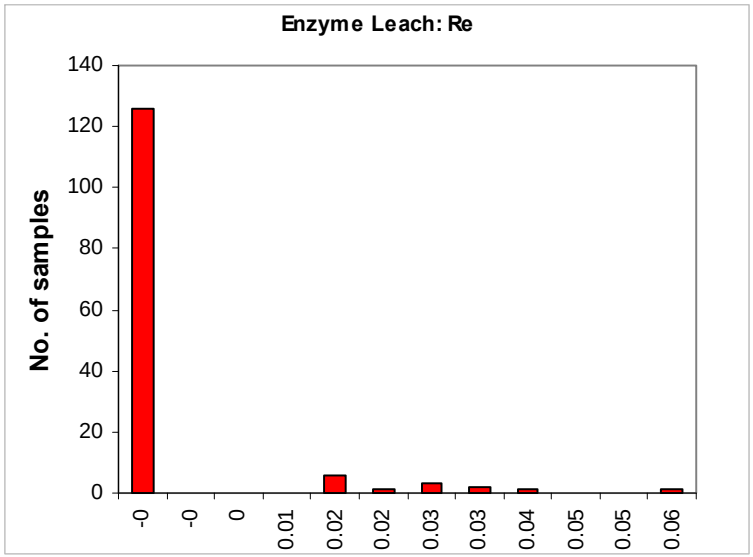
Enzyme Leach: Re
No. of samples
140
120
100
80
60
40
20
0
-0
-0
0
0.01
0.02
0.02
0.03
0.03
0.04
0.05
0.05
0.06

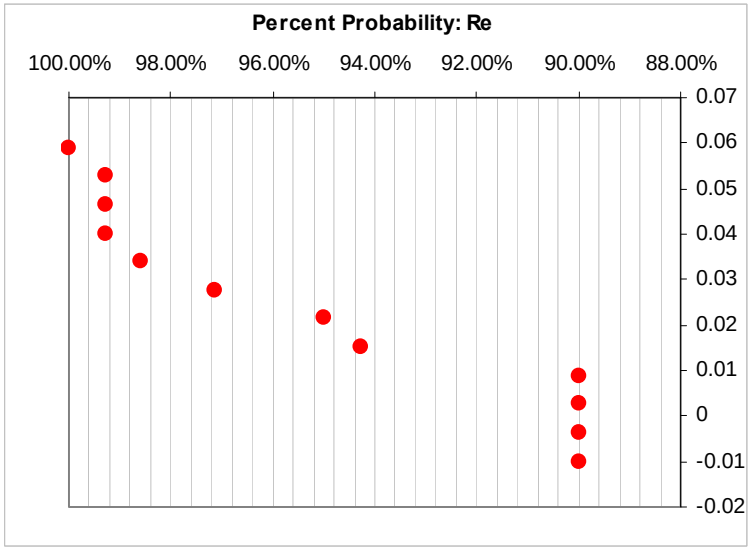
Percent Probability: Re
100.00%
98.00%
96.00%
94.00%
92.00%
90.00%
88.00%
0.07
0.06
0.05
0.04
0.03
0.02
0.01
0
-0.01
-0.02

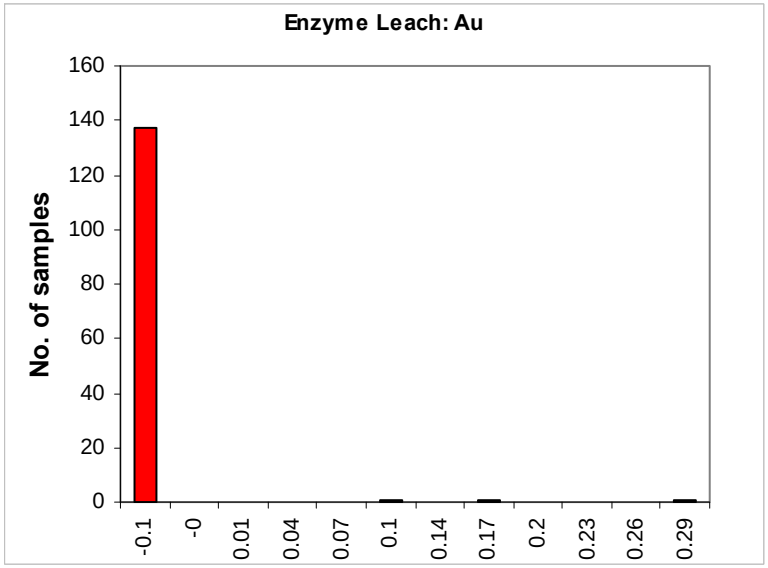
Enzyme Leach: Au
No. of samples
160
140
120
100
80
60
40
20
0
-0.1
-0
0.01
0.04
0.07
0.1
0.14
0.17
0.2
0.23
0.26
0.29

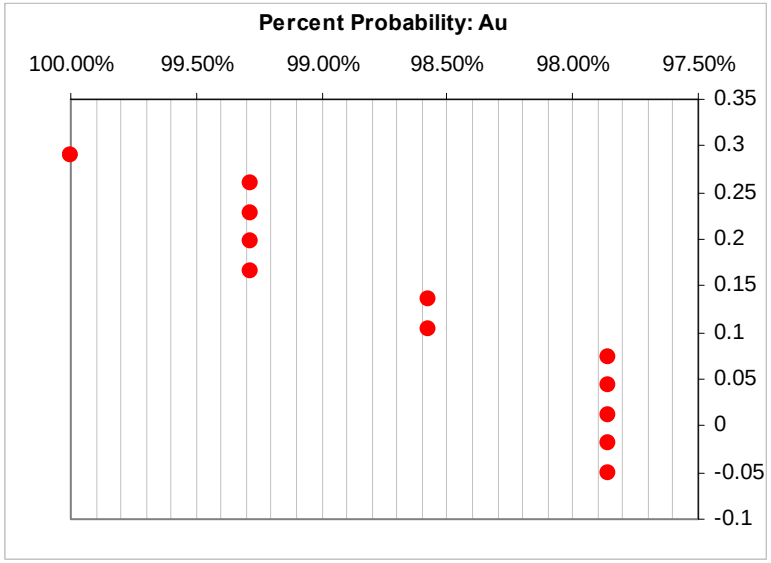
Percent Probability: Au
100.00%
99.50%
99.00%
98.50%
98.00%
97.50%
0.35
0.3
0.25
0.2
0.15
0.1
0.05
0
-0.05
-0.1

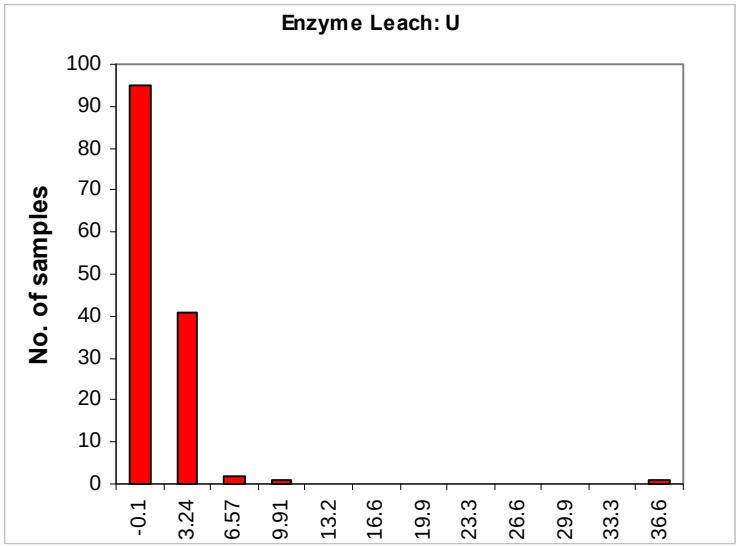
Enzyme Leach: U
No. of samples
100
90
80
70
60
50
40
30
20
10
0
-0.1
3.24
6.57
9.91
13.2
16.6
19.9
23.3
26.6
29.9
33.3
36.6

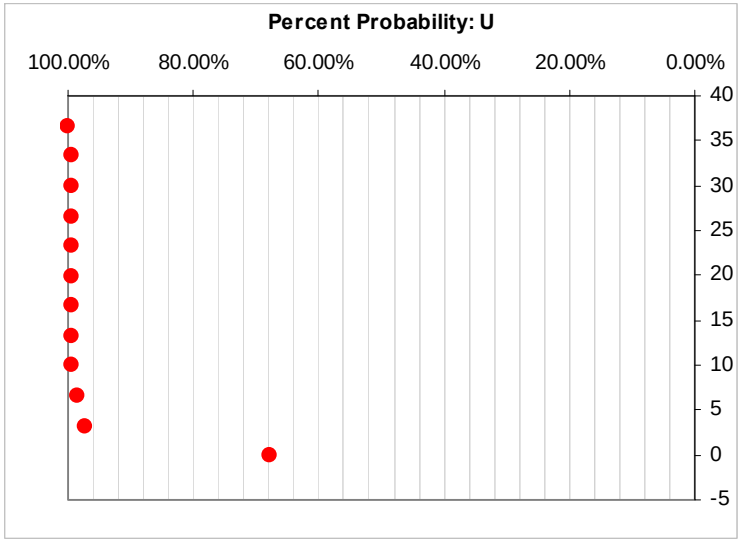
Percent Probability: U
100.00%
80.00%
60.00%
40.00%
20.00%
0.00%
40
35
30
25
20
15
10
5
0
-5

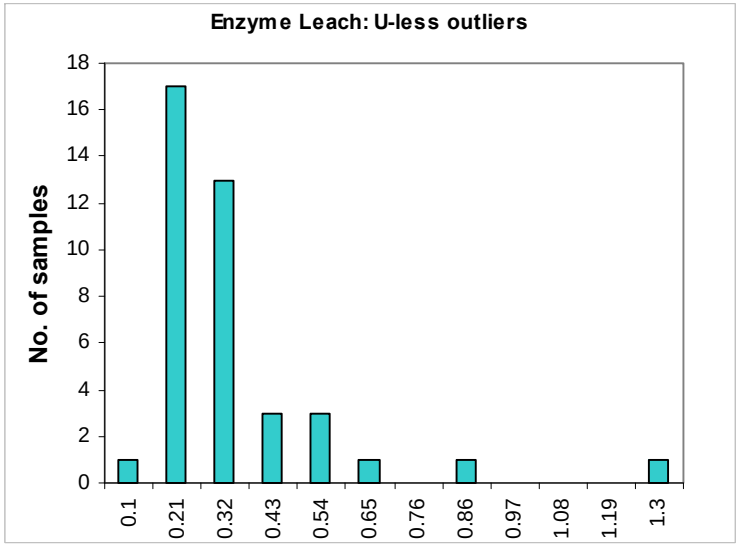
Enzyme Leach: U-less outliers
No. of samples
18
16
14
12
10
8
6
4
2
0
0.1
0.21
0.32
0.43
0.54
0.65
0.76
0.86
0.97
1.08
1.19
1.3

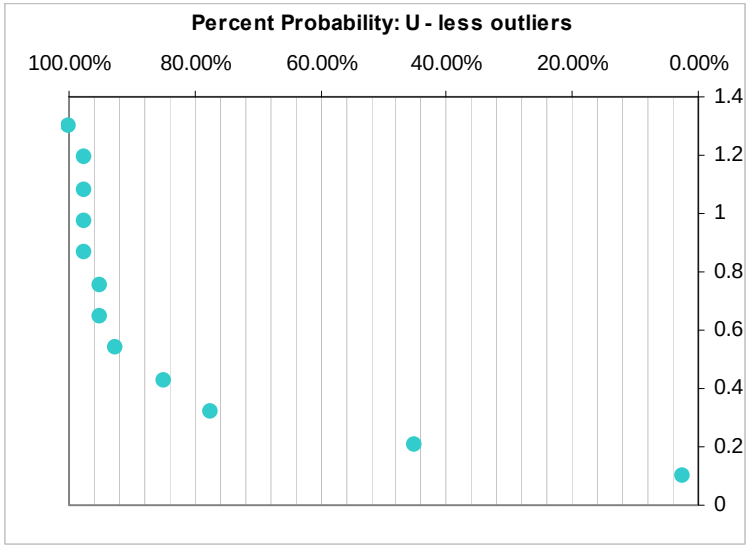
Percent Probability: U - less outliers
100.00%
80.00%
60.00%
40.00%
20.00%
0.00%
1.4
1.2
1
0.8
0.6
0.4
0.2
0

Appendix 5.2 Histograms and cumulative probability plots for EL base metals. Elements with extreme outliers were re-plotted without outlying points to better visualize distribution of data.

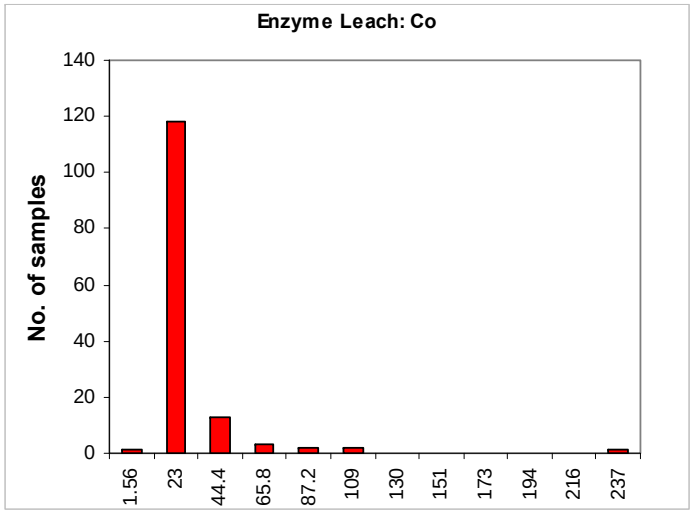

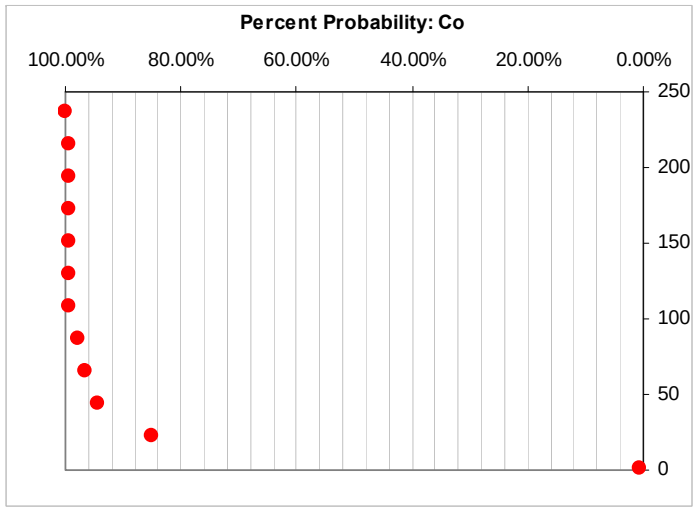

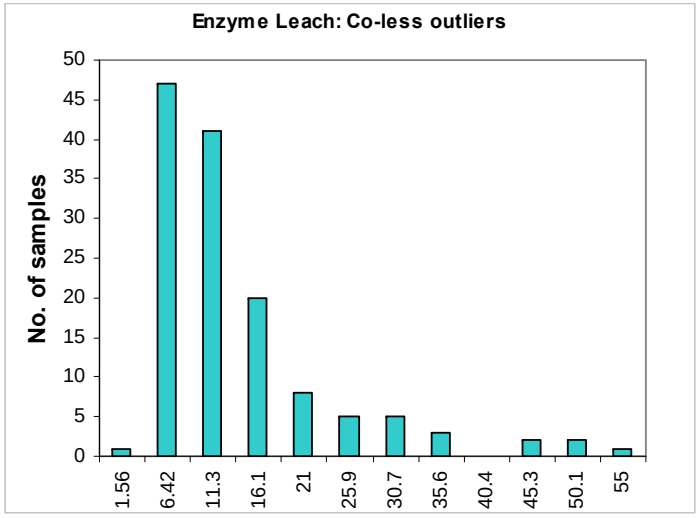

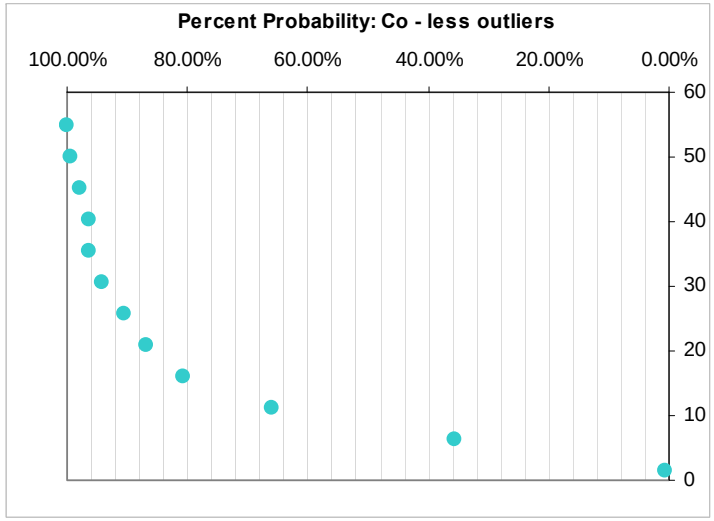

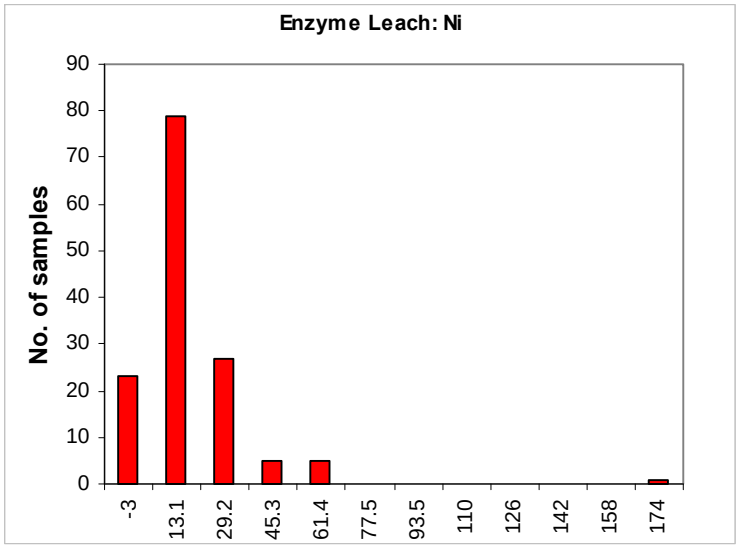
Enzyme Leach: Ni
No. of samples
90
80
70
60
50
40
30
20
10
0
-3
13.1
29.2
45.3
61.4
77.5
93.5
110
126
142
158
174

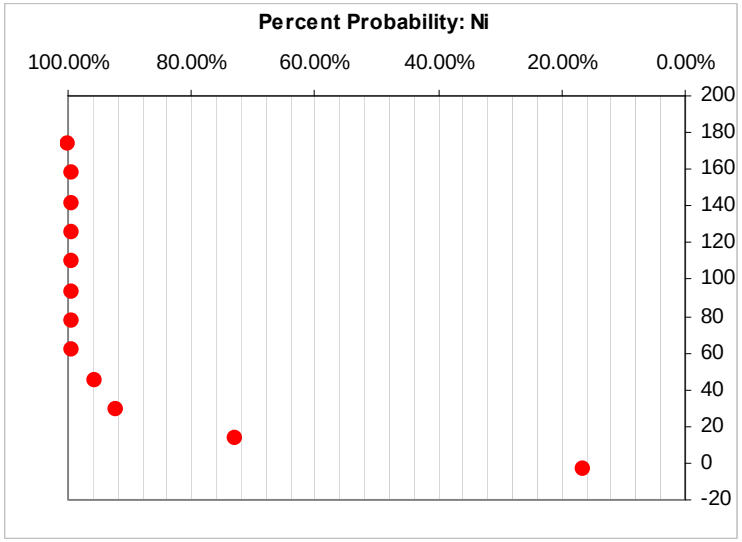
Percent Probability: Ni
100.00%
80.00%
60.00%
40.00%
20.00%
0.00%
200
180
160
140
120
100
80
60
40
20
0
-20

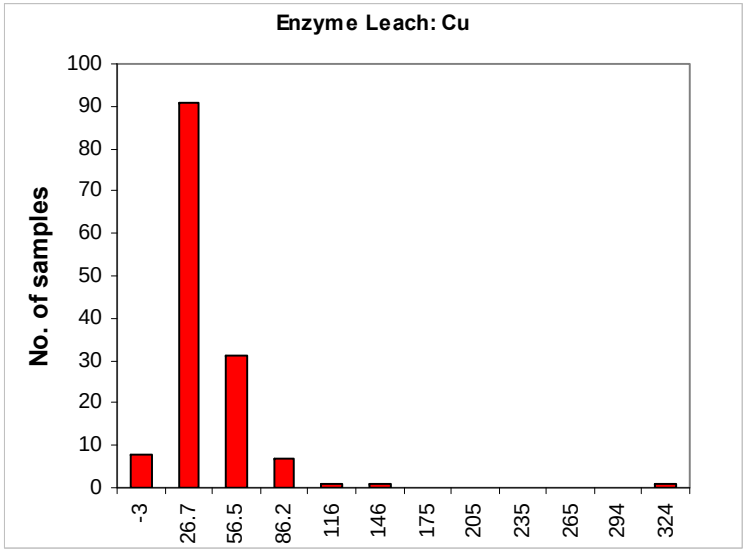
Enzyme Leach: Cu
No. of samples
100
90
80
70
60
50
40
30
20
10
0
-3
26.7
56.5
86.2
116
146
175
205
235
265
294
324

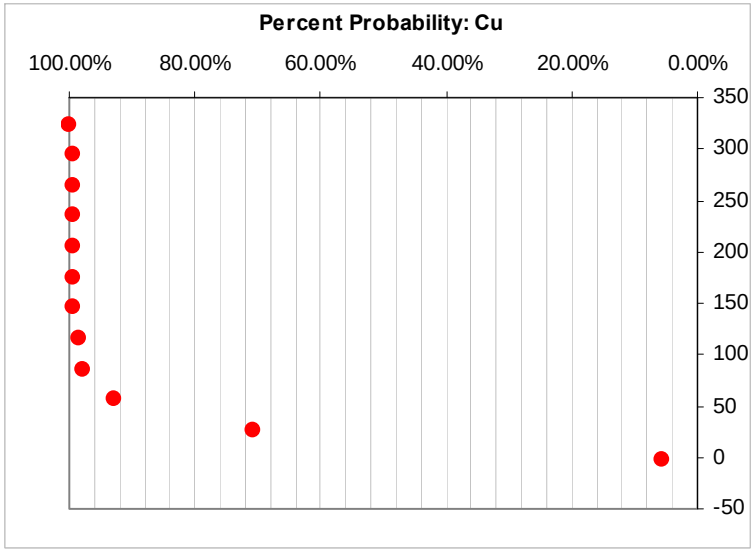
Percent Probability: Cu
100.00%
80.00%
60.00%
40.00%
20.00%
0.00%
350
300
250
200
150
100
50
0
-50

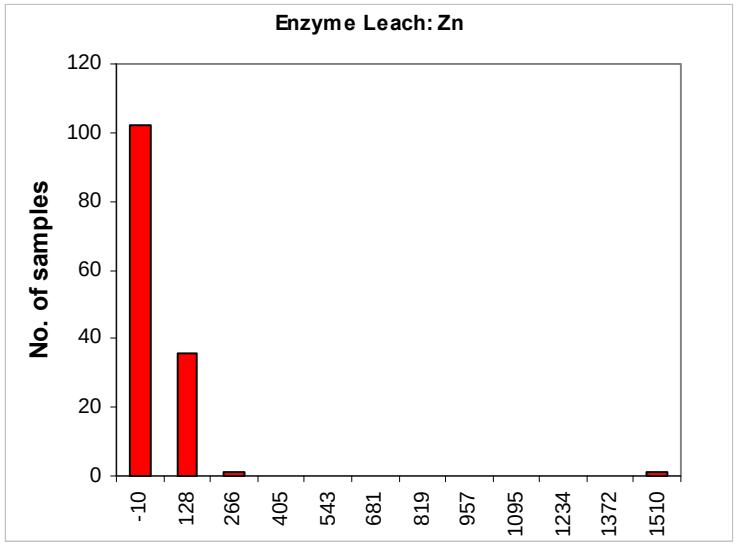
Enzyme Leach: Zn
No. of samples
120
100
80
60
40
20
0
-10
128
266
405
543
681
819
957
1095
1234
1372
1510

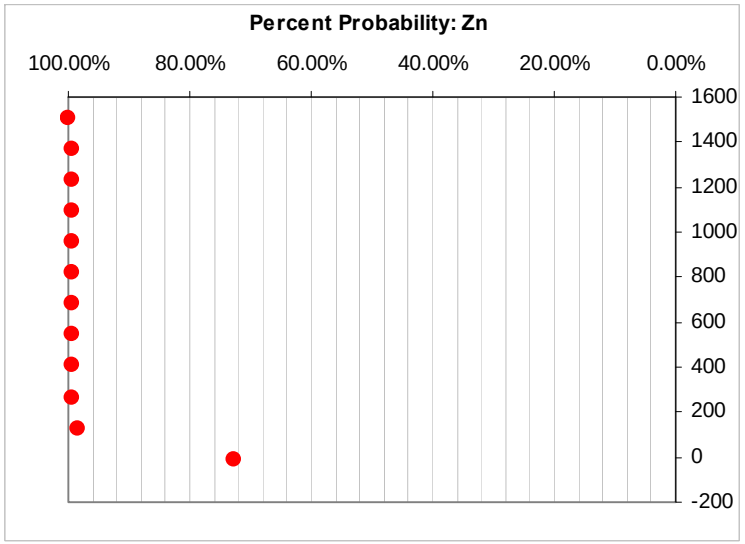
Percent Probability: Zn
100.00%
80.00%
60.00%
40.00%
20.00%
0.00%
1600
1400
1200
1000
800
600
400
200
0
-200

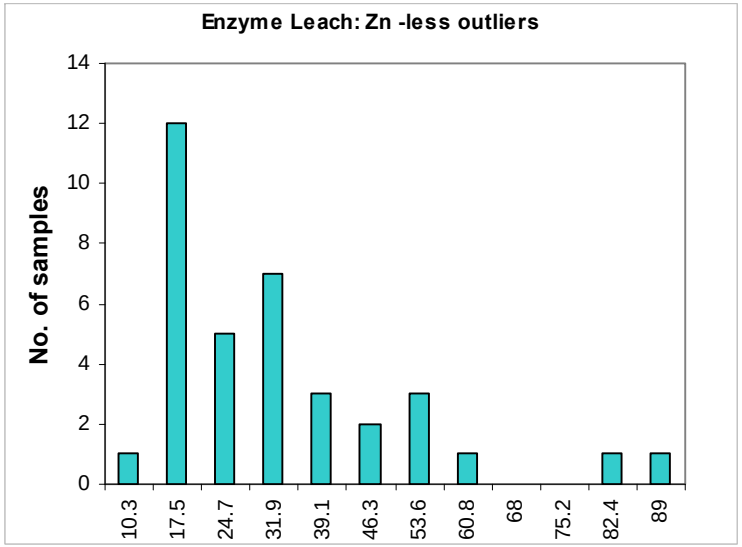
Enzyme Leach: Zn -less outliers
No. of samples
14
12
10
8
6
4
2
0
10.3
17.5
24.7
31.9
39.1
46.3
53.6
60.8
68
75.2
82.4
89

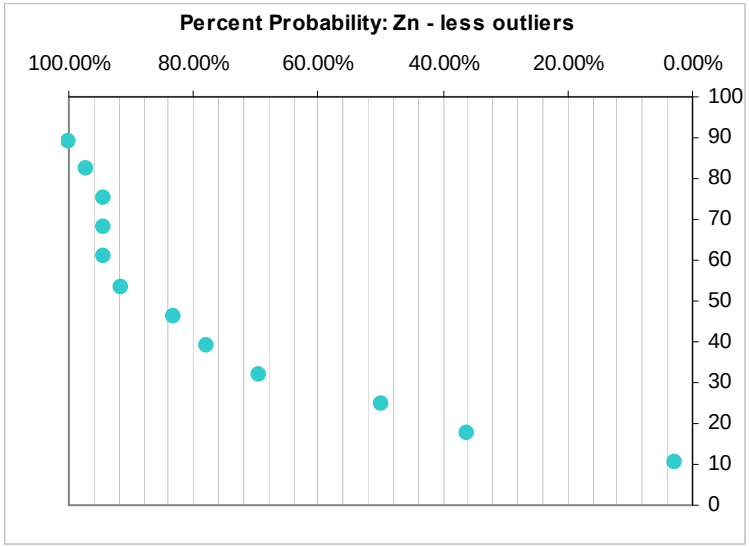
Percent Probability: Zn - less outliers
100.00%
80.00%
60.00%
40.00%
20.00%
0.00%
100
90
80
70
60
50
40
30
20
10
0

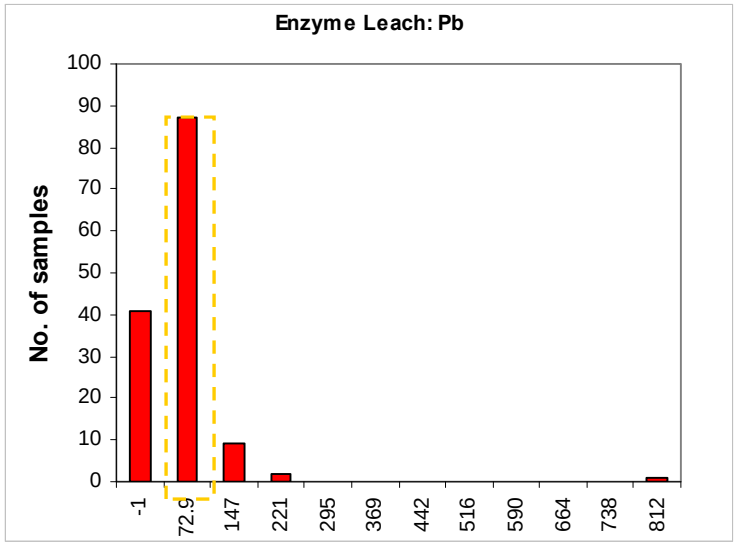
Enzyme Leach: Pb
No. of samples
100
90
80
70
60
50
40
30
20
10
0
-1
72.9
147
221
295
369
442
516
590
664
738
812

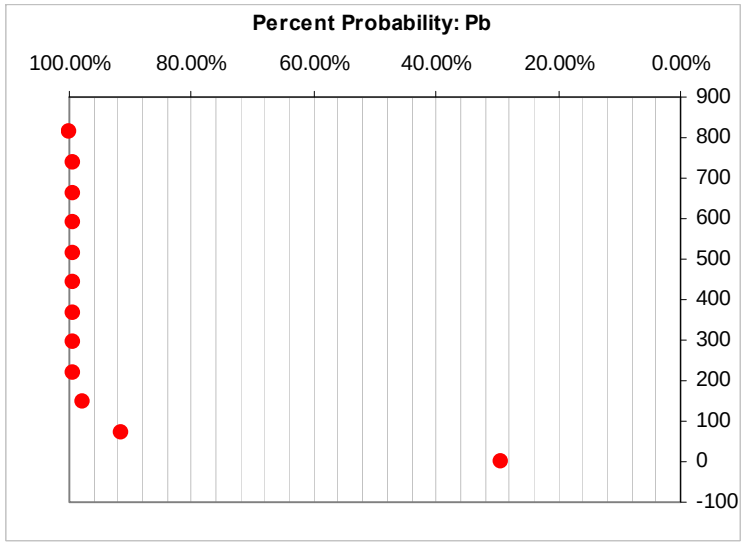
Percent Probability: Pb
100.00%
80.00%
60.00%
40.00%
20.00%
0.00%
900
800
700
600
500
400
300
200
100
0
-100

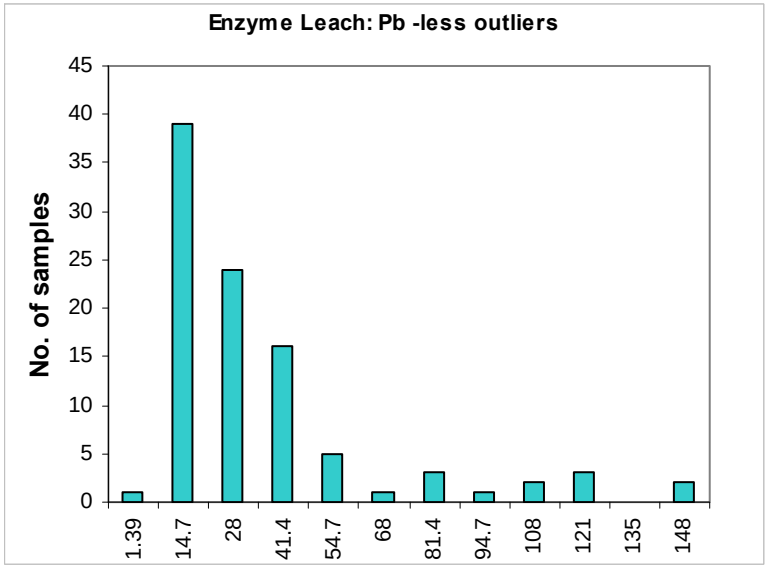
Enzyme Leach: Pb -less outliers
No. of samples
45
40
35
30
25
20
15
10
5
0
1.39
14.7
28
41.4
54.7
68
81.4
94.7
108
121
135
148

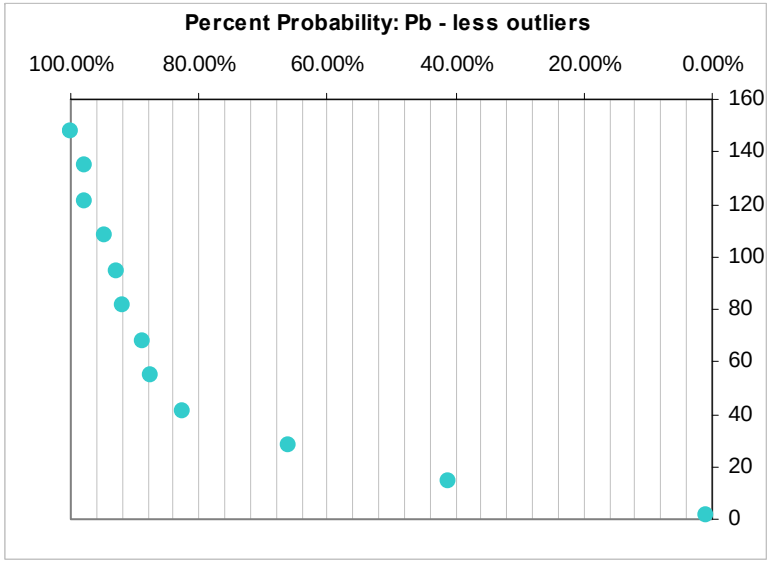
Percent Probability: Pb - less outliers
100.00%
80.00%
60.00%
40.00%
20.00%
0.00%
160
140
120
100
80
60
40
20
0

Appendix 5.3 Histograms and cumulative probability plots for EL Chalcophiles. Elements with extreme outliers were re-plotted without outlying points to better visualize distribution of data.

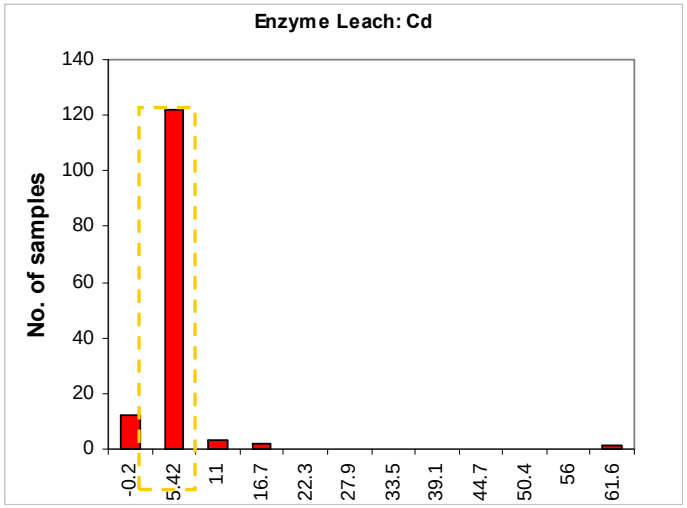

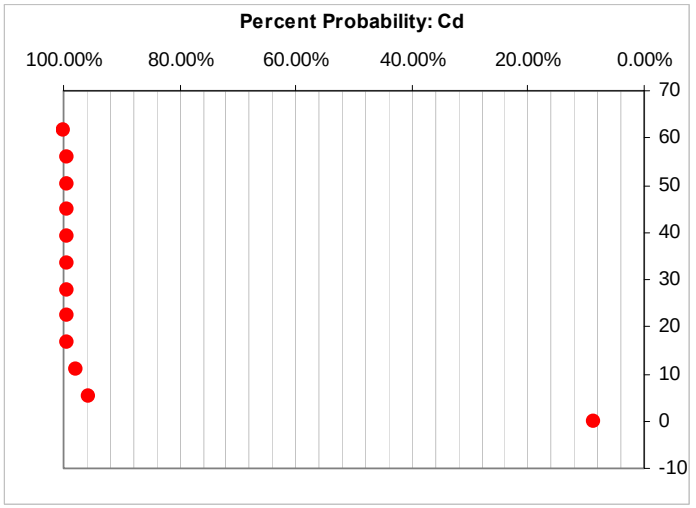

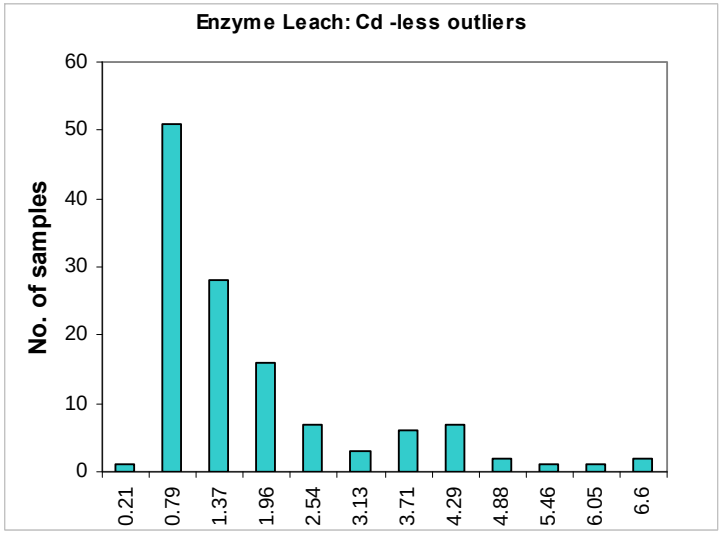

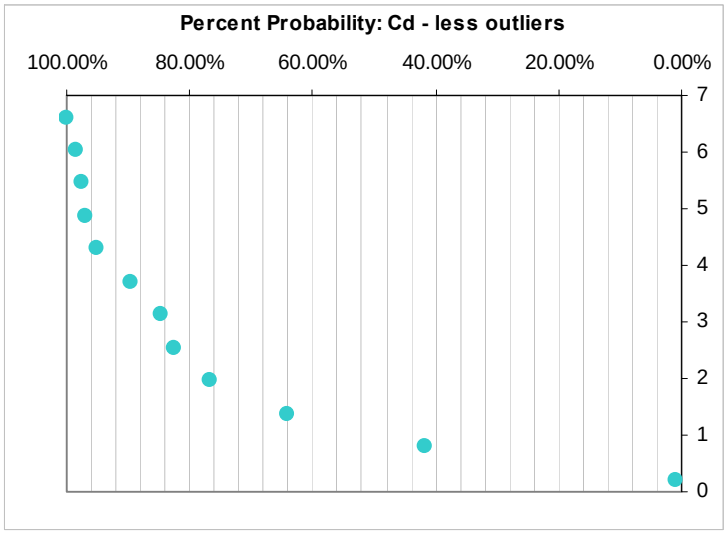

Appendix 5.4 Histograms and cumulative probability plots for EL HFSEs. Elements with extreme outliers were re-plotted without outlying points to better visualize distribution of data.

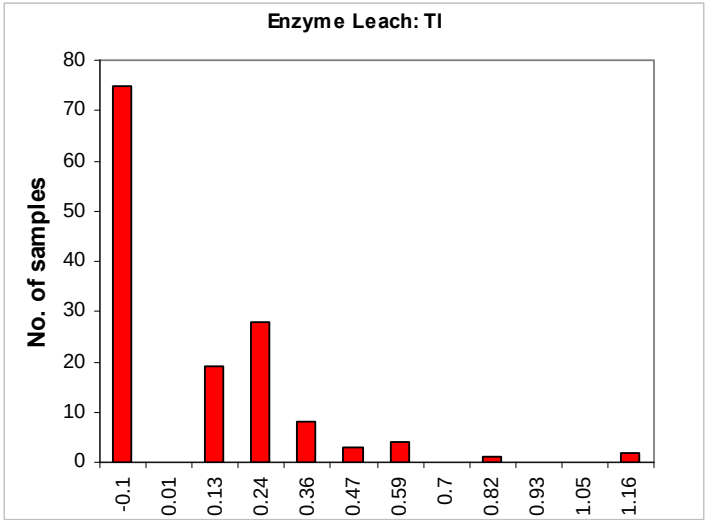

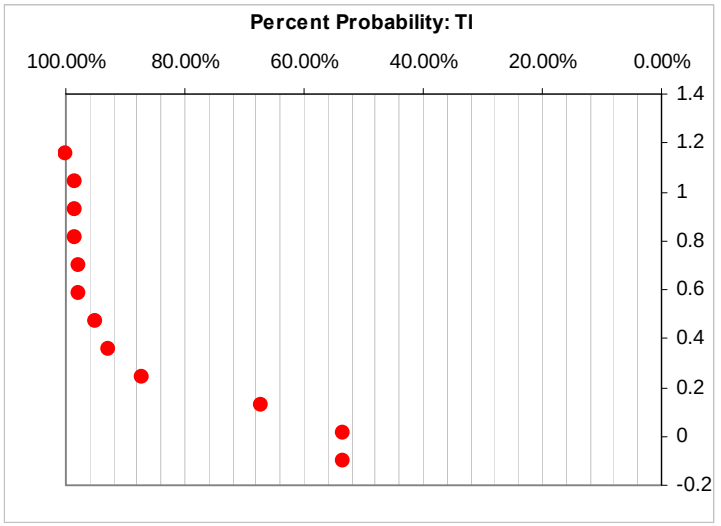

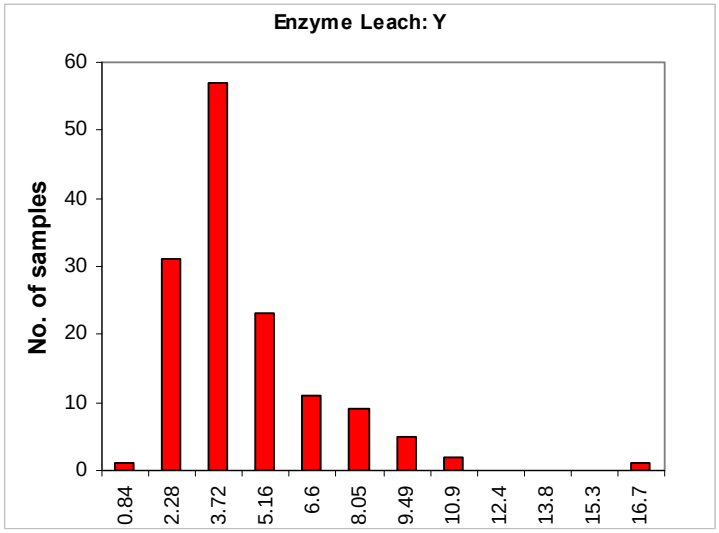

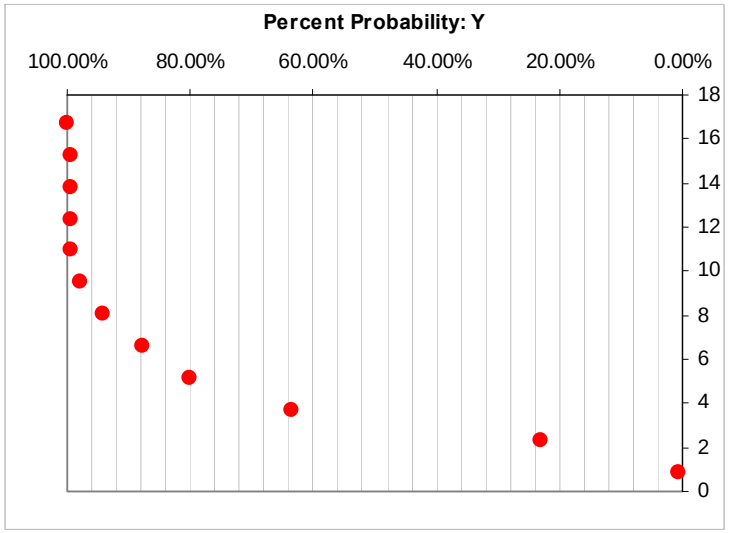

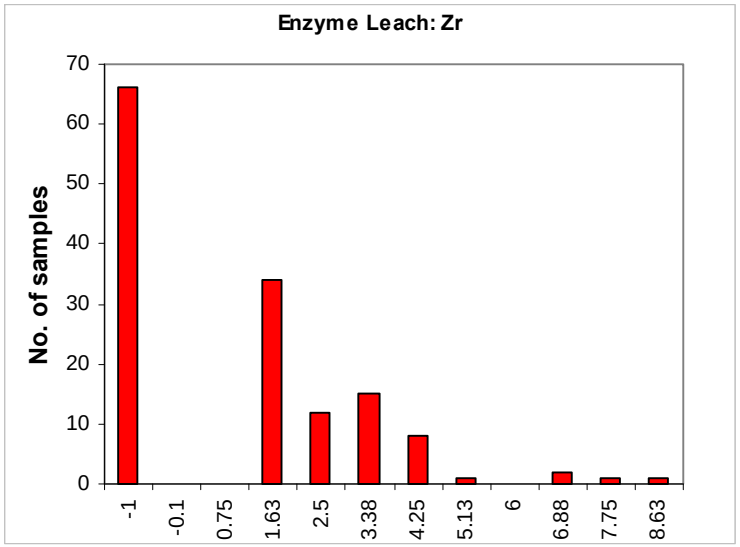
Enzyme Leach: Zr
No. of samples
70
60
50
40
30
20
10
0
-1
-0.1
0.75
1.63
2.5
3.38
4.25
5.13
6
6.88
7.75
8.63

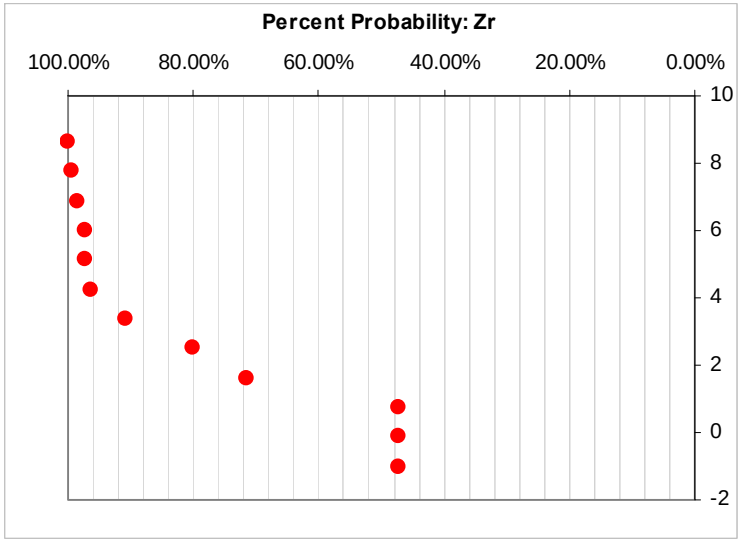
Percent Probability: Zr
100.00%
80.00%
60.00%
40.00%
20.00%
0.00%
10
8
6
4
2
0
-2

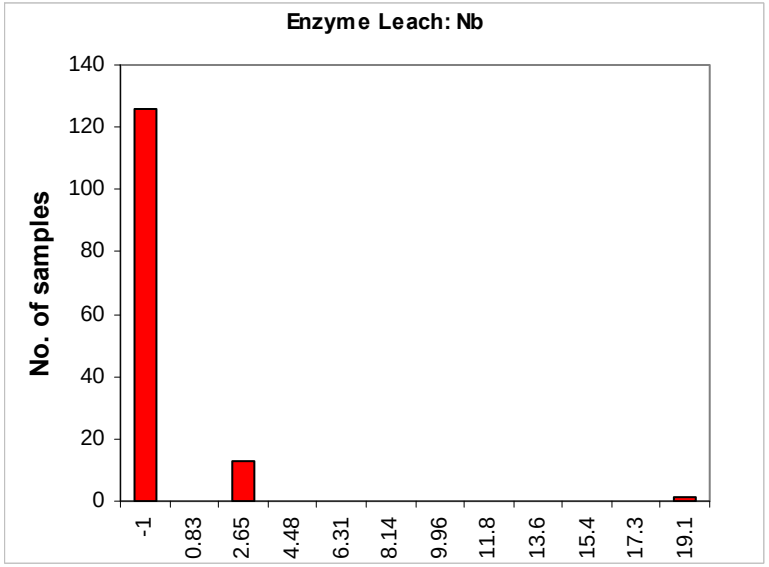
Enzyme Leach: Nb
No. of samples
140
120
100
80
60
40
20
0
-1
0.83
2.65
4.48
6.31
8.14
9.96
11.8
13.6
15.4
17.3
19.1

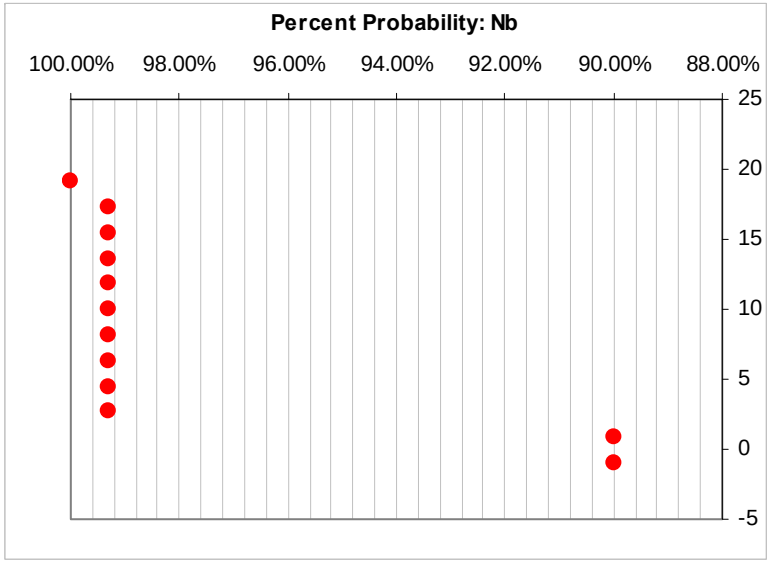
Percent Probability: Nb
100.00%
98.00%
96.00%
94.00%
92.00%
90.00%
88.00%
25
20
15
10
5
0
-5

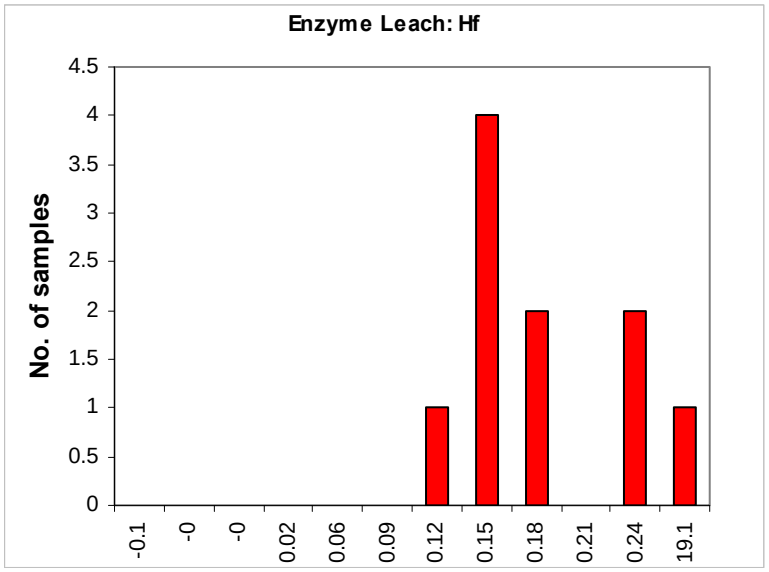
Enzyme Leach: Hf
No. of samples
4.5
4
3.5
3
2.5
2
1.5
1
0.5
0
-0.1
-0
-0
0.02
0.06
0.09
0.12
0.15
0.18
0.21
0.24
19.1

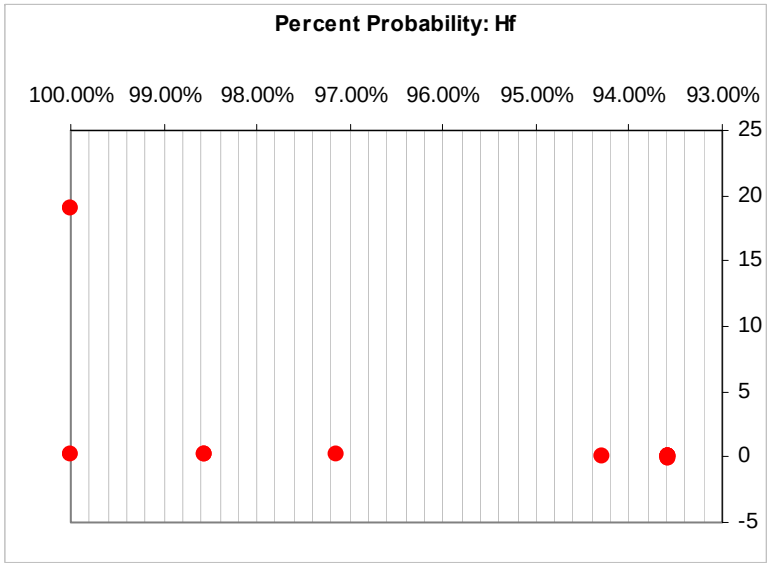
Percent Probability: Hf
100.00%
99.00%
98.00%
97.00%
96.00%
95.00%
94.00%
93.00%
25
20
15
10
5
0
-5

Appendix 5.5 Histograms and cumulative probability plots for EL REEs. Elements with extreme outliers were re-plotted without outlying points to better visualize distribution of data.

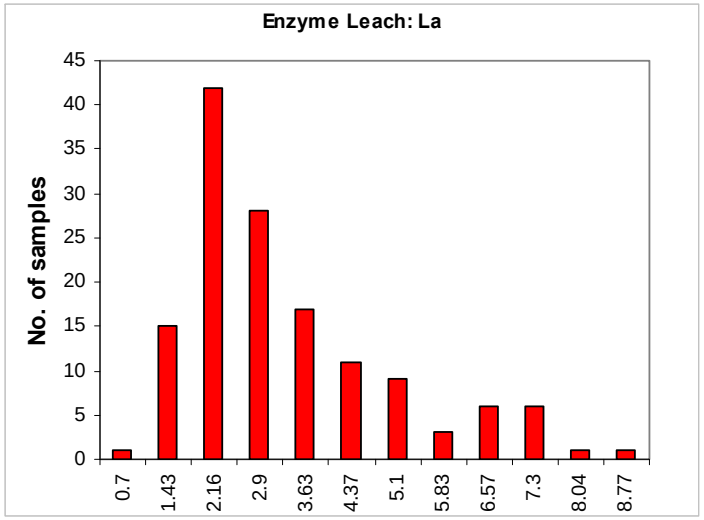

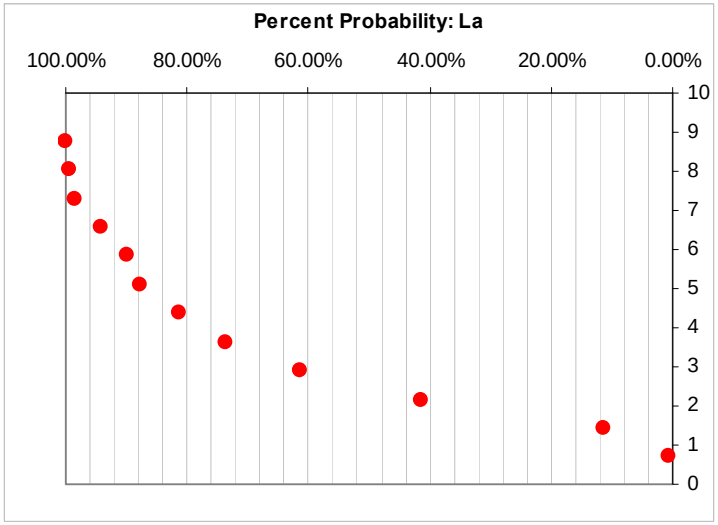

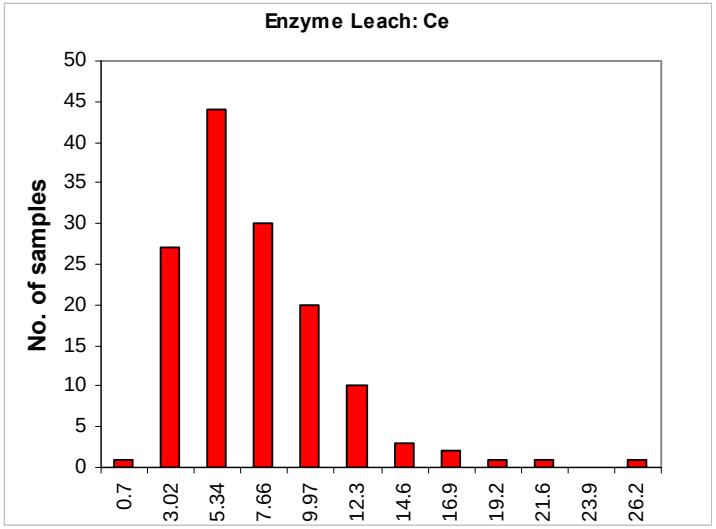

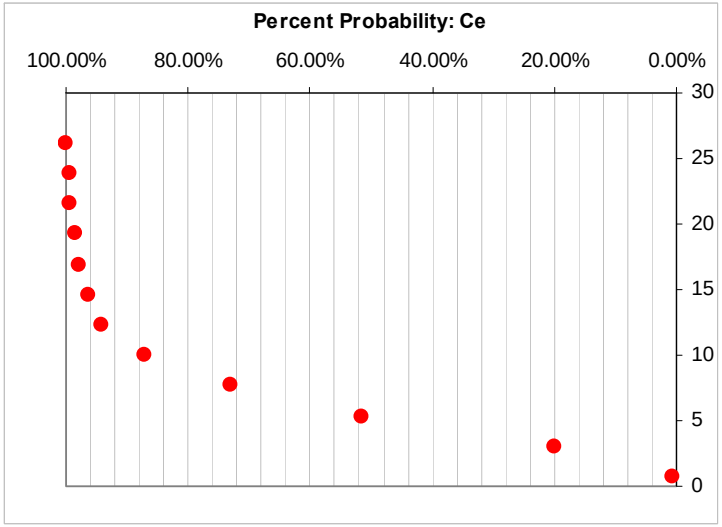

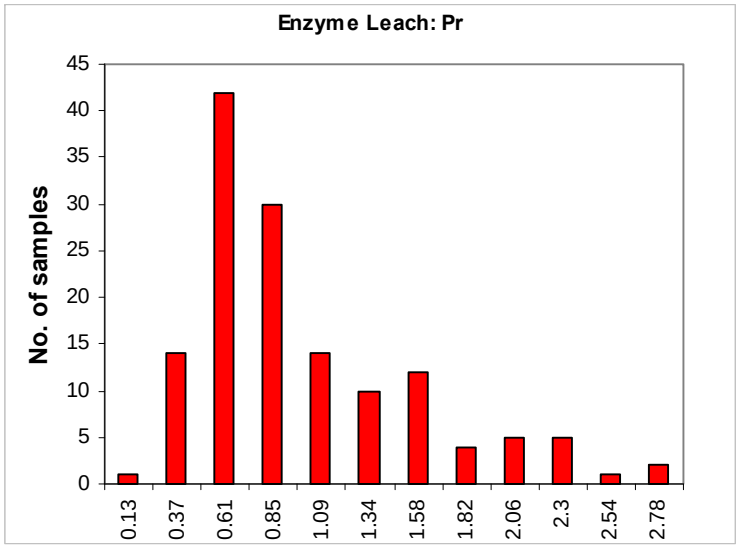
Enzyme Leach: Pr
No. of samples
45
40
35
30
25
20
15
10
5
0
0.13
0.37
0.61
0.85
1.09
1.34
1.58
1.82
2.06
2.3
2.54
2.78

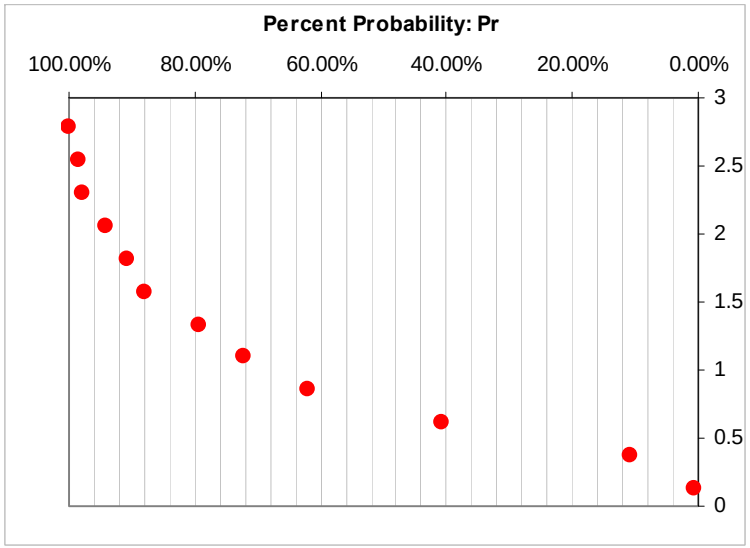
Percent Probability: Pr
100.00%
80.00%
60.00%
40.00%
20.00%
0.00%
3
2.5
2
1.5
1
0.5
0

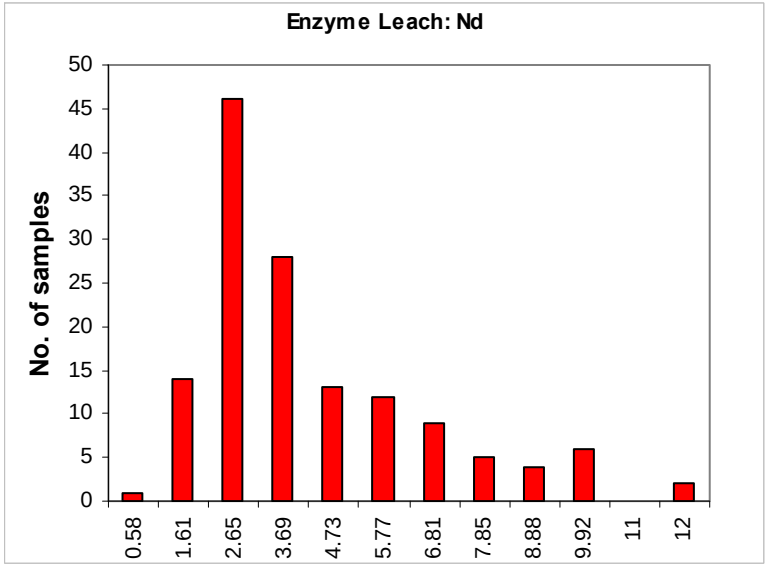
Enzyme Leach: Nd
No. of samples
50
45
40
35
30
25
20
15
10
5
0
0.58
1.61
2.65
3.69
4.73
5.77
6.81
7.85
8.88
9.92
11
12

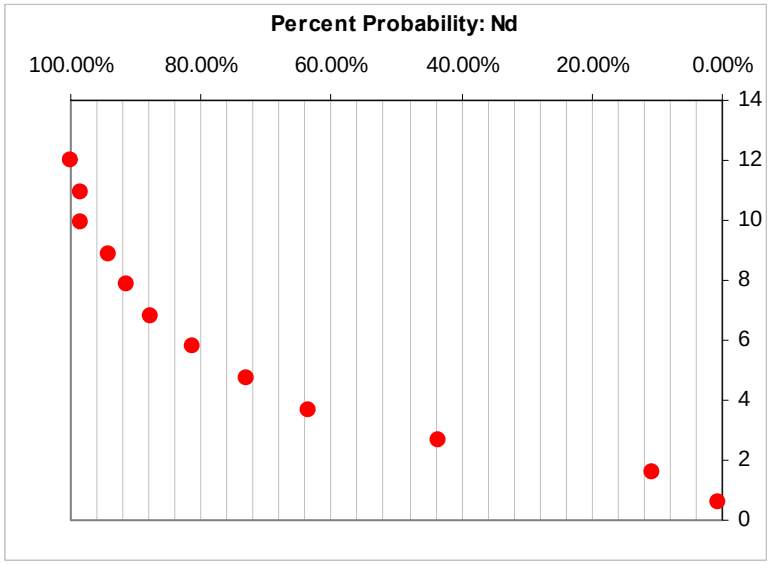
Percent Probability: Nd
100.00%
80.00%
60.00%
40.00%
20.00%
0.00%
14
12
10
8
6
4
2
0

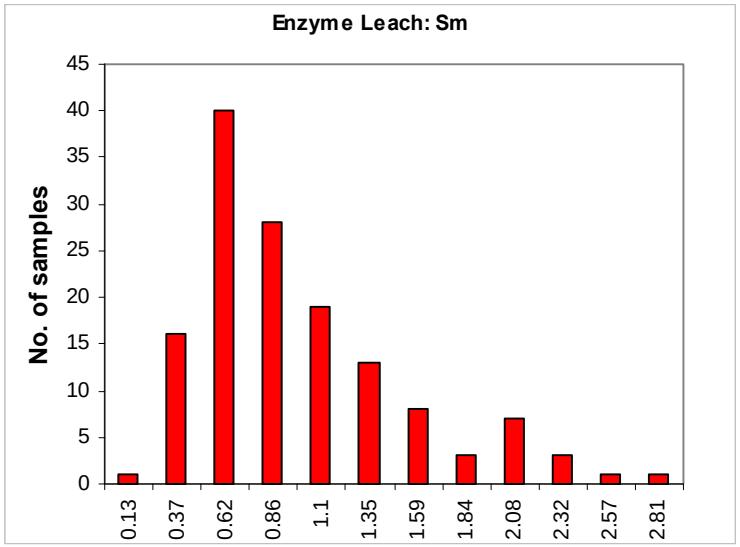
Enzyme Leach: Sm
No. of samples
45
40
35
30
25
20
15
10
5
0
0.13
0.37
0.62
0.86
1.1
1.35
1.59
1.84
2.08
2.32
2.57
2.81

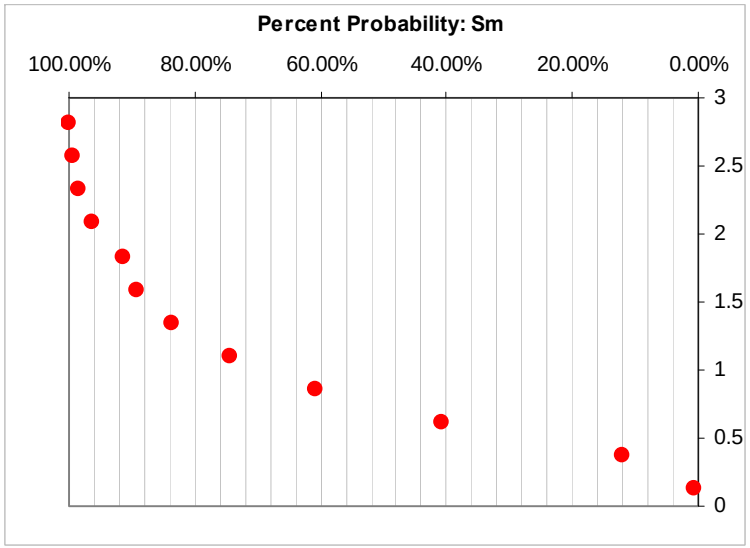
Percent Probability: Sm
100.00%
80.00%
60.00%
40.00%
20.00%
0.00%
3
2.5
2
1.5
1
0.5
0

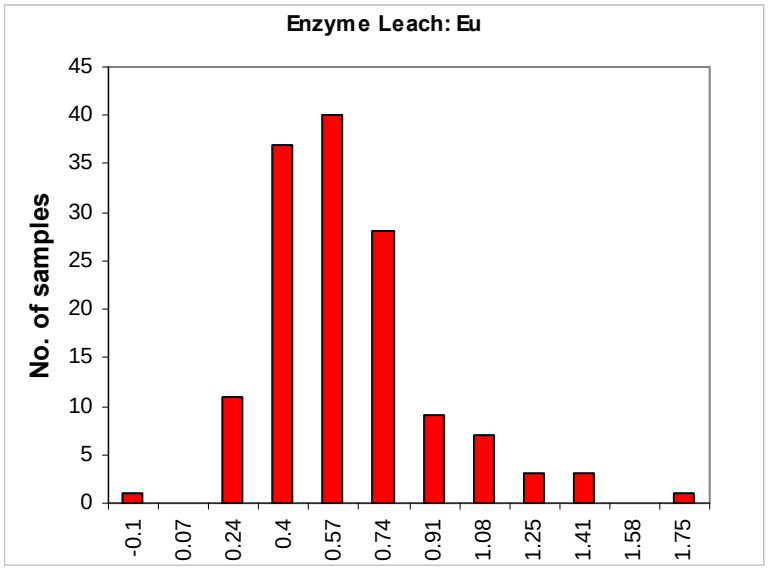
Enzyme Leach: Eu
No. of samples
45
40
35
30
25
20
15
10
5
0
-0.1
0.07
0.24
0.4
0.57
0.74
0.91
1.08
1.25
1.41
1.58
1.75

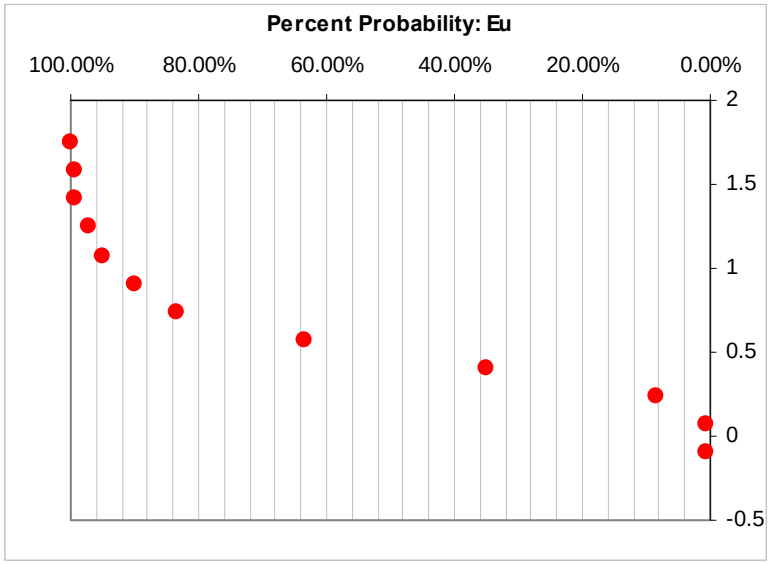
Percent Probability: Eu
100.00%
80.00%
60.00%
40.00%
20.00%
0.00%
2
1.5
1
0.5
0
-0.5

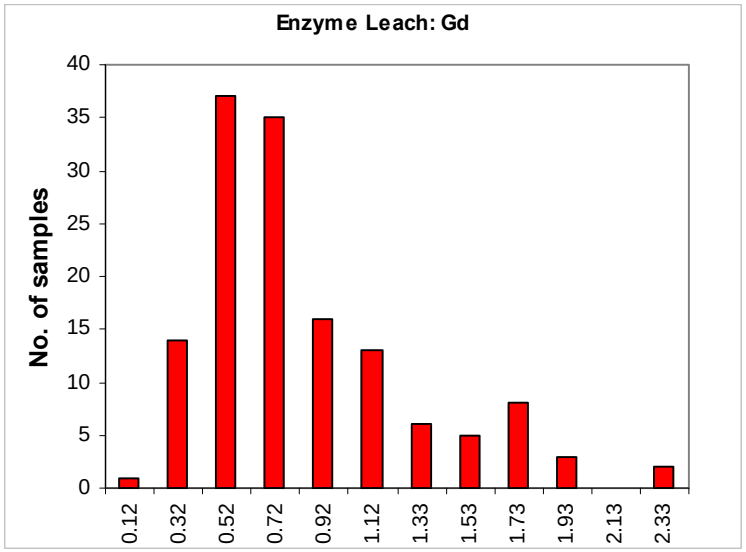
Enzyme Leach: Gd
No. of samples
40
35
30
25
20
15
10
5
0
0.12
0.32
0.52
0.72
0.92
1.12
1.33
1.53
1.73
1.93
2.13
2.33

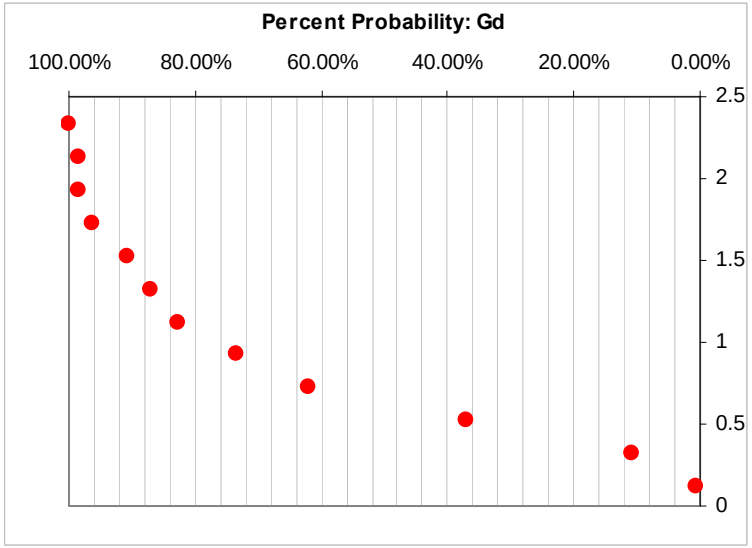
Percent Probability: Gd
100.00%
80.00%
60.00%
40.00%
20.00%
0.00%
2.5
2
1.5
1
0.5
0

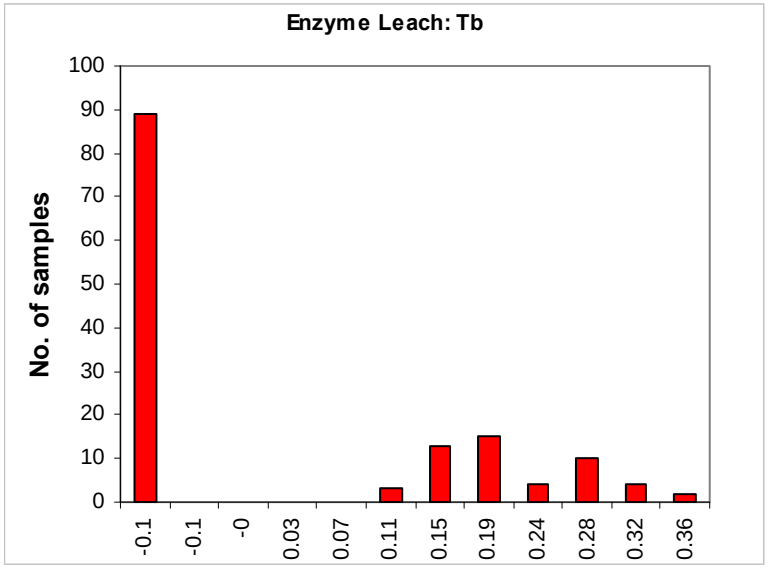
Enzyme Leach: Tb
No. of samples
100
90
80
70
60
50
40
30
20
10
0
-0.1
-0.1
-0
0.03
0.07
0.11
0.15
0.19
0.24
0.28
0.32
0.36

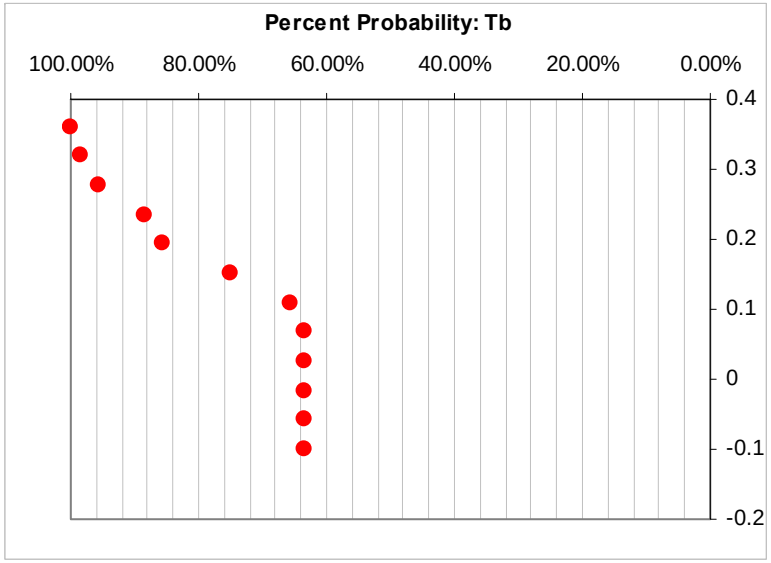
Percent Probability: Tb
100.00%
80.00%
60.00%
40.00%
20.00%
0.00%
0.4
0.3
0.2
0.1
0
-0.1
-0.2

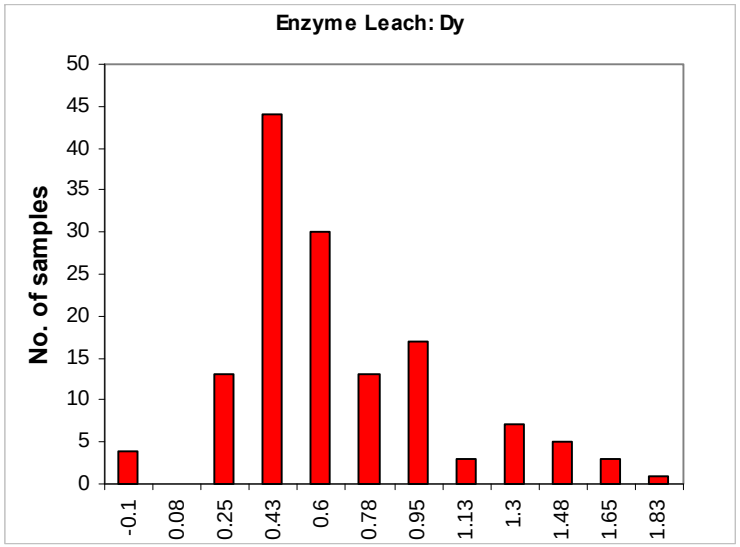
Enzyme Leach: Dy
No. of samples
50
45
40
35
30
25
20
15
10
5
0
-0.1
0.08
0.25
0.43
0.6
0.78
0.95
1.13
1.3
1.48
1.65
1.83

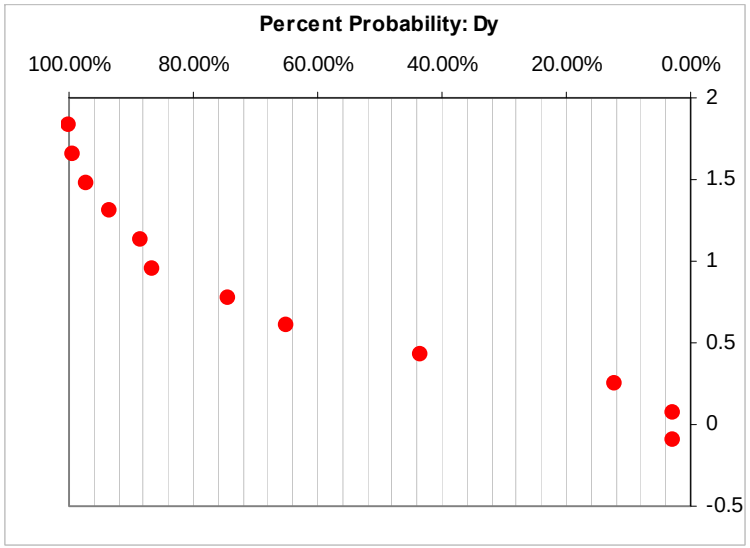
Percent Probability: Dy
100.00%
80.00%
60.00%
40.00%
20.00%
0.00%
2
1.5
1
0.5
0
-0.5

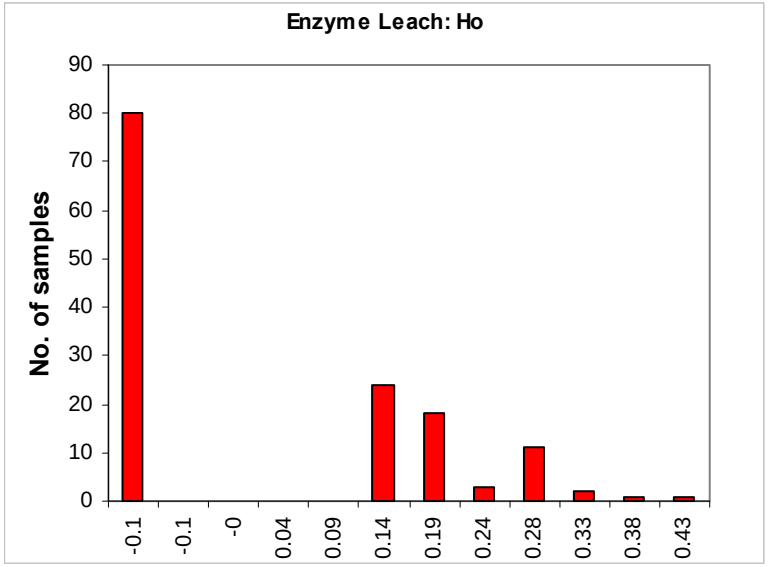
Enzyme Leach: Ho
No. of samples
90
80
70
60
50
40
30
20
10
0
-0.1
-0.1
-0
0.04
0.09
0.14
0.19
0.24
0.28
0.33
0.38
0.43

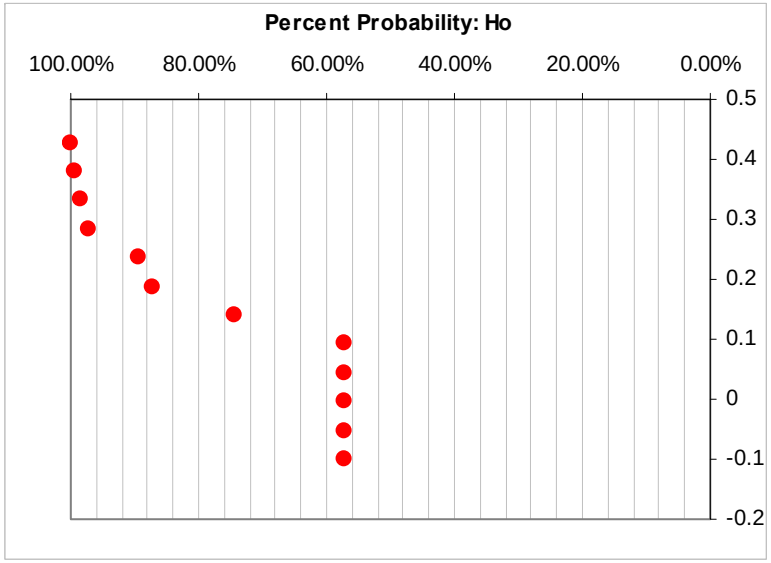
Percent Probability: Ho
100.00%
80.00%
60.00%
40.00%
20.00%
0.00%
0.5
0.4
0.3
0.2
0.1
0
-0.1
-0.2

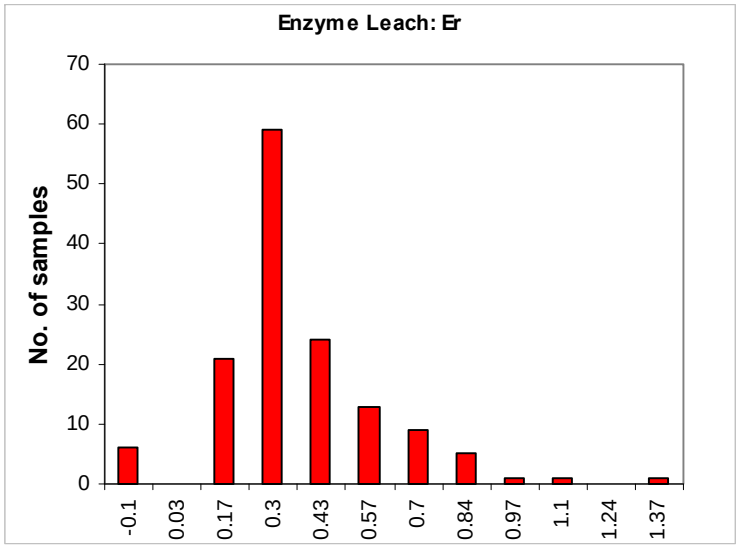
Enzyme Leach: Er
No. of samples
70
60
50
40
30
20
10
0
-0.1
0.03
0.17
0.3
0.43
0.57
0.7
0.84
0.97
1.1
1.24
1.37

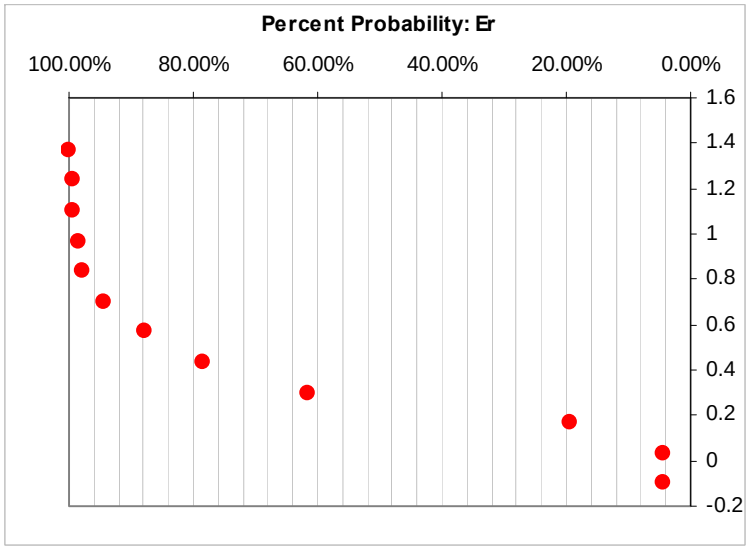
Percent Probability: Er
100.00%
80.00%
60.00%
40.00%
20.00%
0.00%
1.6
1.4
1.2
1
0.8
0.6
0.4
0.2
0
-0.2

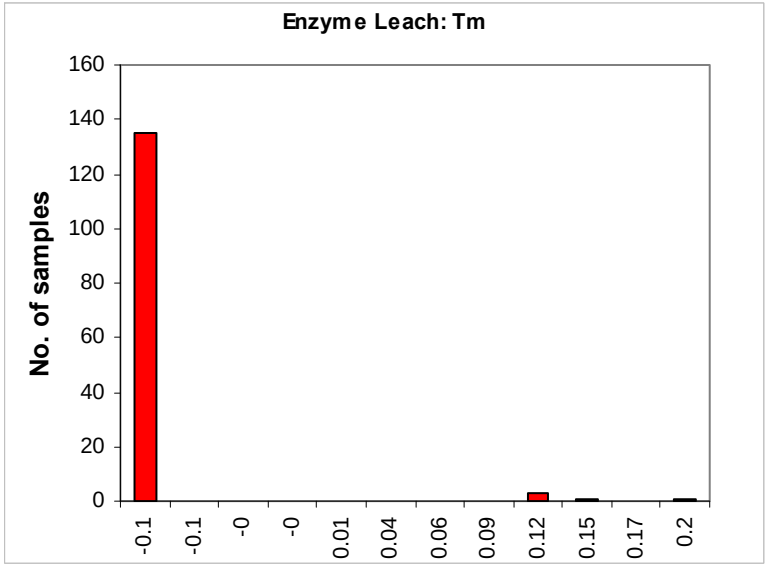
Enzyme Leach: Tm
No. of samples
160
140
120
100
80
60
40
20
0
-0.1
-0.1
-0
-0
0.01
0.04
0.06
0.09
0.12
0.15
0.17
0.2

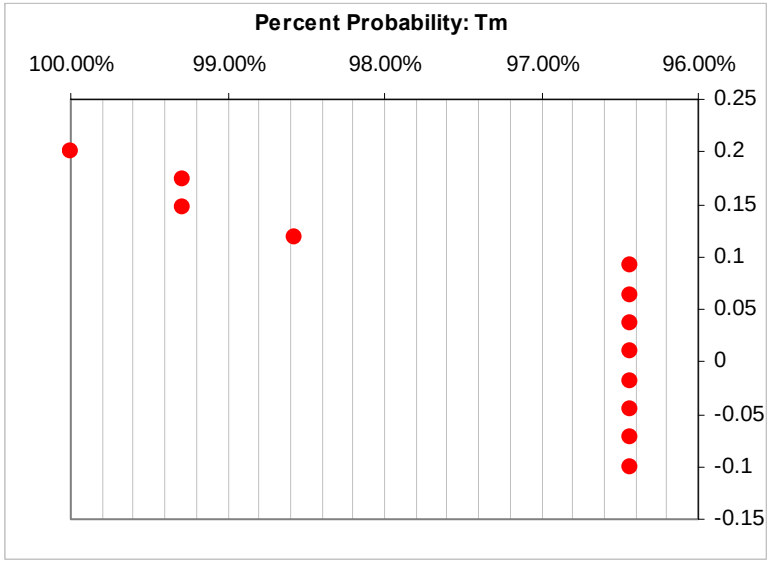
Percent Probability: Tm
100.00%
99.00%
98.00%
97.00%
96.00%
0.25
0.2
0.15
0.1
0.05
0
-0.05
-0.1
-0.15

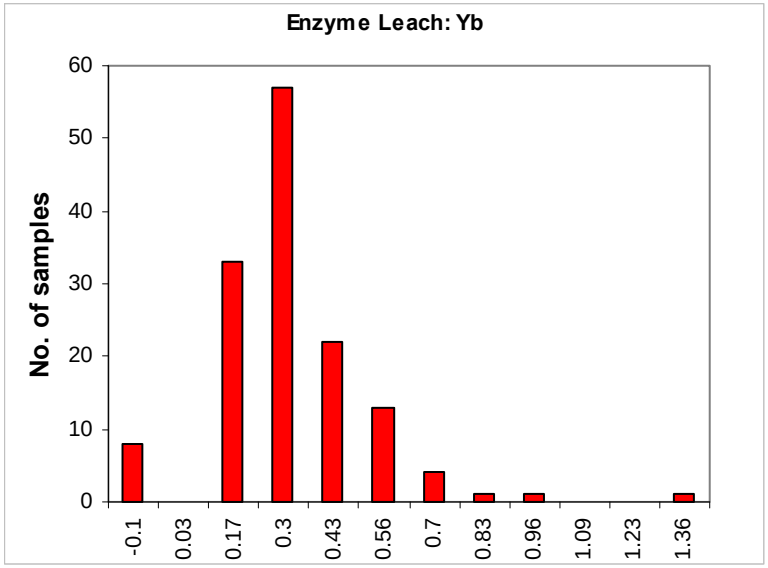
Enzyme Leach: Yb
No. of samples
60
50
40
30
20
10
0
-0.1
0.03
0.17
0.3
0.43
0.56
0.7
0.83
0.96
1.09
1.23
1.36

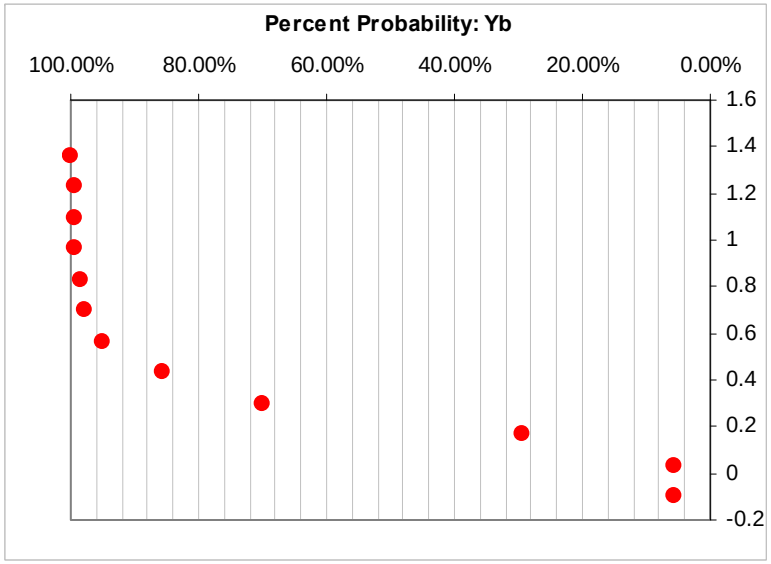
Percent Probability: Yb
100.00%
80.00%
60.00%
40.00%
20.00%
0.00%
1.6
1.4
1.2
1
0.8
0.6
0.4
0.2
0
-0.2

Appendix 5.6 Histograms and cumulative probability plots for EL Lithophiles. Elements with extreme outliers were re-plotted without outlying points to better visualize distribution of data.

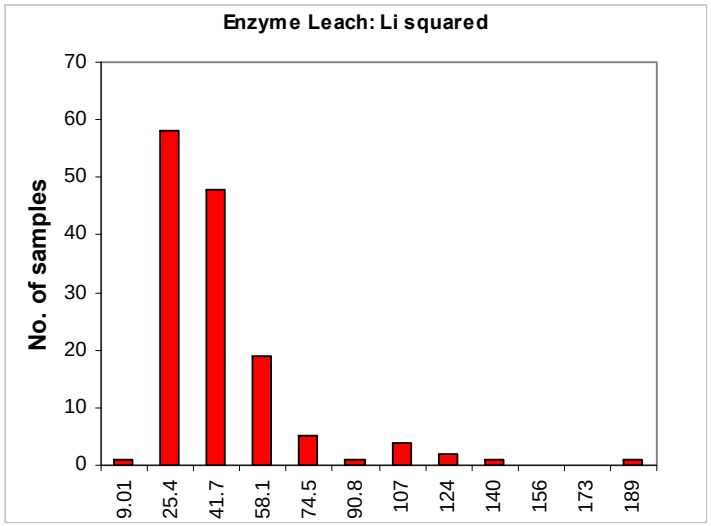

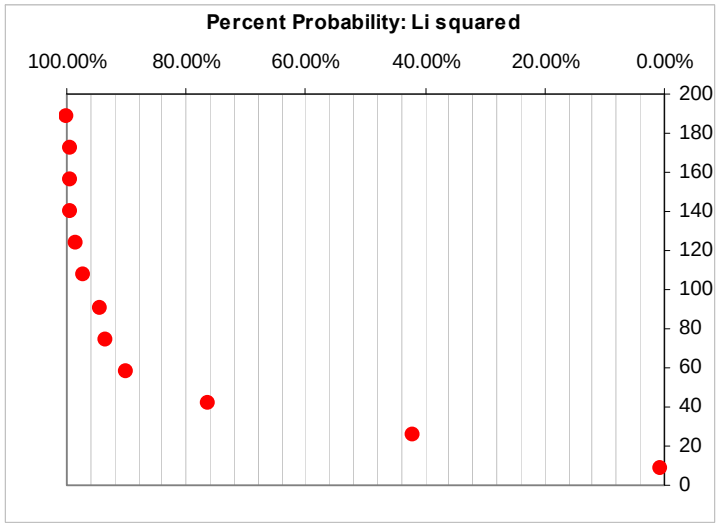

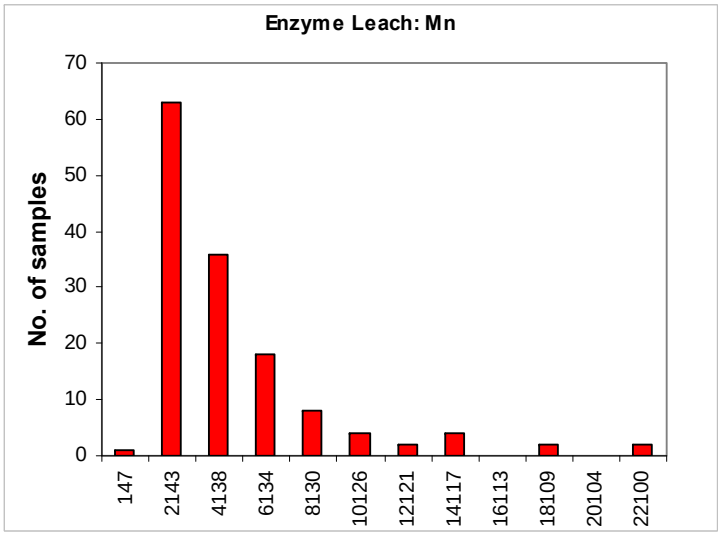

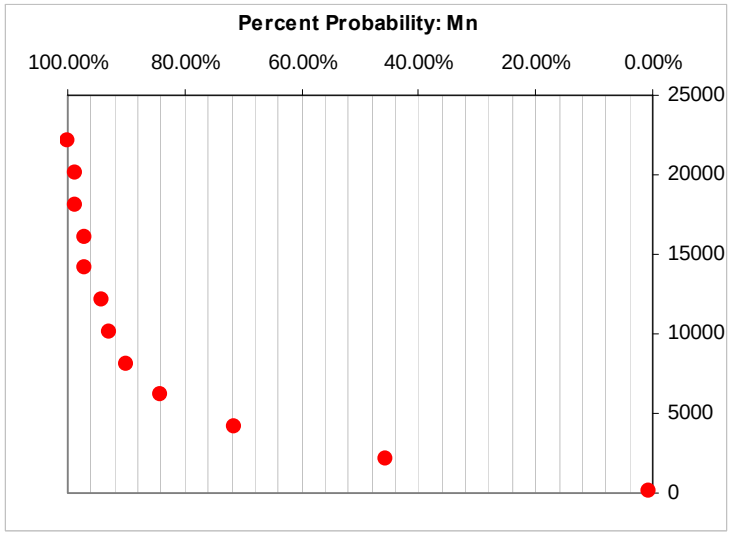

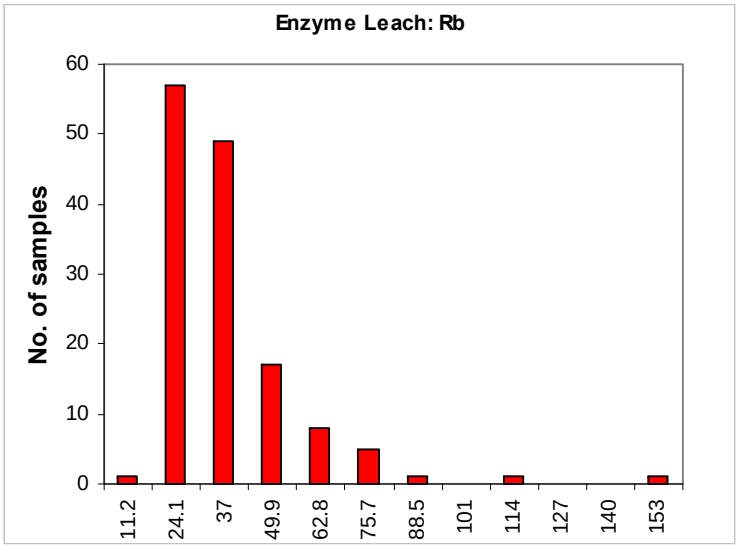
Enzyme Leach: Rb
No. of samples
60
50
40
30
20
10
0
11.2
24.1
37
49.9
62.8
75.7
88.5
101
114
127
140
153

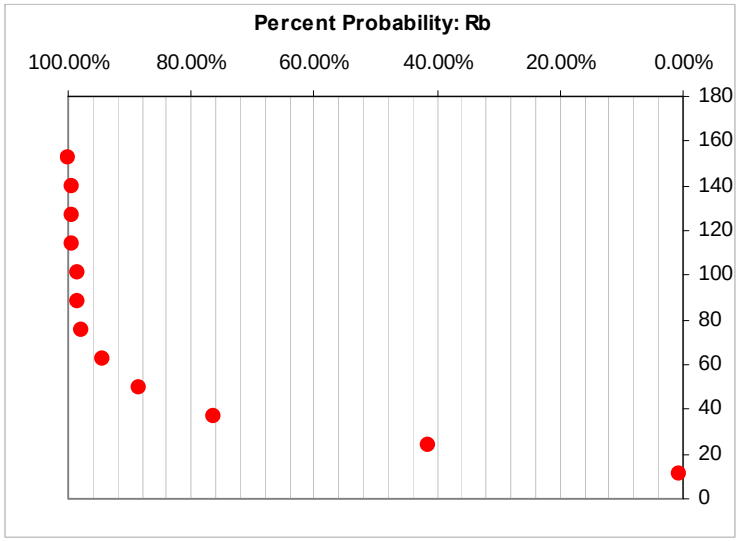
Percent Probability: Rb
100.00%
80.00%
60.00%
40.00%
20.00%
0.00%
180
160
140
120
100
80
60
40
20
0

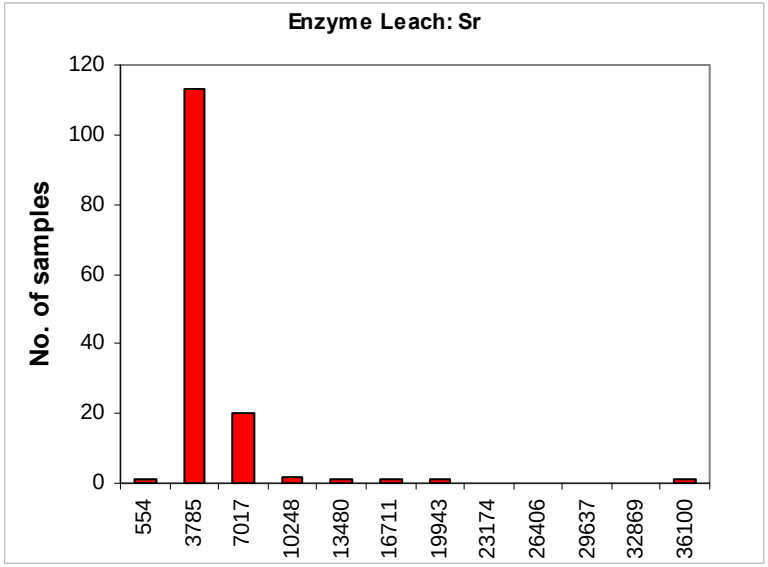
Enzyme Leach: Sr
No. of samples
120
100
80
60
40
20
0
554
3785
7017
10248
13480
16711
19943
23174
26406
29637
32869
36100

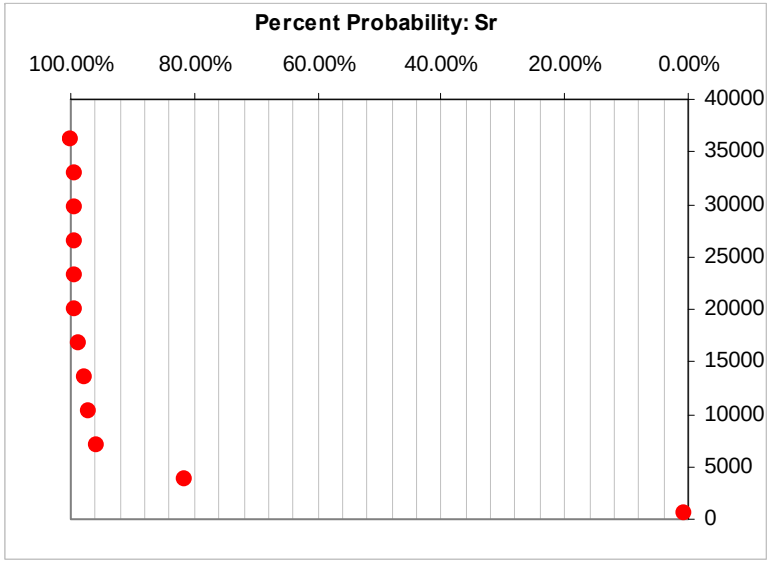
Percent Probability: Sr
100.00%
80.00%
60.00%
40.00%
20.00%
0.00%
40000
35000
30000
25000
20000
15000
10000
5000
0

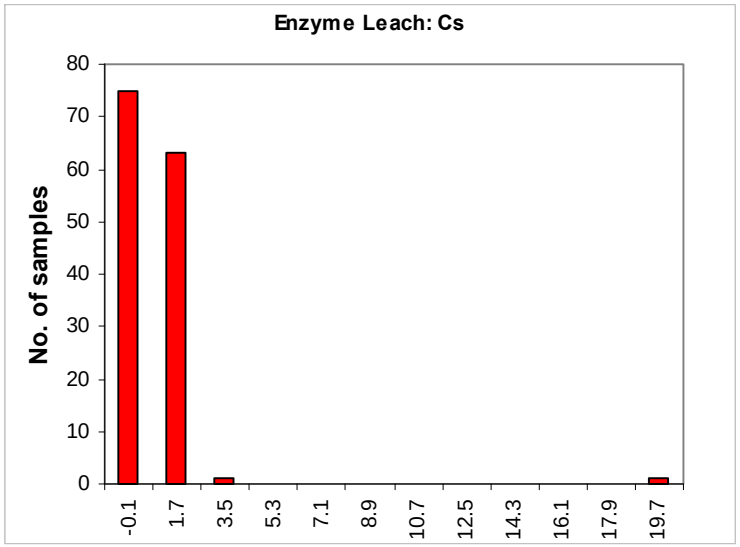
Enzyme Leach: Cs
No. of samples
80
70
60
50
40
30
20
10
0
-0.1
1.7
3.5
5.3
7.1
8.9
10.7
12.5
14.3
16.1
17.9
19.7

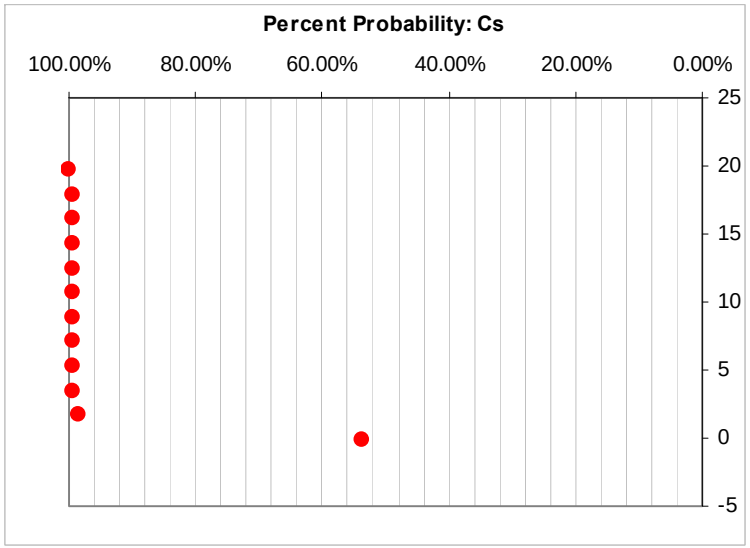
Percent Probability: Cs
100.00%
80.00%
60.00%
40.00%
20.00%
0.00%
25
20
15
10
5
0
-5

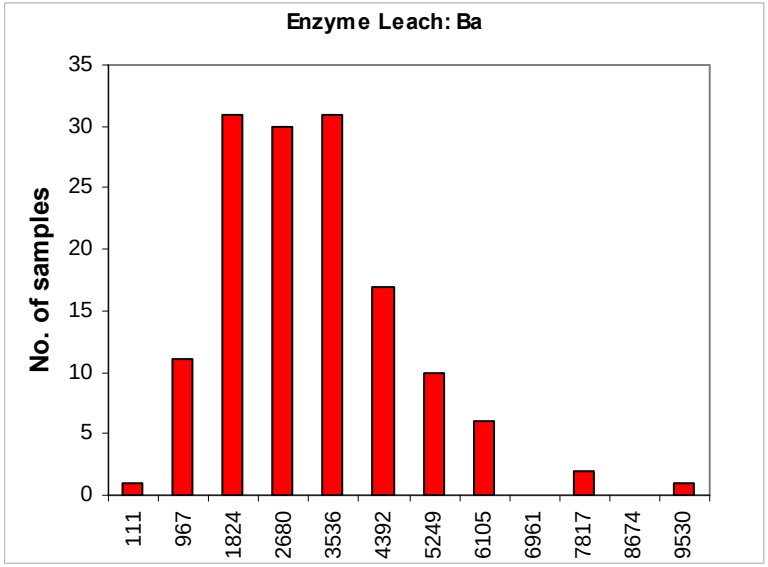
Enzyme Leach: Ba
No. of samples
35
30
25
20
15
10
5
0
111
967
1824
2680
3536
4392
5249
6105
6961
7817
8674
9530

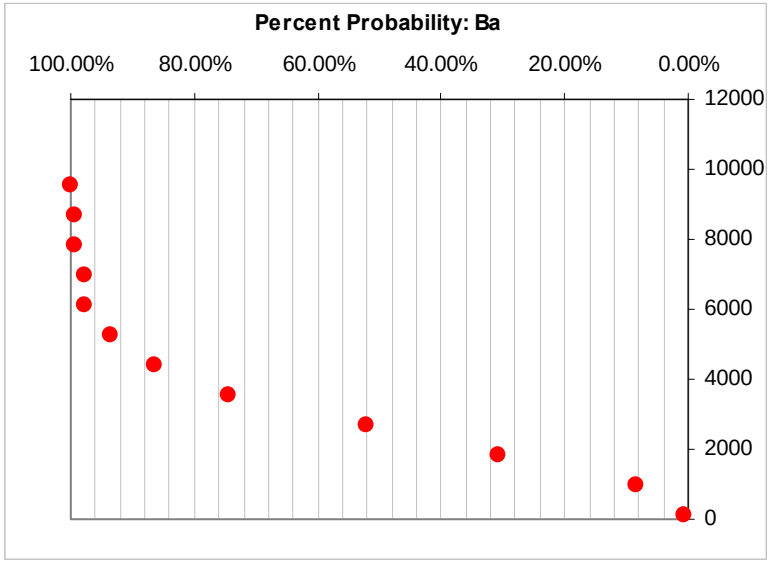
Percent Probability: Ba
100.00%
80.00%
60.00%
40.00%
20.00%
0.00%
12000
10000
8000
6000
4000
2000
0

Appendix 6.1 Histograms and cumulative probability plots for TS Oxide Suite Elements. Elements with extreme outliers were re-plotted without outlying points to better visualize distribution of data.

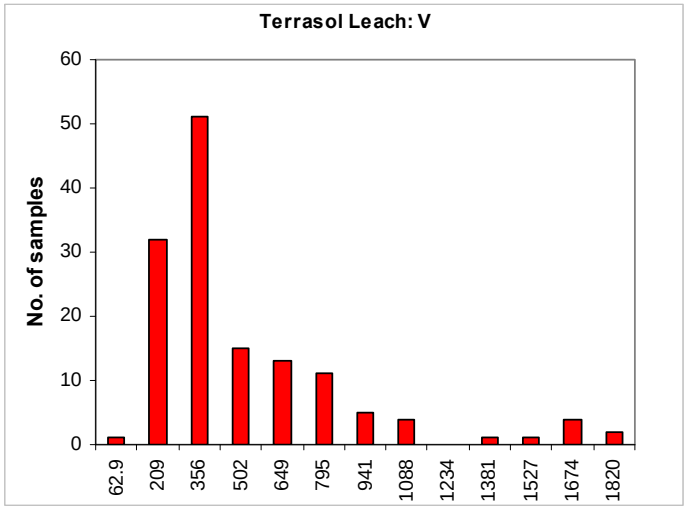

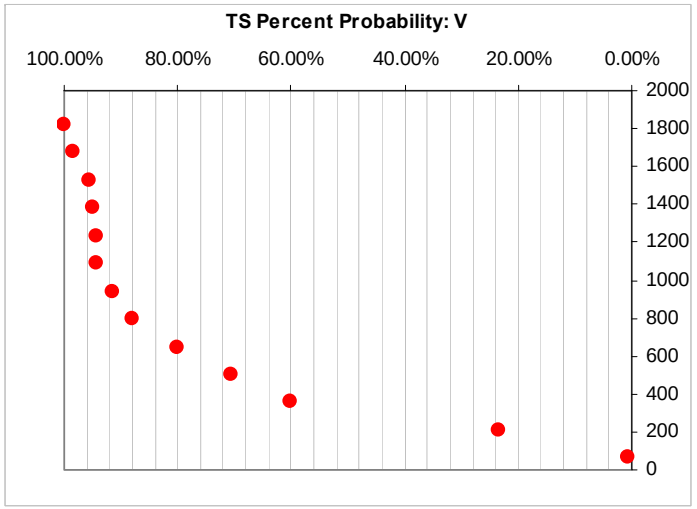

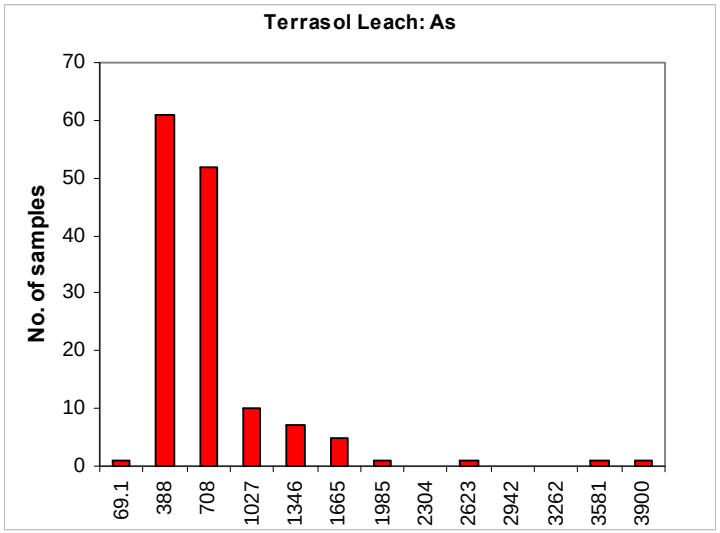

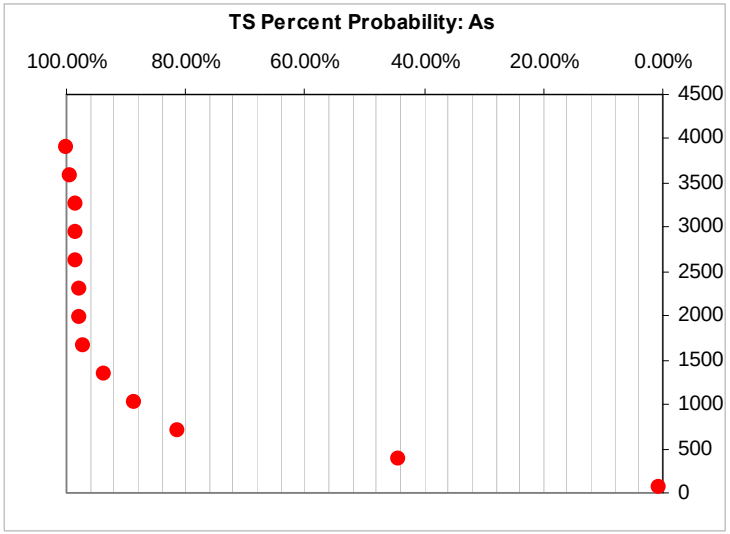

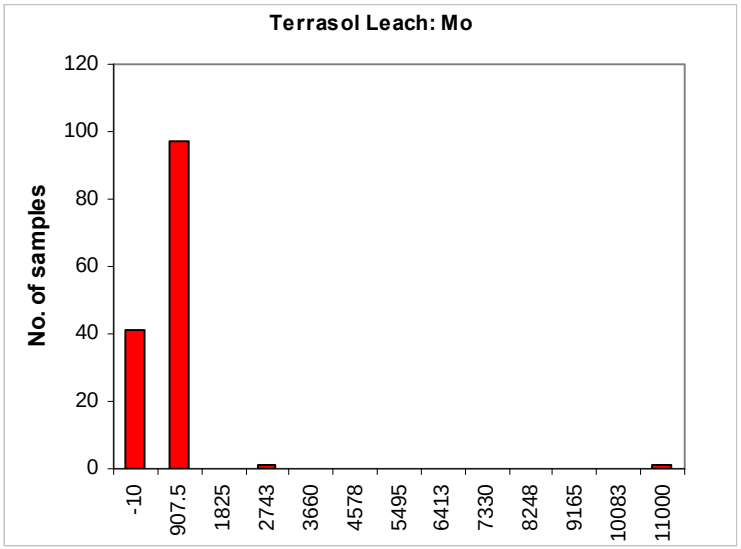
Terrasol Leach: Mo
No. of samples
120
100
80
60
40
20
0
-10
907.5
1825
2743
3660
4578
5495
6413
7330
8248
9165
10083
11000

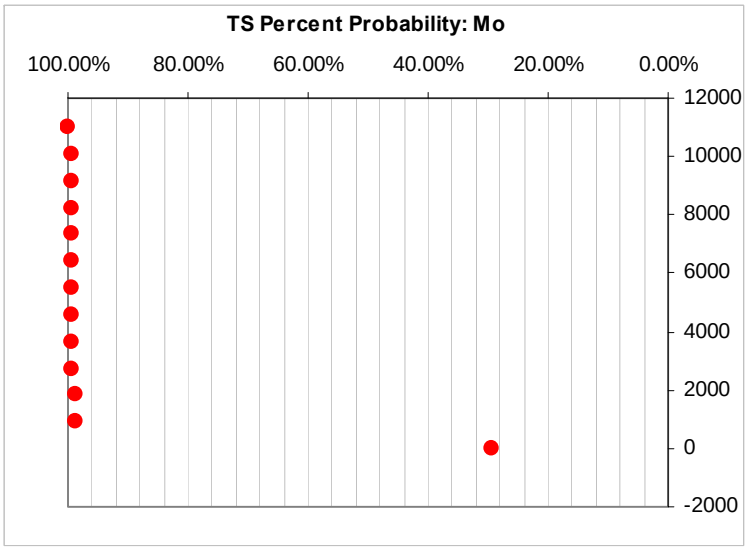
TS Percent Probability: Mo
100.00%
80.00%
60.00%
40.00%
20.00%
0.00%
12000
10000
8000
6000
4000
2000
0
-2000

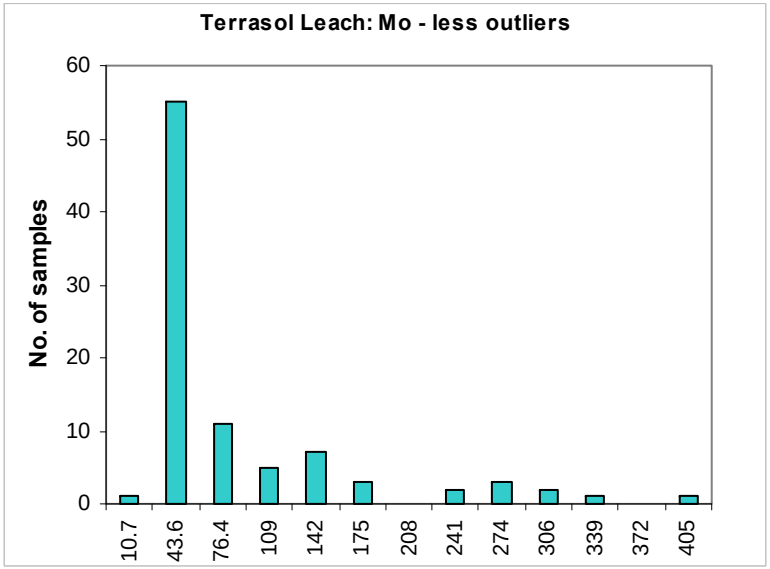
Terrasol Leach: Mo - less outliers
No. of samples
60
50
40
30
20
10
0
10.7
43.6
76.4
109
142
175
208
241
274
306
339
372
405

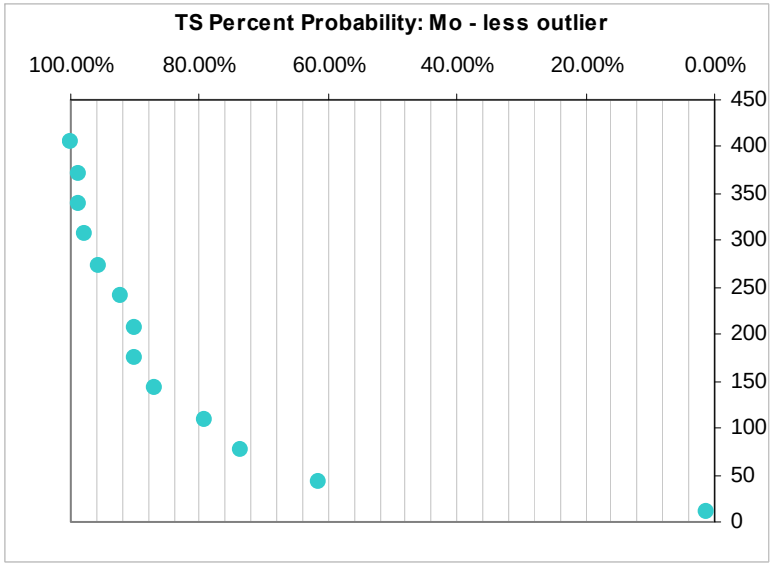
TS Percent Probability: Mo - less outlier
100.00%
80.00%
60.00%
40.00%
20.00%
0.00%
450
400
350
300
250
200
150
100
50
0

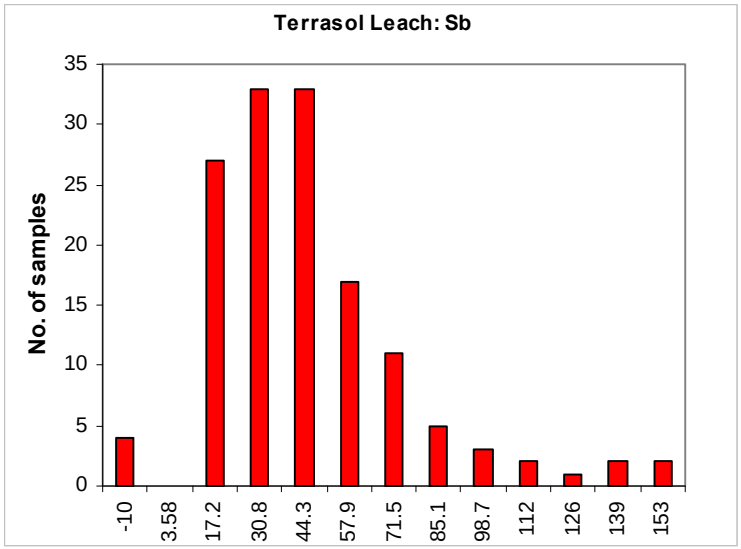
Terrasol Leach: Sb
No. of samples
35
30
25
20
15
10
5
0
-10
3.58
17.2
30.8
44.3
57.9
71.5
85.1
98.7
112
126
139
153

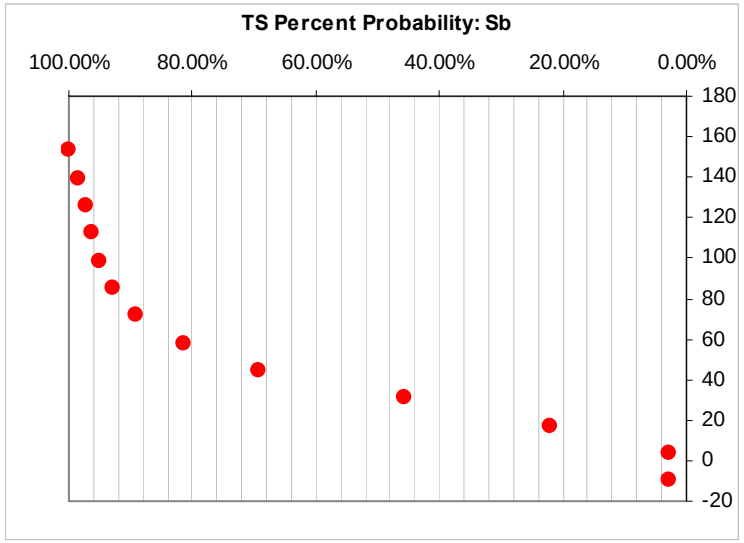
TS Percent Probability: Sb
100.00%
80.00%
60.00%
40.00%
20.00%
0.00%
180
160
140
120
100
80
60
40
20
0
-20

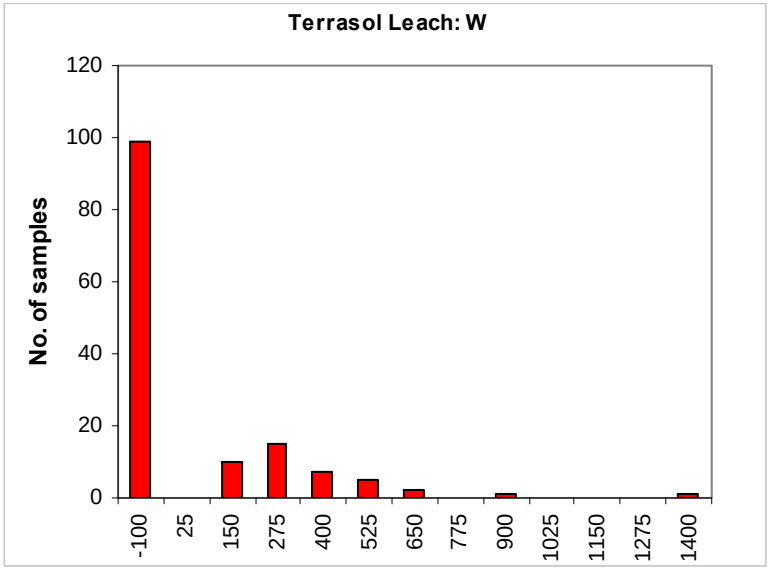
Terrasol Leach: W
No. of samples
120
100
80
60
40
20
0
-100
25
150
275
400
525
650
775
900
1025
1150
1275
1400

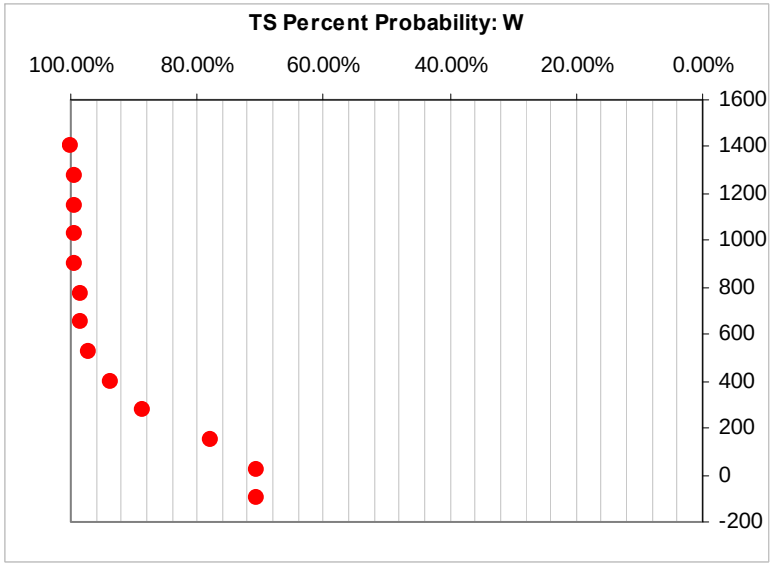
TS Percent Probability: W
100.00%
80.00%
60.00%
40.00%
20.00%
0.00%
1600
1400
1200
1000
800
600
400
200
0
-200

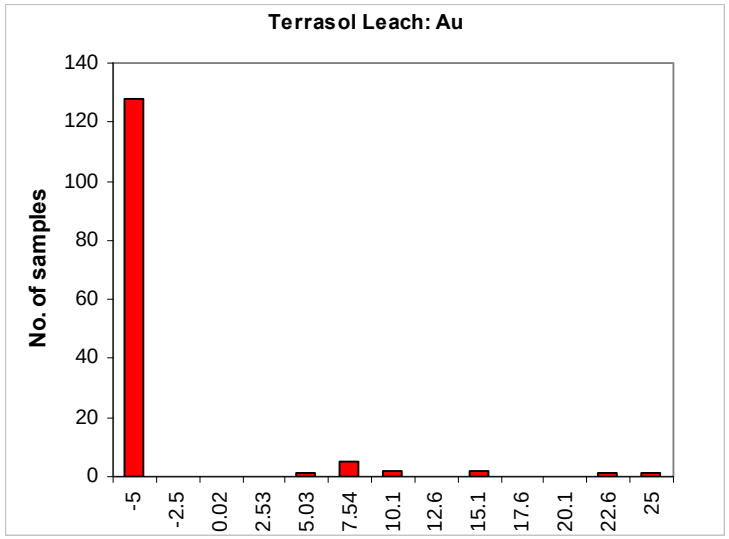
Terrasol Leach: Au
No. of samples
140
120
100
80
60
40
20
0
-5
-2.5
0.02
2.53
5.03
7.54
10.1
12.6
15.1
17.6
20.1
22.6
25

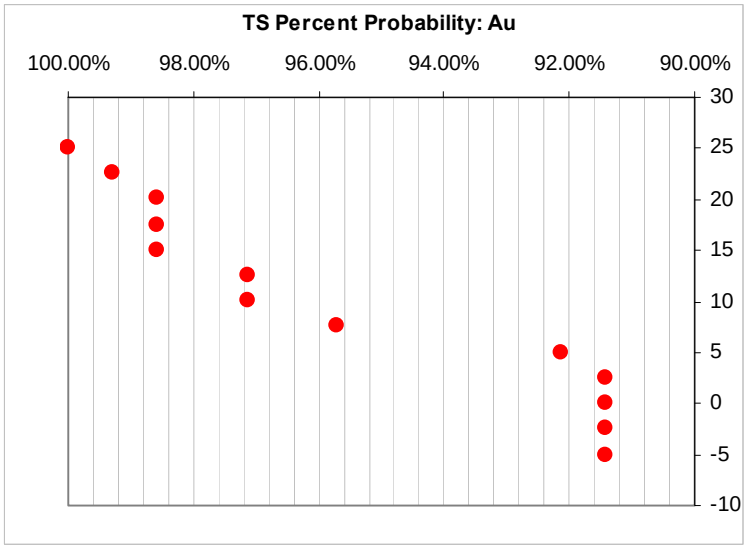
TS Percent Probability: Au
100.00%
98.00%
96.00%
94.00%
92.00%
90.00%
30
25
20
15
10
5
0
-5
-10

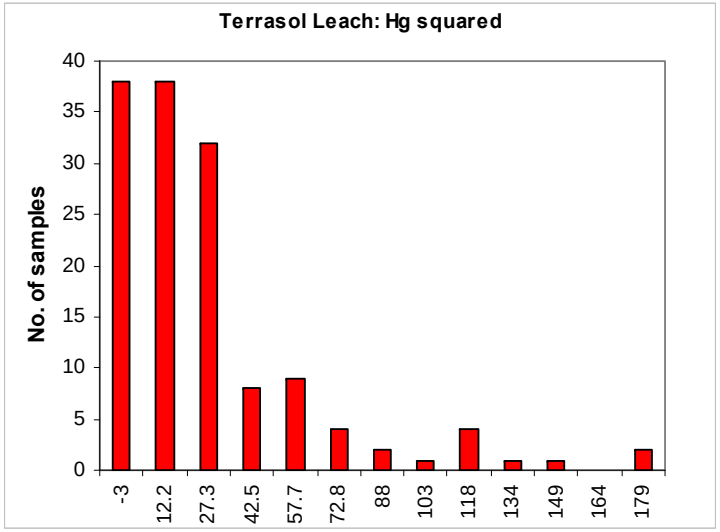
Terrasol Leach: Hg squared
No. of samples
40
35
30
25
20
15
10
5
0
-3
12.2
27.3
42.5
57.7
72.8
88
103
118
134
149
164
179

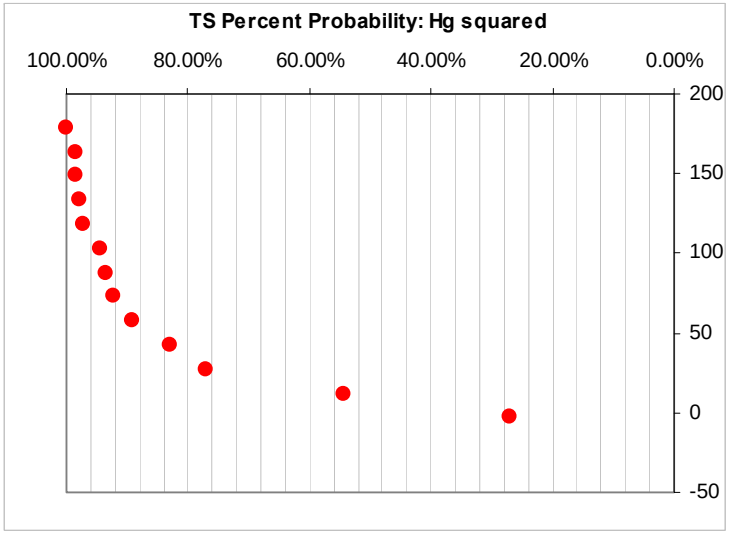
TS Percent Probability: Hg squared
100.00%
80.00%
60.00%
40.00%
20.00%
0.00%
200
150
100
50
0
-50

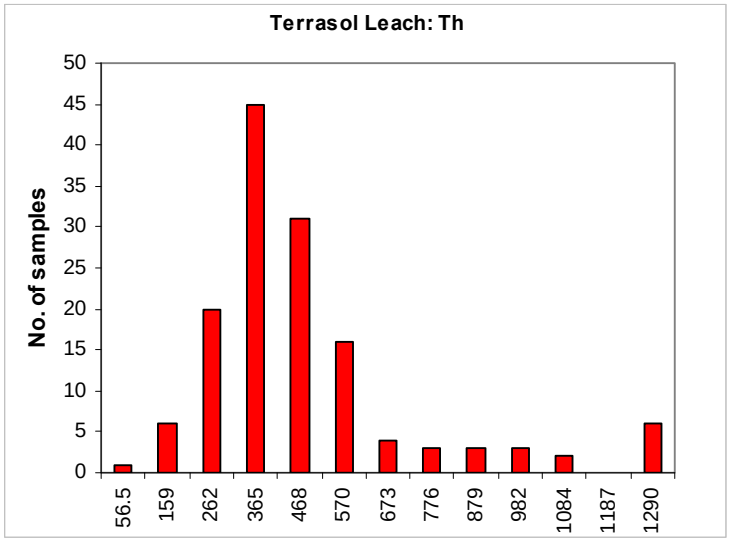
Terrasol Leach: Th
No. of samples
50
45
40
35
30
25
20
15
10
5
0
56.5
159
262
365
468
570
673
776
879
982
1084
1187
1290

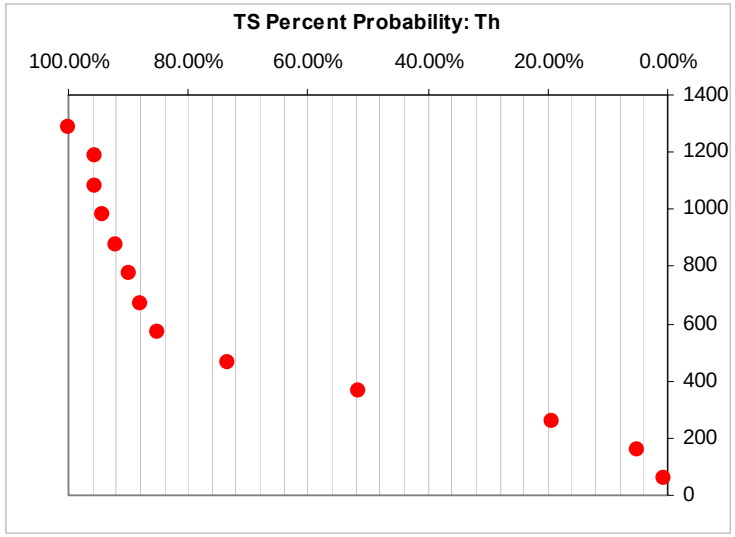
TS Percent Probability: Th
100.00%
80.00%
60.00%
40.00%
20.00%
0.00%
1400
1200
1000
800
600
400
200
0

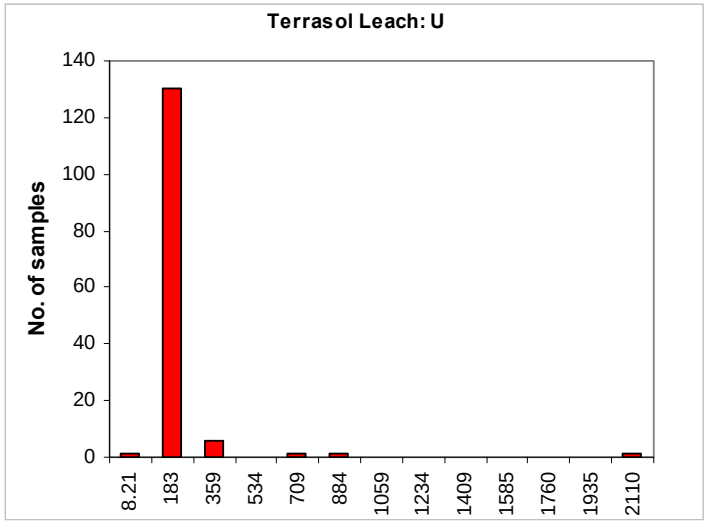
Terrasol Leach: U
No. of samples
140
120
100
80
60
40
20
0
8.21
183
359
534
709
884
1059
1234
1409
1585
1760
1935
2110

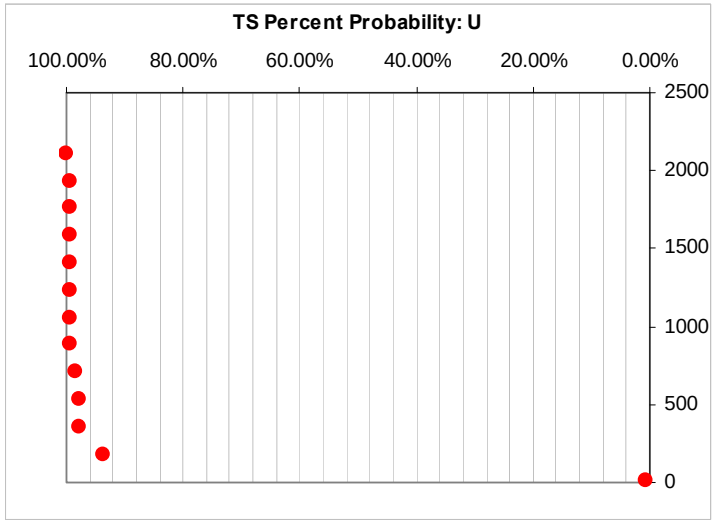
TS Percent Probability: U
100.00%
80.00%
60.00%
40.00%
20.00%
0.00%
2500
2000
1500
1000
500
0

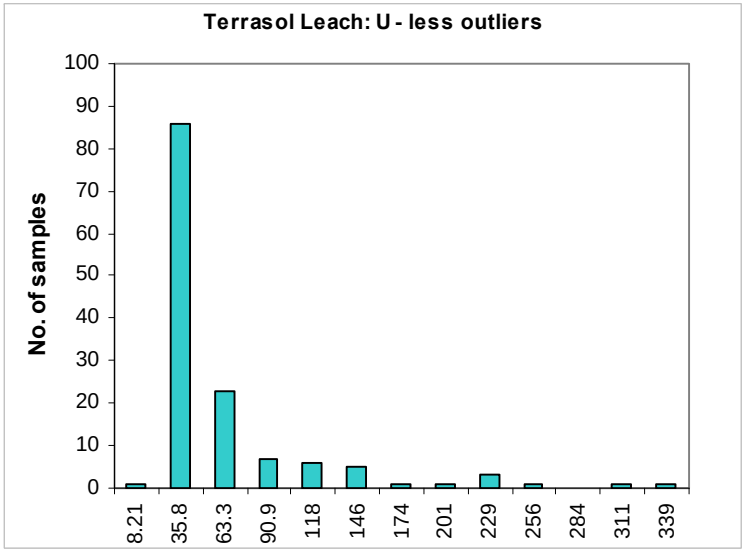
Terrasol Leach: U - less outliers
No. of samples
100
90
80
70
60
50
40
30
20
10
0
8.21
35.8
63.3
90.9
118
146
174
201
229
256
284
311
339

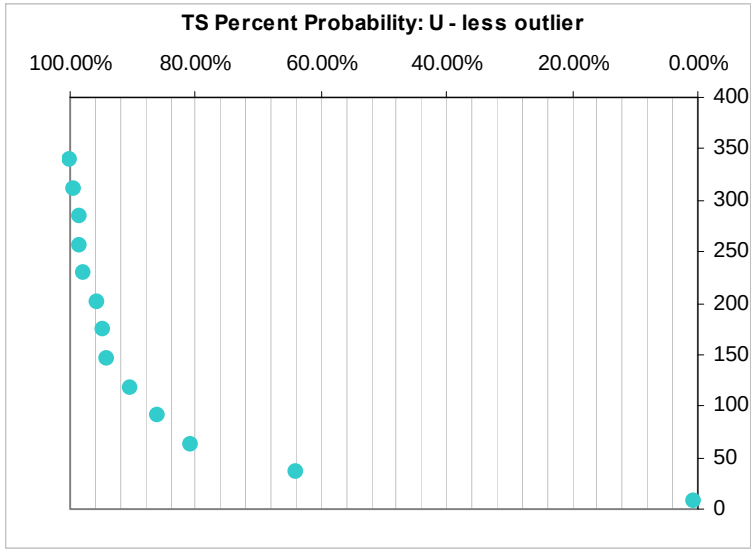
TS Percent Probability: U - less outlier
100.00%
80.00%
60.00%
40.00%
20.00%
0.00%
400
350
300
250
200
150
100
50
0

Appendix 6.2 Histograms and cumulative probability plots for TS base metals. Elements with extreme outliers were re-plotted without outlying points to better visualize distribution of data.

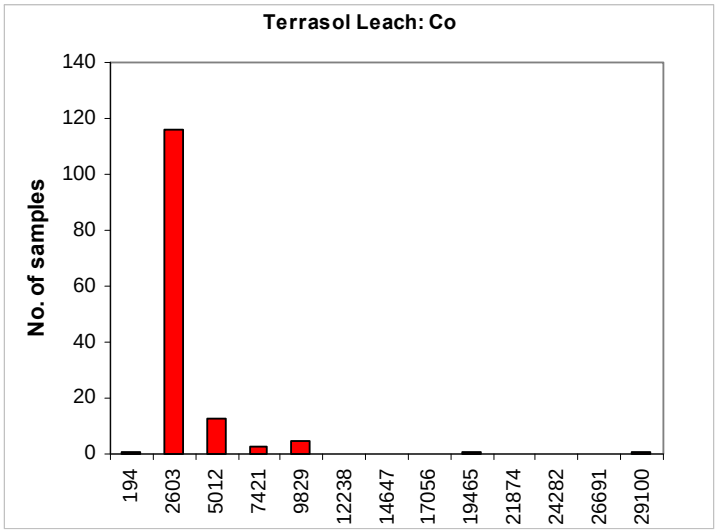

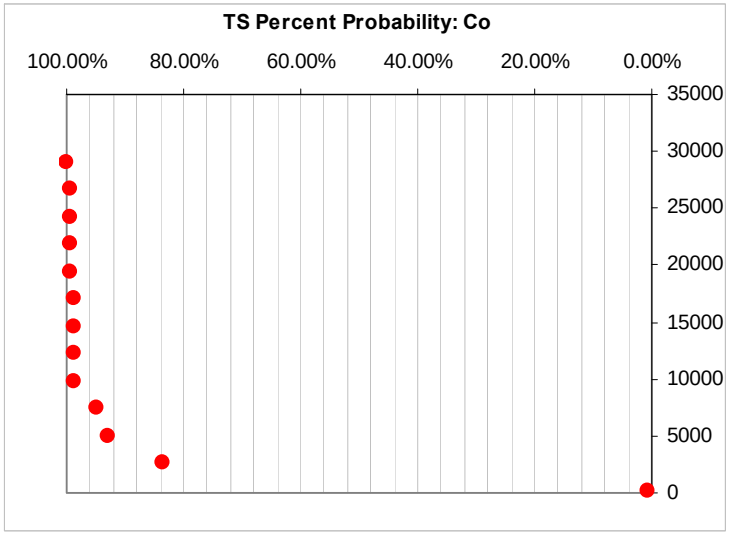

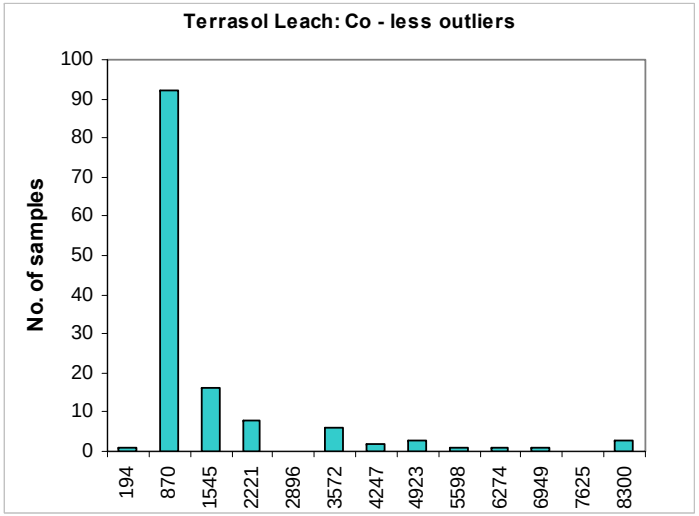

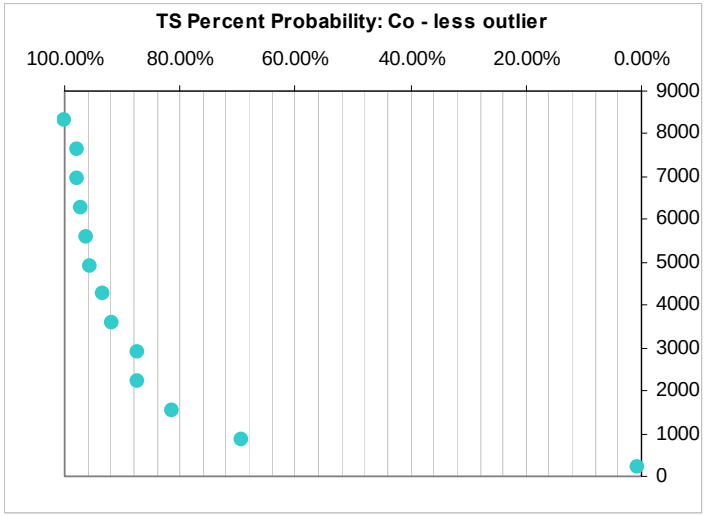

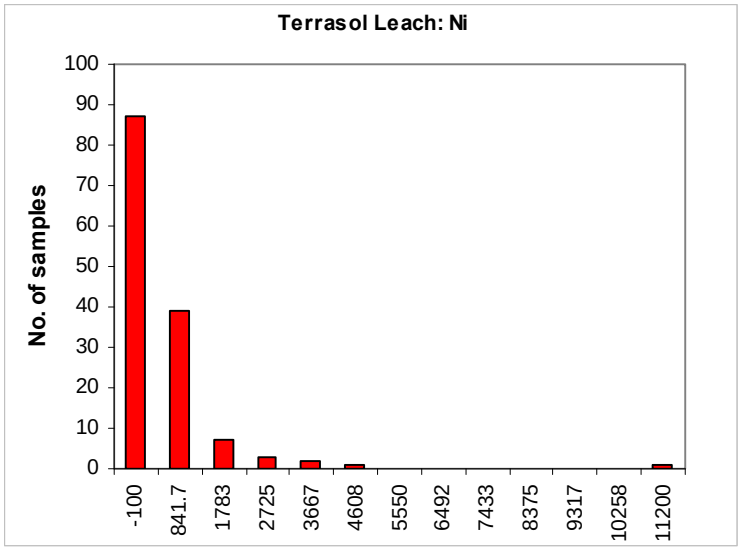
Terrasol Leach: Ni
No. of samples
100
90
80
70
60
50
40
30
20
10
0
-100
841.7
1783
2725
3667
4608
5550
6492
7433
8375
9317
10258
11200

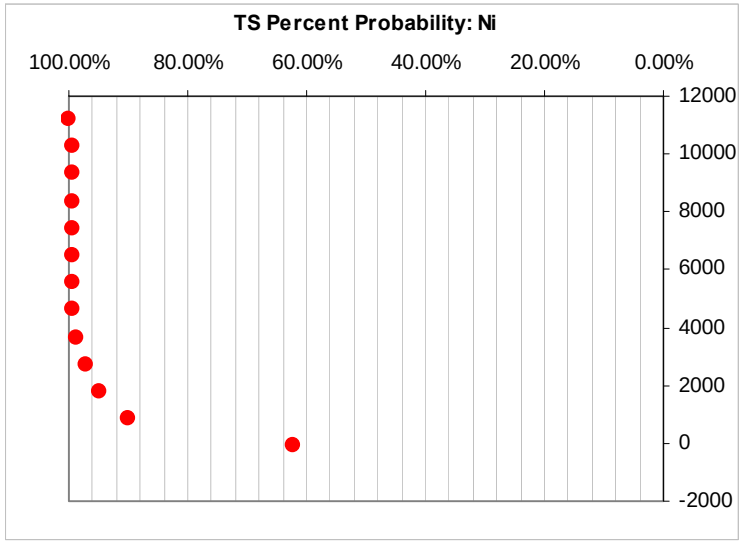
TS Percent Probability: Ni
100.00%
80.00%
60.00%
40.00%
20.00%
0.00%
12000
10000
8000
6000
4000
2000
0
-2000

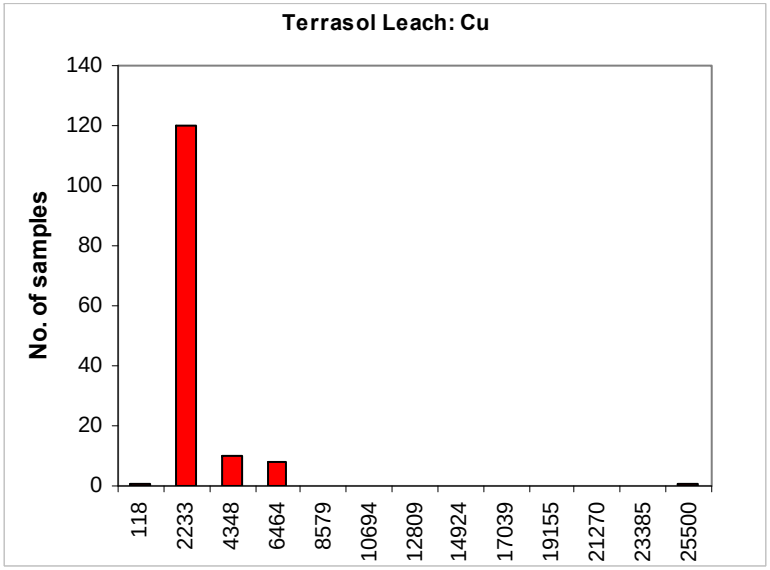
Terrasol Leach: Cu
No. of samples
140
120
100
80
60
40
20
0
118
2233
4348
6464
8579
10694
12809
14924
17039
19155
21270
23385
25500

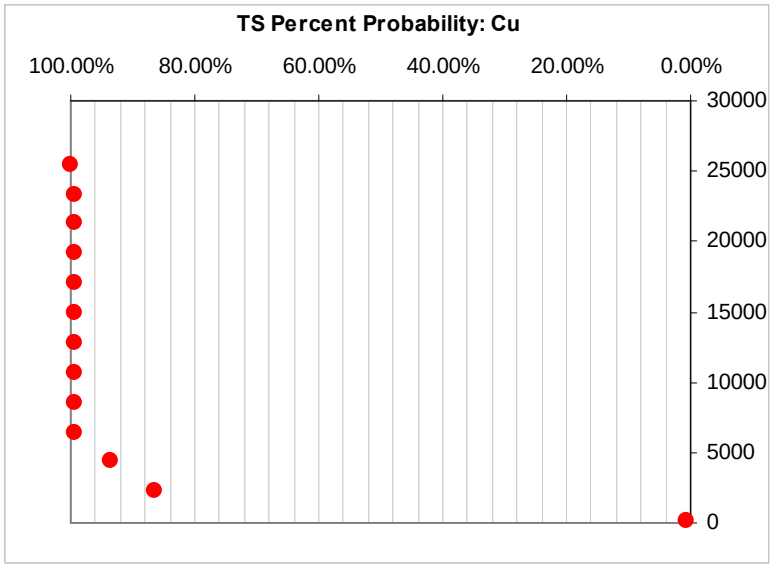
TS Percent Probability: Cu
100.00%
80.00%
60.00%
40.00%
20.00%
0.00%
30000
25000
20000
15000
10000
5000
0

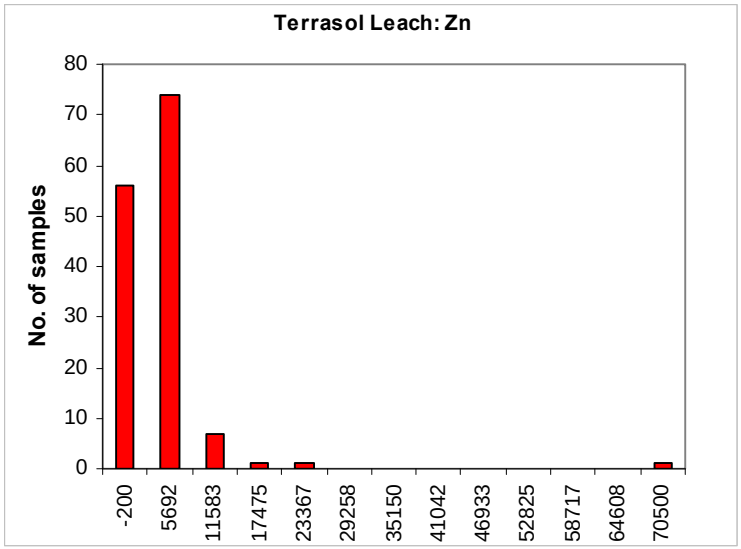
Terrasol Leach: Zn
No. of samples
80
70
60
50
40
30
20
10
0
-200
5692
11583
17475
23367
29258
35150
41042
46933
52825
58717
64608
70500

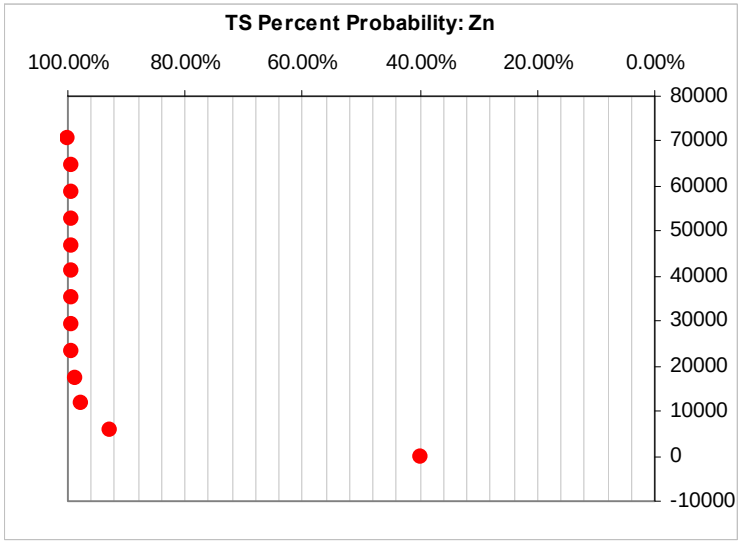
TS Percent Probability: Zn
100.00%
80.00%
60.00%
40.00%
20.00%
0.00%
80000
70000
60000
50000
40000
30000
20000
10000
0
-10000

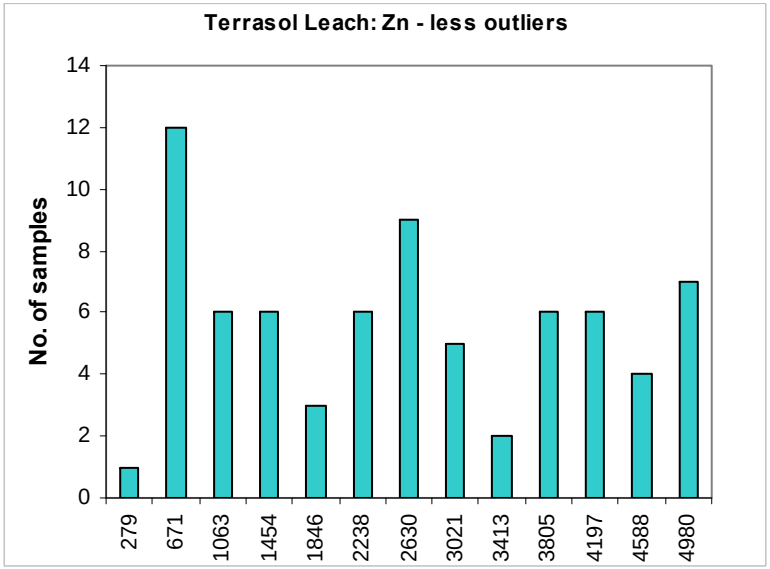
Terrasol Leach: Zn - less outliers
No. of samples
14
12
10
8
6
4
2
0
279
671
1063
1454
1846
2238
2630
3021
3413
3805
4197
4588
4980

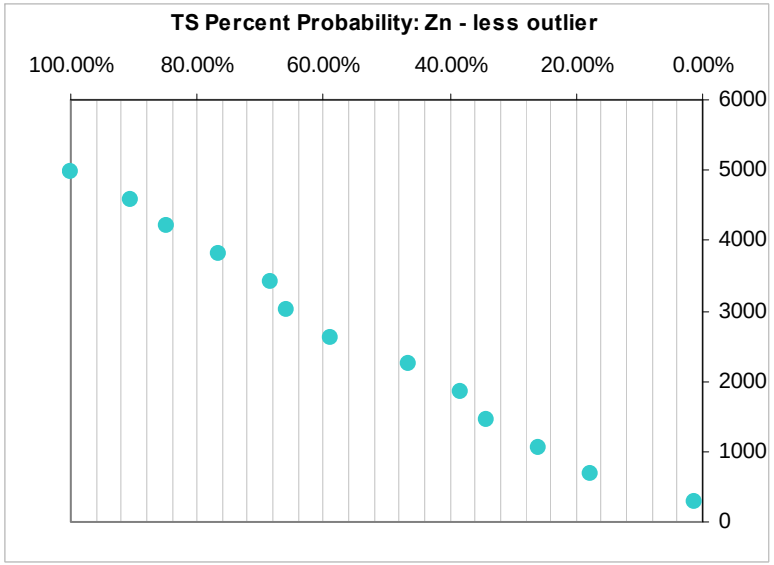
TS Percent Probability: Zn - less outlier
100.00%
80.00%
60.00%
40.00%
20.00%
0.00%
6000
5000
4000
3000
2000
1000
0

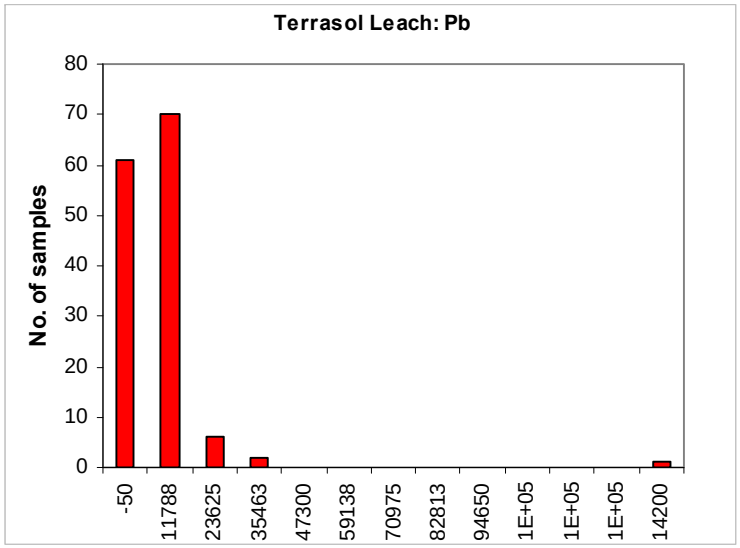
Terrasol Leach: Pb
No. of samples
80
70
60
50
40
30
20
10
0
-50
11788
23625
35463
47300
59138
70975
82813
94650
1E+05
1E+05
1E+05
14200

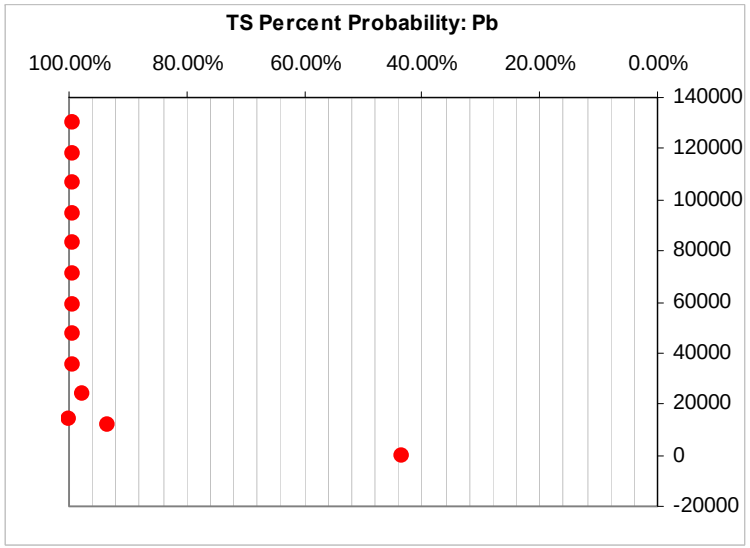
TS Percent Probability: Pb
100.00%
80.00%
60.00%
40.00%
20.00%
0.00%
140000
120000
100000
80000
60000
40000
20000
0
-20000

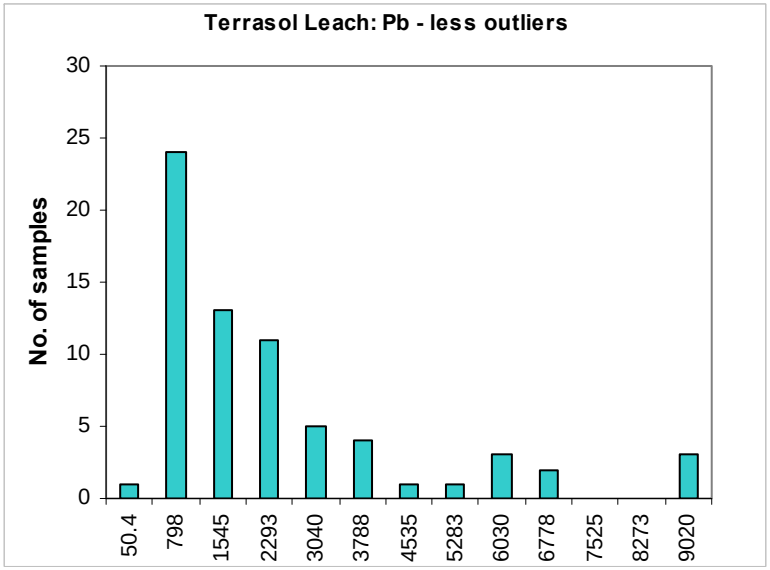
Terrasol Leach: Pb - less outliers
No. of samples
30
25
20
15
10
5
0
50.4
798
1545
2293
3040
3788
4535
5283
6030
6778
7525
8273
9020

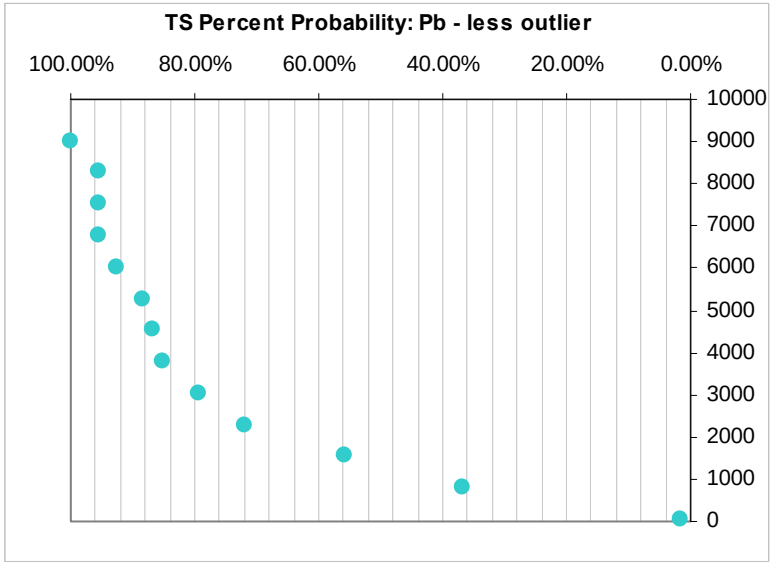
TS Percent Probability: Pb - less outlier
100.00%
80.00%
60.00%
40.00%
20.00%
0.00%
10000
9000
8000
7000
6000
5000
4000
3000
2000
1000
0

Appendix 6.3 Histograms and cumulative probability plots for TS Chalcophiles. Elements with extreme outliers were re-plotted without outlying points to better visualize distribution of data.

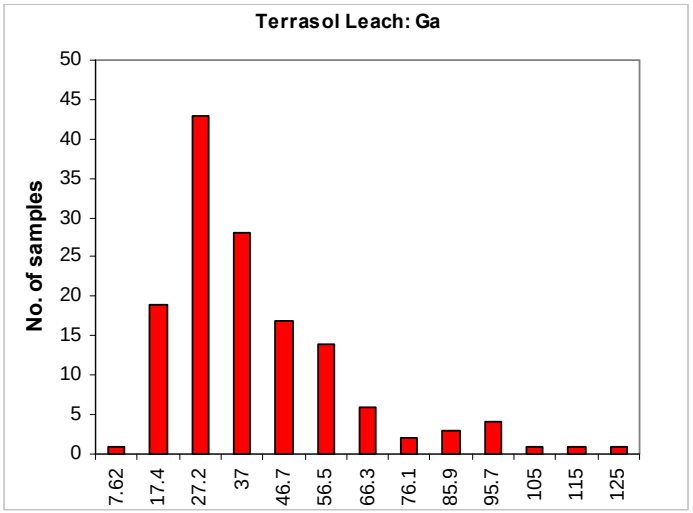

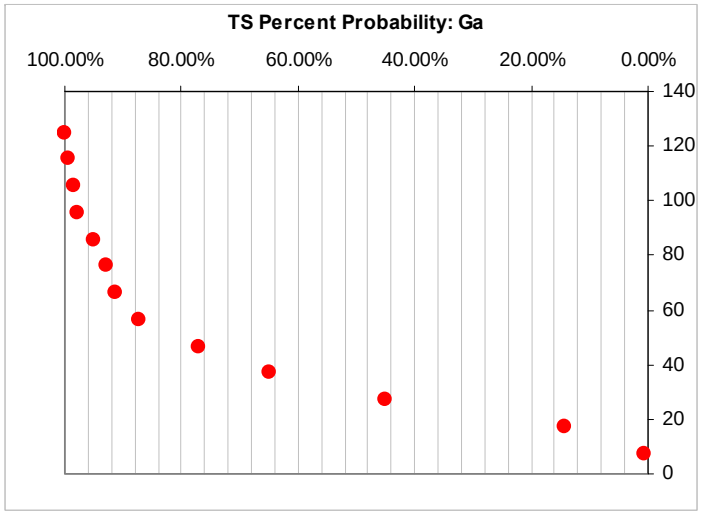

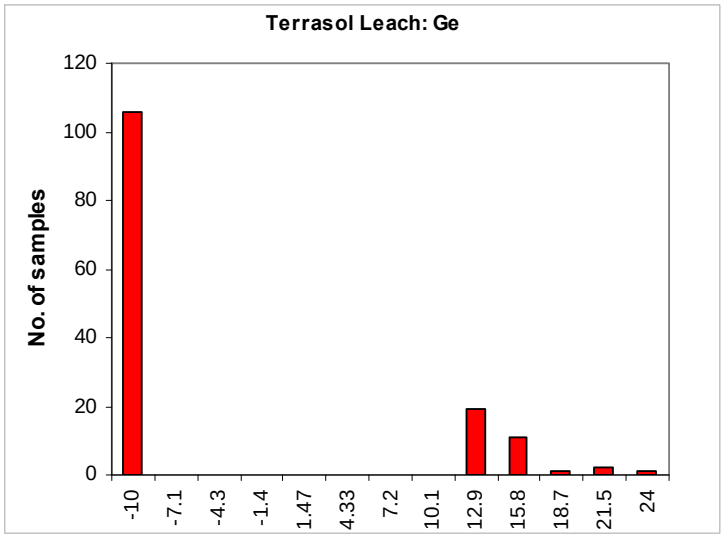

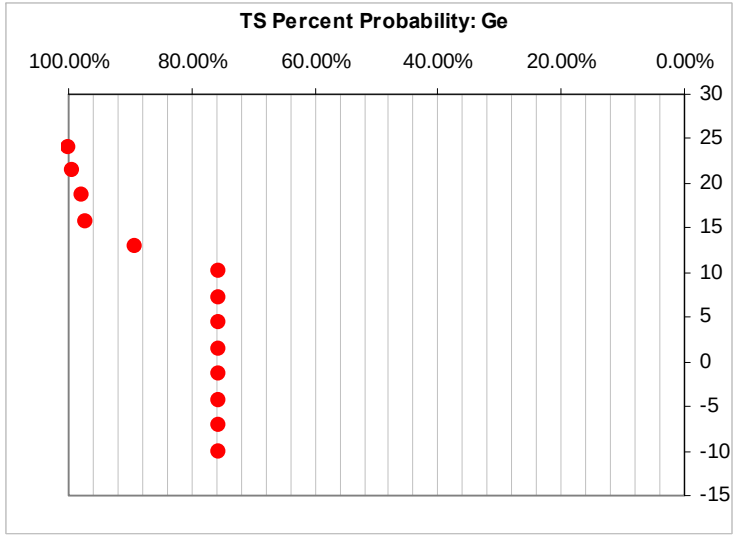

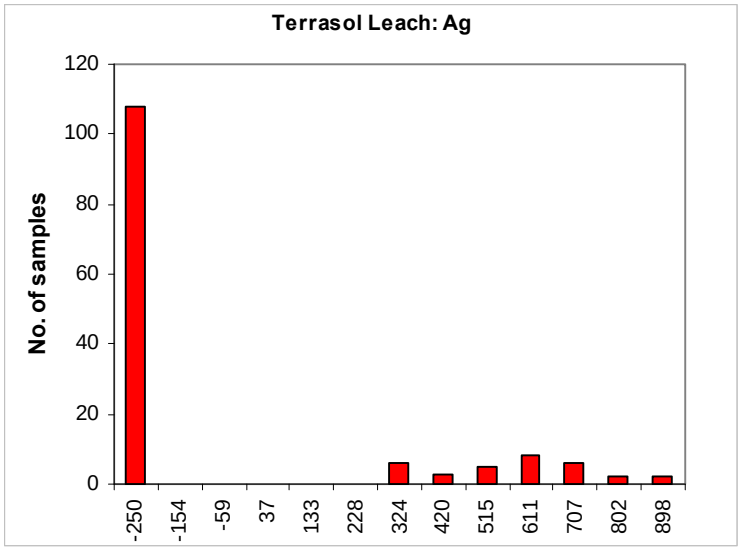
Terrasol Leach: Ag
No. of samples
120
100
80
60
40
20
0
-250
-154
-59
37
133
228
324
420
515
611
707
802
898

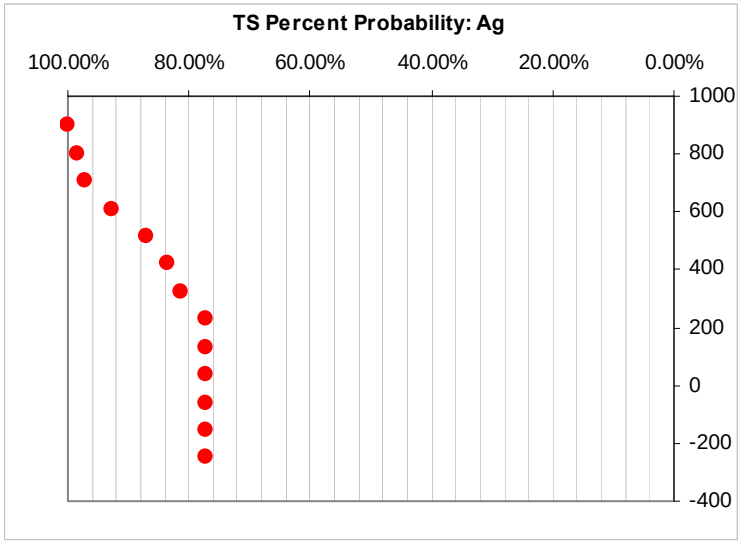
TS Percent Probability: Ag
100.00%
80.00%
60.00%
40.00%
20.00%
0.00%
1000
800
600
400
200
0
-200
-400

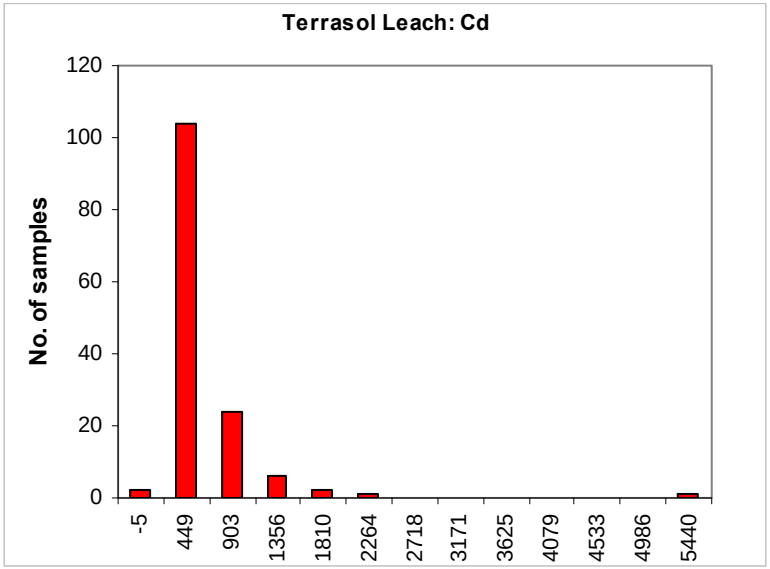
Terrasol Leach: Cd
No. of samples
120
100
80
60
40
20
0
-5
449
903
1356
1810
2264
2718
3171
3625
4079
4533
4986
5440

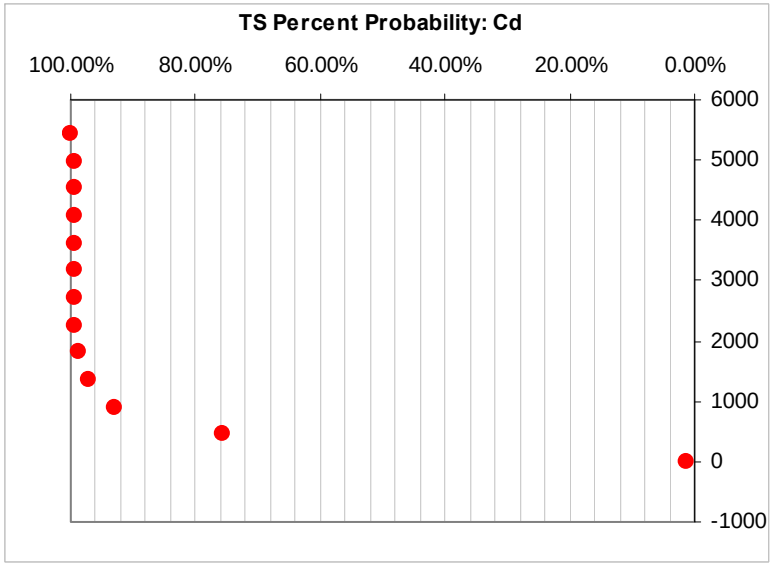
TS Percent Probability: Cd
100.00%
80.00%
60.00%
40.00%
20.00%
0.00%
6000
5000
4000
3000
2000
1000
0
-1000

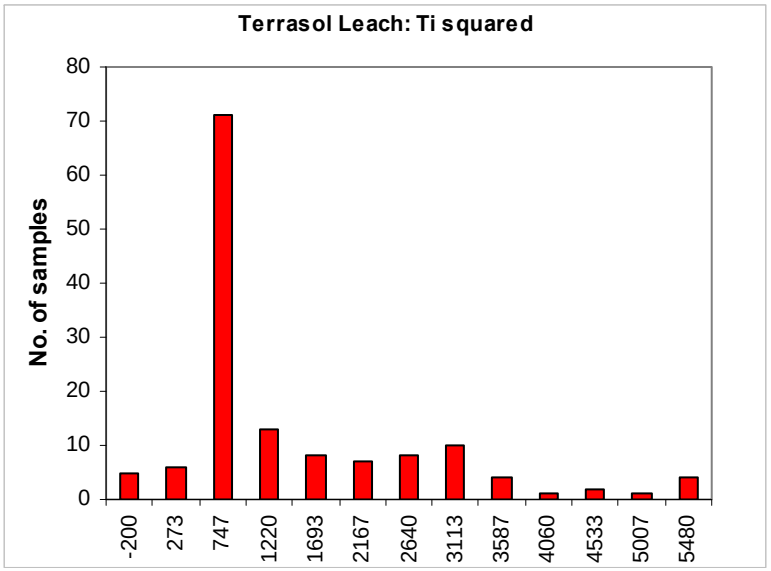
Terrasol Leach: Ti squared
No. of samples
80
70
60
50
40
30
20
10
0
-200
273
747
1220
1693
2167
2640
3113
3587
4060
4533
5007
5480

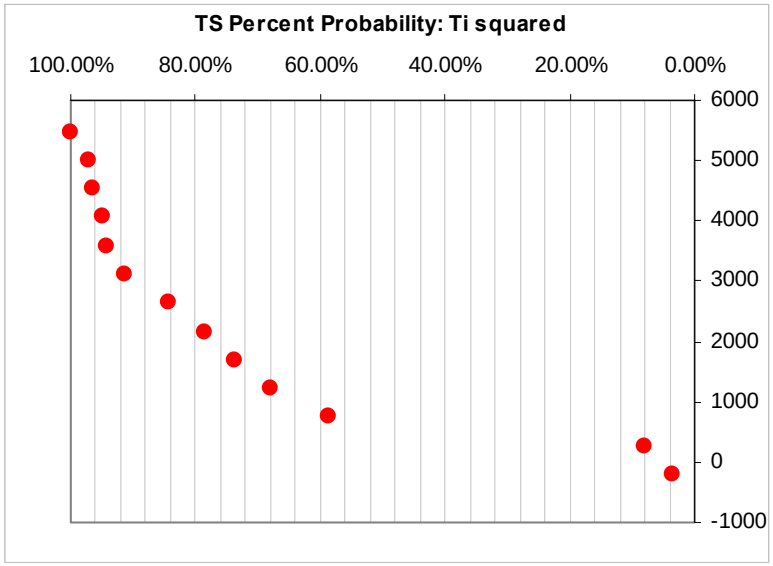
TS Percent Probability: Ti squared
100.00%
80.00%
60.00%
40.00%
20.00%
0.00%
6000
5000
4000
3000
2000
1000
0
-1000

Appendix 6.4 Histograms and cumulative probability plots for TS HFSEs. Elements with extreme outliers were re-plotted without outlying points to better visualize distribution of data.

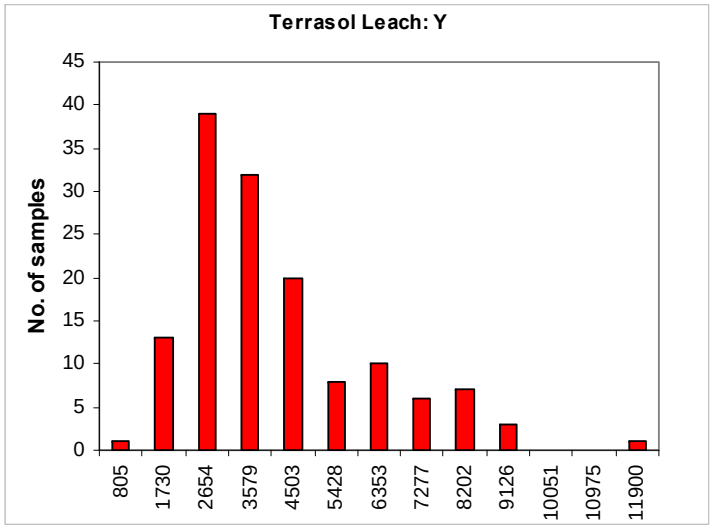

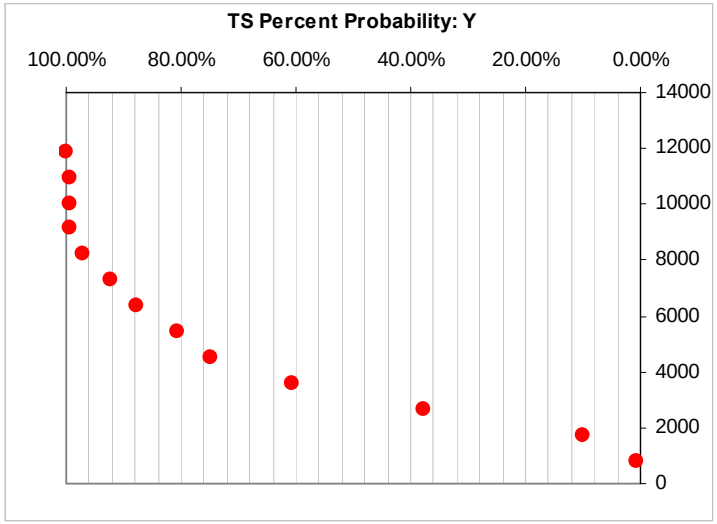

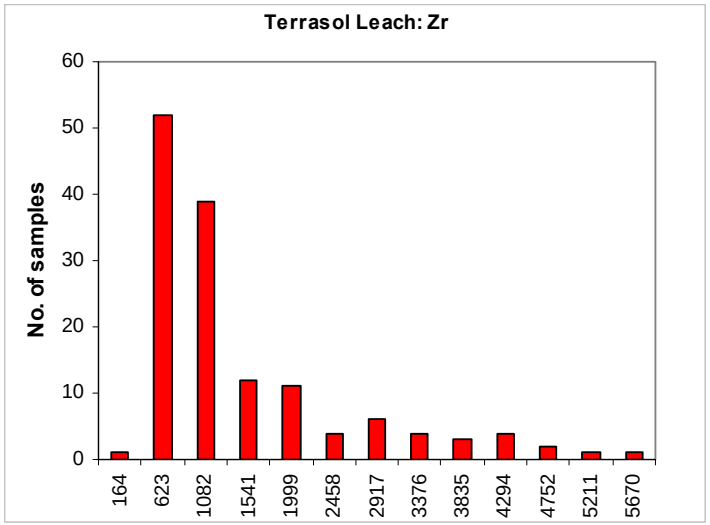

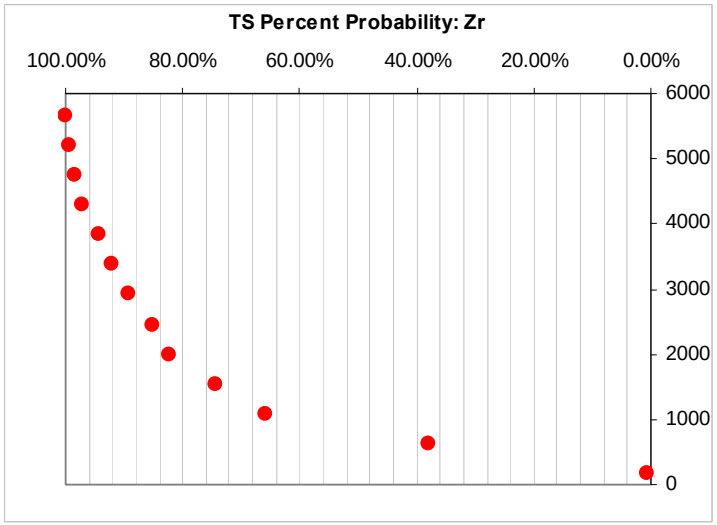

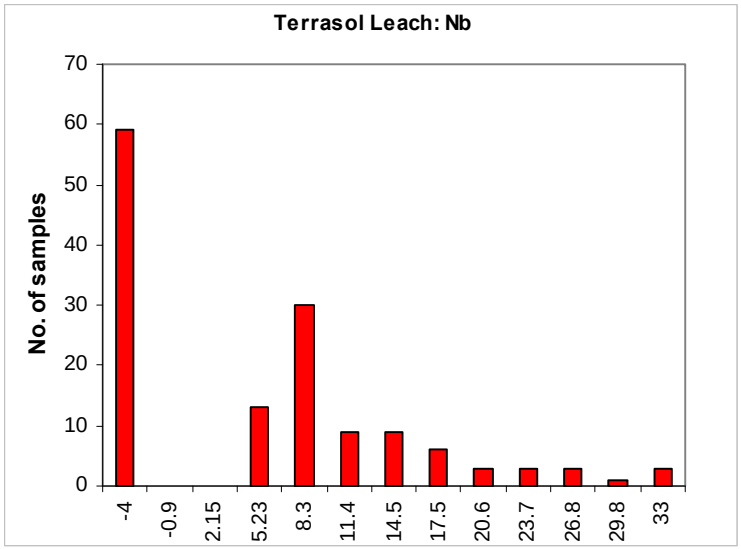
Terrasol Leach: Nb
No. of samples
70
60
50
40
30
20
10
0
-4
-0.9
2.15
5.23
8.3
11.4
14.5
17.5
20.6
23.7
26.8
29.8
33

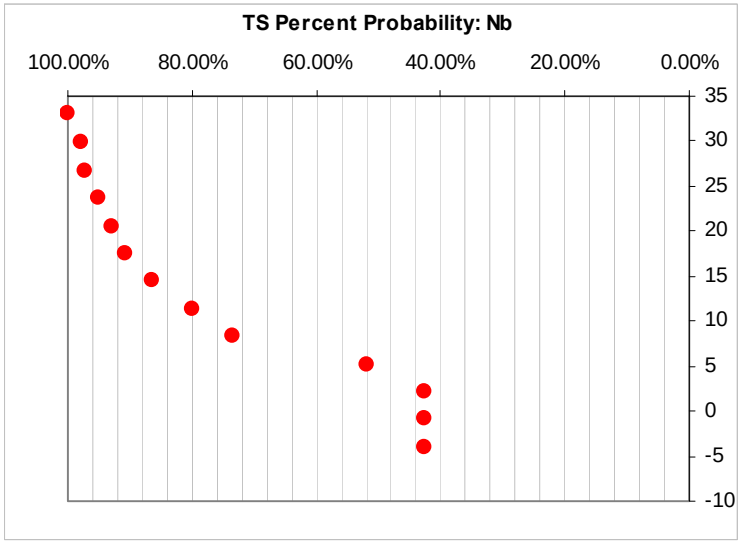
TS Percent Probability: Nb
100.00%
80.00%
60.00%
40.00%
20.00%
0.00%
35
30
25
20
15
10
5
0
-5
-10

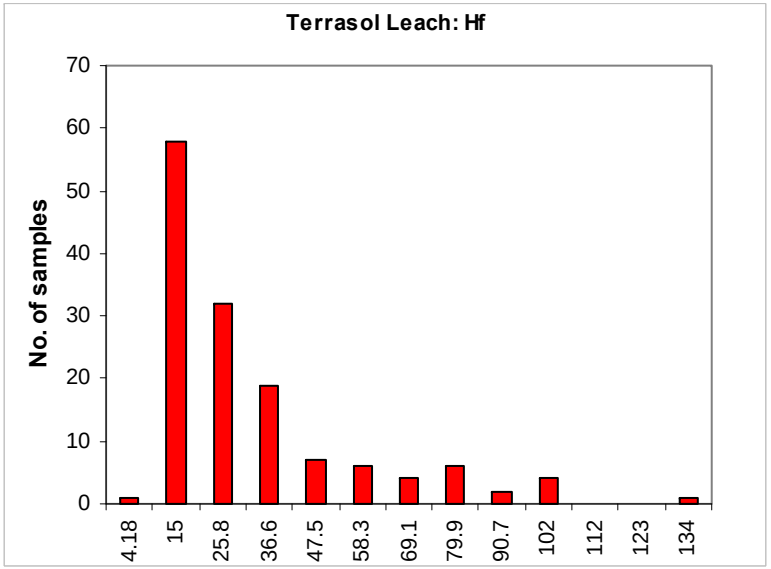
Terrasol Leach: Hf
No. of samples
70
60
50
40
30
20
10
0
4.18
15
25.8
36.6
47.5
58.3
69.1
79.9
90.7
102
112
123
134

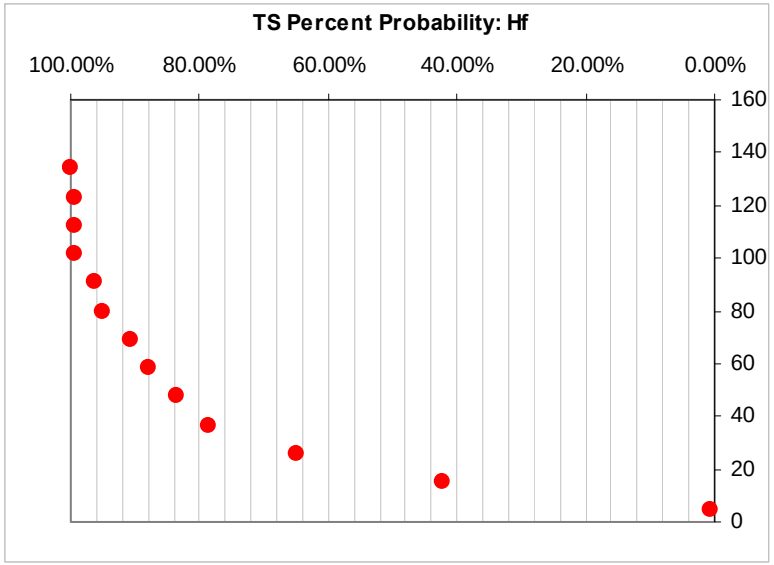
TS Percent Probability: Hf
100.00%
80.00%
60.00%
40.00%
20.00%
0.00%
160
140
120
100
80
60
40
20
0

Appendix 6.5 Histograms and cumulative probability plots for TS REEs. Elements with extreme outliers were re-plotted without outlying points to better visualize distribution of data.

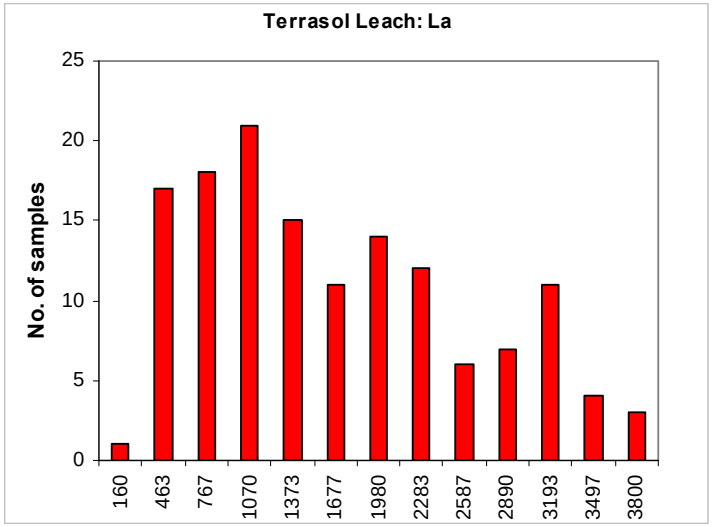

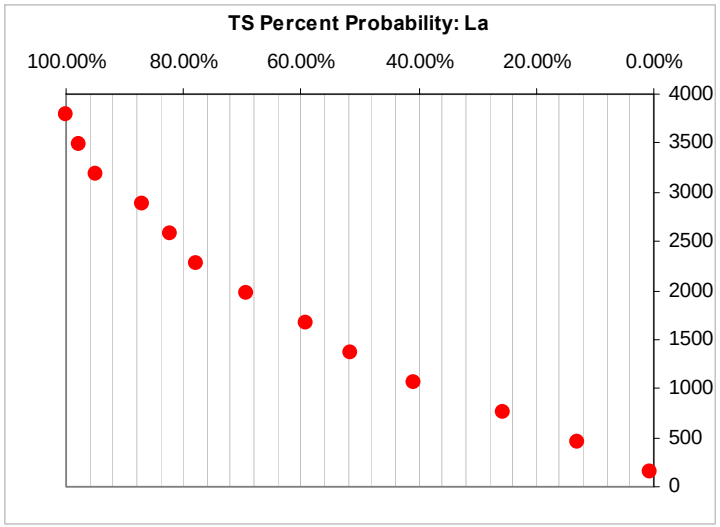

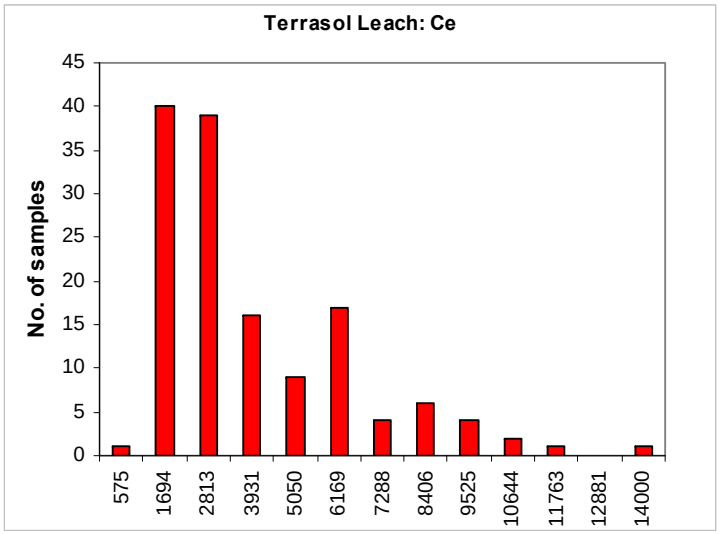

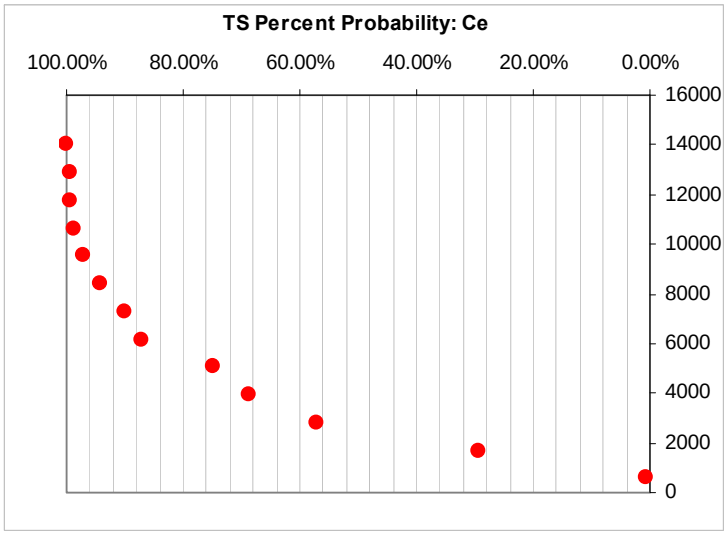

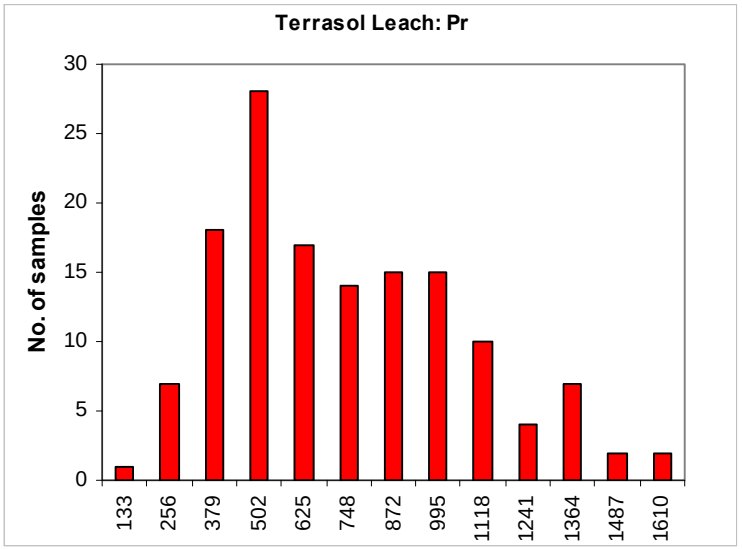
Terrasol Leach: Pr
No. of samples
30
25
20
15
10
5
0
133
256
379
502
625
748
872
995
1118
1241
1364
1487
1610

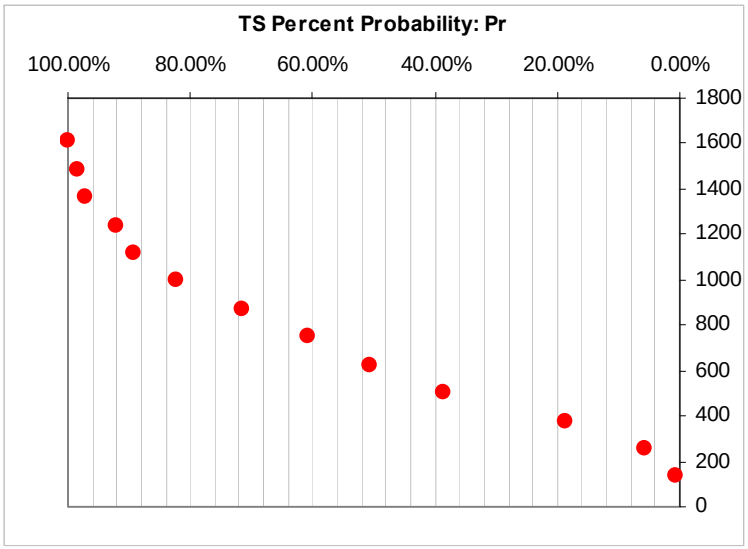
TS Percent Probability: Pr
100.00%
80.00%
60.00%
40.00%
20.00%
0.00%
1800
1600
1400
1200
1000
800
600
400
200
0

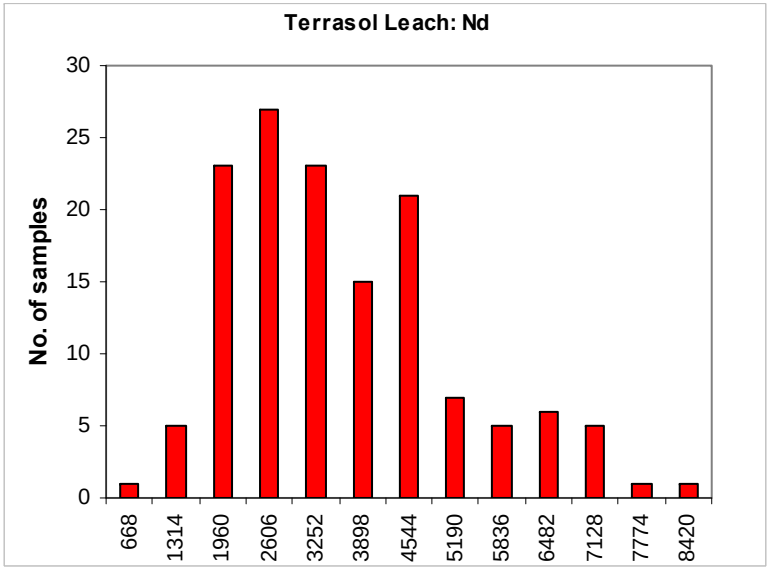
Terrasol Leach: Nd
No. of samples
30
25
20
15
10
5
0
668
1314
1960
2606
3252
3898
4544
5190
5836
6482
7128
7774
8420

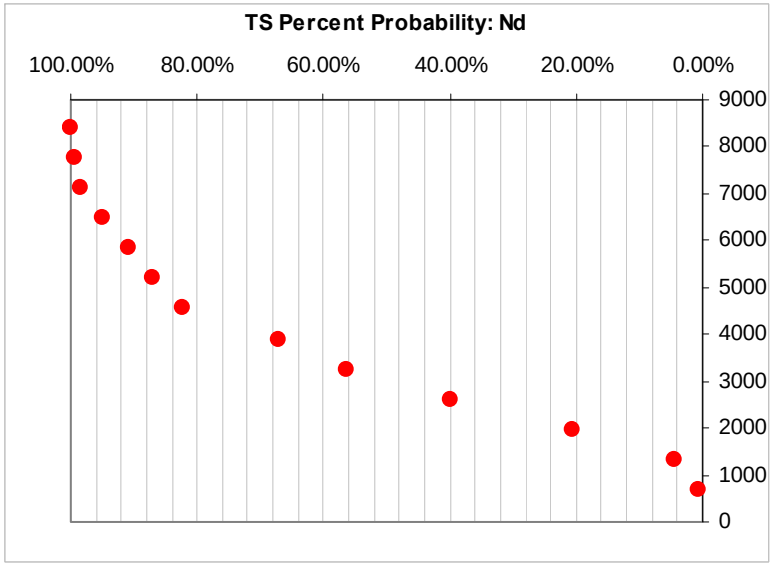
TS Percent Probability: Nd
100.00%
80.00%
60.00%
40.00%
20.00%
0.00%
9000
8000
7000
6000
5000
4000
3000
2000
1000
0

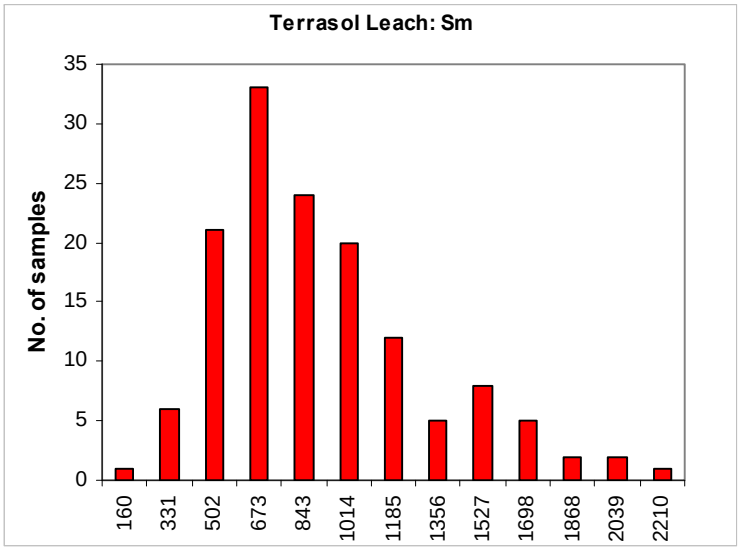
Terrasol Leach: Sm
No. of samples
35
30
25
20
15
10
5
0
160
331
502
673
843
1014
1185
1356
1527
1698
1868
2039
2210

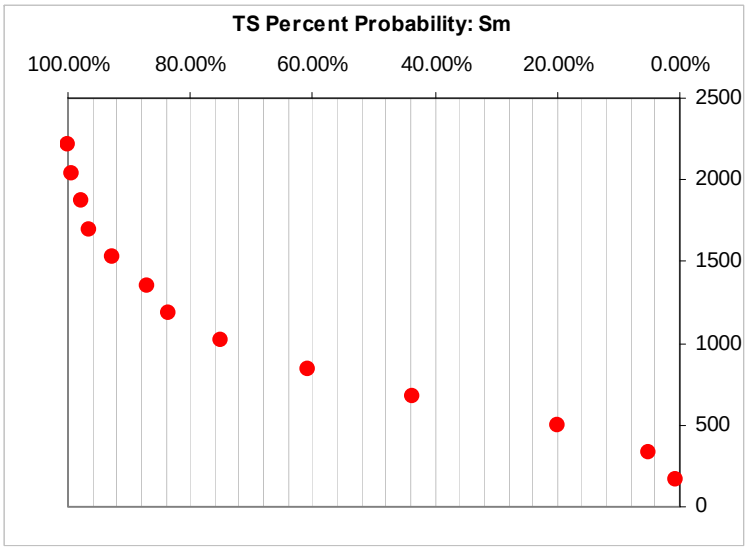
TS Percent Probability: Sm
100.00%
80.00%
60.00%
40.00%
20.00%
0.00%
2500
2000
1500
1000
500
0

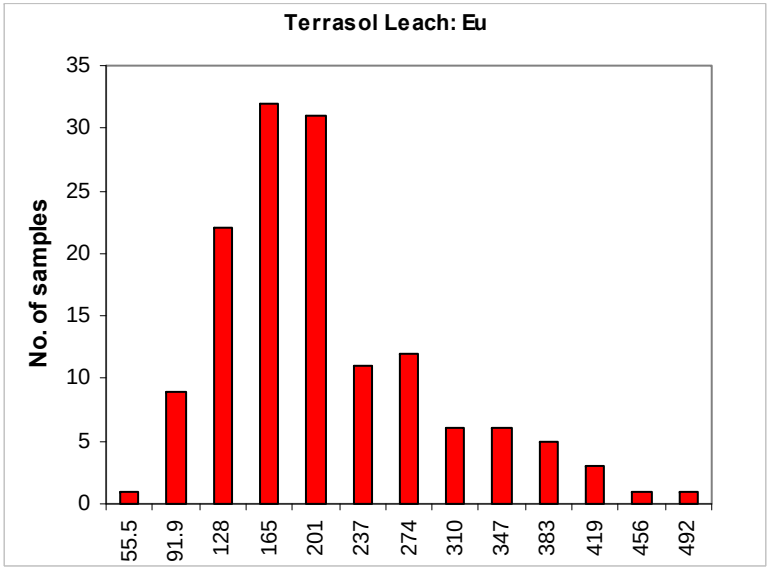
Terrasol Leach: Eu
No. of samples
35
30
25
20
15
10
5
0
55.5
91.9
128
165
201
237
274
310
347
383
419
456
492

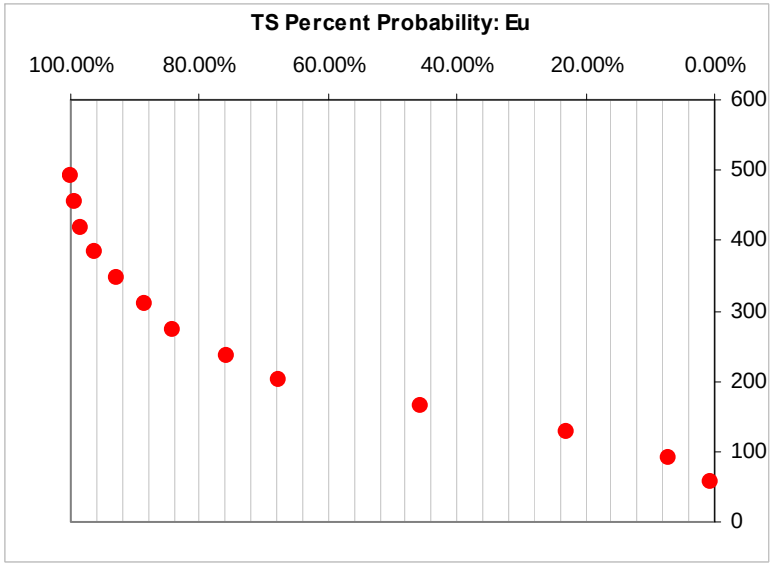
TS Percent Probability: Eu
100.00%
80.00%
60.00%
40.00%
20.00%
0.00%
600
500
400
300
200
100
0

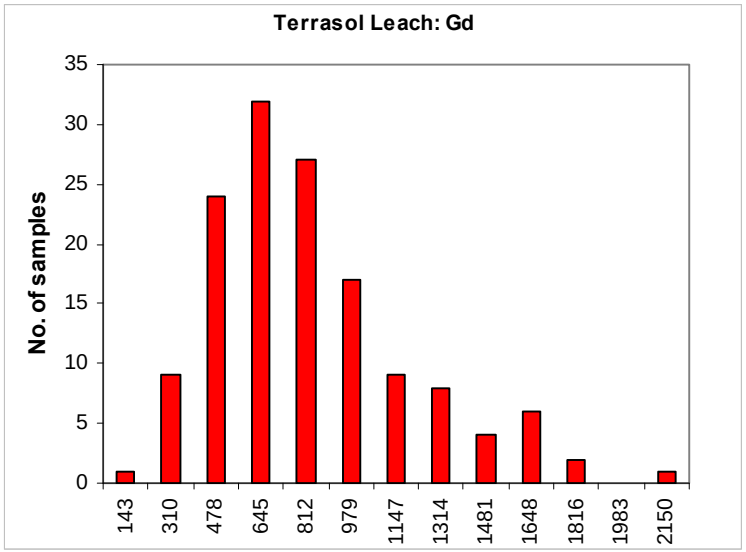
Terrasol Leach: Gd
No. of samples
35
30
25
20
15
10
5
0
143
310
478
645
812
979
1147
1314
1481
1648
1816
1983
2150

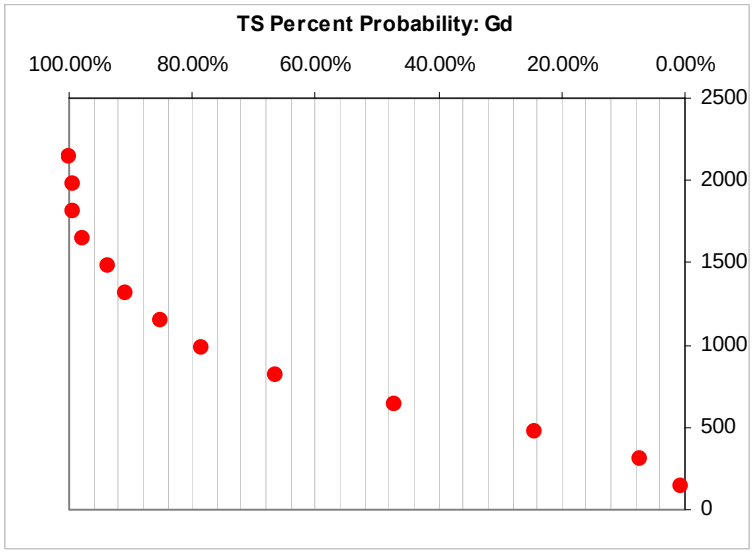
TS Percent Probability: Gd
100.00%
80.00%
60.00%
40.00%
20.00%
0.00%
2500
2000
1500
1000
500
0

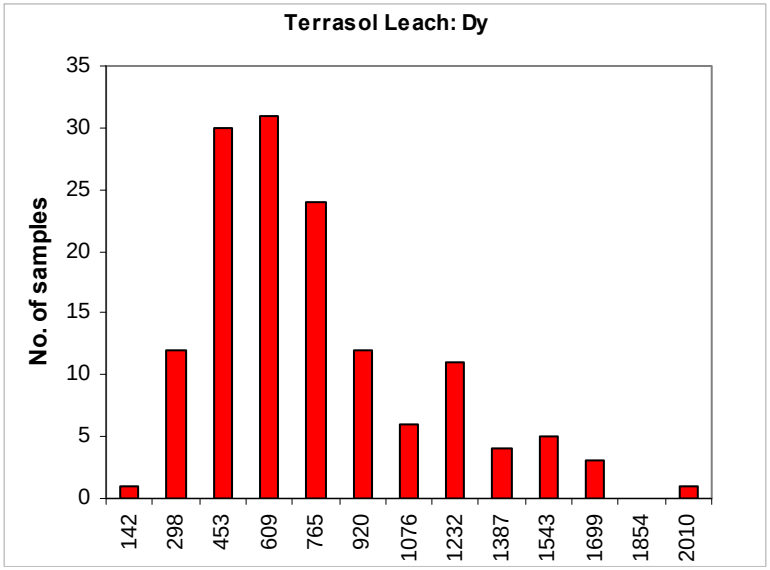
Terrasol Leach: Dy
No. of samples
35
30
25
20
15
10
5
0
142
298
453
609
765
920
1076
1232
1387
1543
1699
1854
2010

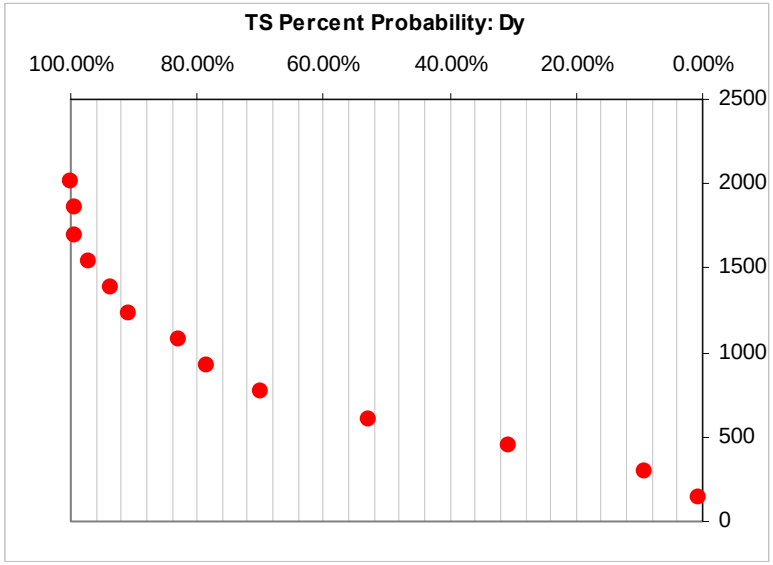
TS Percent Probability: Dy
100.00%
80.00%
60.00%
40.00%
20.00%
0.00%
2500
2000
1500
1000
500
0

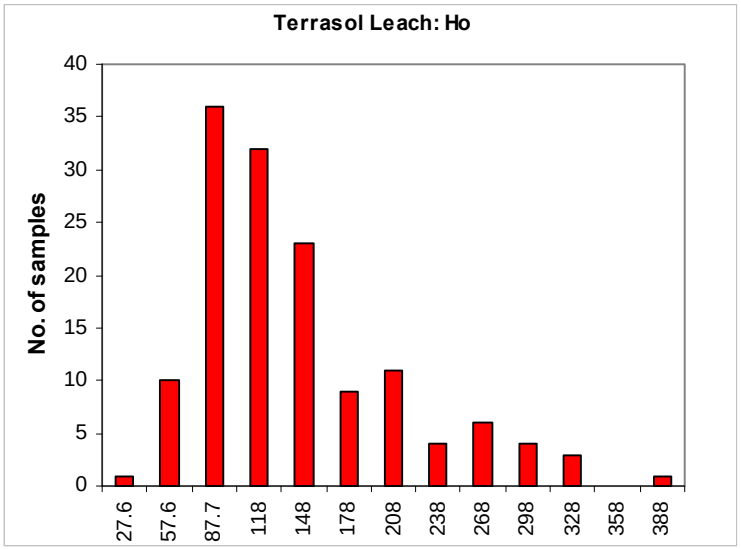
Terrasol Leach: Ho
No. of samples
40
35
30
25
20
15
10
5
0
27.6
57.6
87.7
118
148
178
208
238
268
298
328
358
388

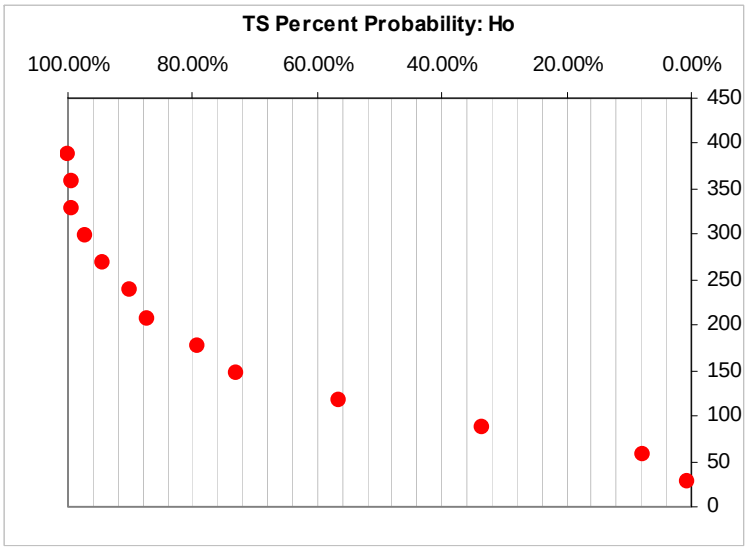
TS Percent Probability: Ho
100.00%
80.00%
60.00%
40.00%
20.00%
0.00%
450
400
350
300
250
200
150
100
50
0

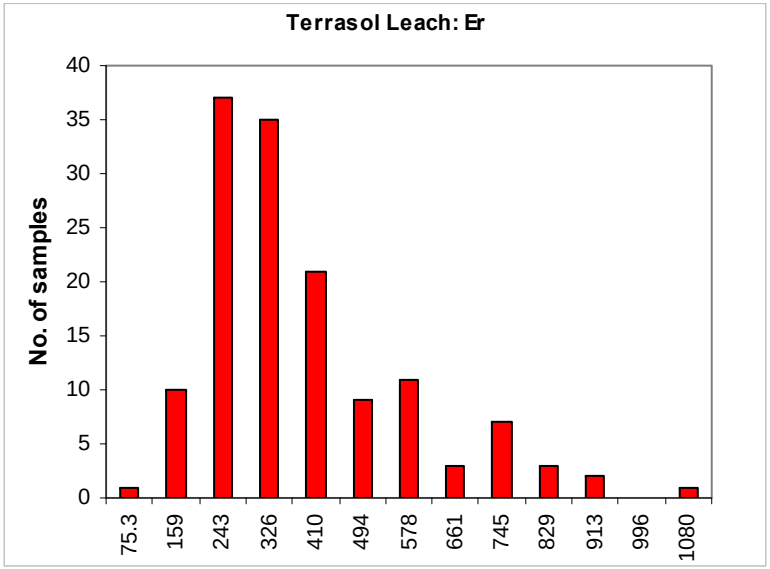
Terrasol Leach: Er
No. of samples
40
35
30
25
20
15
10
5
0
75.3
159
243
326
410
494
578
661
745
829
913
996
1080

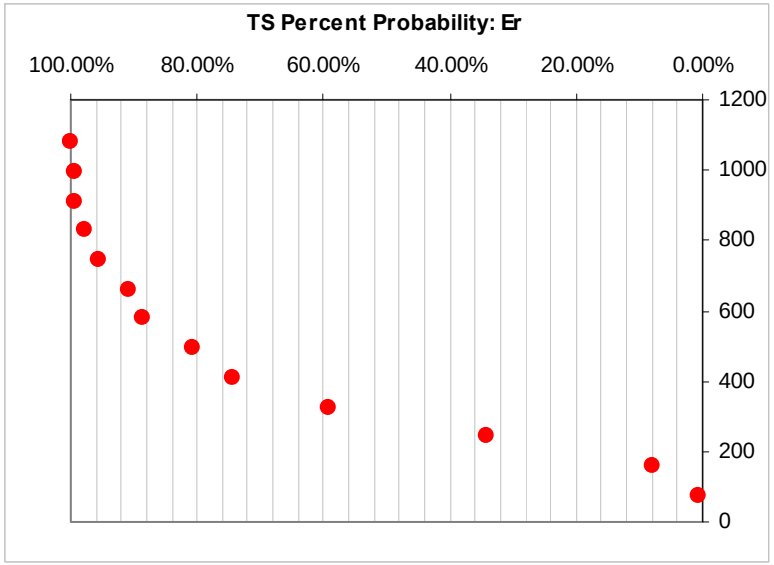
TS Percent Probability: Er
100.00%
80.00%
60.00%
40.00%
20.00%
0.00%
1200
1000
800
600
400
200
0

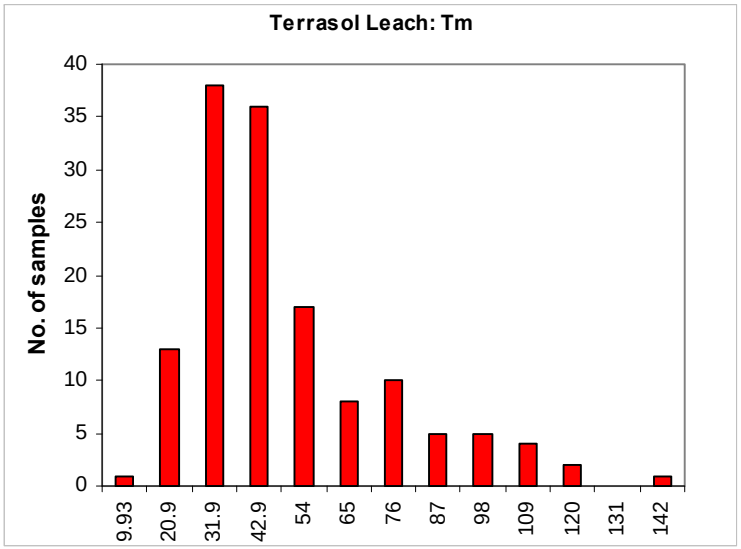
Terrasol Leach: Tm
No. of samples
40
35
30
25
20
15
10
5
0
9.93
20.9
31.9
42.9
54
65
76
87
98
109
120
131
142

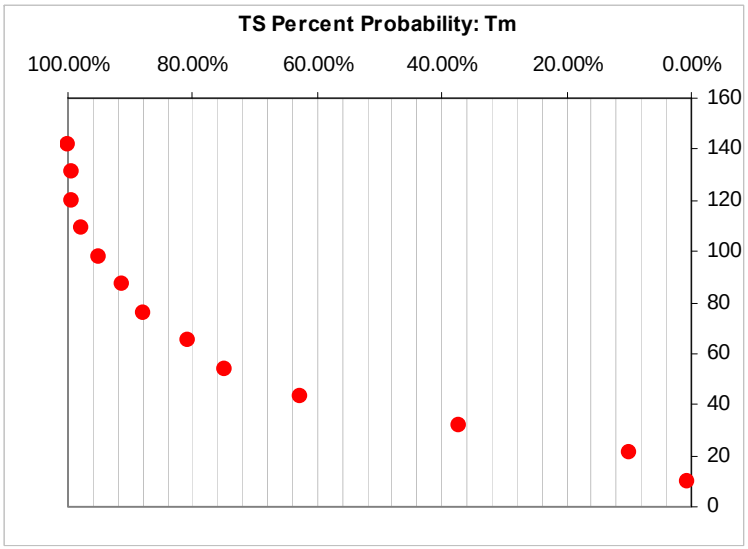
TS Percent Probability: Tm
100.00%
80.00%
60.00%
40.00%
20.00%
0.00%
160
140
120
100
80
60
40
20
0

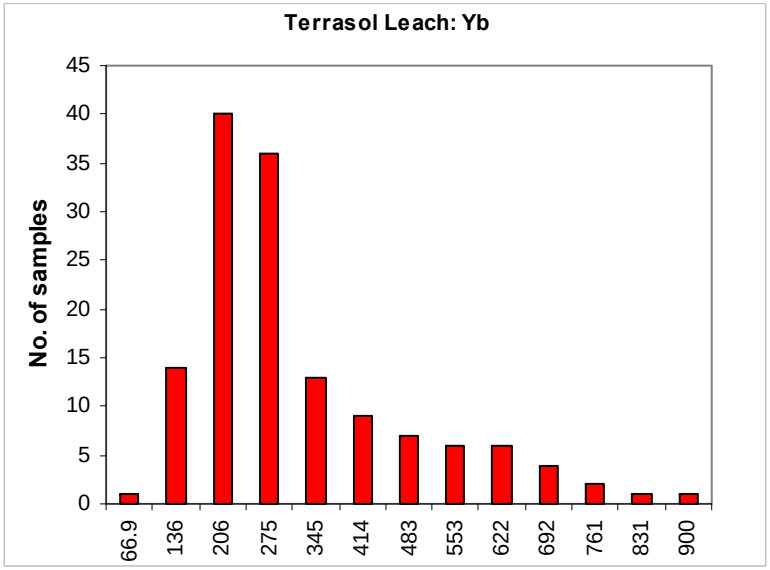
Terrasol Leach: Yb
No. of samples
45
40
35
30
25
20
15
10
5
0
66.9
136
206
275
345
414
483
553
622
692
761
831
900

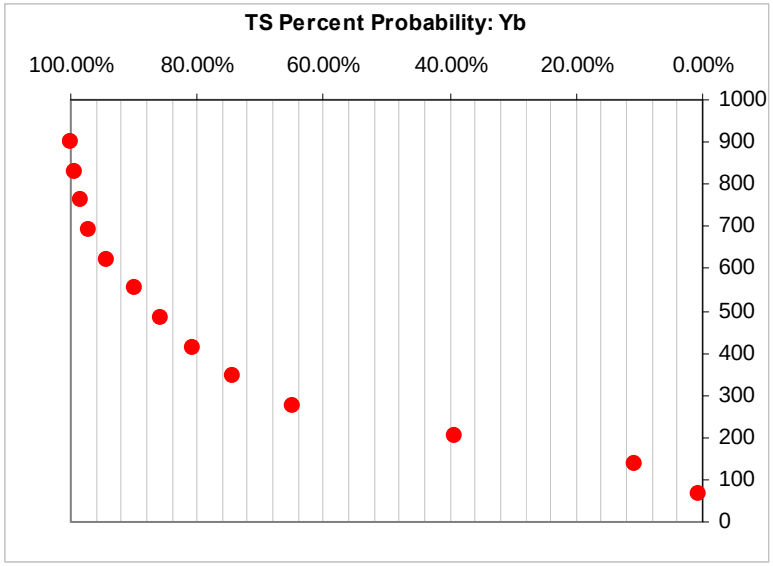
TS Percent Probability: Yb
100.00%
80.00%
60.00%
40.00%
20.00%
0.00%
1000
900
800
700
600
500
400
300
200
100
0

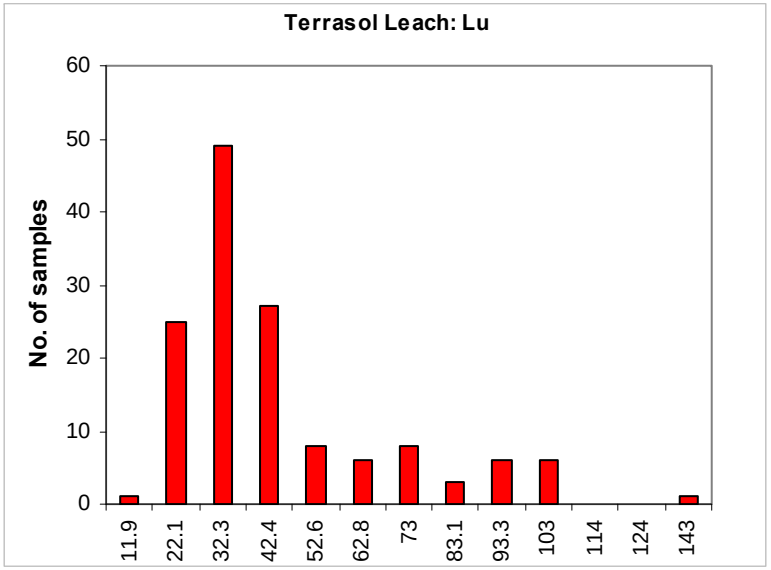
Terrasol Leach: Lu
No. of samples
60
50
40
30
20
10
0
11.9
22.1
32.3
42.4
52.6
62.8
73
83.1
93.3
103
114
124
143

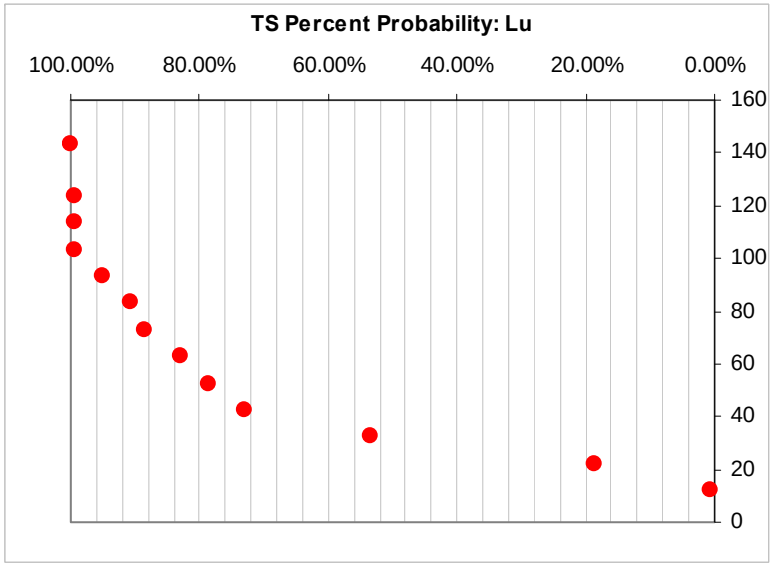
TS Percent Probability: Lu
100.00%
80.00%
60.00%
40.00%
20.00%
0.00%
160
140
120
100
80
60
40
20
0

Appendix 6.6 Histograms and cumulative probability plots for TS Lithophiles. Elements with extreme outliers were re-plotted without outlying points to better visualize distribution of data.

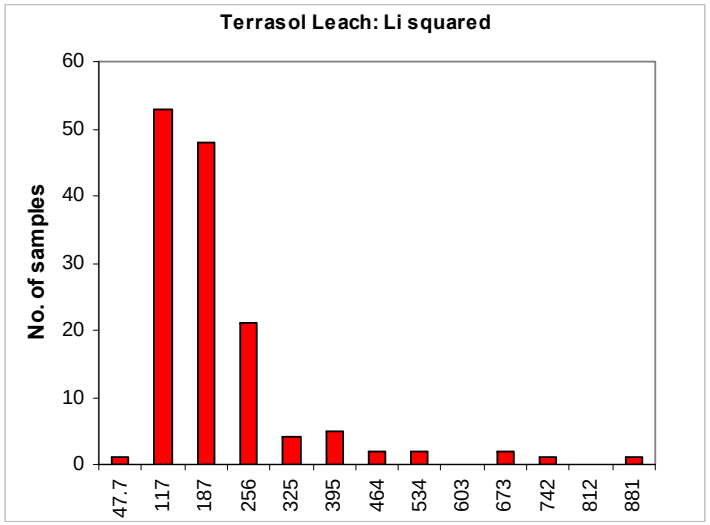

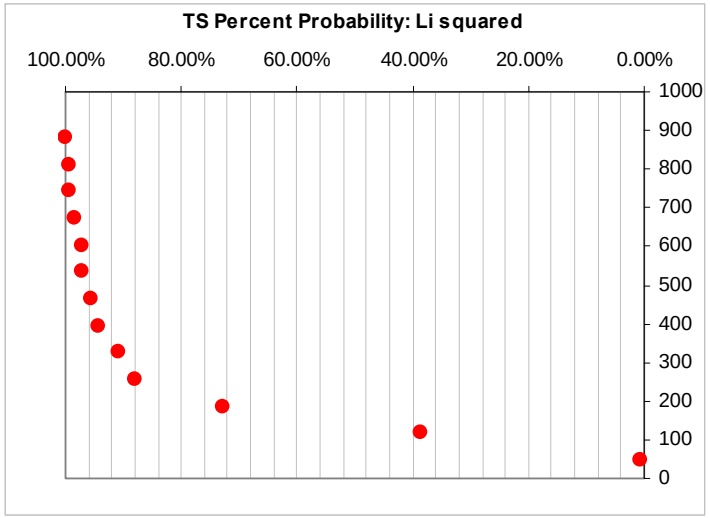

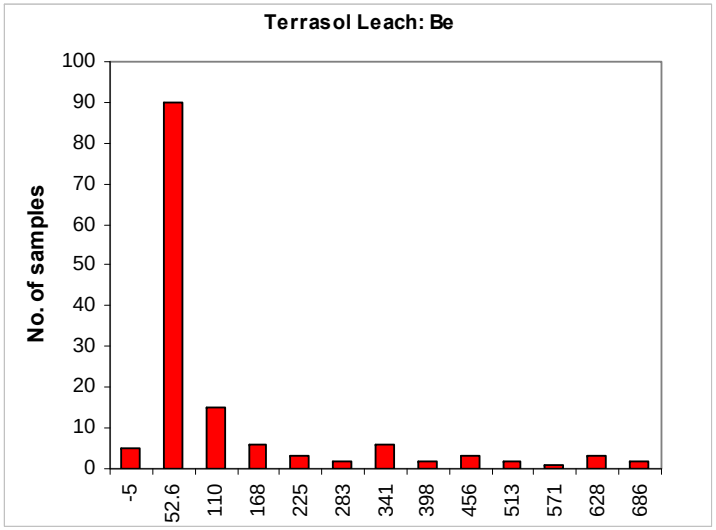

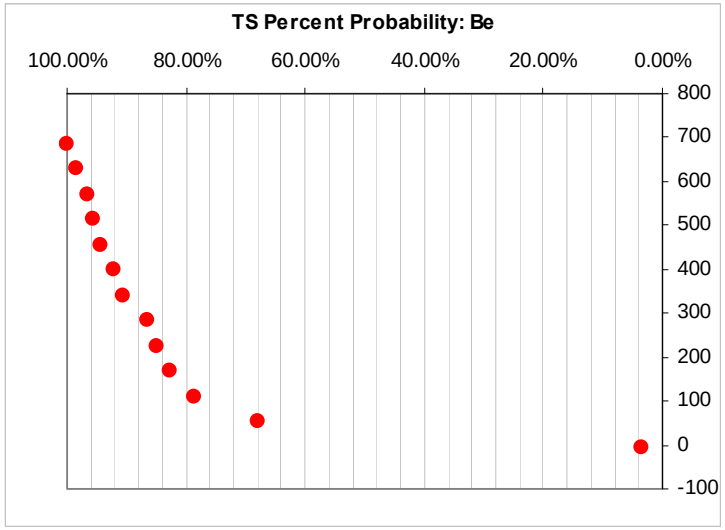

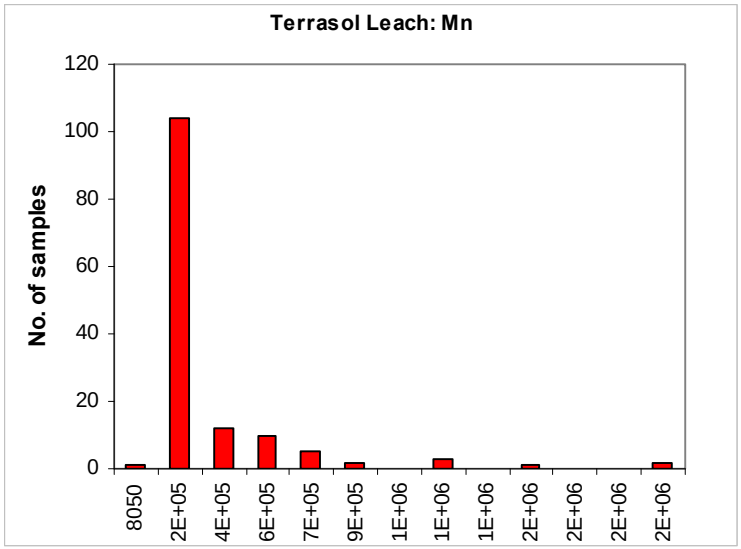
Terrasol Leach: Mn
No. of samples
120
100
80
60
40
20
0
8050
2E+05
4E+05
6E+05
7E+05
9E+05
1E+06
1E+06
1E+06
2E+06
2E+06
2E+06
2E+06

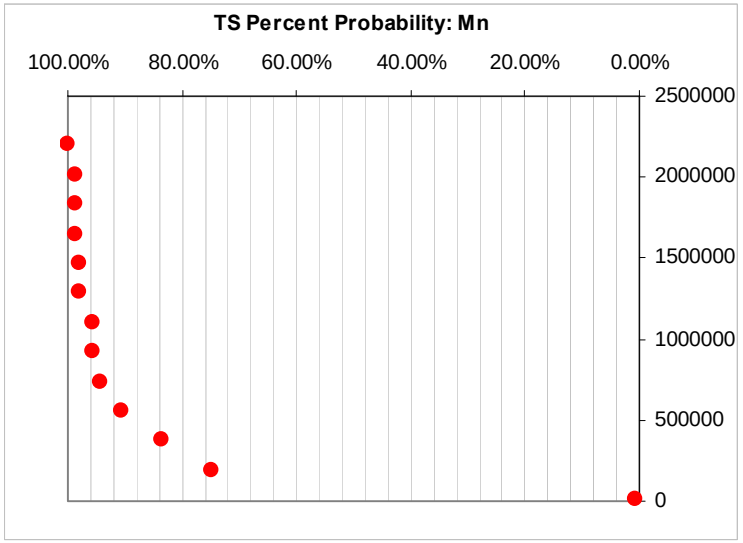
TS Percent Probability: Mn
100.00%
80.00%
60.00%
40.00%
20.00%
0.00%
2500000
2000000
1500000
1000000
500000
0

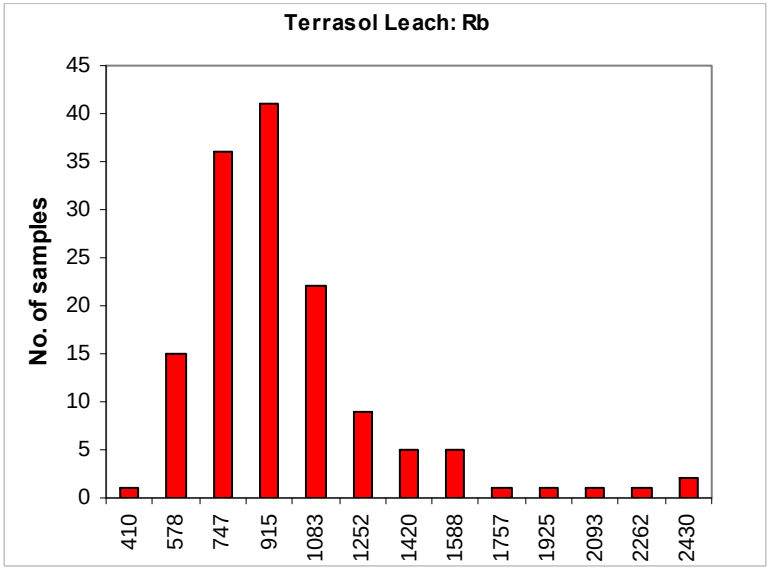
Terrasol Leach: Rb
No. of samples
45
40
35
30
25
20
15
10
5
0
410
578
747
915
1083
1252
1420
1588
1757
1925
2093
2262
2430

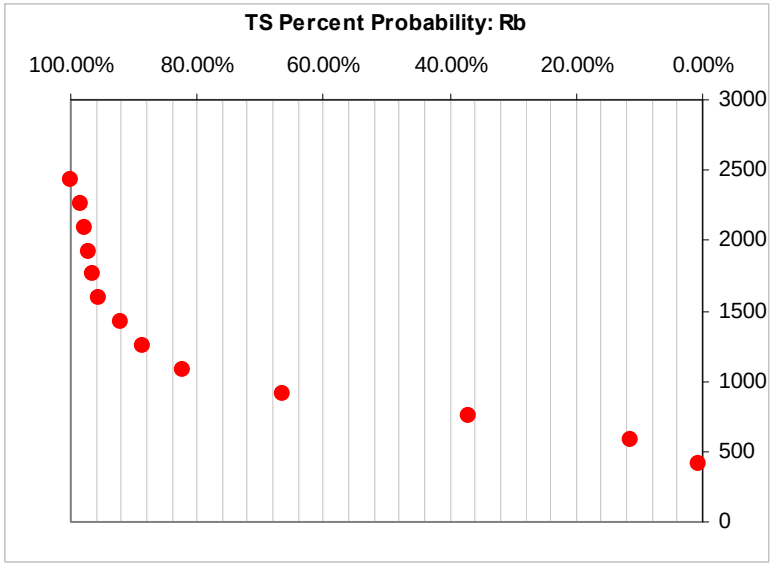
TS Percent Probability: Rb
100.00%
80.00%
60.00%
40.00%
20.00%
0.00%
3000
2500
2000
1500
1000
500
0

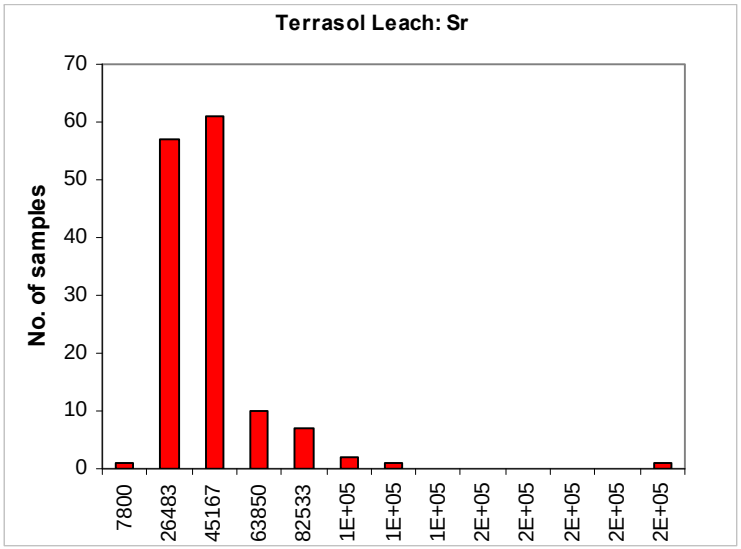
Terrasol Leach: Sr
No. of samples
70
60
50
40
30
20
10
0
7800
26483
45167
63850
82533
1E+05
1E+05
1E+05
2E+05
2E+05
2E+05
2E+05
2E+05

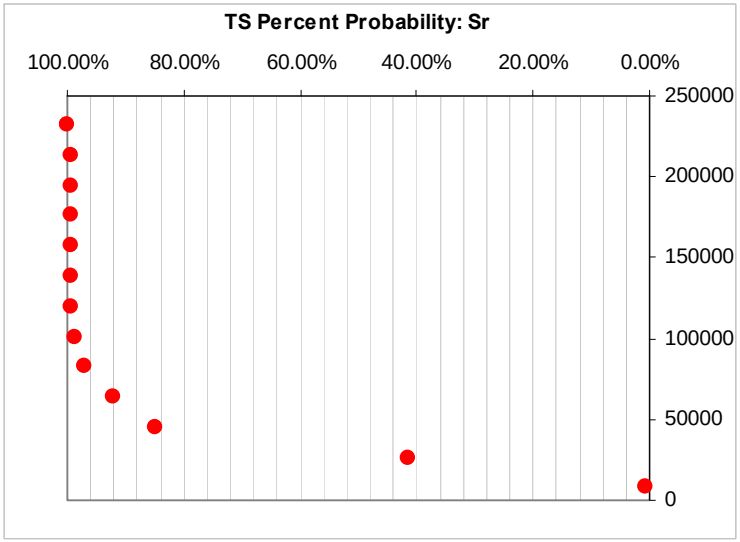
TS Percent Probability: Sr
100.00%
80.00%
60.00%
40.00%
20.00%
0.00%
250000
200000
150000
100000
50000
0

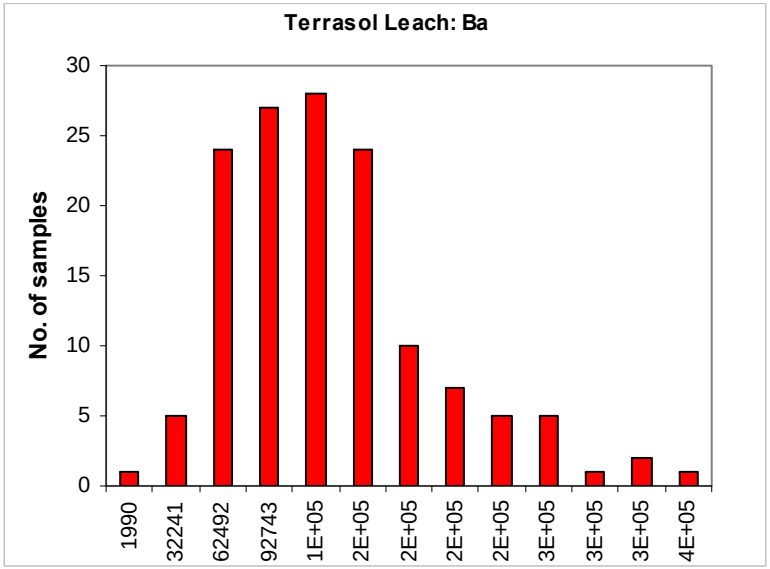
Terrasol Leach: Ba
No. of samples
30
25
20
15
10
5
0
1990
32241
62492
92743
1E+05
2E+05
2E+05
2E+05
2E+05
3E+05
3E+05
3E+05
4E+05

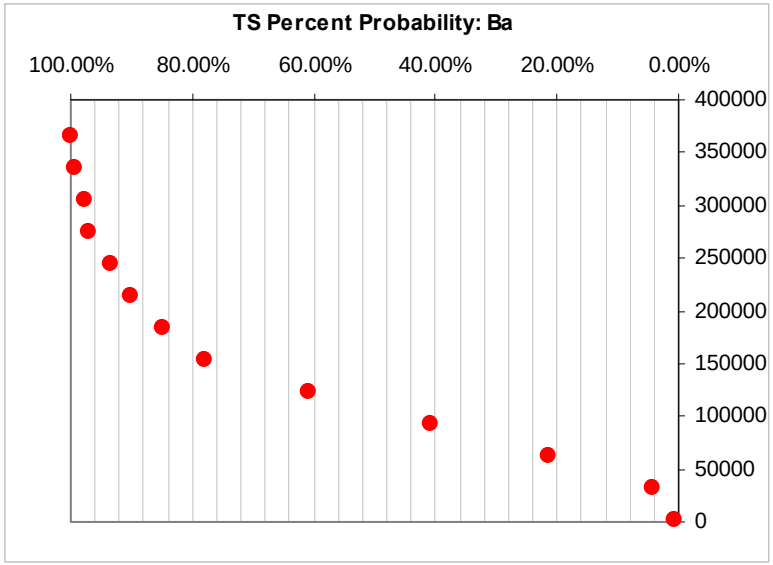
TS Percent Probability: Ba
100.00%
80.00%
60.00%
40.00%
20.00%
0.00%
400000
350000
300000
250000
200000
150000
100000
50000
0

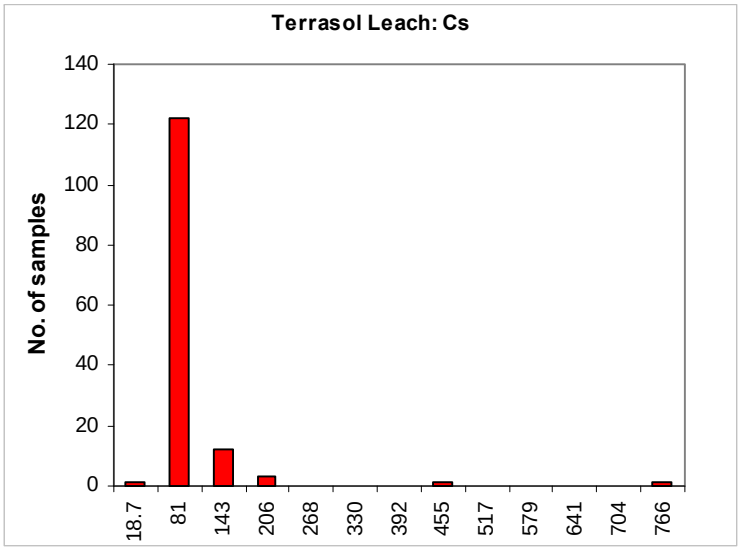
Terrasol Leach: Cs
No. of samples
140
120
100
80
60
40
20
0
18.7
81
143
206
268
330
392
455
517
579
641
704
766

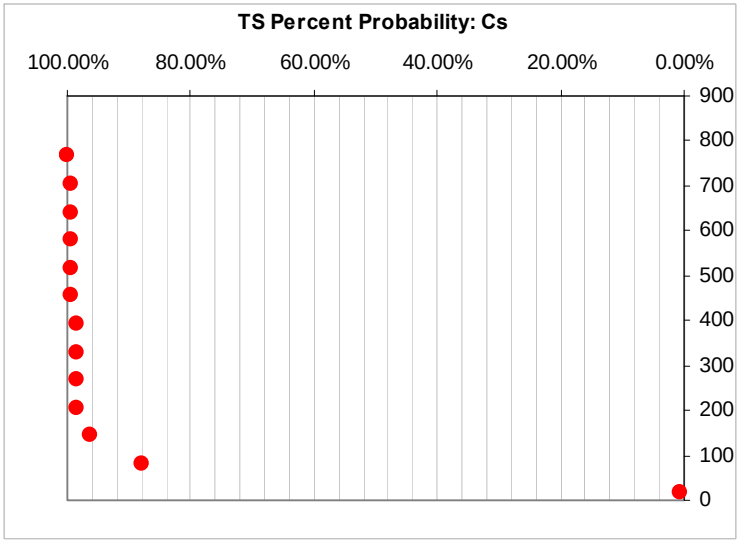
TS Percent Probability: Cs
100.00%
80.00%
60.00%
40.00%
20.00%
0.00%
900
800
700
600
500
400
300
200
100
0

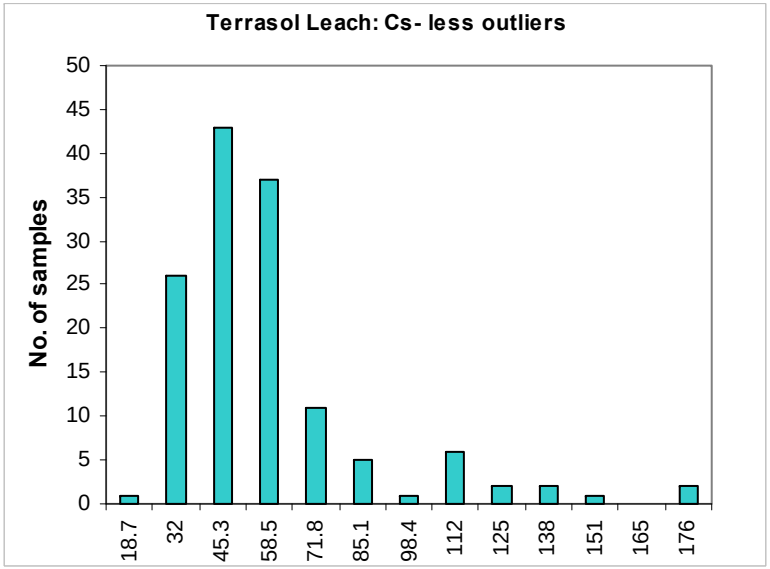
Terrasol Leach: Cs- less outliers
No. of samples
50
45
40
35
30
25
20
15
10
5
0
18.7
32
45.3
58.5
71.8
85.1
98.4
112
125
138
151
165
176

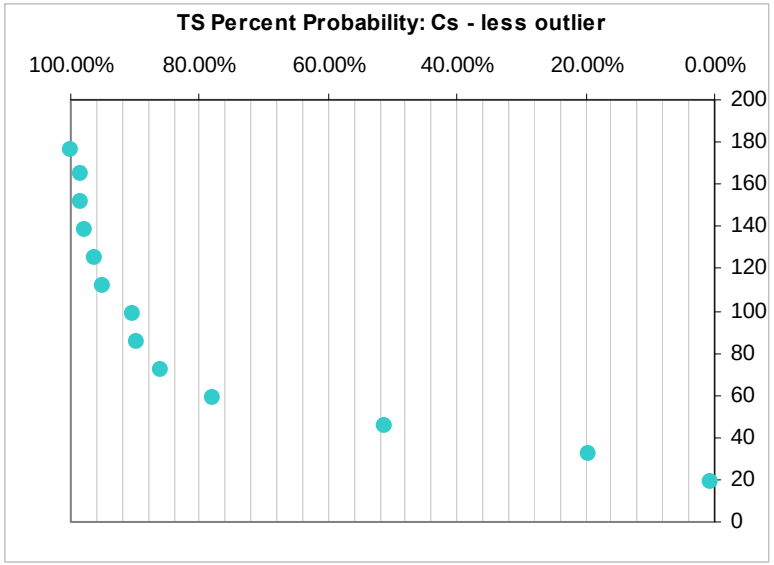
TS Percent Probability: Cs - less outlier
100.00%
80.00%
60.00%
40.00%
20.00%
0.00%
200
180
160
140
120
100
80
60
40
20
0

Appendix 7.1 Declustered Enzyme Leach values. Corresponding surface locations (UTM) for gridding also shown.

Gridding Sample ID	Easting (UTM)	Northing (UTM)	Oxidation Suite Elements														Base Metals						Chalcophile Elements								
			Cl	Br	I	V	As	Se	Mo	Sb	Te	W	Re	Au	Hg	Th	U	Co	Ni	Cu	Zn	Pb	Ga	Ge	Ag	Cd	In	Sn	Tl	Bi
GD.1	320555	3772546	5133	56	<2	66	44	<5	8	16.4	<1	11	<0.01	<0.05	<1	0.5	<0.1	13	10	20	6	8	<1	<0.5	<0.2	0.6	<0.1	<0.8	<0.1	<0.8
GD.2	320953	3772554	<2000	34	<2	73	34	<5	3	15.7	<1	9	<0.01	<0.05	<1	0.5	<0.1	7	5	12	<10	6	<1	<0.5	<0.2	0.3	<0.1	<0.8	<0.1	<0.8
GD.3	321346	3772553	<2000	46	11	148	64	<5	5	19.8	<1	13	<0.01	<0.05	<1	0.6	0.1	9	7	13	<10	4	<1	<0.5	<0.2	0.2	<0.1	<0.8	<0.1	<0.8
GD.4	320167	3772063	12933	80	23	121	42	3	29	14.8	<1	12	0.0	<0.05	<1	0.5	0.1	39	28	29	9	4	<1	<0.5	<0.2	1.7	<0.1	<0.8	0.0	<0.8
GD.5	320356	3771855	12215	86	39	202	104	<5	48	16.0	<1	45	<0.01	<0.05	<1	0.3	0.4	69	36	41	24	87	<1	<0.5	<0.2	9.3	<0.1	<0.8	<0.1	<0.8
GD.6	320623	3771776	5178	71	9	187	339	<5	145	25.3	<1	164	<0.01	<0.05	<1	0.3	0.6	81	29	116	412	264	1	1.1	<0.2	18.6	<0.1	0.3	0.4	0.3
GD.7	321011	3771770	2578	37	<2	136	90	<5	12	32.7	<1	61	<0.01	<0.05	<1	0.2	<0.1	19	18	34	20	68	<1	<0.5	<0.2	2.7	<0.1	<0.8	<0.1	<0.8
GD.8	321368	3771763	6753	95	26	254	116	<5	40	42.3	<1	68	<0.01	<0.05	<1	0.4	0.1	18	27	37	12	31	<1	<0.5	<0.2	1.2	<0.1	<0.8	0.1	<0.8
GD.9	317743	3770089	<2000	40	10	94	15	<5	17	5.5	<1	8	0.0	<0.05	<1	0.5	<0.1	12	4	7	<10	<1	<1	<0.5	<0.2	1.0	<0.1	<0.8	0.1	<0.8
GD.10	318135	3770482	<2000	69	61	146	21	<5	13	4.1	<1	9	<0.01	<0.05	<1	0.4	0.1	9	7	15	<10	2	<1	0.2	<0.2	0.8	<0.1	<0.8	0.3	<0.8
GD.11	318543	3770702	496	79	28	256	86	<5	53	7.8	<1	28	0.0	<0.05	<1	0.2	0.1	44	24	28	10	9	<1	<0.5	<0.2	1.8	<0.1	<0.8	0.5	<0.8
GD.12	318977	3770658	<2000	56	9	140	30	<5	108	13.0	<1	19	0.0	<0.05	<1	0.2	<0.1	36	16	18	<10	3	<1	<0.5	<0.2	1.5	<0.1	<0.8	0.5	<0.8
GD.13	319659	3770768	1644	78	30	190	94	<5	64	27.2	<1	37	0.0	0.1	<1	0.6	<0.1	7	9	22	<10	45	<1	0.1	<0.2	0.8	<0.1	<0.8	0.2	<0.8
GD.14	320121	3770855	3095	66	23	147	76	1	21	34.8	<1	42	<0.01	<0.05	<1	0.5	0.0	6	5	15	<10	<1	0	0.2	<0.2	0.5	<0.1	<0.8	0.2	<0.8
GD.15	320556	3770926	2301	51	25	139	68	<5	31	24.7	<1	32	<0.01	<0.05	<1	0.5	0.1	8	7	29	27	7	<1	0.1	<0.2	2.2	<0.1	<0.8	0.1	<0.8
GD.16	321059	3770947	623	81	29	172	74	1	25	17.4	<1	16	<0.01	<0.05	<1	0.5	0.0	9	11	19	<10	2	0	<0.5	<0.2	0.7	<0.1	<0.8	0.1	<0.8
GD.17	320994	3771217	6220	56	10	85	45	1	20	14.0	1	18	<0.01	<0.05	<1	0.3	<0.1	22	16	44	51	28	<1	<0.5	<0.2	4.1	<0.1	<0.8	0.0	<0.8
GD.18	321463	3771244	4993	52	19	162	56	<5	16	17.4	<1	24	<0.01	<0.05	<1	0.5	0.1	14	11	28	27	30	<1	<0.5	<0.2	2.7	<0.1	<0.8	0.0	<0.8
GD.19	321870	3771232	640	46	14	98	75	<5	7	16.4	<1	14	<0.01	<0.05	<1	0.4	0.0	5	6	24	6	19	<1	<0.5	<0.2	1.3	<0.1	<0.8	0.0	<0.8
GD.20	322315	3771234	<2000	61	43	289	86	<5	7	14.8	<1	10	<0.01	<0.05	<1	0.5	0.2	5	1	6	<10	4	<1	<0.5	<0.2	0.6	<0.1	<0.8	<0.1	<0.8
GD.21	322799	3771215	8620	167	937	315	117	9	556	8.0	<1	33	<0.01	0.0	<1	0.4	8.4	6	37	8	<10	1	<1	<0.5	<0.2	1.3	<0.1	<0.8	<0.1	<0.8
GD.22	320825	3770581	5815	138	50	138	55	<5	11	14.3	0	11	0.0	0.0	<1	0.3	0.1	41	18	101	94	167	<1	<0.5	<0.2	5.0	<0.1	<0.8	0.1	<0.8
GD.23	321249	3770519	3165	47	40	153	60	<5	12	12.3	<1	21	<0.01	<0.05	<1	0.4	0.2	28	16	30	19	27	1	<0.5	<0.2	2.0	<0.1	<0.8	0.1	<0.8
GD.24	321789	3770395	2830	50	47	106	50	1	4	16.7	<1	11	<0.01	<0.05	<1	0.5	0.1	9	4	25	15	20	<1	<0.5	<0.2	1.6	<0.1	<0.8	0.1	<0.8
GD.25	322296	3770327	3094	59	48	97	114	2	5	22.3	<1	7	<0.01	<0.05	<1	0.6	0.2	5	2	26	31	19	<1	<0.5	<0.2	1.0	<0.1	<0.8	0.1	<0.8
GD.26	322753	3770245	3063	50	51	107	100	<5	4	9.8	<1	5	<0.01	<0.05	<1	0.5	0.2	5	<3	30	<10	37	<1	<0.5	<0.2	1.3	<0.1	<0.8	0.1	<0.8
GD.27	319652	3768773	69817	875	355	535	80	5	62	9.9	<1	51	0.0	<0.05	<1	0.5	2.0	9	13	32	5	<1	<1	<0.5	<0.2	<0.2	<0.1	<0.8	<0.1	<0.8
GD.28	320053	3769002	12500	65	481	662	536	<5	265	7.9	<1	28	<0.01	<0.05	<1	0.4	7.0	8	12	33	<10	5	<1	<0.5	<0.2	0.5	<0.1	<0.8	0.3	<0.8
GD.29	320466	3769319	7837	62	47	297	64	2	46	5.4	<1	57	<0.01	0.1	<1	0.7	0.1	14	17	63	13	22	<1	<0.5	<0.2	0.4	<0.1	<0.8	0.1	<0.8
GD.30	321055	3769601	11028	104	11	268	84	<5	13	24.5	<1	36	<0.01	<0.05	<1	0.7	0.0	17	14	29	18	31	<1	<0.5	<0.2	1.2	<0.1	<0.8	0.2	<0.8
GD.31	321554	3769735	3420	43	5	80	36	<5	9	31.0	<1	13	<0.01	<0.05	<1	0.4	<0.1	10	7	14	5	13	<1	<0.5	<0.2	0.3	<0.1	<0.8	0.1	<0.8
GD.32	322070	3769742	1010	38	11	71	40	<5	11	24.9	0	10	<0.01	<0.05	<1	0.7	<0.1	10	4	21	<10	29	<1	<0.5	<0.2	1.7	<0.1	<0.8	0.1	<0.8
GD.33	322481	3769739	<2000	53	31	91	173	<5	8	18.4	0	7	<0.01	<0.05	<1	0.6	0.1	4	1	24	<10	81	<1	<0.5	<0.2	2.8	<0.1	<0.8	0.1	<0.8
GD.34	323057	3769725	<2000	110	129	215	179	3	14	13.5	<1	14	<0.01	<0.05	<1	0.2	0.2	5	5	10	<10	10	<1	<0.5	<0.2	0.9	<0.1	<0.8	0.1	<0.8

Appendix 7.1 cont. Declustered Enzyme Leach values. Corresponding surface locations (UTM) for gridding also shown.

Gridding Sample ID	Easting (UTM)	Northing (UTM)	High-Field Strength Elements						Rare Earth Elements															Lithophile Elements										
			Ti	Cr	Y	Zr	Nb	Hf	Ta	La	Ce	Pr	Nd	Sm	Eu	Gd	Tb	Dy	Ho	Er	Tm	Yb	Lu	Li	Be	Mn	Rb	Sr	Cs	Ba
GD.1	320555	3772546	<100	<20	5.0	<1	<1	<0.1	<0.1	3.8	6.1	1.2	5.6	1.4	0.8	1.1	0.2	0.9	0.2	0.4	<0.1	0.3	<0.1	15	<2	1965	21	1845	0.1	3453
GD.2	320953	3772554	<100	<20	5.9	1	<1	<0.1	<0.1	5.7	8.9	1.8	7.6	1.7	0.7	1.4	0.2	1.1	0.2	0.5	<0.1	0.4	<0.1	11	<2	1046	18	1613	<0.1	2893
GD.3	321346	3772553	<100	<20	7.1	0	<1	<0.1	<0.1	5.9	9.1	1.8	7.6	1.8	0.9	1.5	0.2	1.2	0.2	0.6	<0.1	0.5	<0.1	25	<2	1501	19	2923	0.1	3933
GD.4	320167	3772063	<100	<20	3.2	1	<1	<0.1	<0.1	1.8	4.6	0.6	2.6	0.7	0.4	0.6	0.0	0.4	<0.1	0.2	<0.1	0.2	<0.1	23	<2	6295	30	2108	0.0	2159
GD.5	320356	3771855	<100	<20	5.4	1	<1	<0.1	<0.1	2.4	9.7	1.0	4.6	1.2	0.6	1.0	0.1	0.9	0.1	0.5	<0.1	0.4	<0.1	38	<2	8960	27	2060	<0.1	3370
GD.6	320623	3771776	<100	<20	5.0	1	<1	<0.1	<0.1	3.9	11.3	1.3	5.7	1.3	1.3	1.2	0.2	0.9	0.2	0.5	0.0	0.4	0.0	23	1	13258	59	2110	5.0	6005
GD.7	321011	3771770	<100	<20	5.9	0	<1	<0.1	<0.1	5.3	9.3	1.6	6.6	1.5	1.1	1.3	0.2	1.0	0.2	0.5	<0.1	0.4	<0.1	15	<2	6328	31	2340	<0.1	5173
GD.8	321368	3771763	<100	<20	6.0	1	<1	<0.1	<0.1	5.6	9.8	1.7	6.7	1.6	1.0	1.4	0.2	1.1	0.2	0.5	<0.1	0.4	<0.1	28	<2	4257	52	3183	0.0	4620
GD.9	317743	3770089	<100	<20	2.4	2	<1	<0.1	<0.1	1.8	3.2	0.4	1.7	0.4	0.2	0.3	<0.1	0.3	<0.1	0.2	<0.1	0.2	<0.1	34	<2	2423	21	1259	<0.1	725
GD.10	318135	3770482	<100	<20	3.7	3	1	<0.1	<0.1	2.4	3.5	0.7	2.7	0.6	0.3	0.5	<0.1	0.5	0.0	0.3	<0.1	0.3	<0.1	68	<2	2218	23	2178	0.2	978
GD.11	318543	3770702	23	<20	3.0	2	0	<0.1	<0.1	2.0	5.2	0.6	2.4	0.5	0.4	0.5	<0.1	0.4	<0.1	0.2	<0.1	0.2	<0.1	43	<2	10104	36	1820	0.1	2238
GD.12	318977	3770658	<100	<20	1.9	2	<1	<0.1	<0.1	1.3	4.1	0.4	1.5	0.4	0.1	0.3	<0.1	0.2	<0.1	0.2	<0.1	0.1	<0.1	29	<2	8190	24	1077	0.0	802
GD.13	319659	3770768	<100	<20	3.4	1	0	<0.1	<0.1	2.4	5.3	0.7	3.0	0.7	0.5	0.6	<0.1	0.5	0.0	0.3	<0.1	0.2	<0.1	43	<2	3854	42	2202	0.2	2848
GD.14	320121	3770855	18.3	<20	2.9	1	0	0.0	<0.1	2.5	5.2	0.7	3.0	0.7	0.3	0.6	0.0	0.4	0.0	0.2	<0.1	0.2	<0.1	29	<2	3049	46	2093	0.6	1649
GD.15	320556	3770926	13.9	<20	3.0	1	0	0.0	<0.1	2.2	5.6	0.7	2.9	0.7	0.4	0.6	<0.1	0.4	0.0	0.2	<0.1	0.2	<0.1	28	<2	4209	30	2851	0.2	2073
GD.16	321059	3770947	<100	<20	3.5	2	<1	0.0	<0.1	2.3	4.3	0.7	3.1	0.7	0.4	0.6	0.0	0.5	0.0	0.3	<0.1	0.2	<0.1	44	<2	1830	40	2255	0.4	2007
GD.17	320994	3771217	<100	<20	2.9	1	<1	<0.1	<0.1	2.7	8.0	0.8	3.4	0.8	0.4	0.7	0.0	0.4	0.0	0.2	<0.1	0.2	<0.1	19	<2	7193	24	1053	0.1	2565
GD.18	321463	3771244	24.2	<20	3.6	2	<1	0.0	<0.1	3.3	8.6	1.0	4.1	0.9	0.4	0.8	0.1	0.6	0.1	0.3	<0.1	0.2	<0.1	31	<2	5090	30	1592	0.4	2153
GD.19	321870	3771232	12.3	<20	3.0	1	0	0.0	<0.1	2.9	5.4	0.8	3.4	0.7	0.5	0.6	0.0	0.5	0.1	0.2	<0.1	0.2	<0.1	30	<2	1660	43	2269	0.2	2948
GD.20	322315	3771234	<100	<20	2.5	1	<1	<0.1	<0.1	1.8	2.6	0.5	2.0	0.5	0.6	0.4	0.0	0.3	0.0	0.2	<0.1	0.1	<0.1	59	<2	607	20	3457	0.1	4065
GD.21	322799	3771215	<100	<20	4.7	1	4	<0.1	0.1	2.2	2.7	0.6	2.5	0.6	0.5	0.5	0.1	0.5	0.1	0.4	0.0	0.4	0.1	50	<2	977	20	8144	0.0	2972
GD.22	320825	3770581	25.8	<20	4.7	3	<1	0.1	<0.1	3.2	8.4	1.0	4.6	1.0	0.9	0.9	0.1	0.7	0.2	0.4	0.0	0.4	0.0	64	<2	5150	27	1505	<0.1	5570
GD.23	321249	3770519	<100	<20	3.1	3	<1	0.1	<0.1	2.5	6.2	0.8	3.2	0.8	0.5	0.6	0.0	0.5	0.0	0.3	<0.1	0.2	<0.1	45	<2	5488	25	1323	0.2	3210
GD.24	321789	3770395	25.4	<20	2.8	1	0	0.0	<0.1	2.5	4.1	0.7	2.9	0.7	0.6	0.6	0.1	0.5	0.1	0.2	<0.1	0.2	<0.1	28	<2	2083	25	1876	0.1	3570
GD.25	322296	3770327	<100	<20	2.7	1	<1	0.0	<0.1	2.4	3.7	0.7	3.0	0.6	0.4	0.6	0.1	0.5	0.0	0.3	<0.1	0.2	<0.1	39	<2	738	26	2482	0.1	2454
GD.26	322753	3770245	<100	<20	2.9	0	<1	<0.1	<0.1	2.6	3.6	0.7	2.9	0.7	0.4	0.6	0.0	0.4	0.0	0.3	<0.1	0.2	<0.1	40	<2	628	25	2608	<0.1	2483
GD.27	319652	3768773	<100	<20	4.3	0	<1	<0.1	<0.1	2.9	3.6	0.9	3.6	0.8	0.6	0.7	0.1	0.7	0.1	0.4	0.0	0.4	0.0	110	<2	875	23	8617	0.3	2377
GD.28	320053	3769002	<100	<20	1.9	<1	<1	<0.1	<0.1	1.1	2.2	0.4	1.9	0.4	0.3	0.4	<0.1	0.3	<0.1	0.1	<0.1	0.1	<0.1	129	<2	1400	52	36100	0.7	1300
GD.29	320466	3769319	<100	<20	4.6	0	<1	<0.1	<0.1	4.1	12.4	1.2	5.5	1.2	0.5	1.1	0.1	0.8	0.1	0.4	<0.1	0.3	<0.1	32	<2	2670	31	3640	0.2	1547
GD.30	321055	3769601	<100	<20	7.2	2	0	0.1	<0.1	6.1	13.2	1.9	8.0	1.8	0.7	1.5	0.3	1.3	0.3	0.7	0.1	0.6	0.0	32	<2	3186	29	3300	0.2	2320
GD.31	321554	3769735	<100	<20	3.0	2	0	0.1	<0.1	2.6	6.4	0.8	3.5	0.8	0.5	0.7	0.1	0.5	0.1	0.3	<0.1	0.2	<0.1	20	<2	2894	24	2128	0.6	2454
GD.32	322070	3769742	<100	<20	4.6	2	0	<0.1	<0.1	3.8	7.5	1.1	4.8	1.1	0.5	0.9	0.1	0.7	0.1	0.4	<0.1	0.3	<0.1	19	<2	3104	27	2557	0.1	2316
GD.33	322481	3769739	<100	<20	3.2	1	<1	<0.1	<0.1	2.2	3.7	0.6	2.6	0.6	0.5	0.5	0.0	0.4	0.0	0.3	<0.1	0.2	<0.1	31	<2	593	25	3570	0.1	3265
GD.34	323057	3769725	<100	<20	1.5	<1	<1	<0.1	<0.1	1.0	1.2	0.2	1.0	0.2	0.6	0.2	<0.1	0.1	<0.1	0.1	<0.1	0.1	<0.1	60	<2	508	26	4648	<0.1	3864

Appendix 8. Declustered Soil pH values. Corresponding surface locations for gridding also shown.

	Easting	Northing	*pH*		Easting	Northing	*pH*
GD.35	319378	3773450	***8.91***	**GD.65**	322393	3771944	***9.61***
GD.36	319651	3773451	***9.12***	**GD.66**	320400	3771600	***8.49***
GD.37	319993	3773450	***8.63***	**GD.67**	320650	3771600	***7.36***
GD.38	320355	3773445	***8.8***	**GD.68**	320900	3771599	***7.83***
GD.39	320624	3773449	***9.02***	**GD.69**	321150	3771600	***9.36***
GD.40	320855	3773450	***9.1***	**GD.70**	321380	3771600	***9.36***
GD.41	321205	3773452	***9.07***	**GD.71**	321650	3771604	***9.54***
GD.42	321601	3773445	***9.24***	**GD.72**	321950	3771600	***9.38***
GD.43	320099	3772903	***8.53***	**GD.73**	320947	3771046	***8.3***
GD.44	320376	3772903	***8.01***	**GD.74**	321147	3771050	***8.71***
GD.45	320703	3772902	***8.66***	**GD.75**	321371	3771046	***7.97***
GD.46	321054	3772902	***9.07***	**GD.76**	321684	3771050	***8.25***
GD.47	321400	3772901	***9.19***	**GD.77**	320725	3770599	***6.37***
GD.48	319912	3772353	***7.15***	**GD.78**	320920	3770576	***8.84***
GD.49	320123	3772548	***8.51***	**GD.79**	321161	3770576	***8.17***
GD.50	320383	3772601	***8.87***	**GD.80**	321407	3770569	***8.07***
GD.51	320655	3772603	***9.16***	**GD.81**	321734	3770580	***8.65***
GD.52	320904	3772598	***9.43***	**GD.82**	320475	3769618	***8.47***
GD.53	321180	3772584	***9.49***	**GD.83**	320702	3769618	***9.26***
GD.54	321505	3772580	***9.35***	**GD.84**	320928	3769635	***8.91***
GD.55	321801	3772583	***9.49***	**GD.85**	321200	3769732	***8.95***
GD.56	322105	3772582	***9.6***	**GD.86**	321500	3769873	***9.12***
GD.57	320230	3772000	***9.28***	**GD.87**	321726	3769983	***9.07***
GD.58	320398	3772040	***8.48***	**GD.88**	321881	3770080	***9.07***
GD.59	320636	3772024	***8.89***	**GD.89**	320551	3770269	***7.66***
GD.60	320886	3772010	***9.33***	**GD.90**	320717	3770206	***7.96***
GD.61	321131	3771998	***9.43***	**GD.91**	320927	3770150	***9.07***
GD.62	321334	3771989	***9.33***	**GD.92**	321199	3770154	***8.93***
GD.63	321593	3771961	***9.44***	**GD.93**	321606	3770140	***9.27***
GD.64	321943	3771945	***9.61***	**GD.94**	322001	3770147	***9.25***

Appendix 9. Earthquake magnitude and epicenter data for La Jencia Basin, Socorro peak and Rio Grande Rift, from Stankova-Pursley, 2008. Geographic data in WGS 1984.

Easting	Northing	M_L	Easting	Northing	M_L	Easting	Northing	M_L
322293	3757964	1.11	319332	3770760	0.11	312839	3770812	0.61
312321	3771839	1.58	319247	3770336	-0.21	313052	3770734	0.65
321266	3760757	0.62	319279	3770428	0.21	312397	3771042	0.24
312608	3774700	0.84	317763	3769200	0.11	306993	3714564	1.6
313300	3775462	0.1	319313	3770538	-0.01	304811	3716872	2.3
314008	3773933	0.21	319323	3770316	0.22	326271	3763174	2.2
312758	3770591	0.42	319562	3770755	-0.63	322179	3756816	2.2
322537	3758681	1.31	313082	3766795	-0.26	321262	3757243	2.5
316272	3766954	0.36	319476	3769425	0.62	323187	3761279	2
314340	3771208	0.55	319332	3769946	0.28	324789	3767939	2.1
324177	3771463	0.48	319332	3769946	0.28	319205	3756029	2.5
324502	3771531	0.58	320612	3770883	0.28	318099	3756272	2.1
324173	3772055	0.38	318683	3770642	-0.27	323748	3756675	2
319517	3768390	0.05	319312	3770519	0.24	332821	3752096	2.9
319452	3764175	0.26	318545	3773068	0.3	308637	3768507	2.5
319536	3771773	0.45	319403	3770425	1.25	329125	3762590	2.3
324601	3771104	0.34	319446	3770258	0.47	333006	3773037	2.1
315745	3769109	0.55	319790	3768163	0.44	331932	3780101	2.2
317632	3768795	0.53	319746	3769864	0.5	322154	3784907	2.8
309621	3763110	0.05	319026	3771653	1.47	309793	3766287	2.2
315225	3771652	0.81	315190	3767493	0.64	312174	3769901	2.7
315301	3771595	0.6	315860	3767110	-0.02	310783	3769596	3
315691	3771088	0.26	313547	3766952	0.43	318307	3771867	3.1
316644	3772623	0.22	315713	3768241	0.41	325714	3773025	2.3
315080	3772099	1.36	309953	3767393	-0.69	324067	3773799	2.4
315149	3771728	0.81	313412	3765586	-0.87	327356	3771974	2.5
311949	3766336	0.35	314431	3773499	0.81	324293	3776047	2.6
319545	3762582	0.64	321816	3761263	0.72	324523	3773513	2.9
312282	3771489	0.14	315343	3759557	0.66	328278	3771868	2.2
314923	3771178	0.93	312449	3775240	0.72	309529	3757783	2.8
309119	3754984	0.36	309761	3767786	0.48	329850	3782235	2
309225	3754926	0.49	313688	3764731	0.73	331414	3776915	4.1
309037	3754782	0.5	320197	3762053	0.77	331605	3777278	2
316249	3764920	1.27	320443	3772550	0.25	331513	3777279	2
318277	3763125	0.73	311528	3766826	-0.53	331697	3777265	2.2
313100	3764538	0.58	312049	3765946	-0.49	331610	3777521	2.2
323691	3756939	0.85	311353	3768068	0.58	331329	3777282	2
314598	3764805	0.27	310858	3768762	-0.13	331705	3777708	2.2
311575	3769949	0.39	310846	3768133	0.33	331522	3777767	2.1
319852	3770602	0.13	310880	3768318	0.35	331454	3779111	2.1
317560	3759458	0.76	310878	3768207	0.65	331049	3766826	2.3
315973	3771379	0.69	315853	3772306	1.69	331881	3766845	2.1
313148	3766239	0.71	314453	3771539	1.3	330300	3776513	2.1
318632	3762360	0.65	315789	3770570	0.92	331430	3777769	2.1
311334	3772544	-0.01	314010	3767793	0.97	319364	3754706	2.2
319460	3770239	-0.21	311185	3766611	0.79	322213	3738843	2.3
319345	3769797	-0.91	317718	3760473	0.84	311641	3766339	2.4
319200	3769486	-0.34	312418	3769045	0.72	312755	3766616	2.3
319247	3770336	-0.88	312667	3770686	1.22	328237	3764569	2.6
317454	3770721	0.16	312817	3770498	0.2	327632	3761763	2.3
318762	3769143	-0.94	312560	3770744	0.48	311643	3766416	2.2
313081	3765944	-0.93	312668	3770723	1.28	330209	3776570	2.3
319287	3770003	1.15	312840	3770886	0.24	329118	3777478	2.2
319573	3769646	0.06	312671	3770889	0.36	320153	3776702	2.3
319443	3770128	0.56	312904	3770256	0.02	326309	3780280	2
319536	3770145	2.33	312698	3770704	2.91	304811	3716872	2.3
319124	3770339	0	312543	3770689	0.29	313911	3769001	2.6
319229	3770226	0	312944	3770662	0.54	313682	3762082	2.1
319384	3770240	0.4	312623	3770779	1.15	313425	3763108	2.8
319471	3769999	0.29	312680	3770593	0.1	326796	3766570	2
319332	3770760	-0.51	312604	3770613	0.59	308833	3732301	2.3
						307733	3732933	2.2

Appendix 10. Bromide and chloride compilation values for catalogued waters in Socorro Peak geothermal area and Rio Grande River.

Name	Easting	Northing	Reference	pH	TDS calculated (mg/L)	Bromide (mg/L)	Chloride (mg/L)	Cl/Br
3K West	313611	3773061	*this study*			0.07	5	74
Blue Canyon	319933	3769051	Summers, 1976	7.4		0.54	16	30
Blue Canyon	319933	3769051	Summers, 1976	8.6	145	0.20	20	100
Blue Canyon	319933	3769051	Summers, 1976	7.1		0.50	16	32
Blue Canyon	319933	3769051	WATSTORE, 1997	7.1	0	0.50	16	32
Burris Well	324586	3764619	Summers et al., 1981	8.0	371	0.13	16	123
Bushman	323793	3771184	Summers et al., 1981	8.2	358	0.23	30	132
Bushman	323793	3771184	Summers et al., 1981	7.5	964	0.30	89	297
Bushman	323793	3771184	*this study*	7.7	642	0.21	48	224
D-LLDR3	327612	3758959	Newton, 2004	8.0	1270	0.28	280	1000
D-SMC-91.28	328936	3758018	Newton, 2004	8.6	540	0.14	57	407
D-SRD-87.62	328676	3755140	Newton, 2004	7.6	780	0.28	125	446
D-SRD-87.62	328676	3755140	Newton, 2004	7.6	490	0.12	62	517
D-SRD-87.62	328676	3755140	Newton, 2004	7.7	580	0.13	65	500
D-SRD-91.28	328963	3758017	Newton, 2004	7.9	540	0.14	57	407
Eagle Pitcher	324199	3774727	*this study*	8.1	226	0.06	14	250
Eagle Pitcher	324199	3774727	Summers et al., 1981	7.6	203	0.08	22	275
Evergreen	321544	3768646	*this study*	8.1	428	0.09	68	725
Exp #4 640-700ft	321544	3768646	Glorieta, 2004	8.2	420	0.12	42	350
Exp#1 1080-1140ft	321544	3768646	Glorieta, 2004	8.0	780	0.18	190	1056
Exp#2 940-1000ft	321544	3768646	Glorieta, 2004	8.1	630	0.12	125	1042
Exp#3 800-860ft	321544	3768646	Glorieta, 2004	8.2	440	0.15	50	333
Exp#5 560-620ft	321544	3768646	Glorieta, 2004	8.1	470	0.12	63	525
Exp#6 440-500ft	321544	3768646	Glorieta, 2004	7.9	1070	0.55	350	636
Grefco Well	320976	3765413	Summers et al., 1981	7.9	358	0.08	23	288
Holmes	323685	3771269	Summers et al., 1981	7.8	324	0.08	28	350
Holmes	323685	3771269	*this study*	7.8	301	0.11	22	200
Industrial Park	322985	3767640	City of Socorro, 2003	7.5	690	0.35	190	543
L-109.49	325992	3783830	Newton, 2004	8.0	600	0.16	61	381
L-109.49	325992	3783830	Newton, 2004	7.8	640	0.24	77	321
L-109.49	325992	3783830	Newton, 2004	7.6	690	0.35	76	217
L-109.49	325992	3783830	Newton, 2004	7.9	550	0.14	58	414
L-109.49	325992	3783830	Newton, 2004	7.8	610	0.14	69	493
L-114.60	325020	3790487	Newton, 2004	7.5	730	0.23	105	457
L-114.60	325020	3790487	Newton, 2004	7.4	770	0.13	110	846
L-114.60	325020	3790487	Newton, 2004	7.7	620	0.16	83	519
L-114.60	325020	3790487	Newton, 2004	7.5	740	0.17	105	618
L-68.72	314997	3728092	Newton, 2004	8.0	790	0.24	130	542
L-83.98	328848	3749114	Newton, 2004	8.4	480	0.24	53	221
L-83.98	328848	3749114	Newton, 2004	7.9	540	0.12	66	550
L-83.98	328848	3749114	Newton, 2004	7.9	470	0.13	52	400
L-83.98	328848	3749114	Newton, 2004	8.0	520	0.13	68	523
L-87.62	328768	3755100	Newton, 2004	8.4	490	0.14	53	379
L-87.62	328768	3755100	Newton, 2004	8.3	490	0.27	52	193
L-87.62	328768	3755100	Newton, 2004	8.0	530	0.20	77	385
L-87.62	328768	3755100	Newton, 2004	7.7	560	0.22	65	295
L-87.62	328768	3755100	Newton, 2004	7.7	570	0.27	70	259
L-87.62	328768	3755100	Newton, 2004	7.7	470	0.13	50	385
L-87.62	328768	3755100	Newton, 2004	7.8	550	0.13	69	531

Appendix 10 cont. Bromide and Chloride compilation values for catalogued waters in Socorro Peak geothermal area and Rio Grande River.

Name	Easting	Northing	Reference	pH	TDS calculated (mg/L)	Bromide (mg/L)	Chloride (mg/L)	Cl/Br
L-91.28	329041	3758008	Newton, 2004	8.1	490	0.16	51	319
L-91.28	329041	3758008	Newton, 2004	7.7	470	0.18	53	294
L-91.28	329041	3758008	Newton, 2004	7.6	550	0.59	49	83
L-91.28	329041	3758008	Newton, 2004	7.9	450	0.13	47	362
L-91.28	329041	3758008	Newton, 2004	7.6	500	0.13	56	431
L-99.59	327015	3771077	Newton, 2004	7.8	460	0.23	51	222
L-99.59	327015	3771077	Newton, 2004	7.7	390	0.10	39	390
L-99.59	327015	3771077	Newton, 2004	7.5	420	0.17	33	194
L-99.59	327015	3771077	Newton, 2004	8.0	450	0.13	46	354
L-99.59	327015	3771077	Newton, 2004	7.7	430	0.12	42	350
Main Pad	319932	3768760	*this study*	8.1	1176	0.63	53	84
NMT2-1085	320524	3771972	*this study*	7.9	2092	1.34	935	696
NMT2-633	320524	3771972	*this study*	8.1	2142	1.31	935	713
NMT2-977	320524	3771972	*this study*	8.0	2119	1.33	945	713
NMT4-67T	320524	3771972	*this study*	8.7	1802	1.20	850	708
NMT4-67T	320524	3771972	*this study*	8.2	1868	1.20	865	721
NMT4-67T	320524	3771972	*this study*	7.3	1970	1.38	880	638
R-109.49	326450	3783820	Newton, 2004	8.3	410	0.14	42	300
R-109.49	326450	3783820	Newton, 2004	8.0	390	0.13	34	262
R-109.49	326450	3783820	Newton, 2004	8.2	420	0.16	36	225
R-109.49	326450	3783820	Newton, 2004	8.2	390	0.12	42	350
R-114.60	325224	3790484	Newton, 2004	8.3	410	0.19	44	232
R-114.60	325224	3790484	Newton, 2004	8.1	420	0.23	35	152
R-114.60	325224	3790484	Newton, 2004	8.1	400	0.13	42	323
R-114.60	325224	3790484	Newton, 2004	8.1	500	0.15	53	353
R-68.72	314997	3728092	Newton, 2004	8.4	410	0.14	41	293
R-68.72	314997	3728092	Newton, 2004	8.4	770	0.29	130	448
R-68.72	314997	3728092	Newton, 2004	8.1	630	0.30	82	273
R-68.72	314997	3728092	Newton, 2004	8.1	380	0.12	38	317
R-68.72	314997	3728092	Newton, 2004	8.1	800	0.20	145	725
R-83.98	328997	3749220	Newton, 2004	8.3	400	0.16	41	256
R-83.98	328997	3749220	Newton, 2004	8.7	420	0.19	43	226
R-83.98	328997	3749220	Newton, 2004	8.2	440	0.11	40	364
R-83.98	328997	3749220	Newton, 2004	8.1	390	0.13	43	331
R-87.62	328956	3755078	Newton, 2004	8.4	410	0.14	40	286
R-87.62	328956	3755078	Newton, 2004	8.1	440	0.17	42	247
R-87.62	328956	3755078	Newton, 2004	8.2	450	0.21	40	190
R-87.62	328956	3755078	Newton, 2004	8.1	400	0.12	40	333
R-87.62	328956	3755078	Newton, 2004	8.1	480	0.12	49	408
R-91.28	329267	3757849	Newton, 2004	8.3	410	0.32	42	131
R-91.28	329267	3757849	Newton, 2004	8.2	440	0.17	42	247
R-91.28	329267	3757849	Newton, 2004	7.8	390	0.13	40	308
R-91.28	329267	3757849	Newton, 2004	7.9	470	0.12	48	400
R-99.59	327247	3771052	Newton, 2004	7.9	400	0.28	41	146
R-99.59	327247	3771052	Newton, 2004	8.5	410	0.14	37	264
R-99.59	327247	3771052	Newton, 2004	8.2	470	0.22	52	236
R-99.59	327247	3771052	Newton, 2004	8.2	390	0.13	41	315
Reservoir Well	323770	3769305	Summers et al., 1981	7.4	258	0.08	19	238
Reservoir Well	323770	3769305	Summers et al., 1981	7.8	253	0.05	18	360

Appendix 10 cont. Bromide and Chloride compilation values for catalogued waters in Socorro Peak geothermal area and Rio Grande River.

Name	Easting	Northing	Reference	pH	TDS calculated (mg/L)	Bromide (mg/L)	Chloride (mg/L)	Cl/Br
Rockhouse	315717	3773115	*this study*	8.0	544	0.30	62	207
Rockhouse	315717	3773115	*this study*			0.28	61	218
School of Mines	324916	3770597	City of Socorro, 2003	7.5	640	0.21	82	390
School of Mines	324916	3770597	Summers et al., 1981	8.4	357	0.08	30	375
Sedillo Springs	321378	3768435	Summers et al., 1981	7.9	215	0.12	15	125
Sedillo Springs	321378	3768435	Summers et al., 1981	8.2	211	0.05	14	280
Socorro Springs	321370	3768440	*this study*	8.3	205	0.10	12	123
Socorro Springs	321370	3768440	Summers et al., 1981	7.8	212	0.08	12	150
Torres Lab	320084	3774004	*this study*	8.4	240	0.48	15	31
Torres Lab	320084	3774004	*this study*	8.1	1447	0.76	60	79
Torres Lab	320084	3774004	*this study*			0.67	57	84
W-109.49-2	326096	3783847	Newton, 2004	7.5	400	0.12	38	317
W-109.49-2	326096	3783847	Newton, 2004	7.6	390	0.14	38	271
W-109.49-2	326096	3783847	Newton, 2004	7.4	400	0.13	35	269
W-109.49-3	325951	3783849	Newton, 2004	7.4	960	0.32	100	313
W-109.49-3	325951	3783849	Newton, 2004	7.0	1000	0.27	115	426
W-109.49-3	325951	3783849	Newton, 2004	6.8	940	0.42	95	226
W-109.49-4	325888	3783872	Newton, 2004	7.8	510	0.15	51	340
W-109.49-4	325888	3783872	Newton, 2004	7.4	450	0.14	45	321
W-109.49-4	325888	3783872	Newton, 2004	7.2	510	0.29	56	193
W-114.60-2	325088	3790500	Newton, 2004	8.0	410	0.26	37	142
W-114.60-2	325088	3790500	Newton, 2004	7.5	380	0.13	41	315
W-114.60-2	325088	3790500	Newton, 2004	7.4	450	0.12	45	375
W-114.60-2	325088	3790500	Newton, 2004	7.8	400	0.12	40	333
W-114.60-2	325088	3790500	Newton, 2004	7.7	400	0.12	42	350
W-114.60-3	325953	3783849	Newton, 2004	7.1	860	0.33	80	242
W-114.60-3	325953	3783849	Newton, 2004	6.7	900	0.18	58	322
W-114.60-3	325953	3783849	Newton, 2004	6.7	820	0.13	46	354
W-114.60-3	325953	3783849	Newton, 2004	7.0	810	0.17	57	335
W-114.60-3	325953	3783849	Newton, 2004	6.8	830	0.16	49	306
W-68.72-1	315369	3728480	Newton, 2004	7.5	430	0.21	28	133
W-68.72-1	315369	3728480	Newton, 2004	7.1	490	0.22	41	186
W-68.72-1	315369	3728480	Newton, 2004	6.8	510	0.18	76	422
W-68.72-1	315369	3728480	Newton, 2004	7.0	730	0.20	100	500
W-68.72-1	315369	3728480	Newton, 2004	7.1	720	0.20	89	445
W-68.72-3	315142	3729037	Newton, 2004	7.3	880	0.49	93	190
W-68.72-3	315142	3729037	Newton, 2004	7.0	860	0.47	93	198
W-68.72-3	315142	3729037	Newton, 2004	6.9	800	0.65	90	138
W-68.72-3	315142	3729037	Newton, 2004	7.2	770	0.33	92	279
W-68.72-3	315142	3729037	Newton, 2004	7.0	790	0.32	92	288
W-68.72-4	315099	3729089	Newton, 2004	7.3	830	0.32	55	172
W-68.72-5	315138	3729041	Newton, 2004	7.9	420	0.12	38	317
W-68.72-5	315138	3729041	Newton, 2004	7.4	430	0.10	36	360
W-68.72-6	315136	3729039	Newton, 2004	7.6	600	0.28	30	107
W-68.72-6	315136	3729039	Newton, 2004	7.1	580	0.28	28	100
W-83.98-1	330344	3749068	Newton, 2004	7.4	14010	3.50	4000	1143
W-83.98-1	330344	3749068	Newton, 2004	7.1	14250	3.80	4100	1079
W-83.98-1	330344	3749068	Newton, 2004	6.8	13530	3.60	3800	1056
W-83.98-3	328807	3749129	Newton, 2004	7.6	520	0.19	52	274

Appendix 10 cont. Bromide and Chloride compilation values for catalogued waters in Socorro Peak geothermal area and Rio Grande River.

Name	Easting	Northing	Reference	pH	TDS calculated (mg/L)	Bromide (mg/L)	Chloride (mg/L)	Cl/Br
W-83.98-3	328807	3749129	Newton, 2004	7.4	500	0.17	51	300
W-83.98-3	328807	3749129	Newton, 2004	7.1	560	0.25	63	252
W-83.98-4	328584	3749199	Newton, 2004	7.7	370	0.11	26	236
W-87.62-1	328904	3755094	Newton, 2004	7.5	400	0.13	40	308
W-87.62-2	328852	3755093	Newton, 2004	7.9	420	0.24	36	150
W-87.62-2	328852	3755093	Newton, 2004	7.6	370	0.17	37	218
W-87.62-2	328852	3755093	Newton, 2004	7.5	440	0.28	45	161
W-87.62-2	328852	3755093	Newton, 2004	7.5	450	0.11	39	355
W-87.62-2	328852	3755093	Newton, 2004	7.7	410	0.13	42	323
W-87.62-3	328743	3755123	Newton, 2004	7.7	430	0.19	36	189
W-87.62-3	328743	3755123	Newton, 2004	7.9	610	0.57	65	114
W-87.62-3	328743	3755123	Newton, 2004	7.3	760	0.14	78	557
W-87.62-3	328743	3755123	Newton, 2004	7.7	1330	0.28	330	1179
W-87.62-3	328743	3755123	Newton, 2004	7.7	930	0.18	136	756
W-87.62-4	328685	3755151	Newton, 2004	7.5	1840	0.84	230	274
W-87.62-4	328685	3755151	Newton, 2004	7.4	500	0.24	56	233
W-87.62-4	328685	3755151	Newton, 2004	7.0	620	0.23	65	283
W-87.62-4	328685	3755151	Newton, 2004	7.4	590	0.16	72	450
W-87.62-4	328685	3755151	Newton, 2004	7.1	610	0.15	69	460
W-91.28-1	329576	3757532	Newton, 2004	7.8	390	0.15	26	173
W-91.28-1	329576	3757532	Newton, 2004	7.5	370	0.21	26	124
W-91.28-1	329576	3757532	Newton, 2004	7.2	400	0.22	25	114
W-91.28-3	329098	3757886	Newton, 2004	7.7	460	0.25	38	152
W-91.28-3	329098	3757886	Newton, 2004	7.4	400	0.11	40	364
W-91.28-3	329098	3757886	Newton, 2004	7.3	480	0.15	40	267
W-91.28-3	329098	3757886	Newton, 2004	7.5	490	0.12	45	375
W-91.28-3.5	329008	3758026	Newton, 2004	7.9	1060	0.32	89	278
W-91.28-3.5	329008	3758026	Newton, 2004	7.9	950	0.25	80	320
W-91.28-3.5	329008	3758026	Newton, 2004	7.1	1240	0.83	95	114
W-91.28-3.5	329008	3758026	Newton, 2004	7.6	970	0.17	83	488
W-91.28-4	328720	3758019	Newton, 2004	7.2	1100	0.44	72	164
W-91.28-4	328720	3758019	Newton, 2004	6.8	1060	0.12	78	650
W-91.28-4	328720	3758019	Newton, 2004	6.7	970	0.10	85	850
W-99.59-1	327078	3771072	Newton, 2004	7.7	440	0.17	39	229
W-99.59-4	327085	3771091	Newton, 2004	7.5	380	0.19	32	168
W-99.59-4	327085	3771091	Newton, 2004	7.5	380	0.11	35	318
W-99.59-4	327085	3771091	Newton, 2004	7.5	410	0.14	40	286
W-EB-11-20	314654	3725996	Newton, 2004	7.3	600	0.21	53	252
W-EB-11-20	314654	3725996	Newton, 2004	7.0	580	0.27	98	363
W-EB-11-20	314654	3725996	Newton, 2004	7.1	680	0.39	91	233
W-EB-11-20	314654	3725996	Newton, 2004	7.3	480	0.16	52	325
W-EB-22-18	310599	3719128	Newton, 2004	7.1	1010	0.59	68	115
W-Perini1	327628	3763525	Newton, 2004	7.8	790	0.19	95	500
W-Perini1	327628	3763525	Newton, 2004	7.7	760	0.17	90	529
W-Thomas1	326784	3763540	Newton, 2004	7.6	640	0.19	56	295
W-Thomas1	326784	3763540	Newton, 2004	7.0	620	0.15	57	380
W-Thomas1	326784	3763540	Newton, 2004	6.9	860	0.15	100	667

Appendix 11. Geochemistry for select thermal waters, brines and mixed fluids along the Rio Grande. Concentration values in mg/L.

Name	Reference	Temp C	TDS	Br	Cl	SO4	Na	K	Mg	Ca	As	Ba	B	Li	SiO2	Chalc. Temp_C	Mg -corr. Na-K-Ca_Temp_C	TDS/ SO4	TDS/ Mg
Geothermal																			
MP	*this study*	33.3	233	0.5	17	43	57	2.8	5	19	0.03	0.10	0.10	0.06	21	34	54	5	48
SedS	*this study*	33.1	216	0.1	12	29	50	2.7	4	18	0.04	0.12	0.07	0.05	19	28	53	8	54
Soc S	*this study*	31.8	221	0.1	12	29	50	2.6	4	17	0.04	0.13	0.07	0.06	30	47	53	8	51
G	*this study*	34.0	1510	1.3	865	207	512	21.6	12	69	0.03	0.12	0.72	0.88	37	56	101	7	123
G2	*this study*	42.0	2055	1.3	909	186	614	25.9	18	107	0.03	0.07	0.80	1.11	34	53	100	11	116
MV5	Bothern, 2003	58.7	1960	0.4	554	228	470	53.1	21	162	8.22	102.00	0.20	0.32	78	96	131	9	93
MV6	Bothern, 2003	63.4	1907	0.5	578	236	452	57.6	24	168	22.60	88.60	0.22	0.32	53	75	133	8	79
MV2	Bothern, 2003	68.4	3870	1.2	1620	287	1100	149.0	11	127	13.00	143.00	0.35	0.73	74	93	187	13	352
69	Witcher, 2005	85.5	3540	0.0	1700	260			23	140					71	91		14	154
DA12	Witcher, 2005	53.0	2313	0.0	1630	263												9	
DA12	Witcher, 2005	52.5	3391	2.8	1600		1100	170.0					0.78	1.10	74	93			
RS	Moore et al., 2008		3200	1.2	1300	490			22				0.63					7	145
Chrl	Moore et al., 2008		2600	1.0	1400	75			15				0.27					35	173
Thermal Mixed																			
ISC5	Moore et al., 2008		4500	0.7	1800	1200			19				0.84					4	237
W-14	Brandvolt, 2001	32.7	3110	1.0	973	541	831	33.2	39	124	0.04		0.89	0.93	27	43	67	6	80
DA16	Witcher, 2005	45.0	4790	0.0	1600	860	1400											6	
DA20	Witcher, 2005	42.5	6885	0.0	2700	1700	2100	19.0	10	290					63	84	93	4	688
DA41	Witcher, 2005	31.0	3552	0.0	1200	1000	1200	9.1	24	84					34	54	87	4	148
Brines																			
ISC4	Moore et al., 2008		30000	25.0	18000	6200			670				2.20					5	45
ISC4a	Moore et al., 2008		19000	10.0	7900	5100			340				2.50					4	56
W83	Newton, 2004	19.0	13930	3.7	3967	4546	3817	152.0	285	583			0.76	4.00	54	76	20	3	49

Appendix 12. KJ-39 fluid inclusion molar data and calculated constituents

Sample Number	**KJ39-1**	**KJ39-2**	**KJ39-3**	**KJ39-4**	**KJ39-5**	**KJ39-6**	**KJ39-7**	**KJ39-8**	**KJ39-9**	**KJ39-10**	**KJ39-11**	**KJ39-12**	**KJ39-13**	**KJ39-14**	**KJ39-15**	**KJ39-16**
Depth (m)	2800	2800	2800	2800	*2800*	*2800*	2650	2650	2600	2600	2600	2550	2550	2550	2500	2450
Mole %																
H2	0.21703	0.51755	0.69339	0.41052	0.38433	0.20181	25.29411	3.87333	14.94676	20.43665	5.34072	21.16625	37.12562	29.36277	17.66185	1.59082
He	0.00055	0.00063	0.00070	0.00021	0.00177	0.00034	0.13355	0.04259	0.01389	0.12506	0.01509	0.00801	0.00000	0.00000	0.02387	0.00170
CH4	0.02740	0.05574	0.23152	0.15050	0.10093	0.04989	11.11332	1.79054	7.27541	10.96253	2.66355	12.61814	18.64048	11.43326	23.77966	0.99325
H2O	69.20550	58.19533	65.90920	82.47688	30.34184	76.12252	0.00000	56.15372	36.78949	0.00000	69.59819	36.61981	0.00000	0.00000	33.81135	89.18991
CO	0.00000	0.00000	0.00000	0.00000	0.00000	0.00000	0.00000	0.00000	0.00000	0.00000	0.00000	0.00000	0.00000	0.00000	0.00000	0.00000
N2	2.04363	3.51499	1.75202	1.39289	7.76812	3.96270	37.47781	9.00055	22.41602	32.92486	8.31338	20.12258	26.36166	37.63200	16.24830	2.89961
C2H4	0.00000	0.00000	0.00000	0.00000	0.02774	0.01608	0.00000	0.00000	0.00000	0.00000	0.03012	0.00000	0.66658	0.00000	0.24448	0.00000
C2H6	0.05869	0.06717	0.08991	0.04945	0.25611	0.08934	0.25244	0.00000	0.31552	0.35358	0.02297	0.47789	0.00000	0.01244	0.24555	0.03284
H2S	0.00534	0.00526	0.00394	0.00152	0.01123	0.00270	0.13822	0.00000	0.00000	0.15042	0.02006	0.02250	0.00000	0.09624	0.07100	0.00287
Ar	0.01516	0.01827	0.01080	0.00712	0.03689	0.00986	0.52614	0.05867	0.34769	0.56972	0.08612	0.34920	0.19056	0.44278	0.24175	0.03439
C3H6	0.00000	0.00000	0.00518	0.00081	0.00000	0.00000	0.00000	0.00000	0.01139	0.00000	0.00000	0.04389	0.36340	0.00000	0.00273	0.00205
C3H8	0.11896	0.19973	0.27369	0.11882	0.33784	0.08432	0.00000	0.07271	0.12911	0.67340	0.00000	0.00000	0.00000	0.00000	0.07949	0.02737
CO2	28.28831	37.36643	30.97315	15.36163	60.71388	19.44623	24.51108	28.77240	17.73072	33.80169	13.86244	8.49580	15.97233	20.59131	7.38241	5.21613
C4H8	0.01157	0.04167	0.03272	0.01596	0.00678	0.00158	0.27270	0.07067	0.02355	0.00000	0.00000	0.00000	0.00000	0.10547	0.00000	0.00456
C4H10	0.00569	0.01464	0.02097	0.00995	0.00211	0.00497	0.26939	0.00005	0.00045	0.00208	0.03746	0.00068	0.00000	0.24936	0.00061	0.00443
SO2	0.00126	0.00148	0.00102	0.00266	0.00637	0.00579	0.00000	0.10002	0.00000	0.00000	0.00990	0.03139	0.00000	0.07438	0.00000	0.00000
Benzene	0.00089	0.00110	0.00178	0.00109	0.00406	0.00186	0.01126	0.06474	0.00000	0.00000	0.00000	0.04387	0.67937	0.00000	0.20694	0.00006
total gas	30.79	41.80	34.09	17.52	69.66	23.88	100.00	43.85	63.21	100.00	30.40	63.38	100.00	100.00	66.19	10.81
N2/Ar	134.78	192.35	162.20	195.76	210.56	401.72	71.23	153.40	64.47	57.79	96.54	57.63	138.34	84.99	67.21	84.31
He/Ar	0.04	0.03	0.06	0.03	0.05	0.03	0.25	0.73	0.04	0.22	0.18	0.02	0.00	0.00	0.10	0.05
CO2/N2	13.84	10.63	17.68	11.03	7.82	4.91	0.65	3.20	0.79	1.03	1.67	0.42	0.61	0.55	0.45	1.80
ppm-wt																
H2S	7.10E+01	6.37E+01		2.33E+01					0.00E+00	1.90E+03	3.16E+02		0.00E+00		1.30E+03	5.02E+01
SO2	3.14E+01	3.38E+01	2.50E+01	7.70E+01	1.18E+02	1.58E+02	0.00E+00	2.48E+03	0.00E+00	0.00E+00	2.94E+02	1.07E+03	0.00E+00	2.12E+03	0.00E+00	0.00E+00
H2	1.70E+02	3.69E+02	5.29E+02	3.71E+02	2.22E+02	1.72E+02	2.09E+04	3.00E+03	1.33E+04	1.52E+04	4.95E+03	2.26E+04	3.89E+04	2.61E+04	1.91E+04	1.64E+03
He	8.67E-01	8.91E-01	1.07E+00	3.79E-01	2.05E+00	5.86E-01	2.21E+02	6.59E+01	2.47E+01	1.86E+02	2.80E+01	1.71E+01	2.41E-13	0.00E+00	5.16E+01	3.50E+00
CO2	4.87E+05	5.86E+05	5.20E+05	3.06E+05	7.71E+05	3.65E+05	4.45E+05	4.89E+05	3.47E+05	5.52E+05	2.83E+05	1.99E+05	3.68E+05	4.03E+05	1.76E+05	1.18E+05
CO2/H2S wt/wt	6.86E+03	9.19E+03		1.31E+04						2.91E+02	8.94E+02				1.35E+02	2.36E+03
Geothermometer (°C)																
t(CO2)		427	420	395	442	403	413	417	401	423	392	378	404	408	373	359
t(H2S)-high	275	259		239			325			325	290				318	254
t(H2S+SO2)-high		283	275	267	314	282		336		1004	308	332			339	258
t(H2S)-low	214	191		163			287			287	236				276	184
t(H2)-high	324	325	328	325	320	318	362	344	357	359	348	362	367	364	361	338
t(H2)-low	299	300	306	300	291	287	367	335	360	362	343	369	378	371	366	325

Appendix 12-cont. *KJ-39 fluid inclusion molar data and calculated constituents*

Sample Number	**KJ39-17**	**KJ39-18**	**KJ39-19**	**KJ39-20**	**KJ39-21**	**KJ39-22**	**KJ39-23**	**KJ39-24**	**KJ39-25**	**KJ39-26**	**KJ39-27**	**KJ39-28**	**KJ39-29**	**KJ39-30**	**KJ39-31**	**KJ39-32**
Depth (m)	2450	2400	2400	2250	2250	2200	2150	2150	2050	2050	1950	1950	1850	2250	2050	2050
Mole %																
H2	12.52179	32.89573	1.67542	10.11046	31.14730	2.00241	31.57293	47.09163	55.63995	56.12231	27.49173	31.85342	14.52307	36.47654	5.51762	36.21624
He	0.01045	0.03368	0.00106	0.20649	0.08264	0.00031	0.00000	0.00000	0.03194	0.00000	0.14442	0.17082	0.00000	0.04150	0.00294	0.00000
CH4	6.74315	21.67421	1.02056	47.04539	15.78339	1.33358	16.71190	32.67312	14.49458	17.22948	28.96799	21.89321	9.56868	6.36853	5.35774	27.76404
H2O	38.38366	0.00000	92.61244	28.27028	0.00000	93.42212	36.56488	0.00000	0.00000	0.00000	0.00000	0.00000	59.57858	0.00000	80.68348	0.00000
CO	0.00000	0.00000	0.00000	0.00000	0.00000	0.00000	0.00000	0.00000	0.00000	0.00000	0.00000	0.00000	0.00000	0.00000	0.00000	0.00000
N2	13.83499	33.72998	2.17560	6.45038	42.49107	1.97873	12.83452	16.56408	25.70530	26.25252	32.40794	41.36453	12.95278	53.85018	4.57788	22.13273
C2H4	0.00000	0.00000	0.00445	0.03236	0.00000	0.00000	0.09930	0.00000	0.00000	0.00000	0.00000	0.00000	0.19662	0.16653	0.02889	0.01458
C2H6	0.00000	0.00000	0.00516	1.73192	1.04052	0.03301	0.00000	0.05590	0.24042	0.00000	1.07056	0.00000	0.04232	0.00000	0.23103	1.15714
H2S	0.20716	0.00000	0.00231	0.22940	0.33734	0.00123	0.00000	0.00000	0.00000	0.00000	0.00543	0.00000	0.02477	0.13339	0.01751	0.04302
Ar	0.40549	0.47432	0.03076	0.09309	0.82745	0.03273	0.19434	0.12791	0.56433	0.34218	0.53911	0.93427	0.23395	0.96911	0.05416	0.19126
C3H6	0.00000	0.81735	0.00186	0.00000	0.00000	0.00990	0.17516	0.14725	0.00000	0.02004	0.32645	0.00000	0.05114	0.03578	0.00000	0.00000
C3H8	0.13942	1.64997	0.00000	0.00000	0.00000	0.05079	0.75116	0.00000	0.00000	0.00000	0.00000	0.00000	0.04665	0.00000	0.00000	0.00000
CO2	27.32411	8.17895	2.45814	4.70581	8.25875	1.12499	0.92206	1.64979	2.67352	0.01832	8.60126	2.72983	2.68335	1.89858	3.37208	10.34152
C4H8	0.02885	0.20475	0.00201	0.03247	0.00000	0.00632	0.00000	0.32038	0.00000	0.00361	0.29873	0.00000	0.09795	0.04683	0.02078	0.00000
C4H10	0.00078	0.34046	0.01025	0.50527	0.00165	0.00004	0.17171	1.16697	0.46092	0.00857	0.00000	0.68294	0.00015	0.00028	0.11671	0.82978
SO2	0.40015	0.00000	0.00000	0.31334	0.02989	0.00385	0.00000	0.20294	0.18901	0.00297	0.14637	0.37098	0.00000	0.00000	0.01170	0.60369
Benzene	0.00000	0.00059	0.00000	0.27333	0.00000	0.00000	0.00205	0.00000	0.00000	0.00000	0.00000	0.00000	0.00000	0.01275	0.00746	0.70601
total gas	61.62	100.00	7.39	71.73	100.00	6.58	63.44	100.00	100.00	100.00	100.00	100.00	40.42	100.00	19.32	100.00
N2/Ar	34.12	71.11	70.72	69.29	51.35	60.46	66.04	129.49	45.55	76.72	60.11	44.27	55.37	55.57	84.52	115.72
He/Ar	0.03	0.07	0.03	2.22	0.10	0.01	0.00	0.00	0.06	0.00	0.27	0.18	0.00	0.04	0.05	0.00
CO2/N2	1.98	0.24	1.13	0.73	0.19	0.57	0.07	0.10	0.10	0.00	0.27	0.07	0.21	0.04	0.74	0.47
ppm-wt																
H2S		0.00E+00	4.22E+01				0.00E+00			0.00E+00	9.73E+01			2.49E+03	3.23E+02	
SO2	1.04E+04	0.00E+00	0.00E+00	1.11E+04	9.83E+02	1.36E+02	0.00E+00	1.03E+04	9.68E+03	1.67E+02	4.93E+03	1.32E+04	0.00E+00	0.00E+00	4.06E+02	2.17E+04
H2	1.01E+04	3.51E+04	1.80E+03	1.12E+04	3.20E+04	2.20E+03	4.36E+04	7.45E+04	8.91E+04	9.85E+04	2.90E+04	3.55E+04	1.65E+04	4.01E+04	5.98E+03	4.08E+04
He	1.69E+01	7.19E+01	2.28E+00	4.57E+02	1.70E+02	6.75E-01	1.72E-12	0.00E+00	1.02E+02	2.63E-12	3.04E+02	3.81E+02	0.00E+00	9.12E+01	6.38E+00	1.33E-12
CO2	4.87E+05	1.92E+05	5.82E+04	1.15E+05	1.87E+05	2.72E+04	2.80E+04	5.74E+04	9.42E+04	7.08E+02	1.99E+05	6.70E+04	6.70E+04	4.59E+04	8.04E+04	2.56E+05
CO2/H2S wt/wt			1.38E+03								2.05E+03			1.84E+01	2.49E+02	
Geothermometer (°C)																
t(CO2)	417	376	337	358	375	316	316	336	352	186	378	341	341	330	347	388
t(H2S)-high			251								267			330	290	
t(H2S+SO2)-high	379		253	382	1031	268		1059				1039	308	1024	305	1022
t(H2S)-low			179								203			295	237	
t(H2)-high	355	366	339	356	365	341	368	373	375	376	365	366	359	368	350	368
t(H2)-low	355	376	326	357	374	330	380	389	392	393	373	376	363	378	346	378

Appendix 12-cont. *KJ-39 fluid inclusion molar data and calculated constituents*

Sample Number	**KJ39-33**	**KJ39-34**	**KJ39-35**	**KJ39-36**	**KJ39-37**	**KJ39-38**	**KJ39-39**	**KJ39-40**	**KJ39-41**	**KJ39-42**	**KJ39-43**	**KJ39-44**	**KJ39-45**	**KJ39-46**	**KJ39-47**	**KJ39-48**
Depth (m)	1750	1750	1650	1650	1550	1400	1400	1350	1350	1250	1250	1150	1150	1050	1050	950
Mole %																
H2	12.14620	16.25512	1.22536	1.13980	38.65420	2.74528	1.43018	0.19415	0.34627	0.21459	0.17715	0.09913	0.07471	0.05239	0.04174	0.07863
He	0.00000	0.04021	0.00019	0.00037	0.00000	0.00000	0.00010	0.00010	0.00005	0.00004	0.00008	0.00077	0.00090	0.00003	0.00003	0.00005
CH4	10.66732	10.35386	0.51996	0.31062	6.80527	0.49932	0.17100	0.08737	0.07565	0.03635	0.02158	0.02817	0.01721	0.01327	0.01066	0.03119
H2O	62.99377	51.26761	91.11529	94.22062	29.19874	95.02300	97.72247	99.19325	99.21619	99.38473	99.66799	97.83689	98.60431	99.66054	99.81099	99.49467
CO	0.00000	0.00000	0.00000	0.00000	0.00000	0.00000	0.00000	0.00000	0.00000	0.00000	0.00000	0.00000	0.00000	0.00000	0.00000	0.00000
N2	10.83299	19.52245	1.37016	1.01168	20.33591	1.03077	0.36888	0.22795	0.15410	0.07425	0.04035	0.20321	0.06755	0.08477	0.03485	0.07542
C2H4	0.07322	0.00000	0.00000	0.00000	0.00000	0.00000	0.00000	0.00030	0.00000	0.00021	0.00000	0.00000	0.00000	0.00000	0.00000	0.00000
C2H6	0.34798	0.00000	0.04932	0.01221	0.08490	0.01425	0.00000	0.00133	0.00043	0.00241	0.00065	0.14923	0.08103	0.00010	0.01501	0.04129
H2S	0.06243	0.14230	0.00135	0.00000	0.00828	0.00247	0.00168	0.00008	0.00018	0.00031	0.00025	0.00860	0.00681	0.00193	0.00080	0.00245
Ar	0.16417	0.35546	0.02025	0.01425	0.31849	0.01509	0.00451	0.00412	0.00273	0.00146	0.00073	0.00676	0.00307	0.00164	0.00079	0.00191
C3H6	0.07750	0.00000	0.00000	0.00000	0.15455	0.00855	0.00398	0.00000	0.00055	0.00046	0.00005	0.00000	0.00000	0.00000	0.00000	0.00000
C3H8	0.00000	0.00000	0.00710	0.02016	0.00000	0.00000	0.00000	0.00000	0.00409	0.00136	0.00104	0.00000	0.00000	0.00026	0.00000	0.00000
CO2	2.48338	0.92188	5.67925	3.26659	4.38947	0.63170	0.28255	0.28789	0.19915	0.28233	0.08963	1.65382	1.13481	0.18506	0.08331	0.27043
C4H8	0.00000	0.09194	0.00407	0.00012	0.03090	0.00207	0.00093	0.00016	0.00042	0.00038	0.00015	0.00258	0.00190	0.00000	0.00045	0.00079
C4H10	0.00000	0.96766	0.00646	0.00004	0.01901	0.01777	0.01262	0.00316	0.00000	0.00037	0.00000	0.00319	0.00296	0.00000	0.00066	0.00118
SO2	0.00000	0.00000	0.00000	0.00354	0.00029	0.00295	0.00000	0.00000	0.00013	0.00072	0.00032	0.00517	0.00287	0.00000	0.00047	0.00128
Benzene	0.15104	0.08153	0.00123	0.00000	0.00000	0.00678	0.00110	0.00012	0.00006	0.00002	0.00003	0.00248	0.00187	0.00000	0.00024	0.00070
total gas	37.01	48.73	8.88	5.78	70.80	4.98	2.28	0.81	0.78	0.62	0.33	2.16	1.40	0.34	0.19	0.51
N2/Ar	65.99	54.92	67.67	70.97	63.85	68.30	81.82	55.27	56.42	50.96	55.19	30.05	22.01	51.78	43.88	39.42
He/Ar	0.00	0.11	0.01	0.03	0.00	0.00	0.02	0.02	0.02	0.03	0.11	0.11	0.29	0.02	0.04	0.03
CO2/N2	0.23	0.05	4.14	3.23	0.22	0.61	0.77	1.26	1.29	3.80	2.22	8.14	16.80	2.18	2.39	3.59
ppm-wt																
H2S		2.70E+03		0.00E+00	1.88E+02	4.71E+01	3.19E+01	1.53E+00	3.44E+00	5.90E+00	4.79E+00	1.58E+02	1.27E+02	3.63E+01		
SO2	0.00E+00	0.00E+00	0.00E+00	1.21E+02	1.25E+01	1.06E+02	0.00E+00	0.00E+00	4.52E+00	2.56E+01	1.13E+01	1.79E+02	1.00E+02	0.00E+00	1.67E+01	4.55E+01
H2	1.37E+04	1.81E+04	1.26E+03	1.21E+03	5.16E+04	3.08E+03	1.60E+03	2.15E+02	3.84E+02	2.38E+02	1.97E+02	1.07E+02	8.16E+01	5.81E+01	4.63E+01	8.70E+01
He	0.00E+00	8.96E+01	4.01E-01	7.83E-01	0.00E+00	0.00E+00	2.24E-01	2.25E-01	1.12E-01	9.70E-02	1.86E-01	1.67E+00	1.97E+00	7.58E-02	6.56E-02	1.11E-01
CO2	6.15E+04	2.26E+04	1.29E+05	7.66E+04	1.29E+05	1.56E+04	6.95E+03	7.01E+03	4.86E+03	6.88E+03	2.19E+03	3.94E+04	2.73E+04	4.51E+03	2.03E+03	6.58E+03
CO2/H2S wt/wt		8.38E+00			6.86E+02	3.30E+02	2.18E+02	4.59E+03	1.41E+03	1.17E+03	4.57E+02	2.49E+02	2.16E+02	1.24E+02		
Geothermometer (°C)																
t(CO2)	338	310	362	345	362	300	277	278	266	277	238	326	316	264	235	276
t(H2S)-high		332			280	253	245	186	202	213	209	277	272	248		
t(H2S+SO2)-high	325	345	243	261	301	269	246	187	213	236	224	287	280	248	240	261
t(H2S)-low		297			221	182	171	86	109	124	118	217	210	175		
t(H2)-high	358	360	336	336	370	344	338	320	325	321	319	314	311	308	306	312
t(H2)-low	360	365	320	320	382	335	324	291	300	292	289	279	274	269	265	275

Appendix 12-cont. *KJ-39 fluid inclusion molar data and calculated constituents*

Sample Number	KJ39-49	KJ39-50	KJ39-51	KJ39-52	KJ39-53	KJ39-54	KJ39-55	KJ39-56	KJ39-57	KJ39-58	KJ39-59	KJ39-60	KJ39-61	KJ39-62
Depth (m)	950	850	850	850	750	750	650	650	550	550	550	450	450	450
Mole %														
H2	0.03714	0.14008	0.01907	0.02173	0.00877	0.00615	0.00688	0.00231	0.01962	0.03042	0.04236	0.03948	0.03948	0.03729
He	0.00003	0.00020	0.00000	0.00001	0.00000	0.00002	0.00000	0.00001	0.00001	0.00004	0.00003	0.00001	0.00001	0.00001
CH4	0.02513	0.13557	0.02694	0.02493	0.00607	0.00398	0.00925	0.00409	0.03366	0.05720	0.05231	0.01323	0.01323	0.02078
H2O	99.76894	99.55898	99.91718	99.93047	99.87824	99.93199	99.91433	99.96760	99.78027	99.72342	99.66699	99.78313	99.78313	99.89483
CO	0.00000	0.00000	0.00000	0.00000	0.00000	0.00000	0.00000	0.00000	0.00000	0.00000	0.00000	0.00000	0.00000	0.00000
N2	0.04325	0.10140	0.01746	0.01392	0.05665	0.03481	0.01855	0.01044	0.02312	0.04634	0.06037	0.04154	0.04154	0.01929
C2H4	0.00000	0.00000	0.00000	0.00000	0.00000	0.00000	0.00000	0.00000	0.00000	0.00000	0.00000	0.00000	0.00000	0.00000
C2H6	0.01181	0.00336	0.00268	0.00164	0.00591	0.00295	0.00781	0.00243	0.00693	0.01398	0.01942	0.01205	0.01205	0.00467
H2S	0.00060	0.00000	0.00015	0.00006	0.00029	0.00015	0.00037	0.00010	0.00037	0.00090	0.00151	0.00072	0.00072	0.00004
Ar	0.00095	0.00179	0.00026	0.00018	0.00122	0.00068	0.00038	0.00019	0.00037	0.00084	0.00121	0.00080	0.00080	0.00033
C3H6	0.00000	0.00000	0.00012	0.00017	0.00000	0.00000	0.00000	0.00000	0.00000	0.00000	0.00000	0.00000	0.00000	0.00000
C3H8	0.00000	0.00000	0.00108	0.00050	0.00000	0.00000	0.00000	0.00000	0.00000	0.00000	0.00000	0.00000	0.00000	0.00000
CO2	0.11073	0.05720	0.01466	0.00618	0.04207	0.01871	0.04153	0.01252	0.13486	0.12500	0.15366	0.10727	0.10727	0.02193
C4H8	0.00045	0.00000	0.00000	0.00014	0.00022	0.00019	0.00023	0.00011	0.00016	0.00045	0.00051	0.00041	0.00041	0.00024
C4H10	0.00049	0.00000	0.00000	0.00002	0.00002	0.00010	0.00024	0.00006	0.00028	0.00061	0.00053	0.00057	0.00057	0.00038
SO2	0.00027	0.00143	0.00021	0.00007	0.00030	0.00018	0.00030	0.00010	0.00026	0.00047	0.00059	0.00045	0.00045	0.00010
Benzene	0.00022	0.00000	0.00019	0.00000	0.00023	0.00008	0.00013	0.00004	0.00010	0.00032	0.00050	0.00033	0.00033	0.00012
total gas	0.23	0.44	0.08	0.07	0.12	0.07	0.09	0.03	0.22	0.28	0.33	0.22	0.22	0.11
N2/Ar	45.54	56.72	66.84	79.14	46.56	51.33	49.13	54.13	62.20	55.14	49.73	52.07	52.07	58.11
He/Ar	0.03	0.11	0.00	0.03	0.00	0.03	0.01	0.03	0.04	0.05	0.03	0.02	0.02	0.03
CO2/N2	2.56	0.56	0.84	0.44	0.74	0.54	2.24	1.20	5.83	2.70	2.55	2.58	2.58	1.14
ppm-wt														
H2S	1.13E+01	0.00E+00	2.75E+00	1.14E+00	5.49E+00	2.89E+00	7.07E+00	1.93E+00	6.89E+00	1.71E+01	2.85E+01	1.36E+01	1.36E+01	7.57E-01
SO2	9.68E+00	5.09E+01	7.48E+00	2.48E+00	1.05E+01	6.27E+00	1.06E+01	3.40E+00	9.05E+00	1.68E+01	2.09E+01	1.60E+01	1.60E+01	3.46E+00
H2	4.12E+01	1.56E+02	2.12E+01	2.41E+01	9.74E+00	6.83E+00	7.64E+00	2.57E+00	2.18E+01	3.37E+01	4.70E+01	4.38E+01	4.38E+01	4.14E+01
He	6.48E-02	4.36E-01	3.28E-04	1.36E-02	0.00E+00	4.25E-02	4.31E-03	1.41E-02	3.14E-02	9.49E-02	6.74E-02	3.01E-02	3.01E-02	1.94E-02
CO2	2.70E+03	1.40E+03	3.58E+02	1.51E+02	1.03E+03	4.57E+02	1.01E+03	3.06E+02	3.29E+03	3.05E+03	3.75E+03	2.62E+03	2.62E+03	5.36E+02
CO2/H2S wt/wt	2.40E+02		1.30E+02	1.33E+02	1.87E+02	1.58E+02	1.43E+02	1.58E+02	4.77E+02	1.79E+02	1.32E+02	1.93E+02	1.93E+02	7.08E+02
Geothermometer (°C)														
t(CO2)	246	219	145	79	205	160	204	134	253	250	258	245	245	170
t(H2S)-high	225		198	181	211	199	216	191	216	233	243	229	229	173
t(H2S+SO2)-high	233	242	215	196	225	214	228	204	226	242	250	238	238	197
t(H2S)-low	142		102	77	122	104	129	92	128	154	168	147	147	66
t(H2)-high	305	317	299	300	292	288	289	279	299	303	306	305	305	305
t(H2)-low	263	285	252	254	239	233	235	216	252	260	265	264	264	263

Appendix 13. IDDP-1 fluid inclusion molar data and calculated constituents

Sample Number	**IDDP1-1**	**IDDP1-2**	**IDDP1-3**	**IDDP1-4**	**IDDP1-5**	**IDDP1-6**	**IDDP1-7**	**IDDP1-8**	**IDDP1-9**	**IDDP1-10**	**IDDP1-11**	**IDDP1-12**	**IDDP1-13**	**IDDP1-14**	**IDDP1-15**	**IDDP1-16**
Depth (m)	*2072*	*2072*	*2072*	*2072*	*2072*	*2046*	*2046*	*2046*	*2046*	*2046*	*2046*	*2041*	*2041*	*2041*	*2041*	*2041*
Mole %																
H2	0.43959	1.18786	0.18513	0.39628	0.93280	1.88743	1.52319	1.44948	0.68276	1.39838	2.65284	2.73121	4.51289	19.45205	0.10669	0.09897
He	0.00000	0.02433	0.00005	0.00073	0.00000	0.01066	0.00000	0.00000	0.00034	0.00257	0.00575	0.00000	0.00354	0.03598	0.00103	0.00034
CH4	0.22205	0.56217	0.06996	0.07746	0.16232	2.12967	0.62585	1.24805	0.56997	0.68109	1.17974	2.52253	3.13570	30.92331	0.10122	0.10185
H2O	80.92	77.05	96.16	97.21	96.19	64.97	82.38	68.58	57.91	53.52	47.14	67.00	70.70	2.28	75.74	81.15
CO	0.00000	0.00000	0.00000	0.00000	0.00000	0.00000	0.00000	0.00000	0.00000	0.00000	0.00000	0.00000	0.00000	0.00000	0.00000	0.00000
N2	4.18179	6.04583	0.54839	0.42252	0.45681	5.08137	2.16609	4.58311	5.62726	6.08714	7.72576	10.91357	8.10150	20.12859	2.84776	2.17177
C2H4	0.00000	0.00000	0.00000	0.00000	0.00000	0.00000	0.00871	0.00066	0.00000	0.00000	0.04332	0.00000	0.02427	0.00000	0.00000	0.00000
C2H6	0.02469	0.00000	0.00000	0.00000	0.00000	0.07621	0.00863	0.05049	0.00649	0.05324	0.03527	0.05905	0.16345	0.84837	0.01022	0.01269
H2S	0.00030	0.02260	0.00000	0.00043	0.00000	0.00000	0.00000	0.00000	0.00021	0.00861	0.06293	0.00000	0.01057	0.00000	0.00106	0.00021
Ar	0.02692	0.04902	0.00184	0.00280	0.00129	0.00000	0.00000	0.00189	0.00062	0.00000	0.02280	0.07751	0.09058	0.13722	0.01345	0.01193
C3H6	0.00580	0.00000	0.00602	0.01053	0.00056	0.00000	0.03078	0.00000	0.00317	0.00000	0.00000	0.00000	0.01641	0.00000	0.00000	0.00000
C3H8	0.01949	0.00000	0.05044	0.05894	0.17851	0.33765	0.19008	0.00000	0.31445	0.00000	0.00000	0.00000	0.00000	0.00000	0.03743	0.02995
CO2	14.14050	14.89346	2.96324	1.81333	2.04127	25.33796	12.99729	23.83963	34.82621	38.19590	41.00780	16.39856	13.10558	25.62473	21.13384	16.42059
C4H8	0.00880	0.00000	0.00405	0.00000	0.02017	0.07173	0.05817	0.06674	0.02171	0.01745	0.00000	0.07429	0.00026	0.43215	0.00055	0.00000
C4H10	0.00718	0.15398	0.00369	0.00869	0.00082	0.04052	0.00000	0.16063	0.00007	0.03508	0.11958	0.21122	0.10419	0.01959	0.00019	0.00004
SO2	0.00000	0.00000	0.00295	0.00218	0.01452	0.04378	0.00000	0.00000	0.00527	0.00000	0.00000	0.00778	0.02235	0.00000	0.00170	0.00332
Benzene	0.00253	0.00661	0.00000	0.00055	0.00000	0.01360	0.01565	0.01885	0.02659	0.00000	0.00918	0.00000	0.01369	0.11872	0.00000	0.00028
total gas_mol%	19.08	22.95	3.84	2.79	3.81	35.03	17.62	31.42	42.09	46.48	52.86	33.00	29.30	97.72	24.26	18.85
N2/Ar	155.33	123.34	298.18	150.67	355.26			2430.62	9076.74		338.89	140.80	89.44	146.68	211.74	182.08
He/Ar		0.50	0.03	0.26					0.56		0.25		0.04	0.26	0.08	0.03
CO2/N2	3.38	2.46	5.40	4.29	4.47	4.99	6.00	5.20	6.19	6.27	5.31	1.50	1.62	1.27	7.42	7.56
ppm-wt																
SO2	0.00E+00	0.00E+00	1.00E+02	7.54E+01	5.03E+02	1.12E+03	0.00E+00	0.00E+00	1.22E+02	0.00E+00	0.00E+00	2.16E+02	6.64E+02	0.00E+00	4.59E+01	9.44E+01
H2S	4.66E+00	3.44E+02		7.86E+00					2.59E+00	1.03E+02	7.36E+02		1.67E+02		1.52E+01	3.12E+00
H2	3.99E+02	1.06E+03	1.97E+02	4.29E+02	1.01E+03	1.51E+03	1.42E+03	1.18E+03	4.95E+02	9.87E+02	1.83E+03	2.37E+03	4.19E+03	1.67E+04	8.98E+01	8.80E+01
He	3.44E-14	4.35E+01	1.14E-01	1.57E+00	0.00E+00	1.71E+01	1.09E-13	0.00E+00	4.99E-01	3.63E+00	7.91E+00	0.00E+00	6.58E+00	6.17E+01	1.73E+00	6.06E-01
CO2	2.82E+05	2.93E+05	6.93E+04	4.32E+04	4.86E+04	4.47E+05	2.67E+05	4.28E+05	5.55E+05	5.93E+05	6.21E+05	3.14E+05	2.68E+05	4.84E+05	3.91E+05	3.21E+05
CO2/H2S wt/wt	6.06E+04	8.53E+02		5.49E+03					2.14E+05	5.74E+03	8.43E+02		1.60E+03		2.57E+04	1.03E+05
Geothermometer (°C)																
t(CO2)	411	394	342	328	332	413	390	411	424	427	430	397	390	417	407	398
t(H2S) - high	208	292		218					197	268	307		278		231	200
t(H2S+SO2)high	216	301	257	254	288	317			279	289	331	283	310		260	264
t(H2S)-low	117	239		132					100	205	260		218		150	106
t(H2)-high	325	334	319	326	334	338	337	335	327	334	339	342	347	360	312	312
t(H2)-low	301	317	289	302	317	323	322	319	305	316	326	331	340	364	276	276

Appendix 13-cont. IDDP-1 fluid inclusion molar data and calculated constituents

Sample Number	**IDDP1-17**	**IDDP1-18**	**IDDP1-19**	**IDDP1-20**	**IDDP1-21**	**IDDP1-22**	**IDDP1-23**	**IDDP1-24**	**IDDP1-25**	**IDDP1-26**	**IDDP1-27**	**IDDP1-28**	**IDDP1-29**	**IDDP1-30**	**IDDP1-31**	**IDDP1-32**
Depth (m)	*2041*	*2038*	*2038*	*2038*	*2032*	*2032*	*2032*	*2032*	*2032*	*2024*	*2024*	*2024*	*2000*	*2000*	*2000*	*1980*
Mole %																
H2	0.12119	1.02693	2.00639	4.99022	1.76413	1.62881	2.31480	2.37290	2.11333	0.89052	1.53634	1.49493	8.07370	0.21458	0.67610	1.14146
He	0.00044	0.00418	0.00000	0.00000	0.00235	0.00523	0.00301	0.00000	0.01027	0.00000	0.00155	0.00134	0.00000	0.00106	0.00000	0.00230
CH4	0.15561	0.81658	6.94402	16.23558	1.33564	1.12812	1.05355	1.18786	2.66145	0.68715	1.41891	2.84358	14.79295	0.18636	0.30835	1.51934
H2O	80.80	51.95	40.26	36.37	77.73	75.23	76.93	78.00	71.21	67.74	75.72	73.50	47.56	69.63	60.12	92.25
CO	0.00000	0.00000	0.00000	0.00000	0.00000	0.00000	0.00000	0.00000	0.00000	0.00000	0.00000	0.00000	0.00000	0.00000	0.00000	0.00000
N2	2.40958	7.51583	12.98582	11.48916	3.89918	4.10626	3.23170	2.99083	5.38325	5.29387	2.81044	5.03068	6.92431	3.24076	5.13348	1.77430
C2H4	0.00000	0.00000	0.04789	0.01998	0.00000	0.00000	0.00000	0.00000	0.00000	0.00000	0.00736	0.00000	0.00000	0.00000	0.00000	0.00290
C2H6	0.01223	0.05879	0.03260	0.00000	0.03391	0.06577	0.00000	0.11704	0.20619	0.06584	0.07709	0.10543	0.51280	0.02393	0.02863	0.02067
H2S	0.00000	0.00026	0.02388	0.00000	0.00000	0.00000	0.00230	0.00000	0.00000	0.00319	0.00182	0.00000	0.00000	0.00348	0.00389	0.00000
Ar	0.01202	0.05007	0.06767	0.01673	0.00719	0.00551	0.01504	0.01346	0.02034	0.03951	0.00998	0.02435	0.03438	0.01443	0.02242	0.01165
C3H6	0.00000	0.00000	0.00000	0.00000	0.00000	0.00000	0.00000	0.01027	0.00000	0.00000	0.01510	0.01401	0.06367	0.00000	0.00000	0.00101
C3H8	0.00000	0.01885	0.00000	0.00000	0.16038	0.00000	0.00000	0.00000	0.07572	0.00000	0.01520	0.16421	0.00000	0.05590	0.00000	0.00000
CO2	16.44834	38.55408	37.39087	26.78841	15.06345	17.57915	16.11748	15.18293	18.31664	25.19260	18.34040	16.67080	21.86027	26.61933	33.67961	3.19682
C4H8	0.00000	0.00536	0.01387	1.18719	0.00000	0.10392	0.00000	0.06897	0.00000	0.00114	0.00000	0.09803	0.00000	0.00178	0.00711	0.05180
C4H10	0.02638	0.00004	0.17935	1.11241	0.00004	0.14824	0.33000	0.03895	0.00023	0.06990	0.02392	0.00000	0.17350	0.00006	0.02008	0.00915
SO2	0.00000	0.00000	0.00388	1.20663	0.00056	0.00000	0.00000	0.01225	0.00000	0.00244	0.01283	0.00000	0.00000	0.00586	0.00000	0.00000
Benzene	0.00975	0.00000	0.04396	0.58412	0.00538	0.00000	0.00000	0.00000	0.00687	0.01878	0.00893	0.05484	0.00000	0.00163	0.00504	0.01758
total gas_mol%	19.20	48.05	59.74	63.63	22.27	24.77	23.07	22.00	28.79	32.26	24.28	26.50	52.44	30.37	39.88	7.75
N2/Ar	200.44	150.11	191.91	686.73	542.51	744.61	214.80	222.20	264.71	133.99	281.75	206.59	201.43	224.64	228.95	152.31
He/Ar	0.04	0.08			0.33	0.95	0.20		0.51		0.16	0.05		0.07		0.20
CO2/N2	6.83	5.13	2.88	2.33	3.86	4.28	4.99	5.08	3.40	4.76	6.53	3.31	3.16	8.21	6.56	1.80
ppm-wt																
SO2	0.00E+00	0.00E+00	8.65E+01	2.88E+04	1.64E+01	0.00E+00	0.00E+00	3.58E+02	0.00E+00	6.24E+01	3.60E+02	0.00E+00	0.00E+00	1.49E+02	0.00E+00	0.00E+00
H2S		3.12E+00	2.83E+02				3.51E+01			4.34E+01	2.72E+01			4.68E+01	4.86E+01	
H2	1.08E+02	7.18E+02	1.40E+03	3.72E+03	1.60E+03	1.43E+03	2.08E+03	2.17E+03	1.84E+03	7.13E+02	1.35E+03	1.32E+03	7.04E+03	1.70E+02	4.98E+02	1.21E+03
He	7.76E-01	5.84E+00	0.00E+00	1.76E-13	4.27E+00	9.17E+00	5.42E+00	0.00E+00	1.79E+01	4.68E-14	2.71E+00	2.36E+00	2.18E-12	1.69E+00	1.91E-13	4.89E+00
CO2	3.21E+05	5.93E+05	5.73E+05	4.40E+05	3.01E+05	3.39E+05	3.19E+05	3.05E+05	3.51E+05	4.44E+05	3.54E+05	3.23E+05	4.19E+05	4.64E+05	5.45E+05	7.47E+04
CO2/H2S wt/wt		1.90E+05	2.03E+03				9.08E+03			1.02E+04	1.30E+04			9.91E+03	1.12E+04	
Geothermometer (°C)																
t(CO2)	398	427	425	412	395	400	397	395	402	413	402	398	410	415	423	344
t(H2S) - high		200	288				247			251	242			253	254	
t(H2S+SO2)high		222	318	393	229		257	289		276	293			286	272	
t(H2S)-low		106	233				174			180	167			182	183	
t(H2)-high	314	331	337	346	338	337	341	341	339	331	337	336	352	318	327	336
t(H2)-low	279	311	322	338	324	322	329	329	327	311	321	321	349	287	305	320

Appendix 13-cont. IDDP-1 fluid inclusion molar data and calculated constituents

Sample Number	**IDDP1-33**	**IDDP1-34**	**IDDP1-35**	**IDDP1-36**	**IDDP1-37**	**IDDP1-38**	**IDDP1-39**	**IDDP1-40**	**IDDP1-41**	**IDDP1-42**	**IDDP1-43**	**IDDP1-44**	**IDDP1-45**	**IDDP1-46**	**IDDP1-47**	**IDDP1-48**
Depth (m)	*1980*	*1950*	*1950*	*1950*	*1990*	*1990*	*1900*	*1900*	*1900*	*1850*	*1850*	*1850*	*1800*	*1800*	*1800*	*1700*
Mole %																
H2	1.44452	0.60128	1.30760	0.70354	0.26138	0.81517	0.23125	0.33581	0.36266	0.15337	0.15033	0.17665	0.08956	0.11595	0.17988	0.17789
He	0.00000	0.00255	0.00000	0.00024	0.00041	0.00033	0.00026	0.00006	0.00071	0.00000	0.00000	0.00027	0.00014	0.00007	0.00000	0.00000
CH4	1.39808	0.20653	0.33945	0.25833	0.15567	1.61396	0.02686	0.05864	0.12880	0.08162	0.04544	0.05544	0.09380	0.07627	0.13190	0.09338
H2O	89.60	91.38	90.97	90.99	95.35	87.54	95.22	95.43	95.07	97.25	98.18	97.70	92.78	92.92	93.43	96.23
CO	0.00000	0.00000	0.00000	0.00000	0.00000	0.00000	0.00000	0.00000	0.00000	0.00000	0.00000	0.00000	0.00000	0.00000	0.00000	0.00000
N2	2.01638	2.15105	2.48933	2.22162	1.50447	2.72722	0.80708	1.09476	1.20038	0.69342	0.41747	0.47498	1.35281	1.13793	1.53984	0.83768
C2H4	0.00000	0.00000	0.00554	0.00013	0.00633	0.00078	0.00000	0.00000	0.00000	0.00000	0.00068	0.00000	0.00000	0.00000	0.00000	0.00000
C2H6	0.00000	0.01148	0.00000	0.00656	0.00000	0.04990	0.00411	0.00274	0.00429	0.00188	0.00208	0.00291	0.01084	0.00723	0.00342	0.01012
H2S	0.00000	0.00361	0.00000	0.00117	0.00096	0.00516	0.01401	0.00362	0.00208	0.00075	0.00048	0.00019	0.00224	0.00107	0.00000	0.00000
Ar	0.05020	0.01628	0.02771	0.02393	0.01404	0.02006	0.00927	0.01072	0.01036	0.00620	0.00509	0.00403	0.00985	0.00833	0.01392	0.00493
C3H6	0.00000	0.00144	0.00740	0.00105	0.00389	0.00614	0.00252	0.00272	0.00000	0.00000	0.00000	0.00000	0.00000	0.00000	0.00170	0.00015
C3H8	0.00000	0.00000	0.00000	0.00904	0.00263	0.05043	0.02273	0.01562	0.00000	0.00000	0.00171	0.00237	0.01081	0.01406	0.00706	0.00634
CO2	4.81103	5.60884	4.84072	5.77403	2.69815	7.14694	3.65831	3.03680	3.20542	1.80053	1.19166	1.58537	5.64510	5.70964	4.68161	2.63224
C4H8	0.00000	0.00000	0.00000	0.00634	0.00000	0.00647	0.00402	0.00204	0.00000	0.00006	0.00006	0.00100	0.00269	0.00282	0.00420	0.00732
C4H10	0.54029	0.00372	0.00004	0.00001	0.00002	0.00002	0.00066	0.00130	0.01559	0.00656	0.00000	0.00001	0.00068	0.00001	0.00109	0.00000
SO2	0.13589	0.00170	0.00421	0.00095	0.00000	0.01781	0.00308	0.00125	0.00000	0.00000	0.00144	0.00032	0.00181	0.00269	0.00000	0.00177
Benzene	0.00000	0.01086	0.00728	0.00335	0.00465	0.00000	0.00000	0.00055	0.00000	0.00098	0.00000	0.00000	0.00034	0.00000	0.00082	0.00000
total gas_mol%	10.40	8.62	9.03	9.01	4.65	12.46	4.78	4.57	4.93	2.75	1.82	2.30	7.22	7.08	6.57	3.77
N2/Ar	40.16	132.16	89.82	92.86	107.18	135.96	87.06	102.14	115.82	111.85	82.08	117.86	137.30	136.68	110.65	170.05
He/Ar		0.16		0.01	0.03	0.02	0.03	0.01	0.07			0.07	0.01	0.01		
CO2/N2	2.39	2.61	1.94	2.60	1.79	2.62	4.53	2.77	2.67	2.60	2.85	3.34	4.17	5.02	3.04	3.14
ppm-wt																
SO2	4.46E+03	5.56E+01	1.39E+02	3.09E+01	0.00E+00	5.70E+02	1.04E+02	4.25E+01	0.00E+00	0.00E+00	5.01E+01	1.12E+01	5.91E+01	8.79E+01	0.00E+00	6.05E+01
H2S		6.26E+01		2.03E+01	1.74E+01	8.77E+01	2.51E+02	6.53E+01	3.74E+01	1.37E+01	8.87E+00	3.47E+00	3.88E+01	1.86E+01		
H2	1.48E+03	6.14E+02	1.35E+03	7.17E+02	2.78E+02	8.15E+02	2.43E+02	3.56E+02	3.84E+02	1.66E+02	1.64E+02	1.92E+02	9.14E+01	1.18E+02	1.86E+02	1.90E+02
He	0.00E+00	5.20E+00	0.00E+00	4.80E-01	8.64E-01	6.53E-01	5.42E-01	1.34E-01	1.50E+00	0.00E+00	9.73E-15	5.91E-01	2.89E-01	1.38E-01	8.65E-14	0.00E+00
CO2	1.09E+05	1.26E+05	1.10E+05	1.29E+05	6.31E+04	1.57E+05	8.47E+04	7.09E+04	7.46E+04	4.28E+04	2.86E+04	3.78E+04	1.27E+05	1.28E+05	1.06E+05	6.18E+04
CO2/H2S wt/wt		2.01E+03		6.37E+03	3.63E+03	1.79E+03	3.38E+02	1.09E+03	1.99E+03	3.12E+03	3.23E+03	1.09E+04	3.27E+03	6.88E+03		
Geothermometer (°C)																
t(CO2)	356	361	357	362	339	369	348	343	344	328	317	325	361	362	356	339
t(H2S) - high		259		237	234	265	286	259	249	229	221	202	249	235		
t(H2S+SO2)high	333	270	265	252	235	299	291	267	251	230	248	223	264	262		247
t(H2S)-low		190		159	154	200	230	192	176	148	135	109	177	156		
t(H2)-high	337	329	337	331	322	332	321	324	325	317	317	319	312	314	319	319
t(H2)-low	323	308	321	311	295	313	293	299	300	286	286	289	276	281	288	289

Appendix 13-cont. *IDDP-1 fluid inclusion molar data and calculated constituents*

Sample Number	**IDDP1-49**	**IDDP1-50**	**IDDP1-51**	**IDDP1-52**	**IDDP1-53**	**IDDP1-54**	**IDDP1-55**	**IDDP1-56**	**IDDP1-57**	**IDDP1-58**	**IDDP1-59**	**IDDP1-60**	**IDDP1-61**	**IDDP1-62**	**IDDP1-63**	**IDDP1-64**	**IDDP1-65**	**IDDP1-66**
Depth (m)	*1700*	*1700*	*1608*	*1608*	*1500*	*1500*	*1400*	*1400*	*1400*	*1300*	*1300*	*1300*	*1250*	*1250*	*1250*	*1150*	*1150*	*1150*
Mole %																		
H2	0.09657	0.13642	0.03031	0.06675	0.03839	0.03511	0.10194	0.07663	0.07075	0.18031	0.17960	0.01658	0.04663	0.02860	0.02554	0.03222	0.05778	0.07309
He	0.00020	0.00000	0.00028	0.00050	0.00066	0.00025	0.00112	0.00020	0.00097	0.00223	0.00106	0.00007	0.00020	0.00047	0.00002	0.00075	0.00063	0.00007
CH4	0.05934	0.05355	0.04510	0.05884	0.09069	0.04276	0.03008	0.02961	0.02717	0.02120	0.02503	0.01856	0.01651	0.01110	0.00347	0.01687	0.01187	0.01038
H2O	97.20	97.95	98.48	99.04	94.57	98.47	99.50	99.67	99.45	98.35	98.65	99.72	99.56	99.63	99.92	99.66	99.68	99.80
CO	0.00000	0.00000	0.00000	0.00000	0.00000	0.00000	0.00000	0.00000	0.00000	0.00000	0.00000	0.00000	0.00000	0.00000	0.00000	0.00000	0.00000	0.00000
N2	0.52481	0.38933	0.31670	0.23424	0.31621	0.16594	0.07440	0.06817	0.09737	0.32590	0.32099	0.02779	0.17647	0.09780	0.01627	0.09554	0.05723	0.03788
C2H4	0.00000	0.00000	0.00062	0.00000	0.00000	0.00000	0.00364	0.00249	0.00233	0.00000	0.00000	0.00184	0.00263	0.00272	0.00007	0.00363	0.00298	0.00118
C2H6	0.00429	0.00373	0.01113	0.00317	0.00623	0.00062	0.01782	0.01092	0.01435	0.25078	0.14510	0.00912	0.00952	0.01331	0.00152	0.01723	0.01415	0.00632
H2S	0.00105	0.00017	0.00150	0.00077	0.00246	0.00039	0.00439	0.00281	0.00543	0.02626	0.01870	0.00344	0.00347	0.00470	0.00020	0.00820	0.00654	0.00194
Ar	0.00413	0.00367	0.00373	0.00251	0.00364	0.00131	0.00157	0.00131	0.00197	0.01182	0.00708	0.00050	0.00308	0.00223	0.00029	0.00202	0.00144	0.00077
C3H6	0.00040	0.00000	0.00211	0.00063	0.00162	0.00115	0.00313	0.00206	0.00256	0.00519	0.00000	0.00133	0.00159	0.00247	0.00005	0.00293	0.00251	0.00095
C3H8	0.00768	0.00504	0.00181	0.00000	0.02021	0.01000	0.00000	0.00000	0.00000	0.00000	0.00000	0.00000	0.00000	0.00000	0.00000	0.00000	0.00000	0.00000
CO2	2.10276	1.45068	1.10413	0.58732	4.93738	1.26967	0.25134	0.12714	0.31562	0.79897	0.64305	0.19401	0.18014	0.19595	0.02796	0.15114	0.15869	0.06428
C4H8	0.00205	0.00379	0.00233	0.00000	0.00389	0.00241	0.00222	0.00156	0.00187	0.00443	0.00266	0.00061	0.00081	0.00123	0.00007	0.00164	0.00135	0.00051
C4H10	0.00017	0.00000	0.00229	0.00287	0.00200	0.00081	0.00325	0.00193	0.00319	0.00757	0.00368	0.00154	0.00173	0.00228	0.00050	0.00372	0.00311	0.00140
SO2	0.00076	0.00068	0.00081	0.00000	0.00113	0.00015	0.00206	0.00142	0.00211	0.00840	0.00588	0.00102	0.00128	0.00174	0.00024	0.00229	0.00196	0.00093
Benzene	0.00019	0.00024	0.00091	0.00000	0.00054	0.00003	0.00169	0.00109	0.00150	0.00349	0.00194	0.00053	0.00049	0.00076	0.00011	0.00109	0.00087	0.00033
total gas_mol%	2.80	2.05	1.52	0.96	5.43	1.53	0.50	0.33	0.55	1.65	1.35	0.28	0.44	0.37	0.08	0.34	0.32	0.20
N2/Ar	127.20	106.20	84.94	93.18	86.94	126.83	47.39	51.88	49.47	27.58	45.36	55.92	57.23	43.84	55.98	47.21	39.70	48.89
He/Ar	0.05		0.08	0.20	0.18	0.19	0.72	0.16	0.49	0.19	0.15	0.15	0.06	0.21	0.08	0.37	0.44	0.09
CO2/N2	4.01	3.73	3.49	2.51	15.61	7.65	3.38	1.87	3.24	2.45	2.00	6.98	1.02	2.00	1.72	1.58	2.77	1.70
ppm-wt																		
SO2	2.61E+01	2.37E+01	2.84E+01	0.00E+00	3.75E+01	5.30E+00	7.31E+01	5.04E+01	7.45E+01	2.94E+02	2.07E+02	3.63E+01	4.54E+01	6.17E+01	8.45E+00	8.10E+01	6.96E+01	3.30E+01
H2S	1.92E+01	3.05E+00	2.78E+01	1.44E+01	4.33E+01	7.14E+00	8.27E+01	5.31E+01	1.02E+02	4.89E+02	3.49E+02	6.47E+01	6.53E+01	8.85E+01	3.75E+00	1.54E+02	1.23E+02	3.66E+01
H2	1.04E+02	1.48E+02	3.31E+01	7.35E+01	3.97E+01	3.83E+01	1.13E+02	8.50E+01	7.82E+01	1.98E+02	1.97E+02	1.84E+01	5.16E+01	3.17E+01	2.84E+01	3.57E+01	6.40E+01	8.12E+01
He	4.27E-01	8.08E-15	6.11E-01	1.11E+00	1.36E+00	5.52E-01	2.49E+00	4.54E-01	2.14E+00	4.88E+00	2.34E+00	1.61E-01	4.36E-01	1.03E+00	4.92E-02	1.67E+00	1.40E+00	1.60E-01
CO2	4.98E+04	3.47E+04	2.65E+04	1.42E+04	1.12E+05	3.05E+04	6.12E+03	3.10E+03	7.68E+03	1.93E+04	1.55E+04	4.73E+03	4.39E+03	4.77E+03	6.83E+02	3.68E+03	3.87E+03	1.57E+03
CO2/H2S wt/wt	2.59E+03	1.14E+04	9.54E+02	9.86E+02	2.60E+03	4.27E+03	7.41E+01	5.85E+01	7.52E+01	3.94E+01	4.45E+01	7.31E+01	6.72E+01	5.39E+01	1.82E+02	2.38E+01	3.14E+01	4.30E+01
Geothermometer (°C)																		
t(CO2)	332	322	315	298	357	319	274	251	280	306	300	265	263	266	184	257	259	224
t(H2S) - high	236	200	243	230	251	216	264	255	268	299	292	259	259	265	204	276	272	248
t(H2S+SO2)high	247	232	252	230	261	223	272	263	275	305	298	264	266	272	219	281	277	256
t(H2S)-low	157	105	168	149	180	129	198	186	204	249	239	191	192	200	111	216	210	175
t(H2)-high	313	316	303	310	304	304	314	311	311	319	319	297	307	302	301	303	309	311
t(H2)-low	278	284	259	273	262	262	280	275	274	289	289	249	267	258	257	261	270	274

Appendix 14. KJ-25 fluid inclusion molar data and calculated constituents

Sample Number	**KJ25-1**	**KJ25-2**	**KJ25-3**	**KJ25-4**	**KJ25-5**	**KJ25-6**	**KJ25-7**	**KJ25-8**	**KJ25-9**	**KJ25-10**	**KJ25-11**	**KJ25-12**	**KJ25-13**	**KJ25-14**	**KJ25-15**	**KJ25-16**
Depth (m)	2104	2104	2092	2092	2050	2050	2002	2002	2002	1950	1950	1902	1902	1850	1850	1750
Mole %																
H2	0.65874	1.39232	1.09064	1.59820	0.88650	0.63069	0.63908	0.88432	1.25763	0.63798	0.59830	0.34601	0.31308	0.18148	0.21681	0.06130
He	0.00022	0.00000	0.00086	0.00000	0.00450	0.00070	0.00002	0.00051	0.00000	0.00062	0.00045	0.00000	0.00116	0.00000	0.00024	0.00000
CH4	0.43409	1.55586	0.37255	0.82669	0.67268	0.42852	0.17232	0.37631	0.56412	0.45124	0.34988	0.16669	0.16356	0.06757	0.07010	0.04299
H2O	84.97184	73.60355	66.19177	56.56282	76.74137	83.92638	77.75362	74.30318	70.38602	87.31518	81.13646	89.09091	94.69611	92.71826	93.39850	95.75797
CO	0.00000	0.00000	0.00000	0.00000	0.00000	0.00000	0.00000	0.00000	0.00000	0.00000	0.00000	0.00000	0.00000	0.00000	0.00000	0.00000
N2	3.41822	9.57223	20.76476	23.10060	5.92396	5.78772	5.80424	8.39503	11.19307	7.67986	13.84631	2.76408	2.33699	1.38336	1.60707	3.20841
C2H4	0.00000	0.00000	0.00000	0.00053	0.00000	0.00000	0.02934	0.02682	0.03122	0.00182	0.00579	0.01019	0.00933	0.00000	0.00000	0.00000
C2H6	0.04201	0.08796	0.07382	0.00000	0.04550	0.03179	0.07475	0.06254	0.06996	0.01269	0.00000	0.03627	0.01733	0.02859	0.01652	0.00130
H2S	0.00000	0.00042	0.00251	0.00000	0.00016	0.00152	0.00648	0.00000	0.00000	0.00000	0.00121	0.00186	0.00073	0.00021	0.00056	0.00042
Ar	0.04767	0.14648	0.35061	0.34772	0.08884	0.08514	0.06169	0.08977	0.14294	0.11285	0.22168	0.03242	0.03128	0.02131	0.02255	0.05138
C3H6	0.00000	0.00243	0.00279	0.00826	0.00000	0.00000	0.00594	0.00953	0.02238	0.00568	0.00146	0.00559	0.00804	0.00000	0.00000	0.00036
C3H8	0.04251	0.04664	0.00000	0.05028	0.06875	0.02736	0.05484	0.08959	0.08497	0.00077	0.00000	0.04859	0.01485	0.01946	0.02620	0.00434
CO2	10.37291	13.57840	11.13076	17.46226	15.53471	9.06120	15.38362	15.74666	16.21795	3.77143	3.82788	7.48659	2.40007	5.57035	4.63869	0.87067
C4H8	0.00607	0.00389	0.00736	0.03666	0.01665	0.01062	0.00065	0.00806	0.01702	0.00400	0.00424	0.00586	0.00293	0.00340	0.00160	0.00061
C4H10	0.00005	0.00009	0.00571	0.00010	0.00527	0.00651	0.00333	0.00006	0.00585	0.00369	0.00381	0.00115	0.00455	0.00326	0.00028	0.00001
SO2	0.00478	0.00794	0.00567	0.00589	0.00595	0.00000	0.00902	0.00000	0.00687	0.00218	0.00253	0.00379	0.00000	0.00276	0.00060	0.00026
Benzene	0.00088	0.00178	0.00016	0.00000	0.00517	0.00184	0.00104	0.00764	0.00000	0.00000	0.00000	0.00000	0.00000	0.00000	0.00027	0.00000
total gas	15.03	26.40	33.81	43.44	23.26	16.07	22.25	25.70	29.61	12.68	18.86	10.91	5.30	7.28	6.60	4.24
N2/Ar	71.70	65.35	59.22	66.43	66.68	67.98	94.09	93.52	78.31	68.06	62.46	85.25	74.72	64.92	71.27	62.45
He/Ar	0.00	0.00	0.00	0.00	0.05	0.01	0.00	0.01	0.00	0.01	0.00	0.00	0.04	0.00	0.01	0.00
CO2/N2	3.03	1.42	0.54	0.76	2.62	1.57	2.65	1.88	1.45	0.49	0.28	2.71	1.03	4.03	2.89	0.27
ppm-wt																
H2S	0.00E+00	6.34E+00		0.00E+00					0.00E+00	0.00E+00	2.03E+01	3.14E+01	1.31E+01	3.64E+00	9.85E+00	7.61E+00
SO2	1.46E+02	2.28E+02	1.59E+02	1.53E+02	1.69E+02	0.00E+00	2.56E+02	0.00E+00	1.89E+02	7.09E+01	7.96E+01	1.20E+02	0.00E+00	9.01E+01	1.98E+01	8.83E+00
H2	6.29E+02	1.25E+03	9.53E+02	1.29E+03	7.87E+02	6.05E+02	5.67E+02	7.74E+02	1.08E+03	6.49E+02	5.89E+02	3.43E+02	3.33E+02	1.85E+02	2.24E+02	6.61E+01
He	4.23E-01	5.27E-14	1.51E+00	5.50E-13	7.98E+00	1.35E+00	3.56E-02	8.97E-01	2.72E-13	1.26E+00	8.89E-01	7.57E-14	2.46E+00	1.44E-13	5.01E-01	0.00E+00
CO2	2.18E+05	2.68E+05	2.14E+05	3.11E+05	3.03E+05	1.91E+05	3.01E+05	3.03E+05	3.08E+05	8.44E+04	8.28E+04	1.63E+05	5.61E+04	1.25E+05	1.06E+05	2.07E+04
CO2/H2S wt/wt		4.23E+04									4.08E+03		4.27E+03		1.07E+04	2.71E+03
Geothermometer (°C)																
t(CO2)	381	390	381	396	395	376	395	395	396	348	347	370	336	361	355	308
t(H2S)-high		214					267				237		228		223	218
t(H2S+SO2)-high	263	272	271	264	266	241	284		268	249	259	267	228	255	237	227
t(H2S)-low		126					203				159		146		138	131
t(H2)-high	330	336	333	336	332	329	329	332	335	330	329	324	324	318	320	309
t(H2)-low	309	320	316	321	312	308	307	312	318	309	307	298	298	288	291	271

Appendix 14-cont. KJ-25 fluid inclusion molar data and calculated constituents

Sample Number	KJ25-17	KJ25-18	KJ25-19	KJ25-20	KJ25-21	KJ25-22	KJ25-23	KJ25-24	KJ25-25	KJ25-26	KJ25-27	KJ25-28	KJ25-29	KJ25-30	KJ25-31	KJ25-32
Depth (m)	1750	1602	1602	1450	1450	1348	1348	1252	1252	1150	1150	1050	1050	950	950	850
Mole %																
H2	0.14860	0.04327	0.05867	0.94033	2.13094	1.04269	2.66559	0.85329	1.49336	0.20546	0.22694	0.21041	0.30130	0.11561	0.11638	0.38064
He	0.00004	0.00000	0.00000	0.00281	0.00349	0.00064	0.00051	0.00008	0.00061	0.00000	0.00051	0.00000	0.00049	0.00000	0.00000	0.00000
CH4	0.04150	0.08521	0.05954	0.32922	0.68517	0.29666	0.60943	0.38811	0.62044	0.02593	0.03212	0.02688	0.04104	0.01883	0.02344	0.08908
H2O	94.00684	98.94867	98.73044	95.10250	89.46118	97.50062	94.59311	94.10864	91.42558	99.08290	98.97867	99.58197	99.50147	99.66914	99.77012	99.04249
CO	0.00000	0.00000	0.00000	0.00000	0.00000	0.00000	0.00000	0.00000	0.00000	0.00000	0.00000	0.00000	0.00000	0.00000	0.00000	0.00000
N2	4.73590	0.59648	0.72480	2.00096	4.86467	0.66650	1.32268	1.22814	1.96369	0.35505	0.45681	0.09155	0.07678	0.09144	0.06450	0.27075
C2H4	0.00000	0.00000	0.00000	0.00029	0.01075	0.00000	0.00000	0.00000	0.00090	0.00390	0.00217	0.00000	0.00000	0.00533	0.00000	0.00000
C2H6	0.00176	0.00318	0.00509	0.01150	0.00000	0.00583	0.00134	0.00682	0.00198	0.00480	0.00393	0.00000	0.00000	0.01345	0.00084	0.00000
H2S	0.00024	0.00026	0.00026	0.00086	0.00000	0.00066	0.00000	0.00090	0.00000	0.00000	0.00028	0.00000	0.00003	0.00043	0.00029	0.00000
Ar	0.08075	0.00905	0.01087	0.03166	0.07087	0.00957	0.01861	0.01785	0.02845	0.00450	0.00693	0.00049	0.00000	0.00165	0.00056	0.00000
C3H6	0.00061	0.00000	0.00000	0.00113	0.01752	0.00000	0.00000	0.00000	0.00000	0.00091	0.00000	0.00940	0.00560	0.00179	0.00151	0.01841
C3H8	0.00345	0.00000	0.00000	0.00375	0.00000	0.00000	0.00000	0.02147	0.02334	0.00105	0.00000	0.03677	0.04602	0.00503	0.00607	0.11807
CO2	0.97984	0.31096	0.40813	1.57190	2.74156	0.46346	0.74821	3.37161	4.42773	0.31372	0.28604	0.03516	0.01624	0.07528	0.01459	0.05438
C4H8	0.00010	0.00209	0.00116	0.00090	0.00681	0.00410	0.00099	0.00180	0.00219	0.00102	0.00124	0.00455	0.00549	0.00118	0.00088	0.01767
C4H10	0.00002	0.00063	0.00061	0.00002	0.00003	0.00927	0.02965	0.00039	0.00303	0.00000	0.00389	0.00257	0.00494	0.00002	0.00000	0.00852
SO2	0.00017	0.00020	0.00002	0.00216	0.00000	0.00000	0.00563	0.00080	0.00619	0.00005	0.00022	0.00025	0.00041	0.00038	0.00045	0.00000
Benzene	0.00019	0.00000	0.00039	0.00000	0.00701	0.00000	0.00426	0.00011	0.00251	0.00072	0.00024	0.00000	0.00020	0.00043	0.00039	0.00000
total gas	5.99	1.05	1.27	4.90	10.54	2.50	5.41	5.89	8.57	0.92	1.02	0.42	0.50	0.33	0.23	0.96
N2/Ar	58.65	65.88	66.71	63.20	68.65	69.62	71.09	68.79	69.03	78.91	65.89	185.65		55.32	115.44	
He/Ar	0.00	0.00	0.00	0.09	0.05	0.07	0.03	0.00	0.02	0.00	0.07	0.00		0.00	0.00	
CO2/N2	0.21	0.52	0.56	0.79	0.56	0.70	0.57	2.75	2.25	0.88	0.63	0.38	0.21	0.82	0.23	0.20
ppm-wt																
H2S	4.30E+00	4.92E+00	4.95E+00	1.59E+01	1.86E-13	1.24E+01	0.00E+00	1.62E+01	0.00E+00	0.00E+00	5.35E+00	0.00E+00	4.98E-01	8.11E+00	5.44E+00	0.00E+00
SO2	5.65E+00	7.13E+00	7.95E-01	7.50E+01	0.00E+00	0.00E+00	2.01E+02	2.71E+01	2.07E+02	1.80E+00	7.77E+00	8.75E+00	1.45E+01	1.37E+01	1.60E+01	0.00E+00
H2	1.59E+02	4.77E+01	6.46E+01	1.02E+03	2.26E+03	1.16E+03	2.98E+03	9.05E+02	1.56E+03	2.27E+02	2.51E+02	2.34E+02	3.35E+02	1.28E+02	1.29E+02	4.22E+02
He	9.25E-02	0.00E+00	0.00E+00	6.09E+00	7.40E+00	1.41E+00	1.13E+00	1.61E-01	1.28E+00	0.00E+00	1.12E+00	0.00E+00	1.09E+00	1.64E-15	3.55E-15	0.00E+00
CO2	2.30E+04	7.54E+03	9.88E+03	3.75E+04	6.39E+04	1.13E+04	1.84E+04	7.86E+04	1.02E+05	7.63E+03	6.96E+03	8.60E+02	3.97E+02	1.84E+03	3.57E+02	1.33E+03
CO2/H2S wt/wt		1.53E+03	2.00E+03								1.30E+03			2.27E+02	6.56E+01	
Geothermometer (°C)																
t(CO2)	311	280	288	324	340	292	305	346	354	280	277	196	151	231	144	217
t(H2S)-high		209	209								211			219	211	
t(H2S+SO2)-high	217	220	211	256	-392	227	269	245	270	177	222	208	219	231	229	
t(H2S)-low		119	119								121			133	121	
t(H2)-high	317	306	309	334	341	335	344	333	338	320	321	321	324	315	315	326
t(H2)-low	286	265	270	317	330	319	335	315	324	292	293	292	298	282	282	302

Appendix 14-cont. *KJ-25 fluid inclusion molar data and calculated constituents*

Sample Number	**KJ25-33**	**KJ25-34**	**KJ25-35**	**KJ25-36**	**KJ25-37**	**KJ25-38**	**KJ25-39**	**KJ25-40**	**KJ25-41**	**KJ25-42**	**KJ25-43**	**KJ25-44**	**KJ25-45**
Depth (m)	850	850	750	750	650	650	550	550	550	450	450	350	350
Mole %													
H2	0.22677	0.30908	0.24835	0.13025	0.38034	0.92552	0.05727	0.05284	0.08500	0.01360	0.04071	0.09436	0.09053
He	0.00000	0.00027	0.00018	0.00009	0.00028	0.00005	0.00000	0.00004	0.00000	0.00000	0.00000	0.00009	0.00004
CH4	0.05636	0.06939	0.02577	0.02018	0.02080	0.04554	0.01276	0.01027	0.01557	0.01248	0.00984	0.00817	0.00546
H2O	99.37901	99.10363	99.47689	99.62125	99.42329	98.37076	99.53415	99.65052	99.76805	99.93689	99.86424	99.24000	99.64001
CO	0.00000	0.00000	0.00000	0.00000	0.00000	0.00000	0.00000	0.00000	0.00000	0.00000	0.00000	0.00000	0.00000
N2	0.17416	0.31163	0.13140	0.17158	0.14518	0.15568	0.23609	0.17055	0.07498	0.01510	0.03842	0.42060	0.15548
C2H4	0.00000	0.00000	0.00115	0.00144	0.00107	0.00000	0.00932	0.00634	0.00264	0.00100	0.00185	0.00693	0.00286
C2H6	0.00000	0.00000	0.00332	0.00254	0.00177	0.00000	0.02102	0.01519	0.00506	0.00221	0.00483	0.03795	0.01629
H2S	0.00033	0.00065	0.00023	0.00003	0.00000	0.00000	0.00043	0.00031	0.00000	0.00000	0.00013	0.00100	0.00025
Ar	0.00000	0.00148	0.00165	0.00274	0.00184	0.00000	0.00379	0.00272	0.00123	0.00036	0.00066	0.00745	0.00264
C3H6	0.01976	0.03170	0.00063	0.00085	0.00050	0.00000	0.00181	0.00136	0.00063	0.00027	0.00046	0.00249	0.00116
C3H8	0.09526	0.11297	0.00166	0.00000	0.00000	0.00000	0.00000	0.00064	0.00000	0.00017	0.00000	0.00007	0.00000
CO2	0.02760	0.03051	0.10710	0.04805	0.02395	0.01273	0.12126	0.08783	0.04581	0.01749	0.03749	0.17750	0.08343
C4H8	0.01422	0.01811	0.00083	0.00041	0.00066	0.00000	0.00072	0.00043	0.00040	0.00026	0.00039	0.00107	0.00072
C4H10	0.00652	0.01022	0.00025	0.00048	0.00030	0.32755	0.00056	0.00022	0.00044	0.00000	0.00081	0.00089	0.00055
SO2	0.00000	0.00016	0.00031	0.00009	0.00000	0.00000	0.00044	0.00041	0.00009	0.00000	0.00015	0.00077	0.00029
Benzene	0.00000	0.00020	0.00028	0.00002	0.00000	0.16217	0.00035	0.00035	0.00010	0.00019	0.00000	0.00067	0.00029
total gas	0.62	0.90	0.52	0.38	0.58	1.63	0.47	0.35	0.23	0.06	0.14	0.76	0.36
N2/Ar		210.66	79.46	62.67	78.98		62.26	62.61	60.77	42.28	57.81	56.49	59.00
He/Ar		0.18	0.11	0.03	0.15		0.00	0.01	0.00	0.00	0.00	0.01	0.02
CO2/N2	0.16	0.10	0.82	0.28	0.16	0.08	0.51	0.51	0.61	1.16	0.98	0.42	0.54
ppm-wt													
H2S	6.25E+00	1.22E+01	4.26E+00	5.02E-01	0.00E+00	0.00E+00	8.18E+00	5.76E+00	0.00E+00	0.00E+00	2.52E+00	1.89E+01	4.80E+00
SO2	1.04E-01	5.80E+00	1.11E+01	3.35E+00	0.00E+00	0.00E+00	1.57E+01	1.45E+01	3.07E+00	0.00E+00	5.38E+00	2.73E+01	1.03E+01
H2	2.52E+02	3.43E+02	2.76E+02	1.45E+02	4.24E+02	1.02E+03	6.35E+01	5.86E+01	9.44E+01	1.51E+01	4.52E+01	1.04E+02	1.00E+02
He	0.00E+00	6.00E-01	4.06E-01	2.10E-01	6.33E-01	1.06E-01	0.00E+00	8.17E-02	0.00E+00	1.24E-15	0.00E+00	1.95E-01	9.61E-02
CO2	6.74E+02	7.44E+02	2.62E+03	1.17E+03	5.87E+02	3.10E+02	2.96E+03	2.14E+03	1.12E+03	4.27E+02	9.16E+02	4.32E+03	2.04E+03
CO2/H2S wt/wt		6.11E+01		2.34E+03			3.61E+02	3.72E+02			3.63E+02	2.29E+02	4.25E+02
Geothermometer (°C)													
t(CO2)	183	188	245	211	175	135	249	237	209	156	199	262	235
t(H2S)-high		227		165			219	212			196	235	209
t(H2S+SO2)-high	214	231	223	194			233	229	188		211	246	223
t(H2S)-low		144		54			133	123			100	157	118
t(H2)-high	321	324	322	316	326	334	309	308	312	296	306	313	313
t(H2)-low	293	298	295	284	302	317	270	269	277	246	264	278	278

Appendix 15. KJ-26 fluid inclusion molar data and calculated constituents

Sample Number	**KJ26-1**	**KJ26-2**	**KJ26-3**	**KJ26-4**	**KJ26-5**	**KJ26-6**	**KJ26-7**	**KJ26-8**	**KJ26-9**	**KJ26-10**	**KJ26-11**	**KJ26-12**	**KJ26-13**	**KJ26-14**	**KJ26-15**	**KJ26-16**
Depth (m)	2100	2100	2100	2100	2100	2100	2100	2048	2048	2000	2000	1950	1950	1950	1900	1900
Mole %																
H2	0.26164	7.42337	0.70831	1.02756	1.45395	0.57824	6.47627	0.57309	0.51182	1.20285	1.39488	0.56472	1.09763	1.00345	0.28140	0.44970
He	0.00008	0.00490	0.00000	0.00110	0.00000	0.00000	0.02146	0.00028	0.00019	0.00102	0.00031	0.00035	0.00170	0.00409	0.00012	0.00007
CH4	0.23432	3.57514	0.25251	0.36657	3.32761	0.59461	6.93346	0.81210	0.37469	0.15500	0.22186	0.27718	0.58258	0.61886	0.09928	0.13620
H2O	94.86998	0.00000	89.59076	89.87823	0.00000	88.39969	0.00000	95.94285	94.74613	95.70757	95.00275	92.96705	90.39306	88.00898	98.30644	97.88577
CO	0.00000	0.00000	0.00000	0.00000	0.00000	0.00000	0.00000	0.00000	0.00000	0.00000	0.00000	0.00000	0.00000	0.00000	0.00000	0.00000
N2	1.70072	41.62157	3.83739	5.38035	23.24578	6.16221	41.73301	1.79316	3.56558	1.39929	1.89845	1.42569	3.33311	7.14231	0.51632	0.69780
C2H4	0.00000	0.00000	0.00000	0.00000	0.00000	0.00000	0.00000	0.00000	0.00396	0.00125	0.00000	0.00000	0.00000	0.00000	0.00000	0.00032
C2H6	0.01052	0.10122	0.01992	0.00799	0.99916	0.05654	0.98807	0.04414	0.00332	0.00161	0.00186	0.00000	0.00751	0.06375	0.00359	0.00356
H2S	0.00000	0.00000	0.00033	0.00227	0.07350	0.00362	0.00000	0.00000	0.00049	0.00000	0.00025	0.00042	0.00243	0.00251	0.00044	0.00043
Ar	0.03068	0.80662	0.06701	0.08643	0.38073	0.09930	0.75361	0.02968	0.05318	0.02155	0.03040	0.01831	0.04884	0.11876	0.00863	0.01420
C3H6	0.00000	0.00000	0.00000	0.00492	0.00000	0.00000	0.00000	0.00000	0.00000	0.00000	0.00183	0.00000	0.00000	0.00000	0.00061	0.00092
C3H8	0.00112	0.24438	0.00000	0.00000	0.00000	0.00000	0.00000	0.00000	0.00429	0.01412	0.01631	0.04795	0.00000	0.00000	0.00228	0.00308
CO2	2.88957	45.99019	5.45092	3.20968	69.13777	4.08577	41.11901	0.74880	0.72632	1.44862	1.42142	4.68325	4.45509	2.97613	0.77979	0.80698
C4H8	0.00084	0.05809	0.04724	0.01618	0.00000	0.01655	0.05368	0.00953	0.01003	0.02331	0.00438	0.01506	0.01450	0.02252	0.00058	0.00050
C4H10	0.00001	0.00643	0.02561	0.00794	1.38151	0.00002	0.00000	0.02540	0.00000	0.00000	0.00000	0.00002	0.05011	0.02959	0.00000	0.00000
SO2	0.00052	0.15006	0.00000	0.00000	0.00000	0.00025	0.69344	0.01685	0.00000	0.00993	0.00000	0.00000	0.00000	0.00905	0.00040	0.00000
Benzene	0.00000	0.01803	0.00000	0.01079	0.00000	0.00321	1.22800	0.00413	0.00000	0.01389	0.00532	0.00000	0.01344	0.00000	0.00012	0.00048
total gas	5.13	100.00	10.41	10.12	100.00	11.60	100.00	4.06	5.25	4.29	5.00	7.03	9.61	11.99	1.69	2.11
N2/Ar	55.44	51.60	57.27	62.25	61.06	62.06	55.38	60.42	67.05	64.95	62.45	77.88	68.25	60.14	59.80	49.14
He/Ar	0.00	0.01	0.00	0.01	0.00	0.00	0.03	0.01	0.00	0.05	0.01	0.02	0.03	0.03	0.01	0.00
CO2/N2	1.70	1.10	1.42	0.60	2.97	0.66	0.99	0.42	0.20	1.04	0.75	3.28	1.34	0.42	1.51	1.16
ppm-wt																
SO2	1.77E+01	2.89E+03	0.00E+00	0.00E+00	0.00E+00	8.19E+00	1.34E+04	5.89E+02	0.00E+00	3.46E+02	0.00E+00	0.00E+00	0.00E+00	2.99E+02	1.41E+01	0.00E+00
H2S	0.00E+00	0.00E+00		4.00E+01					9.05E+00	0.00E+00	4.66E+00		4.28E+01		8.13E+00	7.98E+00
H2	2.77E+02	4.47E+03	7.18E+02	1.07E+03	7.50E+02	5.90E+02	3.92E+03	6.26E+02	5.54E+02	1.31E+03	1.52E+03	5.86E+02	1.13E+03	1.04E+03	3.09E+02	4.94E+02
He	1.73E-01	5.90E+00	9.33E-14	2.29E+00	2.71E-13	0.00E+00	2.60E+01	6.02E-01	4.07E-01	2.22E+00	6.76E-01	7.27E-01	3.51E+00	8.44E+00	2.68E-01	1.51E-01
CO2	6.73E+04	6.09E+05	1.22E+05	7.34E+04	7.85E+05	9.17E+04	5.47E+05	1.80E+04	1.73E+04	3.47E+04	3.41E+04	1.07E+05	1.01E+05	6.76E+04	1.88E+04	1.95E+04
CO2/H2S wt/wt				1.83E+03					1.91E+03		7.32E+03		2.37E+03		2.32E+03	2.44E+03
Geothermometer (°C)																
t(CO2)	344		367	349		358		306	305	324	324	360	360	347	306	307
t(H2S)-high			216	253		263			222		209	220	255	256	219	219
t(H2S)-low			128	183		196			138		119	134	185	186	134	133
t(H2S+SO2)-high	224		216	253		264		291	222	281	209	220	255	285	232	219
t(H2)-high	323		333	336		331		330	329	337	338	330	337	336	323	328
t(H2)-low	297		314	320		311		309	308	322	325	310	321	320	297	305

Appendix 15-cont. *KJ-26 fluid inclusion molar data and calculated constituents*

Sample Number	**KJ26-17**	**KJ26-18**	**KJ26-19**	**KJ26-20**	**KJ26-21**	**KJ26-22**	**KJ26-23**	**KJ26-24**	**KJ26-25**	**KJ26-26**	**KJ26-27**	**KJ26-28**	**KJ26-29**	**KJ26-30**	**KJ26-31**	**KJ26-32**
Depth (m)	1900	1900	1900	1900	1850	1850	1850	1850	1850	1800	1800	1800	1800	1800	1800	1800
Mole %																
H2	1.89665	0.86245	1.34097	1.30835	2.82893	10.08920	0.95673	0.53344	1.93811	20.20601	30.18585	43.61648	35.59870	2.56327	3.68228	12.47628
He	0.00056	0.00000	0.00000	0.00140	0.00601	0.00819	0.00000	0.00276	0.01005	0.01598	0.00527	0.01790	0.02586	0.00000	0.00000	0.03173
CH4	1.24267	0.30637	0.27804	0.25511	1.09055	3.06552	0.51773	1.05369	1.97039	17.05768	9.83075	10.43320	6.55549	2.46675	1.75140	8.14802
H2O	87.99945	93.78770	94.09399	95.13847	82.93345	54.16533	95.98759	93.56477	82.43849	0.00000	0.00000	0.00000	19.57830	78.90918	66.62139	0.00000
CO	0.00000	0.00000	0.00000	0.00000	0.00000	0.00000	0.00000	0.00000	0.00000	0.00000	0.00000	0.00000	0.00000	0.00000	0.00000	0.00000
N2	2.58282	2.22145	2.47877	1.74138	6.28817	24.23878	1.24178	2.36295	4.97859	28.35522	37.71382	27.48361	28.87864	4.83563	8.41354	17.66633
C2H4	0.00000	0.01423	0.00000	0.00237	0.00000	0.00000	0.00000	0.00000	0.00000	0.00000	0.15028	0.00000	0.00000	0.00000	0.00000	0.00000
C2H6	0.02027	0.03069	0.00000	0.00000	0.00985	0.00000	0.01185	0.07981	0.12733	1.21175	0.00000	0.03719	0.00000	0.11013	0.00000	0.40643
H2S	0.00000	0.00000	0.00133	0.00000	0.00759	0.00520	0.00856	0.00146	0.02094	0.03220	0.00000	0.01291	0.02384	0.00813	0.00361	0.00000
Ar	0.05085	0.03637	0.04235	0.02630	0.09396	0.37264	0.01782	0.03651	0.12195	0.49776	0.68797	0.31591	0.47178	0.07009	0.09444	0.00000
C3H6	0.00000	0.03934	0.00945	0.01084	0.00000	0.02992	0.02000	0.00000	0.00293	0.00000	0.00000	0.00000	0.00000	0.00924	0.00000	0.00000
C3H8	0.00000	0.00000	0.04416	0.00558	0.05018	0.20039	0.00000	0.00000	0.09332	0.00000	0.17386	0.00000	0.00000	0.07524	0.00000	0.00000
CO2	6.17643	2.60621	1.57034	1.40235	6.50828	7.57728	1.11342	2.26154	8.13505	32.55637	21.25217	15.56169	8.15616	10.94084	19.27781	57.25737
C4H8	0.00000	0.09518	0.11568	0.10119	0.17317	0.24755	0.05585	0.05452	0.16284	0.03660	0.00000	0.87014	0.00000	0.01043	0.00000	1.18241
C4H10	0.01708	0.00000	0.00000	0.00666	0.00000	0.00000	0.00000	0.03718	0.00000	0.03042	0.00002	0.81485	0.69728	0.00015	0.15552	0.00000
SO2	0.00000	0.00000	0.02208	0.00000	0.00176	0.00000	0.00000	0.01137	0.00000	0.00000	0.00000	0.00000	0.00000	0.00091	0.00000	1.02830
Benzene	0.01321	0.00000	0.00285	0.00000	0.00810	0.00000	0.06866	0.00000	0.00000	0.00000	0.00000	0.83611	0.01396	0.00000	0.00000	1.80312
total gas	12.00	6.21	5.91	4.86	17.07	45.83	4.01	6.44	17.56	100.00	100.00	100.00	80.42	21.09	33.38	100.00
N2/Ar	50.79	61.07	58.53	66.22	66.92	65.05	69.69	64.72	40.82	56.97	54.82	87.00	61.21	68.99	89.09	
He/Ar	0.01	0.00	0.00	0.05	0.06	0.02	0.00	0.08	0.08	0.03	0.01	0.06	0.05	0.00	0.00	
CO2/N2	2.39	1.17	0.63	0.81	1.04	0.31	0.90	0.96	1.63	1.15	0.56	0.57	0.28	2.26	2.29	3.24
ppm-wt																
SO2	0.00E+00	0.00E+00	7.63E+02	0.00E+00	5.64E+01	0.00E+00	0.00E+00	3.88E+02	0.00E+00	0.00E+00	0.00E+00	0.00E+00	0.00E+00	2.79E+01	0.00E+00	1.91E+04
H2S		1.27E-14	2.44E+01				1.59E+02			4.21E+02	0.00E+00			1.32E+02	5.26E+01	
H2	1.94E+03	9.17E+02	1.45E+03	1.42E+03	2.84E+03	9.63E+03	1.04E+03	5.68E+02	1.90E+03	1.55E+04	2.69E+04	4.63E+04	4.05E+04	2.45E+03	3.16E+03	7.22E+03
He	1.14E+00	8.29E-14	0.00E+00	3.05E+00	1.20E+01	1.56E+01	3.28E-14	5.88E+00	1.97E+01	2.46E+01	9.38E+00	3.80E+01	5.89E+01	0.00E+00	7.09E-13	3.67E+01
CO2	1.39E+05	6.09E+04	3.73E+04	3.36E+04	1.44E+05	1.59E+05	2.67E+04	5.30E+04	1.76E+05	5.51E+05	4.16E+05	3.63E+05	2.04E+05	2.30E+05	3.64E+05	7.29E+05
CO2/H2S wt/wt		4.80E+18	1.53E+03				1.68E+02			1.31E+03				1.74E+03	6.91E+03	
Geothermometer (°C)																
t(CO2)	372	341	327	323	376	400	317	337	385				458	400	437	
t(H2S)-high			242		278	279	278	244	298				329	281	268	
t(H2S)-low			166		219	220	218	169	248				292	222	204	
t(H2S+SO2)-high			298		282	279	278	286	298				329	283	268	
t(H2)-high	342	334	338	338	346	361	335	330	343				382	346	350	
t(H2)-low	331	317	324	323	339	367	318	309	332				405	338	347	

Appendix 15-cont. *KJ-26 fluid inclusion molar data and calculated constituents*

Sample Number	**KJ26-33**	**KJ26-34**	**KJ26-35**	**KJ26-36**	**KJ26-37**	**KJ26-38**	**KJ26-39**	**KJ26-40**	**KJ26-41**	**KJ26-42**	**KJ26-43**	**KJ26-44**	**KJ26-45**	**KJ26-46**	**KJ26-47**	**KJ26-48**
Depth (m)	1700	1700	1700	1700	1700	1650	1650	1550	1550	1550	1500	1500	1450	1450	1450	1450
Mole %																
H2	41.60384	0.06139	0.09337	0.07434	0.10699	0.12001	0.06412	0.18986	0.16746	0.31684	0.02148	0.01807	0.01400	0.04845	0.06331	0.02115
He	0.03678	0.00003	0.00010	0.00003	0.00008	0.00001	0.00007	0.00004	0.00011	0.00007	0.00000	0.00001	0.00001	0.00002	0.00001	0.00000
CH4	32.67437	0.01505	0.03421	0.01861	0.02905	0.03466	0.03736	0.03196	0.02313	0.04710	0.01863	0.02142	0.02144	0.01303	0.01485	0.01853
H2O	0.00000	99.74903	99.23857	99.48595	99.30746	99.55886	99.76304	99.23388	99.32348	99.22722	99.78378	99.78604	99.74034	99.56274	99.57753	99.64612
CO	0.00000	0.00000	0.00000	0.00000	0.00000	0.00000	0.00000	0.00000	0.00000	0.00000	0.00000	0.00000	0.00000	0.00000	0.00000	0.00000
N2	5.63906	0.10487	0.46549	0.30895	0.44398	0.13485	0.05713	0.11560	0.08121	0.14934	0.08118	0.07074	0.02782	0.05316	0.05894	0.07255
C2H4	0.37268	0.00000	0.00058	0.00000	0.00070	0.00019	0.00000	0.00000	0.00000	0.00000	0.00024	0.00009	0.00035	0.00079	0.00055	0.00000
C2H6	1.40058	0.00032	0.00000	0.00000	0.00000	0.00100	0.00132	0.00208	0.00000	0.00000	0.00086	0.00077	0.00171	0.00307	0.00281	0.00064
H2S	0.03247	0.00007	0.00005	0.00000	0.00005	0.00020	0.00017	0.00032	0.00008	0.00008	0.00008	0.00003	0.00036	0.00276	0.00090	0.00006
Ar	0.00000	0.00184	0.00788	0.00587	0.00748	0.00258	0.00133	0.00240	0.00141	0.00285	0.00125	0.00111	0.00059	0.00089	0.00120	0.00134
C3H6	0.00000	0.00015	0.00136	0.00157	0.00164	0.00025	0.00000	0.00004	0.00242	0.00194	0.00016	0.00014	0.00025	0.00075	0.00062	0.00112
C3H8	0.00000	0.00056	0.00544	0.00283	0.00000	0.00000	0.00000	0.00000	0.00667	0.00467	0.00044	0.00048	0.00000	0.00000	0.00000	0.00441
CO2	17.28181	0.06630	0.13282	0.08300	0.07889	0.14679	0.06555	0.42243	0.38115	0.22783	0.09148	0.10090	0.19152	0.31165	0.27713	0.22505
C4H8	0.00000	0.00024	0.01951	0.01828	0.02103	0.00006	0.00000	0.00019	0.01033	0.01921	0.00018	0.00020	0.00031	0.00053	0.00044	0.00815
C4H10	0.95841	0.00000	0.00000	0.00015	0.00180	0.00029	0.00000	0.00073	0.00000	0.00141	0.00007	0.00000	0.00071	0.00096	0.00075	0.00050
SO2	0.00000	0.00000	0.00063	0.00000	0.00085	0.00020	0.00992	0.00015	0.00256	0.00065	0.00010	0.00000	0.00035	0.00092	0.00072	0.00024
Benzene	0.00000	0.00015	0.00000	0.00041	0.00000	0.00005	0.00000	0.00030	0.00000	0.00079	0.00005	0.00000	0.00026	0.00028	0.00025	0.00014
total gas	100.00	0.25	0.76	0.51	0.69	0.44	0.24	0.77	0.68	0.77	0.22	0.21	0.26	0.44	0.42	0.35
N2/Ar		57.12	59.10	52.65	59.33	52.21	42.93	48.09	57.69	52.32	64.86	63.63	47.54	59.53	49.10	54.29
He/Ar		0.02	0.01	0.01	0.01	0.01	0.05	0.02	0.08	0.02	0.00	0.01	0.01	0.02	0.01	0.00
CO2/N2	3.06	0.63	0.29	0.27	0.18	1.09	1.15	3.65	4.69	1.53	1.13	1.43	6.88	5.86	4.70	3.10
ppm-wt																
SO2	0.00E+00	0.00E+00	2.24E+01	0.00E+00	3.00E+01	7.00E+00	3.52E+02	5.20E+00	9.04E+01	2.32E+01	3.50E+00	0.00E+00	1.22E+01	3.24E+01	2.54E+01	8.38E+00
H2S		1.34E+00		0.00E+00	8.68E-01	3.77E+00	3.13E+00	6.09E+00	1.51E+00	1.46E+00	1.49E+00	5.39E-01	6.74E+00	5.20E+01		
H2	5.09E+04	6.81E+01	1.03E+02	8.24E+01	1.18E+02	1.33E+02	7.12E+01	2.10E+02	1.85E+02	3.51E+02	2.38E+01	2.00E+01	1.55E+01	5.36E+01	7.01E+01	2.34E+01
He	9.01E+01	7.30E-02	2.31E-01	7.24E-02	1.72E-01	3.24E-02	1.55E-01	8.87E-02	2.34E-01	1.50E-01	9.18E-03	1.53E-02	1.82E-02	4.49E-02	2.46E-02	0.00E+00
CO2	4.65E+05	1.62E+03	3.23E+03	2.02E+03	1.92E+03	3.58E+03	1.60E+03	1.03E+04	9.27E+03	5.56E+03	2.23E+03	2.46E+03	4.67E+03	7.58E+03	6.75E+03	5.48E+03
CO2/H2S wt/wt		1.21E+03			2.22E+03	9.51E+02	5.12E+02	1.69E+03	6.15E+03	3.82E+03	1.50E+03	4.57E+03	6.92E+02	1.46E+02		
Geothermometer (°C)																
t(CO2)		226	253	235	233	256	225	289	286	271	239	243	265	280	277	270
t(H2S)-high		184	176		176	204	200	213	186	186	186	166	215	255	233	181
t(H2S)-low		82	70		70	111	106	125	86	84	85	56	128	185	154	77
t(H2S+SO2)-high		184	228		233	217	280	221	254	229	202	166	228	261	245	212
t(H2)-high		309	313	311	315	316	310	320	319	324	300	298	296	307	310	300
t(H2)-low		271	279	275	281	283	272	290	288	299	254	251	247	267	272	254

Appendix 15-cont. *KJ-26 fluid inclusion molar data and calculated constituents*

Sample Number	**KJ26-49**	**KJ26-50**	**KJ26-51**	**KJ26-52**	**KJ26-53**	**KJ26-54**	**KJ26-55**	**KJ26-56**	**KJ26-57**	**KJ26-58**	**KJ26-59**	**KJ26-60**	**KJ26-61**	**KJ26-62**	**KJ26-63**	**KJ26-64**
Depth (m)	1450	1450	1350	1350	1350	1350	1350	1250	1250	1250	1250	1200	1200	1200	1150	1150
Mole %																
H2	0.03188	0.03465	0.01095	0.01032	0.00271	0.00431	0.00495	0.05916	0.04116	0.05431	0.07395	0.01537	0.01413	0.02069	0.01008	0.00000
He	0.00002	0.00001	0.00000	0.00001	0.00000	0.00000	0.00000	0.00004	0.00002	0.00007	0.00007	0.00000	0.00001	0.00000	0.00001	0.00000
CH4	0.01666	0.01223	0.00937	0.01496	0.00689	0.00835	0.00919	0.15994	0.10364	0.05629	0.09821	0.02411	0.01110	0.01382	0.01432	0.00000
H2O	99.58036	99.76668	99.85844	99.81433	99.94539	99.93308	99.92812	99.13304	99.47102	99.30475	98.99375	99.93152	99.87851	99.73248	99.74681	99.94677
CO	0.00000	0.00000	0.00000	0.00000	0.00000	0.00000	0.00000	0.00000	0.00000	0.00000	0.00000	0.00000	0.00000	0.00000	0.00000	0.00000
N2	0.07012	0.04553	0.08818	0.13234	0.02665	0.03307	0.03488	0.37310	0.22318	0.46755	0.68364	0.00563	0.04160	0.07336	0.04709	0.00000
C2H4	0.00000	0.00000	0.00000	0.00000	0.00007	0.00000	0.00000	0.00000	0.00000	0.00130	0.00000	0.00000	0.00041	0.00047	0.00000	0.00000
C2H6	0.00002	0.00000	0.00059	0.00052	0.00024	0.00018	0.00006	0.00601	0.00285	0.00218	0.00352	0.00162	0.00226	0.00207	0.00101	0.00404
H2S	0.00019	0.00003	0.00005	0.00005	0.00000	0.00001	0.00006	0.00039	0.00000	0.00007	0.00063	0.00045	0.00091	0.00074	0.00026	0.00013
Ar	0.00142	0.00089	0.00148	0.00207	0.00047	0.00056	0.00054	0.00665	0.00388	0.00745	0.01094	0.00007	0.00059	0.00132	0.00082	0.00000
C3H6	0.00165	0.00093	0.00002	0.00000	0.00059	0.00057	0.00017	0.00032	0.00000	0.00059	0.00342	0.00023	0.00045	0.00043	0.00017	0.00000
C3H8	0.00744	0.00378	0.00007	0.00000	0.00000	0.00000	0.00068	0.00000	0.00000	0.00110	0.00001	0.00052	0.00000	0.00000	0.00004	0.00519
CO2	0.27646	0.12582	0.03076	0.02517	0.01273	0.01482	0.01753	0.25951	0.15228	0.06893	0.09811	0.01984	0.04859	0.15311	0.17912	0.04125
C4H8	0.01305	0.00913	0.00005	0.00003	0.00378	0.00463	0.00382	0.00037	0.00032	0.03217	0.03167	0.00022	0.00025	0.00029	0.00009	0.00000
C4H10	0.00041	0.00021	0.00001	0.00009	0.00045	0.00036	0.00000	0.00000	0.00143	0.00082	0.00000	0.00023	0.00055	0.00057	0.00004	0.00142
SO2	0.00027	0.00007	0.00000	0.00009	0.00000	0.00000	0.00000	0.00082	0.00003	0.00243	0.00001	0.00012	0.00045	0.00047	0.00000	0.00112
Benzene	0.00004	0.00005	0.00001	0.00002	0.00002	0.00006	0.00000	0.00066	0.00018	0.00000	0.00206	0.00008	0.00019	0.00019	0.00014	0.00009
total gas	0.42	0.23	0.14	0.19	0.05	0.07	0.07	0.87	0.53	0.70	1.01	0.07	0.12	0.27	0.25	0.05
N2/Ar	49.35	51.29	59.76	64.06	56.32	58.76	64.29	56.10	57.53	62.73	62.47	84.73	70.44	55.57	57.46	
He/Ar	0.02	0.01	0.00	0.00	0.00	0.00	0.00	0.01	0.01	0.01	0.01	0.07	0.01	0.00	0.01	
CO2/N2	3.94	2.76	0.35	0.19	0.48	0.45	0.50	0.70	0.68	0.15	0.14	3.53	1.17	2.09	3.80	
ppm-wt																
SO2	9.48E+00	2.36E+00	6.47E-02	3.07E+00	0.00E+00	0.00E+00	0.00E+00	2.91E+01	1.22E+00	8.59E+01	4.79E-01	4.16E+00	1.61E+01	1.67E+01	0.00E+00	3.97E+01
H2S	3.60E+00	4.88E-01	8.54E-01	9.44E-01	5.25E-15	2.56E-01	1.16E+00	7.33E+00	0.00E+00	1.32E+00	1.18E+01	8.44E+00	1.72E+01	1.39E+01	4.93E+00	2.40E+00
H2	3.53E+01	3.84E+01	1.22E+01	1.15E+01	3.01E+00	4.79E+00	5.49E+00	6.54E+01	4.56E+01	6.01E+01	8.17E+01	1.71E+01	1.57E+01	2.29E+01	1.12E+01	0.00E+00
He	5.25E-02	1.35E-02	0.00E+00	1.97E-02	0.00E+00	0.00E+00	0.00E+00	7.83E-02	4.47E-02	1.45E-01	1.49E-01	1.00E-02	1.13E-02	3.50E-03	1.98E-02	0.00E+00
CO2	6.73E+03	3.07E+03	7.51E+02	6.15E+02	3.11E+02	3.62E+02	4.28E+02	6.31E+03	3.71E+03	1.68E+03	2.39E+03	4.85E+02	1.19E+03	3.73E+03	4.37E+03	1.01E+03
CO2/H2S wt/wt	1.87E+03	6.29E+03	8.80E+02	6.51E+02	5.92E+16	1.42E+03	3.68E+02	8.60E+02		1.27E+03	2.03E+02	5.74E+01	6.90E+01	2.69E+02	8.86E+02	4.20E+02
Geothermometer (°C)																
t(CO2)	277	251	189	178	135	145	156	275	258	228	242	164	212	258	263	204
t(H2S)-high	203	164	175	177		152	181	217		184	226	220	233	229	209	195
t(H2S)-low	110	53	69	72		35	78	130		82	144	134	154	148	119	98
t(H2S+SO2)-high	220	189	176	197		152	181	239	170	253	227	224	241	239	209	240
t(H2)-high	303	304	294	293	281	285	286	309	306	308	311	297	296	299	293	
t(H2)-low	260	262	242	242	219	227	229	271	265	269	275	248	247	253	241	

Appendix 15-cont. *KJ-26 fluid inclusion molar data and calculated constituents*

Sample Number	**KJ26-65**	**KJ26-66**	**KJ26-67**	**KJ26-68**	**KJ26-69**	**KJ26-70**	**KJ26-71**	**KJ26-72**	**KJ26-73**	**KJ26-74**	**KJ26-75**	**KJ26-76**	**KJ26-77**	**KJ26-78**	**KJ26-79**	**KJ26-80**
Depth (m)	1100	1100	1100	1050	1050	959	959	904	904	904	850	800	800	750	694	694
Mole %																
H2	0.03504	0.02669	0.02555	0.01395	0.01084	0.01255	0.02775	0.02280	0.02571	0.02197	0.02695	0.00964	0.01764	0.03581	0.04919	0.02901
He	0.00000	0.00001	0.00000	0.00000	0.00001	0.00002	0.00003	0.00001	0.00001	0.00001	0.00003	0.00000	0.00001	0.00004	0.00002	0.00000
CH4	0.01831	0.02893	0.02720	0.01135	0.02034	0.01385	0.02021	0.02685	0.04251	0.03411	0.01429	0.01789	0.01173	0.00953	0.00630	0.00677
H2O	99.82753	99.78093	99.82842	99.81960	99.74804	99.82639	99.81992	99.75113	99.72889	99.62527	99.81441	99.82080	99.74703	99.88186	99.85561	99.83526
CO	0.00000	0.00000	0.00000	0.00000	0.00000	0.00000	0.00000	0.00000	0.00000	0.00000	0.00000	0.00000	0.00000	0.00000	0.00000	0.00000
N2	0.07951	0.10803	0.08537	0.14233	0.20682	0.10434	0.11147	0.03310	0.05259	0.06510	0.08126	0.12896	0.20064	0.05981	0.05761	0.09582
C2H4	0.00000	0.00000	0.00000	0.00000	0.00000	0.00000	0.00000	0.00000	0.00000	0.00000	0.00000	0.00000	0.00000	0.00000	0.00000	0.00000
C2H6	0.00143	0.00116	0.00088	0.00071	0.00072	0.00121	0.00090	0.00253	0.00244	0.00193	0.00154	0.00147	0.00086	0.00080	0.00075	0.00072
H2S	0.00015	0.00014	0.00016	0.00015	0.00018	0.00011	0.00010	0.00029	0.00051	0.00029	0.00019	0.00011	0.00023	0.00035	0.00023	0.00013
Ar	0.00166	0.00177	0.00145	0.00216	0.00282	0.00163	0.00181	0.00048	0.00075	0.00094	0.00137	0.00203	0.00342	0.00104	0.00111	0.00156
C3H6	0.00009	0.00000	0.00009	0.00002	0.00005	0.00000	0.00008	0.00018	0.00012	0.00009	0.00000	0.00000	0.00004	0.00000	0.00000	0.00006
C3H8	0.00000	0.00000	0.00073	0.00000	0.00000	0.00000	0.00000	0.00000	0.00000	0.00000	0.00000	0.00000	0.00000	0.00000	0.00000	0.00000
CO2	0.03559	0.05206	0.03005	0.00941	0.00991	0.03930	0.01738	0.16156	0.14532	0.24932	0.05889	0.01890	0.01808	0.01057	0.02876	0.03015
C4H8	0.00017	0.00010	0.00007	0.00008	0.00008	0.00008	0.00013	0.00019	0.00012	0.00010	0.00029	0.00001	0.00006	0.00015	0.00010	0.00011
C4H10	0.00022	0.00012	0.00000	0.00015	0.00009	0.00030	0.00011	0.00040	0.00055	0.00049	0.00033	0.00012	0.00011	0.00002	0.00009	0.00018
SO2	0.00020	0.00008	0.00000	0.00007	0.00007	0.00019	0.00008	0.00025	0.00030	0.00023	0.00046	0.00000	0.00010	0.00000	0.00012	0.00015
Benzene	0.00010	0.00000	0.00004	0.00002	0.00003	0.00006	0.00005	0.00022	0.00018	0.00015	0.00000	0.00006	0.00005	0.00002	0.00011	0.00009
total gas	0.17	0.22	0.17	0.18	0.25	0.17	0.18	0.25	0.27	0.37	0.19	0.18	0.25	0.12	0.14	0.16
N2/Ar	47.91	61.16	58.86	65.99	73.37	64.09	61.71	69.00	69.69	68.92	59.16	63.38	58.75	57.31	51.94	61.55
He/Ar	0.00	0.00	0.00	0.00	0.00	0.01	0.02	0.02	0.02	0.01	0.02	0.00	0.00	0.04	0.01	0.00
CO2/N2	0.45	0.48	0.35	0.07	0.05	0.38	0.16	4.88	2.76	3.83	0.72	0.15	0.09	0.18	0.50	0.31
ppm-wt																
SO2	7.03E+00	2.88E+00	0.00E+00	2.46E+00	2.51E+00	6.58E+00	2.98E+00	8.99E+00	1.08E+01	8.13E+00	1.63E+01	0.00E+00	3.55E+00	0.00E+00	4.10E+00	5.28E+00
H2S	2.83E+00	2.63E+00	2.96E+00	2.79E+00	3.46E+00	2.04E+00	1.81E+00	5.53E+00	9.58E+00	5.38E+00	3.57E+00	2.15E+00	4.32E+00	6.58E+00	4.33E+00	2.38E+00
H2	3.89E+01	2.96E+01	2.84E+01	1.55E+01	1.20E+01	1.39E+01	3.08E+01	2.53E+01	2.85E+01	2.43E+01	2.99E+01	1.07E+01	1.96E+01	3.98E+01	5.46E+01	3.22E+01
He	7.31E-03	1.28E-02	0.00E+00	8.50E-03	1.97E-02	3.46E-02	6.32E-02	2.46E-02	2.57E-02	2.46E-02	6.58E-02	2.57E-05	3.03E-02	9.68E-02	3.66E-02	6.75E-03
CO2	8.69E+02	1.27E+03	7.34E+02	2.30E+02	2.42E+02	9.60E+02	4.25E+02	3.94E+03	3.54E+03	6.07E+03	1.44E+03	4.61E+02	4.41E+02	2.58E+02	7.03E+02	7.36E+02
CO2/H2S wt/wt	3.08E+02	4.84E+02	2.48E+02	8.23E+01	6.99E+01	4.71E+02	2.35E+02	7.13E+02	3.70E+02	1.13E+03	4.03E+02	2.14E+02	1.02E+02	3.93E+01	1.62E+02	3.09E+02
Geothermometer (°C)																
t(CO2)	197	215	188	113	117	202	156	260	256	274	221	161	158	122	185	188
t(H2S)-high	198	197	199	198	202	192	190	211	222	211	203	193	207	215	207	195
t(H2S)-low	103	101	104	103	109	94	90	122	138	121	110	95	115	127	115	98
t(H2S+SO2)-high	215	206	199	206	209	211	202	224	231	222	227	193	214	215	215	210
t(H2)-high	304	302	301	296	294	295	302	300	301	300	302	293	298	304	307	303
t(H2)-low	262	257	257	247	242	245	258	255	257	254	258	240	250	262	268	259

Appendix 15-cont. *KJ-26 fluid inclusion molar data and calculated constituents*

Sample Number	**KJ26-81**	**KJ26-82**	**KJ26-83**	**KJ26-84**	**KJ26-85**	**KJ26-86**	**KJ26-87**	**KJ26-88**	**KJ26-89**	**KJ26-90**	**KJ26-91**	**KJ26-92**	**KJ26-93**	**KJ26-94**	**KJ26-95**	**KJ26-96**	**KJ26-97**
Depth (m)	694	656	656	656	600	550	550	550	510	510	450	450	400	400	350	350	300
Mole %																	
H2	0.05738	0.00508	0.00856	0.02089	0.03509	0.03035	0.01919	0.03946	0.05667	0.03519	0.00569	0.06140	0.01185	0.01834	0.02341	0.03147	0.01089
He	0.00001	0.00001	0.00000	0.00001	0.00001	0.00000	0.00001	0.00001	0.00000	0.00001	0.00001	0.00000	0.00001	0.00025	0.00001	0.00002	0.00001
CH4	0.00958	0.01485	0.00813	0.01212	0.00757	0.01169	0.02026	0.02428	0.02417	0.02781	0.00340	0.01443	0.00945	0.01420	0.00600	0.01137	0.00331
H2O	99.79103	99.65229	99.81009	99.82277	98.74550	99.55378	99.68128	99.68825	99.59160	99.65361	99.87903	99.63070	99.75330	99.53181	99.86703	99.74545	99.88949
CO	0.00000	0.00000	0.00000	0.00000	0.00000	0.00000	0.00000	0.00000	0.00000	0.00000	0.00000	0.00000	0.00000	0.00000	0.00000	0.00000	0.00000
N2	0.11435	0.05487	0.03937	0.04430	0.00000	0.03940	0.08653	0.09808	0.09138	0.14146	0.02767	0.10442	0.04013	0.04968	0.08997	0.20028	0.03091
C2H4	0.00000	0.00000	0.00000	0.00000	0.00000	0.00000	0.00000	0.00000	0.00000	0.00000	0.00000	0.00000	0.00005	0.00031	0.00000	0.00000	0.00011
C2H6	0.00048	0.00382	0.00338	0.00234	0.00151	0.00111	0.00106	0.00127	0.00217	0.00158	0.00029	0.00092	0.00404	0.00823	0.00106	0.00134	0.00279
H2S	0.00009	0.00112	0.00092	0.00055	0.00087	0.00015	0.00038	0.00031	0.00047	0.00020	0.00003	0.00003	0.00111	0.00634	0.00019	0.00001	0.00075
Ar	0.00201	0.00090	0.00079	0.00091	0.00035	0.00087	0.00128	0.00161	0.00177	0.00232	0.00054	0.00237	0.00082	0.00088	0.00178	0.00425	0.00058
C3H6	0.00004	0.00045	0.00045	0.00031	0.00021	0.00007	0.00008	0.00006	0.00007	0.00000	0.00000	0.00000	0.00063	0.00175	0.00007	0.00000	0.00046
C3H8	0.00000	0.00000	0.00000	0.00000	0.00000	0.00023	0.00027	0.00000	0.00162	0.00000	0.00000	0.00033	0.00000	0.00000	0.00000	0.00006	0.00000
CO2	0.02469	0.26466	0.12639	0.09440	1.20775	0.36180	0.18930	0.14608	0.22942	0.13692	0.08332	0.18532	0.17605	0.36138	0.00995	0.00544	0.05914
C4H8	0.00007	0.00026	0.00024	0.00021	0.00012	0.00000	0.00010	0.00009	0.00022	0.00000	0.00000	0.00008	0.00034	0.00100	0.00004	0.00000	0.00024
C4H10	0.00013	0.00078	0.00078	0.00054	0.00052	0.00014	0.00009	0.00022	0.00000	0.00064	0.00003	0.00000	0.00090	0.00257	0.00025	0.00000	0.00058
SO2	0.00010	0.00067	0.00070	0.00048	0.00033	0.00032	0.00010	0.00021	0.00037	0.00014	0.00000	0.00000	0.00111	0.00256	0.00020	0.00032	0.00062
Benzene	0.00005	0.00024	0.00020	0.00017	0.00016	0.00010	0.00006	0.00008	0.00007	0.00013	0.00000	0.00000	0.00022	0.00069	0.00004	0.00000	0.00013
total gas	0.21	0.35	0.19	0.18	1.25	0.45	0.32	0.31	0.41	0.35	0.12	0.37	0.25	0.47	0.13	0.25	0.11
N2/Ar	56.86	61.17	49.85	48.43	0.00	45.21	67.36	60.82	51.76	60.98	51.18	44.11	49.09	56.75	50.50	47.15	52.88
He/Ar	0.00	0.01	0.01	0.01	0.04	0.00	0.01	0.01	0.00	0.00	0.01	0.00	0.01	0.29	0.00	0.00	0.01
CO2/N2	0.22	4.82	3.21	2.13		9.18	2.19	1.49	2.51	0.97	3.01	1.77	4.39	7.27	0.11	0.03	1.91
ppm-wt																	
SO2	3.45E+00	2.38E+01	2.47E+01	1.71E+01	1.14E+01	1.12E+01	3.71E+00	7.32E+00	1.30E+01	5.07E+00	0.00E+00	0.00E+00	3.93E+01	9.07E+01	7.25E+00	1.14E+01	2.20E+01
H2S	1.69E+00	2.10E+01	1.73E+01	1.04E+01	1.61E+01	2.84E+00	7.07E+00	5.84E+00	8.84E+00	3.84E+00	6.16E-01	5.33E-01	2.09E+01	1.19E+02	3.60E+00	2.38E-01	1.41E+01
H2	6.37E+01	5.63E+00	9.49E+00	2.32E+01	3.83E+01	3.35E+01	2.13E+01	4.37E+01	6.28E+01	3.90E+01	6.32E+00	6.80E+01	1.31E+01	2.03E+01	2.60E+01	3.49E+01	1.21E+01
He	1.86E-02	1.72E-02	1.08E-02	2.31E-02	2.95E-02	4.07E-03	1.69E-02	1.87E-02	2.02E-16	1.61E-02	1.13E-02	3.43E-15	1.70E-02	5.54E-01	1.36E-02	4.22E-02	1.41E-02
CO2	6.03E+02	6.44E+03	3.08E+03	2.30E+03	2.90E+04	8.80E+03	4.61E+03	3.56E+03	5.59E+03	3.34E+03	2.03E+03	4.52E+03	4.29E+03	8.78E+03	2.43E+02	1.33E+02	1.44E+03
CO2/H2S wt/wt	3.57E+02	3.07E+02	1.78E+02	2.22E+02	1.80E+03	3.09E+03	6.52E+02	6.10E+02	6.32E+02	8.70E+02	3.30E+03	8.48E+03	2.06E+02	7.37E+01	6.75E+01	5.58E+02	1.02E+02
Geothermometer (°C)																	
t(CO2)	177	275	251	240	318	285	265	256	271	254	235	264	262	285	117	69	221
t(H2S)-high	188	237	234	224	233	199	216	213	221	204	169	166	237	271	203	150	230
t(H2S)-low	88	160	154	140	153	103	129	124	135	112	60	56	160	209	110	33	148
t(H2S+SO2)-high	203	247	245	236	239	221	221	222	232	215	169	166	251	278	217	214	241
t(H2)-high	309	287	291	300	304	303	299	305	309	304	288	309	294	298	301	303	294
t(H2)-low	270	230	238	253	262	260	252	264	270	262	232	271	244	251	255	260	242

Appendix 15-cont. *KJ-26 fluid inclusion molar data and calculated constituents*

Sample Number	**KJ26-98**	**KJ26-99**	**KJ26-100**	**KJ26-101**	**KJ26-102**	**KJ26-103**	**KJ26-104**	**KJ26-105**	**KJ26-106**	**KJ26-107**	**KJ26-108**	**KJ26-109**	**KJ26-110**	**KJ26-111**	**KJ26-112**	**KJ26-113**	**KJ26-114**
Depth (m)	300	300	300	250	250	250	210	210	210	150	150	100	100	100	50	50	50
Mole %																	
H2	0.04992	0.00865	0.02114	0.00348	0.01335	0.00530	0.01374	0.00926	0.00825	0.00086	0.00462	0.00175	0.00203	0.00903	0.00212	0.00459	0.00911
He	0.00001	0.00001	0.00001	0.00002	0.00002	0.00000	0.00001	0.00001	0.00000	0.00000	0.00000	0.00002	0.00001	0.00000	0.00000	0.00000	0.00000
CH4	0.00577	0.00595	0.00557	0.00388	0.00737	0.00310	0.00337	0.03021	0.00511	0.00528	0.01753	0.02257	0.01269	0.10922	0.00600	0.01317	0.05934
H2O	99.87573	99.89277	99.92395	99.92269	99.89801	99.98185	99.75214	99.88071	99.89804	99.67903	99.58658	99.82030	99.76270	98.97163	99.94548	99.89222	99.56654
CO	0.00000	0.00000	0.00000	0.00000	0.00000	0.00000	0.00000	0.00000	0.00000	0.00000	0.00000	0.00000	0.00000	0.00000	0.00000	0.00000	0.00000
N2	0.02537	0.03457	0.02449	0.03944	0.04918	0.00775	0.01034	0.03148	0.03495	0.06119	0.14847	0.06105	0.06339	0.11153	0.00564	0.01040	0.10475
C2H4	0.00002	0.00025	0.00012	0.00026	0.00018	0.00000	0.00067	0.00000	0.00016	0.00000	0.00000	0.00044	0.00000	0.00025	0.00000	0.00000	0.00080
C2H6	0.00204	0.00255	0.00190	0.00300	0.00324	0.00015	0.00215	0.00249	0.00264	0.00065	0.00089	0.00000	0.00077	0.00504	0.00026	0.00011	0.00089
H2S	0.00045	0.00119	0.00073	0.00271	0.00288	0.00008	0.00089	0.00040	0.00105	0.00007	0.00006	0.00023	0.00015	0.00037	0.00000	0.00003	0.00000
Ar	0.00053	0.00056	0.00066	0.00072	0.00078	0.00000	0.00035	0.00050	0.00054	0.00114	0.00240	0.00102	0.00108	0.00176	0.00009	0.00019	0.00185
C3H6	0.00034	0.00043	0.00031	0.00060	0.00069	0.00000	0.00049	0.00035	0.00039	0.00003	0.00005	0.00079	0.00016	0.00128	0.00004	0.00000	0.00052
C3H8	0.00000	0.00000	0.00000	0.00000	0.00000	0.00000	0.00085	0.00000	0.00000	0.00031	0.00148	0.00027	0.00072	0.00264	0.00055	0.00088	0.00000
CO2	0.03878	0.05149	0.01994	0.02096	0.02200	0.00155	0.21334	0.04380	0.04724	0.25120	0.23753	0.09076	0.15584	0.78436	0.03979	0.07823	0.25365
C4H8	0.00019	0.00024	0.00020	0.00030	0.00034	0.00006	0.00031	0.00016	0.00024	0.00010	0.00024	0.00033	0.00012	0.00062	0.00000	0.00000	0.00004
C4H10	0.00034	0.00054	0.00044	0.00071	0.00074	0.00017	0.00023	0.00032	0.00068	0.00011	0.00008	0.00038	0.00021	0.00227	0.00000	0.00000	0.00171
SO2	0.00043	0.00065	0.00042	0.00103	0.00103	0.00000	0.00086	0.00026	0.00058	0.00002	0.00003	0.00000	0.00008	0.00000	0.00002	0.00019	0.00081
Benzene	0.00009	0.00015	0.00012	0.00019	0.00021	0.00000	0.00026	0.00007	0.00013	0.00002	0.00004	0.00010	0.00004	0.00000	0.00001	0.00000	0.00000
total gas	0.12	0.11	0.08	0.08	0.10	0.02	0.25	0.12	0.10	0.32	0.41	0.18	0.24	1.03	0.05	0.11	0.43
N2/Ar	48.23	61.85	37.34	54.77	63.40		29.59	63.05	64.16	53.68	61.92	59.63	58.47	63.47	64.49	54.71	56.55
He/Ar	0.02	0.01	0.01	0.03	0.02		0.03	0.01	0.01	0.00	0.00	0.02	0.01	0.00	0.01	0.00	0.00
CO2/N2	1.53	1.49	0.81	0.53	0.45	0.20	20.63	1.39	1.35	4.11	1.60	1.49	2.46	7.03	7.05	7.52	2.42
ppm-wt																	
SO2	1.54E+01	2.30E+01	1.50E+01	3.67E+01	3.64E+01	0.00E+00	3.05E+01	9.12E+00	2.05E+01	6.36E-01	1.15E+00	0.00E+00	2.80E+00	0.00E+00	7.37E-01	6.74E+00	2.86E+01
H2S	8.47E+00	2.25E+01	1.37E+01	5.12E+01	5.44E+01	1.45E+00	1.67E+01	7.64E+00	1.98E+01	1.28E+00	1.08E+00	4.42E+00	2.76E+00	7.00E+00	0.00E+00	6.43E-01	0.00E+00
H2	5.54E+01	9.60E+00	2.35E+01	3.86E+00	1.48E+01	5.89E+00	1.52E+01	1.03E+01	9.16E+00	9.46E-01	5.11E+00	1.94E+00	2.25E+00	9.92E+00	2.35E+00	5.09E+00	1.01E+01
He	2.47E-02	1.67E-02	1.96E-02	4.98E-02	4.21E-02	0.00E+00	2.01E-02	1.57E-02	6.96E-03	6.89E-03	9.79E-03	3.95E-02	1.99E-02	1.19E-03	2.75E-03	1.04E-15	4.04E-15
CO2	9.48E+02	1.26E+03	4.87E+02	5.12E+02	5.37E+02	3.80E+01	5.20E+03	1.07E+03	1.15E+03	6.12E+03	5.78E+03	2.21E+03	3.80E+03	1.89E+04	9.72E+02	1.91E+03	6.17E+03
CO2/H2S wt/wt	1.12E+02	5.58E+01	3.55E+01	9.99E+00	9.88E+00	2.62E+01	3.11E+02	1.40E+02	5.83E+01	4.76E+03	5.34E+03	5.01E+02	1.38E+03	2.71E+03		2.97E+03	
Geothermometer (°C)																	
t(CO2)	201	214	164	167	170		269	207	210	274	272	239	258	306	202	233	274
t(H2S)-high	220	239	229	255	256	185	233	218	236	183	180	207	198	216		170	
t(H2S)-low	134	162	148	185	187	84	153	131	158	81	76	116	102	129		61	
t(H2S+SO2)-high	233	247	238	261	262	185	246	227	245	188	188	207	206	216	160	206	231
t(H2)-high	307	292	300	283	295	287	296	292	291	270	286	277	278	292	279	286	292
t(H2)-low	268	239	253	223	246	230	246	240	238	200	228	212	214	239	215	228	239

Appendix 16. KJ-17 fluid inclusion molar data and calculated constituents

Sample Number	**KJ17-1**	**KJ17-2**	**KJ17-3**	**KJ17-4**	**KJ17-5**	**KJ17-6**	**KJ17-7**	**KJ17-8**	**KJ17-9**	**KJ17-10**	**KJ17-11**	**KJ17-12**	**KJ17-13**	**KJ17-14**	**KJ17-15**
Depth (m)	2190	2190	2190	2150	2150	2100	2100	2050	2050	2000	2000	1950	1950	1850	1850
Mole %															
H2	0.07519	0.07870	0.06952	0.29320	0.20033	0.18490	0.13593	0.12087	0.03845	0.07439	0.19158	0.03464	0.03096	0.07268	0.05619
He	0.00001	0.00005	0.00002	0.00000	0.00010	0.00012	0.00004	0.00037	0.00004	0.00011	0.00003	0.00005	0.00005	0.00009	0.00011
CH4	0.04197	0.03008	0.01998	0.27272	0.17569	0.02443	0.02015	0.23824	0.04139	0.03060	0.03731	0.01694	0.01271	0.01751	0.01023
H2O	99.48264	99.50394	99.65994	98.57544	99.00272	99.15622	99.53922	98.87565	99.61915	99.60389	99.48970	99.58866	99.48237	98.86806	99.17484
CO	0.00000	0.00000	0.00000	0.00000	0.00000	0.00000	0.00000	0.00000	0.00000	0.00000	0.00000	0.00000	0.00000	0.00000	0.00000
N2	0.26895	0.29566	0.14686	0.32900	0.35619	0.24028	0.17697	0.68271	0.26363	0.23812	0.21803	0.20487	0.31285	0.40552	0.26529
C2H4	0.00000	0.00000	0.00000	0.00000	0.00000	0.00000	0.00000	0.00135	0.00018	0.00044	0.00068	0.00069	0.00039	0.00000	0.00000
C2H6	0.00000	0.00066	0.00004	0.00000	0.00000	0.00000	0.00000	0.01265	0.00149	0.00143	0.00184	0.00320	0.00346	0.09716	0.06833
H2S	0.00025	0.00013	0.00008	0.00038	0.00024	0.00097	0.00002	0.00039	0.00011	0.00033	0.00017	0.00039	0.00056	0.00224	0.00265
Ar	0.00339	0.00474	0.00219	0.00000	0.00250	0.00248	0.00117	0.00777	0.00357	0.00275	0.00261	0.00324	0.00602	0.00881	0.00557
C3H6	0.00245	0.00166	0.00068	0.02578	0.02334	0.00768	0.01347	0.00220	0.00036	0.00060	0.00099	0.00056	0.00056	0.00000	0.00000
C3H8	0.01200	0.00592	0.00217	0.12179	0.07193	0.02765	0.04109	0.00000	0.00071	0.00000	0.00059	0.00041	0.00047	0.00000	0.00000
CO2	0.11041	0.07670	0.09773	0.34245	0.14386	0.34533	0.05831	0.04669	0.03048	0.04543	0.05475	0.14438	0.14778	0.52383	0.41251
C4H8	0.00213	0.00091	0.00040	0.02075	0.01258	0.00552	0.00903	0.00460	0.00027	0.00048	0.00104	0.00091	0.00074	0.00122	0.00102
C4H10	0.00001	0.00046	0.00028	0.01848	0.01029	0.00272	0.00416	0.00303	0.00000	0.00085	0.00023	0.00062	0.00061	0.00126	0.00156
SO2	0.00024	0.00025	0.00000	0.00000	0.00000	0.00085	0.00000	0.00265	0.00000	0.00000	0.00006	0.00023	0.00021	0.00079	0.00076
Benzene	0.00037	0.00015	0.00012	0.00000	0.00022	0.00085	0.00045	0.00083	0.00016	0.00059	0.00039	0.00020	0.00026	0.00083	0.00093
total gas	0.52	0.50	0.34	1.42	1.00	0.84	0.46	1.12	0.38	0.40	0.51	0.41	0.52	1.13	0.83
N2/Ar	79.34	62.38	67.06		142.35	96.69	150.98	87.88	73.80	86.61	83.58	63.32	52.00	46.05	47.59
He/Ar	0.00	0.01	0.01		0.04	0.05	0.03	0.05	0.01	0.04	0.01	0.02	0.01	0.01	0.02
CO2/N2	0.41	0.26	0.67	1.04	0.40	1.44	0.33	0.07	0.12	0.19	0.25	0.70	0.47	1.29	1.55
ppm-wt															
H2S	4.68E+00	2.38E+00	1.43E+00	7.08E+00	4.51E+00	1.82E+01	3.20E-01	7.29E+00	2.05E+00	6.18E+00	3.22E+00	7.36E+00	1.06E+01	4.19E+01	4.96E+01
SO2	8.36E+00	8.79E+00	0.00E+00	0.00E+00	0.00E+00	3.00E+01	0.00E+00	9.38E+01	0.00E+00	0.00E+00	2.01E+00	8.24E+00	7.40E+00	2.77E+01	2.69E+01
H2	8.33E+01	8.73E+01	7.71E+01	3.24E+02	2.22E+02	2.04E+02	1.51E+02	1.34E+02	4.27E+01	8.25E+01	2.13E+02	3.84E+01	3.43E+01	7.99E+01	6.20E+01
He	2.74E-02	1.11E-01	4.84E-02	3.85E-03	2.23E-01	2.76E-01	7.94E-02	8.29E-01	8.95E-02	2.44E-01	6.84E-02	1.16E-01	1.07E-01	1.96E-01	2.49E-01
CO2	2.69E+03	1.87E+03	2.38E+03	8.31E+03	3.50E+03	8.40E+03	1.42E+03	1.14E+03	7.44E+02	1.11E+03	1.34E+03	3.52E+03	3.60E+03	1.27E+04	1.00E+04
CO2/H2S wt/wt	5.75E+02	7.86E+02		1.17E+03					3.63E+02	1.79E+02	4.15E+02		3.39E+02		2.02E+02
Geothermometer (°C)															
t(CO2)	246	232	241	283	256	283	220	210	189	209	217	256	257	295	289
t(H2S)-high	208	195	185	217	208	235	156	217	192	214	201	217	224	251	254
t(H2S+SO2)-high	221	216	185	217	208	247	156	257	192	214	207	226	230	257	259
t(H2S)-low	117	98	84	129	117	156	42	130	94	125	107	130	141	180	184
t(H2)-high	311	312	310	324	320	319	317	316	305	311	320	304	303	311	308
t(H2)-low	275	275	273	297	291	290	285	283	263	275	290	262	260	274	270

Appendix 16-cont. *KJ-17 fluid inclusion molar data and calculated constituents*

Sample Number	**KJ17-16**	**KJ17-17**	**KJ17-18**	**KJ17-19**	**KJ17-20**	**KJ17-21**	**KJ17-22**	**KJ17-23**	**KJ17-24**	**KJ17-25**	**KJ17-26**	**KJ17-27**	**KJ17-28**	**KJ17-29**	**KJ17-30**
Depth (m)	1750	1750	1650	1650	1550	1550	1450	1350	1350	1250	1250	1150	1150	1050	1050
Mole %															
H2	0.09592	0.09172	0.05374	0.05896	0.21671	0.28526	4.45898	0.18797	0.53864	0.10511	0.25578	0.31524	0.84763	0.08553	0.04942
He	0.00008	0.00008	0.00003	0.00000	0.00033	0.00024	0.00000	0.00000	0.00013	0.00028	0.00000	0.00038	0.00023	0.00006	0.00010
CH4	0.05952	0.03860	0.02111	0.01968	0.06413	0.03494	0.65991	0.00974	0.02661	0.02144	0.02752	0.04025	0.12341	0.03409	0.02135
H2O	99.61812	99.68788	99.64275	99.74486	99.02108	99.33657	91.58773	99.66430	99.25243	99.58778	99.45768	99.28783	98.31397	99.50163	99.81690
CO	0.00000	0.00000	0.00000	0.00000	0.00000	0.00000	0.00000	0.00000	0.00000	0.00000	0.00000	0.00000	0.00000	0.00000	0.00000
N2	0.12477	0.11415	0.18075	0.13392	0.51053	0.25644	2.84474	0.10039	0.15140	0.14303	0.14420	0.22946	0.47597	0.15427	0.04854
C2H4	0.00033	0.00035	0.00024	0.00002	0.00172	0.00016	0.00646	0.00000	0.00000	0.00000	0.00075	0.00000	0.00000	0.00000	0.00000
C2H6	0.00290	0.00130	0.00150	0.00108	0.00357	0.00425	0.00164	0.00215	0.00204	0.00404	0.00040	0.00126	0.00000	0.01956	0.00394
H2S	0.00014	0.00014	0.00024	0.00011	0.00138	0.00011	0.00015	0.00000	0.00000	0.00054	0.00000	0.00032	0.00038	0.00058	0.00019
Ar	0.00209	0.00208	0.00321	0.00230	0.00584	0.00369	0.03352	0.00138	0.00170	0.00189	0.00107	0.00220	0.00123	0.00249	0.00043
C3H6	0.00038	0.00026	0.00016	0.00018	0.00091	0.00038	0.00000	0.00007	0.00000	0.00000	0.00006	0.00292	0.03337	0.00000	0.00032
C3H8	0.00105	0.00025	0.00000	0.00000	0.00000	0.00000	0.00000	0.00053	0.00000	0.00000	0.00000	0.01534	0.11797	0.00000	0.00093
CO2	0.09342	0.06244	0.09531	0.03783	0.17129	0.07578	0.36845	0.03274	0.02235	0.13313	0.11144	0.10134	0.05672	0.19883	0.05674
C4H8	0.00030	0.00003	0.00026	0.00038	0.00096	0.00045	0.00286	0.00049	0.00284	0.00065	0.00060	0.00229	0.01649	0.00108	0.00079
C4H10	0.00055	0.00040	0.00047	0.00050	0.00000	0.00093	0.02384	0.00000	0.00000	0.00163	0.00045	0.00000	0.01103	0.00084	0.00000
SO2	0.00041	0.00018	0.00016	0.00003	0.00000	0.00020	0.00851	0.00023	0.00159	0.00019	0.00006	0.00088	0.00000	0.00033	0.00010
Benzene	0.00003	0.00015	0.00005	0.00014	0.00154	0.00060	0.00322	0.00000	0.00028	0.00028	0.00001	0.00029	0.00159	0.00071	0.00027
total gas	0.38	0.31	0.36	0.26	0.98	0.66	8.41	0.34	0.75	0.41	0.54	0.71	1.69	0.50	0.18
N2/Ar	59.71	54.97	56.40	58.17	87.40	69.58	84.87	72.76	88.91	75.74	135.04	104.25	387.56	62.04	113.87
He/Ar	0.04	0.04	0.01	0.00	0.06	0.06	0.00	0.00	0.08	0.15	0.00	0.17	0.19	0.02	0.23
CO2/N2	0.75	0.55	0.53	0.28	0.34	0.30	0.13	0.33	0.15	0.93	0.77	0.44	0.12	1.29	1.17
ppm-wt															
H2S	2.69E+00	2.65E+00	4.51E+00	2.10E+00	2.59E+01	2.17E+00	2.97E+00	0.00E+00	0.00E+00	1.02E+01	0.00E+00	6.02E+00	7.27E+00	1.10E+01	3.50E+00
SO2	1.46E+01	6.36E+00	5.79E+00	1.16E+00	0.00E+00	7.23E+00	3.08E+02	8.21E+00	5.68E+01	6.78E+00	2.09E+00	3.13E+01	0.00E+00	1.16E+01	3.63E+00
H2	1.06E+02	1.02E+02	5.96E+01	6.55E+01	2.40E+02	3.17E+02	5.04E+03	2.09E+02	6.01E+02	1.17E+02	2.84E+02	3.50E+02	9.43E+02	9.47E+01	5.49E+01
He	1.87E-01	1.86E-01	6.78E-02	5.77E-04	7.30E-01	5.29E-01	1.05E-13	0.00E+00	2.93E-01	6.20E-01	0.00E+00	8.49E-01	5.09E-01	1.30E-01	2.19E-01
CO2	2.28E+03	1.53E+03	2.33E+03	9.24E+02	4.17E+03	1.85E+03	9.17E+03	8.01E+02	5.48E+02	3.25E+03	2.72E+03	2.48E+03	1.39E+03	4.85E+03	1.39E+03
CO2/H2S wt/wt	8.46E+02		5.16E+02	4.40E+02								4.12E+02			3.96E+02
Geothermometer (°C)															
t(CO2)	240	223	240	200	262	231	288	192	171	253	246	243	220	266	219
t(H2S)-high	197	197	207	193	242	193	201			223		213	217	225	203
t(H2S+SO2)-high	224	213	218	198	242	213	279	207	244	229	180	239	217	234	211
t(H2S)-low	102	101	116	95	166	96	106			139		124	130	142	109
t(H2)-high	313	313	308	309	321	323	349	320	329	314	322	324	333	312	307
t(H2)-low	279	278	269	271	292	297	343	290	308	280	295	299	315	277	268

Appendix 16-cont. *KJ-17 fluid inclusion molar data and calculated constituents*

Sample Number	**KJ17-31**	**KJ17-32**	**KJ17-33**	**KJ17-34**	**KJ17-35**	**KJ17-36**	**KJ17-37**	**KJ17-38**
Depth (m)	900	900	692	692	500	500	300	300
Mole %								
H2	0.07121	0.15586	0.12229	0.13017	0.04800	0.07554	0.09622	0.12569
He	0.00012	0.00343	0.00013	0.00007	0.00032	0.00022	0.00015	0.00012
CH4	0.01958	0.03078	0.02083	0.02625	0.02379	0.01947	0.17392	0.12491
H2O	99.34888	98.28688	99.17249	99.12809	99.83929	99.81444	99.01718	99.22108
CO	0.00000	0.00000	0.00000	0.00000	0.00000	0.00000	0.00000	0.00000
N2	0.20187	0.25839	0.23398	0.22177	0.05951	0.06849	0.30055	0.22015
C2H4	0.00000	0.00000	0.00000	0.00000	0.00000	0.00000	0.00000	0.00000
C2H6	0.05117	0.14616	0.02985	0.01620	0.00384	0.00310	0.02977	0.01651
H2S	0.00305	0.01323	0.00104	0.00112	0.00035	0.00010	0.00177	0.00082
Ar	0.00325	0.00941	0.00429	0.00125	0.00049	0.00068	0.00341	0.00259
C3H6	0.00154	0.00321	0.00000	0.01096	0.00000	0.00047	0.00462	0.00528
C3H8	0.00000	0.00000	0.00000	0.04628	0.00000	0.00036	0.01217	0.01685
CO2	0.29516	1.06485	0.41164	0.39914	0.02023	0.01636	0.35447	0.25944
C4H8	0.00141	0.00671	0.00110	0.01178	0.00022	0.00038	0.00245	0.00256
C4H10	0.00095	0.01135	0.00111	0.00562	0.00342	0.00000	0.00207	0.00268
SO2	0.00126	0.00487	0.00057	0.00056	0.00000	0.00038	0.00069	0.00056
Benzene	0.00055	0.00487	0.00067	0.00073	0.00053	0.00000	0.00057	0.00074
total gas	0.65	1.71	0.83	0.87	0.16	0.19	0.98	0.78
N2/Ar	62.19	27.47	54.56	177.26	120.88	100.10	88.19	84.86
He/Ar	0.04	0.37	0.03	0.06	0.66	0.32	0.04	0.05
CO2/N2	1.46	4.12	1.76	1.80	0.34	0.24	1.18	1.18
ppm-wt								
H2S	5.73E+01	2.46E+02	1.94E+01	2.11E+01	6.63E+00	1.80E+00	3.31E+01	1.55E+01
SO2	4.45E+01	1.70E+02	2.03E+01	1.97E+01	0.00E+00	1.35E+01	2.44E+01	1.99E+01
H2	7.87E+01	1.70E+02	1.35E+02	1.44E+02	5.33E+01	8.39E+01	1.06E+02	1.39E+02
He	2.75E-01	7.50E+00	2.87E-01	1.54E-01	7.17E-01	4.82E-01	3.27E-01	2.71E-01
CO2	7.18E+03	2.56E+04	1.00E+04	9.69E+03	4.94E+02	4.00E+02	8.61E+03	6.31E+03
CO2/H2S wt/wt	1.25E+02			4.60E+02		2.23E+02	2.60E+02	4.08E+02
Geothermometer (°C)								
t(CO2)	279	315	288	288	165	152	284	275
t(H2S)-high	257	286	236	238	215	190	247	232
t(H2S+SO2)-high	264	292	245	246	215	221	253	242
t(H2S)-low	188	230	158	160	127	90	173	151
t(H2)-high	311	318	316	316	307	311	313	316
t(H2)-low	274	287	283	284	267	275	279	283

Appendix 17. Geochemical compositions of Erebus Lineage whole rock samples from Kyle et al. (1992).

Sample Name	**83435**	**83437**	**79300**	**83432**	**AW 82044**	**AW 82038**	**83409**	**83415**	**83417**	**83410**	**AW 82015**	**83452**	**83446**	**83448**	**83400**	**80020**	**83412**	**AW 82023**	**83407**	**83454**	**82405**	**82403**	**82431**	**DVDP 105.53**
	Bas Cape Barne	Bas Fang Ridge	Bas Cape Barne	Bas Cape Barne	Bas Turks Head	Pht Turks Head	Pht Inaccessible Island	Pht Tent Island	Pht Tent Island	Tep Inaccessible Island	Tep Turks Head	APh Bomb Peak	Tep Cape Royds	Tep Mt Erebus	APh Mt Erebus	APh 3 Sisters Cone	TA Inaccessible Island	TA Lewis Bay	Ph Inaccessible Island	Tr Aurora Cliffs	Tr Bomb Peak	Xen Summit Mt Erebus	APh Bomb Peak	Bas DVDP basanite
SiO2	43.32	43.97	44.50	44.89	46.20	47.19	48.22	49.53	50.17	50.77	54.22	55.00	55.63	55.93	56.27	56.57	54.28	55.81	58.91	60.59	63.51	52.09	55.04	41.68
TiO2	3.78	3.75	3.69	3.20	3.16	2.72	2.60	2.12	2.18	1.95	1.58	1.36	1.18	1.10	0.99	0.98	1.20	1.07	0.44	0.74	0.43	2.18	1.19	4.06
Al2O3	15.38	16.65	16.77	16.96	16.07	18.24	17.49	19.87	18.64	18.91	18.84	18.29	19.46	19.74	19.25	19.31	18.01	18.03	18.47	15.85	15.33	19.04	20.06	12.92
FeO	12.08	11.44	11.04	11.23	11.11	9.33	9.58	7.41	8.04	7.78	6.76	6.59	5.06	4.59	5.26	4.95	8.46	7.71	5.89	6.79	6.15	7.52	5.13	11.23
MnO	0.22	0.24	0.25	0.23	0.25	0.22	0.23	0.17	0.22	0.22	0.23	0.27	0.20	0.18	0.23	0.23	0.29	0.30	0.26	0.22	0.21	0.24	0.18	0.18
MgO	**6.77**	**4.92**	**4.69**	**4.21**	**4.74**	**3.13**	**3.47**	**3.00**	**2.51**	**2.20**	**1.81**	**1.64**	**1.30**	**1.23**	**0.95**	**0.99**	**1.57**	**1.35**	**0.37**	**0.56**	**0.14**	**2.50**	**1.14**	**12.13**
CaO	10.66	9.62	9.71	9.28	8.05	7.52	6.79	6.93	5.73	5.55	4.22	3.34	3.16	3.20	2.78	2.75	4.40	3.75	2.19	1.94	1.44	5.98	3.73	11.32
Na2O	4.63	4.64	4.84	5.24	4.74	5.89	5.61	6.22	6.44	6.90	6.96	7.77	7.60	7.77	7.72	8.17	6.52	7.06	7.66	6.38	6.56	5.90	7.44	3.16
K2O	1.72	2.07	2.15	2.07	3.11	2.83	3.27	3.00	3.52	3.38	3.90	4.39	4.47	4.33	4.62	4.55	3.38	3.50	4.67	5.16	5.23	2.15	4.00	1.48
P2O5	1.21	1.51	1.56	1.69	1.16	1.22	1.19	0.85	1.10	0.93	0.71	0.56	0.46	0.44	0.40	0.42	0.51	0.41	0.13	0.13	0.05	1.13	0.47	0.84

Rocktype abreviations: Bas-basanite, Tr-trachyte, TA-trachyandesite, Pht-phonotephrite, Tep-Tephriphonolite, APh-Anorthoclase phonolite, Ph-phonolite, Xen-cumulate xenolith.

Appendix 18. Electron Microprobe analysis of Erebus Lineage Glasses. Calculated mean values and standard deviation are reported
**Low Mg endmember samples*

Sample Name	P2O5		SiO2		SO2		TiO2		Al2O3		MgO		CaO		MnO		FeO		Na2O		K2O		F		Cl		Total
LBO-97018-09	0.30		56.24		0.08		0.97		19.44		0.79		1.85		0.30		5.31		9.03		5.76		0.27		0.16		100.47
LBO-97018-010	0.31		55.91		0.08		1.01		19.55		0.88		1.89		0.26		5.65		9.07		5.75		0.09		0.14		100.60
LBO-97018-011	0.35		55.94		0.06		0.93		19.51		0.86		1.96		0.31		5.59		9.24		5.60		0.31		0.14		100.77
LBO-97018-012	0.30		55.93		0.10		0.96		19.62		0.86		1.97		0.24		5.61		9.19		5.63		0.13		0.16		100.70
Mean/1sigma	**0.31**	*0.02*	**56.00**	*0.16*	**0.08**	*0.02*	**0.97**	*0.04*	**19.53**	*0.08*	**0.85**	*0.04*	**1.92**	*0.06*	**0.28**	*0.03*	**5.54**	*0.16*	**9.13**	*0.10*	**5.69**	*0.08*	**0.20**	*0.10*	**0.15**	*0.01*	**100.64**
LBO-EB0603-01	0.26		55.93		0.09		1.02		19.57		0.86		2.06		0.21		5.60		9.23		5.75		0.23		0.16		100.94
LBO-EB0603-02	0.31		55.57		0.06		0.98		19.41		0.79		1.84		0.27		5.27		9.00		5.67		0.23		0.16		99.55
LBO-EB0603-03	0.29		55.77		0.04		1.00		19.63		0.83		1.92		0.25		5.52		9.05		5.72		0.25		0.13		100.40
LBO-EB0603-04	0.29		55.72		0.09		1.06		19.47		0.85		1.98		0.27		5.50		8.90		5.72		0.23		0.14		100.21
	0.28	*0.02*	**55.75**	*0.15*	**0.07**	*0.02*	**1.01**	*0.03*	**19.52**	*0.10*	**0.83**	*0.03*	**1.95**	*0.09*	**0.25**	*0.03*	**5.47**	*0.14*	**9.04**	*0.14*	**5.71**	*0.04*	**0.24**	*0.01*	**0.15**	*0.01*	**100.28**
LBO-82431-01	0.32		57.93		0.04		0.95		20.51		0.94		1.10		0.26		2.57		8.76		6.41		0.22		0.03		100.05
LBO-82431-02	0.53		56.97		0.05		0.92		20.61		0.98		1.07		0.23		2.56		9.29		6.52		0.11		0.03		99.85
LBO-82431-03	0.46		56.97		0.04		0.84		20.71		0.89		1.07		0.24		2.57		9.43		6.55		0.00		0.02		99.78
LBO-82431-04	0.40		57.12		0.01		0.96		20.51		1.00		0.98		0.19		2.65		9.34		6.42		0.02		0.02		99.62
LBO-82431-05	0.50		57.66		0.02		1.02		20.52		0.00		0.99		0.24		2.55		9.11		6.60		0.02		0.02		99.24
LBO-82431-06	0.43		57.58		0.00		0.88		20.72		1.02		0.97		0.27		2.57		9.57		6.59		0.05		0.02		100.64
	0.44	*0.07*	**57.37**	*0.40*	**0.03**	*0.02*	**0.93**	*0.06*	**20.60**	*0.10*	**0.81**	*0.40*	**1.03**	*0.06*	**0.24**	*0.03*	**2.58**	*0.04*	**9.25**	*0.28*	**6.51**	*0.08*	**0.07**	*0.08*	**0.02**	*0.01*	**99.86**
LBO-7713-01	1.08		48.05		0.22		2.94		16.99		2.86		6.94		0.23		10.28		6.61		3.67		0.34		0.09		100.29
LBO-7713-02	1.29		48.02		0.23		2.93		16.74		2.80		6.80		0.31		10.34		6.47		3.62		0.31		0.09		99.94
LBO-7713-03	1.42		50.93		0.24		3.10		18.11		3.03		7.36		0.26		10.93		6.89		3.98		0.18		0.10		106.53
LBO-7713-04	1.23		47.82		0.23		2.88		16.85		2.76		6.77		0.33		10.33		6.57		3.74		0.21		0.08		99.80
LBO-7713-05	1.23		48.02		0.22		2.88		17.06		3.39		6.87		0.30		10.13		6.54		3.86		0.11		0.10		100.71
LBO-7713-06	1.30		48.23		0.23		2.92		17.19		2.83		6.85		0.33		10.39		6.62		3.58		0.08		0.08		100.65
LBO-7713-07	1.27		47.87		0.25		2.97		17.15		2.76		6.69		0.22		10.17		6.50		3.69		0.27		0.10		99.90
LBO-7713-08	1.21		48.41		0.20		2.99		17.31		2.88		6.76		0.23		10.30		6.57		3.66		0.32		0.11		100.94
LBO-7713-09	1.15		48.30		0.22		3.03		17.15		4.04		6.65		0.22		10.20		6.49		3.69		0.19		0.08		101.39
LBO-7713-010	1.21		48.56		0.24		2.94		17.08		2.76		6.89		0.22		10.05		6.47		3.65		0.32		0.09		100.48
LBO-7713-011	1.12		48.14		0.20		2.86		17.07		3.97		6.89		0.29		10.06		6.50		3.60		0.20		0.10		100.99
	1.23	*0.09*	**48.40**	*0.87*	**0.22**	*0.02*	**2.95**	*0.07*	**17.15**	*0.36*	**3.10**	*0.48*	**6.86**	*0.19*	**0.27**	*0.05*	**10.29**	*0.24*	**6.57**	*0.12*	**3.70**	*0.12*	**0.23**	*0.09*	**0.09**	*0.01*	**101.06**
LBO-295-01	1.04		43.52		0.05		4.13		15.44		4.75		13.25		0.22		10.11		4.99		2.22		0.25		0.08		100.04
LBO-295-02	0.76		43.62		0.03		4.34		13.84		7.16		15.54		0.13		10.27		3.22		1.66		0.16		0.04		100.77
LBO-295-03	1.09		43.43		0.03		4.11		14.88		5.46		12.61		0.24		11.77		4.38		2.04		0.11		0.07		100.22
LBO-295-04	1.23		43.87		0.04		4.14		15.67		3.64		10.12		0.26		11.94		5.59		2.80		0.30		0.12		99.71
LBO-295-05	0.84		43.11		0.06		4.49		13.35		7.26		15.78		0.16		10.13		3.14		1.47		0.06		0.05		99.88
	0.99	*0.19*	**43.51**	*0.28*	**0.04**	*0.01*	**4.24**	*0.16*	**14.63**	*1.01*	**5.65**	*1.56*	**13.46**	*2.33*	**0.20**	*0.05*	**10.84**	*0.93*	**4.26**	*1.08*	**2.04**	*0.52*	**0.18**	*0.10*	**0.07**	*0.03*	**100.12**
LBO-AW82033-01	1.12		48.94		0.24		2.69		17.43		3.94		6.47		0.27		10.18		6.43		3.83		0.25		0.08		101.87
LBO-AW82033-02	1.11		48.97		0.20		2.82		17.30		2.83		6.44		0.29		10.07		6.46		3.83		0.27		0.08		100.66
LBO-AW82033-03	1.28		48.56		0.24		2.73		17.25		2.82		6.54		0.30		10.05		6.44		3.80		0.34		0.08		100.41
LBO-AW82033-04*	0.02		55.27		0.00		0.13		27.07		0.04		9.64		0.00		0.29		5.57		0.79		0.00		0.00		98.82
LBO-AW82033-05*	0.06		55.15		0.00		0.12		27.21		0.03		10.03		0.00		0.22		5.30		0.76		0.09		0.02		98.98
LBO-AW82033-06*	0.02		53.91		0.02		0.18		28.05		0.04		10.93		0.00		0.31		5.01		0.70		0.12		0.02		99.33
LBO-AW82033-07*	0.01		53.92		0.01		0.16		27.82		0.00		10.95		0.00		0.31		5.03		0.67		0.04		0.00		98.91
	0.52	*0.61*	**52.10**	*3.11*	**0.10**	*0.12*	**1.26**	*1.39*	**23.16**	*5.47*	**1.39**	*1.73*	**8.72**	*2.14*	**0.12**	*0.15*	**4.49**	*5.25*	**5.75**	*0.68*	**2.05**	*1.65*	**0.16**	*0.13*	**0.04**	*0.04*	**99.86**
EL 82403-013	0.09		36.45		0.06		6.26		12.94		10.57		0.16		0.37		20.23		1.13		8.48		1.10		0.30		98.12
EL 82431-06	0.58		57.19		0.20		1.06		20.56		0.80		1.92		0.24		4.30		8.53		6.18		0.11		0.14		101.80

Appendix 19. Electron Microprobe analysis of Erebus Lineage Olivines.
** Anomalous Mg-composition samples*

Sample	SiO2		Cr2O3		MgO		CaO		MnO		FeO		Total
LBO-97018-01	34.86		0.01		23.39		0.44		2.44		39.58		100.78
LBO-97018-04	34.97		0.02		23.65		0.47		2.35		39.19		100.70
LBO-97018-05	34.94		0.01		23.74		0.47		2.43		39.25		100.87
LBO-97018-06	34.97		0.00		22.85		0.46		2.32		38.90		99.54
LBO-97018-07	34.85		0.01		23.57		0.49		2.28		39.08		100.33
LBO-97018-08	34.72		0.04		23.68		0.47		2.45		39.58		100.97
	34.88	*0.09*	**0.01**	*0.02*	**23.48**	*0.33*	**0.47**	*0.01*	**2.38**	*0.07*	**39.26**	*0.27*	**100.53**
LBO-EB0603-05	36.38		0.00		24.45		0.48		2.57		41.24		105.18
LBO-EB0603-06	34.95		0.01		23.73		0.47		2.39		39.48		101.07
LBO-EB0603-07	34.89		0.00		23.83		0.48		2.47		38.65		100.36
	35.41	*0.84*	**0.00**	*0.01*	**24.00**	*0.39*	**0.48**	*0.00*	**2.48**	*0.09*	**39.79**	*1.32*	**102.20**
LBO-83435-01	39.31		0.03		42.71		0.31		0.26		18.05		100.86
LBO-83435-02	39.21		0.04		41.40		0.31		0.34		19.75		101.23
LBO-83435-03	39.21		0.03		42.82		0.31		0.27		17.40		100.23
LBO-83435-04	39.29		0.02		42.57		0.31		0.22		18.22		100.80
LBO-83435-05	38.46		0.04		40.33		0.40		0.34		20.63		100.38
LBO-83435-06	39.08		0.04		41.62		0.32		0.31		19.46		101.06
	39.09	*0.32*	**0.03**	*0.01*	**41.91**	*0.98*	**0.33**	*0.04*	**0.29**	*0.05*	**18.92**	*1.22*	**100.76**
EL 83410-01	35.73		0.00		28.79		0.41		0.98		34.17		100.08
EL 83410-02	35.90		0.01		29.17		0.39		1.01		33.74		100.20
EL 83410-03	35.82		0.00		29.01		0.40		1.00		33.76		99.99
EL 83410-04	35.95		0.02		29.27		0.43		1.04		33.48		100.20
	35.85	*0.10*	**0.01**	*0.01*	**29.06**	*0.21*	**0.41**	*0.02*	**1.01**	*0.03*	**33.79**	*0.28*	**100.12**
EL AW82044-01	39.54		0.01		43.75		0.39		0.20		15.92		99.80
EL AW82044-06	39.77		0.02		44.33		0.34		0.16		15.11		99.72
	39.65	*0.16*	**0.01**	*0.01*	**44.04**	*0.41*	**0.36**	*0.04*	**0.18**	*0.03*	**15.52**	*0.57*	**99.76**
EL AW82038-01*	38.65		0.01		40.74		0.35		0.27		19.82		99.83
EL AW82038-012*	38.51		0.02		40.32		0.35		0.28		20.11		99.57
EL AW82038-06	36.44		0.01		31.64		0.42		0.67		30.67		99.84
EL AW82038-07	36.75		0.00		31.52		0.45		0.71		30.63		100.05
EL AW82038-08	36.66		0.02		31.35		0.42		0.65		30.63		99.72
EL AW82038-011	36.75		0.00		31.72		0.42		0.75		30.61		100.25
EL AW82038-013	36.36		0.02		31.59		0.42		0.71		30.84		99.94
	37.16	*0.98*	**0.01**	*0.01*	**34.12**	*4.38*	**0.40**	*0.04*	**0.58**	*0.21*	**27.61**	*5.23*	**99.89**
EL 83409-09*	38.00		0.02		36.89		0.26		0.48		24.98		100.62
EL 83409-07	39.63		0.01		43.91		0.33		0.20		16.00		100.07
EL 83409-011	39.33		0.04		44.05		0.30		0.16		15.84		99.72
EL 83409-012	38.05		0.02		39.38		0.25		0.29		22.00		99.99
	39.00	*0.84*	**0.02**	*0.01*	**42.45**	*2.66*	**0.29**	*0.04*	**0.21**	*0.07*	**17.95**	*3.51*	**99.93**

Appendix 19-cont. Electron Microprobe analysis of Erebus Lineage Olivines.
** Anomalous Mg-composition samples*

Sample	SiO2		Cr2O3		MgO		CaO		MnO		FeO		Total
EL 83415-01*	39.63		0.02		44.34		0.35		0.21		15.43		99.98
EL 83415-02*	39.82		0.01		44.52		0.36		0.16		15.10		99.97
EL 83415-03	36.67		0.01		32.72		0.39		0.77		29.94		100.50
EL 83415-04	36.70		0.01		32.62		0.33		0.71		29.76		100.13
EL 83415-014	36.95		0.01		32.78		0.35		0.76		29.76		100.60
EL 83415-015	37.13		0.01		34.25		0.35		0.67		27.11		99.52
	37.82	*1.49*	**0.01**	*0.01*	**36.87**	*5.88*	**0.35**	*0.02*	**0.55**	*0.28*	**24.52**	*7.24*	**100.12**
EL 83417-01	36.53		0.00		31.53		0.34		1.01		30.49		99.90
EL 83417-02	36.47		0.01		31.08		0.38		1.01		31.90		100.86
EL 83417-03	36.68		0.01		31.74		0.38		1.01		30.24		100.05
EL 83417-04	36.50		0.01		31.97		0.40		0.95		30.52		100.34
	36.55	*0.09*	**0.01**	*0.00*	**31.58**	*0.38*	**0.37**	*0.03*	**0.99**	*0.03*	**30.79**	*0.75*	**100.29**
EL AW82015-01	35.34		0.00		26.24		0.49		1.55		36.36		99.97
EL AW82015-02	35.14		0.01		26.16		0.39		1.56		36.92		100.18
EL AW82015-03	35.28		0.02		26.13		0.45		1.55		36.52		99.94
EL AW82015-04	35.23		0.00		25.68		0.41		1.58		37.12		100.02
EL AW82015-05	35.21		0.00		25.45		0.38		1.56		37.28		99.88
EL AW82015-013	35.13		0.01		25.39		0.43		1.56		37.53		100.05
	35.22	*0.08*	**0.01**	*0.01*	**25.84**	*0.38*	**0.42**	*0.04*	**1.56**	*0.01*	**36.95**	*0.45*	**100.01**
EL 83452-01	33.85		0.02		21.09		0.49		2.49		41.62		99.55
EL 83452-02	32.62		0.00		21.03		0.47		2.55		41.17		97.84
EL 83452-011	34.13		0.01		21.04		0.53		2.57		41.37		99.65
	33.53	*0.80*	**0.01**	*0.01*	**21.06**	*0.03*	**0.49**	*0.03*	**2.54**	*0.04*	**41.39**	*0.23*	**99.01**
EL 83446-01	35.40		0.01		26.70		0.39		1.78		35.84		100.13
EL 83446-02	35.50		0.02		27.02		0.37		1.71		35.69		100.31
EL 83446-03	35.52		0.01		26.79		0.44		1.79		35.65		100.19
EL 83446-04	35.65		0.01		26.75		0.42		1.82		35.75		100.39
EL 83446-05	35.60		0.00		26.38		0.42		1.84		35.76		100.00
EL 83446-06	35.69		0.01		26.89		0.42		1.79		35.54		100.34
EL 83446-07	35.60		0.02		26.48		0.44		1.83		35.88		100.26
	35.57	*0.10*	**0.01**	*0.01*	**26.72**	*0.22*	**0.41**	*0.03*	**1.79**	*0.04*	**35.73**	*0.11*	**100.23**
EL 82403-03	30.92		0.02		7.26		0.43		2.69		57.83		99.16
EL 82403-04	31.33		0.01		7.95		0.52		2.62		57.55		99.97
	31.12	*0.29*	**0.02**	*0.01*	**7.61**	*0.49*	**0.47**	*0.06*	**2.65**	*0.05*	**57.69**	*0.20*	**99.56**
EL 82405-01	29.88		0.00		2.40		0.75		2.98		63.52		99.53
EL 82405-02	29.85		0.03		2.32		0.74		3.00		63.41		99.35
EL 82405-03	29.89		0.02		2.36		0.71		3.01		63.54		99.53
EL 82405-04	29.59		0.01		2.42		0.70		3.11		62.97		98.80
EL 82405-014	30.04		0.01		3.32		0.73		2.86		62.59		99.55
	29.85	*0.16*	**0.01**	*0.01*	**2.56**	*0.42*	**0.72**	*0.02*	**2.99**	*0.09*	**63.21**	*0.41*	**99.35**

Appendix 19-cont. Electron Microprobe analysis of Erebus Lineage Olivines.

Sample	SiO2		Cr2O3		MgO		CaO		MnO		FeO		Total
EL 83407-01	31.30		0.00		8.45		0.61		3.04		56.40		99.80
EL 83407-02	31.47		0.00		9.18		0.56		2.83		55.99		100.03
EL 83407-03	31.96		0.02		11.47		0.56		2.47		53.30		99.78
EL 83407-04	30.94		0.00		7.14		0.58		3.12		57.96		99.75
EL 83407-015	30.84		0.00		7.51		0.59		3.07		57.14		99.15
EL 83407-016	31.33		0.01		10.01		0.59		2.78		54.74		99.46
	31.31	*0.40*	**0.00**	*0.01*	**8.96**	*1.62*	**0.58**	*0.02*	**2.89**	*0.24*	**55.92**	*1.68*	**99.66**
EL AW82023-01	33.14		0.00		18.42		0.42		1.96		45.55		99.48
EL AW82023-02	34.36		0.00		22.30		0.34		1.47		41.61		100.09
EL AW82023-03	33.73		0.01		19.13		0.37		1.89		44.83		99.96
EL AW82023-04	34.00		0.00		20.84		0.40		1.72		43.39		100.35
EL AW82023-05	34.29		0.01		21.92		0.36		1.55		41.97		100.10
	33.90	*0.50*	**0.00**	*0.01*	**20.52**	*1.70*	**0.38**	*0.03*	**1.72**	*0.21*	**43.47**	*1.73*	**100.00**
EL 80020-01	34.62		0.01		23.16		0.52		2.38		39.57		100.25
EL 80020-02	34.72		0.01		23.72		0.48		2.36		38.51		99.80
EL 80020-015	34.94		0.01		23.78		0.51		2.34		38.24		99.82
EL 80020-016	35.07		0.01		23.96		0.48		2.35		38.61		100.47
	34.84	*0.20*	**0.01**	*0.00*	**23.65**	*0.34*	**0.49**	*0.02*	**2.36**	*0.02*	**38.73**	*0.58*	**100.08**
EL 83400-01	34.59		0.01		22.42		0.50		2.35		40.36		100.23
EL 83400-02	34.56		0.01		22.66		0.53		2.31		40.03		100.10
EL 83400-03	34.61		0.01		22.74		0.49		2.25		39.96		100.06
EL 83400-012	34.60		0.00		22.84		0.55		2.33		40.36		100.68
EL 83400-013	34.63		0.01		22.69		0.48		2.36		40.11		100.29
	34.60	*0.03*	**0.01**	*0.00*	**22.67**	*0.16*	**0.51**	*0.03*	**2.32**	*0.04*	**40.16**	*0.19*	**100.27**
EL 83448-01	35.44		0.02		26.73		0.43		1.81		35.66		100.10
EL 83448-02	35.72		0.01		27.06		0.41		1.82		35.56		100.58
EL 83448-03	35.64		0.02		26.85		0.40		1.76		35.20		99.88
EL 83448-010	35.63		0.00		26.72		0.46		1.82		35.78		100.42
	35.61	*0.12*	**0.01**	*0.01*	**26.84**	*0.16*	**0.43**	*0.03*	**1.80**	*0.03*	**35.55**	*0.25*	**100.24**
EL DVDP105.53-01	40.80		0.06		48.45		0.14		0.12		9.95		99.52
EL DVDP105.53-02	40.80		0.04		48.59		0.12		0.11		9.91		99.57
EL DVDP105.53-03	40.45		0.04		47.25		0.14		0.12		11.79		99.78
EL DVDP105.53-04	40.65		0.04		48.77		0.11		0.11		9.98		99.66
	40.67	*0.17*	**0.05**	*0.01*	**48.27**	*0.69*	**0.12**	*0.01*	**0.11**	*0.01*	**10.41**	*0.92*	**99.63**

Appendix 20. Electron Microprobe analysis of Erebus Lineage Feldspars.

	SiO2		Al2O3		CaO		FeO		SrO		BaO		Na2O		K2O		Total
LBO-97018-013	62.85		22.65		3.01		0.18		0.30		0.28		7.52		3.38		100.18
LBO-97018-014	62.65		22.92		3.33		0.19		0.33		0.35		7.53		3.05		100.35
LBO-97018-015	62.90		22.64		3.07		0.24		0.28		0.26		7.68		3.26		100.32
LBO-97018-016	63.32		22.55		2.87		0.20		0.29		0.27		7.68		3.61		100.78
	62.93	*0.28*	**22.69**	*0.16*	**3.07**	*0.19*	**0.20**	*0.03*	**0.30**	*0.02*	**0.29**	*0.04*	**7.60**	*0.09*	**3.32**	*0.23*	**100.41**
LBO-EB0603-08	62.54		23.05		3.43		0.21		0.37		0.29		7.60		3.00		100.48
LBO-EB0603-09	61.76		23.66		3.84		0.21		0.30		0.19		7.48		2.63		100.08
LBO-EB0603-010	62.69		22.59		3.11		0.23		0.27		0.23		7.58		3.28		99.98
LBO-EB0603-011	62.34		22.93		3.25		0.21		0.29		0.32		7.45		3.13		99.92
	62.33	*0.41*	**23.06**	*0.44*	**3.41**	*0.32*	**0.21**	*0.01*	**0.31**	*0.04*	**0.26**	*0.06*	**7.53**	*0.07*	**3.01**	*0.28*	**100.11**
LBO-83415-01	56.07		27.81		8.52		0.26		0.41		0.12		5.80		1.00		99.99
LBO-83415-02	55.04		28.71		9.56		0.23		0.35		0.03		5.42		0.75		100.09
LBO-83415-03	54.93		28.70		9.69		0.23		0.36		0.11		5.36		0.78		100.16
LBO-83415-04	56.63		27.42		8.43		0.26		0.38		0.06		6.08		1.04		100.29
LBO-83415-05	56.84		27.29		8.04		0.28		0.43		0.11		6.03		1.03		100.04
LBO-83415-06	56.12		27.56		8.38		0.26		0.40		0.15		5.84		0.97		99.67
EL 83415-06	54.35		27.81		9.80		0.23		0.37		0.09		5.15		0.70		98.49
EL 83415-07	54.57		27.63		9.91		0.27		0.37		0.13		5.11		0.74		98.72
EL 83415-08	55.54		27.01		9.14		0.29		0.42		0.13		5.63		0.88		99.04
EL 83415-09	54.99		27.42		9.51		0.28		0.35		0.09		5.29		0.76		98.69
EL 83415-010	55.53		26.54		8.80		0.26		0.32		0.10		5.61		0.89		98.05
	55.51	*0.82*	**27.63**	*0.64*	**9.07**	*0.66*	**0.26**	*0.02*	**0.38**	*0.03*	**0.10**	*0.03*	**5.57**	*0.34*	**0.87**	*0.13*	**99.38**
EL 83410-06	56.71		26.71		8.02		0.30		0.40		0.10		6.24		1.06		99.54
EL 83410-07	57.49		26.24		7.53		0.26		0.35		0.04		6.33		1.09		99.32
EL 83410-08	57.12		26.42		7.71		0.26		0.35		0.08		6.16		0.98		99.07
EL 83410-10	56.07		27.39		8.56		0.24		0.40		0.03		5.85		0.81		99.34
	56.85	*0.61*	**26.69**	*0.50*	**7.95**	*0.45*	**0.26**	*0.03*	**0.37**	*0.03*	**0.06**	*0.03*	**6.14**	*0.21*	**0.99**	*0.12*	**99.32**
EL AW82044-02	55.67		27.60		9.23		0.26		0.32		0.15		5.60		0.83		99.66
EL AW82044-05	54.49		28.47		9.90		0.33		0.29		0.05		5.12		0.69		99.35
EL AW82044-07	53.24		29.03		10.55		0.32		0.38		0.04		4.68		0.61		98.84
EL AW82044-08	54.60		28.28		9.89		0.29		0.37		0.07		4.78		0.74		99.02
EL AW82044-09	54.95		27.98		9.66		0.27		0.37		0.01		5.17		0.76		99.16
EL AW82044-010	54.87		27.94		9.39		0.26		0.33		0.13		5.23		0.81		98.96
EL AW82044-011	55.23		27.98		9.53		0.25		0.37		0.06		5.47		0.80		99.68
EL AW82044-012	53.83		28.70		10.34		0.30		0.34		0.11		4.88		0.64		99.15
	54.61	*0.77*	**28.25**	*0.47*	**9.81**	*0.46*	**0.29**	*0.03*	**0.35**	*0.03*	**0.08**	*0.05*	**5.12**	*0.32*	**0.73**	*0.08*	**99.23**
EL AW82038-02	54.07		28.69		10.19		0.32		0.42		0.06		4.90		0.63		99.27
EL AW82038-03	53.47		29.01		10.50		0.29		0.37		0.07		4.69		0.59		98.99
EL AW82038-04	52.11		29.11		11.08		0.29		0.36		0.05		4.15		0.54		97.68
EL AW82038-05	53.60		29.00		10.67		0.34		0.40		0.07		4.90		0.59		99.57
EL AW82038-010	54.20		28.58		10.28		0.30		0.35		0.11		5.07		0.63		99.51
EL AW82038-015	53.22		29.54		11.10		0.29		0.41		0.07		4.51		0.54		99.68
	53.44	*0.75*	**28.99**	*0.34*	**10.64**	*0.39*	**0.31**	*0.02*	**0.38**	*0.03*	**0.07**	*0.02*	**4.70**	*0.33*	**0.58**	*0.04*	**99.12**

Appendix 20-cont. Electron Microprobe analysis of Erebus Lineage Feldspars.

	SiO2		Al2O3		CaO		FeO		SrO		BaO		Na2O		K2O		Total
EL 83409-02	54.43		27.68		9.92		0.37		0.38		0.10		5.25		0.65		98.78
EL 83409-03	55.69		27.23		9.04		0.19		0.42		0.07		5.71		0.77		99.12
EL 83409-04	55.65		27.00		8.92		0.34		0.36		0.17		5.67		0.77		98.87
EL 83409-05	55.74		26.94		9.01		0.41		0.38		0.09		5.68		0.74		98.97
EL 83409-06	54.17		27.73		9.98		0.39		0.40		0.08		5.13		0.64		98.52
EL 83409-014	53.25		28.51		10.83		0.30		0.41		0.08		4.89		0.55		98.82
	54.82	*1.04*	**27.51**	*0.59*	**9.62**	*0.76*	**0.33**	*0.08*	**0.39**	*0.02*	**0.10**	*0.03*	**5.39**	*0.34*	**0.69**	*0.09*	**98.85**
EL 83417-09	56.86		25.97		7.85		0.31		0.38		0.17		6.20		1.10		98.84
EL 83417-010	56.83		26.00		7.74		0.24		0.41		0.12		6.15		1.10		98.57
EL 83417-011	56.60		26.08		8.07		0.23		0.37		0.10		6.07		0.97		98.48
EL 83417-012	56.62		26.17		8.01		0.23		0.42		0.10		6.10		0.97		98.60
EL 83417-013	56.36		26.10		8.18		0.23		0.42		0.11		6.01		1.07		98.46
	56.65	*0.20*	**26.06**	*0.08*	**7.97**	*0.18*	**0.25**	*0.03*	**0.40**	*0.02*	**0.12**	*0.03*	**6.11**	*0.08*	**1.04**	*0.07*	**98.59**
EL AW82015-08	59.14		24.45		5.93		0.26		0.35		0.28		6.98		1.45		98.86
EL AW82015-09	59.31		24.06		5.60		0.22		0.38		0.22		6.88		1.74		98.41
EL AW82015-010	59.72		24.11		5.61		0.23		0.33		0.18		7.04		1.67		98.89
EL AW82015-011	59.38		24.32		5.76		0.23		0.44		0.17		7.05		1.53		98.87
EL AW82015-012	59.49		24.26		5.83		0.30		0.41		0.21		6.83		1.57		98.91
	59.41	*0.22*	**24.24**	*0.16*	**5.75**	*0.15*	**0.25**	*0.04*	**0.38**	*0.04*	**0.21**	*0.04*	**6.96**	*0.10*	**1.59**	*0.12*	**98.79**
EL 83452-05	64.43		21.46		2.33		0.24		0.25		0.31		7.75		4.02		100.77
EL 83452-06	64.28		20.99		2.13		0.20		0.11		0.19		7.63		4.03		99.55
EL 83452-07	64.31		20.87		2.10		0.19		0.12		0.20		7.54		4.25		99.58
EL 83452-08	63.84		21.25		2.32		0.24		0.16		0.22		7.53		4.02		99.58
EL 83452-09	63.38		21.53		2.71		0.19		0.16		0.35		7.69		3.53		99.53
	64.05	*0.44*	**21.22**	*0.29*	**2.32**	*0.24*	**0.21**	*0.03*	**0.16**	*0.05*	**0.25**	*0.07*	**7.63**	*0.09*	**3.97**	*0.26*	**99.80**
EL 83446-010	62.50		22.13		3.25		0.20		0.26		0.30		7.35		3.30		99.29
EL 83446-011	62.51		21.95		3.33		0.20		0.28		0.28		7.38		3.22		99.14
EL 83446-012	62.14		22.28		3.43		0.23		0.26		0.21		7.47		3.02		99.05
EL 83446-013	62.23		21.88		3.34		0.20		0.27		0.32		7.36		3.23		98.84
EL 83446-014	62.24		22.23		3.62		0.21		0.28		0.32		7.25		2.99		99.14
	62.32	*0.17*	**22.09**	*0.17*	**3.40**	*0.14*	**0.21**	*0.01*	**0.27**	*0.01*	**0.29**	*0.04*	**7.36**	*0.08*	**3.15**	*0.14*	**99.09**
EL 82403-09	62.57		22.13		3.29		0.18		0.29		0.22		8.03		2.21		98.92
EL 82403-010	63.14		22.13		3.12		0.11		0.31		0.33		8.18		2.10		99.43
EL 82403-011	62.93		22.35		3.26		0.13		0.31		0.21		8.11		2.31		99.61
EL 82403-012	62.33		22.55		3.66		0.15		0.34		0.18		8.18		1.84		99.22
	62.74	*0.36*	**22.29**	*0.20*	**3.33**	*0.23*	**0.14**	*0.03*	**0.31**	*0.02*	**0.24**	*0.06*	**8.13**	*0.07*	**2.12**	*0.20*	**99.29**
EL 82405-08	65.22		19.41		0.66		0.20		0.00		0.21		6.74		6.60		99.03
EL 82405-09	65.67		19.37		0.76		0.21		0.06		0.26		7.11		5.99		99.41
EL 82405-010	65.59		19.38		0.58		0.18		0.00		0.22		6.88		6.55		99.38
EL 82405-011	65.79		19.38		0.63		0.18		0.00		0.20		6.97		6.09		99.22
EL 82405-012	65.58		19.22		0.45		0.18		0.00		0.29		6.73		6.87		99.32
	65.57	*0.21*	**19.35**	*0.07*	**0.61**	*0.11*	**0.19**	*0.01*	**0.01**	*0.02*	**0.23**	*0.04*	**6.88**	*0.16*	**6.42**	*0.37*	**99.27**

Appendix 20-cont. Electron Microprobe analysis of Erebus Lineage Feldspars.

	SiO2		Al2O3		CaO		FeO		SrO		BaO		Na2O		K2O		Total
EL 83407-09	64.58		20.09		1.21		0.13		0.04		0.49		6.96		5.68		99.18
EL 83407-010	65.51		19.89		0.96		0.15		0.01		0.05		7.62		5.33		99.52
EL 83407-011	63.87		21.13		2.37		0.12		0.08		0.27		7.77		3.49		99.09
EL 83407-012	63.78		20.82		2.16		0.18		0.08		0.39		7.83		3.74		98.97
EL 83407-013	64.14		19.58		0.73		0.14		0.05		0.74		5.79		7.73		98.89
EL 83407-014	64.31		20.78		1.92		0.18		0.04		0.36		7.98		3.99		99.56
	64.36	*0.63*	**20.38**	*0.61*	**1.56**	*0.68*	**0.15**	*0.03*	**0.05**	*0.03*	**0.38**	*0.23*	**7.32**	*0.83*	**4.99**	*1.60*	**99.20**
EL AW82023-011	58.03		23.30		0.42		1.15		0.04		0.00		13.16		4.25		100.35
EL 80020-010	62.71		22.14		3.31		0.20		0.28		0.31		7.44		2.99		99.38
EL 80020-011	62.80		21.80		3.13		0.20		0.22		0.26		7.53		3.42		99.35
EL 80020-012	63.38		21.72		2.82		0.20		0.24		0.26		7.59		3.45		99.68
EL 80020-013	63.32		21.54		2.80		0.22		0.19		0.26		7.64		3.52		99.50
EL 80020-014	63.16		21.79		2.96		0.21		0.23		0.18		7.62		3.44		99.58
	63.07	*0.30*	**21.80**	*0.22*	**3.01**	*0.21*	**0.21**	*0.01*	**0.23**	*0.03*	**0.25**	*0.05*	**7.56**	*0.08*	**3.37**	*0.21*	**99.50**
EL 83400-06	63.50		21.64		2.61		0.22		0.20		0.20		7.58		3.76		99.71
EL 83400-07	62.10		22.58		3.88		0.17		0.21		0.20		7.57		2.65		99.34
EL 83400-08	62.95		21.55		2.77		0.19		0.24		0.31		7.36		3.83		99.20
EL 83400-09	62.33		22.48		3.64		0.20		0.27		0.27		7.61		2.61		99.40
EL 83400-010	62.68		21.72		3.20		0.22		0.25		0.38		7.64		3.06		99.14
	62.71	*0.55*	**21.99**	*0.49*	**3.22**	*0.54*	**0.20**	*0.02*	**0.23**	*0.03*	**0.27**	*0.07*	**7.55**	*0.11*	**3.18**	*0.59*	**99.36**
EL 83448-05	61.78		22.63		3.93		0.26		0.31		0.33		7.31		2.72		99.26
EL 83448-06	61.34		23.07		4.47		0.20		0.28		0.18		7.40		2.33		99.26
EL 83448-07	61.94		22.49		3.72		0.23		0.26		0.21		7.42		2.90		99.16
EL 83448-08	62.66		21.88		3.25		0.21		0.21		0.15		7.46		3.23		99.05
EL 83448-09	61.38		23.11		4.55		0.20		0.29		0.20		7.29		2.32		99.34
	61.82	*0.53*	**22.64**	*0.50*	**3.98**	*0.54*	**0.22**	*0.03*	**0.27**	*0.04*	**0.21**	*0.07*	**7.38**	*0.07*	**2.70**	*0.39*	**99.21**
EL 82431-02	57.87		25.41		7.28		0.47		0.26		0.11		6.61		0.94		98.96
EL 82431-03	58.92		25.07		6.57		0.29		0.32		0.28		8.52		1.16		101.12
EL 82431-04	58.45		25.29		7.06		0.33		0.26		0.06		6.75		1.00		99.20
EL 82431-05	58.52		25.54		7.08		0.28		0.31		0.10		8.45		1.09		101.38
	58.44	*0.43*	**25.33**	*0.20*	**7.00**	*0.30*	**0.34**	*0.09*	**0.29**	*0.03*	**0.14**	*0.10*	**7.58**	*1.05*	**1.05**	*0.09*	**100.16**

Appendix 21. Example calculation of modeled melt isotopic composition for Erebus Lineage at increasing stages of differentiation by fractional crystallization. Stages F=of fractionation are derived from Kyle et al. (1992). Final step of isotopic fractionation of convecting anorthoclase phonolite lava lake illustrated here to investigate additional isotopic depletion resulting from equilibrium fraction of anorthoclase megacrysts, magnetite and Raleigh distillation of CO_2 gas. Min-melt fractionation factors from Zhao and Zheng (2003).

Calculations based on initial composition of basanite endmember melt of 6.02 ‰.

	"F" Fraction of Melt		Temp °C	Basalt (Zheng)	Tephrite (Zheng)	Andesite (Zheng)	Trachy-And (Zheng)	frac min × Δ(melt-min)	δ18O Composition Melt (‰)
Wt. fraction Ne hawaiite	**0.45**	**0.45**	1200		Δ(melt-min)				**6.02**
Olivine (Fo88B)		0.12		-0.784	-0.784			-0.091	6.11
Clinopyrox (Diop)		0.35		-0.309		-0.567	-0.599	-0.107	6.22
Cr spinel (Usp.B)		0.04		-1.684				-0.060	6.28
Ti magneti (Usp52B)		0.01		-1.984				-0.025	6.30
Ilmenite		0.02		-1.980				-0.047	6.35
Apatite		0.01		0.147	0.147	-0.106	-0.143	0.001	6.35
*CO2 **		*0.02*		*2.77*					**6.29**
Wt. fraction Ne benmoreite	**0.35**	**0.78**	1150						*0.35*
Olivine (Fo66Nh)		0.01		-0.840				-0.010	6.36
Clinopyrox (En40B)		0.06		-0.331		-0.607	-0.642	-0.021	6.38
Ti magneti (Usp73)		0.04		-2.140				-0.085	6.46
Feldspar (An 64)		0.09		0.213	0.213	-0.061	-0.098	0.019	6.44
Apatite		0.01		0.158	0.158	-0.114	-0.153	0.002	6.44
CO2		*0.02*		*3.1*					**6.38**
Wt. fraction An. phonolite	**0.23**	**0.66**	1100						*0.23*
Olivine (Fo58Ap)		0.00		-0.902					6.45
Clinopyrox (En39Ap)		0.07		-0.355		-0.652	-0.690		6.49
Ti magneti (Usp61Nh)		0.06		-2.302					6.49
Feldspar (An 44)		0.13		0.338	0.338	0.043	0.004		6.49
Nepheline (Ne2)		0.07			0.017				6.49
Apatite		0.02		0.170	0.170	-0.122	-0.164		6.49
CO2		0.02		3.74					**6.42**
Wt. fraction (modern An Phon)	**0.21**	0.90	1000						
feldspar (An 22)		0.04		0.533	0.533	0.189	0.144	0.008	6.41
CO2		0.01					4.100	0.025	6.38
Magnetite		0.05					2.400	0.120	**6.26**

Appendix 22.

Calculation of molar oxygen water-rock ratio required to form altered volcanic units (values represented by isotopically depleted xenolithic phonolite) using the equation:

$$X_W/X_{Rc} = (\delta^{18}O rock_f - \delta^{18}O rock_i)/(\delta^{18}O water_i - \delta^{18}O water_f)$$

*For closer-system box model from Criss and Taylor (1986), representing the minimum water:rock required for rf composition.

Where:

$\delta^f rock = 0.2$ ‰	*(Erebus xenolith)*
$\delta^i rock = 6.02$ ‰	*(WR basanite composition)*
$\delta^i water = -35$ ‰	*(Ross icesheet meteoric water composition Grootes & Suiver, 1986; Dansgaard et al, 1977)*
$\delta^i water = -25$ ‰	*(value of estimated enriched geothermal water in closed system)*
X_w	*number of oxygen atoms in water*
X_r	*number of oxygen atoms in rock*

Xw/Xr	W:R wt/wt	R:W wt/wt
0.58	0.28	3.52

Using:

Calculation of molecular weight of basanite using CIPW normalized composition and calculated number of oxygen moles per mole of basanite for rock/water mass ratio.

Mineral	wt%	Formula	Molecular Weight	Moles of mineral	mol% mineral	moles of Oxygen /mole mineral	moles of Oxygen /mol tephrite	Wt (g) mineral/ mol tephrite
orthoclase	10.2	KAlSi3O8	278.1	28.3	0.0905	8	0.72	25.2
albite	5.9	$NaAlSi_3O_8$	262.0	15.4	0.0491	8	0.39	12.9
anorthoclas	16.1	CaAl2Si2O8	278.1	44.8	0.1433	8	1.15	39.8
nephaline	18.1	Na3KAl4Si4O16	584.4	105.6	0.3376	16	5.40	197.3
diopside	24.0	MgCaSi2O6	216.6	51.9	0.1660	6	1.00	36.0
olivine	15.8	(Mg,Fe)2SiO4	172.3	27.2	0.0869	4	0.35	15.0
ilmentite	7.2	FeTiO3	151.7	10.9	0.0348	3	0.10	5.3
apatite	2.9	$Ca_{10}(PO_4)_6(OH)_2$	1004.8	28.7	0.0919	26	2.39	92.3
TOTAL				**312.8**	**1**	**79**	**11.50**	**423.7**

Appendix 23. Fractionation Model 1: Calculation of isotopic composition of Erebus lineage with the incorporation of depleted, altered volcanic edifice. Crustal contamination calculated in wt% added to new melt fraction prior to crystallization of new mineral species.

	"F" Fraction of Melt		Temp	ΔBasalt-Min	ΔTephrite-Min	ΔAndesite-Min	ΔTrachy-And-Min	frac min * Δ(melt-min)	δ18O composition melt (‰)
Wt. fraction basanite	**0.45**	**0.45**	**1200**						**6.02**
Altered Units		0.07		0.170					5.60
Olivine (Fo88B)		0.12		-0.784				-0.091	5.69
Clinopyrox (diop)		0.35		-0.309				-0.107	5.80
Cr spinel (Usp.B)		0.04		-1.684				-0.060	5.86
Ti magneti (Usp52B)		0.01		-1.984				-0.025	5.88
Ilmenite		0.02		-1.687				-0.040	5.92
Apatite		0.01		0.147				0.001	**5.92**
Wt. fraction phonote	**0.35**	**0.78**	**1150**						
Altered Units		0.06			0.170				5.57
Olivine (Fo66Nh) O0117		0.01			-0.840				5.58
Clinopyrox (En40B) 00624		0.06			*-0.469*				5.61
Ti magneti (Usp73)		0.04			-1.649				5.68
Feldspar 64		0.09			0.213				5.66
Apatite		0.01			0.158				**5.66**
Wt. fraction phonoli	**0.23**	**0.66**	**1050**						
Altered Units		0.11				0.170			5.05
Olivine (Fo58Ap)		0.00				0.257			5.05
Clinopyrox (En39Ap)		0.07				-0.703			5.10
Ti magneti (Usp61Nh)		0.06				-2.222			5.23
Feldspar 44		0.13				0.046			5.22
Nepheline (Ne2)		0.07			0.018				5.22
Apatite		0.02				-0.131			**5.22**
Wt. fraction modern	**0.21**	**0.90**	**1000**						**melt**
Altered Units		0.00				0.170			5.22
feldspar 22		0.30					0.144		5.39
CO2		0.06					4.100		5.14
Magnetite		0.15					-2.450		**5.51**

Appendix 23. cont. Fractionation Model 2: Calculation of isotopic composition of Erebus lineage with the incorporation of depleted, altered volcanic edifice. Crustal contamination calculated in wt% added to new melt fraction prior to crystallization of new mineral species.

	"F" Fraction of Melt		Temp	ΔBasalt-Min	ΔTephrite-Min	ΔAndesite-Min	ΔTrachy-And-Min	frac min * Δ(melt-min)	δ18O composition melt (‰)
Wt. fraction basanite	**0.45**	**0.45**	**1200**						**6.02**
Altered Units		0.07		0.170					5.60
Olivine (Fo88B)		0.12		-0.784				-0.091	5.69
Clinopyrox (diop)		0.35		-0.309				-0.107	5.80
Cr spinel (Usp.B)		0.04		-1.684				-0.060	5.86
Ti magneti (Usp52B)		0.01		-1.984				-0.025	5.88
Ilmenite		0.02		-1.687				-0.040	5.92
Apatite		0.01		0.147				0.001	**5.92**
Wt. fraction phonote	**0.35**	**0.78**	**1150**						
Altered Units		0.06			0.170				5.57
Olivine (Fo66Nh) O0117		0.01			-0.840				5.58
Clinopyrox (En40B) 00624		0.06			*-0.469*				5.61
Ti magneti (Usp73)		0.04			-1.649				5.68
Feldspar 64		0.09			0.213				5.66
Apatite		0.01			0.158				**5.66**
Wt. fraction phonoli	**0.23**	**0.66**	**1050**						
Altered Units		0.25				0.170			4.29
Olivine (Fo58Ap)		0.00				0.257			4.28
Clinopyrox (En39Ap)		0.07				-0.703			4.34
Ti magneti (Usp61Nh)		0.06				-2.222			4.46
Feldspar 44		0.13				0.046			4.45
Nepheline (Ne2)		0.07			0.018				4.45
Apatite		0.02				-0.131			**4.45**
Wt. fraction modern	**0.21**	**0.90**	**1000**						**melt**
Altered Units		0.00				0.170			4.45
feldspar 22		0.30					0.144		4.62
CO2		0.06					4.100		4.37
Magnetite		0.20					-2.450		**4.86**